

Polymers for Biomedical Applications

August 5, 2012 | <http://pubs.acs.org>
Publication Date: March 28, 2008 | doi: 10.1021/bk-2008-0977.fw001

ACS SYMPOSIUM SERIES **977**

Polymers for Biomedical Applications

Anil Mahapatro, Editor
Norfolk State University

Ankur S. Kulshrestha, Editor
BD Medical, BD

**Sponsored by the
Division of Polymeric Materials: Science
and Engineering, Inc.**



American Chemical Society, Washington, DC

In *Polymers for Biomedical Applications*; Mahapatro, A., et al.;
ACS Symposium Series; American Chemical Society: Washington, DC, 2008.



Library of Congress Cataloging-in-Publication Data

Polymers for biomedical applications / [edited by] Anil Mahapatro, Ankur S. Kulshrestha.

p. cm.—(ACS symposium series ; 977)

Based on papers from the 223rd National Meeting of the American Chemical Society. San Francisco, 2006.

Includes bibliographical references and index.

ISBN 978-0-8412-3966-1 (alk. paper)

I. Polymers in Medicine—Congresses.

I. Mahapatro, Anil. II. Kulshrestha, Ankur S. III. American Chemical Society. Meeting (232nd : 2006 : San Francisco, Calif.)

R857.P6P6222 2007
610.28'4—dc22

2007060792

The paper used in this publication meets the minimum requirements of American National Standard for Information Sciences—Permanence of Paper for Printed Library Materials, ANSI Z39.48-1984.

Copyright © 2008 American Chemical Society

Distributed by Oxford University Press

All Rights Reserved. Reprographic copying beyond that permitted by Sections 107 or 108 of the U.S. Copyright Act is allowed for internal use only, provided that a per-chapter fee of \$36.50 plus \$0.75 per page is paid to the Copyright Clearance Center, Inc., 222 Rosewood Drive, Danvers, MA 01923, USA. Republication or reproduction for sale of pages in this book is permitted only under license from ACS. Direct these and other permission requests to ACS Copyright Office, Publications Division, 1155 16th Street, N.W., Washington, DC 20036.

The citation of trade names and/or names of manufacturers in this publication is not to be construed as an endorsement or as approval by ACS of the commercial products or services referenced herein; nor should the mere reference herein to any drawing, specification, chemical process, or other data be regarded as a license or as a conveyance of any right or permission to the holder, reader, or any other person or corporation, to manufacture, reproduce, use, or sell any patented invention or copyrighted work that may in any way be related thereto. Registered names, trademarks, etc., used in this publication, even without specific indication thereof, are not to be considered unprotected by law.

PRINTED IN THE UNITED STATES OF AMERICA

Foreword

The ACS Symposium Series was first published in 1974 to provide a mechanism for publishing symposia quickly in book form. The purpose of the series is to publish timely, comprehensive books developed from ACS sponsored symposia based on current scientific research. Occasionally, books are developed from symposia sponsored by other organizations when the topic is of keen interest to the chemistry audience.

Before agreeing to publish a book, the proposed table of contents is reviewed for appropriate and comprehensive coverage and for interest to the audience. Some papers may be excluded to better focus the book; others may be added to provide comprehensiveness. When appropriate, overview or introductory chapters are added. Drafts of chapters are peer-reviewed prior to final acceptance or rejection, and manuscripts are prepared in camera-ready format.

As a rule, only original research papers and original review papers are included in the volumes. Verbatim reproductions of previously published papers are not accepted.

ACS Books Department

Preface

The field of biomaterials has seen an exponential growth during the past few years. This growth has been catalyzed by the need to propel the progress of emerging strategies such as tissue engineering and the delivery of bioactive agents for treating, repairing, and restoring function of tissues. The emergence of these new biomaterial-based technologies has resulted from the convergence of principles from various disciplines such as materials science, bio-engineering, molecular biology, biochemistry, and nanotechnology.

Polymers represent the most versatile class of biomaterials, being extensively applied in biomedical applications including surgical devices, implants and supporting materials, drug delivery systems and drug device combination, surface modification, biosensors, components of diagnostic assays, tissue adhesives, ocular devices, and orthopaedic and tissue engineering applications. This versatility results from the fact that polymers can be prepared in different compositions with a wide variety of structures and appropriate physicochemical, interfacial, and biomimetic properties to meet specific end applications. Motivations to improve health and lower long-term treatment costs to consumers and insurers has fueled continuous innovation toward developing novel polymeric compositions that can be used to manufacture medical devices with markedly lower risk of failure and adverse immune reactions.

The purpose of this book is to publish, in one volume, the latest findings of the leading researchers in the field of polymers for biomedical applications. A total of 22 chapters are included in this book. Chapter 1 (by Kulshrestha and Mahapatro) provides an overview of this field, covering the new developments. The remaining chapters have been grouped into five broad categories:

- synthesis of polymeric biomaterials
- characterization of polymeric biomaterials

- polymers for drug delivery applications
- polymeric surfaces
- other examples of use of polymers for biomedical applications

This book is based on a successful international symposium *Polymers for Biomedical Applications* held at the 232nd National Meeting of the American Chemical Society (ACS) in San Francisco from September 10–14, 2006. The purpose of the symposium was to create a forum to foster dialogue and the exchange of information among researchers, educators, and developers of medical devices who are seeking to create new knowledge and technology by using polymeric biomaterials for various biomedical applications. Leaders in this field gathered to present their interesting findings. Participants represented many countries and included scientists from academics, industry, and government laboratories. Hopefully this book serves to transmit the latest information to the readers and also captures some of the excitement of the symposium in the process.

We thank the authors for their contributions and wish them success in their ongoing pursuit for novel biomaterials and advanced technologies that contribute to improvement in healthcare and quality of life. Thanks are also due to the ACS Division of Polymeric Materials: Science and Engineering, Inc. for sponsoring the symposium and to the ACS books department for being patient through the compilation of this symposium series book.

Ankur S. Kulshrestha

BD Medical–Medical Surgical Systems, MC 212
BD, 1 Becton Drive
Franklin Lakes, NJ 07417

Anil Mahapatro

Center for Biotechnology and Biomedical Sciences
Department of Chemistry
Norfolk State University
700 Park Avenue
Norfolk, VA 23504

Chapter 1

Polymers for Biomedical Applications

Ankur S. Kulshrestha¹ and Anil Mahapatro²

¹BD Medical–Medical Surgical Systems, BD, 1 Becton Drive, MC 212,
Franklin Lakes, NJ 07417

²Center for Biotechnology and Biomedical Sciences, Department
of Chemistry, Norfolk State University, Norfolk, VA 23504

Polymers represent the largest and versatile class of biomaterials being extensively applied in multitude of biomedical applications. This versatility is attributed to the relative ease with which polymers can be designed and prepared with a wide variety of structures and appropriate physical, chemical, surface and biomimetic properties. As described in this book a new arsenal of synthetic and applied methodologies are under study that provides an enhanced range of tools to greatly expand the biomedical applications of polymeric materials.

Technological advancements over the last two decades particularly in the field of biomaterials have revolutionized the biomaterials-based health care industry. These technological developments have enhanced the survival and quality of life and have resulted in production of more efficient and sophisticated medical devices available in the market today. These advancements have been driven by several factors including significant changes in the life style pattern, increasing medical needs of the growing and aging world population, social pressures to reduce health care costs and increasing awareness among the public regarding the efficiency and improved performance of using biomaterials in medical devices (1).

The field of biomaterials represents the platform technology necessary to propel the progress of emerging strategies such as tissue engineering,

nanotechnology, and the delivery of bioactive agents for treating, repairing, and restoring function of tissues. Biomaterials can be broadly classified into: metals, ceramics, natural or synthetic polymers and composites (1).

Polymers represent the largest and most promising class of biomaterials. This is attested by their widespread use in various medical applications. A large number of polymeric biomaterials have been developed and new developments continue to appear in both open and patent literatures. Several excellent books and reviews are also available (1). The key to the success of polymer-based biomaterials is the relative ease coupled with low cost with which they can be synthesized with wide range of properties and functionality. This has resulted in research on various aspects of polymeric biomaterials and advanced technologies based on them being conducted in environment that foster the seamless convergence of concepts, ideas and research tools at the interface between disciplines of polymer chemistry, materials science, biomedical engineering, surface science, biophysics and biology. This symbiotic relationship has driven the maturation of polymeric biomaterial based technologies from scientific breakthroughs to the commercial applications at a very rapid pace over the past few years.

This chapter provides a brief overview of some of the recent developments in the field of polymeric biomaterials with a particular emphasis on the articles included in this book (2-22). The research being done in this field is diverse and takes on several directions due to its multi disciplinary nature. It helps to organize these developments broadly into three sections: (a) Synthetic approaches to polymer based biomaterials (b) characterization related development and (c) polymeric surfaces and (d) other biomedical applications of polymers.

New Synthetic Approaches and Polymer based Biomaterials

The wide range and scope of the reactions involved in polymer science makes it highly desirable to discover and devise new synthetic strategies and to generate new polymeric biomaterials from these strategies. Furthermore, recent developments in the field of tissue engineering and drug delivery have renewed the quest for more efficient and biocompatible and biodegradable polymers. Many chapters in this book give excellent examples of new synthetic strategies or polymers.

With regards to new polymeric biomaterial, Gomurashvilli and co-workers (2) have developed new biodegradable and tissue-resorbable co-poly(ester amides) (PEAs) using a versatile Active PolyCondensation (APC) method which involves di-*p*-toluenesulfonic acid salts of bis-(*L*- α -amino acid)- α,ω -alkylene diesters and active diesters of dicarboxylic acids as monomers. A wide range of

mechanical properties and biodegradation rates were achieved by varying the three components in the backbone: α -amino acids, diols and dicarboxylic acids. These poly(esteramides) may find potential applications in drug delivery and tissue engineering. Novel chitosan-PEG superabsorbent gel prepared at room temperature by Chirachanchai et al. (3) may be useful as injectable carrier for bioactive agents. Polymeric Metal complexes developed by Fraser et al. (7) may find applications in biological systems as catalysts, stimuli responsive centers and structural materials.

As far as development of new synthetic approaches are concerned, Cooper et al. (5) have developed a synthetic technique for preparing radiation sterilizable aromatic poly(anhydride)s with high molecular weights, high tensile properties and melt processability. Nicholas and coworkers (6) have devised a new strategy for the synthesis of fluorescent bioconjugates by living radical polymerization using protein-derived macroinitiators. These fluorescent bioconjugates are expected to have improved traceability in biological environments, during biomedical assays. Click cycloaddition reactions have been explored by Grayson et al. (4) to prepare macrocyclic poly (hydroxylstyrene). The presence of phenolic hydroxyl group on each repeat unit in the cyclic polymer provides site for further modification and incorporation of bioactive moieties. The cyclization technique described is believed to have broad application for preparing a wide range of functionalized macrocycles.

Several papers in this book dealt with synthesis and characterization of polymeric biomaterials for drug delivery applications. Smith and coworkers (11) found Poly(N-vinylpyrrolidinone) hydrogels functionalized with drug molecules as a promising hydrogels for sustained release of drugs over several days. Kumar et al. in chapter (12) have developed a green route to pegylated amphiphilic polymers with the use of immobilized enzyme, *Candida antarctica* lipase B. The ability of these polymers to form the nano-micelles make them attractive candidates for application not only in drug delivery but also in cancer diagnostics. In chapter (13) Gong et al. developed a new highly innovative two photon activated photodynamic therapy (PDT) triad agent, which incorporates (1) a photosensitizer: a porphyrin that has been substituted on the meso positions by chromophores with large two-photon absorption and activated in the Near Infra red Region (NIR) in the tissue transparency window and efficiently producing singlet oxygen as the cytotoxic agent; (2) a small molecule targeting agent that can target over-expressed receptor sites on the tumor, and (3) a NIR imaging agent that can accurately image the tumor for treatment. Adronov et al. (14) synthesized carborane functionalized dendronized polymers and found them to be useful as potential Boron Neutron Capture Therapy (BNCT) agents. Nederberg and coworkers (15) have developed a series of telechelic biodegradable ionomers based on poly (trimethylene carbonate) carrying zwitterionic, anionic or cationic functional groups for protein drug delivery. The ability to absorb water and the open swollen structure of these telechelic

biodegradable ionomers was utilized for protein loading simply by letting the material swell in an aqueous protein solution. Furthermore, near quantitative release was achieved either directly after loading or following an additional drying step. Moreover, protein activity is maintained following release, suggesting that these ionomers may favourably interact with guest proteins such that denaturation is suppressed.

Characterization of Polymeric Biomaterial

An in-depth understanding of physical, chemical, biological and engineering properties is highly relevant to the performance and development of any polymer based medical devices. This requires development of advanced instrumentation and characterization techniques, coupled with mathematical models to understand structure-property and functional performance relationships of various polymeric systems thereby opening the way towards more efficient polymer based medical devices, therapies and other biomedical applications such as tissue engineering. In this symposium proceeding, chapter (8) by Henderson et al. introduces selected aspects of the NIST measurement toolkit for tissue engineering which consist of high-throughput, combinatorial methods to produce test specimens varying in materials properties and advanced instrumental techniques for collecting data like high-resolution, non-invasive multi-modal imaging of cells and 3D visualization. Hassan et al. (9) demonstrated the application of broadband dielectric spectroscopy as a powerful tool to study the degradation of biodegradable polymeric materials.

The increasing use of mass spectrometry (MS) in polymer characterization is attributed to the development of ionization techniques such as MALDI and ESI coupled with innovations in mass analyzers such as reflectron-TOF and FT-ICR. This has greatly augmented the capabilities of MS to better understand the detailed composition of polymeric materials. Furthermore, increased mass resolution and accuracy coupled to hyphenated techniques permits greater detail about even minor components in polymeric biomaterials to be assessed, especially with regard to composition of repeat and end groups. In this book Maziarz and coworkers (10) review the application of mass spectrometry in characterization of polymeric biomaterials.

Polymeric surfaces

It is of cardinal importance to have an in depth understanding of surface/interface characteristics of polymeric biomaterials along with a precise control on interaction between their surface and biological milieu. This is highly relevant for their successful and safe performance in various applications including

biosensing, diagnostics and medical devices. Hence a major thrust over the past few years has been towards development of versatile, convenient and cost-effective strategies for rendering surface resistant to fouling by proteins, cells and microorganisms. Glasgow et al. (16) reviews the biocompatibility of surfaces of various hydrophobic, hydrophilic and heterogenic polymeric biomaterials with reference to their interactions with proteins and blood platelets. Nandivada et al. (17) reviews the applications of reactive polymer surfaces created by chemical vapor deposition (CVD) polymerization as stable platforms for biomimetic modifications. Wingkono and co-workers (18) report on the investigation of phase-separated micro domains in a PEG-PCL polyurethane and their effect on osteoblast adhesion. Combinatorial libraries were employed to optimize microphase domain size and shape of polyethylene glycol (PEG) - poly(caprolactone) (PCL) polyurethanes following which the effect of these surface structures on osteoblast adhesion was investigated by culturing cells directly on the libraries.

Other Biomedical Applications

A few chapters in this book dealt with applications of polymers in tissue engineering and as biosensors. The field of tissue engineering represents an interdisciplinary field that applies the principles of engineering and the life sciences toward the development of biological substitutes that restore, maintain, or improve tissue functions (1b). He et al. (19) reviews the materials requirements for tissue engineering application, and focus on polymer materials including both natural and synthetic polymers. Furthermore, they also describe the frequently used and newly developed fabrication technologies for constructing tissue-engineering scaffolds along with surface modification/functionalization approaches to the tissue engineering scaffolds. Konno et al. (20) developed a novel covalently crosslinked hydrogel system from a phospholipid polymer bearing 2-methacryloyloxyethyl phosphorylcholine units and *p*-vinylphenylboronic acid (PMBV) with polyvinyl alcohol as cell container. The hydrogel formed not only in water but also in saline including cell culture medium. Furthermore, the viability of the cells in the entrapped in the hydrogel was not affected. Hence, it was concluded that the novel hydrogel system based on the phospholipid polymer might be applied as cell container to preserve and transport the cells in tissue engineering applications. Cooper et al. (21) present the evaluation of bioabsorbable, aliphatic polyester blends comprising a 50:50 mole: mole poly(50, 50 D, L-lactide) (D, L-PLA) and a 95:5 mole mole poly(ϵ -caprolactone-co-*p*-dioxanone) (PCL:PDO) for application as a cranial fixation device, CraniosorbTM. Duran and coworkers (22) fabricated poly (γ -benzyl-*L*-glutamate) (PBLG) polypeptide nanotubes for optical biosensor applications

using technique based on the synthesis of nanostructures within the pores of a nanoporous membrane.

In summary, an attempt has been made in this book to capture some of the recent developments made by researchers in the field of polymeric biomaterials and their applications. However, many recent developments by eminent researchers could not be incorporated. Nevertheless, we hope that this book will provide a useful insight to the readers on some of the new directions taken up by researchers in this dynamic field.

References

1. (a) *An Introduction to Biomaterials*; Guelcher, S.; Hollinger, J.; CRC Press, 2006. (b) *Biomaterials Science*; Ratner, B.D.; Hoffman, A.S.; Schoen, F.J.; Lemon, J.E. Eds; Academic Press, Orlando, 1996. (c) *Biomedical Polymers, Designed to Degrade Systems*, Shalaby, S.W. Hanser Gardner Publications, Inc., Cincinnati, 1994. (d) Angelova, N.; Hunkeler, D.; *Tibtech*, 1999, 17, 409. (e) *Biomaterials: Principles and Applications*; Park, J.B.; Bronzino, J.D.; CRC Press, 2002. (f) Frost and Sullivan database.
2. Gomurashvili, Z.; Zhang, H.; Da, J.; Jenkins, T.D.; Hughes, J.; Wu, M.; Lambert, L.; Grako, K.A.; DeFife, K.M.; MacPherson, K.; Vassilev, V.; Katsarava, R.; Turnell, W.G.; *ACS Symp. Ser.* (this volume), Chapter 2.
3. Chirachanchai, S.; Fangkangwanwong, J. *ACS Symp. Ser.* (this volume), Chapter 3.
4. Laurent, B.A.; Eugene, D.M.; Grayson, S.M. *ACS Symp. Ser.* (this volume), Chapter 4.
5. Cooper, K.; Scopelianos, A. *ACS Symp. Ser.* (this volume), Chapter 5.
6. Nicolas, J.; SanMiguel, V.; Mantovani, G.; Haddleton, D.M. *ACS Symp. Ser.* (this volume), Chapter 6.
7. Fraser, C. L.; Fiore, G.L. *ACS Symp. Ser.* (this volume), Chapter 7.
8. Henderson, L.A.; Kipper, M.J.; Chiang, M.Y.M. *ACS Symp. Ser.* (this volume), Chapter 8.
9. Hassan, M.K.; Wiggins, J.S.; Storey, R.S.; Mauritz, K.A. *ACS Symp. Ser.* (this volume), Chapter 9.
10. Maziarz, E.P.; Liu, X.M.; Wood, T.D. *ACS Symp. Ser.* (this volume), Chapter 10.
11. Smith, L.E.; Collins, S.; Liu, Z.; Neil, S.C.; Williams, R.; Rimmer, S. *ACS Symp. Ser.* (this volume), Chapter 11.
12. Kumar, R.; Pandey, M.K.; Tyagi, R.; Parmar, V.S.; Watterson, A.C.; Kumar, J. *ACS Symp. Ser.* (this volume), Chapter 12.
13. Gong, A.; Meng, F.; Starkey, J.R.; Moss, B.L.; Rebane, A.; Drobizhev, M.; Spangler, C.W. *ACS Symp. Ser.* (this volume), Chapter 13.

14. Benhabbour, S.R.; Adronov, A.; *ACS Symp. Ser.* (this volume), Chapter 14.
15. Nederberg, F.; Atthoff, B.; Bowden, T.; Welch, K.; Strömme, M.; Hilborn, J. *ACS Symp. Ser.* (this volume), Chapter 15.
16. Glasgow, K.; Dhara, D. *ACS Symp. Ser.* (this volume), Chapter 16.
17. Nandivada, H.; Chen, H-Y.; Elkasabi, Y.; Lahann, J. *ACS Symp. Ser.* (this volume), Chapter 17.
18. Wingkono, G.; Meredith, C. *ACS Symp. Ser.* (this volume), Chapter 18.
19. He, W.; Feng, Y.; Ramakrishna, S. *ACS Symp. Ser.* (this volume), Chapter 19.
20. Konno, T.; Ishihara, K. *ACS Symp. Ser.* (this volume), Chapter 20.
21. Cooper, K.; Li, Y.; Lowenhaupt, B.; Overaker, D.; Poandl, T.; Trenka-Benthin, S.; Yuan, J.; Zimmerman, M. *ACS Symp. Ser.* (this volume), Chapter 21.
22. Duran, H.; Lau, K.H.A.; Lübbert, A.; Jonas, U.; Steinhart, M.; Knoll, W. *ACS Symp. Ser.* (this volume), Chapter 22.

Chapter 2

From Drug-Eluting Stents to Biopharmaceuticals: Poly(ester amide) a Versatile New Bioabsorbable Biopolymer

Zaza Gomurashvili¹, Huashi Zhang¹, Jane Da¹, Turner D. Jenkins¹,
Jonathan Hughes¹, Mark Wu¹, Leanne Lambert¹,
Kathryn A. Grako¹, Kristin M. DeFife¹, Kassandra MacPherson¹,
Vassil Vassilev¹, Ramaz Katsarava², and William G. Turnell¹

¹MediVas LLC, 6275 Nancy Ridge Drive, San Diego, CA 92121

²Center for Medical Polymers and Biomaterials, Georgian Technical
University, 69, Kostava Strasse, 0175 Tbilisi, Georgia

New biodegradable and tissue-resorbable co-poly(ester amides) (PEAs) useful for biomedical applications were prepared using a versatile Active PolyCondensation (APC) method, which involves di-*p*-toluenesulfonic acid salts of bis-(L- α -amino acid)- α,ω -alkylene diesters and active diesters of dicarboxylic acids as monomers. APC reactions were carried out at mild temperatures (40-60°C) and allowed the synthesis of regular, linear, polyfunctional PEAs with high molecular weights. The physical properties of PEAs are critically dependent upon the structure of the polymer backbone. A wide range of mechanical properties and biodegradation rates can be achieved by varying the three components in the backbone: α -amino acids, diols and dicarboxylic acids. Indeed, there is a growing need for wider variations of biocompatible PEA compositions and methods for the delivery of different therapeutic molecules at controlled rates, while affording enhanced mechanical and physical properties. Therefore, various types of new non-toxic building blocks based upon bulky diols (isosorbide, 17 β -estradiol), unsaturated (fumaric) and aromatic diacids (hydroxycinnamic acid, 1,3-bis(4-carboxyphenoxy)-propane) were developed and successfully

incorporated into the main backbone of PEA. *In vitro* biodegradation tests with enzymes have shown that changes in the polymer backbone and functional groups resulted in a wide range of degradation rates that further exemplify the usefulness of these compositions in biomedical applications.

Introduction

α -Amino acids-based poly(ester-amide)s, (PEAs), belong to the class of AA-BB type heterochain polymers. This relatively new class of amino acid based PEAs have been extensively studied (1-4) because they combine favorable properties of both polyesters and polyamides, such as good thermal stability, tensile strength and modulus, increased hydrophilicity, biodegradation and biocompatibility. The amino acid rich compositions give these polymers natural protein-like qualities, resulting in a high capacity for hydrogen bonding between polymer chains, between polymer and loaded therapeutic, and/or between polymer and water. Entirely composed of nontoxic building blocks, such as essential α -amino acids, aliphatic dicarboxylic acids and aliphatic α,ω -diols, AA-BB type PEAs have proved to be promising biodegradable materials for various biomedical applications. PEAs have been successfully tested in animals and humans for cardiovascular applications (5) and *ex-vivo* cell based assays have strongly supported recent human trial data indicating that PEAs are blood and tissue compatible, with advantageous properties for implantation (6).

The PEAs reported in this work were prepared in a simple way by solution or interfacial polycondensation, where di-*p*-toluenesulfonic acid salts of bis-(α -amino acid)- α,ω -alkylene diesters react with chlorides of dicarboxylic acids (interfacial polycondensation) or their active diesters (Active Polycondensation, APC). The APC method involves the condensation of two partners: (I) bis-electrophilic, activated dicarboxylic acids, and (II) bis-nucleophilic, acid salts of bis-(α -amino acid)- α,ω -alkylene diesters in combination with di-*p*-toluenesulfonic acid salts of L-lysine benzyl ester. This reaction proceeds under mild conditions in common organic solvents and leads to polymer of high molecular weight (up to 300 KDa). A detailed review of the APC method has been recently summarized by Katsarava (7).

In addition to the functionalizable end-groups, assuming one amino and one carboxylic (or *p*-nitrophenyl ester) end group, the PEA polymer backbone can accommodate pendant functional groups (charged or uncharged, but polar) introduced on multifunctional monomers, for example C-protected L-lysine, that are useful for covalent conjugation of biologically active compounds. Novel polyelectrolyte type PEAs with polar pending groups along the chain will significantly change the physico-chemical and biological properties of the polymer, such as the ability to diffuse through cell membranes.

The tremendous value that PEAs have in the health science industry relates directly to the polymers' compatibility in biological systems and the mechanism by which they degrade and loaded drugs are released. PEA's mechanism of biodegradation and drug release is by surface erosion and primarily follows zero order kinetics (8,9). These unique material properties have shown that PEAs have a multiuse potential as a new family of biodegradable biomaterials useful as drug delivery platforms or as components of resorbable surgical implants.

Extensive research at MediVas has lead to a vast assortment of PEA copolymers confirming that the APC method has virtually unlimited possibilities for designing new polymeric materials with a wide variety of mechanical, physico-chemical and biological properties that are easily achieved by varying the three component building blocks. In addition, because these polymers have a significant number of lateral functional groups, functionalized PEAs can be subjected to subsequent chemical attachment of bioactive agents. thereby making this group of polymers effective for stabilizing biologics in addition to serving as platforms for drug delivery. These new polyfunctional non-toxic, bio-compatible compounds with improved mechanical properties are suitable for specific clinical applications, such as coating materials for drug-eluting stents, stabilization and oral delivery of biologics, targeted delivery of drugs to the front and back of the eye, topical or transdermal drug delivery, and therapeutic wound dressings for surgical procedures.

Experimental

Materials

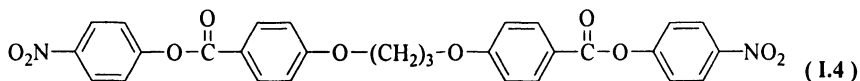
All starting materials and solvents were obtained from commercial sources (Sigma-Aldrich, Fisher Scientific Int.). Active di-esters (of **Formula I**): di-*p*-nitrophenyl adipate, **I.1** (1), di-*p*-nitrophenyl sebacate, **I.2** (1), di-*p*-nitrophenyl fumarate, **I.3** (10), and bis-nucleophilic monomers: (of general **Formula II**) di-*p*-toluenesulfonic acid salts of bis(α -aminoacyl)- α,ω -alkylene diesters (1, 2), and di-*p*-toluenesulfonic acid salt of L-lysine benzyl ester (11,12) were prepared as described previously.

Monomer Synthesis

Preparation of Di-*p*-Nitrophenyl Ester of 1,3-Bis(4-carboxyphenoxy) propane (I.4)

Precursor diacid 1,3-bis(4-carboxyphenoxy) propane (CPP) was prepared by refluxing 2.1 mol. eq. of 4-hydroxybenzoic acid with 1 mol. eq. of 1,3-

dibromopropane in alkaline water solution for 8-12 h. Solution was then poured into 700 mL of 1M HCl and filtered. An off-white solid obtained was suspended in water/ethanol 1:1 mixture, re-filtered and dried under vacuum which gave 62 % yield. Product was recrystallized from DMF:water, (1:1 v/v), mp. 310 °C.



7.9 g. (25 mmol) of CPP, 7.3 g (52.5 mmol) of p-nitrophenol and a few drops of DMF were suspended in 100 mL of dry chlorobenzene under nitrogen. Then a diluted solution of 4 mL (54.8 mmol) thionyl chloride in 10 mL of chlorobenzene was added drop-wise to reaction mixture at ambient temperature for 20 min, heated to 75°C while a slow stream of nitrogen was introduced to evacuate formed gases. After 8 h, the reaction mixture became homogenous. The cooled solution was diluted with 120 mL hexane and left over night at 0°C. Yellow crystals of compound **1.4** were collected, washed with hexane and dried in vacuum over night at 45°C. Yield was 10.3 g, (74 %). Recrystallization from acetone yielded pale yellow crystals, mp 161.6°C; ¹H NMR, (DMSO-*d*₆, 500 MHz) δ: 8.33 (d, 4H, Ar), 8.10 (d, 4H, Ar), 7.58 (d, 4H, Ar), 7.17 (d, 4H, Ar), 4.29 (t, 4H, -O-CH₂-), 2.27 (m, 2H, -CH₂-CH₂-).

Preparation of Di-p-Toluenesulfonic Acid Salts of Bis-(α-amino acid)-α,ω-Alkylene Diester Monomer (Formula II)

General procedure: 2 eq. of α-amino acid and 1 eq. of diol were suspended and refluxed in toluene in the presence of 2.2 eq. of TsOH monohydrate, with the resulting water seized in a Dean-Stark condenser. Monomers were thoroughly purified by multiple recrystallizations (1).

Preparation of Di-TFA Salt of Bis-(L-Leu)-estradiol-3,17β-diester (Compound II.5)

bis(Boc-L-leucine)estradiol-3,17β-diester, (II.5): 1.5 g (5.51 mmol) of 17,β-estradiol, 3.43 g (13.77 mmol) Boc-L-leucine monohydrate and 0.055 g (0.28 mmol) of p-toluenesulfonic acid monohydrate were dissolved into 20 mL of dry N,N-dimethylformamide at room temperature under argon; 0.067 g of DMAP and 5.4g (26.17 mmol) of DCC were introduced and stirring was continued for 6 h. At the end of reaction, 1 mL of acetic acid was added to destroy the excess of DCC. Precipitated urea was filtered off and filtrate poured into 80 mL of water. Product was extracted three times with 30 mL of ethylacetate, dried over sodium sulfate, solvent evaporated, and remainings

subjected to chromatography on a column (7:3 hexanes: ethylacetate). A colorless glassy solid of analytically pure compound (**II.5a**) obtained a 2.85 g, 74% yield. De-protection of (**II.5a**) Boc-protected monomer proceeded quantitatively in 10 mL of dry dichloromethane and 4 mL of dry TFA. After 2 h of stirring at room temperature, a homogenous solution was diluted with 300 mL of anhydrous ether and left at 0°C over night. White crystals were collected, washed twice with ether, and dried in a vacuum oven at 45 °C. Yield 2.67 g, (90%). Mp = 187.5°C.

Co-PEA Synthesis by Solution Active Polycondensation

This method involves equimolar amounts of (**I**) and (**II**), and organic base as the acceptor of liberated *p*-toluenesulfonic acid. Polymers with high molecular weights, and yields from 68 to 95% (depending on mol. weights) were characterized by GPC, ¹H NMR spectroscopy and DSC. Their enzymatic hydrolysis (lipase, α -chymotrypsin) was studied.

A general procedure is described for preparation of copolymer 4-(Leu-6)_{0.50}-Lys(Bz)_{0.50}. A 0.1 mole of a bis-nucleophile monomer **II** (here, a mixture of 0.05 mol. of L-Leu-6 and 0.05 mol. of **II.3**), 0.1 mol of di-*p*-nitrophenyl adipate (monomer **I**) stirred in 52 mL of *N,N*-dimethylformamide (DMF) at 60°C and dry triethylamine (NEt₃) added (30.8 mL, 0.22 mol.) corresponded to total monomer concentration 1.2 mol/L. The reaction was conducted over 24 h and crude samples monitored by GPC. The purification of co-PEAs was achieved by multiple precipitation from solvent (ethanol, dichloromethane) into non-solvent (water or cold ethylacetate) until no *p*-nitrophenol was detected in the UV spectrum.

New co-PEAs were labeled in the following way: $y\text{-[AA-x}_1\text{]}_m\text{-[AA-x}_2\text{]}_n$, where AA stands for amino acid, *y*, diacid fragment (or number of methylene group in diacid) in monomer **I**; and *x* is the diol fragment (or the number of methylene group in linear aliphatic diol) in monomer **II**. Therefore, in the above example polymer is composed of adipic acid, bis-(L-Leu)-1,6-hexanediol diester and benzylated L-Lysine. Scheme 3 shows the chemical structure of some representative co-PEAs synthesized. Due to the equal reactivity of diamines, integration of ¹H NMR signals of copolymers display in most cases exactly the same monomer feed ratios as in the starting mixture.

Deprotection of Polymeric Benzyl Esters

Catalytic hydrogenolysis of co-PEA(Bz) was conducted under dry H₂ in combination with Pd/C catalyst as described (13). The deprotected co-PEA was designated co-PEA(H). The covalent conjugation of nitroxyl radicals (4-amino-2,2,6,6-tetramethylpiperidine-1-oxyl) onto co-PEA(H) was performed according to the published and patented method (Chu *et al.*, 12, 13).

***In Vitro* Enzyme Catalyzed Biodegradation Studies**

Biodegradation studies by weight loss were performed for four PEAs (fig 2). Circular PEA films were cast (ethanol) on stainless steel discs of 11 mm diameter with ca. 16.8 mg film weight on each. Films were placed into glass vessels containing 2 mL of Dulbecco's phosphate buffered saline solution at pH 7.0 containing 8.5 U/mL concentration of enzyme (α -chymotrypsin). Glass vessels were maintained at 37°C and gently shaken. Enzyme solution was renewed twice weekly. Discs were taken out at 7, 14, 21 and 28 day time points, washed three times with DI water and dried up to constant weight at 50°C (about another 24 hr). Weight loss (%) was calculated as:

$$\% \text{ weight loss} = [\text{polymer start weight} - \text{polymer end weight}] / [\text{polymer starting weight} \times 100]$$

Comparison of Endothelial Cell Viability in the Presence of Monocyte-mediated Co-PEA and Therapeutic PEA Degradation Products

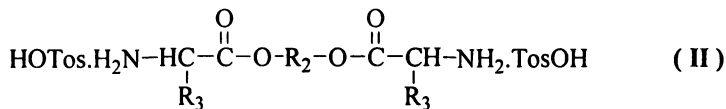
PEA monocyte degradation experiments were conducted as follows: polymer film was cast into glass wells, dried and sterilized. Freshly isolated human monocytes were plated into the polymer coated wells (2×10^6 cells per well) in 2 mL of cell growth media (RPMI media with autologous serum). Plates were placed at 37°C in a CO₂ incubator and media replaced every third day for two weeks. The collected media with degradation products (PEA 8-Leu(6)_{0.75}-Lys(Bz)_{0.25} or co-PEA17 β supernatants) were used to grow human coronary artery endothelial cells (ECs). ATP assays were conducted using a ViaLight Plus assay kit (Cambrex) at 24 and 48 hour time points to determine the percent viability of the ECs grown in the two polymer degradation product supernatants.

Results and Discussion

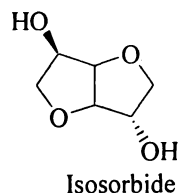
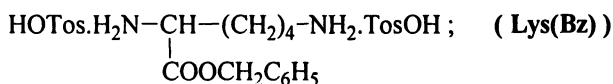
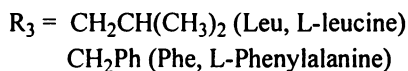
Monomer Synthesis

The following amino acids were selected for new co-PEA designs: L-Lys - for the purpose of incorporating free lateral carboxylate groups into the polymeric backbones; L-Leu - for imparting elastomeric properties, based upon prior studies (1,4,8); and L-Phe for enhancing mechanical properties of the resulting PEAs.

Amino acid-based bis-nucleophilic monomers (II) are represented in scheme 1.

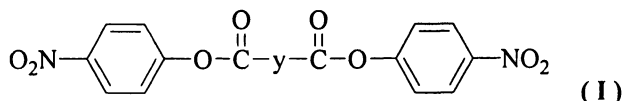


where $\text{R}_2 = (\text{CH}_2)_3$, designated as "3", for 1,3-propanediol
 $(\text{CH}_2)_6$, designated as "6", for 1,6-hexanediol
 Isosorbide, designated as DAS;



Scheme 1

Other bis-electrophilic monomers prepared have the general structure shown in scheme 2, where y represents a dicarboxylic acid.



Scheme 2

Synthesis of PEA Copolymers

The co-PEAs were synthesized by solution polycondensation with equal molar amounts of diamine salts **II** and active diesters **I** in an amide type solvent (DMA) under optimal reaction conditions previously described for homo-PEAs (1). The close chemical nature of the salts **II** and di-*p*-nitrophenyl esters **I** easily allowed us to carry out the polycondensation with combinations of multiple monomers (minimum three), which resulted in copolymers with randomly distributed components with the same ratio as in the starting reaction mixture. Synthesized co-PEAs achieved high yields (up to 90 %) and high weight average molecular weights from 85 000 Da to 300 000 Da. Complete incorporation of monomers into polymer backbone was confirmed by ^1H NMR spectroscopy, which showed the same unit content in the main backbone as in the starting reaction mixture. The co-PEAs obtained have a reduced viscosity (η_{red}) as high as 1.50 dL/g (8-leu(6) $_{0.50}$ - lys(Bz) $_{0.50}$) and excellent film-forming properties, an indication of relatively high molecular weights of the co-PEAs synthesized.

Polydispersity indices estimated by GPC ranged from 1.24 to 1.9, which is typical for PEAs prepared by active polycondensation (1,2). Sample copolymer structures are depicted in scheme 3.

Mechanical Properties of the Co-PEAs

Table I shows tensile properties of selected co-PEAs, all containing Lys(Bz) units at 25% of total di-amine monomers. The tensile property data showed that 8-Leu(6)_{0.75}-Lys(Bz)_{0.25} was the weakest of the co-PEA samples tested. Decrease in the length (*y*) of polymethylene groups in the diacid monomer **I**, or the incorporation of phenylalanine increased the tensile strength of the resulting co-PEAs. Following a general trend, shortening the polymethylene chain in the diol or diacid caused a decrease of film elasticity and increased the Young's modulus (2.5 GPa). The tensile strength can be further increased by processing conditions that induce molecular orientation

Introduction of bulky aliphatic fragments of isosorbide contributed significantly to a higher T_g and an increased Young's modulus whilst maintaining biocompatibility and solubility in ethanol. From the data in Table I, we observe that the monomer bis(L-Leu)-isosorbide-diester (Leu(DAS)) contributed higher T_g; whereas the monomer bis(L-Leu)-hexanediol-diester, (Leu(6)) led to increased elongation. Incorporation of both monomers in various feed ratios resulted in new PEAs with different combinations of mechanical properties and glass transitions (Figure 1).

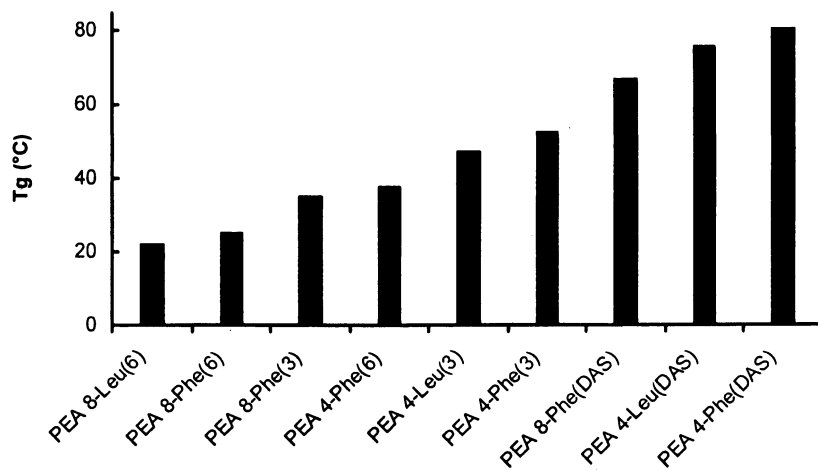
In Vitro Enzyme Catalyzed Biodegradation

The effect of co-PEA composition on enzymatic biodegradation was studied in enzyme phosphate buffer solution. Figure 2 summarizes lipase-catalyzed weight loss data from four different types of co-PEA films: **a**) 4-Leu(6)_{0.75}-Lys(Bz)_{0.25}, **b**) 8-Leu(6)_{0.75}-Lys(Bz)_{0.25}, **c**) 4-Leu(6)_{0.5}-Phe(6)_{0.25}-Lys(Bz)_{0.25}, **d**) 8-Leu(6)_{0.5}-Phe(6)_{0.25}-Lys(Bz)_{0.25}. There was virtually no weight loss in the PBS control during the same testing period. Several of these co-PEAs show close to zero order kinetics, a property important for sustained and controlled release of drugs.

As illustrated in Figure 2, an increase of polymethylene chain in diacid **y** from 4 (samples **a** and **c**) to 8 (samples **b** and **d**) significantly decreased weight loss rates. The effect of α -amino acids on enzyme-catalyzed biodegradation is evident when comparing sample **a** with sample **c**, or sample **b** with sample **d**: The replacement of the L-leucine component with L-phenylalanine led to a sharp increase in weight loss, particularly in the shorter **y** acids (samples **a** and **c**). The increase in the biodegradation rate due to the L-Phe is consistent with the data of previous studies (1,8,9). The solution viscosity (η_{inh}) measurements before and after 120 h of biodegradation showed no changes, an indication of a surface erosion mechanism, without compromising bulk properties (8,9).

Table I. Co-PEA Tensile Properties

<i>Sample</i>	<i>T_g</i> (°C)	<i>Stress at Break</i> (MPa)	<i>Elongation at Break</i> (%)	<i>Young's Modulus</i> (MPa)
<i>PEA-co-Lys(Bz)_{0.25}</i>				
8-Leu(6)	22	29	609	15
8-Leu(3)	30	29	389	329
4-Leu(6)	45	26	446	462
8 _{0.5} -CPP _{0.5} -Leu(6)	44	52	6	1306
8-Phe(6)	25	26	361	825
8-Phe(3)	35	41	106	1842
4-Phe(3)	52	37	152	2533

*Figure 1. Co-PEA glass transition temperatures*

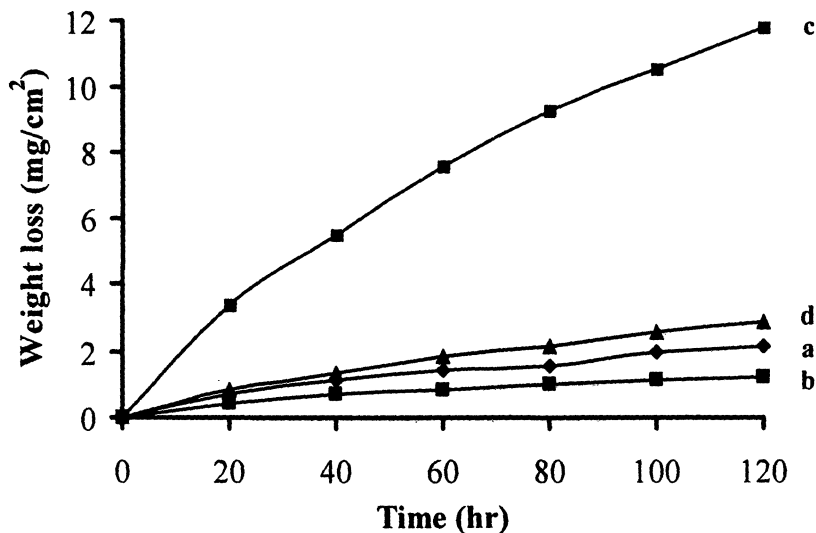


Figure 2. Lipase-mediated weight loss profiles of co-PEA films: a) 4-Leu(6)_{0.75}-Lys(Bz)_{0.25}, b) 8-Leu(6)_{0.75}-Lys(Bz)_{0.25}, c) 4-Leu(6)_{0.5}-Phe(6)_{0.25}-Lys(Bz)_{0.25}, d) 8-Leu(6)_{0.5}-Phe(6)_{0.25}-Lys(Bz)_{0.25}.

The α -chymotrypsin-catalyzed biodegradation profiles of PEA - 4-amino-TEMPO radical conjugate, 8-Leu(6)_{0.75}-Lys(TEMPO)_{0.25} (a) as well as its Bz-protected homolog 8-Leu(6)_{0.75}-Lys(Bz)_{0.25} (b) are depicted in Figure 3. Compared with these polymers, a decrease of amide group density by lowering the Lys(Bz) concentration in co-PEA 4-Leu(6)_{0.6}-Leu(DAS)_{0.3}-Lys(Bz)_{0.1} increased degradation by α -chymotrypsin: only 10 % of polymer film remained on the metal disc surface after 28 days of enzyme treatment.

PEA Copolymers Based on Aromatic Diacids

Gliadel[®] - a controlled-delivery polymer wafer is the combination of a copolyanhydride matrix consisting of CPP and sebacic acid (20/80 mol. ratio) in which an anticancer agent is physically admixed. Clinical investigations of Gliadel[®] implants in rabbit brains have shown limited toxicity, initial activity and fast excretion of decomposition products as free acids (14).

It was expected that incorporation of less-toxic aromatic CPP fragments in the PEA backbone would increase mechanical strength, T_g and thermal stability, as well as decrease hydrophilicity. For these reasons an active diester of CPP was prepared according to Scheme 4:

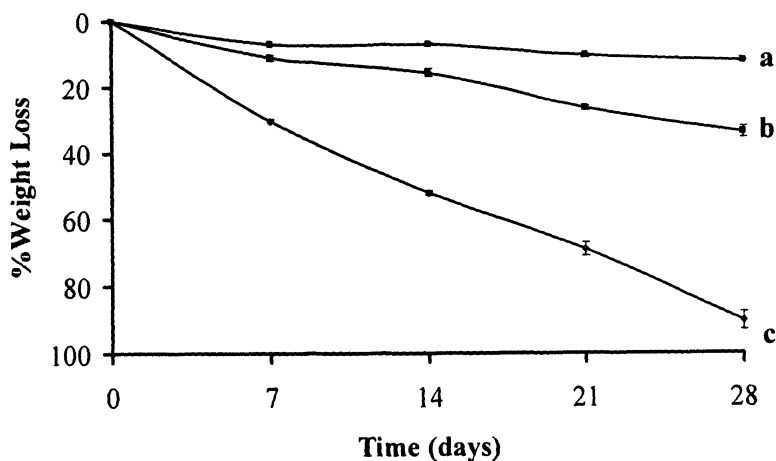
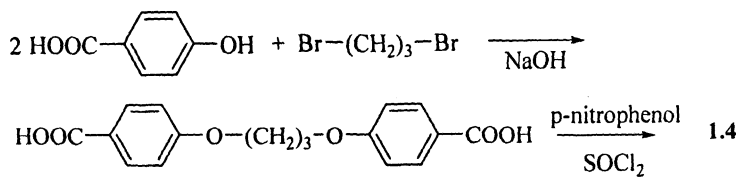


Figure 3. Co-PEA film degradation weight loss profiles in α -chymotrypsin/PBS buffer: a) 8-Leu(6)_{0.75}-Lys(TEMPO)_{0.25}, b) 8-Leu(6)_{0.75}-Lys(Bz)_{0.25}, c) 4-Leu(6)_{0.6}-Leu(DAS)_{0.3}-Lys(Bz)_{0.1}



Scheme 4

Copolymer [8_{0.5}-CPP_{0.5}]-Leu(6)_{0.75}-Lys(Bz)_{0.25} (Table 1) with Mw = 82 000 Da and polydispersity (PDI) = 1.66 was isolated with 76 % yield. As a result, the incorporation of 50% CPP-unit in sebacic acid based PEA raised the Tg from 22 to 44°C. An additional sharp melting endotherm in differential scanning calorimetry (DSC) curves at 286°C was also observed, indicating a semi-crystalline nature of the co-polymer. The polymer is soluble in chlorinated non-polar and aprotic polar solvents. but not in ethanol. Because of its high hydrophobicity, the CPP-co-polymer does not swell in aqueous media, and equilibrium water content is about 2-3% w/w.

PEA Copolymers Based on Fumaric Acid

Among unsaturated di-acids, fumaric acid is one of the most useful building blocks, since it is a naturally occurring metabolite. Aliphatic polyesters, poly(propylene fumarates) have recently been considered as biodegradable and photo-crosslinkable polymeric material used for scaffold applications (15).

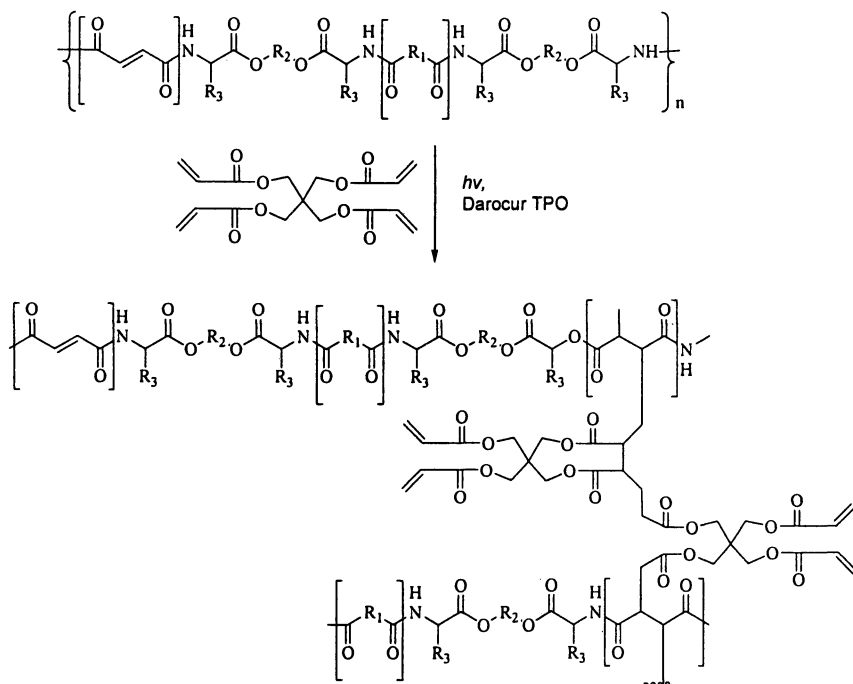
As reported, AABB type PEAs of fumaric acid display limited solubility in common organic solvents. In most cases the polymerization solution turns to gel, due to partial crosslinking (10). We have observed that unsaturated PEA (UPEA) copolymers with less than 35 % mol. ratio of fumaric acid to aliphatic diacid maintain reactivity during radical reactions and remain soluble over long storage periods.

Photoinitiated radical crosslinking of UPEAs was investigated further. For this study, the photoinitiator diphenyl (2,4,6-trimethylbenzoyl)-phosphine oxide (Darocur TPO, research sample CIBA Speciality Chemicals) and the crosslinker, pentaerythritol tetraacrylate were employed. UPEA polymer films of [8]_{0.75} – Fum_{0.25} – Leu(6) composition (Scheme 3), with Mw = 56 000 Da, PDI = 1.73, Tg = 19.7°C were cast onto a hydrophobic surface with 4 % w/w photoinitiator and 1 to 5 % w/w crosslinker (Scheme 5). Films of ca. 0.13 mm thickness were exposed to a broadband UV mercury lamp with the exposure rate 10 000 mW/cm². Sample was mounted 4 cm away from the source, irradiation time was 5 min. Tensile properties after exposure were measured.

Young's modulus of cured UPEA increased over 2500 % as tetraacrylate content reached 4 % w/w (Figure 4). Therefore, UPEAs display obvious reactivity and the potential to fabricate into solid scaffolds with a wide range of applications.

Therapeutic PEAs

In most drug-eluting applications, the drug is physically matrixed by dissolving or melting with a polymer. Another approach has also been reported in which a drug is chemically attached as a side group to a polymer (16). If a



Scheme 5. UV-photocrosslinking of co-PEA [8]_{0.75} – Fum_{0.25} – Leu(6) and pentaerythritol tetraacrylate in the presence of 4 % Darocur TPO.

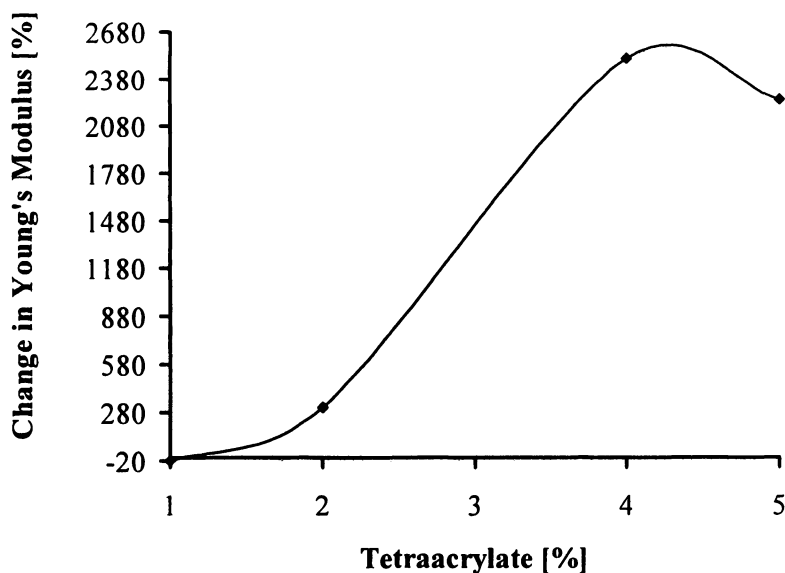
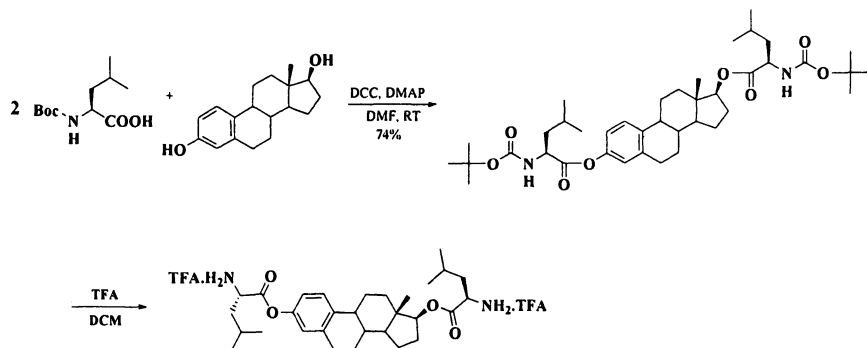


Figure 4. Change of Young's modulus after photocrosslinking of UPEA

drug or other therapeutic agent is covalently incorporated into a biodegradable polymer backbone, a therapeutic polymer is formed. Such compositions represent synthetic polymers that combine therapeutic or palliative bioactivity with desirable mechanical and physical properties, and degrade into therapeutic active compounds. Incorporation of hormones and non-steroidal anti-inflammatory drugs (NSAIDs) into a biodegradable polymer backbone can solve many problems of drug therapy. Some of the drugs exhibit high immunogenicity in human subjects; whereas prodrugs can show less toxicity. Besides, most of the drugs are removed quickly from the bloodstream after their administration (i.e. the concentration of the drug in the plasma decreases rapidly). Thus, there is a need for new compositions and methods for incorporating therapeutic molecules, such as drugs and other bioactive agents, into the backbones of polymers for use in polymer delivery systems in which a controlled rate of therapeutic release is combined with desirable mechanical and physical properties.

A naturally occurring therapeutic-diol, 17- β -estradiol is an endogenous hormone, useful in preventing restenosis and tumor growth (17,18). Steroid-diol 17 β -estradiol was introduced in a PEA backbone via the di-TFA salt of the new monomer bis-(L-Leu)-17 β -estradiol-diester (II.5). This monomer was prepared in ca. 70% yield, followed by the reaction in scheme 6 and then directly introduced into the APC reaction.



Scheme 6

Therapeutic co-polymer composition 8-Leu(6)_{1.5}-Leu(17 β)_{1.5}-co-Lys(Bz) depicted in scheme 3(c) inherently contains ca. 34 % w/w of 17 β -estradiol. The polymer formed tough films. Further characterization showed a high molecular weight at 82 000 Da (GPC, PS, DMAc), with T_g = 41°C and a sharp melting endotherm at 220°C (DSC). According to ¹H NMR, component feed ratios in the backbone correspond to the designed architecture.

This new therapeutic polymer was subjected to monocyte degradation. Comparison of endothelial cell (EC) viability in the presence of monocyte-mediated degradation products from two copolymers 8-Leu(6)_{0.75}-co-Lys(Bz) and 8-Leu(6)_{0.5}-Leu(17 β)_{0.50}-co-Lys(Bz) showed promising results. Two independent assays showed that, in the presence of the PEA-17 β monocyte-mediated degradation products, viability of ECs was enhanced at both 24 hours and 48 hours by 30% and 20%, respectively.

Acknowledgements

The authors are grateful for John Crison for insightful discussion, for support from the MediVas team and for G. Jokhadze and M. Machaideze for degradation tests.

References

1. Katsarava, R.; Beridze, V.; Arabuli, N.; Kharadze, D.; Chu, C.C.; Won, C.Y. *J. Polym. Sci.: Part A: Polym. Chem.* **1999**, *37*, 391.
2. Gomurashvili, Z.; Katsarava, R.; Kricheldorf, H.R. *J. Macromol. Sci.-Pure and Appl. Chem.* **2000**, *37*, 215.

3. Fan, Y.; Kobayashi, M.; Kize, H. *J. Polym. Sci.: Part A: Polym. Chem.* **2001**, *39*, 1318.
4. Okada, M.; Yamada, M.; Yokoe, M.; Aoi, K. *J. Appl. Polym. Sci.* **2001**, *81*, 2721
5. Lee, S.H.; Szinai, I.; Carpenter, K.; Katsarava, R.; Jokhadze, G.; Chu, C.C.; Huang, Y.; Verbeken, E.; Bramwell, O.; De Scheerder, I.; Hong, M.K. *Coronary Artery Disease.* **2002**, *13(4)*, 237.
6. DeFife K. *et al.* Poly(ester amide) Amino Acid Based Copolymers Promote Blood and Tissue Compatibility; Transcatheter Cardiovascular Therapeutics - TCT **2004**; Washington, DC, 2004; Poster.
7. Katsarava, R. *Macromol. Symp.* **2003**, *199*, 419
8. Tsitlanadze, G.; Kviria, T.; Chu, C.C.; Katsarava, R. *J. Mater. Sci. Mater. in Medicine.* **2004**, *15*, 185.
9. Tsitlanadze, G.; Machaidze, M.; Kviria, T.; Djavakhishvili, N.; Chu, C.C.; Katsarava, R. *J. Biomater. Sci. Polymer Ed.* **2004**, *15*, 1.
10. Guo, K.; Chu, C.C.; Chkhaidze, E.; Katsarava, R. Synthesis and Characterization of Novel Biodegradable Unsaturated Poly(ester amide)s. *J. Polym. Sci. Part A: Polym. Chem.* **2005**, *43*, 1463-1477.
11. Keun-Ho Lee & C. C. Chu, "Molecular Design of Biologically Active Biodegradable Polymers for Biomedical Applications", *Macromol. Symposium*; Huthig & Wepf Verlag, Zug, **1998**, *130*, 71.
12. Lee, K.-H.; Chu, C.C.; Freed, J. Aminoxyl-containing Radical Spin Labeling In Polymers and Copolymers, *U.S. Patent 5,516,881*, May 16, 1996.
13. Chu CC, Katsarava R., Elastomeric Functional biodegradable copolyester amides and copolyester urethanes, US 6,503,538 B1, Jan 7, 2003.
14. Domb, A.J.; Rock, M.; Perkin, C.; Yipchuck, G.; Broxup B.; Villemure J.G. *Biomaterials.* **1995**, *16*, 1069
15. Fisher, J. P.; Dean, D.; Mikos A.G. *Biomaterials*, **2002**, *23*, 4333.
16. Ghosh, M. Appl. Bioactive Polym. Mater. In *Polym. Sci. and Tech.* Vol 38, Plenum Press, **1988**, p. 115-123.
17. Klauber, N.; Parangi, S.; Flynn, E.; Hamel, E.; D'Amato R.J. *Cancer Res.* **1997**, *57*, 81
18. Fotsis, T.; Zhang, Y.; Pepper, M.S.; Adlercreutz, H.; Montesano, R.; Nawroth, P.P.; Schweigerer, L. *Nature*, **1994**, *368*, 237

Chapter 3

Chitosan Water-Soluble System: An Approach to Prepare Superabsorbent Gel

Suwabun Chirachanchai and Juthathip Fangkangwanwong

The Petroleum and Petrochemical College, Chulalongkorn University, Soi Chula 12, Phya Thai, Bangkok 10330, Thailand

A novel chitosan-PEG superabsorbent gel is proposed. The gel is directly formed by conjugating chitosan with dicarboxylated polyethylene glycol. The reaction is simple but effective as chitosan aqueous solution with a water soluble conjugating (WSC) agent of 1-ethyl-3-(3-dimethylaminopropyl-carbodiimide) hydrochloride (EDC·HCl) favors the gelation with PEG at room temperature and in water without adding any organic solvents. The super-water absorptivity can be controlled by the molecular weight and the content of PEG. The hydroxyapatite is successfully impregnated by alternate soaking in calcium chloride and phosphate solution.

Introduction

Hydrogel is a class of polymer that absorbs water and swells at least 20% of the total weight of the starting polymer (*1*). In forming hydrogel, the system needs a hydrophilic polymer chain for the interaction with water molecules and the covalent or ionic crosslinks to form a three dimensional network and avoid the dissolution of hydrophilic polymer chains into water phase. The difunctional molecules (e.g. dialdehydes, diacids, diamines) or divalent ions (e.g., Mg^{2+} , Cu^{2+} , SO_4^{2-}) or ionic interaction (i.e., $NH_3^+ \dots ^-OOC$) or hydrogen bond thus play an important role in crosslinking, to result in hydrogels.

For the loosely crosslinked hydrogel, especially the polymer network with dissociated ionic functional group, the water absorption may possibly be up to above 95% of the total weight of the starting polymer, resulting in a superabsorbent polymer (SAP). Weaver *et al.* (2) demonstrated the first SAP as a “Super Slurper”, obtained from the saponified starch-graft-polyacrylonitrile copolymers. Presently, numerous superabsorbent products, such as soil conditioners, disposable diapers, feminine napkins, surgical pads, etc., are available. Synthetic polymers, such as polyacrylic acid, polyacrylamide, polyacrylonitrile, etc. and their derivatives, including their salts, are well recognized for the production of SAPs as the structures contribute the hydrophilicity, charge repulsion, osmosis, and the effective crosslinking.

Naturally derived Superabsorbent Polymer

Biopolymer-based SAPs have their advantages in their biocompatibility and non-toxicity. Various specific applications, such as alternative diuretic therapy (3), controlled drug delivery (4), cultivation of the cell (5), hypocaloric dietary treatment (6) have been proposed for decades. Potential natural polymers are cellulose or starch, chitin-chitosan, alginate, hyaluronic acid, etc.

Cellulose has received much attention because it is the most abundant naturally occurring substance with the unique properties of water swelling and gelatinization. The etherification of cellulose to carboxymethylcellulose (CMC) and its sodium salts produces a soft gel with a water absorbency up to 27 times the dry weight (7). Zhang *et al.* demonstrated the starch-*g*-poly(acrylic acid-*co*-sodium acrylate) with water absorbency of 417 times the dry weight (8). Sannino *et al.* proposed the use of the non-toxic carbodiimide conjugating agent to provide the chemically crosslinked SAP of hydroxyethylcellulose, carboxymethylcellulose sodium salt and hyaluronic acid. The SAP obtained had a water absorption up to 425 times the dry weight (6).

Chitin-Chitosan for Superabsorbent Polymer

Chitin-chitosan is the second-most abundant naturally occurring polysaccharide, existing in the exoskeleton of crustaceans, insects, and fungi. In making chitin-chitosan based products, one has to realize the difficulty in dissolving chitin-chitosan due to its strong hydrogen bond network. In the case of chitin (degree of acetylation above 0.3), only a few solvents, i.e. the mixture of lithium chloride and *N*-methyl-2-pyrrolidone (11), hexafluoroisopropanol and hexafluoroacetone (12) are good. Yoshimura *et al.* (13) demonstrated the esterification of chitin with succinic anhydride in the specific mixture of tetrabutylammonium fluoride and dimethylsulfoxide to give an SAP with a water absorption of 300 times. The work is unique in terms of its overcoming the

hydrogen-bonded packing structure of chitin to achieve the water swollen chitin-succinate. However, the uses of specific solvents and complicated steps might be points for further development.

The materialization of chitosan is simpler than that of chitin since it dissolves in acids, i.e., carboxylic and Lewis acids. In these cases, the hydrogel can be obtained by simply crosslinking with dialdehydes. Kulkarni *et al.* (14) proposed the modification of chitosan with PEG-dialdehyde and demonstrated that the PEG functioned in improving the swelling ratio to as high as 306. Fangkangwanwong *et al.* (15) proposed the crosslink network by introducing the epoxy group onto chitosan in which the gelation was obtained via the ring opening of the oxirane ring. The complexation of chitosan salts with polyanionic polymers, such as carboxymethyl cellulose, alginic acid, carboxymethyl dextran, heparin (16), etc., is a simple approach to prepare the SAP based on the loose packing network with effective hydrogen bonding with water molecules. Hagino and Huang (17) showed that the swelling in water of a chitosan-alginate complex was increased as high as 150 times as compared to the dry gel.

Modifying chitosan to become a water soluble species, such as carboxymethylchitosan, is another way to enhance gelation as the structure effectively allows the interaction with water molecules. Pourjavadi *et al.* (18) and Yu *et al.* (19) demonstrated the grafting of anionic polymers, i.e. poly(acrylonitrile), poly(acrylic acid) onto water soluble chitosan to obtain SAP, and the products showed a swelling of ~200 and ~500 times, respectively.

Superabsorbent Gel for Tissue Engineering

Recently, hydrogels and SAPs have received much attention for their applications, such as space filling agents, delivery vehicles for bioactive molecules, and three dimensional structures for cell organization in stimulating tissue formation in the field of tissue engineering (20). It is challenging to develop a chitosan superabsorbent gel with good physical and mechanical properties combined with biocompatibility, biodegradability, and especially, biomedical safety. As mentioned above, although the ionic crosslinked gels can be obtained from the simple preparation step, the low mechanical properties need the improvement. The covalently bonded hydrogel via crosslinkers, such as glutaraldehyde, diethyl squarate, oxalic acid, etc., gives high mechanical strength and good thermal stability, however, most of the crosslinkers possibly initiate irritation to the bio-system.

Previously, we clarified the complexation of chitosan with hydroxybenzo triazole, resulting in a water soluble system of chitosan (21-23). The system is attractive since it provides the reaction, and especially the conjugation, in aqueous media. Based on this approach, the present work, thus, (i) demonstrates a simple but effective crosslink reaction by using poly(ethylene glycol) as the crosslinker to obtain a superabsorbent gel in aqueous, and (ii) proposes

hydroxyapatite impregnation to develop a novel SAP chitosan. The SAP obtained might be a good model for preparing the bone tissue scaffold.

Materials and Methods

Materials

Chitosan (95% DD, M_v of 5.6×10^5) was supplied from Seafresh Chitosan (Lab) Company Limited, Thailand. Poly(ethylene glycol) (PEG) with M_n of 1450, 3350 Da were purchased from Sigma-Aldrich, Inc., USA. 1-Hydroxybenzotriazole monohydrate (HOBt·H₂O) and 1-ethyl-3-(3-dimethylaminopropyl-carbodiimide) hydrochloride (EDC·HCl) were purchased from Wako Pure Chemical Industries Co. Ltd., Japan. Succinic anhydride was provided from Fluka Chemika, Switzerland. All chemicals were used without further purification.

Synthesis of Dicarboxylated Poly(ethylene glycol), 1

PEG (3.3 mmol) was reacted with succinic anhydride (6.7 mmol) in the presence of a catalytic amount of pyridine at 65°C for 24 hours. The crude product was reprecipitated in diethyl ether, washed several times and dried in vacuo to obtain dicarboxylated poly(ethylene glycol).

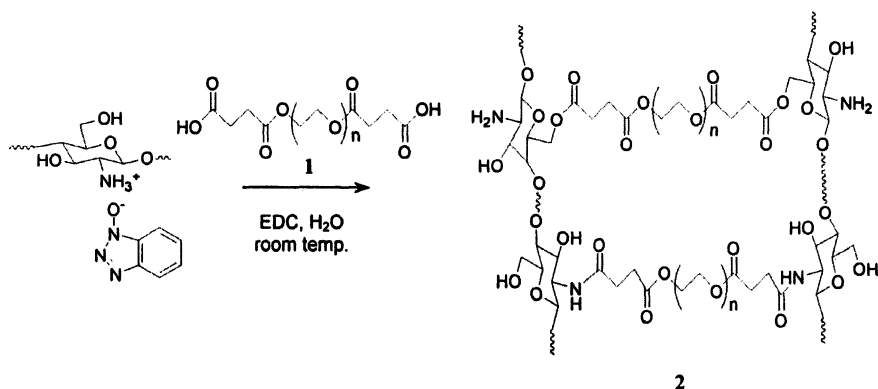
Synthesis of Chitosan-PEG Superabsorbent Gel, 2

Chitosan-HOBt aqueous solution was prepared as reported previously (21-23). In brief, chitosan (1.00 g) was vigorously stirred with HOBt·H₂O (0.94 g, 6.1 mmol equivalent to pyranose ring) in 80 mL of deionized water at ambient temperature until a clear solution was obtained.

To the chitosan-HOBt aqueous solution (0.61 mmol, 8 mL), 1 was added, followed by the aqueous solution of EDC·HCl (3 mol equivalent to PEG, 2 mL). The solution was stirred in a cylinder mold for 5 minutes at ambient temperature to obtain a gel, and was left for 24 h. The obtained gel was immersed in deionized water for 3 days. The swelling ratio of the chitosan hydrogels were calculated from a ratio of the weight of the swollen gel to the weight of the dry gel.

Impregnation of Hydroxyapatite (HAp)

Impregnation of HAp was done as reported by Tachaboonyakiat *et al.* (24). Gel 2 was soaked in a CaCl₂ (200mM)/Tris-HCl (pH 7.4) aqueous solution for 2



Scheme 1. Preparation of chitosan-PEG.

h, followed by thorough rinsing with deionized water several times. The product was soaked in a Na_2HPO_4 (120 mM) aqueous solution for 2 h and washed thoroughly with water. This alternating soaking was carried out five times.

Results and Discussion

When chitosan and HOBt were mixed in an equimolar amount in water, the chitosan is easily dissolved, even at room temperature. Figure 1 (a) shows a typical ^1H NMR pattern of HOBt in D_2O with two triplets at 7.41 and at 7.51 (for H-b), and two doublets at 7.60 and at 7.66 ppm (for H-a). Figure 1 (b) shows the spectrum of the chitosan (%DD ~ 95) and HOBt mixture in a mole ratio of 1:2 (equimolar to the pyranose ring). The peaks at 7.3 and 7.6 ppm are for the H-b and H-a benzene proton of HOBt, respectively. Comparing Figure 1 (a) to Figure 1 (b), the changes in chemical shift of the HOBt benzene protons indicate the formation of a complex with chitosan as an organic salt.

The mixture of chitosan and HOBt at 1:1 mole ratio was freeze-dried for further characterization. Chitosan (Figure 2 (a)) shows peaks at 1646 cm^{-1} (amide I), and 1589 cm^{-1} (amide II), whereas chitosan-HOBt (Figure 2 (b)) gives a peak at 1534 cm^{-1} , implying the protonation of NH_3^+ .

Synthesis of Chitosan-PEG Superabsorbent Gel

The crosslinking of chitosan-HOBt in water without using organic solvents was considered. Dicarboxylated poly(ethylene glycol), 1, was considered for the conjugation with chitosan, as it dissolves well in water. Systematic studies were done by varying the molar ratios of chitosan and PEG and the PEG molecular

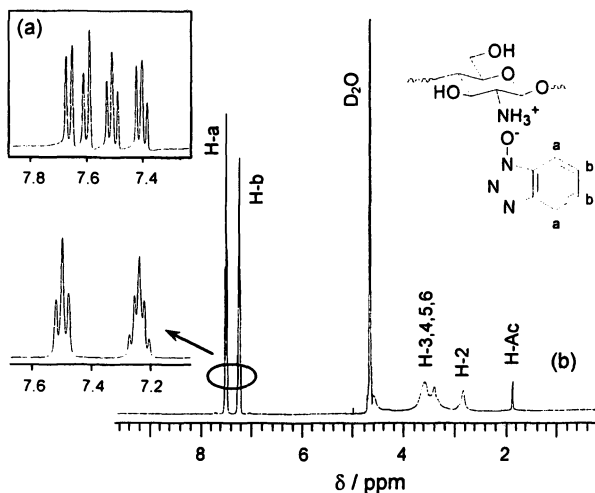


Figure 1. ^1H NMR spectra of (a) HOBt and (b) the mixture of chitosan and HOBt in D_2O at room temperature (Reproduced from reference 23. Copyright 2006 Wiley-VCH).

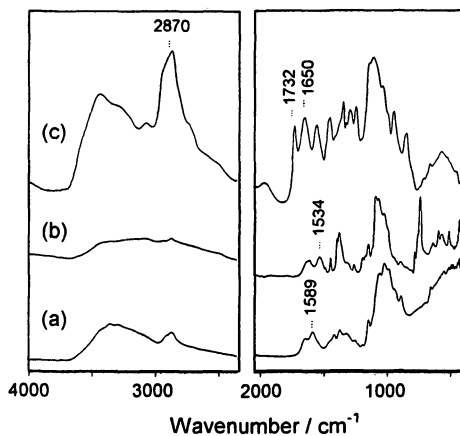


Figure 2. FTIR spectra of (a) chitosan, (b) chitosan-HOBt, and (c) chitosan-PEG3350 (mole ratio of chitosan : PEG 3350 = 1:0.2) (Reproduced from reference 22. Copyright 2006 Wiley-VCH).

weights. For example, after adding **1**, which has the molecular weight of 3350, into the chitosan aqueous solution (Figure 3 (a)) for the mole ratio of chitosan:PEG:WSC = 1:0.2:0.6 and being left for 5 minutes, the gelation of chitosan-PEG3350 started. The transparent and colorless swollen gel was obtained within a few hours when the gel was left in water (Figure 3 (b) and (c)).

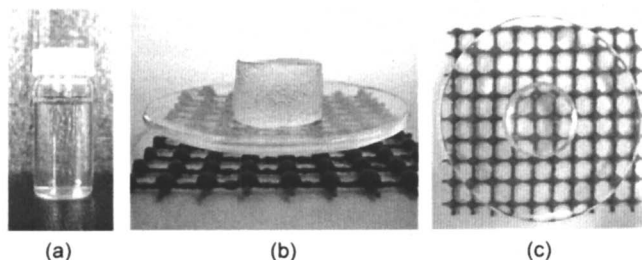


Figure 3. (a) chitosan-HOBt aqueous solution, and chitosan-PEG 3350 (mole ratio of chitosan : PEG 3350 = 1:0.2) at (b) side view, and (c) top view.

The gelation was confirmed by FTIR from the peaks at 2870, 1732, and 1650 cm^{-1} , corresponding to CH-stretching, C=O ester, and amide I, respectively (Figure 2 (c)).

Here, chitosan was reacted with PEG 1450 and PEG 3350 at various mole ratios of chitosan and PEG. The PEG crosslinker with different molecular weights related to the swelling properties was observed. The swelling ratios of chitosan gels with PEG 1450 and PEG 3350 at the mole ratio of chitosan:PEG = 1:0.1 are 532, and 224, respectively (Figure 4). This implies that conjugation with dicarboxylated PEG gives the SAP. The low swelling of chitosan with PEG 3350 might come from the fact that the crosslink of the long chain PEG was not effective and, as a result, a certain amount of chitosan aqueous solution remained in the water during the experiment.

The mole ratios of chitosan and PEG1450 were varied from 1:0.1 to 1:0.3 to observe the effect of crosslinking density on the stress at maximum load of the SAP. The SAPs with the mole ratios of 1:0.1, 1:0.2, 1:0.3 gave the stress at the maximum load for 4, 5 and 6 kPa, respectively. This implies that PEG is a practical crosslinker to control the hydrogels with different properties resulting in SAP chitosan.

One application for superabsorbent gel is the space filling scaffold for tissue engineering. Here, the hydroxyapatite impregnation was further studied. Previously, Tachaboonyakiat *et al.* reported the formation of hydroxyapatite (HAp) by alternate soaking of the chitosan gel with calcium chloride and sodium hydrogen phosphate (24). The gel was soaked in a calcium chloride solution in the first step to replace the water molecules followed by soaking in a sodium

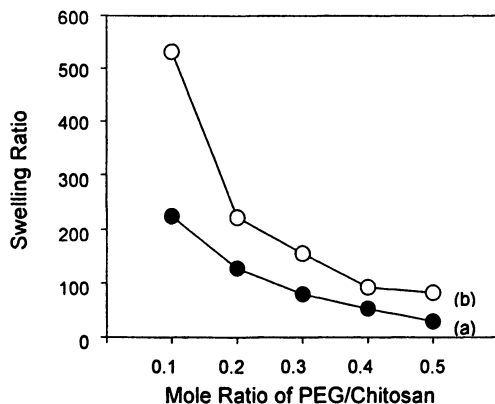


Figure 4. Swelling ratio of (a) chitosan-PEG1450 and (b) chitosan-PEG3350 under various mole ratios of PEG/Chitosan.

hydrogen phosphate solution. FTIR and WAXD analyses were used to trace the HAP formation. It was found that after soaking for five cycles, the phosphate peak (561 cm^{-1}) was identified, implying the existence of HAP. The WAXD showed peaks at $26^\circ 2\theta$ and $32^\circ 2\theta$ to confirm the HAP in the gel. TGA was applied to quantify the amount of HAP in the gel. Figure 5 shows that the ash content of the gel increases as the number of soaking cycles increase. Considering the ash content of the starting chitosan-PEG3350 for 10%, it was found that the HAP amount of the first and second cycles are 40% and 50%, respectively. The HAP content is saturated at 66% after four to five soaking times. It is important to note that after HAP mineralization, the gel became white and the texture was quite hard, as compared to the soft gel at the beginning.

Conclusions

The present work demonstrated an effective pathway to achieve SAP chitosan-PEG gel. The aqueous systems of chitosan-HOBt gave a successful conjugation at room temperature by using a water soluble conjugating agent. The materials obtained were superabsorbent gel with the swelling ratio as high as 500 times. The swelling and the mechanical properties of the gel were related to the PEG contents and PEG molecular weights. The impregnation of hydroxyapatite was as high as 66%, which shows the potential application for a space filling scaffold.

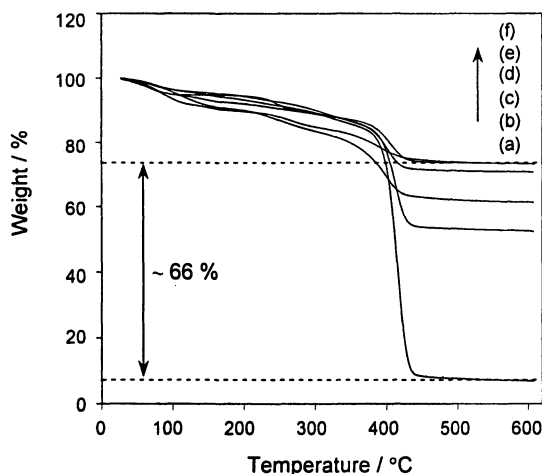


Figure 5. TGA thermograms of chitosan-PEG3350 (mole ratio of chitosan:PEG3350 = 1:0.5), after alternate soaking in $\text{CaCl}_2/\text{Na}_2\text{HPO}_4$ for the (b) 1st cycle, (c) 2nd cycle, (d) 3rd cycle, (e) 4th cycle, and (f) 5th cycle.

Acknowledgements

The authors would like to thank Seafresh Chitosan (Lab) Company Limited, Thailand for the chitosan material. They extend the acknowledgment to the Thailand Research Fund for the Royal Golden Jubilee Ph.D. Program Scholarship (Grant No. PHD/0112/2546). The project leader (S.C.) wishes to express his appreciation to the National Research Council of Thailand.

References

1. Park, H., Park, K. In *Hydrogels and Biodegradable Polymers for Bioapplications*; Ottenbrite, R.M., Huang, S.J., and Park, K., Eds.; ACS Symposium Series 627; American Chemical Society: Washington, DC, 1996; pp 2-10.
2. Weaver, M.O.; Bagley, E.B.; Fanta, G.F.; Doane, W.M. U.S. Patent 3,981,100, 1976.
3. Sannino, A.; Esposito, A.; De Rosa, A.; Cozzolino, A.; Ambrosio, L.; Nicolais, L. *J. Biomed. Mater. Res.* **2003**, *67A*, 1016-1024.
4. Chen, J.; Park, H.; Park, K. *J. Biomed. Mater. Res.* **1999**, *44*, 53-62.

5. Schneider, G.B.; Dnglish, A.; Abraham, M.; Zaharias, R., Stanford, C.; Keller, J. *Biomaterials* **2004**, *25*, 3023-3028.
6. Sannino, A.; Pappadà, S.; Madaghiele, M.; Maffezzoli, A.; Ambrosio, L.; Nicolais, L. *Polymer* **2005**, *46*, 11206-11212.
7. Ning, X.; Sun, T. U.S. Patent 5,247,072, 1993.
8. Zhang, J.; Wang, L.; Wang, A. *Macromol. Mater. Eng.* **2006**, *291*, 612-620.
9. Li, A.; Zhang, J.; Wang, A. *Bioresource Technol.* **2006**, in press.
10. Wu, J.; Lin, J.; Zhou, M.; Wei, C. *Macromol. Rapid Commun.* **2006**, *27*, 1039-1046.
11. Uragami, T.; Ohsumi, Y.; Sugihara, M. *Polymer* **1981**, *22*, 1155.
12. Capozza, R.C. German Patent 2,505,305, 1975.
13. Yoshimura, T.; Uchikoshi, I.; Yoshiura, Y.; Fujioka, R. *Carbohydr. Polym.* **2005**, *61*, 322-326.
14. Kulkarni, A.R.; Hukkeri, V.I.; Sung, H.-W.; Liang, H.-F. *Macromol. Biosci.* **2005**, *5*, 925-928.
15. Fangkangwanwong, J.; Yoksan, R.; Chirachanchai, S. *Polymer* **2006**, in press.
16. Dutkiewicz, J. *Advances in Polymer Materials for Medicine and Hygiene*;
17. Hagina, Y.; Huang, S. *Polym. Mater. Sci. Eng.* **1995**, *72*, 249-250.
18. Pourjavadi, A.; Mahdavinia, G.R.; Zohuriaan-Mehr, M.J. *J. Appl Polym. Sci.* **2003**, *90*, 3115-3121.
19. Yu, C.; Hui-min, T. *Carbohydr. Res.* **2006**, *341*, 887-896.
20. Drury, J.L.; Mooney, D.J. *Biomaterials* **2003**, *24*, 4337-4351.
21. Fangkangwanwong, J.; Yoksan, R.; Chirachanchai, S. Thai Patent Application, patent pending.
22. Fangkangwanwong, J.; Akashi, M.; Kida, T.; Chirachanchai, S. *Macromol. Rapid Commun.* **2006**, *27*, 1039-1046.
23. Fangkangwanwong, J.; Akashi, M.; Kida, T.; Chirachanchai, S. *Biopolymers* **2006**, *82*, 580-586.
24. Tachaboonyakiat, W.; Serizawa, T.; Akashi, M. *J. Biomater. Sci.* **2002**, *13*, 1021.

Chapter 4

The Cyclization and Functionalization of Styrenic Polymers

Boyd A. Laurent, Dawanne M. Eugene, and Scott M. Grayson

Department of Chemistry, Tulane University, New Orleans, LA 70118

Macrocyclic poly(styrene) and poly(4-acetoxystyrene) have been successfully synthesized utilizing a highly efficient “click” coupling of a terminal alkyne and azide. This technique has been shown to give high yields of well-defined polymeric macrocycles consisting of molecular weights of 2200 Da and 4200 Da prepared via atom transfer radical polymerization (ATRP). This procedure also enables the facile functionalization of the backbone of the macrocycles in order to incorporate a range functional materials or tune the molecule’s physical properties.

Introduction

The exploration of new polymer architectures has been the focus of significant recent research, motivated by the fundamental hypothesis that a polymer’s properties are intimately related to its structure. This concept has led to the development and optimization of synthetic techniques for the preparation of graft, star, dendritic, ladder, and hyperbranched polymers as well as a variety of hybrid and more complex architectures. Cyclic polymers are of particular interest because their circular shape and lack of end groups has a profound effect on their physical properties such as intrinsic viscosity and hydrodynamic volumes (*I*).

The preparation of cyclic polymers has been particularly challenging for polymer chemists as the vast majority of polymerization methods involve the linear propagation from an initiator to a terminal end group. A post

polymerization coupling of the initiating and terminating groups would then be required, and such reactions are usually complicated by both incomplete reactions and side reactions. The resultant mixture of linear and cyclic macromolecules is extremely difficult to purify because of the minor differences in size, polarity and solubility. Techniques that have been used with limited success for purification of these mixtures include fractionation and preparative gel permeation chromatography (GPC).

One of the first cyclization techniques used historically was the quenching of α,ω -homodifunctional anionic polymers with a difunctional electrophilic agent. Roovers *et al.* were pioneers in this field, synthesizing cyclic poly(styrenes) through anionic polymerization from a difunctional initiator and quenching with a dimethyldichlorosilane under extreme dilution conditions (2). A variety of other quenching agents have also been explored with the anionic polymerization method (3). However, because this quenching reaction is bimolecular, the dilute conditions required to favor cyclization over linear oligomerization also slow the reaction significantly.

A related cyclization technique is the coupling of two ends of a linear α,ω -heterodifunctional polymer. Deffieux and Schappacher have used this technique extensively for the synthesis of a number of cyclic architectures including monocyclic polymers, bi-cycle figure 8's, and even tri-cyclic compounds from anionic polymerized precursors (4-7). This technique has become extremely popular and has been utilized by numerous of research groups. An efficient synthesis using this technique requires a synthetic design that addresses the two primary synthetic challenges:

- Quantitative modification of the polymer's end groups to activate the coupling reaction, and
- Suppression of the rate of intermolecular coupling with respect to the intramolecular cyclization, typically achieved through extreme dilution.

High yielding end group transformations are particularly attractive because otherwise the cyclization reaction will be incomplete causing the presence of linear impurities. These linear polymers can be challenging to remove, and even small percentages of these non-cyclic impurities can have a detrimental effect on the bulk properties of cyclic polymers.

Control of the concentration of polymer during the cyclization is also vital in order to yield high purity macrocyclics. More concentrated solutions favor the bimolecular oligomerization reaction while more dilute solutions favor the unimolecular cyclization reaction (Figure 1). As a result, the key cyclization reaction is typically carried out in a vast excess of solvent to discourage intermolecular oligomerization.

Recently, a number of alternate cyclization techniques have been developed to improve the synthesis of macrocycles without the requirement of high

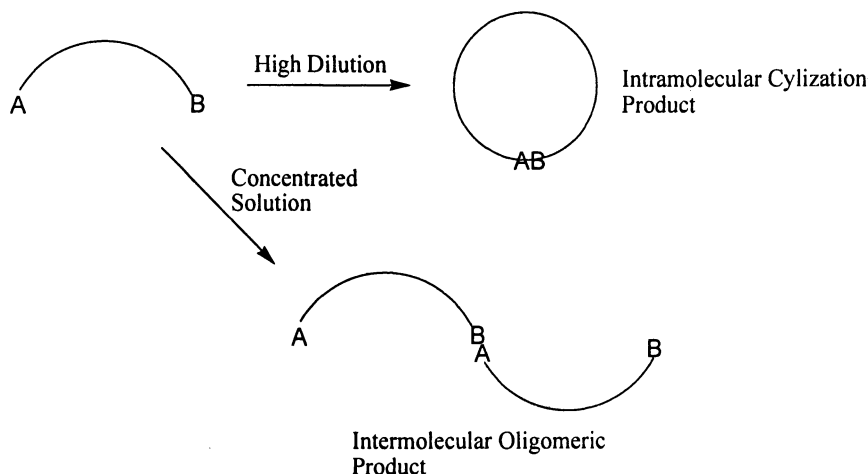


Figure 1. General scheme of the coupling of α,ω -heterodifunctional polymers under dilute or concentrated conditions

dilution. Bielawski *et al.* reported the preparation of well-defined macrocycles employing a “cyclic” ruthenium ring opening metathesis polymerization (ROMP) catalyst to produce macrocyclic hydrocarbon type polymers (8). Shea *et al.* utilized ring expansion of cyclic boranes in which a methylene type ylide inserts itself into the carbon-boron bond thus expanding the cyclic initiator (9). Ring expansion utilizing the insertion of strained lactones into cyclic dibutyltin initiators has also been reported by Kricheldorf *et al.* (10). And most recently, using a cyclic dithiocarbonyl type initiator, He *et al.* synthesized cyclic poly(methyl acrylate) polymers through a radical polymerization mechanism (11). The authors attribute this system’s utility to the fact that the formed radical does not diffuse quickly enough through the monomer solution to react with other active radical chains. Instead the formed radical reacts with monomer and is sequentially “trapped” by the initiating dithiocarbonyl radical when the reaction is performed at temperatures low enough to ensure minimal diffusion (-30 °C).

Synthetic Design

While these techniques demonstrate a variety of cyclization methods not requiring linear precursors, most of these methods have drawbacks, including the use of only very specialized monomers and the poor control of product molecular weight and polydispersity. The limited compatibility with functional

monomers is particularly disappointing, since functionalized cyclic macromolecules are expected to have a range of useful applications. Therefore, our efforts to prepare functionalized macrocycles has focused on the cyclization of α,ω -heterodifunctional precursors. Ideal systems for preparing functionalized linear precursors are controlled radical polymerization (CRP) methods such as atom transfer radical polymerization (ATRP), nitroxide-mediated polymerization (NMP), and radical addition fragmentation chain transfer polymerization (RAFT). These techniques provide polymers with controlled molecular weights and low polydispersities, but most importantly, enable the use of diverse functional monomers since they demonstrate a significantly wider range of functional group tolerance than traditional cationic or anionic polymerizations. Of these techniques, ATRP polymerization seems the best candidate for preparing cyclic polymers because the resultant polymer contains a terminal bromide end group which can be easily converted into a variety of other functional groups (12).

Typically for polymer substrates, highly efficient reactions must be utilized to afford quantitative transformations. This low reactivity can be attributed to steric bulk of the polymer shielding of the intended site of reaction. Therefore, we have envisioned using a high-conversion “click”-type cyclization reaction, specifically the copper-catalyzed Huisgen cycloaddition of a terminal alkyne and azide to yield a 1,2,3-triazole (13). Recently, “click” chemistry has become extremely popular in the polymer field due to its simplicity, high efficiency, and suppression of side reactions. The utility of the Huisgen cycloaddition in building complex architectures has been demonstrated in the synthesis of dendrimers, block copolymers, dendronized linear polymers, and even in doubly dendronized linear systems (14-18). The triazole linkages provide the additional advantage that their hardness will decrease the likelihood of undesired ring openings. Previous coupling techniques presented in the literature afforded relatively labile cyclic acetals, esters, and amides, as the vital linkage, all of which are prone to hydrolysis in either acidic or basic media.

Since ATRP polymerization yields a polymer with a terminal bromide moiety, this provides an ideal substrate for nucleophilic conversion to the requisite azide. The complimentary alkyne group necessary for “click” cyclization can then be incorporated into the initiating group. Poly(styrene) was selected for model studies because it provides an ideal substrate for this transformation as the terminal bromide is benzylic, and therefore highly activated towards nucleophilic substitution with sodium azide.

In order to prevent the use of a large excess of organic solvent, a slow addition technique via syringe pump was employed (19). This has been shown to favor intramolecular coupling over intermolecular reactions and avoids the complications involved with the isolation of the polymer from excess solvent. This method allows for the infinitesimal dilution of the polymer as it is sequentially added to the catalyst solution, thus keeping the concentration of linear, uncoupled α,ω -heterodifunctional polymer to a minimum. If the polymer

solution is added at an appropriately slow rate and the reaction vessel stirred vigorously, each drop will be diluted to a near infinitesimal concentration enabling the near quantitative formation of cyclic polymers before the next drop is added. Once the intramolecular coupling has been accomplished, the resultant macrocycle should become inert and not interfere with subsequent cyclizations. This process is continually repeated for the duration of addition as long as the catalyst solution remains active.

By using this technique, small amounts of the α,ω -heterodifunctional polymer can be added at a pre-specified rate into a dilute solution of Cu(I) catalyst. The rate of addition (mL/hr) can also be meticulously controlled via syringe pump, thus enabling the direct comparison of the cyclization results from different addition rates and experimental conditions.

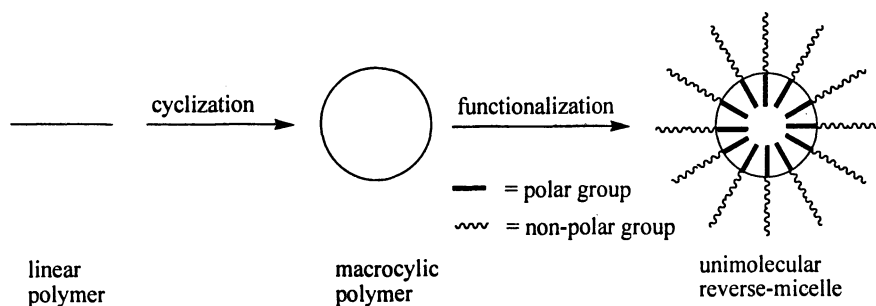


Figure 2. General method for the synthesis of unimolecular reverse micelles from linear polymer precursors.

Cyclic polymers should be an excellent substrate for the preparation of invertible unimolecular micelles (Figure 2). Traditional micelles are formed in solution as a thermodynamic minima resulting from the self-assembly of surfactant type amphiphilic molecules. Because of this self-assembly process, they are subject to two significant limitations:

- The micelle structure is only stable in a certain concentration regime, and dilution below the critical micelle concentration leads to disaggregation.
- The self-assembly is controlled by inherent properties of the amphiphiles, making it difficult to tune the size and shape of the resultant micelles.

Both of these problems limit their application for a range of biomedical applications, but can be addressed by using unimolecular micelles, micelle-like structures that are covalently linked to prevent disaggregation. In particular, if a bifurcated amphiphile is attached to each repeat unit of a cyclic polymer, (Figure 3) a unique architecture is afforded that will adapt to its environment. For

example, in the presence of a non-polar solvent, the non-polar chains would extend out into the hydrophobic medium in order to solvate the molecule while the polar chains would point inwards in order to minimize interaction with the non-polar solvent. If the solvent polarity is significantly increased, the system will invert with polar groups facing outward from the core and the non-polar groups oriented inward. Because ATRP demonstrates exceptional functional group tolerance as well as excellent molecular weight control, the size as well as the functionality of the unimolecular micelles can be tuned to address each potential application.

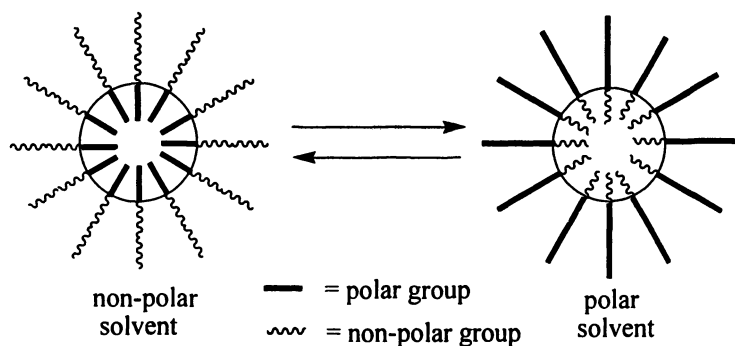


Figure 3. Behavior of invertible unimolecular micelles in both polar and non-polar solvents.

Results

Cyclic poly(styrene) was synthesized by coupling the end groups of an α -alkynyl- ω -azido poly(styrene) (Figure 4). In order to incorporate the alkynyl functionality on the initiating end of the polymer chain, an alkynyl ester was synthesized by esterification of 2-bromoisobutyryl bromide with propargyl alcohol. The resultant tertiary bromide ester was used to initiate styrene polymerization using ATRP. ATRP of styrene was performed using traditional conditions with a Cu(I)Br catalyst using *N, N, N', N'', N'''*-pentamethyldiethylenetriamine (PMDETA) as the ligand at 75 °C. This technique produced polymers of controlled molecular weight and relatively low polydispersity (PDI) after extraction from water into dichloromethane followed by precipitation into an excess of methanol. The presence of the terminal benzyl bromide was verified by ¹H-NMR (4.3-4.7 ppm). The terminal benzylic bromide was successfully converted to the terminal azide by reaction with an excess of sodium azide (NaN₃) in *N,N*-dimethyl formamide (DMF). The

quantitative nature of this reaction could be verified by the disappearance of the benzyl bromide protons (4.3-4.7 ppm) and the appearance of the benzyl azide protons (4-4.5 ppm) in the $^1\text{H-NMR}$ spectra as shown in Figure 5 (20). Additional proof of this transformation was provided by the appearance of the azide stretch in the infrared spectrum (2100 cm^{-1}) in Figure 6. As expected, no change in the retention time or the polydispersity of the two polymers in the gel permeation chromatograms was seen.

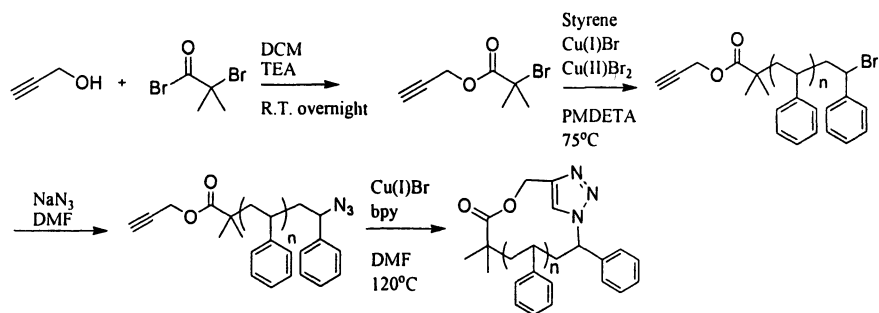


Figure 4. Synthetic scheme for the preparation of macrocyclic poly(styrene) via ATRP polymerization and "click" coupling.

As was previously mentioned, the polymer concentration of linear precursors is the most important factor in a post-polymerization cyclization to form high-purity polymer macrocycles. To probe the effect of precursor concentration, the concentration of polymer in solution as well as the rate of addition to the catalyst solution was varied. GPC was crucial in the characterization of the relative amounts of both cyclic and oligomeric product. Since GPC separates components based upon size in solution, cyclic polymers should have a predictably different retention times from their linear counterparts. This can be attributed to smaller hydrodynamic volume of the cyclic polymers when compared to linear polymers of same molecular weight, a consequence of the "locked" smaller configuration of the cyclic polymer. As a result the cyclic polymers demonstrate a longer retention time due to their smaller perceived molecular size. The linear precursors are then expected to have a shorter retention time, whereas higher molecular weight oligomers will demonstrate the shortest retention time.

When attempting to optimize conditions, cyclizations reactions were performed by varying the concentration of polymer in solution, the concentration of Cu(I) catalyst in solution, and the temperature of reaction. The crude polymer solutions were then extracted out of water into dichloromethane, washed with a

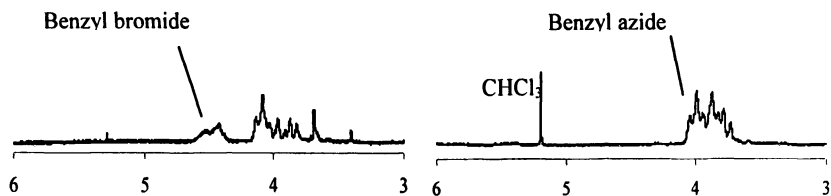


Figure 5. $^1\text{H-NMR}$ spectra indicating the resonances of the terminal benzyl bromide protons (left) and the terminal benzyl azide protons (right).

large volume of aqueous NaHSO_4 , and then precipitated into an excess of methanol. The polymer samples were then analyzed by GPC in order to determine the relative ratios of cyclic and oligomeric polymer.

An initial attempt to form of cyclic poly(styrene) was performed by addition of a 10 mM linear precursor solution at a rate of 0.4 ml/min into a solution of the Cu catalyst at 40 °C resulting in a final polymer concentration of 0.36 mM. While the GPC chromatograph clearly shows that cyclic product was favored under these conditions, (Figure 7) there is still a large amount of oligomeric product present in the reaction mixture. As a result, the reaction conditions were altered to reduce the oligomeric by-product. If the rate of the “click” reaction is slower than the addition of the precursor, then the concentration of the unreacted precursor will build-up causing to formation of oligomer; however, if the rate of the “click” reaction is faster than the rate of dilution, a localized high concentration of precursor can also form oligomers. To increase the rate of the “click” cyclization, the concentration of the copper was increased, as was the temperature of the reaction. But to expedite dilution, the concentration of the polymer solution being added via syringe pump was diluted, and the volume of copper solution to which it was added was increased.

Optimization of these four variables led to a successful procedure which utilized a 2.2 mM solution of the linear precursor dissolved in DMF added via syringe pump at a rate of 0.2 mL/hr to 110 ml of a 9 mM solution of Cu(I)Br in DMF at 120 °C. The above mentioned conditions were used to successfully cyclize poly(styrenes) of M_n 2200 and 4200 Da yielding cyclic polymers with PDI values less than 1.2 (21). The GPC chromatographs of each of these cyclic and linear precursors are shown in Figures 8 and 9 respectively. It is evident from these chromatograms that the cyclic polymers indeed have the predicted increase in retention time compared to their linear counterparts. The resultant cyclized polymers were further characterized using matrix assisted laser desorption ionization-time of flight mass spectroscopy (MALDI-TOF MS.) The molecular weights determined by this technique were identical for both the linear and cyclized samples confirming that the molecular formula remained unchanged

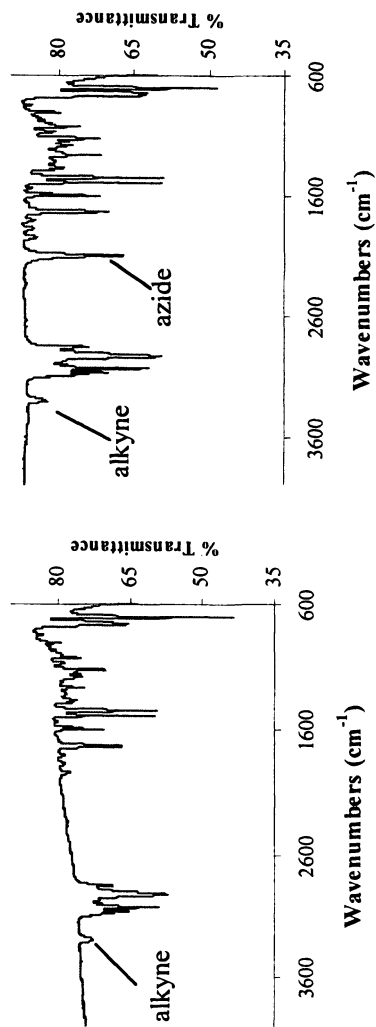


Figure 6. IR spectra of the terminal bromide (left) and terminal azide (right.)

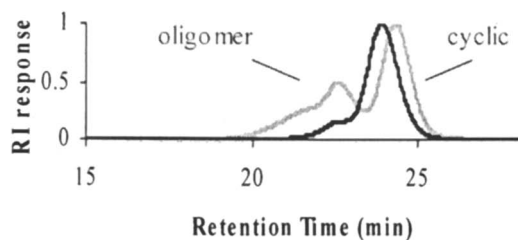


Figure 7. GPC chromatogram of linear polystyrene (black) and a mixture of cyclic and oligomeric product (gray) after an unoptimized cyclization.

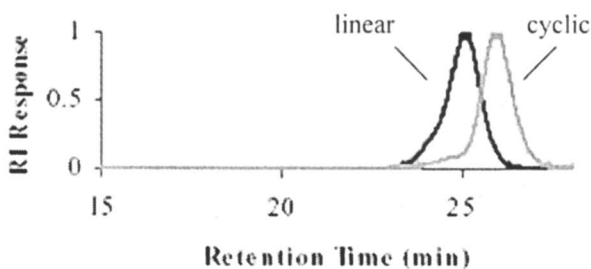


Figure 8. GPC chromatogram of linear (black) and cyclic (gray) poly(styrene) of $M_n = 2200$ Da.

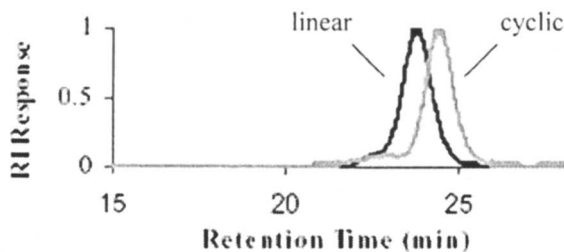


Figure 9. GPC chromatogram of linear (black) and cyclic (gray) poly(styrene) of $M_n = 4200$ Da.

during this transformation (Figure 10). Further verification of the cyclization was apparent from the IR spectra in which both the alkyne C-H stretch and the azide $-N_3$ stretch disappeared upon reaction, suggesting near quantitative transformation to the triazole.

In each of the two GPC chromatograms, it can clearly be seen that near quantitative yields of cyclic polymer have been produced. This method has been reproduced with numerous polymers of similar molecular weights. Currently in our laboratories, we are exploring the limitations of this technique. A number of larger molecular weights are currently being investigated in order to define size limitations to the cyclization procedure. Also underway in our laboratories is the attempted synthesis of non-styrenic type polymers (e.g. acrylates). It is thought that this "click" cyclization technique should be general if the required α,ω -heterodifunctional polymers can be prepared.

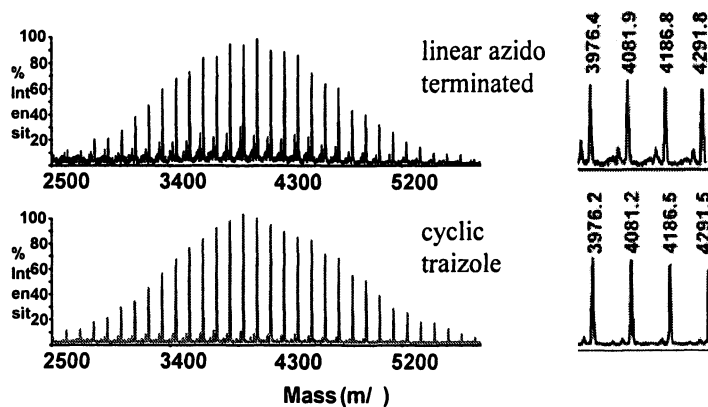


Figure 10. MALDI-TOF mass spectra indicating no change in molecular weight upon transformation from linear to cyclic polymers.

This methodology has also been extended to 4-acetoxystyrene, which was successfully polymerized with a Cu(I) catalyst with bipyridine as the ligand (22). The resultant 2700 Da bromide terminated polymer was then successfully converted to the azide and cyclized using analogous reaction conditions as used for styrene cyclization (Figure 11). The deprotection of poly(acetoxystyrene) was carried out in a 1.5 M solution of KOH in a 1:1 water / methanol solution for 12 hours at room temperature. This transformation was verified by the complete loss of the acetate protons in the $^1\text{H-NMR}$ (2.15 ppm).

The synthesis of cyclic poly(hydroxystyrene) is extremely important as it provides a hydroxyl group on each monomer that can be easily modified to attach a range of functional moieties. Recently in our labs (23), we have

demonstrated the esterification of each hydroxyl unit using the benzylidene protected acid anhydride of bis(hydroxymethyl) propanoic acid (Figure 12). Removal of the benzylidene protecting groups enables attachment of subsequent generations of dendrons through repeated esterification and deprotection steps. This technique has been proven to work effectively on the corresponding linear analogues (24, 25) and yields a unique toroidal polymer architecture. Additional work in our labs is presently investigating the attachment of bifurcate amphiphiles to afford the unique invertible unimolecular micelle architecture.

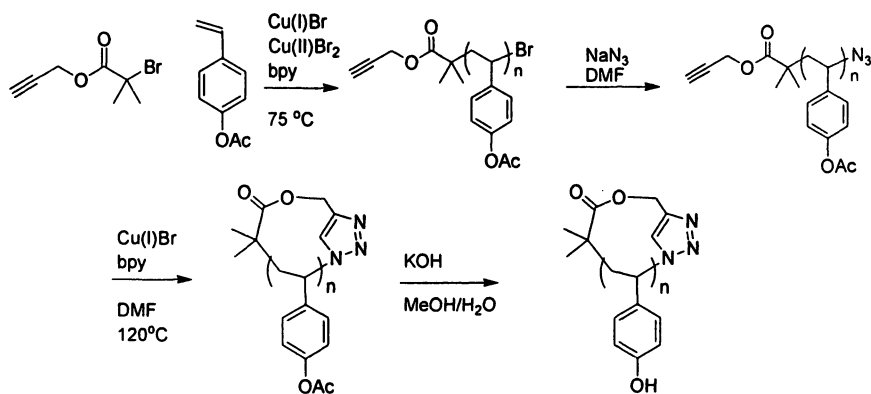


Figure 11. Synthetic scheme for the preparation of cyclic poly(4-acetoxystyrene) and its hydrolysis to yield cyclic poly(hydroxystyrene).

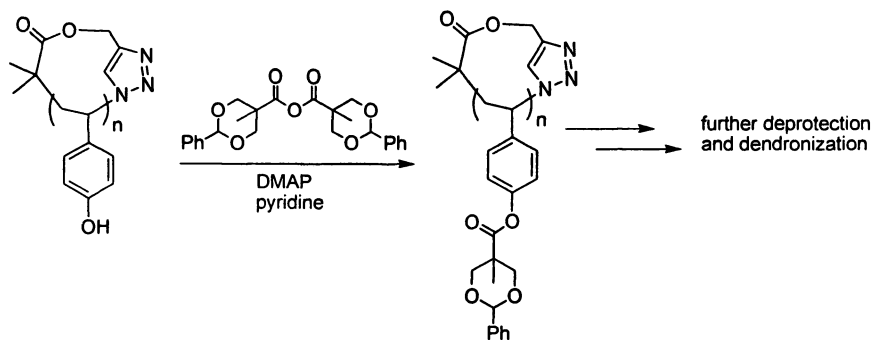


Figure 12. Synthetic methodology for the functionalization of cyclic poly(hydroxystyrene).

Conclusions

The Huisgen “click” cycloaddition reaction has been explored for the cyclization of linear poly(styrene) precursors prepared by ATRP. Using an optimized slow, continuous addition technique, nearly quantitative yields of the cyclic polymer can be achieved without the need for fractionation or further purification. The versatility of ATRP provides extremely well defined linear precursors and enables the incorporation of diverse functionality. As a demonstration of this versatility, acetoxystyrene was polymerized, cyclized, and hydrolyzed to yield macrocyclic poly(hydroxystyrene). This cyclic polymer is extremely useful as the phenols on each repeat unit can be easily modified to incorporate further functionality, such as the quantitative esterification described. We are currently investigating the attachment of bifurcated amphiphiles in order to synthesize the target invertible unimolecular micelle. The cyclization technique described is believed to have broad application for preparing a wide range of functionalized macrocycles.

References

1. J.A. Semylen, *Cyclic Polymers*, Kluwer Academic, Dordrecht, The Netherlands, ed. 2, 2000.
2. Roovers, J.; Toporowski, P. M. *Macromolecules* **1983**, *16*, 843-849.
3. Hadjichristidis, N.; Pitsikalis, M.; Pispas, S.; Iatrou, H. *Chem. Rev.* **2001**, *101*, 3747-3792.
4. Schappacher, M.; Deffieux, A. *Macromolecules* **2001**, *34*, 5827-5832.
5. Beinart, S.; Schappacher, M.; Deffieux, A. *Macromolecules*, **1996**, *29*, 6737-6743.
6. Schappacher, M.; Deffieux, A. *Macromolecules*, **1995**, *28*, 2629-2636.
7. Schappacher, M.; Deffieux, A. *Macromolecules*, **1992**, *25*, 6744-6751.
8. Bielawski, C. W.; Benitez, D.; Grubbs, R. H. *J. Am. Chem. Soc.* **2003**, *125*, 8424-8425.
9. Shea, K. J.; Lee, S. Y.; Busch, B. B. *J. Org. Chem.*, **1998**, *63*, 5746-5747.
10. Kricheldorf, H. R.; Lee, S. *Macromolecules* **1995**, *28*, 6718-6725.
11. He, T.; Zheng, G. H.; Pan, C. *Macromolecules* **2003**, *36*, 5960-5966.
12. Lutz, J. F.; Börner, H. G.; Weichenhan *Macromol. Rapid Comm.* **2005**, *26*, 514-518.
13. Rostovtsev, V. V.; Green L. G.; Fokin V. V.; Sharpless, K. B. *Angew. Chem. Int. Ed.* **2002**, *41*, 2596-2599.
14. Wu, P.; Feldman, A. K.; Nugent, A. K.; Hawker, C. J.; Scheel, A.; Voit, B.; Pyun, J.; Fréchet, J. M. J.; Sharpless, B.; Fokin, V. V. *Angew. Chem. Int. Ed.* **2004**, *43*, 3928-3932.

15. Joralemon, M. J.; O'Reilly, R. K.; Matson, J. B.; Nugent, A. K.; Hawker, C. J.; Wooley, K. L. *Macromolecules* **2005**, *38*, 5436-5443.
16. Opsteen, J. A.; van Hest, J. C. M. *Chem. Comm.* **2005**, 57-59.
17. Helms, B.; Mynar, J. L.; Hawker, C. J.; Fréchet, J. M. J. *J. Am. Chem. Soc.* **2004**, *126*, 15020-15021.
18. Mynar, J. L.; Choi, T. L.; Yoshida, M.; Kim, V.; Hawker, C. J.; Fréchet, J. M. J. *Chem. Comm.* **2005**, 5169-5171.
19. Harth, E.; Van Horn, B.; Lee, Y. Y.; Germack, D. S.; Gonzales, C. P.; Miller, R. D.; Hawker, C. J. *J. Am. Chem. Soc.* **2002**, *124*, 8653-8660.
20. Tsarevsky, N. V.; Sumerlin, B. S.; Matyjaszewski, K. *Macromolecules* **2005**, *38*, 3558-3561.
21. Laurent, B. A.; Grayson, S. M. *J. Am. Chem. Soc.* **2006**, *128*, 4238-4239.
22. Gao, B.; Chen, X.; Ivan, B.; Kops, J.; Batsberg, W. *Macromol. Rapid Commun.* **1997**, *18*, 1095-1100.
23. Laurent, B. A.; Grayson, S. M. *Polym. Prepr.* **2006**, *49*(2), 246.
24. Grayson, S. M.; Fréchet, J. M. J. *Macromolecules* **2001**, *34*, 6542-6544.
25. Yoshida, M.; Fresco, Z. M.; Ohnishi, S.; Fréchet, J. M. J. *Macromolecules* **2005**, *38*, 334-344.

Chapter 5

High-Strength, Melt Processable, Aromatic Poly(anhydride)s

Kevin Cooper and Angelo Scopelianos

Center for Biomaterials and Advanced Technologies, Medical Devices Group, A Division of Ethicon Inc., A Johnson & Johnson Company, Route 22 West, Somerville, NJ 08876

A synthetic technique for preparing aromatic poly(anhydride)s with high molecular weights has been developed that yields polymers with high tensile properties and melt processability. The high molecular weight aromatic poly(anhydride)s (inherent viscosities greater than 1.0 dl/g) were prepared by a three-step synthesis in which highly pure aromatic dicarboxylic acids were converted to highly pure dianhydrides followed by high temperature melt polycondensation to form the polyanhydrides. It has been determined that these high molecular weight poly(anhydride)s have excellent thermal stability, are melt processable, yield high strength fibers and molded articles, and are radiation sterilizable.

In the 1930's, Carothers prepared a series of aliphatic poly(anhydride)s for potential use as fibers in the textile industry (1). However, the hydrolytic stability of these materials was very poor. By the mid-1950's, Conix was able to synthesize aromatic poly(anhydride)s with improved film and fiber forming properties (2). Despite these properties, the polyanhydrides' poor thermal and hydrolytic stability resulted in their limited use, and no commercial applications were found. By the late 1960's, however, hydrolytic instability became an important factor for polymers utilized in the manufacture of medical devices such as absorbable sutures and drug delivery systems.

By the early 1970's, Domb and Langer determined that not only were aromatic poly(anhydride)s hydrolytically unstable, but under certain circumstances followed zero-order drug release breakdown kinetics via surface erosion (3a,b). This, along with the fact that aromatic poly(anhydride)s have been shown to degrade into monomeric diacids which are highly biocompatible, led to their use as matrices for controlled delivery of biologically active substances. However, due to the low molecular weights, degradation and gelation as well as poor thermal stability and melt processability, Domb and Langer's aromatic poly(anhydride)s have been restricted to the narrow field of drug delivery, where microspheres of the drug in the polymer matrix can be prepared at low (ambient) temperatures utilizing solvent casting techniques.

High molecular weight, thermally stable, melt processable aromatic poly(anhydride)s are required for biomedical devices such as staples, clips, and sutures since superior mechanical properties are a necessity for good product results. Good polymer mechanical properties are a requirement for certain biomedical devices such as staples, clips, and sutures. These devices are advantageously made by traditional melt processing techniques such as injection molding or fiber extrusion. To be able to achieve the high mechanical properties required, the polymer must generally be high molecular weight. To utilize melt processing fabrication techniques, the resin must have excellent melt stability; that is to say it must not degrade at temperatures at which it can be rendered molten. We describe in this work the preparation of high molecular weight aromatic poly(anhydride)s that exhibit excellent melt stability and have been fabricated into high strength test articles. In addition, in-vitro experimental evidence is provided that strongly suggests that materials may provide higher in-vivo strength retention than is possible with bulk erosion bioerodible polymers such as poly(glycolide).

Also, since the practice of sterilization of biomedical devices by ethylene oxide is diminishing due to concerns for the environment, along with health and safety factors, it may also be necessary for future biomedical devices to be irradiation sterilizable (i.e., Cobalt/gamma, E-beam). From work at Ethicon on polymers with aromatic substituents in the backbone (4a,b), it is believed that aromatic groups lead to an enhancement in the radiation stability of a polymer.

Therefore, aromatic poly(anhydride)s may prove useful for their potential as irradiatable devices.

Despite the desirability of such a polymer, the development of high molecular weight (I.V. >1.0 dl/g), non-crosslinked, non-gel forming, bioerodible aromatic poly(anhydride)s incorporating these properties has not progressed. This report describes for the first time a process for preparing high molecular weight (I.V. > 1.0 dl/g), non-crosslinked, non-gel forming, high strength, thermally stable, melt processable and irradiation sterilizable, aromatic poly(anhydride)s.

In detail, a synthetic technique for preparing aromatic poly(anhydride)s with high molecular weights, as characterized by inherent viscosities, in excess of 1.0 dl/g in chloroform at room temperature (25°C) has been developed. In this synthetic process, the high molecular weight aromatic homo or copoly(anhydride)s (I.V. > 1.0 dl/g) were prepared by a three-step synthesis. The high molecular weight aromatic poly(anhydride)s were synthesized from highly pure aromatic dianhydrides that were prepared from highly pure aromatic dicarboxylic acids. The highly pure dicarboxylic acid was formed in the first step by a nucleophilic substitution reaction between a hydroxybenzoic acid and a dibromoalkane. Batch sizes of up to half a kilogram have been prepared. Once a salt free product was obtained it was then further purified by three recrystallizations with N-methylpyrrolidinone (NMP) or dimethylacetamide (DMAC). The highly pure aromatic dicarboxylic acid was then refluxed with acetic anhydride for several hours to form a highly pure aromatic mixed anhydride. This was followed by recrystallization with acetic anhydride, isolation and drying. Batch sizes of up to 150 grams have been prepared by this method. The isolated, pure, dry mixed anhydride was then polymerized under melt condensation conditions at temperatures between 180°C and 240°C for a time of 90 to 360 minutes utilizing high vacuum (<20 microns). Batch sizes of up to 60 grams have been prepared by this technique. In the examples, higher molecular weight (I.V. > 1.0 dl/g), non-crosslinked, non-gel forming, aromatic poly(anhydride) homo and co-polymers are prepared from monomers 1,6-bis(p-carboxyphenoxy)hexane, 1,4-bis(pcarboxyphenoxy)butane, and 1,2-bis(p-carboxyphenoxy)ethane. It was also determined that some of the high molecular weight poly(anhydride)s display a linear decrease in breaking strength, while all showed excellent thermal stability and melt processability. They also exhibit excellent radiation stability and have yield strengths similar to or greater than that of poly(p-dioxanone) molded articles.

Results and Discussion

The preparation of poly(anhydride)s can be considered a three-step process in which an aromatic dicarboxylic acid is formed in the first step followed by the

preparation of a mixed anhydride which is then melt polymerized by a method initially described by Carothers (1). This method was then modified by Domb and Langer (3,5).

From the methods described by Domb and Langer, high molecular weight (I.V. > 1.0 dl/g) aliphatic poly(anhydride)s have been prepared. However, only low molecular weight (I.V. < 0.55 dl/g) fully aromatic homo and co-poly(anhydride)s can be synthesized by Domb and Langer's methods, due to the formation of a rubbery gel, which swells extensively in chloroform. This is explained by a depolymerization process during extensive heating that yields entangled cyclic macromers (3a). Domb and Langer state that the depolymerization process occurs at longer polymerization times and higher polymerization temperatures. Consequently, it was believed that high molecular weight (I.V. > 1.0 dl/g) fully aromatic homo and co-poly(anhydride)s could not be prepared due to the longer reaction times and higher reaction temperatures necessary to polymerize the higher glass/melting transition aromatic poly(anhydride)s.

In the results described herein, it has been determined that high molecular weights can be obtained for aromatic homo or co-poly(anhydride)s if high purity monomers are utilized along with higher melt polymerization temperatures and longer reaction times.

Hence, it was concluded that the dicarboxylic acid prepared in the first step of the three-step polymerization synthesis must be of the highest purity (99.9%). This was successfully established by first preparing an "ash free", salt free acid product (Example 1). The salt free monomer was prepared by suspending the highly insoluble sodium salt in a strongly acidic aqueous solution. This procedure was repeated one to two more times, since it was found that 10 to 15 percent ash remained after one treatment (Elemental analysis, Table 1).

Once ash free monomer had been prepared, the dicarboxylic acid was purified by three recrystallizations using N-methylpyrrolidinone (NMP) or dimethylacetamide (DMAC) as a solvent (Examples 1 and 4). This was necessary, since it was determined by NMR that the purity after the first and second recrystallizations was not polymer grade. It was also necessary to wash the purified acid monomer after the third recrystallization with hot, distilled water to remove NMP bound to the acid.

However, as can be seen in Example 4, recrystallization with DMAC yielded a complex of the solvent bound to the acid which could not be removed by washing with hot water (Table 1). Nevertheless, high molecular weights were obtained (Table 2). This will be discussed in greater detail in later descriptions. Whether the purified acid was recrystallized with NMP or DMAC, it was washed in the final preparation step with acetone for ease of drying.

In contrast, Domb and Langer prepared the bis(p-carboxyphenoxy)alkanes according to the method described by Conix (6) and purified by extraction with ether before use, leaving the monomers impure (Example 8). It would appear

Table 1. Carbon, Hydrogen and Nitrogen elemental analysis of bis-1,n-(p-carboxyphenoxy)alkane aromatic acids

Aromatic Acid	Recrystallization Solvent	Theoretical			Found*		
		C	H	N	C	H	N
1,6-NMP Complex	NMP	63.1	7.51	5.26	62.76	7.46	5.44
1,6-Free Acid	NMP	67.0	6.19	0	66.92	6.11	0
1,4-Free Acid	NMP	65.4	5.48	0	65.06	5.42	0

*Swarzkopf Microanalytical Labs

Table 2. Inherent Viscosities of poly[1,6-bis(carboxyphenoxy)hexane anhydride] as a function of time (minutes) at a reaction temperature of 200°C

Experiment	Recrystallization Solvent	120 ^a	160 ^a	200 ^a	240 ^a
A	NMP	1.1 ^b			
B	NMP		1.2 ^b		
C	NMP		1.4 ^b		
D	NMP			1.3 ^b	
E	DMAC		1.1 ^b		
F	DMAC			1.3 ^b	
G	DMAC				1.3 ^b

^aReaction Time (minutes), ^bInherent Viscosity (dl/g)

that impurities remaining after this process partially contribute to the lower molecular weight (I.V. < 0.5 dl/g) aromatic bis(p-carboxyphenoxy)alkane poly(anhydride)s synthesized in the past. We have repeated this procedure, and have found our molecular weights to be less than 0.3 dl/g, similar to Domb and Langer's results (Table 7). As expected, the results indicate that purification by recrystallization with NMP leads to higher molecular weights at a reaction temperature of 180°C (I.V. > 0.60 dl/g). Purification by washing with a non-solvent (acetone/ether, i.e., Domb's method) leads to low molecular weights (0.2 to 0.3 dl/g), even at higher reaction temperatures (200°C). Therefore, by purifying the acid and using higher reaction temperatures and longer reaction times, it is possible to obtain much higher molecular weights.

Once our purified dicarboxylic acid monomer had been synthesized, isolated and purified, the mixed anhydride was prepared (Examples 2 and 5). The mixed anhydride is synthesized by reacting acetic anhydride with the acid monomer at reflux for several hours under a nitrogen atmosphere followed by removal of a portion of the acetic anhydride. The homogeneous solution was then allowed to crystallize at 0°C overnight, filtered, and then washed with dry ethyl ether to remove traces of acetic anhydride. The mixed anhydride was then filtered, and dried for 24 hours at low temperature (50°C) under vacuum to yield the highly pure anhydride monomer. Recrystallization with acetic anhydride was also performed (Example 5).

Domb and Langer state that the acid monomer is refluxed in acetic anhydride for 15 minutes and then the unreacted diacid (10-20%) was removed by filtration (3a). As discussed above, it is unclear as to the quantity of trace amounts of the impurity, the diacid, that might remain after filtration (Example 8). This would lead to an anhydride monomer that is impure and, therefore, cannot be polymerized to high molecular weight.

Our isolated, pure, dry mixed anhydride was then polymerized under typical melt condensation conditions, utilizing elevated temperatures (200°C to 220°C) under high vacuum with reaction times ranging from 90 to 360 minutes. Under these conditions, high molecular weights (Examples 3, 6 and 9) were formed.

Domb and Langer stated that polymerizing at temperatures above 180°C for greater than 150 minutes not only leads to the formation of insoluble gel, but a decrease in molecular weight with the formation of insoluble gel through a depolymerization process that yields cyclic macromers.

No decrease in molecular weight or the formation of insoluble gel was observed with our aromatic poly(anhydride) polymerizations at even higher temperatures (i.e., 200 to 220°C). NMR and FT-IR also indicates no formation of branching, crosslinking or degradation side products (Figure 3). Inherent viscosities as high as 1.4 dl/g (Tables 2 and 7, Figure 5) were found. This clearly indicates that high molecular weight (I.V. > 1.0 dl/g) aromatic homo and co-poly(anhydride)s can be synthesized. In fact, recrystallization of the anhydride monomer (Example 5) along with the recrystallization of the diacid by

DMAC (Example 4), also leads to high molecular weights (Table 2) without the formation of gel or crosslinking.

To examine the potential of these high molecular weight aromatic poly(anhydride)s for melt processing methods such as injection molding and melt extrusion, melt stability measurements were made. Typically the resin was introduced and packed into the barrel of a capillary rheometer at a temperature just below the melting point of the resin. The barrel temperature setting was then reset and quickly brought up to the test temperature, while continuing to lower the piston to facilitate packing. A clock was started as soon a set temperature was reached. With a die diameter and piston speed combination selected to result in a shear rate of about 100 sec^{-1} , piston travel was activated (once the barrel had equilibrated to the test temperature) to obtain an initial viscosity measurement. Once a value was obtained, the piston travel was arrested and the remaining polymer melt was allowed to reside in the temperature-controlled rheometer barrel. After about 10 minutes, the piston travel was again reactivated and a second measurement made. This start-and-stop procedure was employed until at least six data points were obtained over the course of about one hour. A plot of log melt viscosity versus total residence time in the barrel at the test temperature was found to be linear. The slope value was used to calculate the percent change in melt viscosity with unit time. A cone and plate rotational rheometer was often employed with similar results. Melt viscosity (i.e., molecular weight) remained constant over a one-hour period under an inert, dry nitrogen atmosphere at 220°C (Figure 5). This is a strong indication that degradation/gelation does not occur at processing temperatures above 200°C . This had not been previously established for aromatic poly(anhydride)s.

Additionally, monofilament fibers were produced using a capillary rheometer as an extruder. The ground resin was introduced and packed into the barrel as described above. Typically a 40-mil die with an L/D of 25 was used. A piston speed was selected to result in a shear rate of 236 sec^{-1} . The extrudate was passed through an ice-water quench bath and subsequently collected on a roll at constant speed. A jet-stretch of about 4 was used to get an extrudate diameter of about 20 mils. The spool of extrudate was typically placed into a vacuum oven for drying and storage purposes. To develop mechanical strength in the fiber, molecular orientation was imparted by drawing the extrudate. The fiber was stripped from a supply spool at constant speed using a first set of pinch rollers. The fiber was then directed by a series of rollers into a glycerin bath heated to a preset temperature; since the fiber was passed through a second set of pinch rollers rotating at a higher speed, a draw tension was established that caused permanent deformation of the fiber. The deformation, or drawing, occurred in the glycerin bath. The draw ratio can be calculated by dividing the linear speed of the fiber exiting the bath by the linear supply speed. The exiting fiber was in-line water-washed and subsequently dried and stored under vacuum.

If the fiber was annealed, it was racked wound and heated under nitrogen at the annealing temperature.

Using the above conditions at an extrusion temperature of 250°C, and a shear rate of 236 sec⁻¹, a poly[1,4-bis(p-carboxyphenoxy)butane] resin displayed a melt viscosity of approximately 28,000 poise. The 18 to 19.5 mil diameter monofilament extrudate was taken-up through an ice-water quench and subsequently drawn 4X at 100°C resulting in a 9.6 mil fiber (Table 3). This fiber was subjected to a higher temperature (105°C) second-stage draw at 1.105X resulting in slightly higher strength and lower elongation.

A sample of poly[1,4-bis(p-carboxyphenoxy)butane-co-1,6-bis(p-carboxyphenoxy)hexane] exhibiting a melting point of 170°C was extruded using similar conditions as described above. Using an extrusion temperature of 270°C, and a shear rate of 236 sec⁻¹, the resin displayed a melt viscosity of approximately 11,000 poise. The monofilament extrudate was taken-up through an ice-water quench. The extrudate was subjected to a two-stage drawing process, 5X at 84°C immediately followed by 2X at 112°C resulting in an 8.1 mil fiber. This 10X fiber was subjected to a further draw at 1.368X conducted at 106°C, again resulting in slightly higher strength and lower elongation (Table 3).

Cylindrical dumbbells were also prepared at high temperatures (220 to 260°C) utilizing a CSI Mini-max small injection molder to determine baseline as well as in-vitro (pH=7.27, 37°C) physical properties. For example, the poly[bis-1,6(p-carboxyphenoxy) hexane anhydride], 1,6 PA, was processed at 220°C. 1,6 PA processed at 220°C, was still soluble (i.e., no gelation), and had no observable changes in chemical structure as determined by NMR (Figure 4).

The mechanical properties as well as in-vitro testing of cylindrical dumbbells were also studied (Tables 4-6 and 8-14). As can be seen from the tables, the yield strength and modulus of the aromatic poly(anhydride)s developed by the methods described herein are similar to or greater than poly(p-dioxanone), an absorbable polyester used extensively for medical devices, and poly(anhydride)s described by other researchers. This is another indication that the aromatic poly(anhydride)s have the high molecular weights (I.V. > 1.0 dl/g), and consequently, the high strengths required in wound closure devices.

As stated earlier, it was believed that aromatic poly(anhydride)s would be cobalt sterilizable since previous work at Ethicon (4a,b) established that incorporation of aromatic substituents in the polymer backbone yielded irradiation stability.

Consequently, test coupons of the aromatic poly(anhydride)s were subjected to cobalt (gamma) irradiation. No loss in the strength or modulus was observed. Also, no observable chemical structural changes were found by NMR (Figure 6). Molecular weight (I.V.) and solubility was also unchanged for coupons (Table 4). Therefore, it has been established that our aromatic poly(anhydride)s can be cobalt irradiated without loss in physical properties, molecular weight (I.V.), solubility, or changes occurring in chemical structure (NMR).

Table 3. Fiber Tensile Properties of Aromatic Poly(anhydride)s as a Function of Draw Ratio

PA	Draw Ratio	Dia. (mil)	Straight Tensile Str. (kpsi)	Knot Tensile Str. (kpsi)	Young's Modulus (kpsi)	Elong to Break (%)
1,4	4X	9.6	45.45	33.57	363	26
	4.42X	8.8	52.12	37.65	339	14
1,4-co-1,6	10X	8.1	52.20	29.30	374	38
	13.68X	6.7	57.06	40.84	394	23

Table 4. Physical properties of annealed of poly[1,6-bis(carboxyphenoxy)hexane anhydride]

	Tensile Strength (psi)	Elongation@ Yield (%)	Tensile Modulus (psi)	Strength Retained (%)
Unannealed	4500	9.5	44000	---
Annealed*	5600	7	76000	---
1 wk in-vitro	5000	6.6	75500	88
3 wk in-vitro	3700	5.8	58000	66
6 wk in-vitro	2100	3.2	43000	35
Annealed, Irradiated (2.5Mrad)	5900	6	75000	100
Irradiated, 1 wk in-vitro	6200	8	77500	100
Irradiated, 3 wk in-vitro	5100	6.3	70000	85
Irradiated, 6 wk in-vitro	2500	3.6	39000	42

*Annealing 85°C/6hrs., data an avg. of 8-12 cylindrical dumbbells

Table 5. Physical properties of unannealed of poly[1,4-bis(carboxyphenoxy)butane anhydride]

	Tensile Strength (psi)	Elongation@ Yield (%)	Tensile Modulus (psi)	Strength Retained (%)
Unannealed	7400	11.5	76000	---
1 wk in-vitro	6300	9.3	77000	85
3 wk in-vitro	6700	9.6	79000	90
6 wk in-vitro	5400	8.7	58000	73
9 wk in-vitro	1800	3	52000	24
Unannealed, Irradiated 2.5Mrad	6500	8	94000	88
Irradiated, 1 wk in-vitro	6500	9.5	79000	100
Irradiated, 3 wk in-vitro	6500	9.2	80000	100
Irradiated, 6 wk in-vitro	4800	6	59000	74
Irradiated, 9 wk in-vitro	2200	3.3	55000	30

Table 6. Physical properties of annealed of poly[1,4-bis(carboxyphenoxy)butane anhydride]

	Tensile Strength (psi)	Elongation@ Yield (%)	Tensile Modulus (psi)	Strength Retained (%)
Annealed	8700	11.1	94000	---
1 wk in-vitro	7000	9	94000	80
3 wk in-vitro	4500	6	72000	52
6 wk in-vitro	2700	2	108000	30
9 wk in-vitro	1500	1	102000	17
Annealed, Irradiated 2.5Mrad	8500	8	85000	98
Irradiated, 1 wk in-vitro	6500	8	81000	76
Irradiated, 3 wk in-vitro	3400	3	100000	40
Irradiated, 6 wk in-vitro	2500	2	105000	30
Irradiated, 9 wk in-vitro	1800	2	105000	21

Data an avg. of 8-12 cylindrical dumbbells

Even though no loss in physical properties was observed for aromatic poly(anhydride)s subjected to gamma irradiation, it is important to establish the polymers physical characteristics as a function of exposure time in-vitro. This is a necessary requirement, since past work has shown that absorbable polymers, and devices formed from them (PDSTM, VicrylTM), subjected to cobalt may indicate little change in physical properties, but when tested in-vitro rapidly lose strength. However, no difference is observed in in-vitro properties between coupons subjected to cobalt versus unirradiated coupons. In fact, yield strength as a function of weeks in-vitro appears to follow a linear decrease profile for annealed test coupons. However, unannealed test coupons display an induction period (6 weeks) prior to the linear decrease in physical strength.

Like the 1,6 PA, poly[1,4-bis(p-carboxyphenoxy)butane anhydride] (1,4 PA) was also molded into cylindrical dumbbells, and baseline as well in-vitro physical properties were determined (Tables 5, 6 and 8-10). As can be seen from these tables, the yield strength and modulus is greater than that of 1,6 PA. This is as expected, since the 1,4 PA contains two less methylene groups per repeat unit. This leads to a polymeric chain, which is slightly stiffer and, therefore, causes a corresponding increase in yield strength and modulus.

More importantly, like the 1,6 PA, unannealed test coupons of the 1,4 PA display no change in physical strength between coupons subjected to cobalt and unirradiated test samples. In addition, like the 1,6 PA an induction period in the in-vitro physical strength is observed. However, unlike the 1,6 PA, the 1,4 PA displays only a 3 week induction period, followed by a linear decrease strength profile. The nature of this difference between 1,6 PA and 1,4 PA is believed to be due to the increased hydrolyzability and hydrophilicity of the 1,4-bis acid in comparison to that of the 1,6-bis acid monomer. It should be noted that similar behavior to that of the annealed 1,6 PA is observed for annealed coupons of the 1,4 PA.

Additionally, 1,4 PA subjected to a dosage of 4.5 Mrad shows almost identical in-vitro results to that of 1,4 PA subjected to 2.5 Mrad (Table 8). This is another clear indication that this series of poly(anhydride)s are radiation sterilizable.

Also of significance, is the establishment that the 2.5 Mrad in-vivo BSR profile for the 1,4 PA is almost identical to that of the 2.5 Mrad in-vitro BSR profile. This indicates that for the polyanhydride systems studied, in-vitro BSR results can be correlated to in-vivo BSR results.

Physical properties of poly[1,2-bis(p-carboxyphenoxy)ethane anhydride] (1,2 PA) were also determined. Unannealed test coupons gave results at baseline (zero day) of a yield strength of 11300 psi, a yield at elongation of 13%, and a modulus of 114500 psi. As expected, the strength and modulus of the 1,2 PA, in comparison with 1,6 PA and 1,4 PA, increased. Results also indicate that little change (< 10% decrease) occurs in the strength and modulus in the first week in-vitro, but is followed by a sharp decrease in strength at 3 weeks (33% retained

Table 7. Inherent Viscosities of poly[1,6-bis(carboxyphenoxy)hexane anhydride] as a function of time (minutes) at a reaction temperature of 180 or 200°C

Experiment	Recrystallization Solvent	120 ^a min	240 ^a min	120 ^a min	240 ^a min
A	NMP	0.7 ^b		1.1 ^c	
B	NMP		0.7 ^b		1.3 ^c
C (Control)	None	0.2 ^b		0.25 ^c	
D (Control)	None		0.2 ^b		0.3 ^c

Controls performed via Domb and Langer, ^aReaction Time, ^bInherent viscosity (dl/g) at 180°C, ^cInherent viscosity (dl/g) at 200°C

Table 8. Physical properties of unannealed of poly[1,4-bis(carboxyphenoxy)butane anhydride] irradiated at 4.5Mrad

	Tensile Strength (psi)	Elongation@ Yield (%)	Tensile Modulus (psi)	Strength Retained (%)
Unannealed	7000	11	71000	---
1 wk in-vitro	6800	11	63000	97
3 wk in-vitro	6900	9.8	76000	99
6 wk in-vitro	4200	8	43000	60
9 wk in-vitro	1200	2	56000	17

Data an avg. of 8-12 cylindrical dumbbells

Table 9. In-vivo physical properties of unannealed of poly[1,4-bis(carboxyphenoxy)butane anhydride]

	Tensile Strength (psi)	Elongation@Yield (%)	Tensile Modulus (psi)	Strength Retained (%)
Unannealed	7800	11.3	89000	---
1 wk in-vivo	7000	11.1	74000	90
3 wk in-vivo	7400	10	84000	95
6 wk in-vivo	5900	10	90000	75
9 wk in-vivo	2800	5.7	52000	35
Unannealed, Irradiated 2.5Mrad	7900	10.6	82000	100
Irradiated, 1 wk in-vivo	6900	10.3	81000	87
Irradiated, 3 wk in-vivo	7400	10	82000	94
Irradiated, 6 wk in-vivo	5700	9	98000	73
Irradiated, 9 wk in-vivo	2000	5.6	10000	25

Data an avg. of 8-12 cylindrical dumbbells

Table 10. Physical properties of unannealed of poly[1,4-bis(carboxyphenoxy)butane anhydride]

	Tensile Strength (psi)	Elongation@Break (%)	Tensile Modulus (psi)	Strength Retained (%)
Unannealed	6300	84	62000	---
1 wk in-vitro	5600	78	55000	90
3 wk in-vitro	6300	56	58000	100
6 wk in-vitro	5400	18	70000	85

Data an avg. of 8-12 cylindrical dumbbells

Table 11. Physical properties of unannealed of poly[1,6-bis(carboxyphenoxy)hexane anhydride]

	Tensile Strength (psi)	Elongation@ Break (%)	Tensile Modulus (psi)	Strength Retained (%)
Unannealed	5500	120	79000	---
1 wk in-vitro	5700	135	49000	100
3 wk in-vitro	6200	155	54000	100
6 wk in-vitro	5500	77	56000	100
9 wk in-vitro	4500	10	50000	75

Data an avg. of 8-12 cylindrical dumbbells

strength) (Table 12). This is as expected, since it is believed, from the literature, that the 1,2 PA is even more hydrophilic than the 1,4 PA or 1,6 PA. In fact, although the modulus is not as high as BTC-1(4*a,b*) and PGA, this type of yield strength breakdown profile appears to be quite similar to radiation sterilizable BTC-1, and ethylene oxide sterilized PGA (Tables 13, 14).

In conclusion, we have developed a process by which high molecular weight homo and co-poly (anhydride) polymers (I.V. > 1.0 dl/g) can be synthesized at polymerization temperatures above 200°C without degradation or gelation at reaction times greater than 300 minutes by utilizing highly purified dicarboxylic acid and anhydride monomers under highly inert, high vacuum (< 10 microns) conditions.

Also, the high molecular weight poly(anhydride)s are melt processable under inert atmospheric conditions at temperatures greater than 200°C. The high molecular weight poly(anhydride)s are also stable to Cobalt irradiation without loss of mechanical properties, molecular weight, or changes in chemical structure.

The aromatic poly(anhydride)s also display various physical strength breakdown profiles, from that of low strength/slow breakdown (i.e., 1,6 PA) to that of high strength/fast breakdown (i.e., 1,2 PA), with behavior between the two extremes (i.e., 1,4 PA).

Experimental

The present report describes a synthetic process for preparing aromatic poly(anhydride)s, potentially useful as biomedical devices, with high molecular weights as characterized by inherent viscosities in excess of 1.0 dl/g in common organic solvents such as chloroform at ambient (25°C) temperature.

Table 12. Physical properties of unannealed of poly[1,2-bis(carboxyphenoxy)ethane anhydride]

	Tensile Strength (psi)	Elongation@Yield (%)	Tensile Modulus (psi)	Strength Retained (%)
Unannealed	11300	12.9	114000	---
1 wk in-vitro	9900	10.6	116000	88
3 wk in-vitro	3700	4.1	74000	33
4 wk in-vitro	1500	2	56000	13

Data an avg. of 8-12 cylindrical dumbbells

Table 13. In-vivo physical properties of annealed BTC-1

	Tensile Strength (psi)	Elongation@Yield (%)	Tensile Modulus (psi)	Strength Retained (%)
Annealed	19200	12	201000	---
1 wk in-vivo	11500	42	166000	60
2 wk in-vivo	11100	24	136000	57
3 wk in-vivo	3100	5	44000	16
4 wk in-vivo	1300	4	29000	7
Annealed, Irradiated 2.5Mrad	18400	9	180000	96
Irradiated, 1 wk in-vivo	10700	41	160000	58
Irradiated, 2 wk in-vivo	8100	12	98000	44
Irradiated, 3 wk in-vivo	2100	6	42000	11
Irradiated, 4 wk in-vivo	0	0	0	0

Data an avg. of 8-12 cylindrical dumbbells

Table 14. In-vivo physical properties of annealed PGA

	Tensile Strength (psi)	Elongation@Yield (%)	Tensile Modulus (psi)	Strength Retained (%)
Annealed	16700	13	203000	---
1 wk in-vivo	12700	33	184000	76
2 wk in-vivo	4800	6	67000	29
3 wk in-vivo	0	0	0	0
4 wk in-vivo	0	0	0	0
Annealed, Irradiated 2.5Mrad	19100	11	173000	100
Irradiated, 1 wk in-vivo	10000	7	48000	52
Irradiated, 2 wk in-vivo	3200	7	39000	17
Irradiated, 3 wk in-vivo	0	0	0	0
Irradiated, 4 wk in-vivo	0	0	0	0

Data an avg. of 8-12 cylindrical dumbbells

In this synthetic process, the high molecular weight poly(anhydride) was prepared by a method consisting of selecting a highly pure aromatic mixed anhydride that was synthesized by reacting acetic anhydride at reflux under a stream of nitrogen for several hours with a highly pure dicarboxylic acid. The anhydride was then isolated, purified, and dried.

It was then polymerized under melt condensation conditions at temperatures between 180°C and 240°C for a time of 90 to 360 minutes utilizing high vacuum (< 20 microns) to remove the condensation product formed during the polymerization.

The various times and temperatures of the polymerization collaborate to yield aromatic homo- and co-poly(anhydride)s with high molecular weights (I.V. > 1.0 dl/g). In the examples, higher molecular weight (I.V. > 1.0 dl/g), non-crosslinked, aromatic homo and co-poly(anhydride) polymers were prepared from 1,6-bis(pcarboxyphenoxy)hexane, 1,4-bis(p-carboxyphenoxy)butane, and 1,2-bis(p-carboxyphenoxy)ethane.

The polymers and monomers were characterized for chemical composition and purity (NMR, FT-IR, elemental analysis), thermal analysis (DSC), melt rheology (melt stability and viscosity), molecular weight (inherent viscosity), crystallinity (XRD). Baseline and in-vitro mechanical properties (Instron stress/strain) were determined on molded and extruded samples.

FT-IR was performed on a Nicolet FT-IR. Polymer samples were melt pressed into thin films. Monomers were pressed into KBr pellets. ^1H NMR was performed on a 200 MHz NMR using CDCl_3 as a reference. Elemental analysis was performed at Schwarzkopf Microanalytical Laboratories.

Thermal analysis of polymers and monomers was performed on a Dupont 912 Differential Scanning Calorimeter (DSC) at a heating rate of $10^\circ\text{C}/\text{min}$. A Fisher-Johns melting point apparatus was also utilized to determine melting points of monomers. Thermal gravimetric analysis was performed on a Dupont 951 TGA at a rate of $10^\circ\text{C}/\text{min}$. under a nitrogen atmosphere. A Rheometrics Dynamic Analyzer RDA II also determined isothermal melt stability of the polymers for a period of 1 hour at temperatures ranging from 220°C to 260°C under a nitrogen atmosphere. Melt viscosity was also determined utilizing a Rheometrics Dynamic Analyzer RDA II at temperatures ranging from 160°C to 290°C at rate of $1^\circ\text{C}/\text{min}$. to $10^\circ\text{C}/\text{min}$. at frequencies of lcm^{-1} to 100cm^{-1} under a nitrogen atmosphere.

Inherent viscosities (I.V.) of the polymers were measured using a 50 bore Cannon-Ubbelohde dilution viscometer immersed in a thermostatically controlled water bath at 25°C at a concentration of 0.025 gms/25 ml.

The cylindrical dumbbells were prepared by utilizing a CSI Mini-max injection molder equipped with a dry nitrogen atmospheric chamber at temperatures ranging from 220°C to 260°C with a residence time of 3 minutes.

The aromatic poly(anhydride)s were also extruded into fibers. For example, a sample of poly[1,4-bis(p-carboxyphenoxy)butane] exhibiting a melting point of 190°C was extruded using an Instron capillary rheometer equipped with a 40-mil die with an L/D of 25.

Baseline and in-vitro mechanical properties of the cylindrical dumbbells of the poly(anhydride) polymers so produced were performed on an Instron model 1122 at a crosshead rate of 0.35 in/min. Specimen gauge length was 0.35 in., with a width of 0.06 in. Results are an average of 8 to 12 dumbbell specimens.

In-vitro studies were determined in a buffer solution ($\text{pH}=7.27$) at a temperature of 37°C for periods of 1, 3, 6, and 9 weeks. Eight to ten cylindrical dumbbells (2.4 to 3.0 grams) were placed in 100 ml of buffer solution. The buffer solution was replaced on a weekly basis. Sterilization of the dumbbells was conducted by Cobalt-60 irradiation at a dosage of 2.5 Mrad.

Several monomer and polymer synthesis examples will be described in the following few pages.

Example 1. Synthesis of 1,4-bis(p-carboxyphenoxy)butane with N-methylpyrrolidinone (NMP) recrystallization

To a nitrogen purged 5L 3-neck round bottom flask equipped with a reflux condenser, two addition funnels, and a mechanical overhead stirrer, 127.2 grams (3.2 moles) of sodium hydroxide (reagent grade, Fisher) and 600 ml of distilled

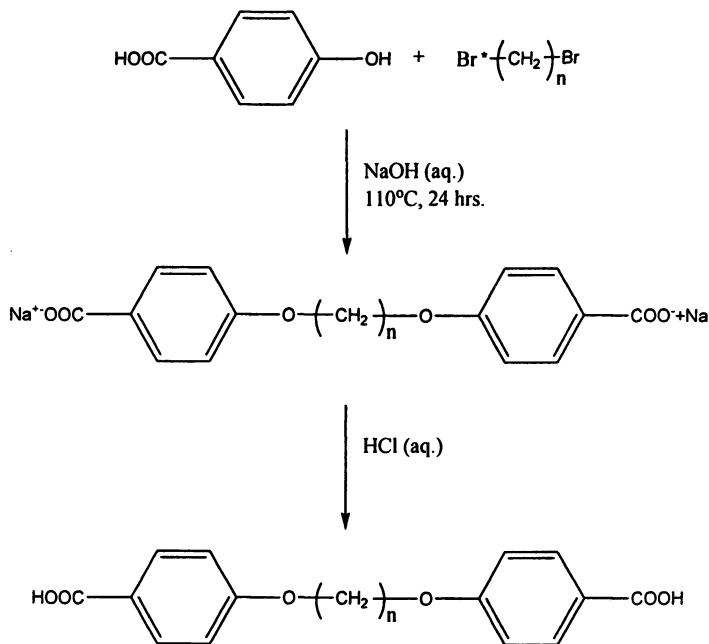


Figure 1. Synthesis of 1,n-bis(p-carboxyphenoxy)alkane

water were added. The vigorously stirred solution was cooled with an ice-water bath and 219.4 grams (1.6 moles) of p-hydroxybenzoic acid (99%, Aldrich) was slowly added (Figure 1).

The temperature of the homogeneous solution was then slowly raised to reflux (110°C) via a heating mantle, and 173.4 grams (0.80 moles) of 1,4-dibromobutane (99%, Aldrich) was slowly added, dropwise, through an addition funnel over the course of 6 hours. Over the same time frame, 900 ml of distilled water was slowly added through a second addition funnel to help control the reflux temperature.

The temperature of the white slurry was then lowered below the refluxing temperature (80-90°C), and the reaction was allowed to continue for an additional 16 hours. The suspended dicarboxylic sodium salt was then cooled to 60°C and a solution of 33 grams of sodium hydroxide in 100 ml of distilled water was slowly added through the addition funnel. The suspension was then brought to reflux (110°C) for 15 to 30 minutes, cooled to room temperature (25°C), and partially converted to the free dicarboxylic acid by adding one-third portions of the suspended salt to three stirring solutions of 500 ml of hydrochloric acid and 500 ml of distilled water. The stirred suspensions of

partially free acid were then heated to 70°C for 2 hours, and suction filtered through a coarse glass frit and allowed to air-dry overnight.

Typically, the partially acidified (10 to 15% salt remaining after one acidification as determined by an ash test) monomer was washed one to two more times with 1500 ml of hydrochloric acid and 1500 ml of distilled water, as described above, until an ash free product was formed.

The ash free product was allowed to air-dry overnight, and then was washed twice with 750 ml of acetone (99.6%, Fisher) to remove excess water and hydrochloric acid. It was then suction filtered through a Buchner funnel with a coarse glass frit and allowed to air-dry overnight. The air-dried monomer was then dried at room temperature under vacuum to a constant weight (3 to 4 days). The final yield was 220 grams (70%).

The white, crude 1,4-bis(p-carboxyphenoxy)butane was then placed in a 4L Erlenmeyer flask and 1750 ml of N-methylpyrrolidinone (99+%, Aldrich) was added to yield an 8 to 1 ratio of solvent to monomer. The stirred solution was then heated to 110°C. After 1 to 2 hours, the acid monomer dissolved. The clear, brown solution was then suction filtered to remove particulates, and allowed to stand overnight in a freezer (0°C).

The white crystals that formed were isolated by suction filtration and allowed to air dry for 1 to 2 hours. The partially dried monomer was then placed in a 4L Erlenmeyer flask and 1500 ml of NMP was added to yield a 7 to 1 ratio. The stirred solution was then heated to 110°C. After 1 to 2 hours the monomer dissolved, and the light brown solution was suction filtered to remove particulates. The clear solution was placed in a freezer at 0°C and allowed to stand overnight.

The white crystals that formed were again isolated by suction filtration, and allowed to air dry for 1 to 2 hours. The partially dried monomer was recrystallized for a third time as described above, yielding a clear, light yellow solution that was allowed to stand overnight at 0°C.

The highly pure, white crystals were then isolated for a third time as described above and allowed to air dry for 2 to 3 hours. The crystals were then transferred to a 4L beaker and 1000 ml of distilled water was added (5 to 1 ratio of water to monomer). The stirred white slurry was then heated to 90°C for 2 hours, suction filtered and washed with an additional 1000 ml of hot (90°C) distilled water.

The monomer was allowed to air dry for 1 to 2 hours, and then was placed in a 4L beaker along with 1000 ml (5 to 1 ratio) of acetone (99.6%, Fisher), stirred for 1 to 2 hours, suction filtered, washed with an additional 1000 ml of acetone and dried under vacuum at 50°C for 24 hours. The final yield of polymer grade 1,4-bis(p-carboxyphenoxy)butane (99.9% pure) was 50 to 60 percent. The preparation, isolation and purification of 1,6-bis(p-carboxyphenoxy)hexane was done in a similar fashion to that described above.

Example 2. Synthesis of 1,4-bis(acetoxycarboxyphenoxy)butane

To a 5L 1-neck round bottom flask equipped with a magnetic stir bar, distillation head/trap and water condenser, 220 grams of purified 1,4-bis(p-carboxyphenoxy)butane and 2750 ml of acetic anhydride (99+%, Aldrich) were added to give a 12.5 to 1 ratio (ml acetic anhydride to monomer). The stirred white suspension was heated to reflux (135°C), giving a clear red-brown solution. The clear solution was concentrated to 875 ml (4 to 1 ratio) by removing acetic acid and acetic anhydride via the distillation head. The solution was slowly cooled to room temperature and then allowed to stand at 0°C overnight (Figure 2).

The off-white product, 1,4-bis(acetoxycarboxyphenoxy)butane, was isolated by suction filtration under a blanket of nitrogen and allowed to stand for 1 to 2 hours. The anhydride monomer was then transferred to a 2 L beaker and 900 ml of dry ethyl ether (reagent grade, Fisher) was added.

The white slurry was stirred for 2 hours under a blanket of nitrogen, suction filtered and dried under vacuum at 50°C for 24 hours. The final yield was 70 to 75 percent. 1,6-bis(acetoxycarboxyphenoxy)hexane was synthesized and isolated as described above.

Example 3. Polymerization of 1,4-bis(acetoxycarboxyphenoxy)butane

To a flamed-out, dry 250 ml 1-neck round bottom flask equipped with an overhead mechanical stirrer, vacuum adapter, 75° adapter, distillate bend with a vacuum take-off and a 50 ml collection flask, 40 grams of freshly prepared 1,4-bis(acetoxycarboxyphenoxy)butane was added via a nitrogen purged glove box.

The assembly was then secured to a high vacuum (<10 microns) diffusion pump and placed in a high temperature oil bath at 220°C. The stirred anhydride monomer immediately began to melt. Shortly thereafter, a high volume of distillate (acetic anhydride) began to evolve and was collected. After 15 to 20 minutes, the viscous melt was no longer stirrable. At such time, the polymerization was allowed to continue under high vacuum (10 to 30 microns) without stirring for a total reaction time of 90 to 360 minutes (Figure 2).

The high molecular weight polymer, poly[1,4-bis(pcarboxyphenoxy)butane anhydride], was removed from the bath, cooled to room temperature under a stream of nitrogen and isolated by deglassing and grinding. The polymer was then placed under vacuum at 50°C for 24 hours. The final yield was 25 to 30 grams (70 to 75 percent).

Poly[1,6-bis(p-carboxyphenoxy)hexane anhydride] was prepared and isolated by the method described above except the typical polymerization temperature was 200°C.

Example 4. Synthesis of 1,6-bis(p-carboxyphenoxy)hexane with dimethylacetamide recrystallization

The preparation of 1,6-bis(p-carboxyphenoxy)hexane by this method was similar to the method described in Example 1, except dimethylacetamide (DMAC) was used as a recrystallization solvent. It has also been shown that this preparation yields a complex of the dicarboxylic acid and the solvent. Washing with hot water does not break this complex, and consequently, the monomer was not washed with hot water.

Therefore, once the white, crude, dry, ash free 1,6-bis(p-carboxyphenoxy)hexane had been prepared, it was placed in a 4L Erlenmeyer flask along with dimethylacetamide (DMAC) (99+%, Aldrich) to yield an 8 to 1 ratio of solvent to monomer. The stirred solution was then heated to 110°C. After 1 to 2 hours, the acid monomer dissolved. The clear, brown solution was then suction filtered to remove particulates, and allowed to stand overnight in a freezer (0°C).

The white crystals that formed were isolated by suction filtration, and allowed to air dry for 1 to 2 hours. The partially dried monomer was again placed in a 4L Erlenmeyer flask along with DMAC at an 8 to 1 solvent to monomer ratio. The stirred solution was then heated to 110°C. After 1 to 2 hours the monomer dissolved, and the light brown solution was suction filtered to remove particulates. The clear solution was placed in a freezer at 0°C and allowed to stand overnight.

The white crystals that formed were again isolated by suction filtration, and allowed to air dry for 1 to 2 hours. The partially dried monomer was recrystallized for a third time as described above, yielding a clear, light yellow solution that was allowed to stand overnight at 0°C.

The highly pure, white crystals were then isolated for a third time as described above and allowed to air dry for 2 to 3 hours. The crystals were then transferred to a 4L beaker along with acetone (99.6%, Fisher) (5 to 1 ratio of solvent to monomer), stirred for 1 to 2 hours, suction filtered, washed with additional acetone and dried under vacuum at 50°C for 24 hours. The final yield of the complex, 1,6-bis(p-carboxyphenoxy)hexane-DMAC, was 60 percent.

Example 5. Synthesis of 1,6-bis(acetoxycarboxyphenoxy)hexane and recrystallization with acetic anhydride

To a 2L 1-neck round bottom flask equipped with a magnetic stir bar, distillation head/trap and water condenser, 80 grams of purified 1,6-bis(p-carboxyphenoxy)hexane-DMAC and 1000 ml of acetic anhydride (99+%, Aldrich) were added to give a 12.5 to 1 ratio (ml acetic anhydride to monomer). The stirred white suspension was heated to reflux (135°C), giving a clear red-

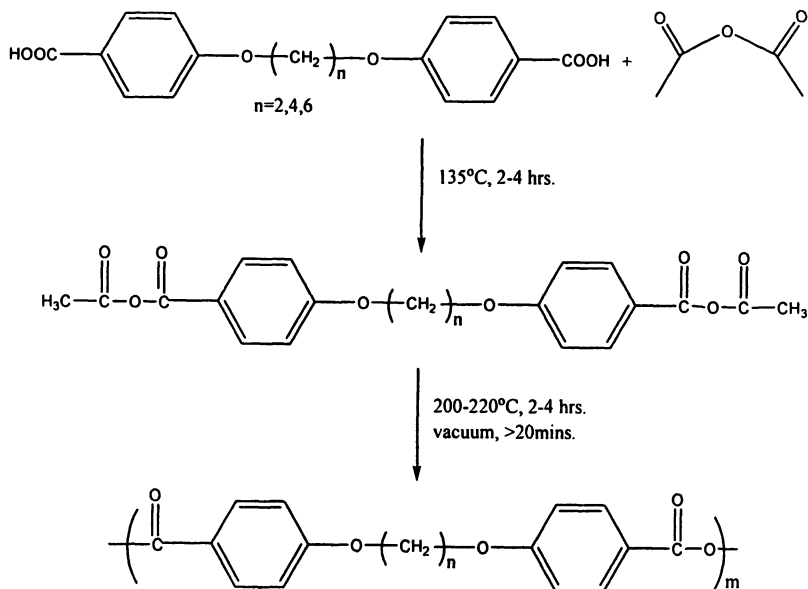


Figure 2. Synthesis of poly[1,n-bis(p-carboxyphenoxy)alkane anhydride]

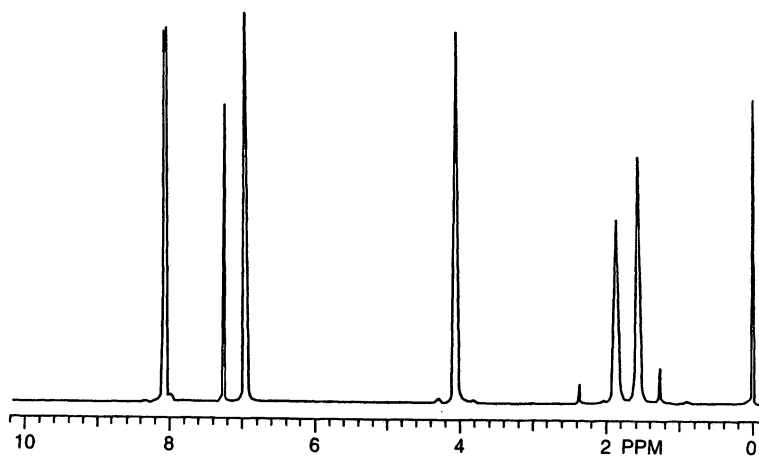


Figure 3. $^1\text{H NMR}$ of poly[1,6-bis(p-carboxyphenoxy)hexane anhydride]

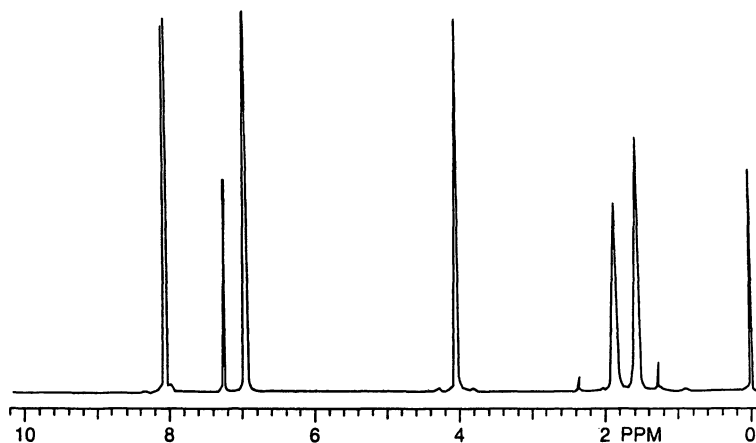


Figure 4. ^1H NMR of poly[1,6-bis(*p*-carboxyphenoxy)hexane anhydride] processed at 220°C

brown solution. The clear solution was concentrated to 700 ml (4 to 1 ratio) by removing acetic acid and acetic anhydride via the distillation trap. The solution was slowly cooled to room temperature and then allowed to stand at 0°C overnight (Figure 2).

The off-white product, 1,6-bis(acetoxycarboxyphenoxy)hexane, was isolated by suction filtration under a blanket of nitrogen and allowed to stand for 1 to 2 hours. The anhydride monomer was then transferred to a 2 L beaker and 300 ml of dry ethyl ether (reagent grade, Fisher) was added. The white slurry was stirred for 2 hours under a blanket of nitrogen, suction filtered and dried under vacuum at 50°C for 24 hours. The final yield was 70 to 75 percent.

Twenty-five grams of the mixed anhydride was then added to a 250 ml Erlenmeyer flask along with 125 ml of acetic anhydride and heated, with stirring, to 75°C. After 15 to 30 minutes, the anhydride monomer dissolved. The mixed anhydride was allowed to slowly cool to room temperature and then was cooled to 0°C overnight. The purified anhydride was washed with ethyl ether as described above, and dried overnight under vacuum at 50°C. The final yield was 50 to 60 percent.

Example 6. Polymerization of 1,6-bis(acetoxycarboxyphenoxy)hexane from recrystallized anhydride monomer

To a flamed-out, dry 250 ml 1-neck round bottom flask equipped with an overhead mechanical stirrer, vacuum adapter, 75° adapter, distillate bend with a vacuum take-off and a 50 ml collection flask, 12 grams of recrystallized

(Example 5) 1,6-bis(acetoxycarboxyphenoxy)hexane was added via a nitrogen purged glove box.

The assembly was then secured to a high vacuum (<10 microns) diffusion pump and placed in a high temperature oil bath at 200°C. The stirred anhydride monomer immediately began to melt. Shortly thereafter, a high volume of distillate (acetic anhydride) began to evolve, and was collected. After 15 to 20 minutes, the viscous melt was no longer stirrable. At such time, the polymerization was allowed to continue under high vacuum (10 to 30 microns) without stirring for a total reaction time of 240 minutes (Figure 2).

The high molecular weight polymer, poly[1,6-bis(pcarboxyphenoxy)hexane anhydride], was removed from the bath, cooled to room temperature under a stream of nitrogen and isolated by deglassing and grinding. The polymer was then placed under vacuum at 50°C for 24 hours.

Example 7. Polymerization of 1,6-bis(acetoxycarboxyphenoxy)hexane via modified Domb and Langer method

The method described below is the same as Domb and Langer's method except that the monomer, 1,6-bis(pcarboxyphenoxy)hexane, was recrystallized three times from NMP.

Therefore, to a flamed-out, dry 100 ml 1-neck round bottom flask equipped with an overhead mechanical stirrer, vacuum adapter, 75⁰ adapter, distillate bend with a vacuum take-off and a 50 ml collection flask, 33.5 grams of freshly prepared 1,6-bis(acetoxycarboxyphenoxy)hexane was added via a nitrogen purged glove box. The assembly was then secured to a high vacuum (<10 microns) diffusion pump and placed in a high temperature oil bath at 180°C. The stirred anhydride monomer immediately began to melt. Shortly thereafter, a high volume of distillate (acetic anhydride) began to evolve, and was collected. After 15 to 20 minutes, the viscous melt was no longer stirrable. At such time, the polymerization was allowed to continue under high vacuum (10 to 30 microns) without stirring for a total reaction time of 120 minutes.

The high molecular weight polymer, poly[1,6-bis(pcarboxyphenoxy)hexane anhydride], was removed from the bath, cooled to room temperature under a stream of nitrogen and isolated by deglassing and grinding. The polymer was then placed under vacuum at 50°C for 24 hours. The final yield was 70 to 75 percent.

A second poly[1,6-bis(p-carboxyphenoxy)hexane anhydride] was also prepared and isolated by the method described above, except the polymerization time was 240 minutes.

Example 8. Polymerization of 1,6-bis(acetoxycarboxyphenoxy)hexane via Domb and Langer method

The method described below is the same as Domb and Langer's method. That is, the monomer, 1,6-bis(pcarboxyphenoxy)hexane, was not recrystallized three times from NMP, but was simply washed with acetone without further purification as described in Example 1.

The anhydride monomer was also prepared by Domb and Langer's method. That is, after refluxing for 15 minutes, the unreacted monomer/impurities were removed by filtration. The remaining acetic anhydride was removed as described by Domb and Langer (3a).

To a flamed-out, dry 100 ml 1-neck round bottom flask equipped with an overhead mechanical stirrer, vacuum adapter, 75° adapter, distillate bend with a vacuum take-off and a 50 ml collection flask, 33.5 grams of freshly prepared 1,6-bis(acetoxycarboxyphenoxy)hexane was added via a nitrogen purged glove box.

The assembly was then secured to a high vacuum (<10 microns) diffusion pump and placed in a high temperature oil bath at 180°C. The stirred anhydride monomers immediately began to melt. Shortly thereafter, a high volume of distillate (acetic anhydride) began to evolve, and was collected. The low viscosity melt polymerization was allowed to continue under high vacuum (10 to 30 microns) with stirring for a total reaction time of 120 minutes.

The low molecular weight polymer, poly[1,6-bis(pcarboxyphenoxy)hexane anhydride], was removed from the bath, cooled to room temperature under a stream of nitrogen and isolated by deglassing and grinding. The polymer was then placed under vacuum at 50°C for 24 hours. The final yield was 70 to 75 percent.

A second poly[1,6-bis(p-carboxyphenoxy)hexane anhydride] was also prepared and isolated by the method described above, except the polymerization time was 240 minutes.

Example 9. Copolymerization of 1,4-bis(acetoxycarboxyphenoxy)butane and 1,6-bis(acetoxycarboxyphenoxy)hexane

To a flamed-out, dry 250 ml 1-neck round bottom flask equipped with an overhead mechanical stirrer, vacuum adapter, 75° adapter, distillate bend with a vacuum take-off and a 50 ml collection flask, 11 grams of freshly prepared 1,4-bis(acetoxycarboxyphenoxy)butane (Example 3) and 33 grams of 1,6-bis(acetoxycarboxyphenoxy)hexane (Example 6) were added via a nitrogen purged glove box.

The assembly was then secured to a high vacuum (<10 microns) diffusion pump and placed in a high temperature oil bath at 220°C. The stirred anhydride monomer immediately began to melt. Shortly thereafter, a high volume of distillate (acetic anhydride) began to evolve, and was collected. After 15 to 20

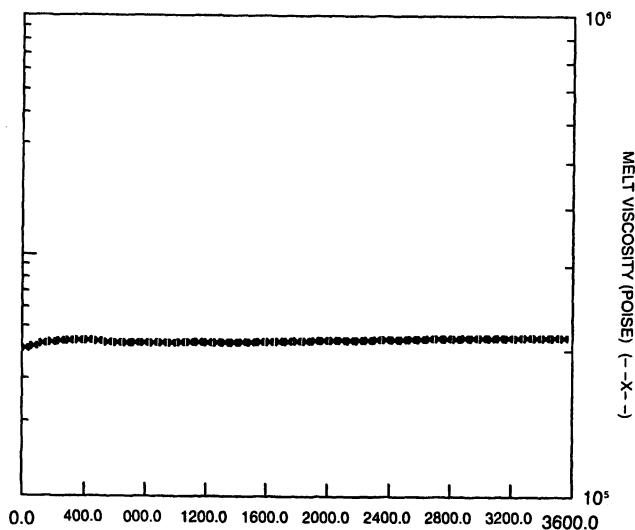


Figure 5. Isothermal (220°C) melt viscosity of poly[1,6-bis(p-carboxyphenoxy)hexaneanhydride]

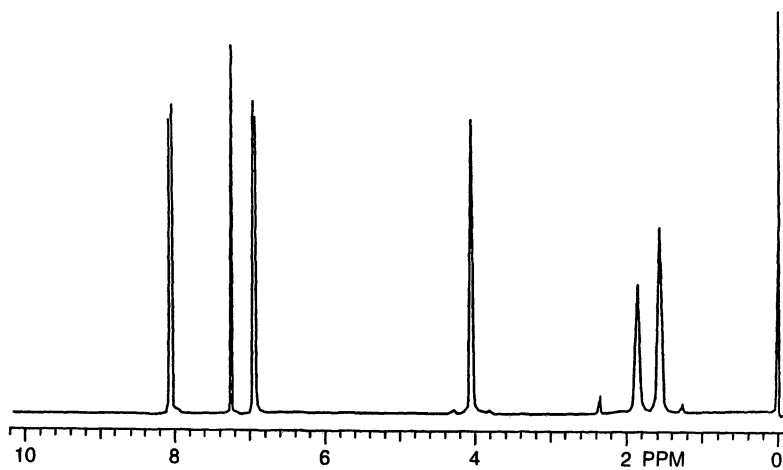


Figure 6. ¹H NMR of poly[1,6-bis(p-carboxyphenoxy)hexane anhydride] after exposure to 2.5 Mrad Cobalt irradiation

minutes, the viscous melt was no longer stirrable. At such time, the polymerization was allowed to continue under high vacuum (10 to 30 microns) without stirring for a total reaction time of 90 to 360 minutes.

The high molecular weight poly[1,4-bis(pcarboxyphenoxy)butane anhydride]-co-[-1,6-bis(pcarboxyphenoxy)hexane anhydride], was removed from the bath, cooled to room temperature under a stream of nitrogen and isolated by deglassing and grinding. The polymer was then placed under vacuum at 50°C for 24 hours. The final yield after grinding was 70 to 75 percent.

References

1. Carothers, W., *J. Am. Chem. Soc.*, 1932, 54, 1569
2. Conix, *J. Polym. Sci.*, 1958, 29, 343
3. (a) Domb, A.; Langer, R.; *J. Polym. Sci.*, 1987, 25, 3373, (b) Domb, A.; Langer, R., *Macromol.*, 1992, 25, 12
4. (a) Bezwada, R.; Shalaby, S.W.; Jamiolkowski, D.D., U.S. Patent 4,510,295, 1985, (b) Shalaby, S.W. and Jamiolkowski, D. D., U.S. Patent 4,689,424, 1987
5. Domb, A. and Langer, R., U.S. Patent 4,757,128, 1988
6. Conix, *Macromol. Synth.*, 1966, 2, 95
7. (a) Cooper, K., Wasserman, D., Scopelianos, A., Jamiolkowski, D.D., U.S. Patent 5264540, 1993.

Chapter 6

Fluorescently Labeled Protein–Polymer Bioconjugates Using Protein-Derived Macroinitiators from Living Radical Polymerization

Julien Nicolas¹, Veronica San Miguel², Giuseppe Mantovani¹,
and David M. Haddleton^{1,*}

¹Department of Chemistry, University of Warwick,
Coventry CV4 7AL, United Kingdom

²Instituto de Ciencia y Tecnología de Polímeros, CSIC, Juan de la Cierva 3,
28006 Madrid, Spain

Bovine Serum Albumin (BSA) and lysozyme have been chemically transformed into macroinitiators for the synthesis of fluorescent bioconjugates by living radical polymerization. A new fluorescent monomer based on rhodamine B has been synthesized and incorporated into the polymer backbone of the bioconjugate by copolymerization. This provides a new strategy for the synthesis of fluorescent bioconjugates with improved traceability in biological environments, during biomedical assays.

Introduction

Protein-polymer conjugates is an emerging research area, representing an established way to new and more efficient therapeutics for application in biotechnology and medicine. Bioconjugation often refers to the linking of a (macro)molecule to (poly)peptides/proteins in order to form new chemical entities which are able to retain the bioefficacy and features of the peptide whilst enjoying enhancements from the polymer. The most significant example is the covalent modification of proteins with poly(ethylene glycol) (PEG), *pegylation* (1,2,3,4). The resulting conjugates exhibited multiple benefits including improved biodistributions and pharmacokinetics, improved resistance to proteolysis, reduced immunogenicity/antigenicity, longer plasma half-life and improved solubility when compared to non-pegylated counterparts (5). The emergence of living radical polymerization (LRP) has provided an efficient tool to design the nature and characteristics of the polymer conjugated to the protein. Transition-metal-mediated living radical polymerization (also called atom transfer radical polymerization, ATRP) (6,7), nitroxide-mediated polymerization (NMRP) (8) and reversible transfer as reversible addition fragmentation transfer (RAFT) (9) allow various tailor-made polymers featuring unique properties in terms of molecular weight, molar mass distribution and chain-end functionality to be synthesized. This provides a powerful tool for protein/peptide biology. Protein and peptides currently constitute approximately 10% of the market for molecular medicines (total > 400 bn USD) which is growing year on year. As such; technological developments can have a real and immediate impact in this area.

We have recently reported studies involving the “*grafting to*” strategy for synthesizing bioconjugates by copper-mediated living radical polymerization, the conventional route for pegylation. α -Functional well-defined polymers were used as alternative pegylation agents and reacted with residual amines (lysine and *N*-terminal α -amino residues) and thiols (cysteine residues) present at the surface of proteins (10,11,12). In contrast, the “*grafting from*” synthetic route, which consists of transforming a protein into a macroinitiator for subsequent polymerization, has not been as widely investigated (13,14).

In this present work, we present a strategy for synthesizing fluorescent bioconjugates by LRP starting from previously modified proteins as macroinitiators. Materials containing fluorescent tags are extremely useful due to their increased traceability in biological systems during biomedical assays as the location of the material can be observed and hence its effectiveness may be determined. In addition, they can be observed using fluorescence microscopy and especially laser scanning confocal microscopy.

Experimental Part

Materials

Albumin, from bovine serum (BSA, molecular weight ~66 kDa, V fraction), lysozyme (molecular weight ~14.3 kDa), poly(ethylene glycol) methyl ether methacrylate (PEGMA₄₇₅, average $M_n = 475 \text{ g.mol}^{-1}$, Aldrich), 2-(dimethylamino)ethyl methacrylate (DMAEMA, Aldrich, 99%) and methacryloyl chloride (Aldrich, 97%) were used as received without further purification. Copper(I) bromide was purified by stirring over glacial acetic acid and followed by rinsing with ethanol and diethyl ether. Anhydrous dimethyl sulfoxide (DMSO, Aldrich, 99%), triethylamine (TEA, Fischer, 99%, stored over potassium hydroxide pellets), dichloromethane (DCM, Fischer, >99%), acetonitrile (BDH, 99.9%, HPLC grade) and trifluoroacetic acid (TFA, Aldrich, 99%) were used as received. *N*-(Ethyl)-2-pyridylmethanimine was prepared as described earlier (15) and stored under dinitrogen atmosphere at 4 °C. Hostasol methacrylate fluorescent monomer, maleimide and *N*-succinimidyl 2-bromo-2-methylpropionate initiators were prepared as described elsewhere (16,11,12).

Analytical techniques

¹H NMR and ¹³C NMR spectra were recorded on a Bruker DPX 400 spectrometer using deuterated chloroform (CDCl₃, Aldrich) as a solvent. Fluorescence spectroscopy was performed on a Perkin Elmer LS 50B spectrofluorometer with 1 cm quartz cuvette at 200 nm.min⁻¹ scan speed, 2.5 nm excitation and emission slit widths, ambient temperature in phosphate buffer (10 mM, pH = 7.1). U.V.-Visible spectroscopy analysis was performed on a Jasco V-550 spectrophotometer with 1 cm quartz cuvette, 0.5 nm data pitch, 200 nm.min⁻¹ scan speed, ambient temperature in phosphate buffer (10 mM, pH = 7.1). Circular Dichroism (CD) analysis was performed on a Jasco J715 spectropolarimeter with 0.1 cm quartz cuvette, 0.2 nm data pitch, 100 nm.min⁻¹ scan speed, 8 accumulations, ambient temperature in phosphate buffer (10 mM, pH = 7.1) for a concentration of 0.1 mg.mL⁻¹. Percentages of α -helices and β -sheets were determined by applying the protein CD structure-fitting program, CDSSTR (18).

The RP-HPLC system was fitted with a Phenomenex column (Jupiter, C₁₈, 4.6 × 250 mm, 5 μ m, 300 Å) and a U.V. detector (Gilson, UV-VIS-155) at 280 nm under a flow rate of 1 mL.min⁻¹. The separation was performed under a gradient between mobile phase A (acetonitrile/water, 90/10, v/v and 0.05% TFA) and mobile phase B (100% acetonitrile, 0.04% TFA). The gradient

involved several linear steps: 0 min 90% A, 27 min 40% A, 35 min 40% A, 37 min 90% A, and 45 min 90% A. SEC-FL-HPLC system was carried out on two BioSep-SEC-S3000 columns with fluorescence detection (Hitachi, L-7480) continuously measuring the relative intensity of the mobile phase. The system was eluted with 0.1 vol.% TFA in water and acetonitrile (69/31, v/v) at a flow rate of 0.5 mL.min⁻¹.

SDS-PAGE was conducted using a stacking polyacrylamide gel of 5% cross-linking, a resolving polyacrylamide gel (8% cross-linking for BSA conjugates; 12% cross-linking for lysozyme conjugate) and a running buffer consisting of 25 mM of TRIS base, 250 mM of glycerol, 0.1% of SDS at pH 8.7, bromophenol blue with addition of DTT for reducing conditions (17).

Synthesis of rhodamine B methacrylate monomer

Both TEA (1.44 g, 14.3 mmol) and methacryloyl chloride (0.97 g, 10.7 mmol) were sequentially added at 0 °C to a solution of rhodamine B alcohol (19) (5.93 g, 9.80 mmol) in DCM (100 mL). After 1 h, the temperature was raised to ambient temperature and the mixture stirred for a further 12 h. The volatiles were then removed under reduced pressure and the residue purified by a pre-eluted flash chromatography (SiO₂) using methanol/triethylamine (95/5), to give rhodamine B methacrylate monomer as purple glassy solid in 72% yield.

¹H NMR (400.03 MHz, CDCl₃, 298 K): δ = 1.20 (t, *J* = 7.0 Hz, 12H), 1.67–1.76 (q, *J* = 6.8 Hz, 2H), 1.78 (s, 3H), 2.24 (br s, 4H), 2.31 (t, *J* = 7.2 Hz, 2H), 3.30 (br s, 4H), 3.50–3.55 (q, *J* = 7.3 Hz, 8H), 4.02 (t, *J* = 6.4 Hz, 2H), 5.38–5.45 (m, 1H), 5.91–5.96 (m, 1H), 6.63–6.68 (d, *J* = 2.5 Hz, 2H), 6.80–6.91 (dd, *J* = 2.3, 9.5 Hz, 2H), 7.07–7.15 (d, *J* = 9.5 Hz, 2H), 7.19–7.25 (m, 1H); 7.41–7.49 (m, 1H), 7.51–7.61 (m, 2H). ¹³C NMR (100.59 MHz, CDCl₃, 298 K): δ = 12.50, 18.12, 25.51, 41.34, 46.01, 47.17, 52.19, 52.88, 54.48, 62.52, 96.11, 113.52, 114.32, 125.40, 127.51, 129.77, 129.99, 130.06, 130.46, 131.91, 135.17, 136.02, 155.44, 155.70, 157.54, 167.12, 167.22. IR (solid, ATR cell): ν (cm⁻¹) 3070 (=CH₂), 1709 (C=O ester carbonyl), 1635 (C=O amide), 1582 (C=C aromatic), 1460 (C=C aromatic), 1250 (C-O ester), 1169 (C-O ester), 1070 (C-O ether). High resolution MS-ES calcd. for C₃₉H₄₉N₄O₄ (M⁺): 637.3754; found: 637.3760.

Preparation of protein-macroinitiators

BSA-macroinitiator

BSA (34 mg, 0.52 μmol) was dissolved in 4.6 mL of 100 mM phosphate buffer (pH = 7.0). A solution of 15 mg of maleimide initiator (51.7 μmol) in 0.2

mL of DMSO was slowly added. The mixture was gently stirred for 12 h at ambient temperature and the solid residue was removed by centrifugation. The supernatant was diluted with deionized water and dialyzed with a 12,000-14,000 molecular weight cut-off (MWCO) membrane against deionized water for several days. The solution was then lyophilized to isolate the BSA-macroinitiator.

Lysozyme-macroinitiator

N-Hydroxysuccinimide-2-bromo-2-methylpropionate (37 mg, 140 μmol) in 400 μL of DMSO was added to lysozyme (100 mg, 7.0 μmol) dissolved in 20 mL of phosphate buffer (100 mM, pH = 7.0). To this, 50 μL of a TEA solution of 2.26 mM, prepared by dissolving 50 μL of TEA in 0.16 mL of phosphate buffer (100 mM, pH = 7.0), was added. The mixture was incubated at ambient temperature during 48 h under gentle stirring. The suspension was diluted with water and the solid residue was removed by centrifugation. The supernatant was dialyzed using a 6,000-8,000 MWCO membrane against deionized water for several days. The solvent was removed by lyophilization to isolate the lysozyme-macroinitiator.

Preparation of fluorescent bioconjugates

BSA-poly(PEGMA₄₇₅-co-rhodamine B methacrylate)

BSA-macroinitiator (100 mg, 1.5 μmol), PEGMA₄₇₅ (0.11 g, 0.38 mmol) and Cu(I)Br (32 mg, 0.23 mmol) were placed in a Schlenk tube and were dissolved in 23.8 mL of deionized water. 200 μL of a stock solution of rhodamine B monomer (3.8 μmol), previously prepared by dissolving 25 mg of the rhodamine B monomer in 2 mL of deionized water, was added. The solution was then deoxygenated by three freeze-pump-thaw cycles. Subsequently three vacuum-nitrogen cycles were applied and the Schlenk was placed in an oil bath at 25 °C. *N*-(Ethyl)-2-pyridylmethanimide (59 μL , 0.48 mmol) was added and the reaction mixture immediately turned dark brown/red. After 48 h under nitrogen atmosphere, the reaction medium was diluted with deionized water and bubbled with air overnight. The solid residue was removed by centrifugation and the supernatant was dialyzed using a 12,000-14,000 MWCO membrane against deionized water. The solution was lyophilized and the BSA-poly(PEGMA₄₇₅-co-rhodamine B methacrylate) conjugate was obtained as a purple solid.

BSA-poly(PEGMA₄₇₅-co-hostasol methacrylate)

BSA-macroinitiator (75 mg, 1.1 μmol), PEGMA₄₇₅ (85 mg, 0.28 mmol) and Cu(I)Br (24 mg, 0.17 mmol) were placed in a Schlenk tube and dissolved in DMSO (17.8 mL). The hostasol monomer (1.3 mg, 2.8 μmol) was added and the mixture deoxygenated by three freeze-pump-thaw cycles. The Schlenk tube was placed in an oil bath at 25 °C and *N*-(ethyl)-2-pyridylmethanimide (44 μL , 0.36 mmol) as a polymerization initiator (the reaction medium turned a dark brown/orange color). The mixture was stirred under inert atmosphere for 48 h prior to dilution with DMSO and bubbled with air overnight. The suspension was centrifuged and the supernatant was then diluted with deionized water. The solid residue was removed by centrifugation and the supernatant was dialyzed using a 12,000-14,000 MWCO membrane against deionized water. The solvent was removed by lyophilization in order to isolate a yellow solid.

BSA-poly(DMAEMA-co-rhodamine B methacrylate)

BSA macroinitiator (100 mg, 1.5 μmol) was dissolved in 23.6 mL of degassed water. A solution of DMAEMA (200 μL , 0.38 mmol) was added (prepared by dissolving 630 μL of DMAEMA in 2 mL of deionized water and adding some drops of HCl until pH 6.6). To this, 200 μL of a rhodamine B monomer solution (3.8 μmol), obtained by dissolving 25 mg of the fluorescent monomer in 2 mL of deionized water, was added. The mixture was deoxygenated with three freeze-pump-thaw cycles. Cu(I)Br (32 mg, 0.23 mmol) was subsequently added to the frozen mixture and three vacuum-nitrogen cycles were applied. Then, the Schlenk tube was placed in an oil bath at 25 °C under a nitrogen atmosphere. *N*-(Ethyl)-2-pyridylmethanimide (59 μL , 0.48 mmol), reaction mixture turned a dark brown/red color. After 17 hours, the polymerization medium was diluted with deionized water and bubbled with air overnight. The solid residue was removed by centrifugation and the supernatant dialyzed using a 12,000-14,000 MWCO membrane against deionized water for several days. The solution was lyophilized to give the conjugate as a purple solid.

Lysozyme-poly(PEGMA₄₇₅-co-rhodamine B methacrylate)

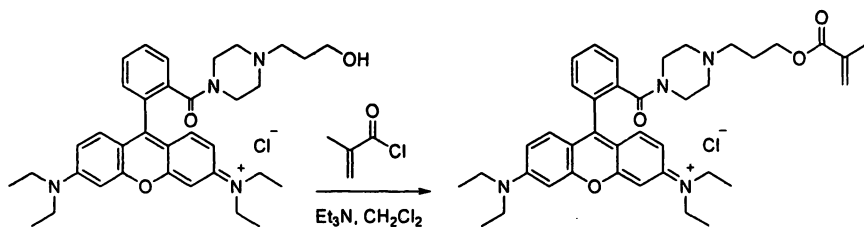
Lysozyme-macroinitiator (18 mg, 1.1 μmol), PEGMA₄₇₅ (83 mg, 0.28 mmol) and Cu(I)Br (24 mg, 0.17 mmol) were dissolved in 15 mL of deionized water. Rhodamine B monomer solution, 150 μL (2.8 μmol), 19 mg of the fluorescent monomer in 2 mL of deionized water, was added. The solution was

subsequently deoxygenated by three freeze-pump-thaw cycles and placed in an oil bath at 25 °C. *N*-(Ethyl)-2-pyridylmethanimide (44 μ L, 0.35 mmol) was added, the reaction mixture immediately turning dark brown/red. The mixture was stirred for 48 hours under nitrogen. The reaction medium was then diluted with deionized water and bubbled with air overnight. The mixture was centrifuged to remove the solid residue and the supernatant dialyzed using a 12,000-14,000 MWCO membrane against deionized water. The solution was then lyophilized to isolate the desired conjugate as a purple solid.

Results and Discussion

Synthesis of the rhodamine B methacrylate monomer as a fluorescent probe

Fluorescent bioconjugates were prepared by *in situ* incorporation of the fluorescent probe during the synthesis of the polymer by copolymerization of fluorescent monomers with poly(ethylene glycol) methyl ether methacrylate (PEGMA₄₇₅) or with dimethyl aminoethyl methacrylate (DMAEMA). Both the hostasol methacrylate monomer (*16*) and novel fluorescent methacrylate monomer derived from rhodamine B (Scheme 1) were employed.



Scheme 1. Synthesis of the rhodamine B methacrylate monomer.

The method proposed by Francis *et al.* (19) allowed the preparation of a rhodamine B-based alcohol which was subsequently transformed into the corresponding methacrylate monomer by reaction with methacryloyl chloride. This synthetic route was chosen for three main beneficial reasons: (i) contrary to secondary amides of rhodamine, tertiary amides do not undergo intramolecular cyclization which results in a loss of fluorescence; (ii) this fluorescent compound is highly soluble in aqueous solutions and retains its fluorescence emission under a broad range of pH and (iii) it enlarges our range of fluorescent probes.

The resulting rhodamine B methacrylate monomer was obtained with high purity and gave a $\lambda_{\text{ex.}} = 566$ nm with $\lambda_{\text{em.}} = 587$ nm in 10 mM PBS buffer (pH

7.1) (Figure 1), leading to a Stokes shift of 21 nm in agreement with rhodamine B-tertiary amide spectral properties (19).

BSA fluorescent bioconjugates

Synthesis and characterization of the BSA-macroinitiator

Bovine Serum Albumin (BSA) is a 66 kDa commercially available protein which was been selected as a model protein. The synthetic route for the synthesis of fluorescent bioconjugates based on BSA is represented in Scheme 2. The synthesis of the BSA-macroinitiator utilized the free cysteine residue (Cys-34) as a reactive functional group towards the maleimide initiator. It is known that only approximately 40-60% of free cysteine residues are available for protein modification in native BSA (20) and the number of thiols at the protein surface can be increased by appropriate reduction of disulfide bridges, although the latter approach mainly led to statistical multisite conjugation (13). In the present work we chose to prepare a BSA-monoinitiator using native BSA as the starting material, with unreacted non-thiol-containing BSA being the only observed byproduct.

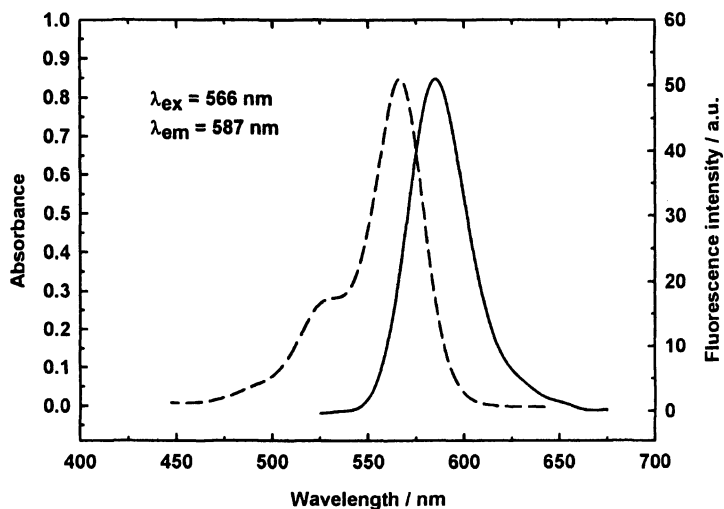
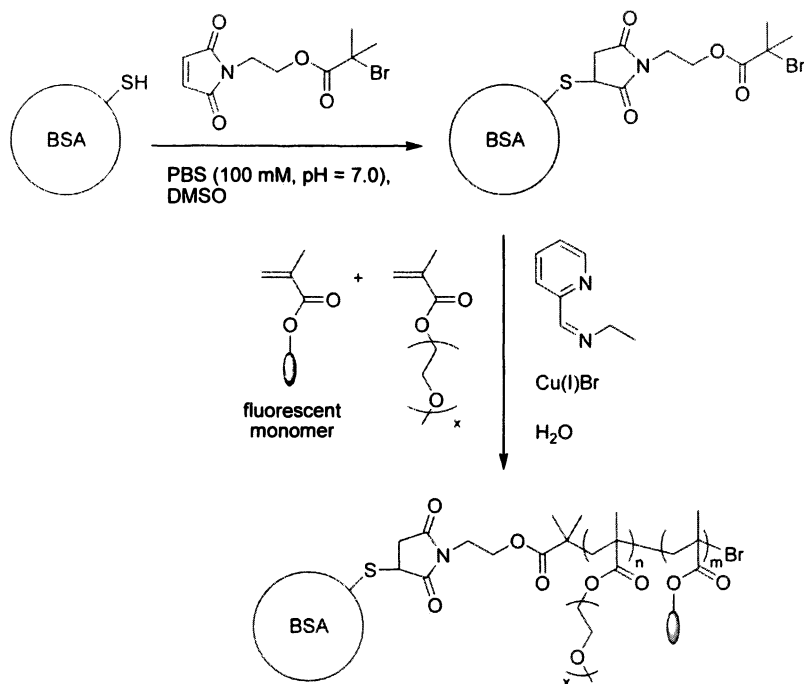


Figure 1. Absorption (dashed line) and emission (solid line) spectra of the rhodamine B methacrylate monomer in 10 mM PBS buffer (pH 7.1).



Scheme 2. Synthesis of the BSA fluorescent bioconjugates.

Each step of the synthesis of the bioconjugate was monitored by Sodium Dodecyl Sulfate Polyacrylamide Gel Electrophoresis (SDS-PAGE). Compared to the native BSA (band at 66 kDa), the BSA-macroinitiator exhibited two visible bands: The most significant band was slightly higher than 66 kDa and the second was spread out from 200 kDa to higher molecular weight (Figure 2). The presence of the second band can be ascribed to the aggregation phenomenon in which BSA oligomerizes *via* intermolecular thiol-disulfide interchange reaction (21). However, the relative intensities of the two bands indicate that only a minor fraction of BSA starting material undergoes oligomerization. SDS-PAGE analysis also revealed that traces of high molecular weight oligomers were already present in the commercially available native BSA.

BSA oligomerization has been reported to induce some protein conformational changes, especially a decrease of the α -helix accompanied by an increase of β -sheet substructures (21). Circular dichroism (CD) analysis of native BSA and BSA-macroinitiator revealed that the α -helix content decreased from 54 to 43% whereas the β -sheet content increased from 1 to 8% by passing from the former to the latter. This may be ascribed to the presence of oligomeric impurities in the BSA-macroinitiator, although a conformational change due to the attachment of the initiator moiety to the BSA cannot be ruled out.

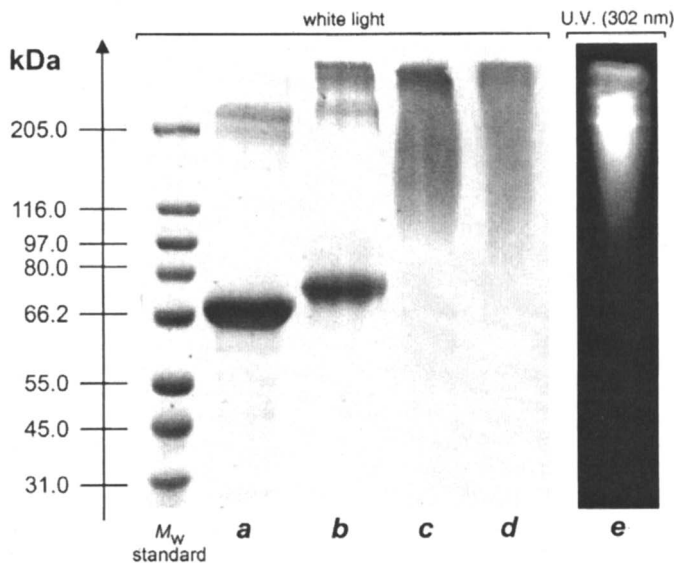


Figure 2. SDS-PAGE of (a) native BSA, (b) BSA-macroinitiator, (c) BSA-poly(DMAEMA-co-rhodamine B methacrylate), (d) BSA-poly(PEGMA₄₇₅-co-rhodamine B methacrylate) and (e) BSA-poly(PEGMA₄₇₅-co-rhodamine B methacrylate) under U.V. light at $\lambda = 302$ nm.

RP-HPLC using a C₁₈ column (Figure 3) showed separation between native BSA (retention time = 17.0 min) and BSA-macroinitiator (retention time = 19.5 min), The BSA-macroinitiator also presented small peak observed at 14.6 min, ascribed to the presence of BSA oligomers.

Synthesis and spectral properties of the BSA fluorescent bioconjugates

The isolated BSA-macroinitiator was used to initiate the polymerization of PEGMA₄₇₅ and DMAEMA using both hostasol and rhodamine B methacrylate fluorescent comonomers. After 48 h of polymerization at ambient temperature, the bioconjugates were purified and isolated by dialysis and lyophilization in order to remove unreacted monomers, especially remaining fluorescent monomers. The bioconjugation reaction was assessed by SDS-PAGE (Figure 2) where a shift from the BSA-macroinitiator to higher molecular weight was observed for both PEGMA₄₇₅ and DMAEMA polymerizations. Due to the incorporated rhodamine B fluorescent probe, the bioconjugate can also be detected by U.V. excitation ($\lambda = 302$ nm).

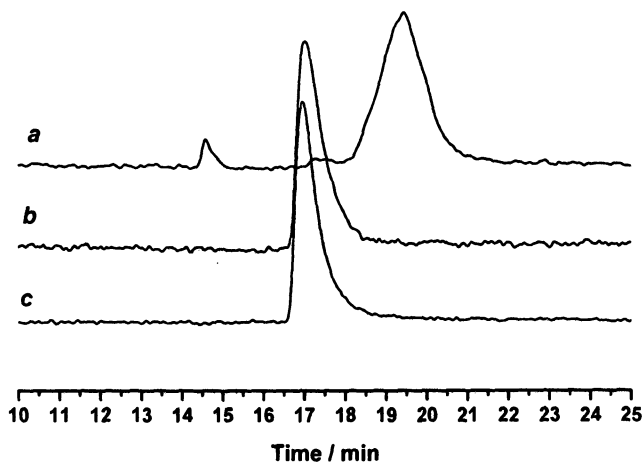


Figure 3. RP-HPLC of native (a) BSA, (b) control experiment and (c) BSA-macroinitiator. Control experiment: BSA in PBS (100 mM, pH = 7.0) with DMSO, stirred overnight at ambient temperature.

As expected, solutions of the bioconjugates in phosphate buffer (10 mM, pH = 7.1) exhibited a strong fluorescence in agreement with the respective excitation/emission spectra of the rhodamine B and hostasol methacrylate fluorescent monomers (Figure 4).

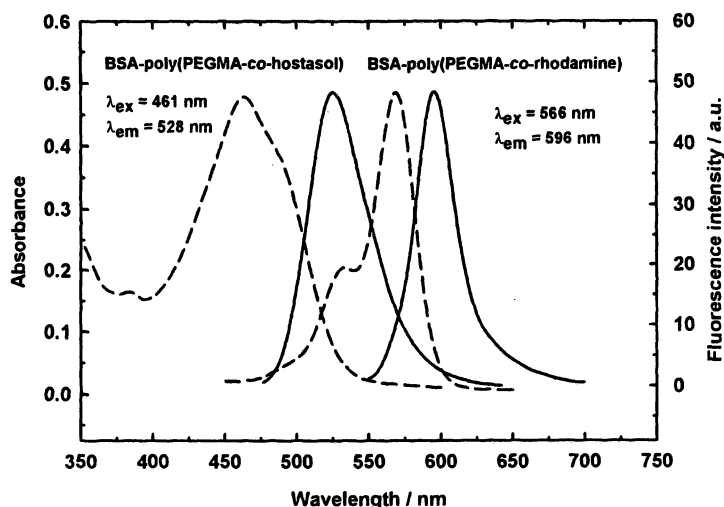


Figure 4. Absorption (dashed line) and emission (solid line) spectra of BSA-poly(PEGMA₄₇₅-co-hostasol methacrylate) and BSA-poly(PEGMA₄₇₅-co-rhodamine B methacrylate) fluorescent bioconjugates.

With both copolymerized fluorescent monomers the obtained fluorescent bioconjugates could be detected by SEC-HPLC with fluorescence detection (at appropriate λ_{ex} and λ_{em} for each fluorescent monomer) (Figure 5). This confirmed that the fluorescent probes had been incorporated *in situ* into the synthetic polymer-protein conjugate during the polymerization. In addition, SEC-FL-HPLC analysis revealed the absence of unreacted fluorescent monomers in the bioconjugate samples.

Lysozyme fluorescent bioconjugate

Synthesis of the lysozyme-macroinitiator

In order to demonstrate the flexibility of this approach, a similar synthetic route was investigated with lysozyme. The strategy for conducting bioconjugation was to target the free amine groups for multi-site attachment with the *N*-succinimidyl 2-bromo-2-methylpropionate (Scheme 3).

RP-HPLC analysis showed an almost complete disappearance of the native lysozyme peak along with the appearance of the lysozyme-macroinitiator peak. The relative broadness of the latter may indicate the presence of a statistical macroinitiators mixture in which different number of bromoisobutyrate initiator moieties are bound to the lysozyme core. The SDS-PAGE did not show any noticeable difference between the native lysozyme and the lysozyme-macroinitiator (Figure 6); in particular no formation of side products at higher molecular weight was observed.

Synthesis and characterization of the lysozyme fluorescent bioconjugate

The lysozyme-macroinitiator was used for the polymerization of PEGMA₄₇₅ in aqueous solution under living radical polymerization conditions with the rhodamine B monomer as a fluorescent probe. After polymerization, the lysozyme-poly(PEGMA₄₇₅-*co*-rhodamine B methacrylate) conjugate was purified and isolated by dialysis and lyophilization in order to remove unreacted monomers. The spectral properties of the fluorescent lysozyme bioconjugate were determined and, as expected, absorption and emission spectra of the bioconjugate are in very good agreement with those of pure rhodamine B monomer (Figure 7).

The lysozyme-poly(PEGMA₄₇₅-*co*-rhodamine B methacrylate) conjugate was observed by SEC-HPLC equipped with fluorescence detection (λ_{ex} = 566 nm and λ_{em} = 596 nm), which confirmed the incorporation of the fluorescent probe *in situ* during the polymerization reaction of PEGMA₄₇₅ initiated by the

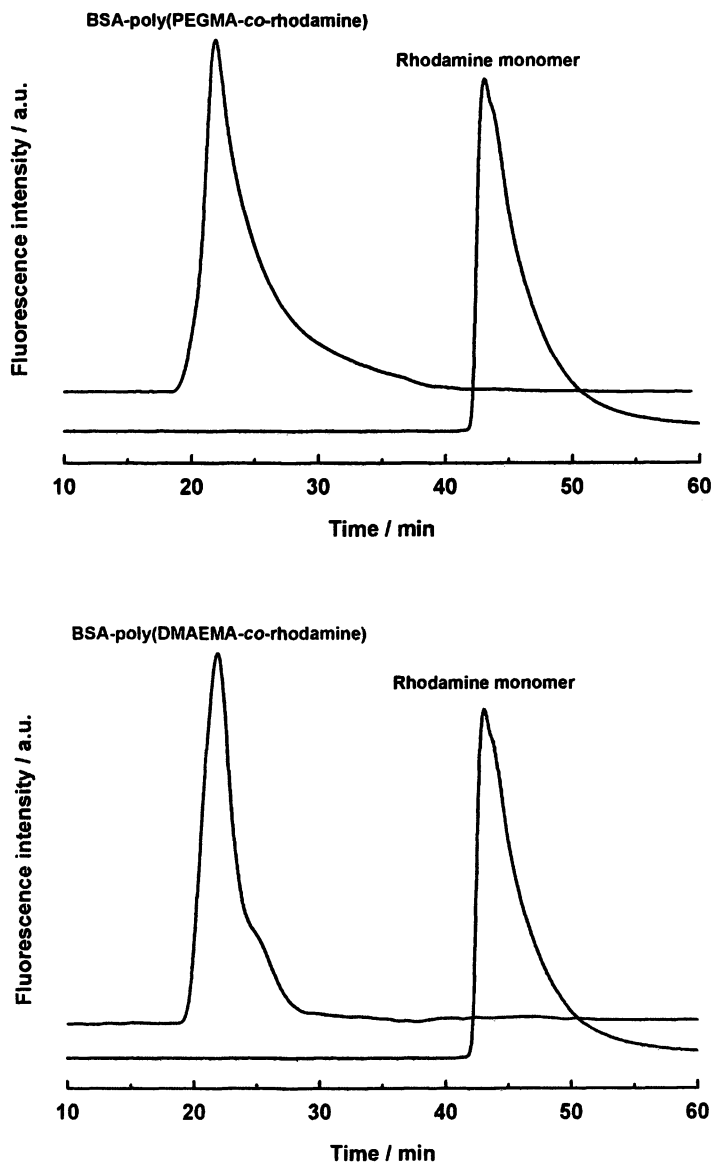
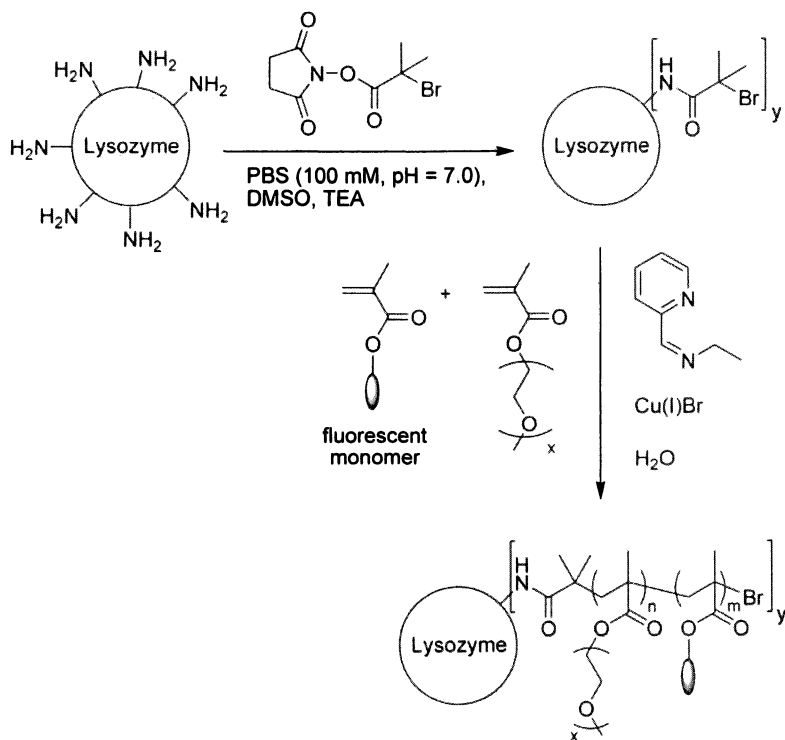


Figure 5. *Top:* SEC-FL-HPLC of BSA-poly(PEGMA₄₇₅-co-rhodamine B methacrylate) bioconjugate and of the rhodamine B methacrylate monomer. *Bottom:* SEC-FL-HPLC of the BSA-poly(DMAEMA-co-rhodamine B methacrylate) bioconjugate and of the rhodamine B monomer, $\lambda_{\text{ex.}} = 566 \text{ nm}$ and $\lambda_{\text{em.}} = 596 \text{ nm}$.



Scheme 3. Synthesis of the lysozyme fluorescent bioconjugate by living radical polymerization.

lysozyme-macroinitiator (Figure 8). A broad peak for the lysozyme bioconjugate was observed, probably due to the use of lysozyme-macroinitiators featuring a different number of initiating centers, which induced a broader molar mass distribution in the resulting biohybrid material, a behaviour that is commonly observed in living radical polymerization using multifunctional initiators.

Conclusions

Bovine serum albumin and lysozyme have been transformed into macroinitiators for the synthesis of fluorescent bioconjugates exploiting living radical polymerization. For this purpose, we have designed and synthesized a new fluorescent methacrylate monomer derived from rhodamine B. The bioconjugation reactions were assessed and these bioconjugates were detected by HPLC with fluorescent detection, giving rise to a new strategy for *in situ*

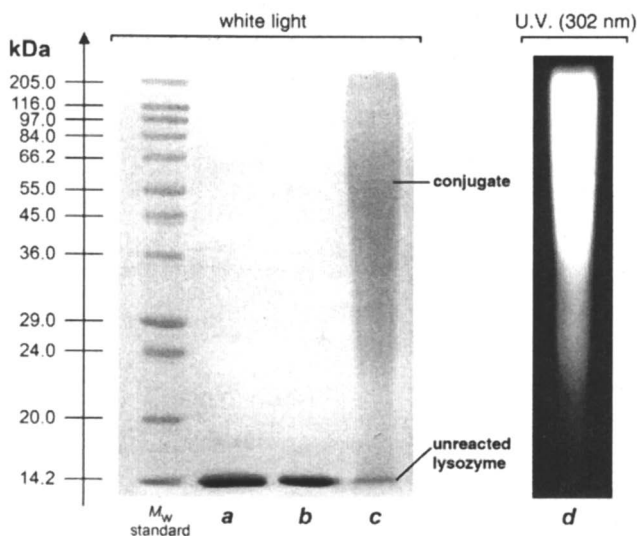


Figure 6. SDS-PAGE of (a) native lysozyme, (b) lysozyme-macroinitiator, (c) lysozyme-poly(PEGMA₄₇₅-co-rhodamine B methacrylate) and (d) lysozyme-poly(PEGMA₄₇₅-co-rhodamine B methacrylate) under U.V. light at 302 nm.

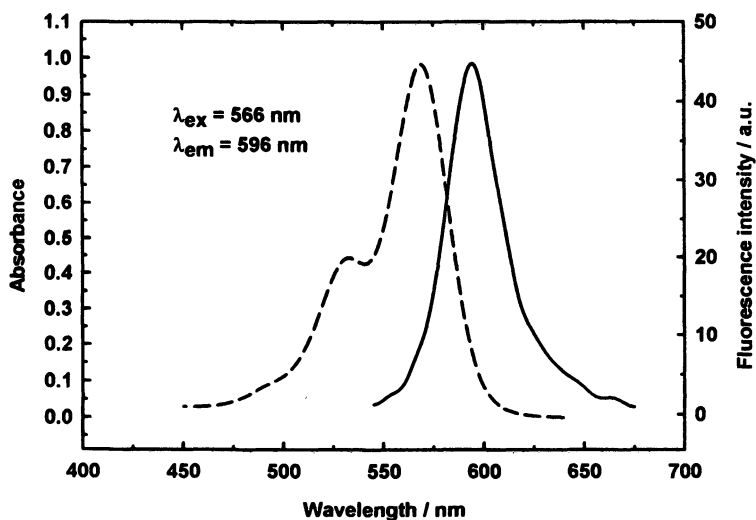


Figure 7. Absorption (dashed line) and emission (solid line) spectra of the lysozyme-poly(PEGMA₄₇₅-co-rhodamine B methacrylate) fluorescent bioconjugate.

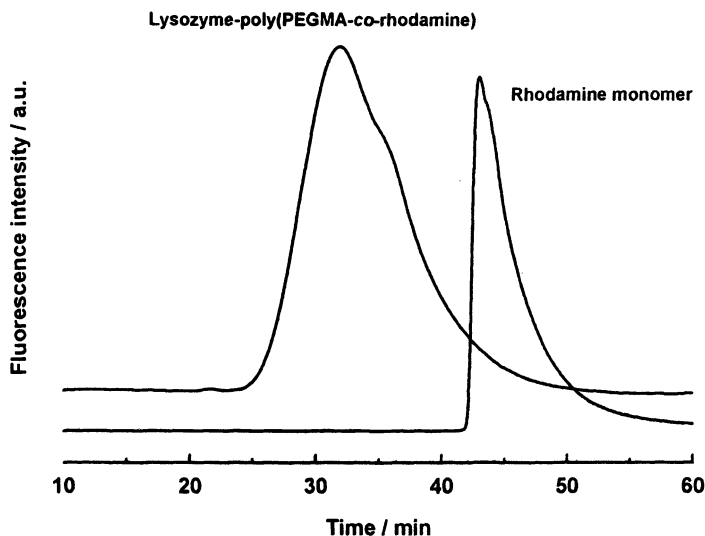


Figure 8. SEC-FL-HPLC of lysozyme-poly(PEGMA₄₇₅-co-rhodamine B methacrylate) bioconjugate and of the rhodamine B methacrylate monomer (λ_{ex} = 566 nm and λ_{em} = 596 nm).

observation of delivered compounds.²² This strategy is quite generic and applicable to a wide range of proteins and peptides.

References

1. Abuchowski, A.; Van Es, T.; Palczuk, N. C.; Davis, F. F. *J. Biol. Chem.* **1977**, *252*, 3578.
2. Harris, J. M.; Chess, R. B. *Nat. Rev. Drug Discov.* **2003**, *2*, 214.
3. Veronese, F. M.; Harris, J. M. *Adv. Drug Deliver. Rev.* **2002**, *54*, 453.
4. Roberts, M. J.; Bentley, M. D.; Harris, J. M. *Adv. Drug Deliver. Rev.* **2002**, *54*, 459.
5. Veronese, F. M. *Biomaterials* **2001**, *22*, 405.
6. Matyjaszewski, K.; Xia, J. *Chem. Rev.* **2001**, *101*, 2921.
7. Kamigaito, M.; Ando, T.; Sawamoto, M. *Chem. Rev.* **2001**, *101*, 3689.
8. Hawker, C. J.; Bosman, A. W.; Harth, E. *Chem. Rev.* **2001**, *101*, 3661.
9. Perrier, S.; Takolpuckdee, P. *J. Polym. Sci., Part A: Polym. Chem.* **2005**, *43*, 5347.
10. Tao, L.; Mantovani, G.; Lecolley, F.; Haddleton, D. M. *J. Am. Chem. Soc.* **2004**, *126*, 13220.

11. Lecolley, F.; Tao, L.; Mantovani, G.; Durkin, I.; Lautru, S.; Haddleton, D. M. *Chem. Commun.* **2004**, 2026.
12. Mantovani, G.; Lecolley, F.; Tao, L.; Haddleton, D. M.; Clerx, J.; Cornelissen, J. J.; Velonia, K. *J. Am. Chem. Soc.* **2005**, *127*, 2966.
13. Heredia, K. L.; Bontempo, D.; Ly, T.; Byers, J. T.; Halstenberg, S.; Maynard, H. D. *J. Am. Chem. Soc.* **2005**, *127*, 16955.
14. Bhalchandra, S. L.; Hironobu, M.; Matyjaszewski, K.; Russell, A. J. *Biomacromolecules* **2005**, *6*, 3380.
15. Haddleton, D. M.; Crossman, M. C.; Dana, B. H.; Duncalf, D. J.; Heming, A. M.; Kukulj, D.; Shooter, A. J. *Macromolecules* **1999**, *32*, 2110.
16. Limer, A. J.; Rullay, A. K.; San Miguel, V.; Peinado, C.; Kelly, S.; Fitzpatrick, E.; Carrington, S. D.; Brayden, D.; Haddleton, D. M. *React. Funct. Polym.* **2006**, *66*, 51.
17. Laemmli, U. K. *Nature* **1970**, *227*, 680.
18. Johnson, W. C. *Proteins Struct. Funct. Genet.* **1999**, *35*, 307.
19. Nguyen, T.; Francis, M. B. *Org. Lett.* **2003**, *5*, 3245.
20. Janatova, J. F.; Fuller, J. K.; Hunter, M. J. *J. Biol. Chem.* **1968**, *243*, 3612.
21. Maruyama, T.; Katoh, S.; Nakajima, N.; Nabetani, H. *Biotechnol. Bioeng.* **2001**, *75*, 233.
22. Nicolas, J.; San Miguel, V.; Mantovani, G.; Haddleton, D. M. *Chem. Commun.* **2006**, 4697.

Chapter 7

Adapting Polymeric Metal Complexes for Biomedical Applications

Cassandra L. Fraser and Gina L. Fiore

Department of Chemistry, University of Virginia, Charlottesville, VA 22904

Metal complexes play many roles in biological systems as catalysts, stimuli responsive centers and structural materials. Introduction of metals into synthetic biomaterials can result in similarly diverse functions, useful for imaging, degradation, and bioactivity. Biomaterials with single well-defined metal centers can result from the combination of coordination chemistry and controlled polymerizations. Efforts in our laboratory to adapt these reactions to bipyridine (bpy) and dibenzoylmethane (dbm) ligand and metal complex reagents, and to explore the ways that metals and polymers mutually affect each other are reviewed below, with poly(lactic acid) (PLA), poly(ethylene glycol) (PEG), poly(ethylenimine) (PEI), and selected acrylate systems, poly(*t*-butyl acrylate) (PtBA) and poly(acrylic acid) (PAA), as examples.

Introduction

Polymeric metal complexes (PMCs) consist of metal centers in well defined macromolecular environments (1,2,3,4) (Figure 1) and have many desirable features for biomedical applications. Metal complexes, consisting of metal ions and ligands, are modular systems that can undergo structural and physical property changes in response to environmental stimuli, relevant to imaging and controlled release applications. Metals can function as reactive centers to facilitate materials synthesis or degradation, and introduce new kinds of biological activities into polymeric biomaterials. Sometimes the ligands themselves display therapeutic potential (5) (e.g. as anticancer agents), (6,7,8) and coordination of chelates to metals can influence biochemical pathways *in vitro* (9) and *in vivo* (10). Metal based drugs are also known (11,12,13). Modification of ligands with polymers (14,15) and delivery alone or as responsive metal complex prodrugs, therapeutics (16), or imaging agents (17,18,19) could lead to increased circulation time, improved bioavailability, altered mechanical properties, and new kinds of triggered release mechanisms. Metal crosslinks in biomaterials (20,21) can respond differently than organic materials to changes in pH, temperature, and other stimuli (22,23), and targeting can also be introduced (24,25).



Figure 1. Schematic representation of a polymeric metal complex (left) and two stage degradation mechanism, at the metal center via macroligand dissociation (center) and along the polymer backbone (right).

Progress has been made in combining coordination chemistry with controlled polymerization to generate PMCs (1,2,3,4) however, new strategies and design criteria are required to adapt these systems for biomedical uses. Biocompatible and biodegradable polymers (26) accessible by controlled polymerizations are needed, and known synthetic methods must be tested and adapted for compatibility with ligand and metal complex reagents if well defined metallo-biomaterial architectures are to be achieved. Additionally, it is important to consider ligand and metal complex properties in polymeric, aqueous, and biological environments, and how these might change in response to likely

stimuli. Some results of our efforts to begin to explore these areas are described below for bipyridine (bpy) model systems and dibenzoylmethane (dbm) chelates. The latter system and its derivatives are of interest for their reported anti-cancer properties (7,8,27,28,29) and for the wide ranging physical properties and reactivity of diketone metal complexes (30) for incorporation into polymers.

Modifying Ligands and Metal Complexes with Biocompatible and Biodegradable Polymers

Polymers commonly used in medicine range from neutral to charged, water soluble, swellable, and insoluble, to hybrid materials of various types (26). Biomaterials attainable by controlled polymerization methods to produce well defined PMC architectures include biocompatible polyesters such as poly(lactic acid) (also known as polylactide), and the crystalline poly(ϵ -caprolactone) (31). Physical properties and degradation of these hydrophobic polymers can be tuned by monomer choice (32). For example, PLGA is a lactide glycolide copolymer that degrades more readily than PLA or PCL. These materials have been formulated in many ways (33,34,35,36) as bulk material devices, fibers, meshes, microspheres, nanoparticles, solution assemblies and other configurations for drug delivery and tissue engineering. Poly(ethylene glycol) (PEG), in contrast, is a ubiquitous water soluble polymer used in medical applications (37). Its protein non-adhesive qualities are desirable for surface modification (38) and lending stealth-like properties (39,40) to drug delivery vehicles. Drugs remain in circulation longer once PEGylated, and numerous bioconjugation methods have been reported for PEG in active targeting (41,42,43). Many PEG-based hydrogels are also known (44,45). Charged polymers include poly(ethylenimine) (PEI), a cationic polymer that is used to entrap DNA for gene delivery (46,47), and negatively charged poly(acrylic acid) (PAA), with known mucoadhesive properties (48,49,50) and capability of forming polyplexes with cationic polymers. Each of these kinds of materials presents unique challenges for adaptation with ligand and metal complex functionality by initiation, termination or coupling routes.

Polyesters

Polymeric metal complexes with polyester macroligands have been generated by initiation from hydroxyl functionalized ligand and metal complex reagents. Ligand initiators lead to macroligands which can be combined with metal precursors in coordination reactions to produce PMCs (51). Metalloinitiators, on the other hand, produce PMCs directly (2).

Bipyridine

Hydroxyl functionalized bipyridines, $\text{bpy}(\text{CH}_2\text{OH})_2$, serve as initiators for ring opening polymerization (ROP) of lactide, caprolactone and glycolide monomers using tin(II) octoate ($\text{Sn}(\text{oct})_2$) as the catalyst (52,53). Reactions with lactide and caprolactone exhibited good control and the resulting bpyPLA_n and bpyPCL_n ($n = 1, 2$) macroligands can be coordinated to metals (Figure 2A) such as iron, ruthenium (52,53), or lanthanides (54) to produce PMCs of varying kinetic stability. Hybrid systems have also been investigated, both star blocks (55) and heteroarm stars (56) in which the macroligands themselves are block copolymers (57), and heteroarm stars comprised of homopolymer macroligand combinations (58,59). For certain block combinations, e.g. $\text{bpy}(\text{PS})(\text{PCL})$ and $\text{bpy}(\text{PEG})(\text{PLA})$, better control was noted with Et_3Al in toluene solution versus bulk polymerization with $\text{Sn}(\text{oct})_2$ (57). Care must be taken in chelation reactions involving inert metals such as Ru (58) or Pt (60) to avoid polyester backbone cleavage. A range of molecular weights and polymer architectures are compatible with this chelation approach. Metalloinitiation was also demonstrated for hydroxyl functionalized Ru tris(bpy) reagents with DMAP as the catalyst for lactide ROP (Figure 2B) (61).

Dibenzoylmethane

Drawing on experience from bpy ligand and metal complex reagents, lactide ROP reactions were also run with hydroxyl functionalized dbm , dbmOH , and $\text{Sn}(\text{oct})_2$ under bulk conditions (54,62). In contrast to bpy , with neutral nitrogen heterocycles, dbm is a negatively charged ligand with oxygen donors. Though dbmPLA (54) and dbmPCL_n ($n = 1, 2$) (63) macroligands were achieved with lactide, dbmOH and the tin catalyst, reactions took longer than for bpy and displayed diminished molecular weight control (i.e. higher polydispersity indices, PDIs, and non-linear behavior in kinetics experiments and M_n vs percent conversion plots.) (Figure 3 top). Control experiments suggest that dbm interferes with catalyst function, perhaps by serving as a competitive ligand for tin.

To address this issue and obtain higher molecular weight materials with good control (i.e. >10 kDa), protecting group strategies were pursued. In previous work, we have employed metal complexation as a way of reversibly masking incompatible ligand functionality during polymerization (64,65). Here too, this approach was adopted by binding dbmOH to iron(III) to produce $\text{Fe}(\text{dbmOH})_3$ (66,67). Subjection of this trifunctional iron initiator to bulk polymerization conditions, both with and without the tin catalyst, resulted in much faster polymerization rates and low PDI materials to reasonably high monomer conversion ($\sim 70\%$) (Figure 3, bottom). Thus, iron serves as both a protecting group and a catalyst for ring opening polymerization to generate iron

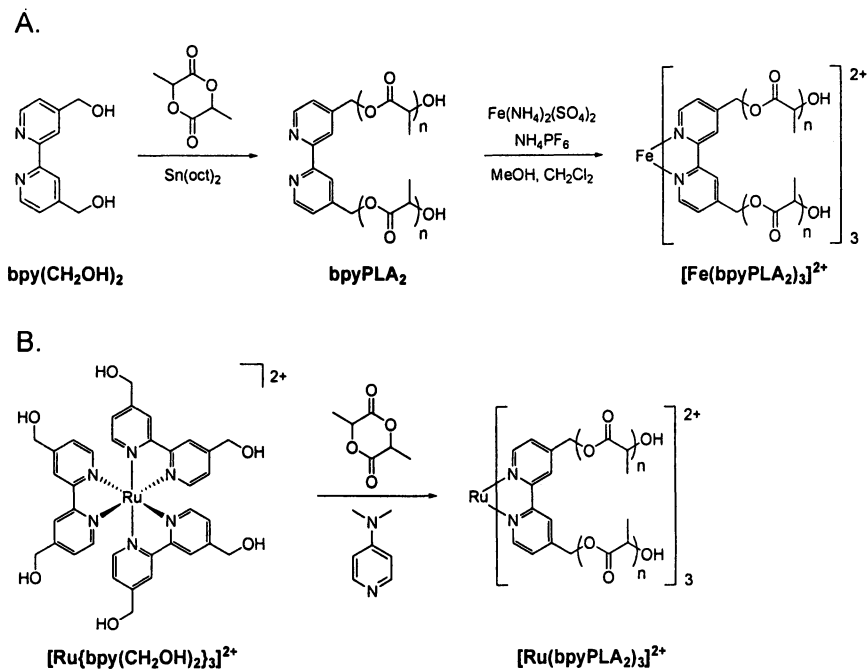


Figure 2. (A) Macroligand chelation and (B) metalloinitiation approaches to metal complexes with bipyridine polyester macroligands.

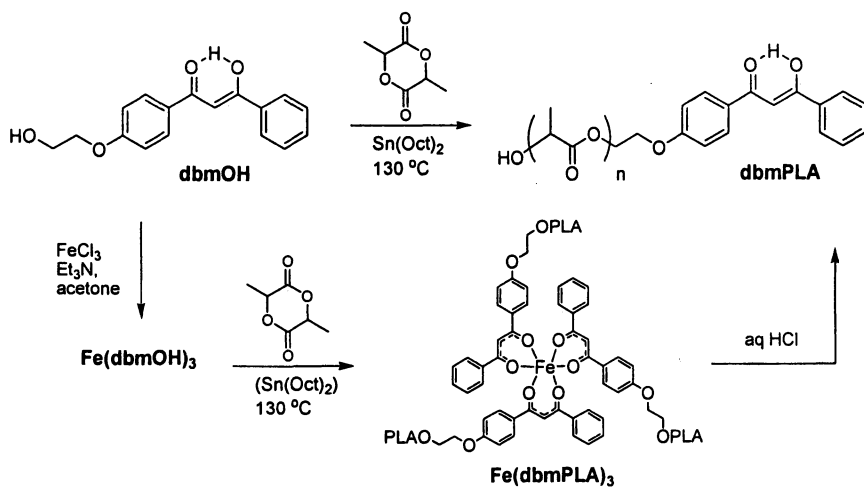


Figure 3. Synthetic routes to PLA macroligands and polymeric iron complexes based on dibenzoylmethane (dbm).

tris(dbm) centered PLA and also analogous PCL materials. These red orange materials are of interest for cosmetics applications and as new kinds of responsive biomaterials subject to a two stage degradation mechanism at the metal center upon ligand dissociation and along the polyester backbone (Figure 1). Presently these polymers are being formulated as nanoparticles for more detailed degradation studies and also to test cytotoxicity and cell growth effects. If nanoparticles are taken up into the acidic environment of endosomes and lysosomes in cells (68,69), the metal complex may be destabilized and polyester hydrolysis facilitated. In fact, treatment with weak acid under mild conditions serves as a synthetic demetallation procedure too, to decolorize the sample and liberate macroligands from iron. (Figure 3, bottom right). The resulting dbmPLA materials may be subsequently coordinated to other metal centers to generate new PMC materials. Luminescent systems based on lanthanides and boron are currently under investigation.

These findings with multifunctional iron dbm reagents are exciting for a number of reasons. The iron complexes play many roles, as a dbm protecting group, polymerization initiator, catalyst and activator, and as chromophores and reactive, responsive features in the resulting materials. Demetallation leads to macroligand building blocks for modular metal template polymer synthesis. Additionally, a green synthesis is employed to generate these responsive state-of-the-art materials. Lactide is derived from corn, a renewable resource, and a solvent-free process is employed to generate a multifunctional biodegradable and biocompatible polymer product. In comparison to many reagents used in chemical synthesis that can be toxic, iron is a common metal in biological systems, and dbm has documented health benefits with respect to anti-cancer activity. Dbm serves a protective role (70,71) when administered prior to food mutagen (72) and carcinogen exposure (73,74,75), and furthermore, treatment of cancer cells or tumor bearing animals with dbm analogues can help to diminish cancer growth in model systems (7,8,27,28,29). As UV light absorbers, dbm analogues are active components in sunscreens and play a protective role in this respect (28,75,76). As these examples illustrate, dbm is not just a spectator ligand, only there to enhance metal properties, or a synthetic impurity; it can also introduce beneficial prophylactic or therapeutic features into the material. Clearly, the methods by which materials are made can impact human health. Green syntheses, processes, and materials that are safe or beneficial for biological systems can help to diminish health problems, such as cancer, that subsequent therapies are designed to address.

Poly(ethylene glycol)

For many biomaterial applications, water soluble polymers are required. Given the prevalence of PEG as a polymeric biomaterial

(37,38,39,40,41,42,43,44,45) and the many points of comparison in the literature, it is a good place to start to understand the effects of ligand and metal complex adaptations on biomaterials properties.

Iron Bipyridine

Recently we reported the synthesis of bpy centered PEG macroligands, bpyPEG₂, by anionic polymerization and the coordination chemistry of these systems with iron(II) in aqueous solution (Figure 4) (77). Though iron tris(bpy) complexes are normally very stable in water and air for long periods of time (>1 year) (78,79), in the presence of PEG the red violet iron tris(bpy) chromophores bleach over time (e.g. $M_n = 6200$; $t_{1/2} = 7.1$ h). Samples that are generated and kept under an inert argon atmosphere do not degrade, thus suggesting an important role for oxygen in this process. Rates of bleaching depend upon whether PEG is introduced as a blend or covalently attached to the metal complex; the latter systems fade more rapidly. Furthermore, complex degradation rates show molecular weight dependence. Higher molecular weight $[\text{Fe}(\text{bpyPEG}_2)_3]\text{SO}_4$ degrades more rapidly once bleaching commences. The exact cause of this process is not known; however, it is known that peroxides develop in PEG upon exposure to air and also, that iron chemistry and peroxides can lead to Fenton chemistry, namely the generation of reactive oxygen species by radical processes (80,81,82). The fact that acrylate modified bpyPEG₂ formed gels spontaneously upon addition of iron salts, without the addition of light and a photoinitiator, is consistent with the presence of radical intermediates (83,84).

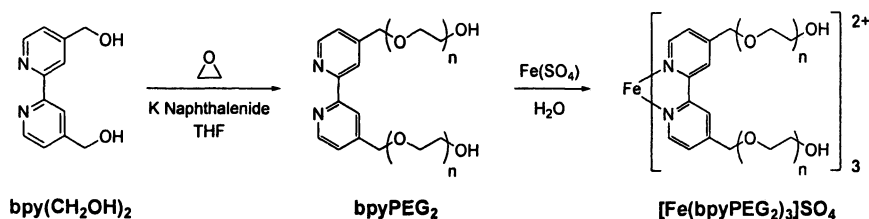


Figure 4. Synthesis of iron tris(bpy) centered PEG stars.

Recently, the synthesis of bpyPEG₂ has been optimized, and better molecular weight control has been achieved in polymer synthesis (85). To ensure that minor impurities were not responsible for side reactions in first generation bpyPEG₂ polymers, these new materials were tested for air sensitivity and stability as well. When these new PEG macroligand samples were generated and stored under strictly air-free conditions in attempt to prevent peroxide

formation, and subsequently were subjected to iron coordination under air-free conditions, chromophores were again stable. However, when these aqueous iron tris(bpyPEG₂) solutions are opened to air, they too degrade at rates comparable to first generation bpyPEG₂ samples that were stored under air for long periods of time. Thus, PEG storage method and time do not seem to have a measurable effect on this degradation process. Reactive species seem to form rapidly within minutes, and chromophore degradation occurs within hours, upon exposure of PMC solutions to air. In addition to chromophore bleaching, gel permeation chromatographic (GPC) analysis shows evidence of enhanced PEG backbone degradation too, in the presence of iron tris(bpy). An iron tris(bpy) sample with starting molecular weight of $M_n \text{ star} = 47,700$; $M_n \text{ macroligand} = 15,900$, PDI = 1.12 was exposed to air and the red violet color faded. After ~40 days, $M_n = 6200$, PDI = 1.57. Since iron tris(bpy) polymers fragment during GPC analysis, this value likely corresponds to the degradation products of the dissociated macroligand. Presently we are conducting systematic studies of PEG macroligand degradation and acrylate crosslinking in the presence of iron tris(bpy). Effects of metal centers on hybrid PEG-PLA materials and their assemblies are also under investigation. Though radicals and other reactive species can be damaging to cells (86), they are also integral to certain drug therapies (87) when appropriately targeted to sites of pathological tissue (e.g. tumors) and to tissue repair and remodeling processes (88,89). In these respects, enhanced two stage degradation involving ligand dissociation from metal centered stars, and along the polymer backbone could prove useful for drug delivery and tissue engineering (Figure 1).

Ruthenium Bipyridine

A typical reactivity is also noted for PEG with luminescent ruthenium tris(bpy) systems, but in this case during preparation. Coordination reactions with polymeric ligands are typically slower than those with non-polymeric analogues, and in a comparative study of different macroligands, reactions involving PEG were the slowest among the compositions explored (58). Ru tris(bpy) complexes have been generated from low molecular weight bpy PEG macroligands (90,91), but for higher molecular weights, products do not always form efficiently. Other investigators working with Ru diimine PEG materials have noted similar effects (92). GPC analysis suggests that degradation is occurring and bimodal traces are sometimes observed, with only one of the two peaks showing evidence of associated metal complex chromophores (93). Presently, we hypothesize that chain scission occurs at bpy-PEG junctions to form PEG and bpyPEG, before or after metal binding. Thus, macroligand chelation is not consistently effective method for generating Ru tris(bpyPEG₂) materials.

As an alternative approach to model systems for water soluble materials with built in imaging agents, we are pursuing coupling approaches involving Ru tris(bpy) reagents (94) and activated PEGs. Though Ru tris(bpy) luminescence is quenched by oxygen, this sensitivity can be exploited for sensing applications (95), and polymers can influence optical properties of Ru and other metal complexes (96). In some cases, polymers facilitate luminophore degradation. For example, Demas and coworkers have shown that the entrapment or caging of singlet oxygen in Ru tris(bpy)/PEG blends can lead to photochemical decomposition (97). In other instances, metal site isolation in polymers enhances luminescence properties by minimizing metal-metal self quenching processes (98). Given the challenges of PEG macroligand chelation and the need for greater fundamental understanding of polymer effects on metal optical properties, we are also pursuing coupling reactions to Ru complexes with activated groups in their ligand peripheries. Previously, we (58) and other groups (90,99,100,101) have explored coupling approaches to bpy PEG macroligands via covalent attachment. Reactions between PEG nucleophiles and alkyl or acid halides to form ethers and esters respectively tend to work best for low molecular weight polymers and coupling agents with lower functionality (e.g. mono or difunctional reagents, vs hexafunctional systems). In order to increase coupling efficiency, reactions involving PEGs with stronger nucleophiles such as thiols at the chain termini were targeted. Disulfide and other forms of thiol coupling reactions are common bioconjugation strategies (37,43), which can be extended to ligand (102) and metalloreagent coupling as well (Figure 5) (103). Since sulfur based compounds, such as 4-mercaptopyridine, are known quenchers for Ru tris(bpy) luminescence (104), covalent attachment via thiol ether, thiol ester or disulfide ligands could result in enhanced responsiveness. Indeed, this is the case in non-polymeric thiol ester model systems, however this also correlates with impressive oxygen sensitivity in some analogues. Currently, we are extending methodologies from model systems to functionalized PEG derivatives (Figure 5), to see if covalent attachment of PEG to Ru tris(bpy) via these kinds of sulfur-based linkages results in sensor materials with enhanced properties and processibility. Ultimately, methodologies developed for Ru tris(bpy) modification with PEGs could be extended to other metal systems with desirable optical properties for *in vitro* molecular probes or *in vivo* imaging.

Poly(ethylenimine)

Polymeric vectors for gene delivery are typically based on cationic polymers that can entrap and condense DNA, and protect it during delivery (46,47,105).

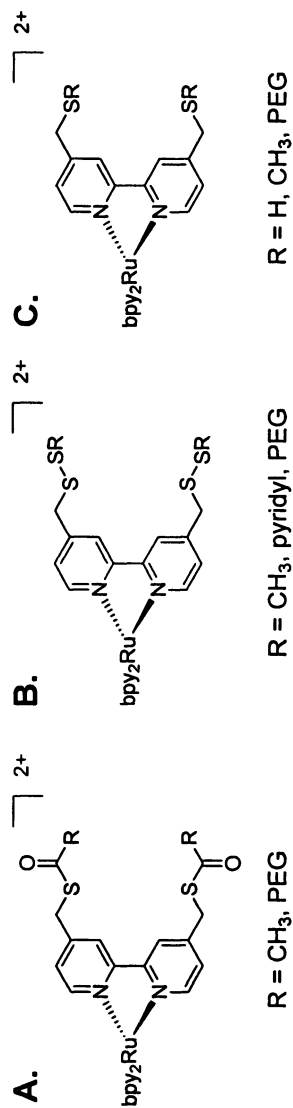


Figure 5. Model systems and Ru tris(bpy)-centered PEG materials involving thioester, disulfide, and thioether linkages.

One of the most common polymers used for this purpose is poly(ethylenimine) (PEI) (106), which serves as a point of comparison for new state-of-the-art materials incorporating targeting, degradation and other functions designed to overcome obstacles in the delivery pathway that can diminish transfection efficiency (105,107). One way to lower toxicity of cationic PEI vectors is to combine them with PEG or other materials, such that the molecular weight is increased but the overall cationic charge density is lowered (108). Through metal template synthesis too, different kinds of polymeric ligands may be combined and a variety of architectures are accessible. Toward this end of combining PEI and PEG and generating models for gene delivery vectors with built-in imaging agents, we also conducted methodological studies involving Ru PEI (109,110). One of the first systems employed by our group (111,112) and others (113) to demonstrate the metalloinitiator concept involved ruthenium tris(bpy) complexes with chloride sites (114) and 2-oxazoline monomers to generate Ru centered polyoxazolines such as six arm stars, $[\text{Ru}(\text{bpyPEOX}_2)_3]^{2+}$ from hexafunctional initiators or linear polymers, $[\text{Ru}(\text{bpy})_2(\text{bpyPEOX}_2)]^{2+}$ from difunctional reagents (PEOX = poly(2-ethyl-2-oxazoline)). Though PEI is typically generated in a branched fashion by cationic ROP of aziridine (115,116), amide hydrolysis of polyoxazolines yields PEI in linear form (117,118). Labile metal complexes are sensitive to acid and base and thus are not expected to survive amide hydrolysis conditions, however more robust Ru tris(bpy) complexes and other inert metal systems could be compatible with these conditions. To test this idea, Ru tris(bpyPEOX₂) samples were synthesized and subjected to acid hydrolysis to generate Ru tris(bpy) centered PEI (Figure 6). Red orange chromophores present in the Ru PEOX starting materials persisted in the Ru PEI products upon acid hydrolysis, though metal complexes degraded when basic conditions (i.e. pH>10) were employed, as evidenced by the disappearance of the red orange color and corresponding absorptions ($\lambda_{\text{max}} = 466 \text{ nm}$) in UV/vis spectra. Ru PEI materials were combined with DNA for gel retardation assays and transfection studies. Gel retardation assays show that star shaped Ru PEI ($M_n = 7.9 \text{ kDa}$) entraps DNA at an N:P ratio of 2, comparable to commercial linear PEI (L-PEI) ($M_n = 22 \text{ kDa}$). Transfection of GFP plasmids was evident in LNCaP prostate cancer cells (a cell type studied by our biological collaborator but reported to present challenges for PEI gene delivery (119)), but at a lower efficiency than linear PEI (~50% relative transfection efficiency, N/P ratio: 48 for Ru PEI vs 12 for L-PEI). These model studies demonstrate that inert metal centers may be incorporated into cationic polymers used as vectors for gene delivery. Ultimately, these strategies could be extended to new state-of-the-art polymers and other metal systems with functionalities (e.g. optical, magnetic, reactivity) that are useful for imaging and other applications.

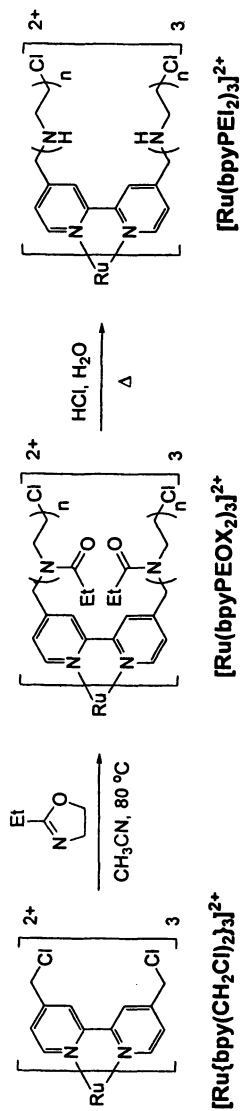


Figure 6. Synthesis of Ru tris(bpy) centered poly(ethylenimine) via Ru centered poly(2-ethyl-2-oxazoline) precursors.

Poly(acrylic acid)

Ruthenium Bipyridine

Presently, many new polymeric biomaterials, water soluble and both cationic and anionic charged systems, are being generated by ATRP and other controlled radical methods (120,121). Poly(acrylic acid) (PAA) is a mucoadhesive anionic material (48,49,50) used in drug delivery (122). It has also been coupled with PEG to form gels (50), and with PLA and other degradable polyesters to form hybrid film (123) and assembly forming materials (124,125) with neutral hydrophobic and charged hydrophilic domains. A common route to PAA involves the ATRP of t-butyl acrylate, followed by cleavage of the resulting t-butyl ester side chains of poly(t-butyl acrylate) (PtBA) with hydrolysis or thermolysis (55,61,124,126). Accordingly, Ru tris(bpy) ATRP initiators with α -bromoester functionalities (127,128) were employed in combination with t-butyl acrylate to generate $[\text{Ru}\{\text{bpy}(\text{PtBA})_2\}_3]^{2+}$ stars (49). Subsequent reaction with TMSI in dry dichloromethane and hydrolysis using 0.1 N HCl led to the corresponding Ru PAA materials. Hybrid PLA-PtBA star block materials (129) were generated via $[\text{Ru}(\text{bpyPLA})_2]^{2+}$ by esterification of PLA hydroxyl chain ends with 2-bromoisobutyryl bromide to generate ATRP macroinitiators. Deprotection of t-butyl groups as described above afforded amphiphilic $[\text{Ru}\{\text{bpy}(\text{PLA-PAA})_2\}_3]^{2+}$ with little PLA degradation evident upon NMR analysis (61). Though Ru tris(bpy) luminescence is often quenched by oxygen in aqueous solutions, when entrapped in a protective PLA shell, these Ru PLA-PAA materials formed assemblies that continued to luminescence quite brightly upon excitation with UV light.

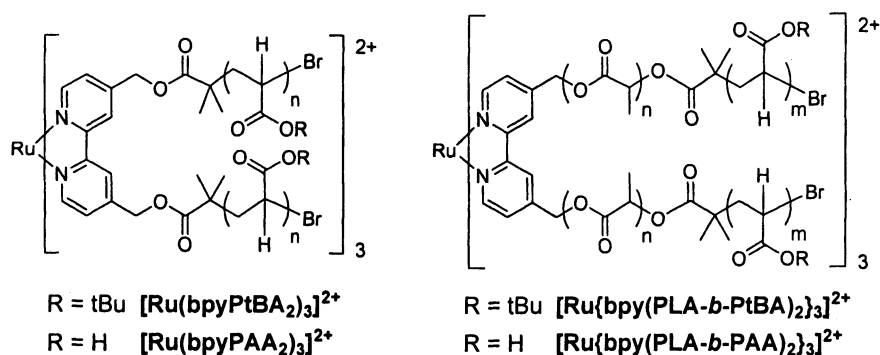


Figure 7. Ru tris(bpy)-centered PMCs based on poly(t-butyl acrylate), poly(acrylic acid), and PLA-PtBA and PLA-PAA block copolymers.

Iron Bipyridine

Though labile iron tris(bpy) complexes are not expected to be stable in the presence of carboxylic acid or negatively charged carboxylate PAA side chains, nor under the conditions used to generate PAA from PtBA, fundamental studies were conducted with bpyPtBA₂ macroligands and iron salts for comparison with other iron tris(bpy) PMCs. Initial experiments showed anomalous behavior compared to bpy PMCs based on neutral polymer chains (e.g. PMMA, PS, PLA, PCL, etc.) (130) Rather than obtaining red violet solutions upon mixing bpyPtBA₂ with Fe²⁺, instead the reaction mixture turned yellow and then colorless over time. Initially, we hypothesized the formation of mono bpy complexes, based on correspondence of spectral data with literature precedent (131), with possible transformation to bis complexes over time (Figure 8).

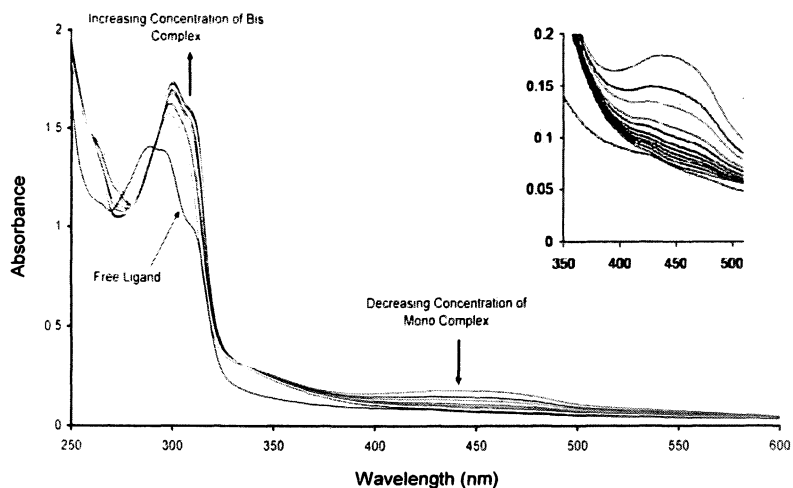


Figure 8. UV/vis spectral data for 1:3 Fe(II):bpy(PtBA)₂ ($M_n = 23$ kDa) as a function of time in 3:1 CH₂Cl₂:MeOH. (Spectra were collected at 5 min intervals except the final three were collected at 20 min intervals). Labels reflect the initial hypothesis that mono then bis bpy complexes were formed. Spectral data for the free bpyPtBA₂ macroligand is provided for comparison.

However, spectral data for known Fe(II) bis(bpy) complexes were not well matched to the colorless solutions that were noted (132,133,134). Further investigation revealed that red violet iron tris(bpy) complexes could be generated under air- and light-free conditions; whereas, yellow, then colorless solutions form in the presence of air and light (135). This suggests possible oxidation of

an Fe^{2+} species (e.g. to Fe^{3+}), which could occur via a mono or bis bpy intermediate. As for bpyPEG₂, these observations with bpyPtBA₂ also point to outer sphere effects upon inner sphere reactivity. Additional studies are merited here, to better understand the observed processes and increase fundamental understanding of the ways that polymeric environments influence metal complex behavior.

Conclusion

Metallobiomaterials have been generated from ligand and metal complex initiators using controlled polymerization. As these examples with bipyridine and dibenzoylmethane illustrate, ligand and metal sites can influence the outcome of polymerizations and common coupling reactions. For example, alternative strategies were required with dibenzoylmethane initiators, dbm(OH)_n, in lactide or caprolactone ROP with Sn(oct)₂ in order for molecular weight control to be achieved. Protection of dbm(OH)_n as iron(III) complexes also results in initiator activation and ROP catalysis, obviating the need for an additional, potentially more toxic metal catalyst. Unexpected reactivity, namely chain scission, was also noted for bpyPEG₂ macroligands in chelation reactions with Ru centers. Not only can metals affect polymer reactions, just as in metalloproteins, polymers can influence metal reactivity in synthetic biomaterials too. For example, iron centers in PEG and PtBA environments show unusual oxygen sensitivity compared to the corresponding non-polymeric metal complexes. Metals introduce new properties and can serve as responsive structural elements in materials, offering the possibility of a two stage degradation mechanism, namely macroligand dissociation and polymer chain scission (Figure 1). In many cases these steps may be synergistic. That is, once ligand dissociation has occurred the metal can help to initiate or activate chain scission processes. For example, iron can participate in Fenton chemistry with peroxides that develop in PEG polyethers. As Lewis acids, metals could foster ester hydrolysis in Fe PLA materials. Better understanding of the properties of metals in polymeric biomaterials environments is relevant to adapting PMCs and harnessing their properties and reactivities as multifunctional responsive materials for biomedicine. These tunable model systems can also help to shed light on possible effects of trace metals and residual catalysts in biomaterials, or likely interactions between leaching metals and polymers in inorganic/organic hybrid material implants and devices. Metals encountered *in vivo* might influence polymeric biomaterials degradation, and from the opposite perspective, macroligands can chelate metals in biological systems, and alter metal concentrations and thus, reactivity of targeted biochemical pathways. Many cancer therapies, for e.g., are based on this concept, and chelator effects could be enhanced or prolonged by polymer conjugation. Ongoing development of

synthetic methodology, ligand and metallobiomaterials characterization, and studies of materials fabrication, degradation and bioactivity will to help to shed light on these many processes and generate new uses for polymeric ligand and metal complex materials.

Acknowledgments

We thank the National Science Foundation, the Petroleum Research Fund, Dupont, the Commonwealth Health Research Board, the American Cancer Society, and the University of Virginia FEST program for support for research described in this account.

References

1. Fraser, C. L.; Smith, A. P. *J. Polym. Sci., Part A: Polym. Chem.* **2000**, *38*, 4704-4716.
2. Hoogenboom, R.; Schubert, U. S. *Chem. Soc. Rev.* **2006**, *35*, 622-629.
3. Schubert, U. S.; Eschbaumer, C. *Angew. Chem. Int. Ed.* **2002**, *41*, 2892-2926.
4. Andres, P. R.; Schubert, U. S. *Adv. Mater.* **2004**, *16*, 1043-1068.
5. *Iron chelators*: Liu, Z. D.; Hider, R. C. *Coord. Chem. Rev.* **2002**, *232*, 151-171.
6. *Iron chelators in cancer therapy*: Buss, J. L.; Greene, B. T.; Turner, J.; Torti, F. M.; Torti, S. V. *Cur. Top. Med. Chem.* **2004**, *4*, 1623-1635.
7. *Dbm and breast cancer*: Lin, C.-C.; Tasi, Y.-L.; Huang, M.-T.; Lu, Y.-P.; Ho, C.-T.; Tseng, S.-F.; Teng, S.-C. *Carcinogenesis* **2006**, *27*, 131-136.
8. *Dbm and prostate cancer*: Jackson, K. M.; DeLeon, M.; Verret, C. R.; Harris, W. B. *Cancer Lett.* **2002**, *178*, 161-165.
9. *Beta-diketones and iron*: Nakano, K.; Nakayachi, T.; Yasumoto, E.; Morshed, S. R.; Hashimoto, K.; Kikuchi, H.; Nishikawa, H.; Sugiyama, K.; Amano, O.; Kawase, M.; Sakagami, H. *Anticancer Research* **2004**, *24*, 711-717.
10. *Curcumin and copper*: Nair, J.; Strand, S.; Frank, N.; Knauff, J.; Wesch, H.; Galle, P. R.; Bartsch, H. *Carcinogenesis* **2005**, *26*, 1307-1315.
11. Zhang, C. X.; Lippard, S. J. *Curr. Op. Chem. Bio.* **2003**, *7*, 481-489.
12. Clarke, M. J.; Zhu, F.; Frasca, D. R. *Chem. Rev.* **1999**, *99*, 2511-2533.
13. Clarke, M. J. *Coord. Chem. Rev.* **2003**, *236*, 209-233.
14. Duncan, R. *Nat. Rev. Drug Discov.* **2003**, *2*, 347-360.
15. Lee, C. C., MacKay, J. A., Fréchet, J. M. J., Szoka, F. C. *Nature Biotech.* **2005**, *23*, 1517-1526.

16. Bronich, T. K.; Keifer, P. A.; Shlyakhtenko, L. S.; Kabanov, A. V. *J. Am. Chem. Soc.* **2005**, *127*, 8236-8237.
17. Torchilin, V. P. *Curr. Pharm. Biotechnol.* **2000**, *1*, 183-215.
18. Santra, S.; Xu, J.; Wang, K.; Tan, W. *J. Nanosci. Nanotechnol.* **2004**, *4*, 590-599.
19. Lowe, M. P. *Curr. Pharm. Biotechnol.* **2004**, *5*, 519-528.
20. Wang, C.; Stewart, R. J.; Kopeček, J. *Nature* **1999**, *397*, 417-420.
21. Hutchison, J. B.; Stark, P. F.; Hawker, C. J.; Anseth, K. S. *Chem. Mater.* **2005**, *17*, 4789-4797.
22. Kost, J.; Langer, R. *Adv. Drug Deliv. Rev.* **2001**, *46*, 125-148.
23. Hoffman, A. S. et al. *J. Biomed. Mater. Res.* **2000**, *52*, 577-586.
24. Meares, C. F.; Chmura, A. J.; Orton, M. S.; Corneillie, T. M.; Whetstone, P. A. *J. Mol. Recognit.* **2003**, *16*, 255-259.
25. Nori, A.; Kopeček, J. *Adv. Drug Deliv. Rev.* **2005**, *57*, 609-636.
26. Ratner, B. D.; Hoffman, A. S.; Schoen, F. J.; Lemons, J. E. In *Biomaterials Science: An Introduction to Materials in Medicine*, 2nd Ed.; Elsevier: San Diego, 2004.
27. Frazier, M. C.; Jackson, K. M.; Jankowska-Stephens, E.; Anderson, M. G.; Harris, W. B. *Proteomics* **2004**, *4*, 2814-2821.
28. Nogueira, M. A.; Magalhaes, E. G.; Magalhaes, A. F.; Biloti, D. N.; Laverde, A. J.; Pessine, B. T.; Carvalho, J. E.; Kohn, L. K.; Antonio, M. A.; Marsaioli, A. J. *Il Farmaco* **2003**, *58*, 1163-1169.
29. Pan, M.-H.; Sin, Y.-H.; Lai, C.-S.; Wang, Y.-J.; Lin, J.-K.; Wang, M.; Ho, C.-T. *J. Agric. Food Chem.* **2005**, *53*, 9039-9049.
30. Pettinari, C.; Marchetti, F.; Drozdov, A. In *Comp. Coord. Chem. II*; McCleverty, J. A., Meyer, T. J., Eds.; Elsevier Ltd.: Oxford, UK, 2004; Vol. 1, pp. 97-115.
31. Dechy-Cabaret, O.; Martin-Vaca, B.; Bourissou, D. *Chem. Rev.* **2004**, *104*, 6147-6176.
32. Alexis, F. *Polym. Int.* **2005**, *54*, 36-46.
33. Albertsson, A.-C.; Varma, I. K. *Biomacromolecules* **2003**, *4*, 1466-1486.
34. Jain, R. A. *Biomaterials* **2000**, *21*, 2475-2490.
35. Griffith, L. G. *Acta Materialia* **2000**, *48*, 263-277.
36. Uhrich, K. E.; Cannizzaro, S. M.; Langer, R. S.; Shakesheff, K. M. *Chem. Rev.* **1999**, *99*, 3181-3198.
37. *Poly(ethylene glycol) Chemistry and Biological Applications*; Harris, J. M., Zalipsky, S., Eds.; American Chemical Society: Washington, DC, 1997; Vol. 680.
38. Leckband, D.; Sheth, S.; Halperin, A. *J. Biomater. Sci. Polym. Ed.* **1999**, *10*, 125-147.
39. Sapra, P.; Allen, T. M. *Prog. Lipid Res.* **2003**, *42*, 439-462.
40. Molineux, G. *Cancer Treat. Rev.*, **2002**, *28 Suppl A*, 13-16.

41. Roberts, M. J.; Bentley, M. D.; Harris, J. M. *Adv. Drug Delivery Rev.* **2002**, *54*, 459-476.
42. Greenwald, R. B.; Choe, Y. H.; McGuire, J.; Conover, C. D. *Adv. Drug Deliv. Rev.* **2003**, *55*, 217-250.
43. Zalipsky, S. *Bioconjugate Chem.* **1995**, *6*, 150-165.
44. Anseth, K. S.; Metters, A. T.; Bryant, S. J.; Martens, P. J.; Elisseeff, J. H.; Bowman, C. N. *J. Controlled Release* **2002**, *78*, 199-209.
45. Peppas, N. A.; Huang, Y.; Torres-Lugo, M.; Ward, J. H.; Zhang, J. *Annu. Rev. Biomed. Eng.* **2000**, *2*, 9-29.
46. Merdan, T.; Kopecek, J.; Kissel, T. *Adv. Drug Deliv. Rev.* **2002**, *54*, 715-758.
47. Pack, D. W.; Hoffman, A. S.; Pun, S.; Stayton, P. S. *Nat. Rev. Drug Discov.* **2005**, *4*, 581-593.
48. Valenta, C. *Adv. Drug Deliv. Rev.* **2005**, *57*, 1692-1712.
49. Bernkop-Schnurch, A. *Adv. Drug Deliv. Rev.* **2005**, *57*, 1569-1582.
50. Huang, Y.; Leobandung, W.; Foss, A.; Peppas, N. A. *J. Controlled Release* **2000**, *65*, 63-71.
51. For another illustration of macroligand chelation see: Peter, K.; Thelakkat, M. *Macromolecules* **2003**, *36*, 1779-1785.
52. Corbin, P. S.; Webb, M. P.; McAlvin, J. E.; Fraser, C. L. *Biomacromolecules* **2001**, *2*, 223-232.
53. Also see: Holder, E.; Marin, V.; Alexeev, A.; Schubert, U. S. *J. Polym. Sci., Part A: Polym. Chem.* **2005**, *43*, 2765-2776.
54. Bender, J. L.; Corbin, P. S.; Fraser, C. L.; Metcalf, D. H.; Richardson, F. S.; Thomas, E. L.; Urbas, A. M. *J. Am. Chem. Soc.* **2002**, *124*, 8526-8527.
55. Johnson, R. M.; Fraser, C. L. *Macromolecules* **2004**, *37*, 2718-2727.
56. Smith, A. P.; Fraser, C. L. *Macromolecules* **2002**, *35*, 594-596.
57. Smith, A. P.; Fraser, C. L. *Macromolecules* **2003**, *36*, 2654-2660.
58. Smith, A. P.; Fraser, C. L. *Macromolecules* **2003**, *36*, 5520-5525.
59. Fraser, C. L.; Smith, A. P.; Wu, X. *J. Am. Chem. Soc.* **2000**, *122*, 9026-9027.
60. Smith, A. P.; Fraser, C. L. Unpublished results.
61. Johnson, R. M.; Fraser, C. L. *Biomacromolecules* **2004**, *5*, 580-588.
62. Gorczynski, J. L.; Chen, J.; Fraser, C. L. *J. Am. Chem. Soc.* **2005**, *127*, 14956-14957.
61. Bender, J. L.; Shen, Q.-D.; Fraser, C. L. *Tetrahedron* **2004**, *60*, 7277-7285.
64. McAlvin, J. E.; Fraser, C. L. *Macromolecules* **1999**, *32*, 1341-1347.
65. McAlvin, J. E.; Scott, S. B.; Fraser, C. L. *Macromolecules* **2000**, *33*, 6953-6964.
66. Gorczynski, J. L.; Chen, J.; Fraser, C. L. *J. Am. Chem. Soc.* **2005**, *127*, 14956-14957.
67. Gorczynski, J. L.; Chen, J.; Fraser, C. L. *Polym. Prepr. (Am. Chem. Soc., Div. Polym. Chem.)* **2005**, *46*, 928.

68. Panyam, J.; Sahoo, S. K.; Prabha, S.; Bargar, T.; Labhasetwar, V. *Int. J. Pharm.* **2003**, *262*, 1-11.
69. Shenoy, D.; Little, S.; Langer, R.; Amiji, M. *Mol. Pharm.* **2005**, *2*, 357-366.
70. Aggarwall, B. B.; Dorai, T. *Cancer Lett.* **2004**, *215*, 129-140.
71. Manson, M. M.; Farmer, P. B.; Gescher, A.; Steward, W. P. *Recent Results Cancer Res.* **2005**, *166*, 257-275.
72. Shishu, S. A. K.; Kaur, I. P. *Phytomedicine* **2003**, *10*, 575-582.
73. Singletary, K.; MacDonald, C.; Iovinelli, M.; Fischer, C., Wallig, M. *Carcinogenesis* **1998** *19*, 1036-1043.
74. Huang, M.-T.; Lou, Y.-R.; Xie, J. G.; Ma, W.; Lu, Y.-P., Zhu, B. T.; Newmark, H.; Ho, C.-T. *Carcinogenesis* **1998**, *19*, 1697-1700.
75. Huang, M. T.; Liu, Y.; Xie, J. G.; Newmark, H. H.; Ho, C. T. In *Food Factors in Health Promotion and Disease Prevention*; American Chemical Society: Washington, DC, 2003; Vol. 851, pp 196-207.
76. Simeoni, S.; Scalla, S.; Benson, H. A. E. *Int. J. Pharm.* **2004**, *280*, 163-171.
77. Pfister, A.; Fraser, C. L. *Biomacromolecules* **2006**, *7*, 459-468.
78. Hill, R. *Proc. Roy. Soc.* **1930**, *B107*, 205-214.
79. Moss, M. L.; Mellon, M. G. *Ind. Eng. Chem., Anal. Ed.* **1942**, *14*, 862-865.
80. Liochev, S. I. In *Metal Ions in Biological Systems*; Sigel, A., Sigel, H., Eds.; Marcel Dekker: New York, 1999; Vol. 36, pp 1-39.
81. Wardman, P.; Candeias, L. P. *Radiation Research* **1996**, *145*, 523-531.
82. *Free Radicals in Biology and Medicine*; Halliwell, B.; Gutteridge, J. M. C. Eds. Oxford Sci. Pub.: Oxford, 1999.
83. Rydholm, A. E.; Bowman, C. N.; Anseth, K. S. *Biomaterials* **2005**, *26*, 4495-4506.
84. Napoli, A.; Valentini, M.; Tirelli, N.; Muller, M.; Hubbell, J. A. *Nat. Mater.* **2004**, *3*, 183-189.
85. Fiore, G. L.; Pfister, A.; Fraser, C. L., Unpublished results.
86. For e.g., see: Valko, M.; Morris, H.; Cronin, M. T. D. *Curr. Med. Chem.* **2005**, *12*, 1161-1208.
87. Kemsley, J. N.; Zaleski, K. L.; Chow, M. S.; Decker, A.; Shishova, E. Y.; Wasinger, E. C.; Hedman, B.; Hodgson, K. O.; Solomon, E. I. *J. Am. Chem. Soc.* **2003**, *125*, 10810-10821.
88. Sen, C. K.; Khanna, S.; Babiator, B. M.; Hunt, T. K.; Ellison, E. C.; Roy, S. J. *Biol. Chem.* **2002**, *277*, 33284-33290.
89. Cho, M.; Hunt, T. K.; Hussain, M. Z. *Am. J. Physiol. Heart Circ. Physiol.* **2001**, *280*, H2357-2363.
90. Chujo, Y.; Naka, A.; Kramer, M.; Sada, K.; Saegusa, T. J. *Macromol. Sci., Pure Appl. Chem.* **1995**, *A32*, 1213-1223.
91. Masui, H.; Murray, R. W. *Inorg. Chem.* **1997**, *36*, 5118-5126.
92. Personal communication, L. De Cola.
93. Pfister, A.; Wedge, T. J.; Fraser, C. L. Unpublished results.

94. For an early example of this approach, see: Peters, M. A.; Belu, A. M.; Linton, R. W.; Dupray, L.; Meyer, T. J.; DeSimone, J. M. *J. Am. Chem. Soc.* **1995**, *117*, 3380-3388.
95. Demas, J. N.; DeGraff, B. A. *J. Chem. Educ.* **1997**, *74*, 690-695.
96. Kose, M. E.; Crutchley, R. J.; DeRosa, M. C.; Ananthakrishnan, N.; Reynolds, J. R.; Schanze, K. S. *Langmuir* **2005**, *21*, 8255-8262.
97. Fuller, Z. J.; Bare, W. D.; Kneas, K. A.; Xu, W.-Y.; Demas, J. N.; DeGraff, B. A. *Anal. Chem.* **2003**, *75*, 2670-2677.
98. Kawa, M.; Frechet, J. M. *J. Chem. Mater.* **1998**, *10*, 286-296 and references therein.
99. Long, J. W.; Velazquez, C. S.; Murray, R. W. *J. Phys. Chem.* **1996**, *100*, 5492-5499.
100. Naka, K.; Kobayashi, A.; Chujo, Y. *Macromol. Rapid Commun.* **1997**, *18*, 1025-1032.
101. Marin, V.; Holder, E.; Meier, M. A. R.; Hoogenboom, R.; Schubert, U. S. *Macromol. Rapid Commun.* **2004**, *25*, 793-798.
102. Thiol and disulfide bipyridine reagents have been prepared by U. S. Schubert and V. N. Marin (Marin, V. N. Ph.D. thesis, Eindhoven University, Netherlands, 2006) via a xanthogenate intermediate: Gibson, M.S.; Bradshaw, R. W. *Angew. Chem. Int. Ed. Engl.* **1968**, *7*, 919-930.
103. Meier, M. A. R.; Schubert, U. S. *J. Polym. Sci., Part A: Polym. Chem.* **2003**, *41*, 2964-2973.
104. Miyashita, T.; Matsuda, M. *Bull. Chem. Soc. Jpn.* **1985**, *58*, 3031-3032.
105. Park, T. G.; Jeong, J. H.; Kim, S. W. *Adv. Drug Deliv. Rev.* **2006**, *58*, 467-486.
106. Kircheis, R.; Wightman, L.; Wagner, E. *Adv. Drug Deliv. Rev.* **2001**, *53*, 341-358.
107. Little, S. R.; Lynn, D. M.; Ge, Q.; Anderson, D. G.; Puram, S. V.; Chen, J.; Eisen, H. N.; Langer, R. *Proc. Natl. Acad. Sci. USA* **2004**, *101*, 9534-9539.
108. Banerjee, P.; Weissleder, R.; Bogdanov, A. *Bioconjugate Chem.* **2006**, *17*, 125-131.
109. Fiore, G. L.; Edwards, J. M.; Klinkenberg, J. L.; Demas, J. N.; Gioeli, D. G.; Fraser, C. L. *Polym. Mater. Sci. Eng.* **2006**, *95*.
110. Fiore, G. L.; Edwards, J. M.; Klinkenberg, J. L.; Demas, J. N.; Gioeli, D. G.; Fraser, C. L. Manuscript in preparation.
111. Lamba, J. J. S.; Fraser, C. L. *J. Am. Chem. Soc.* **1997**, *119*, 1801-1802.
112. McAlvin, J. E.; Fraser, C. L. *Macromolecules* **1999**, *32*, 6925-6932.
113. Schubert, U.; Nuyken, O.; Hochwimmer, G. *J. Macromol. Sci., Pure Appl. Chem.* **2000**, *37*, 645-658.
114. Collins, J. E.; Lamba, J. J. S.; Love, J. C.; McAlvin, J. E.; Ng, C.; Peters, B. P.; Wu, X.; Fraser, C. L. *Inorg. Chem.* **1999**, *38*, 2020-2024.

115. Peterson, H.; Martin, A. L.; Stolnik, S.; Roberts, C. J.; Davies, M. C.; Kissel, T. *Macromolecules* **2002**, *35*, 9854-9856.
116. Fischer, D.; Bieber, T.; Li, Y.; Elsasser, H.-P.; Kissel, T. *Pharm. Res.* **1999**, *16*, 1273-1279.
117. Brissault, B.; Kichler, A.; Guis, C.; Leborgne, C.; Danos, O.; Cheradame, H. *Bioconjugate Chem.* **2003**, *14*, 581-587.
118. Akiyama, Y.; Harada, A.; Nagasaki, Y.; Kataoka, K. *Macromolecules* **2000**, *33*, 5841-5845.
119. Frønsdal, K.; Engedal, N.; Saatcioglu, F. *The Prostate* **2000**, *43*, 111-117.
120. Oh, J. K.; Tang, C.; Gao, H.; Tsarevsky, N. V.; Matyjaszewski, K. *J. Am. Chem. Soc.* **2006**, *128*, 5578-5584.
121. Becker, M. L.; Liu, J.; Wooley, K. L. *Biomacromolecules* **2005**, *6*, 220-228.
122. Yan, X.; Gemeinhart, R. A. *J. Controlled Release* **2005**, *106*, 198-208.
123. Janorkar, A. V.; Metters, A. T.; Hirt, D. E. *Macromolecules* **2004**, *37*, 9151-9159.
124. Zhang, Q.; Remsen, E. E.; Wooley, K. L. *J. Am. Chem. Soc.* **2000**, *122*, 3642-3651.
125. Choucair, A.; LimSoo, P.; Eisenberg, A. *Langmuir* **2005**, *21*, 9308-9313.
126. Davis, K. A.; Matyjaszewski, K. *Macromolecules* **2000**, *33*, 4039-4047.
127. Farah, A. A.; Pietro, W. J. *J. Poly. Sci Part A.: Polym. Chem.* **2005**, *43*, 6057-6072.
128. Viau, L.; Even, M.; Maury, O.; Haddleton, D. M.; Le Bozec, H. *C. R. Chimie* **2005**, *8*, 1298-1307.
129. For another example of metal-centered star blocks by radical polymerization (i.e. RAFT), see: Chen, M.; Ghiggino, K. P.; Launikonis, A.; Mau, A. W. H.; Rizzardo, E.; Sasse, W. H. F.; Thang, S. H.; Wilson, G. J. *J. Mater. Chem.* **2003**, *13*, 2696-2700.
130. Johnson, R. M.; Pfister, A.; Fraser, C. L. In *Metal-Containing and Metallosupramolecular Polymers and Materials*; Schubert, U. S., Newkome, G. R., Manner, I., Eds.; American Chemical Society: Washington, DC, 2006; Vol. 928, pp 17-29.
131. Krumholz, P. *J. Am. Chem. Soc.* **1949**, *71*, 3654-3656.
132. Blandamer, M. J.; Burgess, J.; Chambers, J. G. *J. C. S. Dalton* **1976**, 606.
133. Josceanu, A. M.; Moore, P. *J. Chem. Soc, Dalton Trans.* **1998**, 369.
134. Collomb, M-N.; Deronzier, A.; Gorgy, K.; Leprêtre, J-C. *New J. Chem.* **2000**, *24*, 455.
135. Johnson, R. M.; Fraser, C. L.; Turro, C. Unpublished results.

Chapter 8

Beyond Trial and Error: Tools to Advance the Engineering of Biomaterials

Lori A. Henderson, Matt J. Kipper, and Martin Y. M. Chiang

**Polymers Division, Materials Science and Engineering Laboratory,
National Institute of Standards and Technology,
Gaithersburg, MD 20899–8543**

Tissue engineering and advanced medical technologies have the potential to dramatically improve the quality of human life. In order to move beyond empirical trial and error into design, biomaterials development is in urgent need of reliable measurement tools and techniques to engineer structures that meet specific physiological requirements for clinical use. This requires the development of design principles based on the physical understanding of how cells respond to molecular signals and integrate multiple inputs to generate a given biological response to their environment. Biomaterial scaffolds, for example, support cells, give tissues their form, and are an important source of information that drives cell fate. The definition and quantification of the type of relationships that trigger specific cell response to polymer composition and structure will enhance the rational design of tissue-engineered products. To meet this need, NIST is developing instruments, methodologies, and standards for the measurement of materials properties and cell response to properties on surfaces and in 3D scaffolds. Many tools and techniques were adapted (*e.g.*,

combinatorial libraries, biochemical assays, electron-, atomic force-, and fluorescence microscopy, etc.) to examine cell characteristics like adhesion, morphology, and migration as a function of the physical properties of biomaterials. This chapter introduces the characterization techniques and modeling tools used to obtain chemical, physical, and structural information that describe cell morphology and migration on different polymeric surfaces. The results identified key variables that impact the engineering and design of biomaterials.

Introduction

Tissue engineering¹ is a rapidly developing field that offers a new approach to treat the loss or malfunction of various tissues and organs. The capability to engineer new functional tissues will have an enormous impact on the quality of life of patients and rising healthcare costs in the near future. Between 1990 and 2002, the worldwide cumulative capital investment in the tissue engineering industry was over \$4.5 billion (*1*), with more than 90 % from the private sector, resulting in a limited number of commercially available tissue-engineered therapies thus far.

Many countries are rapidly stepping up research to develop the landscape in tissue engineering. The most recent global assessment of tissue engineering acknowledged (2):

- Major efforts to create biotechnology incubators
- Diverse and widespread interest across Europe and Japan
- The establishment of research centers in Japan, China, Germany, and the United Kingdom

In the US, commercial support has principally been directed in the area of applied research whereas the 10 % governmental support focused on more basic research. In Japan and Europe, tissue engineering is largely driven by

¹ Tissue Engineering is defined in this text as the application of principles and methods of engineering and life sciences to understand structure-function relationships in mammalian tissues, and the development of biological substitutes to restore, maintain, or improve tissue function.

government funding, doing more basic research and thus generating intellectual property as a mode of operation. Many centers in Europe and Japan devote their attention to cell-based technologies combining “off-the-shelf” products with cells whereas the US has focused on design principles based on cell interactions leading to *novel* biomaterials. These different approaches to research and technology developments suggest the need for cross-disciplinary interactions among different laboratories worldwide to advance tissue engineering products and applications.

Global regulatory issues present an additional challenge to the development of the tissue engineering industry. The Food and Drug Administration approach to regulate products involving human tissues depends upon classifying the product as a drug, biologic, or a device and is not fully implemented (*i.e.*, the classification scheme is still in flux). The lack of an established European Union regulatory program has also complicated the international application of new technologies resulting in an array of classification schemes (2). This controversy in regulatory compliance based on classification is but one critical barrier to commercialization. Along with this is the lack of “universal” standards and test methods to characterize, evaluate, and certify such products. Many government programs and standards organizations are working together to provide the measurement infrastructure and standard protocols to accelerate regulatory acceptance and promote tissue-engineering industries. Examples include Versailles Advanced Materials and Standards (VAMAS) committee on pre-standards, American Society for Testing and Materials (ASTM) F04.41 committee on tissue-engineered medical products (TEMP’s), the International Organization of Standards technical committee on surgical and medical devices (ISO TC-150 & 210), and NIST reference materials.

NIST is developing a series of measurement tools, solutions, and test methods in order to examine how cells, the fundamental units of tissues, respond to different types of materials to engineer structures that meet specific physiological requirements for clinical use. Our work focuses on the development of characterization techniques and analytical and modeling tools that can be used to predict adhesion, migration, and differentiation of cells grown on biomaterials that are designed to promote healing, improve existing tissues and organs, or serve as tissue substitutes. This common measurement infrastructure that leads to predictive models is necessary for all phases of tissue-engineering innovation, from basic research to production. For example, it would enable manufacturers of prospective tissue-engineered products to progress from costly, time-consuming “try-it-and-see” approaches to well defined design methodologies. These tools, methods, and models will also help industry to rapidly evaluate and select materials, cells, and manufacturing processes. This will result in substantial savings in time and money as industry passes only the most promising materials through the regulatory processes.

This chapter introduces an approach to biomaterials research that focuses on the development of *design principles*² for biomaterials that can guide the design of tissue-engineered materials. The following sections will cover: Strategies used to develop models and resulting design principles; tools and methodologies to model bioactive materials, fundamentals of cell-surface interactions; mathematical modeling of cell migration on combinatorial libraries; and the influence of polymer mechanical properties on cell migration and morphology.

Strategic Approaches to Design Principles

Design principles provide a platform for engineering new solutions and are based upon informed models of the way a system behaves. Only recently have modeling theories centered on examining the interface between materials and biology to understand the complexity of cell-material interactions. As our understanding of these interactions continues to grow, there still lacks comprehensive³ predictive design models that can be used to make functional materials for tissue engineering applications.

Developing models at the onset is very complex. There are several approaches to consider in conducting experiments that lead to predictive models for engineering. It is generally better to: (i) use multivariate rather than univariate testing due to higher throughput and the ability to test interactions, (ii) have well defined targets for the end product, and (iii) incorporate a feedback system wherein results from an experiment inform the next experiments. These criteria are then incorporated into the strategies used to develop design principles. Figures 1 and 2, for example, illustrate two among many types of strategies in which to develop design principles for engineering. Both figures use the example of modifying a synthetic biomaterial with a peptide moiety to potentially induce/enhance a particular cellular response. The *iterative optimization* approach in Figure 1 is defined as the culmination of data from studies that were conducted and optimized independently (Study II & III) – unable to evaluate synergistic effects from the onset. A univariate test method with a feedback loop is frequently used to optimize different materials, peptides, peptide surface concentrations, and other experimental parameters by conducting

²Design principles are defined herein as the application of principles in mathematics, science, and engineering to the design and evaluation of biomaterials for medical applications. The focus is on molecular designs of polymeric surfaces by evaluating cell response as a function of surface chemistry and mechanical properties.

³ Refers to multi-parametric based models.

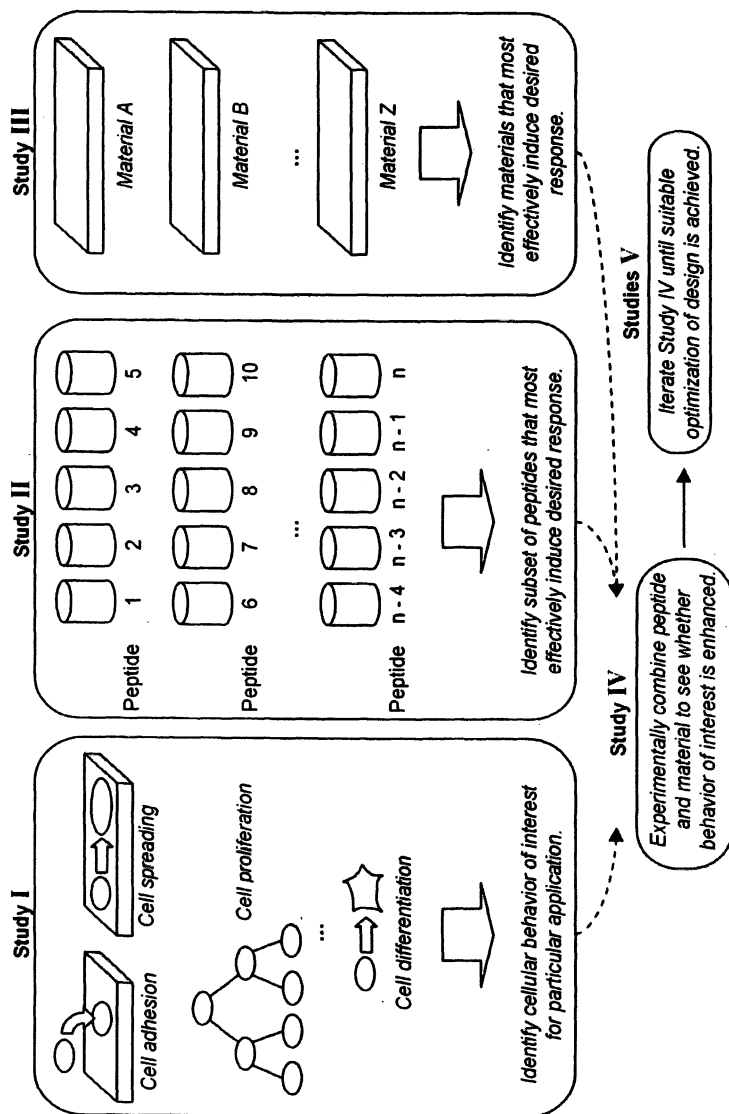


Figure 1. Schematic of the iterative optimization approach to designing a tissue engineering scaffold with the addition of a biologically active peptide.

several independent, generally single parametric studies. The optimal design of biologically active tissue-engineered scaffolds and surfaces then results from further experimentation (Study IV, V). Some examples of this type of approach to modeling are listed in Table II, Cell response to mechanical stimuli section.

Alternatively, design principles can be synthesized by taking a holistic approach to understanding the interface between cells and surfaces. These model studies are guided by an *information network* (Figure 2) that encompasses the combination of molecular information of various types to describe and predict function at the cellular, tissue, or even whole organism levels. Here, the purpose is to derive multi-parametric models from several variables - data sets built from characterizing the chemical, physical, mechanical, and structural properties of materials and their overall biological function. Figure 2 also illustrates a multi-variate approach to experimentation with a feedback system (Study II') that can deal with the large parameter space associated with complex bioactive materials. Although the information network is important and extremely useful for engineering designs, it is a tremendous undertaking to construct a bioinformatic-like system due to a lack of an established database in which to handle large data sets generated and the need for highly sensitive, low cost, analytical technologies to make broad range measurements of clinically relevant biomaterials. The NIST Biomaterials Program is working on the latter.

In this chapter, we will demonstrate the advantages of a multi-variate, approach with examples of investigations conducted at NIST to evaluate cell morphology and migration as a function of different characteristics of bioactive surfaces. First, we briefly discuss some of the tools and technologies that are required to make this approach feasible.

Tools and Methodologies to Model *Bioactive Materials*

The development of biomaterials for tissue engineering requires the use of physical, chemical, biological and engineering processes to direct the aggregate behavior of cells. Advanced instrumentation and measurement techniques, coupled with mathematical models, will help tissue engineering to connect and assemble the many and varied pieces in an extremely complex biological puzzle, opening the way to powerful medical treatments and therapies. This advanced measurement toolkit for tissue engineering will employ high-throughput, combinatorial methods wherein test specimens are many different (yet related) material samples combined into one (3,4,5). Specimens may vary systematically and incrementally in surface roughness or structural rigidity (6,7) – two of the many properties shown to influence cell morphology, growth, and viability (8). NIST studies on cell-surface interactions also includes advanced instrumental techniques used to collect the data – high resolution, non-invasive multi-modal

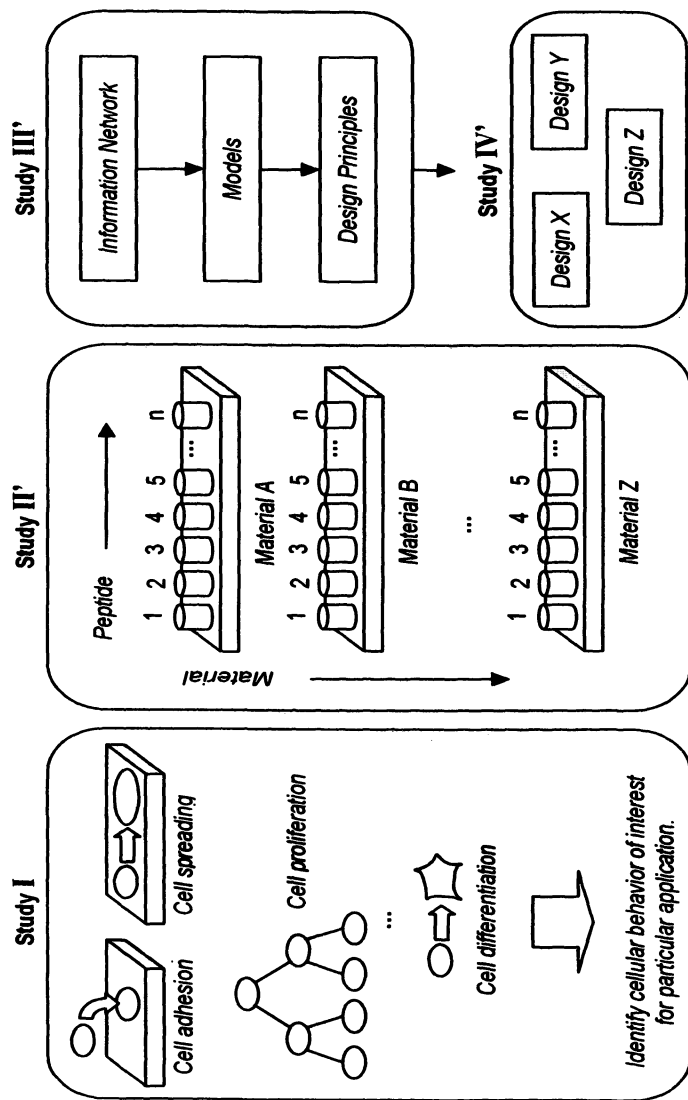


Figure 2. Schematic of the information network approach to designing a tissue engineering scaffold by modifying polymer materials with peptides to achieve a desired response.

imaging of cells, cell-based assays, and 3D immersive visualization software as described below⁴ and illustrated in Figure 3:

- *Optical imaging with collinear optical coherence and confocal fluorescence microscopy (OCM-CFM)*. This noninvasive imaging technique combines the use of reflection confocal microscopy in tandem with optical coherence microscopy to characterize scaffolds and tissue constructs. It can probe the interior of scaffolds with the same resolution as conventional laser scanning confocal microscopy but with greater sensitivity (9).
- *Spectroscopic imaging with broadband coherent anti-Stokes Raman spectroscopy (CARS)*. This high-resolution, chemically sensitive volumetric imaging method allows rapid, non-invasive study of processes on tissue scaffolds and constructs. This technique involves the phenomenon of four-wave mixing, takes advantage of the high efficiency of coherent Raman scattering, and has the applicability of conventional Raman spectroscopy (10).
- *Immersive visualization using Rave Engine*. A computer based virtual reality environment that utilizes a combination of hardware, software, and interaction devices to create 3D representations of data. This technology allows scientist to work within a virtual setting for analyzing materials. This virtual imaging laboratory ties 3D representations and interactions with data through image analysis, visualization, and data mining tools (11).

These instrumental tools and visual workstation are just a few techniques used to characterize and measure structural and chemical properties of materials or cells cultured on them (Figure 3). Incorporating these advanced imaging techniques into our measurement toolkit allows us to translate this work into standard reference materials and methods to aid discovery, research, and regulatory issues.

The characterization of bioactive materials also requires an interdisciplinary approach to evaluate test parameters related to different classes of biomaterials and their clinical applications. Among the two primary applications for biomaterials – therapeutic⁵ and diagnostic⁶ – requisite material properties can

⁴ See references for details on how these techniques were applied to biological investigations.

⁵ Since tissues and scaffolds are grown and transplanted, respectively, properties such as degradation, resorption, biocompatibility, and inflammatory response are critical.

⁶ Applications based on tissue made *in vitro* like drug metabolism and uptake also require degradation, toxicity, and pathogenecity testing.

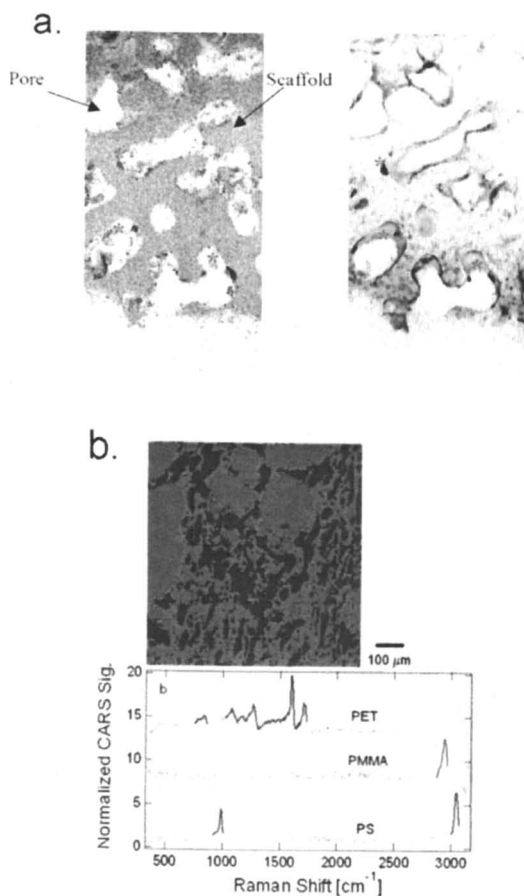


Figure 3. These images represent the types of structural and chemical information that can be obtained using the OCM-CFM dual-mode technique (a.), CARS (b.), and immersive visualization (c.). The OCM-CFM images (a) are of fetal chick osteoblasts cultured on porous polycaprolactone scaffolds. Differences in pore size and crystalline regions of the polymer could be determined at 145 μm from the surface. Figure b is a broadband CARS micrograph of a phase-separated ternary polymer blend. The colors green, blue, and red represent polystyrene, poly(ethylene terephthalate) and poly(methyl methacrylate), respectively. Figure c is a 3D representation of cells on polycaprolactone scaffold taken from the immersive visualization laboratory. This visual image provides additional information on cell shape, orientation, and position within the scaffold.

C.

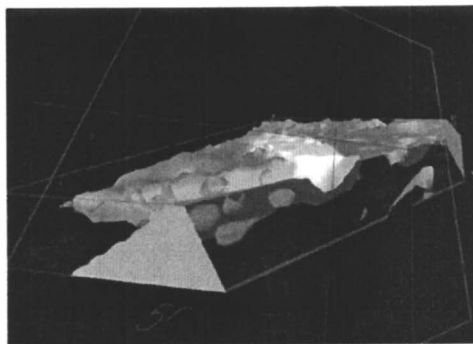


Figure 3. Continued.

vary drastically. Tissue engineered medical products often consist of a 3D synthetic scaffold that provides form and foundation for the cells as they produce the tissue of interests. Synthetic scaffolds can be designed to mimic the salient features of naturally-derived polymers or their physiological environment. They vary in physical state from porous sponges, meshes, and felts, to gels and depend on the type of engineered tissue (*e.g.*, bone, cartilage, skin, tendon, cornea, bladder, blood vessels). Therefore, design of bioactive materials for tissue engineering requires control of many physical, chemical, structural, mechanical, and biological characteristics simultaneously. Of particular importance are the composition, microstructures (*e.g.*, porosity, pore size, interconnectivity, and pore-wall microstructure), surface chemistry, surface morphology, biodegradability and mechanical properties. These include microstructures to facilitate cell adhesion and distribution, biodegradability to match tissue formation, and transfer of mechanical forces to surrounding tissue. Table I lists some features of biomaterials and medical devices monitored for clinical performance and regulatory testing. The modeling studies discussed later are examples where polymer stiffness and surface chemistry are modified to affect cell migration.

Contributions from Cell-Surface Interactions

Recent advances in design principles have resulted from a systematic study of the mechanics of cells and cell surface interactions. Cell attachment, or lack of it, to biomaterials is a critical factor influencing both mechanotransduction and migration processes. It is a complicated, time dependent, process involving significant morphological changes of the cell and deposition of extracellular matrix components. The quality of the adhesive bond between a cell and a surface depends on a range of biological and physical factors that include the culture history, the age of the cell, the cell type, and both the chemistry and morphology of the underlying surface. The next section describes how these and other important characteristics of cells may affect cell motility and migration. This includes a description of the types of interactions known to trigger specific cellular phenomena used experimentally or empirically in the development of the two cell migration models at NIST. One model describes cell migration as a function of polymer rigidity, and the other describes cell migration on covalently bound surface peptide gradients.

Cell Response to Peptide Gradients

A recent popular strategy for enhancing the performance of synthetic biomaterials for tissue engineering scaffolds is to tailor the surface chemistry of

Table I. Examples of important properties in characterizing tissue engineered materials

<i>Chemical-Physical Characterization</i>	<i>Structural Characterization</i>	<i>Biological Characterization</i>
Chemical composition	Porosity	Focal adhesion complexes
Phase behavior - Domain sizes	Density	Protein adsorption
Degradability	Tortuosity	Cell shape & size
Solubility	Permeability	Apoptosis
Stiffness	Network architecture	Necrosis
Strength		Inflammation
Viscoelasticity		Phenotype
		Cell viability
		Biocompatibility
		Hemoecompatability

the material with some biochemical moiety that induces or triggers a favorable biological response. The biochemical moiety may be an adhesion ligand for a cell surface receptor, a cofactor that potentiates a particular enzyme activity, or it may bind a secondary biomolecule for activation. The ability to functionalize surfaces of materials is commonly used to strengthen interfacial adhesion or alter molecular dynamics at interfaces to improve the material's function. Scientists have found ways to extend these techniques to biomaterials by functionalizing surfaces with chemistries that enhance the cell/surface interactions. For example, the integrin ligand peptide RGD can be used to improve cellular attachment and guidance. RGD is the cell adhesive sequence (Arg-Gly-Asp) that supports the attachment and proliferation of a variety of cells. A similar surface engineering strategy was also employed in our studies on tracking cell motility and migration.

The goal of this research activity is to develop measurement solutions that characterize biologically active peptides on polymer surfaces and describe the motility of connective tissue cells. In these studies, the focus was on a group of bioactive peptides derived from the laminin family of proteins, which are found in the basal lamina of a variety of tissues, and have been shown to promote cell adhesion, migration, and angiogenesis. The 90 kDa laminin-1 protein has been exhaustively investigated with 671 overlapping peptide sequences, of which 20 have been identified as having some potential to promote cell adhesion, when bound to a surface, or cell migration when presented in soluble form (12,13,14). Two short sequences of laminin-1, A10 and B160, were linked to poly (L-lysine) surfaces in a gradient fashion to promote cell attachment and spreading of cells.

The peptide sequence for the laminin-1 A10 (heparin mediated adhesion ligand) and B160 (integrin mediated adhesion ligand) were $^{95}\text{GTNNWWQSPSIQN}^{107}$ and $^{1607}\text{VILQSSAADIAR}^{1618}$ respectively. A combinatorial method was also used to make gradient libraries that varied in peptide surface concentration for testing. Experiments were conducted to evaluate fibroblast motility on peptide gradient surfaces. These experiments provide information that can be used to inform models of cell migration and also determine design parameters for bioactive tissue engineering scaffolds that promote cell migration.

Studying cell motility as a function of material surface design and properties (Model Study 1) also impacts the understanding of the wound healing process. The mechanisms of cell migration have been well characterized for several cell types important to the early (inflammation) stage of wound healing (*e.g.*, neutrophils, macrophages) (15,16,17,18,19). These cells migrate relatively quickly, compared to connective tissue cells (*e.g.*, fibroblasts, keratinocytes) whose migration is important during the later stages of wound healing (proliferation and remodeling). Migration of the slower moving connective tissue cells can be one to three orders of magnitude slower than the faster migrating cells, and is therefore much more difficult to accurately observe and precisely characterize. This technique for studying cell migration can be a powerful diagnostic tool to study the growth and organization of cells and tissues, design standard reference materials for exploratory research, or to modify scaffolding materials to promote the migration of connect tissue cells within scaffolds.

The covalent attachment of functional peptides is also beneficial to enhancing the biocompatibility of materials and surfaces used in biomedical applications. Although, many labs have reported results on the performance of chemically modified surfaces and structures designed to improve compatibility, this research field for the most part, remains exploratory and often uses a “try it and see” approach to experimentation. This “try it and see” approach can be built on basic principles where it is known that:

- Cells will interact more favorably with surfaces to which they can form stable adhesive contacts, than with surfaces to which they can only poorly adhere.
- Cells have surface receptors (integrins) that bind to known peptide sequences, such as RGD.
- Some (broad) range of surface peptide concentration should be targeted, below which the cells may not recognize the peptide and above which the surface may be excessively adhesive.

In the “try it and see” approach a great deal of experimentation is still required in order to obtain the optimal chemical and structural design of compatible surfaces. However, by modeling the cell migration in the context of the materials and peptides of interest, more comprehensive predictive models can be developed and used to design functional materials for specific applications.

Cell Response to Mechanical Stimuli

The biological cell performs a variety of functions: the synthesis, sorting, storage and transport of molecules; the expression of genetic information; the recognition, transmission and transduction of signals; and the powering of molecular motors. The cell also converts energy from one form to another and responds to external environments by continually altering its structure. For the cell body to move forward during cell migration, contractile forces must be generated within the cell. With the development of instruments capable of mechanically probing, imaging, and manipulating single cells and biomolecules with forces smaller than a piconewton (20), the tissue engineering community has learned a great deal about the cytoskeletal and adhesive machinery underlying the generation and transmission of motile forces – local protrusive and contractile forces coming from molecular motors – and interactions within cells and between cells and substrates. These advances, coupled with advanced imaging techniques, have provided key insights into the mechanotransduction process (transfer of forces to proteins, nucleic acids, etc.) and improved the understanding of cellular responses to mechanical stimuli.

Figure 4 illustrates some of the various phenomena that lead to cell migration. Some of these phenomena have been successfully formulated into mathematical models of cell migration and are marked with an asterisk in Figure 4. Table II lists some of the most significant models from the literature. These models account for such effects as the population dynamics, the individual cell movements, mechanical force balances between the cell and its substrate, intra- and extracellular signaling, and ligand-receptor binding. Other phenomena that are essential to cell migration, such as cytoskeletal rearrangement and focal adhesion formation have not been exhaustively modeled.

From these model studies and advances in instrumentation, researchers have learned a great deal about the cytoskeletal and adhesive machinery underlying the generation and transmission of motile forces within cells: cells use a variety of mechanisms to change their shape, move through their environment and internally transport chemical cargo and cellular subunits. The simplest dynamic mechanism involves growth and shrinkage of the cytoskeletal filaments actin and tubulin (30):

Table II. Theoretical descriptions of cell migration

<i>Features described</i>	<i>Model description</i>	<i>Authors</i>
Individual cell movements	A discrete form of the persistent random walk is shown to accurately describe the individual movements of fibroblasts studied at high resolution	G.A. Dunn; A.F. Brown (21)
Individual cell movement Cell population dynamics	Relationship between persistent random walk model to individual cell movement measurements confirmed for macrophages in isotropic and directionally biased motility	B.A. Farrell; R.P. Daniele; D.A. Lauffenburger (16)
Cell population dynamics	Methods for obtaining persistent random walk model parameters from regression of experimental data are discussed	R.B. Dickinson; R.T. Tranquillo (22)
Individual cell movements Cell population dynamics	Stochastic differential equations for cell movements are related to cell population dynamics	R.B. Dickinson; R.T. Tranquillo (23)
Individual cell movements Cell population dynamics Extracellular signaling	A continuous form of the persistent random walk is shown to accurately describe endothelial cell migration and effects of adding acidic fibroblast growth factor are investigated	C.L. Stokes; D.A. Lauffenburger; S.K. Williams (24)
Intracellular signaling Individual cell movement Cell population dynamics	Hypothetical kinetics for intracellular signaling mechanisms are related to stochastic cell movements and shown to be consistent with biased random walk model for population dynamics	Alt, W. (25)

Table II. (continued)

<i>Features described</i>	<i>Model description</i>	<i>Authors</i>
Population dynamics Receptor-ligand binding Extracellular signaling	Receptor-ligand binding of chemoattractants is shown to be sufficient to introduce stochastic elements observed in persistent random walk population dynamics	R.T. Tranquillo; D.A. Lauffenburger; S.H. Zigmond (26)
Individual cell movement Extracellular signaling	Differences among cell types, their membrane receptors and mechanisms of interaction with extracellular environment are invoked to describe large differences in cell speed among different cell types	P. Friedl; K.S. Zanker; E.-B. Broeker (27)
Cell/substrate force balance Receptor-ligand binding	Cell speed obtained from force balance and is biphasic in ligand surface concentration	M.H. Zaman; R.D. Kamm; P. Matsudaira; D.A. Lauffenburger (28)
Cell population dynamics	Parameters describing persistent random walk are allowed to change with time to more accurately describe population dynamics	A.J. Bergman; K. Zygorakis (19)
Cell population dynamics Intracellular signaling	Parameters of persistent random walk population dynamics are allowed to change at different stages of the cell cycle	P.S. Walmod; R. Hartmann-Petersen; S. Prag; E.L. Lepekkin; C. Roepke; V. Berezin; E. Brock (29)

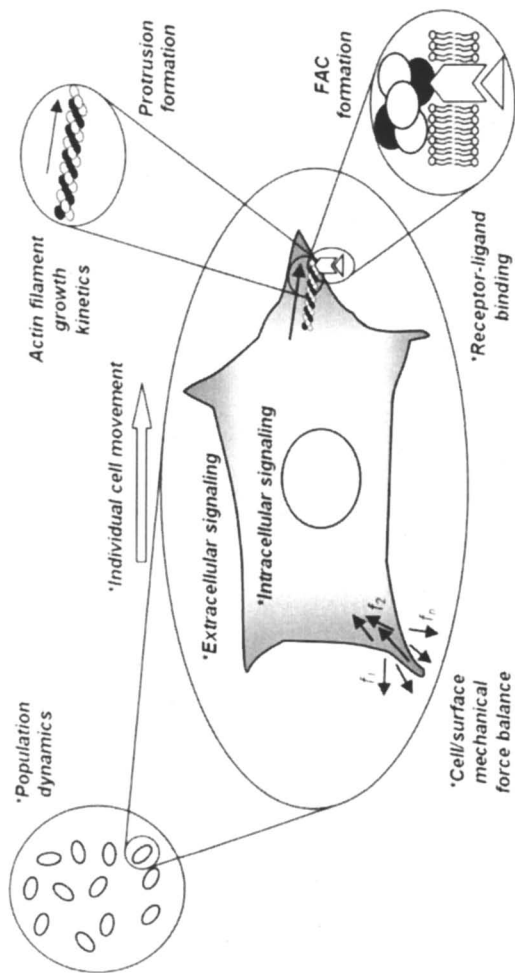


Figure 4. Phenomena that play key roles in cell migration. The phenomena marked with asterisks have been incorporated into some of the theoretical modeling studies listed in Table II.

- Actin and tubulin are dynamic polymers: their fundamental protein building blocks (G-actin or tubulin heterodimer) can both polymerize and depolymerize to change the length of a filament. The growth rates of individual actin filaments depend on the concentration of actin monomer, which varies from cell to cell.
- More complex machinery for cell movement and transport is provided by special motor proteins capable of walking along actin filaments or microtubules. These motor proteins generate a force of a few piconewtons.
- Mechanical properties (elasticity) of filaments in isolation and as components of networks play a key role in cell movement.
- Cells subject to applied stress achieve a balance between internal and external forces.

Cells also undergo mechanical deformation when subjected to external forces and geometric constraints in a similar manner to engineering materials. Many normal and diseased conditions of cells are dependent on or regulated by their mechanical environment, and the deformation characteristics of cells can provide important information about their biological and structural functions (31). However, little is known about how the underlying polymer surfaces and bulk material properties influence the stimulation of cells and transfer of forces. NIST has recently developed mathematical solutions to explain how cells respond to rigid and elastic polymeric surfaces. The scope of this work is provided elsewhere (32) with brief highlights provided in Model Study 2 of this chapter. As a result, a thermodynamic based model was developed that demonstrates how substrate rigidity alters the morphology and migration of cells.

Model Study 1: Cell Migration on Bioactive Gradient Materials

In 1965, S.B. Carter proposed that all cell movements in physiological processes such as metastasis, wound healing, and embryonic development are the result of a process he termed “haptotaxis” (33). He explained these migration phenomena in terms of an adhesion differential that a cell might experience in contact with its surroundings and investigated fibroblast haptotaxis experimentally by creating adhesion gradients of palladium on cellulose acetate-coated glass (34, 33). Since these experiments, there has been a substantial amount of literature on cell migration. In the intervening four decades, usage of the term haptotaxis has evolved somewhat to indicate the particular stimulus to

which the cells are responding (*i.e.*, a gradient in a surface chemistry), rather than a universal mechanism of motility. Other terms are used to distinguish migration to other stimuli such as galvanotaxis, in which the stimulus is an electric field, durotaxis, in which the stimulus is related to the substrate mechanics (35,36,37), and topotaxis, in which the stimulus is a topographical feature of the substrate, are just a few examples. The exploration of many types of stimuli, cells, and physiological processes leaves us with a wealth of experimental observations of cell migration for which there is no single comprehensive model describing connective tissue cell motility. There are multiple models for cell motility cited in the literature (Table II examples), most of which have been formulated to describe a particular set of experiments rather than to describe cell motility holistically or to be used in designing materials to promote cell migration. Models that are formulated to account for multiple phenomena focus on biophysics and biochemistry of cell migration and are not oriented toward materials design. Therefore, the probability of successfully designing an appropriate tissue engineering scaffold to promote the migration of a population of connective tissue cells such as fibroblasts from this body of work is not very high. Design principles are likely to be the product of predictive models from experimental observations of cell migration that include well characterized chemical, physical, structural, and mechanical properties of biomaterials.

An ideal pursuit would be a more comprehensive⁴ theoretical description of cell migration that could be used by material scientists to model the biological response to materials such that design principles could be used in the development of new tissue-engineered medical products. In NIST studies, a pragmatic approach that encompasses multivariate analysis for optimization was chosen as outlined in Study II' of Figure 2. Experiments were designed to explore as broad a parameter space as possible within a set of conditions closely simulating practical wound healing applications. This strategy affected the design of experiments in two ways: the method chosen to prepare peptide modified surfaces and the technique used to assay the cell migration phenomenon. A discussion of these two elements of the experimental design is provided below along with the results and how they can be used to construct useful models of optimal materials design for cell migration.

Peptide gradient surfaces

Synthetic laminin-1 A10 and B160 peptide sequences were coupled to poly (L-lysine) coated glass or fibrin gels. In order to investigate a broad range of peptide surface concentrations in a single test specimen, a gradient in the peptide concentration on the polymer surfaces was prepared in one direction. The

surface peptide concentration gradients allow the investigation of many concentrations on a single sample surface and also the effects of the gradient magnitude itself. A variety of techniques have been proposed in the recent literature for preparing such gradient surfaces. These include among others, microfluidic devices (38,39,40), electrochemical potential gradients (41), and photoinitiated chemistries (42,43). A review of surface chemistry methods is provided by Ruardy *et al.* (44). These techniques can be used to reliably produce gradients, but have some important restrictions regarding the chemistry or geometry of the material. In the NIST gradient model study, only peptide gradient fabrication techniques that can easily be translated to a variety of platforms relevant for tissue engineering scaffolds, such as three-dimensional microporous structures were considered. The technique chosen uses a heterobifunctional coupling agent that reacts with primary amines on the surface via a succinimidyl ester and a cysteine-terminated peptide via a thiol reactive portion, covalently binding the peptide to the surface. The gradient is established by controlling the residence time of the coupling agent with the surface. Controlling the gradient by controlling the residence time is a very general technique, which has already been extended from surfaces to other platforms including hydrogels and electrospun nanofibers. This procedure for fabricating and characterizing the peptide gradients is detailed in (45).

Assaying cell migration

Cell migration was assayed by automated time-lapse video microscopy. In this technique, cells are imaged on the surfaces and the individual cell tracks are reconstructed from the position of each cell at successive time points. The automation enables time lapse videos to be taken from multiple locations on the same surface at the same time. Thus, the entire gradient can be imaged at once. This high-throughput technique combined with the combinatorial sample preparation enables the exploration of a relatively large parameter space quickly.

This approach is illustrated in Figure 5. Several gradient materials that differ in the type of peptide and concentration were prepared and seeded with fluorescently labeled fibroblast cells. The cells were cultured in an incubated, humidified chamber that is built around the stage of a microscope so that the cells can be imaged over long periods of time. This apparatus for monitoring populations of relatively slowly migrating connective tissue cells such as fibroblasts worked well. The stage of the microscope is robotically controlled so that time-lapse videos can be collected from multiple fields of view on multiple surfaces in a single experiment. In a typical experiment, 9 fields of view on each of 4 surfaces are simultaneously imaged by programming the stage controller to raster through all 36 fields of view at each time point. The details of these

experiments are described elsewhere (45,46). From these data, the paths of individual cells were reconstructed. All of the cells within a particular field of view of the microscope are considered as a single population.

Examples of cell tracks from populations at three different fields of view of one of the laminin peptide gradients are shown in Figure 6. The data shown in Figure 6 represent the reconstructed cell tracks from 30 cells in each of the 3 fields of view. There are typically between 50 and 100 cells per field of view, but only 30 are shown in Figure 6 to improve the clarity. The cell tracks are all plotted with their origins coincident (*i.e.*, the position of each cell is plotted relative to its position at time zero rather than relative to its actual position on the surface or relative to the other cells). The cell tracks shown represent 20 hours of observation. Figure 6 illustrates how the B160 peptide concentration affects the cell motility. The cells from the field of view on the left are from the low peptide concentration end of the surface and have a relatively low motility, indicated by the distance the cells travel from their origin over the course of the experiment. The cells at the intermediate peptide concentration (the center population) interrogate a larger surface area, by moving further from their respective origins during the experiment. This population is characterized by a higher motility. Finally, at the very high peptide concentration, on the right side of the gradient, cells exhibit lower motility, similar to the cells on the right side of the gradient. This biphasic response is typical of migration responses to a variety of stimuli, including surface chemistry gradients as well as gradients in soluble chemo attractants (47,48,18,15). More experimental details and discussion of these results can be found in (45,46).

Comparisons can also be made among populations on steep and shallow peptide gradients. On relatively shallow peptide gradients there is very little observable response to the gradient itself. The cell motility within each population appears to be isotropic. However, if the gradient magnitude is increased, the cells respond to both the peptide concentration and the relative change in concentration (data not shown). In this case the motility of the population is not isotropic, and there is a preference for the cells to move in the direction of higher adhesive ligand concentration. This haptotactic response is characterized elsewhere (45).

In conclusion, the multivariate analysis of peptide gradient libraries identified optimal concentrations for both A10 and B160 on poly (L-lysine). The results demonstrate that fibroblasts behave differently at different positions along peptide gradient surfaces from $(35 \text{ to } 91) \times 10^3 \mu\text{m}^{-1}$. A dramatic increase in cell speed was determined in the range of $(63 \text{ to } 91) \times 10^3 \mu\text{m}^{-1}$. Although diffusivity increased initially with increasing peptide concentration for both A10 and B160, the persistence time decreased with increasing B160 concentrations. Therefore, it was possible to distinguish fibroblast response to different adhesion ligands and to fine tune the migration behavior. These data provide insight into the

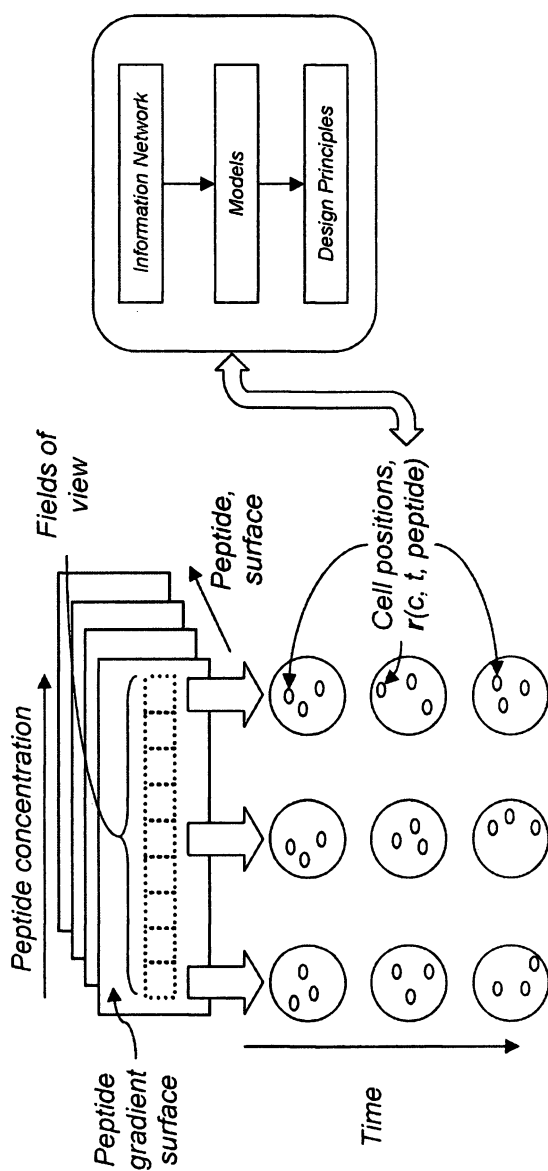


Figure 5. Schematic of NIST's experimental research on cell migration using combinatorial peptide gradient surfaces.

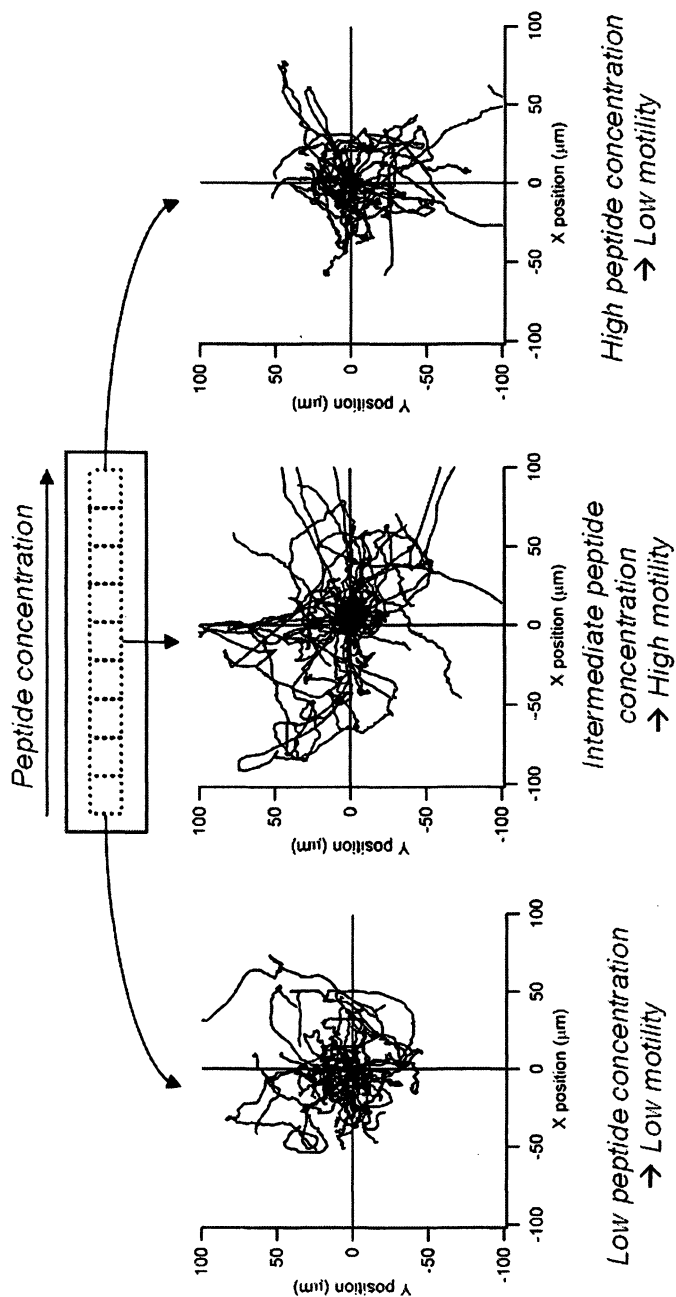


Figure 6. Tracks of 30 cells for 20 hours at each of 3 fields of view along a combinatorial BI60 peptide gradient surface.

molecular design of biomaterials⁷ to promote migration of connective tissue cells. The experimental design can be further used to investigate the biological function of the peptide adhesion ligands. The accurate determination of cell motility parameters (*i.e.*, speed, persistence time, and diffusivity) allows researchers to also conduct comparative analysis of peptides that: (*i*) provide signals to cells through different biochemical mechanisms (*e.g.*, integrin-mediated versus syndecan-mediated adhesion), (*ii*) enhance cell-extracellular matrix and cell-biomaterial interactions, and (*iii*) contribute to the dynamics of cellular biophysics. This new understanding of the activities of peptides can enhance the predictions of cell population dynamics near the edge of a wound or tissue-biomaterial interfaces and has led to the development of a new method for modeling cell migration. The methodology and tools can also be adapted to a variety of surface bound peptides and scaffold geometries with complex 3D network structures like gels and fibers. The significance of the aforementioned cell migration data to modeling migration based on the well-characterized persistent random walk models is presented below.

Modeling cell migration with persistent random walk models

NIST has developed a new technique for analyzing the cell migration data which accounts for important sources of uncertainty in the cell speed determination. This method accounts for uncertainty in determination of the precise position of each cell from the microscopy images as well as variation in cell speed within the population. The details of this analysis are reported elsewhere (46). This analysis permits us to accurately discern differences in cell populations migrating on different regions of a peptide gradient and to compare results from gradients of different peptides.

Persistent random walk models for the mean squared displacement, $\langle d^2 \rangle$ take the form (50,21,26):

$$\langle d^2 \rangle = n_d \langle S^2 \rangle P t \left[1 - \frac{P}{t} \left(1 - e^{-t/P} \right) \right] \quad (1)$$

Here, t is time and n_d is the number of dimensions in which the cells are migrating. This model assumes that the isotropic migration of the cell population can be described by some characteristic mean squared speed, $\langle S^2 \rangle$, and some persistence time in direction, P . One of the primary difficulties in fitting experimental data of cell migration to this model is that there is a very large variance in the squared displacements of the population of the individual

⁷Pertinent to current activities in elastic protein based polymers used for soft tissue augmentation and generation (49).

cells. This is in part because the cell population has a large variance in speed. A single cell can move relatively fast at some times and stop moving altogether at other times. For connective tissue cells such as fibroblasts, which move relatively slowly, this model may be appropriate but very difficult to accurately fit to experimental data in order to obtain the parameters P and $\langle S^2 \rangle$.

The common engineering strategy to improve the fit of experimental data to a model is to reduce the variance in the data as much as possible. However, in this particular case there are two sources of large variance to be dealt with. The first is experimental error. The experimental error arises from uncertainty in determining the true cell position from the micrographs. The second source of the variance is the actual variance in the speed within the cell population. This source of variance, due to heterogeneity in the cell speed, represents part of the biological response, and should therefore be conserved, rather than eliminated, in our analysis.

The method for analyzing the cell migration data accounts for this variation within the population by measuring the cell speed for each cell, i , at each time interval, j , as well as the displacement for each cell. Then, rather than leaving the mean squared speed for the population as a fit parameter to the model, it is assumed that the population is accurately described by a single persistence time, but that the cells do not necessarily have the same speed and that the speed of each cell may change. Furthermore, we recognize that cells with relatively higher speed will likely have larger displacements than cells that have relatively slower speeds. This leads us to defining a time dependent normalized migration parameter, $\xi_i(t)$:

$$\xi_i(t) = \frac{d_i^2(t)}{n_d \bar{S}_i^2(t)} = \frac{d_i^2(t)}{n_d \frac{1}{\tau} \sum_{j=1}^{\tau} S_{i,j}^2} \quad (2)$$

In equation 2, \bar{S}_i^2 is a cumulative mean squared speed for cell i , averaged over all of the previous time intervals. A cell with a relatively small displacement is normalized by a relatively small value of \bar{S}_i^2 , and a cell with a relatively large displacement is normalized by a relatively large value of \bar{S}_i^2 . This effectively reduces the standard error on $\xi_i(t)$. Then a model was derived for the mean normalized migration parameter, $\langle \xi \rangle$, to which the data can be more accurately fit in order to obtain the persistence time, P . The details of this procedure are given in (46).

The uncertainty in the cell position is propagated to the values of d_i^2 , $S_{i,j}^2$, and ξ_i^2 . This uncertainty is dealt with analytically and we develop a method to estimate the uncertainty in the cell position from displacement measurements over varying time intervals, Δt .

An additional source of error is also dealt with analytically in this method. This error arises from approximating the cell speed from the displacements at successive time intervals. This approximation assumes that the cell path is linear. In fact, the cell path is not linear and this path length approximation can be dealt with analytically, assuming that the cells behave according to the persistent random walk represented by equation 1.

By accounting for the large variance in the cell speed, the persistence time of the population can much more accurately be determined. However, without accounting for the error arising from the path length approximation and the error associated with the determination of the cell position, the model still does not fit the data. Once these two sources of error are accounted for the data is accurately described by the model. Finally, a mean squared speed $\langle S^2 \rangle$ for the population was computed. The mean squared speed is no longer a fit parameter, but is computed from the speed measurements and corrected for the two sources of error mentioned above.

With accurate determination of the persistence time and mean squared speed, a diffusion coefficient for the cell population, D , can be obtained in two dimensions and is given by $D = 0.5 \langle S^2 \rangle P$. The diffusion coefficient is a single parameter that describes how dispersive the cell population is. Diffusivity, speed, and persistence time data from two different peptide gradients are compared in Figure 7.

Model Study 2: Cell Morphology and Migration on Rigid Polymeric Surfaces

Cells are endowed with the ability to sense their chemical and mechanical environment and to alter their shape, migration, and proliferation in response to environmental cues. These responses lead to the self-organizing behavior that drives morphogenesis, and are affected by changes in the balance of mechanical forces within and around the cell. The discovery of the importance of cell shape, cytoskeletal tension, and motion for control of the cell-cycle progression requires a study of the micromechanics, cellular architecture, and structural complexity of supporting materials.

Thermodynamic Based-Model to Examine Cell Morphology

In order to more fully understand how the mechanical properties of substrates affect the behavior of adherent cells, a thermodynamic model of the cell/substrate system was developed. This approach models the cell and the

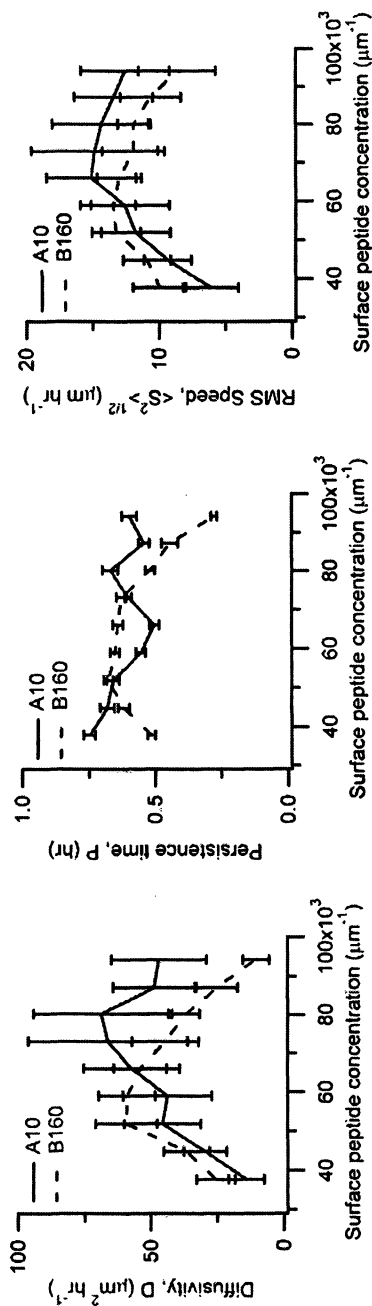


Figure 7. Cell population migration parameters from populations of human foreskin fibroblasts on laminin peptide gradients on poly(L-lysine) coated surfaces. The two laminin peptides used are the B160 peptide, which is an integrin ligand, and the A10 peptide, which is a heparin ligand. These results are taken from references (45) and (46).

substrate as two elastic materials with an adhesive force coupling them at the boundary of the cell. Minimization of the free energy of the cell/substrate system is used to predict changes in cell morphology and cell migration. This model also sheds light on the results from recent experimental investigations of cell behavior on materials of different elastic modulus.

Recent experimental reports on the effects of substrate mechanical properties on cell morphology and migration have demonstrated that substrate rigidity can profoundly affect cell behavior. For example, in some cases, increasing substrate stiffness can result in increased cell branching (6,7), while other reports, particularly with neurons, indicate the opposite trend (51,52,53). Cell alignment induced by substrate strain (54,55,56) and cell migration in response to changes in substrate compliance have also been observed (35,36,37). Thus, experimental observations provide information about the behavior of particular systems. The objective of this research is to derive a numerical solution that can interpret this information and shed light on the mechanisms that give rise to the observed phenomena. First, previous experimental reports in the literature were used as our information network. Second, a thermodynamic approach based on strain energies of the cell and substrate and the mechanism of cell adhesion at cell/substrate interfaces was employed. Finally, predictions of the resulting model were tested against literature findings.

Total Free Energy in Cell-Substrate Systems

The total free energy E_{tot} is given by the sum of the strain energy, E_1 , and the interfacial energy, E_2 .

$$E_{tot} = E_1 + E_2 \quad (3)$$

The strain energy is computed from an isotropic elastic modulus assumed for the (two-dimensional) cell and the (three-dimensional) substrate. The interfacial energy is computed from a uniform interfacial energy density at the cell periphery. Changes in E_1 and E_2 occur as cell morphology changes (*i.e.*, the cell area and periphery path length). The assumptions and details of the free-energy model for the cell/substrate system are given in (57). Extensions of the model account for effects of gradients in substrate rigidity to determine how such variations in mechanical properties of the substrate may influence cell behavior. Here, the cell migration occurs as the cell substrate system relaxes to a free energy minimum.

These results demonstrated that relaxation of the system free energy is sufficient to account for changes in cell morphology, cell orientation, and cell migration from a softer region of a substrate to a stiffer region. As substrate stiffness changes, the ratio of the interfacial energy density to the strain energy density, and the cell can respond by minimizing its free energy through either

reducing or increasing the number of branches. Figure 8a shows the normalized total free energy of the cell/substrate system for different values of β , where β is the ratio of the interfacial energy density to the strain energy density of the cell/substrate system. β is modeled as (57):

$$\beta = \frac{E_2}{E_1} = \frac{\mu^S \gamma \left(1 + \frac{\mu^C}{\mu^S} \right)^2}{(1 - \nu^S) \sigma_0^2} \quad (4)$$

In equation 4, μ^S and μ^C are the shear moduli of the substrate and the cell, respectively, γ is the interfacial energy per unit length at the cell periphery, ν^S is the Poisson's ratio of the substrate, and σ_0 is the magnitude of the initial isotropic stress of a cell.

In Figure 8a, n is the integer mode of the perturbation of the cell outline. For $n = 1$, the cell is modeled as a circle. For $n > 1$, the cell has a harmonic perturbation to its periphery with wave number n . The insets in Figure 8a represent the shape of a cell with n set to the wave number that minimizes the free energy for the corresponding value of β . Figure 8b shows the progression of cell migration along a gradient in substrate compliance (indicated by a gradient in β). The cell migrates from the softer region of the substrate to the stiffer region. The time variable t^* is normalized by a time constant for focal adhesion assembly and disassembly.

In summary, this model shows how the destabilizing forces of the cell and substrate strain energy compete with the stabilizing force of the interfacial energy to affect cell morphology and migration. Interactions between the surface and the cell will be manifested by changes in cell morphology (or cell position on surface with a non-uniform elastic modulus) when the modulus of the cell is on the same order of magnitude as the modulus of the substrate. This new understanding of the cell/surface mechanical interactions provides important physical and structural information for engineering materials with mechanical properties that interact with cells in different ways. Knowing the effective modulus is important for designing biomimetic structures, tissue constructs, gene delivery systems, and active biocomposites in tissue engineering (58,59). The model can be used to predict cell response to microstructures obtained from the self-assembly of supramolecular structures, microcontact printing (soft lithography), layer-by-layer deposition or microfluidics and other fabrication techniques that can fine tune surface properties (60,61,62,63). Recent advances in “designer” scaffolds, porous materials created using computational topography design (CTD) and solid free-form fabrication (SFF) shows great promise in tailoring structures with mechanical modulus in the range of hard (10-1,500) MPa or soft tissue (0.4-350) MPa at scales above 100 μm (64). Recent

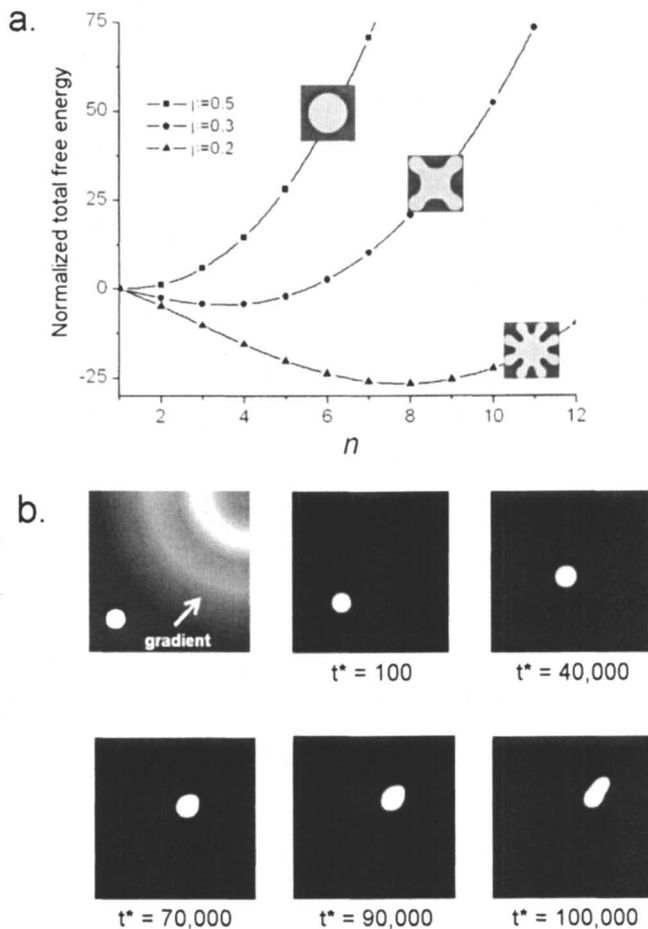


Figure 8. Effects of substrate rigidity on cell morphology (a) and cell migration (b). In (a) the free energy of a cell is computed as a function of the number of branches, n , for different values of the substrate stiffness. Insets in (a) show the cell shape with the lowest free energy for the corresponding value of β . In the first panel in (b) the color scale indicates the gradient in β on a surface on which a cell (white spot) is allowed to minimize its free energy. The free energy minimization results in a migration and elongation of the cell in the direction of the gradient. (See page 4 of color inserts.)

studies also indicate that not only surface properties, but also, geometries can be tailored through the cross-linking or blending of polymers or copolymers (65,66) The composition and processing conditions of polymer blends, for example, can result in different phase-separated morphologies where pattern size and stiffness is a function of film thickness (*i.e.*, spinodal-like structures that vary in height, crystallinity, or surface energy) (66). These surface directed or pattern formation processes to perturbations allows us to control the morphology of the evolving patterns and leads to a multiplicity of microstructures for engineering materials. It is interesting to note that the results of this cell migration model also suggests that it may be possible to estimate the modulus of cells by observing differences in their morphological characteristics on surfaces with varying mechanical properties.

Summary

The development of biomaterials requires the understanding of physical, chemical, biological and engineering processes that direct the aggregate behavior of cells. Advanced instrumentation and measurement techniques, coupled with mathematical models, will help to connect and assemble these components, opening the way to powerful medical treatments and therapies in tissue engineering. This chapter introduced selected aspects of the NIST measurement toolkit for tissue engineering consisting of high-throughput, combinatorial methods to produce test specimens varying in materials properties and advanced instrumental techniques used to collect data like high-resolution, non-invasive multi-modal imaging of cells and 3D visualization. A series of characterization techniques - spectroscopic, microscopic, and other analytical technologies that measure the physical and chemical properties of materials were also used in NIST investigations into cell-surface interactions but not mentioned. Many laboratories have identified key factors influencing cell response with only a few able to integrate multiple inputs to generate a series of models that map cell motility and migration. The two NIST models described herein focused on either cell migration as a function of covalently bound peptide gradients or as a function of polymer rigidity. In the gradient model study, an automated time-lapse video microscope was used to map the migrating path of fibroblast cells on surfaces with laminin peptide gradients. This high-throughput technique combined with the combinatorial sample preparation enabled many parameters (*i.e.*, type and concentration of peptide, gradient magnitude, etc.) to be tested simultaneously. From this, a new technique for analyzing the cell migration data was derived that resulted in an accurate determination of the persistence time, mean squared speed, and a diffusion coefficient for the cell population. This persistent random walk model takes into account important sources of uncertainty thereby enabling the identification of different migration patterns on different regions of a peptide gradient.

The discovery of the importance of cell shape, cytoskeletal tension, and motion to cell-cycle progression is predicated on the study of the cell's architecture, mechanics, and the structural integrity of supporting scaffold materials. The 2D thermodynamic-based model developed by NIST, examined how certain mechanical properties of polymer substrates affect the behavior of adherent cells. This numerical solution is driven by the need to minimize the system's total energy and predicts changes in cell morphology, orientation, and migration due to differences in stiffness across a polymer surface. The ratio of the interfacial energy density to the strain energy density of a system is a function of the shear moduli of the substrate and cell. The model sheds light on the results of recent experimental investigations of cell behavior on materials of different elastic modulus. In conclusion, these two models provide chemical, structural, and/or physical information that can be used in the engineering or fabrication of novel biomaterials. In the absence of predictive models and design principles, engineering structures to meet physiological requirements from experimentation amounts to little more than trial and error.

References

1. Lysaght, M. J.; Hazlehurst, A. L. *Tissue Eng*, **2004**, *10*, pp 309-320.
2. McIntyre, L. V.; Greisler, H.; Griffith, L.; Johnson, P.; Mooney, D. J.; Mrksich, M.; Parenteau, N. L.; Smith, D. *WTEC Panel Report on Tissue Engineering Research* International Technology Research Institute, World Technology (WTEC) Division, 2002, <http://www.wtec.org/loyola/te/>.
3. Tweedie, C. A.; Anderson, D. G.; Langer, R.; Van Vliet, K. J. *Adv Mater*, **2005**, *17*, p 2599.
4. Bhat, R. R.; Tomlinson, M. R.; Genzer, J. *J Polym Sci, Part B: Polym Phys*, **2005**, *43*, pp 3384-3394.
5. Khademhosseini, A.; Langer, R.; Borenstein, J.; Vacanti, J. P. *Proc Natl Acad Sci USA*, **2006**, *103*, pp 2480-2487.
6. Pelham, R.J.; Wang, Y.L. *Proc Natl Acad Sci USA*, **1997**, *94*, pp. 13661-13665.
7. Yeung, T.; Georges, P.C.; Flanagan, L.A.; Marg, B.; Ortiz, M.; Funaki, M.; Zahir, N.; Ming, W.Y.; Weaver, V.; Janmey, P.A. *Cell Motil Cytoskeleton* **2005**, *60*, 24-34.
8. Bailey, L. O.; Becker, M. L.; Stephens, J. S.; Gallant, N. D.; Mahoney, C. M.; Washburn, N. R.; Rege, A.; Kohn, J.; Amis, E. J. *J Biomed Mater Res, Part A*, **2006**, *76A*, pp 491-502.
9. Dunkers, J. P.; Cicerone, M. T.; Washburn, N. R. *Opt Express*, **2003**, *11*, pp 3074-3079.
10. Kee, T. W.; Cicerone, M. T. *Opt Lett*, **2004**, *29*, pp 2701-2703.

11. Devaney, J. E.; Satterfield, S. G.; Hagedorn, J. G.; Kelso, J. T.; Peskin, A. P.; George, W. L.; Griffin, T. J.; Hung, H. K., and Kriz, R. D. *Science at the speed of thought*; 2005.
12. Malinda, K. M.; Nomizu, M.; Chung, M.; Delgado, M.; Kuratomi, Y.; Yamada, Y.; Kleinman, H. K.; Ponce, M. L. *FASEB J.*, **1999**, *13*, pp 53-62.
13. Nomizu, M.; Kuratomi, Y.; Malinda, K. M.; Song, S. Y.; Miyoshi, K.; Otaka, A.; Powell, S. K.; Hoffman, M. P.; Kleinman, H. K.; Yamada, Y. *J Biol Chem.*, **1998**, *273*, pp 32491-32499.
14. Nomizu, M.; Kim, W. H.; Yamamura, K.; Utani, A.; Song, S. Y.; Otaka, A.; Roller, P. P.; Kleinman, H. K.; Yamada, Y. *J Biol Chem.*, **1995**, *270*, pp 20583-20590.
15. Tranquillo, R. T.; Zigmond, S. H.; Lauffenburger, D. A. *Cell Motil Cytoskeleton*, **1988**, *11*, pp 1-15.
16. Farrell, B. E.; Daniele, R. P.; Lauffenburger, D. A. *Cell Motil Cytoskeleton*, **1990**, *16*, pp 279-293.
17. Haddox, J. L.; Pfister, R. R.; Sommers, C. I. *J Immunol Methods*, **1991**, *141*, pp 41-52.
18. Moghe, P. V.; Nelson, R. D.; Tranquillo, R. T. *J Immunol Methods*, **1995**, *180*, pp 193-211.
19. Bergman, A. J.; Zygourakis, K. *Biomaterials*, **1999**, *20*, pp 2235-2244.
20. Van Vliet, K. J.; Bao, G.; Suresh, S. *Acta Mater*, **2003**, *51*, pp 5881-5905.
21. Dunn, G. A.; Brown, A. F. *J Cell Sci Suppl*, **1987**, *8*, pp 81-102.
22. Dickinson, R. B.; Tranquillo, R. T. *AIChE J*, **1993**, *39*, pp 1995-2010.
23. Dickinson, R. B.; Tranquillo, R. T. *SIAM J Appl Math*, **1995**, *55*, pp 1419-1454.
24. Stokes, C. L.; Lauffenburger, D. A.; Williams, S. K. *J Cell Sci*, **1991**, *99*, pp 419-430.
25. Alt, W. *J Math Biol*, **1980**, *9*, pp 147-177.
26. Tranquillo, R. T.; Lauffenburger, D. A.; Zigmond, S. H. *J Cell Biol*, **1988**, *106*, pp 303-309.
27. Friedl, P.; Zanker, K. S.; Broucker, E. B. *Microsc Res Tech*, **1998**, *43*, pp 369-378.
28. Zaman, M. H.; Kamm, R. D.; Matsudaira, P.; Lauffenburger, D. A. *Biophys J*, **2005**, *89*, pp 1389-1397.
29. Walmod, P. S.; Hartmann-Petersen, R.; Prag, S.; Lepekkin, E. L.; Ropke, C.; Berezin, V.; Bock, E. *Exp Cell Res*, **2004**, *295*, pp 407-420.
30. Boal, D. H. *Mechanics of the cell*. Cambridge University Press: Cambridge, UK, **2002**; pp. 23-35.
31. Suresh, S. *J Mater Res*, **2006**, *21 (8)*, pp. 1871-1877.
32. Ni, Y.; Chiang, M. Y. M. *Biophys J (Submitted)*, **2006**,
33. Carter, S. B. *Nature*, **1965**, *208*, pp 1183-1187.
34. Carter, S. B. *Nature*, **1967**, *213*, pp 256-260.
35. Lo, C. M.; Wang, H. B.; Dembo, M.; Wang, Y. L. *Biophys J*, **2000**, *79*, pp 144-152.

36. Gray, D. S.; Tien, J.; Chen, C. S. *J Biomed Mater Res, Part A*, **2003**, *66A*, pp 605-614.
37. Wong, J. Y.; Velasco, A.; Rajagopalan, P.; Pham, Q. *Langmuir*, **2003**, *19*, pp 1908-1913.
38. Dertinger, S. K. W.; Jiang, X. Y.; Li, Z. Y.; Murthy, V. N.; Whitesides, G. M. *Proc Natl Acad Sci USA*, **2002**, *99*, pp 12542-12547.
39. Jeon, N. L.; Dertinger, S. K. W.; Chiu, D. T.; Choi, I. S.; Stroock, A. D.; Whitesides, G. M. *Langmuir*, **2000**, *16*, pp 8311-8316.
40. Gunawan, R. C.; Choban, E. R.; Conour, J. E.; Silvestre, J.; Schook, L. B.; Gaskins, H. R.; Leckband, D. E.; Kenis, P. J. A. *Langmuir*, **2005**, *21*, pp 3061-3068.
41. Plummer, S. T.; Wang, Q.; Bohn, P. W.; Stockton, R.; Schwartz, M. A. *Langmuir*, **2003**, *19*, pp 7528-7536.
42. Adams, D. N.; Kao, E. Y.; Hypolite, C. L.; Distefano, M. D.; Hu, W. S.; Letourneau, P. C. *J Neurobiol*, **2005**, *62*, pp 134-147.
43. Hypolite, C. L.; McLernon, T. L.; Adams, D. N.; Chapman, K. E.; Herbert, C. B.; Huang, C. C.; Distefano, M. D.; Hu, W. S. *Bioconjugate Chem*, **1997**, *8*, pp 658-663.
44. Ruardy, T. G.; Schakenraad, J. M.; vanderMei, H. C.; Busscher, H. J. *Surf Sci Rep*, **1997**, *29*, pp 3-30.
45. Kipper, M. J.; Kleinman, H. K.; Wang, F. W. *Anal Biochem*, (Submitted), **2006**.
46. Kipper, M. J.; Kleinman, H. K.; Wang, F. W. *Biophys J* (Submitted), **2006**.
47. Dimilla, P. A.; Stone, J. A.; Quinn, J. A.; Albelda, S. M.; Lauffenburger, D. A. *J Cell Biol*, **1993**, *122*, pp 729-737.
48. Wu, P.; Hoying, J. B.; Williams, S. K.; Kozikowski, B. A.; Lauffenburger, D. A. *Ann Biomed Eng*, **1994**, *22*, pp 144-152.
49. Shoichet, M. S.; Hubbell, J. A.; *Polymers for Tissue Engineering*; Brill Academic Publishers: New York, N.Y., 1998; pp. 19-24.
50. Dunn, G. A. *Agents Actions Suppl*, **1983**, *12*, pp 14-33.
51. Balgude, A. P.; Yu, X.; Szymanski, A.; Bellamkonda, R. V. *Biomaterials*, **2001**, *22*, pp 1077-1084.
52. Georges, P. C.; Miller, W. J.; Meaney, D. F.; Sawyer, E. S.; Janmey, P. A. *Biophys J*, **2006**, *90*, pp 3012-3018.
53. Flanagan, L. A.; Ju, Y. E.; Marg, B.; Osterfield, M.; Janmey, P. A. *Neuroreport*, **2002**, *13*, pp 2411-2415.
54. Dartsch, P. C.; Betz, E. *Basic Res Cardiol*, **1989**, *84*, pp 268-281.
55. Neidlinger-Wilke, C.; Groot, E. S.; Wang, J. H. C.; Brand, R. A.; Claes, L. *J Orthop Res*, **2001**, *19*, pp 286-293.
56. Wang, J. H. *J Theor Biol*, **2000**, *202*, pp 33-41.
57. Ni, Y.; Chiang, M. Y. M. *Biophys J* (Submitted), **2006**.
58. Saltzman, M. W.; Olbricht, W. L. *Nat Rev Drug Discov*. **2002**, *1*, pp. 177-186.

59. Chesnoy, S.; Huang, L. *Annu Rev Biophys Biomo Struct* **2000**, *29*, pp. 27-47.
60. Whitesides, G. M.; Grzybowski, B. *Science*. **2002**, *29*, pp. 2418-2421.
61. Tan, J.; Saltzman, M. W. *Biomaterials*. **2004**, *25*, pp. 3593-3601.
62. Quist, A. P.; Pavlovic, E.; Oscarsson, S. *Anal Bioana Chem*. **2005**, *381*, pp. 591-600.
63. Tan, W.; Desai, T. A. *Biomaterials*. **2004**, *25*, pp. 1355-1364.
64. Hollister, S. J. *Nat Mater*, **2005**, *4*, pp. 518-590.
65. Zhang, Y.; Ge, S.; Rafailovich, M. H.; Sokolov, J. C.; Colby, R.H. *Polymer*. **2003**, *44*, 3327-3332.
66. Smith, A.P.; Douglas, J.F.; Carson, J.M.; Amis, E.J.; Karim, A. *J Polym Sci Part B: Polym Phys*. **2001**, *39*, pp. 2141-2158.

Chapter 9

Broadband Dielectric Spectroscopic Characterization of the Hydrolytic Degradation of Hydroxyl-Terminated Poly(D,L-lactide) Materials

Mohammad K. Hassan^{1,2}, Jeffrey S. Wiggins¹, Robson F. Storey¹,
and Kenneth A. Mauritz^{1,*}

¹School of Polymers and High Performance Materials, The University
of Southern Mississippi, 118 College Drive, Hattiesburg, MS 39406

²Permanent address: Chemistry Department, Faculty of Science,
Bani Suef University, Bani Suef, Egypt

*Corresponding author: Kenneth.mauritz@usm.edu

Broadband dielectric spectroscopy was used to examine hydroxyl-terminated poly(D,L-lactide) samples that were hydrolytically degraded in 7.4pH phosphate buffer solutions at 37° C. The dielectric spectral signatures of degraded samples were considerably more distinct than those of undegraded samples and a T_g – related relaxation associated with long range chain segmental mobility was seen. For both degraded and undegraded samples, a relaxation peak beneath T_g was observed, which shifts to higher frequency with increasing temperature. Linear segments on log-log plots of loss permittivity vs. frequency, in the low frequency regime, are attributed to d.c. conductivity. An upward shift in peak frequency maximum was observed after 95 days of immersion in buffer solution. This behavior implies a decrease in the time scale of long range chain segmental motions. Permittivity data for degraded and undegraded materials were fitted to the Havriliak-Negami equation with subtraction of the d.c. conductivity contribution to uncover pure relaxation peaks.

Parameters extracted from these fits were used to construct Vogel-Fulcher-Tammann-Hesse (VFTH) and distribution of relaxation time, $G(\tau)$, curves. The relaxation time for this α -transition in both degraded and undegraded samples showed VFTH temperature behavior. $G(\tau)$ curves showed a general broadening and shift to lower τ with degradation, which can be explained in terms of a broadening of molecular weight within degraded samples and faster chain motions.

Introduction

Biodegradable polyesters and co-polyesters have been the focus of extensive research for several decades due to their ease of manufacturing and desirable characteristics. Their ranges of physical properties and hydrolytic degradation profiles have made them attractive candidates for use in a variety of biomedical products such as degradable sutures (1), temporary orthopedic fixtures (2) and controlled pharmaceutical delivery matrices (3,4).

Degradation mechanisms vary among biodegradable polyesters as a function of chemical composition and are categorized as hydrolytic and/or microbial. Factors that influence degradation rate include material hydrophilicity, morphology, crosslink density and surface chemistry. Additives such as monomers, acidic or basic compounds, superoxide ions, drug composition, and catalysts have been shown to affect degradation kinetics (5). Polymer endgroups and endgroup modifications can also influence degradation. In general, studies have shown that the presence of free carboxylic acid moieties, whether on the polymer endgroup or blended into the sample as an additive or active ingredient, will accelerate the hydrolytic degradation rates of polyesters (5-8). Another study revealed that carboxylic acid modifications of a biodegradable polymer have a greater influence on degradation than the acidity of the external aqueous environment (9).

Modern broadband dielectric spectroscopy is a very useful tool to interrogate the molecular dynamics of polymers because response over a broad frequency range from the milli- to giga-Hertz region is possible (10). Therefore, motional processes which take place in polymers on extremely different time scales can be investigated vs. temperature. Moreover, the motional process depends on the morphology of the system.

Dielectric spectroscopy, in the context of this system, deals with the interaction of an applied alternating electric field with the orientable dipoles in matter that account for polarizability. Macroscopic polarization is microscopically related to the dipole density of N permanent molecular dipoles of moment $\overline{\mu}_i$ in a volume V . In low molecular weight molecules, the net dipole moment can

often be represented by a single rigid vector, while in polymers there are different geometric possibilities for the orientation of the component molecular dipole vectors along the backbones owing to conformational fluctuations. The net dipole moment per unit volume (i.e., polarization) of a polymer is the vector sum over all molecular dipoles in a repeat unit, and this is summed over the entire chain, and finally over all chains in the system (11):

$$\vec{P} = \frac{1}{V} \sum_{\text{all chains}} \sum_{\text{chain}} \sum_{\text{repeat unit}} \vec{\mu}_i \quad (1)$$

From the standpoint of chain dynamics, these dipoles are interactively coupled and long range chain segmental mobility that is affected at the glass transition upon heating from the glassy state is a cooperative process.

Molecular motions in amorphous entangled polymer chains can have considerable restrictions and exist on very different time and length scales; therefore, different vector components that contribute to the net dipole moment can undergo reorientation in different motional processes. Thus, the dielectric spectrum of an amorphous polymer generally shows multiple relaxations, depending on temperature, where each process is indicated by a peak in loss permittivity (ϵ'') and an associated step decrease in storage permittivity (ϵ') versus frequency (f) at a fixed temperature. Most amorphous polymers exhibit a secondary β -relaxation in the glassy state and a primary α -relaxation at lower frequencies (or higher temperature) than the β -relaxation. Useful information on the structural and dynamic states of a polymer material can be extracted by monitoring macromolecular mobility in this way. The structural aspect of interest in these studies is the molecular weight distribution.

This chapter reports the use of modern broadband dielectric spectroscopy as a novel approach in the study of the degradation of hydroxyl-terminated poly(D,L-lactide) materials from the perspective of modified macromolecular motions. As this technique is largely unfamiliar to the community engaged in the pursuit of biodegradable materials, fundamental explanations are provided where needed in this chapter. The analysis outlined here can be considered as useful in a broader context of materials that are degraded in similar ways, such as proton exchange membranes that are exposed to generated peroxide in fuel cells.

Experimental

Materials and Degradation Study. The biodegradable polyester material used in this study, described in a previous report (8), is hydroxyl-terminated

poly(D,L-lactide) having a molecular weight of 20,000 g/mol. These materials were degraded by exposure to phosphate-buffered aqueous solutions (7.4 pH, 0.05M) at 37° C for different time intervals up to 180 days and were tested for relative moisture uptake and weight loss behaviors. Sample discs of diameter 2.54 cm and thickness of ~ 1 mm were prepared for degradation studies by melt pressing them at 100° C for 15 min.

Sample Preparation and Dielectric Spectroscopy Measurements. Dielectric relaxation spectra were collected using a Novocontrol GmbH Concept 40 broadband dielectric spectrometer over the frequency range 0.01 Hz – 3 MHz and over the temperature range of 0 to 100° C. The temperature stability of the instrument was controlled to within $\pm 0.2^\circ$ C.

Degraded sample discs were carefully dried by melting at 100° C for 20 min under vacuum to remove residual moisture from the degradation procedure. The discs were then melt pressed between two gold coated copper electrodes at 100° C using a hot press. This process was done in two steps using polyimide non-stick films between the sample and one of the electrodes to visually examine the sample while it was attached to the other electrode. This procedure allowed for inspection of possible air bubbles in the sample before conducting the dielectric spectroscopy experiment. The upper electrode was 2 cm in diameter and the lower electrode was 3 cm in diameter.

Results and Discussion

Dielectric Spectra of Undegraded Poly(D,L-lactide)

The glass transition peak and shift of the associated relaxation time to shorter values with increasing temperature is seen in the ϵ'' vs. f plots for the same sample at different temperatures in Figure 1. There is a relaxation peak beneath the previously determined, DSC-based T_g ($= 51^\circ$ C) (8) which becomes more distinct and shifts to higher f with increasing temperature. A relaxation time, τ_{max} , can be extracted as usual from the frequency corresponding to the peak maximum, f_{max} , as $\tau_{max} = (2\pi f_{max})^{-1}$. Havriliak and Negami pointed out that the value of f for which ϵ'' is maximum is not exactly the relaxation time for cases for which the Cole-Cole plots (ϵ'' vs. ϵ') (12) are not strict semicircles but rather are arcs skewed toward the left, that is, in the progression of increasing f (13-15). When such curve asymmetry exists, the actual relaxation time is longer than that derived from the condition $\partial\epsilon''/\partial\omega = 0$, where $\omega = 2\pi f$.

In the low- f region and for $T > T_g$ the $\log \epsilon''$ vs. $\log f$ plots are linear such that the slopes are slightly less 1.0. This reflects d.c. conductivity which is characterized by the relationship $\epsilon''_{dc} = G_{dc}/(\omega C_0)$, where G_{dc} is the d.c. conductance and C_0 is the vacuum capacitance of the unfilled cell in which the

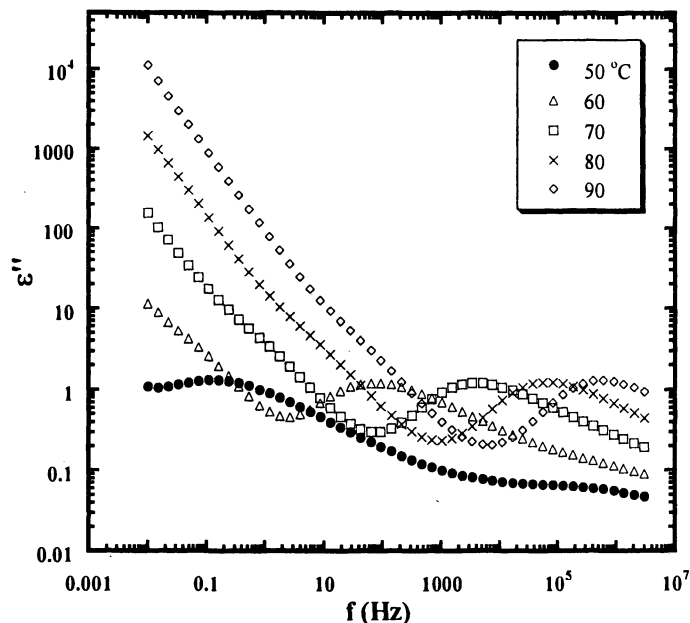


Figure 1. $\log \epsilon''$ vs. $\log f$, at various fixed temperatures, for a dry untreated 20 kg/mol hydroxyl-terminated poly(D,L-lactide) sample.

electrode plate spacing is equal to the sample thickness (16). For 'ideal' conduction the d.c. curve segment is characterized by the relationship $\epsilon'' \propto \omega^{-1}$. Often, the general power law $\epsilon'' \propto \omega^{-N}$, where N is the slope of the line, is obeyed. An additional spectral feature, caused by sample-electrode interfacial polarization, can be present as characterized by N being considerably less than 1.00 and ϵ'' being inordinately large with decreasing f at the lowest frequencies. This effect was discussed in reports of dielectric relaxation studies of hydrated perfluorosulfonate ionomer membranes (17-22). Also, there is another small peak, to the left of the primary α -relaxation peak, which seems to be obscured by the d.c. conductivity linear upturns at low frequency. This additional relaxation will be clearly seen on the distribution of relaxation times later in this report. Here, however, we will confine our comments to the relaxation associated with the α process.

Dielectric Spectra of Hydrolyzed Polymers

Figure 2 consists of $\log \epsilon''$ vs. $\log f$ plots, at different fixed temperatures, for a dried 20 kg/mol hydroxyl-terminated sample that was immersed in buffer

solution for 95 days at 37° C. After the hydrolysis reaction was terminated, the samples were melted under vacuum at 100° C to remove residual water before conducting the dielectric spectroscopic analysis. In addition to minimizing the obscuring effect of d.c. conduction due to residual water, this procedure is considered to be important for the following reason. With increasing degradation time, the surfaces of sample discs show voids due to erosion. While these voids disappear upon melting, the original degraded morphology is expected to be destroyed. On the other hand, the dielectric relaxation associated with the glass transition is mainly dependent on molecular weight which is reduced, on the average, by hydrolytic scission along the chain.

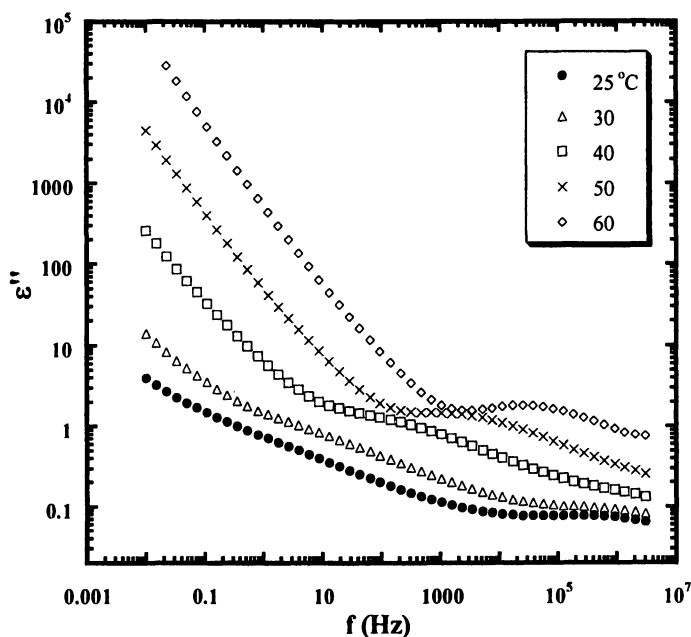


Figure 2. $\log \epsilon''$ vs. $\log f$, at various fixed temperatures, for a dry 20 kg/mol hydroxyl-terminated sample that underwent degradation by hydrolysis for 95d.

The overall rightward trend in peak shift with increasing temperature is similar to that for the untreated sample. The α -relaxation peak, that is weak at 25° C but becomes increasingly more clear with increase in temperature, shifts to lower temperature with degradation. As in Figure 1, there is an upward vertical curve displacement with increasing temperature although ϵ'' attains

considerably higher values than those for the untreated sample in the low frequency regime. This, as well as an enhanced polarizability that is given evidence by an upward vertical displacement of the ϵ' vs. f curves (data not shown), could be due to the hydrolytic cleavage of main chain ester linkages which increases the number density of polar carboxylic acid endgroups.

Effect of Degradation Time on Dielectric Relaxation Spectra

Figure 3 shows ϵ'' vs. f curves at 30 and 60° C for dried 20 kg/mol hydroxyl-terminated samples that were immersed in buffer solution for 95 days at 37° C as well as for untreated control sample. At 30° C, a broad peak is observed for the 95 days degraded sample while no peak is shown for the untreated sample at this temperature. This is taken to indicate the presence of low molecular weight segments in the degraded sample that would have shorter α relaxation times. At 60° C, which is considerably above T_g for the untreated sample, f_{\max} associated with the time scale of long range segmental motions increases with increased degradation time. Likewise, this behavior reflects an increase in chain segmental motion caused by molecular weight degradation.

Jamshidi, Hyon and Ikada (23) established that T_g vs. number average molecular weight (M_n) for polylactic acid follows the Flory-Fox equation (24,25):

$$T_g = T_g^\infty - K/M_n \quad (2)$$

K is a constant for the polymer under study and T_g^∞ is its glass transition temperature at infinite molecular weight. These investigators found that T_g^∞ for poly(D,L-lactide) and poly(L-lactide) are 57 and 58° C, respectively. While this equation is largely empirical, it can be rationalized on the simple basis of excess free volume associated with inefficient packing of chains around chain ends, although intra- and inter-chain polar and hydrogen bonding interactions are expected to influence T_g , as well. In any case, the validity of this equation is important as it allows for interpreting upward shifts in the T_g - related f_{\max} value with a decrease in average molecular weight due to polymer chain degradation. A decrease in molecular weight causes an increase in excess free volume.

An alternate explanation of these results comes from the perspective of the Rouse-Zimm model that predicts that the relaxation time for simple polymers above T_g is directly proportional to the product of the molecular weight and viscosity, where the latter increases with increasing molecular weight (*ref. 16, p 147*).

With either view, complications caused by water plasticization can be discounted because the samples were carefully dried.

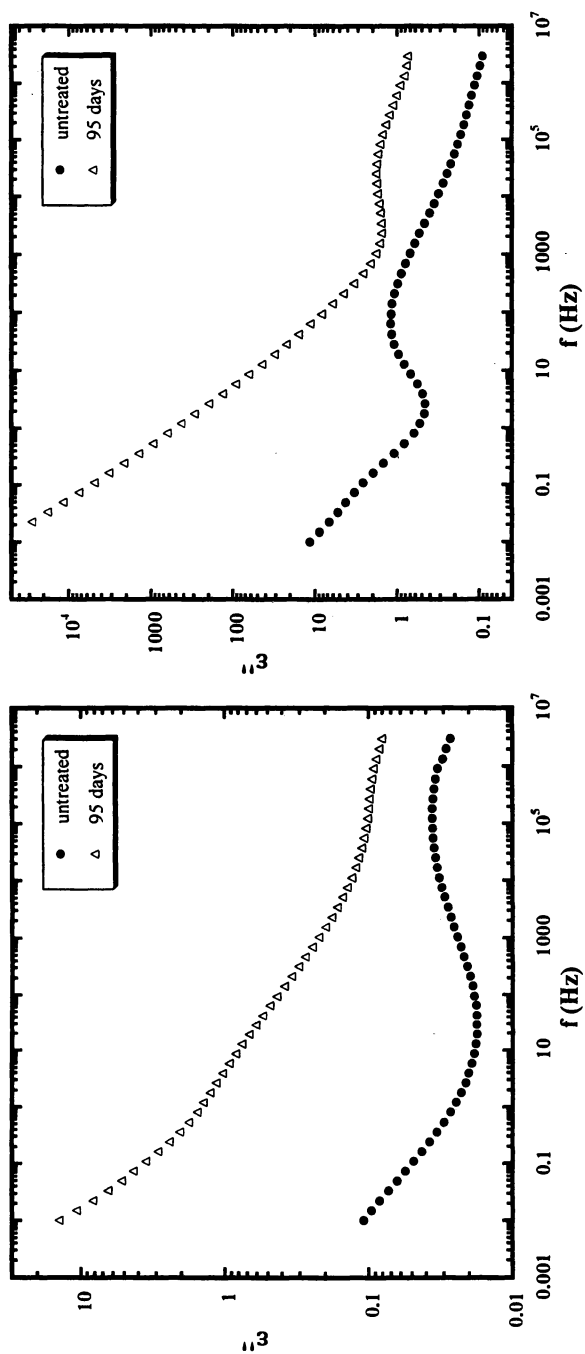


Figure 3. $\log \epsilon''$ vs. $\log f$, at 30°C (a) and 60°C (b), for a dry 20 kg/mol hydroxyl-terminated untreated and a 95d degraded sample.

Linear low frequency upturns to the left of the relaxation peaks observed in Figure 3, attributed to d.c. conduction, are displaced upward with increasing degradation time. While the exact nature of the charge carrier in the conduction process is not clear, an increasing density of COOH groups resulting from ester linkage hydrolysis with increased chain scission must be implicated. d.c. conductivity, in essence, involves the sampling of charge hopping pathways that become progressively longer at increasingly lower frequencies. As the experimental time scale, or half period of oscillation = $(2f)^{-1}$, increases, charge carriers, possibly protons in this case, can execute more elementary hops throughout the free volume of the polymer before the applied field reverses. This phenomenon likely reflects an increase in the number of carboxylic endgroups as hydrolytic degradation progresses.

Data Analysis using the Havriliak-Negami (HN) and Vogel-Fulcher-Tammann-Hesse (VFTH) Equations

In order to extract more information on degraded chemical structure and chain dynamics, the phenomenological Havriliak-Negami (HN) equation was fitted to the permittivity data shown in Figures 1 and 2 (13-15):

$$\varepsilon^*(\omega) = \varepsilon' - i\varepsilon'' = -i \left(\frac{\sigma_0}{\varepsilon_0 \omega} \right)^N + \sum_{k=1}^3 \left[\frac{\Delta\varepsilon_k}{(1 + (i\omega\tau_{HN})^{\alpha_k})^{\beta_k}} + \varepsilon_{\infty k} \right] \quad (3)$$

$\Delta\varepsilon_k = (\varepsilon_R - \varepsilon_{\infty})_k$, the difference between the real permittivities (ε') at very low and very high frequencies, respectively, is the relaxation strength for the k th relaxation and ε_0 is the vacuum permittivity. τ_{HN} is the Havriliak-Negami relaxation time, α and β ($0 < \alpha < 1$, $\alpha\beta \leq 1$) are permittivity curve shape constants where α quantifies the breadth of the distribution of relaxation times and β accounts for distribution asymmetry for the k th relaxation. σ_0 is the d.c. conductivity in units of S/cm. The exponent N ($0 < N \leq 1$), that was referred to earlier, characterizes the conduction process in terms of charge hopping pathways and mobility constraints. σ_0 , N , τ_{HN} , $\Delta\varepsilon$, α , and β are treated as free variables that are obtained by fitting the HN equation to the loss (ε'') spectra. Equation 3 allows for up to three different relaxations that might overlap, and in practice, three were used in the fitting. Curve fitting was performed using the WinFit program (Novocontrol) and the parameters extracted from fitting the data are listed in Table I. τ_{HN} is related to τ_{max} by the following equation (ref. 10, p 64):

$$\tau_{\max} = \tau_{HN} \left[\frac{\sin\left(\frac{\pi\alpha\beta}{2(\beta+1)}\right)}{\sin\left(\frac{\pi\alpha}{2(\beta+1)}\right)} \right]^{\frac{1}{\alpha}} \quad (4)$$

Note that $\tau_{HN} = \tau_{\max}$ when $\beta=1$.

The first, d.c. conductivity, term in equation 3 is not a relaxation but a spectral-obscuring factor that is subtracted for the purpose of uncovering the actual relaxation signatures of macromolecular motions. This subtraction is especially necessary to resolve relaxation times at temperatures approaching T_g at which d.c. conduction becomes stronger (26). Even in the absence of intended ions, water, or in some rare cases, free electrons, there can be unknown impurity charges in polymers and a low concentration of these is sufficient for this effect to be seen.

Spectra for the untreated control sample vs. temperature are in Figure 4. Subtraction of the d.c. contribution causes the peaks to be more distinct and their progressive shift to greater frequency with increased temperature is more clearly visualized.

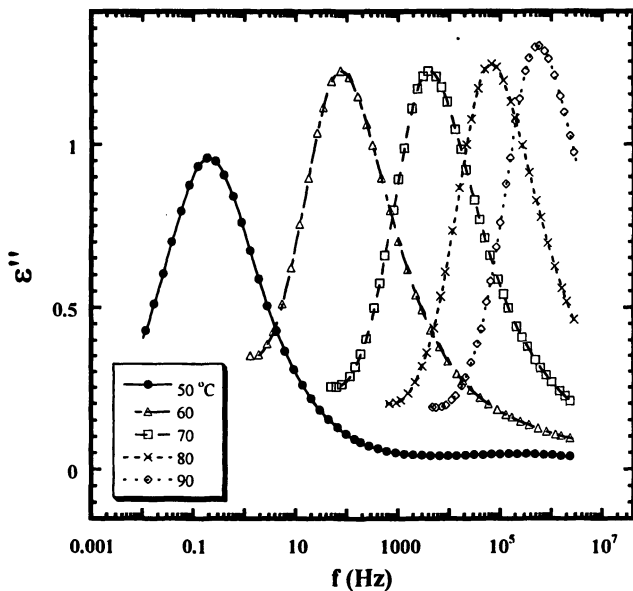


Figure 4. ϵ'' vs. $\log f$, at various fixed temperatures, for a dry undegraded sample with the conductivity contribution subtracted. The curves show an excellent fit of the HN equation to the data points.

As seen in the d.c.-subtracted loss spectra in Figure 5 for the fixed temperature of 60° C, f_{\max} shifts to higher values with increased time of degradation. Accordingly, as seen in Table I, $\tau_{\max} = 1/(2\pi f_{\max})$ decreases by decades reflecting more rapid chain motions. Notice also that the peak is less symmetric for the non-degraded sample. The Rouse-Zimm model predicts that the relaxation time for long range chain motions in the rubbery state decreases with decreasing molecular weight (*ref. 16, p 147*). Hence, if the average molecular weight shifts to lower values through degradation, f_{\max} will necessarily shift to higher values. This, in essence, is the main link between degradation by chain scission and dielectric relaxation spectra.

Segmental relaxation is a non-Arrhenius process having a time scale with a temperature dependence that follows the Vogel-Fulcher-Tammann-Hesse (VFTH) equation (27):

$$\tau(T) = \tau_0 \exp\left(\frac{E_a}{k_B(T - T_V)}\right) \quad (5)$$

τ_0 , E_a , and T_V are treated as adjustable parameters obtained by fitting equation 5 to experimental data. τ_0 is a hypothetical relaxation time at infinite temperature.

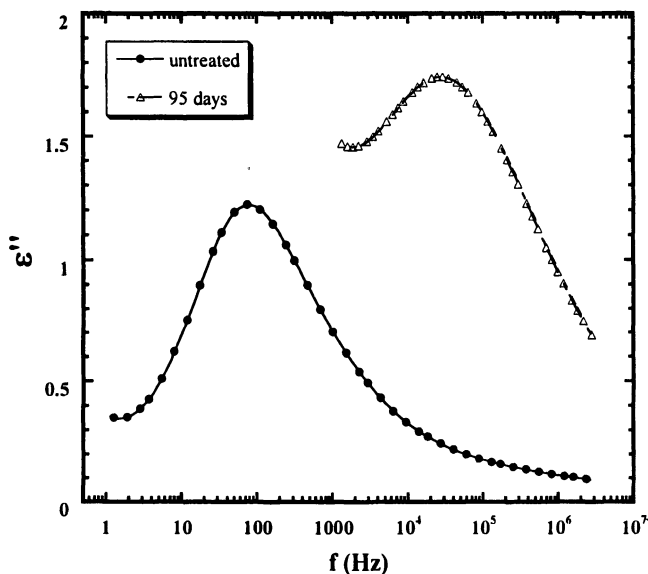


Figure 5. ϵ'' vs. $\log f$ at 60° C for dry untreated and 95 days degraded samples with the conductivity contribution subtracted.

Table I. Havriliak-Negami equation and VFTH equation fit parameters for 95 days degraded vs. untreated samples at 60° C.

Sample	Relaxation time (s) ¹	α	β	T_V (K)
undegraded	2.05×10^{-3}	0.77	0.51	284
95 days-degraded	4.70×10^{-6}	0.51	0.75	240

¹As calculated by eq 4.

E_a , while having units of energy, is a quantity of uncertain meaning that is not associated with an activated process in the usual sense and can, in fact, have values that are unrealistically much greater than the binding energy for a C-C bond near the glass transition (*ref 11, p 89*). T_V , the Vogel temperature, is viewed as the temperature at which chain segments become immobile, or frozen-in, in a hypothetical experiment in which a polymer is cooled very slowly (quasi-static) from the rubbery state. Given this prescription, T_V is expected to be lower than T_g and is given by the equation (*ref. 10, p 103*)

$$T_V = T_g - \frac{f_g}{\alpha_f} \quad (6)$$

f_g is the free volume fraction at T_g and α_f is the temperature coefficient of free volume expansion. For quasi-static cooling, in the absence of kinetic effects inherent in all experiments to determine T_g , f_g would be zero.

Figure 6 shows VFTH plots for the untreated and 95 days degraded samples over a range of temperatures. The plots are nonlinear, i.e., non-Arrhenius like. Also, there is a distinct separation between the curves for the non-degraded and degraded samples. The VFTH equation can be well fitted to the data for both degraded and non-degraded samples as in cases for the α -transition for other polymers (*16*). Curve-fitted values of T_V , listed in Table I, show that T_V decreased with immersion in buffer solution for 95 days. T_V would be expected to decrease with increased degradation time as the free volume increases and it was discussed above how smaller, degraded chains insert more excess free volume into the system.

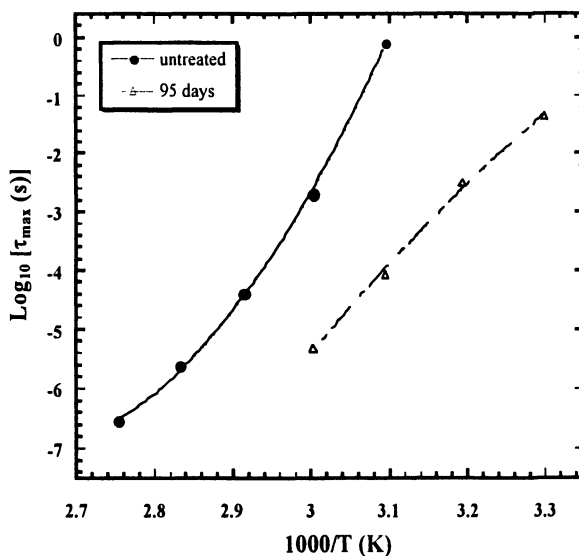


Figure 6. VFTH plot for dry untreated and 95 days degraded samples with the conductivity contribution subtracted from spectra.

Effect of Degradation on the Distribution of Relaxation Times

In the Havriliak-Negami treatment, α and β determine the distribution of relaxation times, $G(\tau)$. α characterizes the breadth of the distribution while β characterizes the extent of skew from curve symmetry (14). $G(\tau)$ is given by the following equation (14):

$$G(\tau) = \frac{\left(\frac{\tau}{\tau_{0i}}\right)^{\beta_i \alpha_i} \sin(\beta_i \Theta_i)}{\pi \tau \left[\left(\frac{\tau}{\tau_{0i}}\right)^{2\alpha_i} + 2 \left(\frac{\tau}{\tau_{0i}}\right)^{\alpha_i} \cos(\pi \alpha_i) + 1 \right]^{\frac{\beta_i}{2}}} \quad (7)$$

In equation 7,

$$\Theta_i = \arctan \left(\frac{\sin(\pi \alpha_i)}{\left(\frac{\tau}{\tau_{0i}}\right)^{\alpha_i} + \cos(\pi \alpha_i)} \right)$$

The quantity Θ has units of an angle in radians such that ($0 \leq \Theta_i \leq \pi$).

$G(\tau)$ plots for degraded vs. non-degraded samples are shown in Figure 7. The obscuring d.c. contribution was subtracted from the loss spectra to yield pure relaxation information. Both degraded and undegraded samples showed a bimodal distribution but there is distinct curve broadening with less asymmetry for the 95d degraded sample. This feature is related to the loss permittivity asymmetry seen in Figure 5. Based on the rationale presented above, the unsymmetric distribution is interpreted in terms of molecular weight degradation and molecular weight distribution broadening with time. The shift in curve maximum to lower τ reflects faster chain motions as would be expected of shorter chains. It is also seen that α , β and $G(\tau)$ are temperature dependent (data not shown).

In polymer blends, such broadening is usually attributed to two possible mechanisms; concentration fluctuation or intrinsic mobility differences between the blend components (28). Within the context of the system at hand, at some point of degradation, one can consider a 'blend' of chains of lengths that are so diverse as to create microstructural heterogeneity, in part because the solubility of chains depends on molecular weight and the effect is more pronounced at low

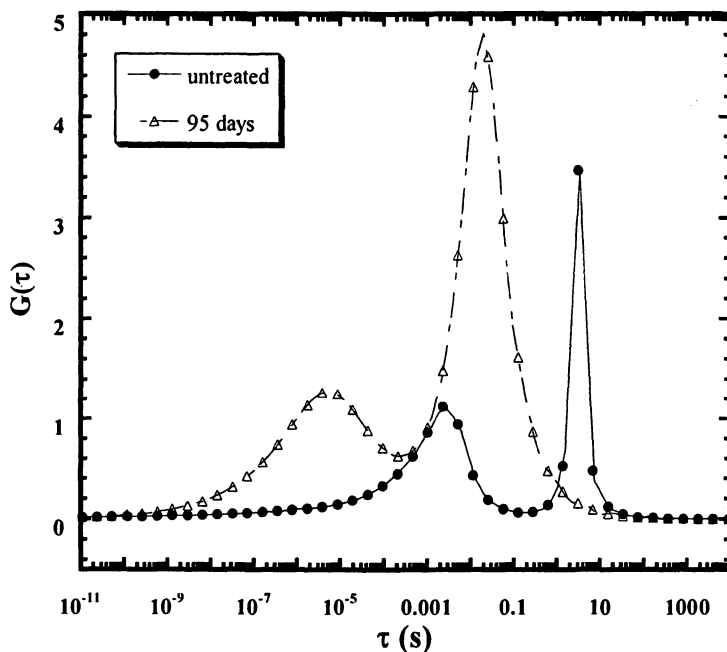


Figure 7. Distribution of relaxation times at 60° C for dry untreated and 95 days degraded samples.

molecular weight. Thus, there will also be distribution in chain dynamics, i.e. relaxation times.

In a concentration fluctuation model, Fisher and co-workers assumed that there are many dynamically heterogeneous domains in polymer blends. Different domains have different compositions which follow a Gaussian distribution centered around the global composition (29,30). Roland and Ngai modeled the dynamics of polyisoprene/poly(vinylethylene) blends by assuming that concentration fluctuations lead to normally distributed coupling parameters for each component and the observed relaxation time distribution is a summation of all of these components (31). It should be noted that intermolecular hydrogen bonding is capable of damping concentration fluctuations (28), which could be true for the system here as the number of carboxylic acid groups is expected to increase with degradation as a result of ester linkage hydrolysis. The geometric distribution of hydrogen bonding throughout the entire system could broaden the relaxation time distribution as some segments may have formed one or two hydrogen bonds while others may be in an environment where such intermolecular interactions are minimal (28). Segments with different degrees of coupling will exhibit different relaxation times, thus broadening the $G(\tau)$ curves of degraded samples.

All the above observations support the interpretation of the weight loss measurement results that were reported earlier, which showed considerable degradation at 95d (8).

Conclusions

The relaxation signature on dielectric loss permittivity vs. frequency curves of hydrolytically degraded hydroxyl-terminated poly(D,L-lactide) samples is considerably more distinct than those of undegraded samples. Specifically, for both degraded and undegraded samples, there is a relaxation peak at temperatures just beneath T_g , assigned to the α process, which becomes more distinct and shifts to higher frequency with increased temperature. In addition, there is a linear section in the low frequency regime on log-log ϵ'' vs. f plots that is attributed to d.c. conductivity which shifts upward with degradation and is most likely related to the increased concentration of COOH groups resulted from ester linkage hydrolysis with increased chain scission.

A distinct shift in f_{\max} for these T_g - related peaks to higher values after 95d degradation implies a decrease in the time scale of the underlying long range chain segmental motions. Experimental data for degraded and undegraded materials were fitted to the Havriliak-Negami equation for the complex permittivity with subtraction of the d.c. contribution to uncover pure relaxation peaks. Relaxation parameters extracted from these fits were used to construct

the VFTH and distribution of relaxation time functions. The relaxation time of this α -transition in both degraded and undegraded samples showed VFTH temperature behavior. The Vogel temperature decreased with immersion in buffer solution for 95d which suggests an increase in free volume as chains become shorter due to degradation and chain packing becomes less efficient. Distribution of relaxation time curves showed a general broadening with degradation and shift to lower times which can be explained in terms of a broadening of molecular weight by hydrolytic scission as well as faster chain motions. Thus, it can be concluded that the technique of modern broadband dielectric spectroscopy can be a powerful tool in the interrogation of biodegradable materials degradation.

Acknowledgements

The authors gratefully acknowledge The Office of Naval Research Grant No. N00014-04-1-0703 for financial support.

References

1. Greenwald, D.; Shumway, S.; Albear, P.; Gottlieb, L. *J. of Surg. Res.* **1994**, *56*, 372.
2. Hickey, T.; Kreutzer, D.; Burgess, D.; Moussy, F. *J. of Biomed. Mat. Res.* **2002**, *61*, 180.
3. LeCorre, P.; Rytting, J.; Gajan, V.; Chevanne, F.; LeVerge, R. *J. of Microencap.* **1997**, *14*, 243.
4. Witt, U.; Einig, T.; Yamamoto, M.; Kleeburg, I.; Deckwer, W.; Muller, R. *Chemosphere* **2001**, *44*, 289.
5. Yu, F.; Zhuo, R. *Polym. J.* **2003**, *35*, 671.
6. Lee, S.; Kim, S.; Han, Y.; Kim, Y. *J. Polym. Sci.: Polym. Chem. Ed.* **2001**, *39*, 973.
7. Tracy, M.; Ward, K.; Firouzabadian, L.; Wang, Y.; Dong, N.; Qian, R.; Zhang, Y. *Biomaterials* **1999**, *20*, 1057.
8. Wiggins, J. S.; Hassan, M. K.; Mauritz, K. A.; Storey, R. F. *Polymer* **2006**, *47*, 1960.
9. Huffman, K.; Casey, D. *J. Polym. Sci.: Polym. Chem. Ed.* **1985**, *23*, 1939.
10. Kremer, F.; Schönhals, A. *Broadband Dielectric Spectroscopy*; Springer: Berlin, 2003; p 225.
11. Runt, J. P.; Fitzgerald, J. J. *Dielectric Spectroscopy of Polymeric Materials: Fundamentals and Applications*; ACS Publications: Washington, DC, 1997; p 83.
12. Cole, K. S.; Cole, R. H. *J. Chem. Phys.* **1941**, *9*, 341.

13. Havriliak, S.; Negami, S. *J. Polym. Sci.: Polym. Symp.* **1966**, *14*, 99.
14. Havriliak, S.; Negami, S. *Polymer* **1967**, *8*, 161.
15. Negami, S.; Ruch, R. J.; Myers, R. R. *J. Colloid Interface Sci.* **1982**, *90*, 117.
16. McCrum, N. G.; Read, B. E.; Williams, G. *Anelastic and Dielectric Effects in Polymeric Solids*; Dover: New York, 1991.
17. Mauritz, K. A.; Fu R-M. *Macromolecules* **1988**, *21*, 1324-1333
18. Mauritz, K. A. *Macromolecules* **1989**, *22*, 4483-4488
19. Deng, Z. D.; Mauritz, K. A. *Macromolecules* **1992**, *25*, 2369-2380
20. Mauritz, K. A.; Yun, H. *Macromolecules* **1989**, *22*, 220-225
21. Mauritz, K. A.; Yun, H. *Macromolecules* **1988**, *21*, 2738-2743
22. Deng, Z. D.; Mauritz, K. A. *Macromolecules* **1992**, *25*, 2739-2745
23. Jamshidi, K.; Hyon, S.-H.; Ikada Y. *Polymer* **1988**, *29*, 2229.
24. Fox, T. G.; Flory, P. J. *J. Appl. Phys.* **1950**, *21*, 581.
25. Fox, T. G.; Flory, P. J. *J. Polym. Sci.* **1954**, *14*, 315.
26. Zhang, S.; Painter, P. C.; Runt, J. P. *Macromolecules* **2004**, *37*, 2636.
27. Vogel, H. *Phys. Z.* **1921**, *22*, 645; Tammann, G.; Hesse, W. *Z. Anorg. Allg. Chem.* **1926**, *156*, 245; Fulcher, G. S. *J. Am. Ceram. Soc.* **1923**, *8*, 339.
28. Zhang, S.; Painter, P. C.; Runt, J. P. *Macromolecules* **2002**, *35*, 9403.
29. Zetsche, A.; Fisher, E. W. *Acta Polym.* **1994**, *45*, 168.
30. Katana, G.; Fisher, E. W.; Hack, T.; Abetz, V.; Kremer, F. *Macromolecules* **1995**, *28*, 2714.
31. Roland, C. M.; Ngai, K. L. *Macromolecules* **1991**, *24*, 2261.

Chapter 10

The Expanding Role of Mass Spectrometry as a Tool for Polymer Chemistry

E. Peter Maziarz, III¹, X. Michael Liu², and Troy D. Wood^{1,2,*}

¹Ethicon, A Johnson & Johnson Company, Route 22 West,
Somerville, NJ 08876

²Bausch & Lomb, Global Scientific Programs, 1400 North Goodman Street,
Rochester, NY 14609

³Departments of Chemistry and Structural Biology, University at Buffalo,
State University of New York, Buffalo, NY 14260-3000

*Corresponding author: twood@acsu.buffalo.edu

Innovations to mass spectrometry (MS) ionization sources and mass analyzers have helped usher in a new era in polymer chemistry in which the mass spectrometer is viewed as an essential tool that complements classical methods of polymer characterization. MS can be employed for the direct characterization of individual molecules, enabling not only determination of molecular mass and molecular mass distributions, but also determination of structural aspects of polymers such as end-group composition, repeat unit composition and sequence, and the presence of impurities and unintended side products. Here, we review some particular challenges faced for polymer characterization by MS. Synthetic polymers are polydisperse and require fractionation to reduce the complexity of samples analyzed by MS. Different approaches integrating gel permeation chromatography (GPC) with MS analysis for this application are compared and discussed. Next, several different MS

methods for characterizing polymer repeat unit and/or end group composition are reviewed, and how this structural discovery process can lead to new directions in synthesis. Finally, recent efforts to process seemingly intractable polymers for MS analysis are described.

Introduction

Synthetic polymers play pivotal roles as materials for a vast array of applications throughout industrialized modern society. Unlike organic or biological compounds, which exist as homogeneous materials, synthetic polymers are largely polydisperse (i.e., they consist of an ensemble of polymer chains with a distribution of molar masses). Both the average molar mass (sometimes more commonly referred to as molecular weight, MW) and the molar mass distribution (MMD) are fundamental properties of polymeric materials that contribute greatly to their physical properties. Because of this correlation, characterization of a polymeric material's repeat unit structure and composition as well as the end group structure and composition is of prime interest and is essential for providing insight into the physico-chemical and mechanical properties of a polymeric material. This is particularly relevant in the industrial setting, where batch-to-batch consistency in such properties for polymeric materials is required.

Numerous techniques have been developed for characterizing the molar mass and molar mass distribution of polymeric materials (1,2). These include gel permeation chromatography (GPC), nuclear magnetic resonance (NMR), low-angle light scattering, osmometry, and end group titration. Chemical composition of polymeric materials, both with regard to the repeat units and end groups, has also been performed by NMR, infrared (IR) spectroscopy, X-ray photoelectron spectroscopy (XPS). Mass spectrometry (MS) has emerged as a complementary technique in characterizing polymeric materials because of its ability to provide simultaneous information on the molar mass and molar mass distribution along with chemical composition.

At first glance, the use of MS for the characterization of polymeric materials is not straightforward. MS relies upon the analysis of volatilized gas-phase ions whose mass-to-charge (m/z) ratios can be measured by an instrument known as a mass spectrometer. Polymeric materials are in the condensed phase. Thus, volatilization of polymeric materials from the condensed phase to a vapor state, and conversion into charged ions, is essential for their analysis by MS.

Ionization techniques. Major advances in the development of ionization techniques capable of volatilizing large molecules into the gas-phase as intact species have been made in the past two decades. Frequently these techniques are referred to as "soft" ionization methods because they do not deposit enough

energy into internal modes in large molecules to cause them to fragment. Of these techniques, two have been in particular use in the field of polymer MS (1,3), including our own laboratories, and they are called matrix-assisted laser desorption ionization (MALDI) (4,5) and electrospray ionization (ESI) (6). Descriptions of each of these techniques and how they result in ionization of polymeric species will now be discussed.

MALDI is a novel soft ionization technique that generates high mass, predominantly singly-charged ions from a condensed phase analyte and matrix mixture via irradiation of a pulsed laser beam directly onto the mixture. In MALDI, a matrix species is applied with the analyte in a large molar excess to absorb the majority of incident radiation (usually ultraviolet, although sometimes infrared) (7) the matrix possesses a chromophore capable of absorbing radiation at the output wavelength of the pulsed laser. In the case of synthetic polymer analysis, a salt which provides a source of cations (e.g., Na^+ or Ag^+) is also added to the sample to serve as a charging agent for the neutral oligomers in the initial plume of material ablated by the laser (8).

Sample preparation has a tremendous influence on the success of MALDI analysis and serves to achieve homogenous distribution of the analyte throughout the matrix (3,9). Consideration must be given to the choice of the matrix and solvents employed, concentration of analyte and matrix in the solution, the method of sample deposition, the molar ratio of matrix to analyte, the addition of salts for cationization, and pH. Most compatible matrixes are organic acids, and after deposition of the matrix/analyte solution to the sample probe, evaporation proceeds and crystals of the matrix/analyte mixture are formed. Cocrystallization is favored in MALDI because this minimizes undesired chemically- and photochemically-induced reactions between the matrix, analyte, and charging agent. Large matrix/analyte ratios are particularly important for larger molar mass polymeric materials, which is believed to prevent polymer entanglement and formation of inhomogeneous, microcrystalline regions (10). A number of methods for application of the matrix/analyte solution onto the MALDI probe tip have been the subject of recent investigations (11-15).

Despite the numerous "entanglements" which must be avoided for successful analysis of polymeric materials, MALDI has emerged as the major ionization method because of its distinct features. Chief amongst these is that analyte polarity is not particularly critical, enabling a wide range of water-soluble, polar organic-soluble, and nonpolar organic-soluble polymeric materials to be ionized by MALDI. For synthetic polymeric materials, ionization by MALDI is relatively insensitive to the concentration of the charging agent, lending versatility to examine polymers that can be difficult to ionize by cation adduction. Lastly, MALDI's ability to produce predominantly singly-charged ions keeps the mass spectra much less complicated than ESI, as we will discover below.

For ESI, the polymeric material is solubilized and infused continuously through a small diameter (ca. 50 μm) needle held at high voltage (2-5 kV) at ambient pressure to create an aerosol of charged droplets. As is the case with MALDI, the solution is often admixed with a salt to provide a source of cations needed to produce charged ions (16). The droplets are desolvated by the combined effects of heat, inert gas flow, and transfer into the vacuum of a mass spectrometer. As a consequence, solvent properties heavily influence spray characteristics. In general, polar or semi-polar solvents are employed because their solution properties are conducive to forming stable sprays and in encouraging charge formation between neutral analyte and charging agent. The choice of solvent places some limitation onto the types of polymeric materials which can be analyzed using ESI. A unique feature of ESI is its ability to generate multiply-charged analyte ions. The redundant molar mass information obtained from the multiple charge state distributions allows highly accurate determination of molar mass; however, it also produces extremely complicated mass spectra because polymeric materials consist of an ensemble of oligomer lengths, leading to overlapping polymeric distributions. Spectral complexity is exacerbated with increasing molar mass. Therefore, a detailed analysis of such polymeric materials requires high resolving power of the mass analyzer, and even so ESI is limited to polymers of relatively low molar mass.

Mass analyzers. MALDI is ideally coupled to time-of-flight (TOF) for polymer analysis (17). This combination is ideal due to the pulsed nature of the laser and the theoretically unlimited mass range and high transmission efficiency of TOF. Ions are produced by laser ablation of the dried matrix/analyte mixture and are then accelerated by a fixed potential into a drift tube that does not contain an external electric field. The ions continue moving toward a detector. Since all the ions are accelerated at the same potential, the kinetic energy (KE) of a given ion can be given by eq. 1:

$$KE = \frac{1}{2} mv^2 = qV \quad (1)$$

where m is the mass of the ion, v is the velocity of the ion, q is the charge on the ion and V represents the accelerating potential. Assuming that all ions have the same KE entering the drift tube of fixed length (d), the velocity of an ion is related to the time it takes an ion to traverse the drift tube (t , or time-of-flight) as indicated in eq. 2:

$$v = d/t \quad (2)$$

Substitution of eq. 2 into eq. 1 leads to the relationship in eq. 3 between time-of-flight and the mass and charge on a given ion.

$$t = d(m/2qV)^{1/2} \quad (3)$$

Mass resolution, or the ability of a mass analyzer to separate ion signals from ions of similar mass, is typically 500-800 on a linear TOF. Resolution can be improved in TOF by using a reflectron instrument (18) which compensates

for the initial distribution in KE ions possess upon entering the drift tube using a series of grids that creates a sequential increase in potential field that slows the ions down until their KE reaches zero; at this point, the ions reverse direction and are directed toward a second detector. Mass resolution is substantially increased by using reflectron mode TOF. The advantage of using reflectron mode TOF is that the improved mass resolution enables determination of exact molar masses for individual oligomers, which is essential for repeat unit composition and end group composition information.

A disadvantage of TOF-MS, however, is the inability to mass select oligomer ions and subsequently cause them to fragment inside the mass spectrometer for tandem mass spectrometry (MS/MS) experiments that provide detailed structural information for individual ions. In such cases, MS/MS can only be achieved by placing a mass selective filter between the ionization source and the drift tube; the development of the quadrupole-TOF (QTOF) mass spectrometer (19), typically coupled to ESI, was a response to the need for enabling MS/MS with TOF.

High mass resolution can be combined with MS/MS capabilities for polymer analysis using Fourier transform ion cyclotron resonance (FT-ICR) MS (20). FT-ICR is an ion trapping technique that confines ions in a magnetic field coupled to a DC electric field. Ions in a magnetic field (B) will rotate about the magnetic field axis with a characteristic ion cyclotron frequency (ω) which is related to the mass and charge of the ion, according to eq. 4:

$$\omega = qB/m \quad (4)$$

Because cyclotron frequency can be measured to ppm precision, so can m/z . Also of importance is the ability to mass-select individual ions for subsequent MS/MS experiments. For polymer analysis, the combined effects of simultaneous high resolving power (and mass accuracy) with MS/MS capability enables detailed analyses of polymer structure to be conducted. The high mass resolution also enables direct determination of charge state in ESI analyses because of the ability to separate the masses of individual isotope peaks in large macromolecules.

Importance of Mass Spectrometry in Polymer Analysis. Although MS is amongst the more recent analytical techniques for characterizing polymeric materials, the data which can be acquired from MS has become recognized as indispensable to polymer chemists. MS can be used to determine the molar masses of individual oligomers directly, which is useful in determining the repeat unit and end group composition. It can also reveal the presence of low level impurities in polymer compositions and sequence distributions within copolymers. These are highly significant capabilities in product development efforts because they enable the ability to compare batch-to-batch synthetic processes and provide complementary information to other techniques. For implantable biological devices, this is especially crucial, because Federal

regulations require strict identification and characterization of the constituent materials. In this way, MS plays an important role not only in quality control, but also in providing important information that can guide polymer chemists during the synthesis process.

GPC Methods Integrated with MS

While MS has proved a valuable tool for polymer chemists, its ability to determine average molar mass values of polymeric materials is generally limited. In polymer science, the molecular weights and molecular weight distributions are determined by the following formulae:

$$M_n = \Sigma (N_i \times M_i) / \Sigma M_i \quad (5)$$

$$M_w = \Sigma (N_i \times M_i^2) / \Sigma (N_i \times M_i) \quad (6)$$

$$M_z = \Sigma (N_i \times M_i^3) / \Sigma (N_i \times M_i^2) \quad (7)$$

$$PD = M_w/M_n \quad (8)$$

where M_n , M_w and M_z represent the number-average, weight-average, and z-average molar masses, respectively, and N_i represents the number of polymer molecules at a given molar mass M_i . The general consensus in the scientific community is that the accuracy of average molar mass determination measurements by MS is limited to materials having relatively narrow PD (< 1.2) (10,21-24). Mass discrimination effects for more polydisperse materials tend to bias against the higher molar mass oligomers so that they are under-represented (if detected at all), introducing considerable error in the average molar mass determination. An example of this is illustrated in Figure 1 for the direct MALDI-TOF MS analysis of α,ω -bis(4-hydroxybutyl) poly(dimethylsiloxane) (HB-PDMS) having a nominal number average mass of 5,000 Da and a polydispersity of approximately 1.86. Here PDMS oligomers are observed from 900 to approximately 4,000 Da where eventually the poor S/N impedes analysis. One could argue here that although the relatively high mass oligomers (i.e. those predicted by the GPC trace to be present in the sample) are not detected, there is informative data obtained from this analysis. For example the inset in Figure 1 illustrates that there are four distributions denoted by closed circle, closed diamond, closed square and open circle. Each peak within a distribution differs by a nominal mass of 74 Da and therefore these represent poly(dimethylsiloxane) ($C_2H_6OSi = 74$ Da) distributions that differ from one another based on a chemistry that is not defined within the repeat unit sequence (e.g. end group chemistry). We determined the composition of these distributions from a previous study (25). Here two of the distributions, denoted as closed circle and open circle, contain middle group chemistries that separate repeat unit distributions; this is often recognized in a GPC trace as having a bimodal

distribution. The important composition detail here from the product development perspective was how the C-O-Si bond sequence, occurring in closed and open circle distributions, might affect material performance. With this question in mind it becomes important to obtain the relative change in distribution varieties as a function of increasing mass for as much of the MMD as possible. Although only one example is provided here, the desire for detailed information is what drives polymer-MS practitioners to overcome the effects of mass discrimination for polydisperse polymer analysis. Several reports have examined the fundamental causes of this mass discrimination behavior (22,26-31) and it will not be discussed further here.

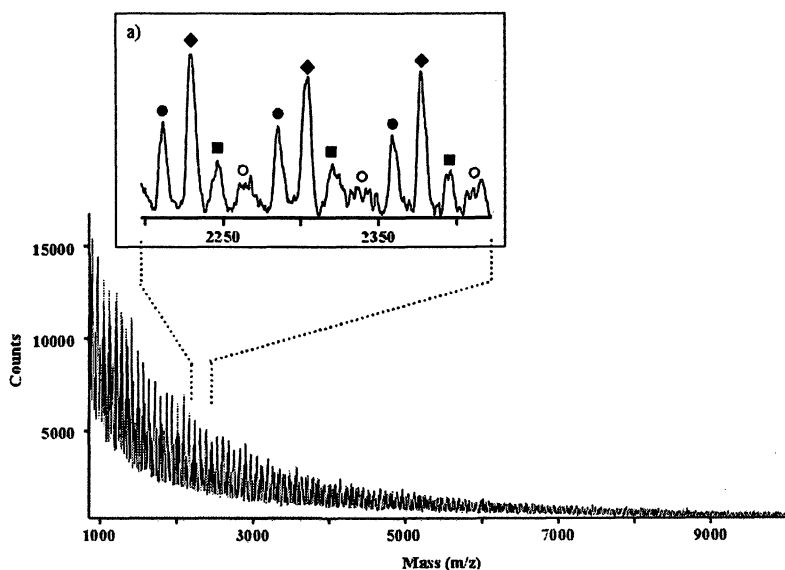


Figure 1. direct MALDI-TOF MS analysis of α,ω -bis(4-hydroxybutyl) poly(dimethylsiloxane) (HB-PDMS) having a nominal number average mass of 5,000 Da and a polydispersity of approximately 1.86. (Inset) A region of the mass spectrum containing the four different distributions denoted in Table 1.

One strategy that has been employed in our laboratories in an effort to minimize mass discrimination effects has been to couple GPC, either off-line or directly on-line to MS. In GPC, the separation mechanism involves an equilibrium between solutes in the mobile phase and those which can permeate the inner volume of a stationary phase that is porous. Molecules with hydrodynamic volumes (or size in solution) that are smaller than the pore sizes in the stationary

phase can exchange between the void volume (free volume external to the gel matrix), v_o , and the internal volume of the pores in the stationary phase, v_i . Thus, small molecules have relatively long elution times because they can exchange between the void volume and the pore volume; large molecules are hindered from entering the pore volume, and elute relatively quickly. The volume of solvent needed to elute a given species is known as the elution volume (v_e) and it is related to the void volume and pore volume by eq. 9:

$$v_e = v_o + K v_i \quad (9)$$

where K is the fraction of internal pore volume penetrated by the given oligomer, which is dependent on hydrodynamic volume and hence molar mass. Thus, the MMD is minimized by collecting individual fractions separated by GPC. Since many of the most important and interesting polymeric materials possess broad MMD, the coupling of GPC to MS provides an attractive means of minimizing mass discrimination. In addition, the narrow MMD fractions can be used for absolute recalibration of the GPC curves (log MW vs. v_e).

On-line GPC-ESI MS: GPC and ESI share in common solution infusion, and it was recognized and demonstrated that these two techniques could be merged for on-line MS analysis of polymeric materials (16). The conventional GPC-ESI-TOF MS setup used in our laboratories (32) is illustrated in Fig. 2a. The hyphenated system uses analytical bore GPC columns and introduces the charging agent/cosolvent solution via syringe pump through a Valco tee positioned after the column and before the ESI source. Initially, we used the GPC-ESI-TOF MS system to analyze hydroxyl-terminated poly-(dimethylsiloxane) (OH-PDMS) samples and to compare the GPC-ESI-TOF MS approach to traditional GPC and an automated GPC MALDI-TOF MS approach. Quantitatively, a notable difference was observed in that GPC-ESI-TOF MS effectively reported low mass oligomers of OH-PDMS but underestimated the higher mass oligomers, whereas low mass oligomers were masked by matrix interference in automated GPC-MALDI-TOF MS (32). The underestimation of high mass oligomers by GPC-ESI-TOF MS was observed to be the result of ion suppression. This is illustrated in Fig. 3, which shows a comparison between (a) the total ion chromatogram (TIC) and (b) the differential refractive index chromatogram for OH-PDMS. Ion current suppression in the higher MW region is observed in the TIC. The ion suppression of high mass oligomers can ultimately limit the use of GPC-ESI MS analysis to evaluate only the low mass end of the molecular weight distribution. Since information is also required on the moderate to high mass portion of the MMD, our intent to harness the advantages of true on-line analysis offered by GPC-ESI MS was initially impeded.

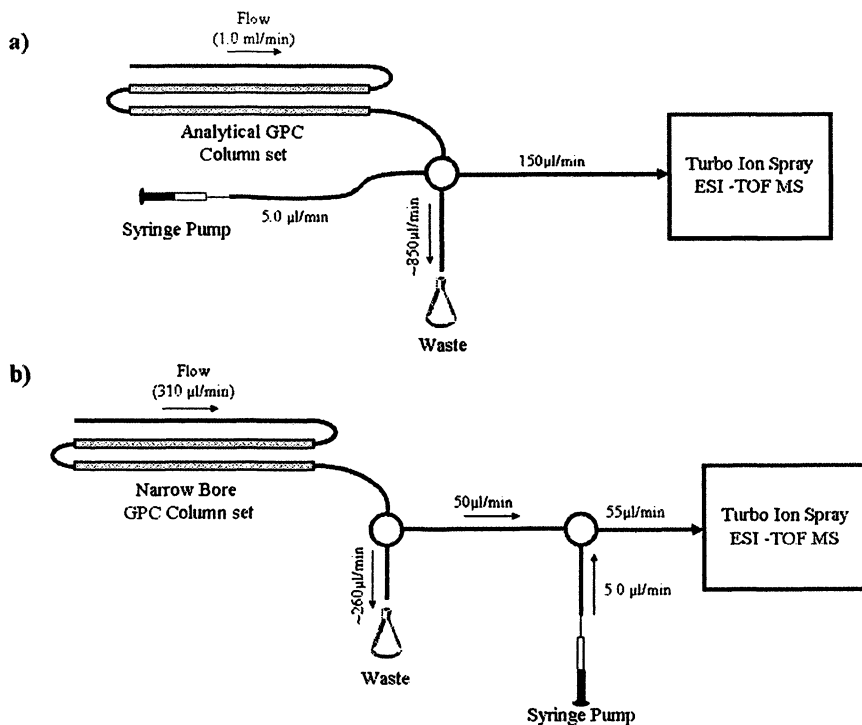


Figure 2 (a) Schematic diagram of conventional GPC-ESI MS experimental set-up used in our laboratory. Introduction of the charging agent solution into the mobile phase and mobile phase splitting occurs in one Valco tee. (b) Schematic diagram of improved GPC-ESI MS experimental set-up. Mobile phase splitting occurs in the first Valco tee and a second downstream Valco tee is used to introduce the charging agent.

Subsequently we have designed an on-line system that provides improved results compared to the conventional on-line GPC-ESI MS system that enables the detection of higher mass oligomers. A schematic of this set-up is shown in Fig. 2b. The modified design utilizes narrow bore GPC columns as opposed to the analytical bore columns used in Fig. 2a. The modified design also introduces the charging agent/cosolvent solution through a second Valco tee positioned further downstream from the Valco tee used to control the split, whereas in Fig. 2a these events occur at a single post-column Valco tee. Figs. 3a and 3b illustrate analysis of an OH-PDMS polymer using the instrumental designs illustrated in Figs. 2a and 2b, respectively. All experimental conditions were identical except for the mobile phase flow rate going to the ESI source. The narrow bore GPC columns were operated at a flow rate of 55 $\mu\text{l}/\text{min}$, while the analytical bore GPC columns were operated at 150 $\mu\text{l}/\text{min}$. Comparatively it can

be observed that the ion suppression that occurs in Fig. 3a is not present in Fig. 3b. Repeated measurements confirm that this improvement is real. Originally we proposed that ion suppression could occur from precipitation of the high mass less soluble OH-PDMS oligomers during desolvation (32). Figs. 4d and 4e illustrate mass spectra of the highest mass oligomers achieved from the Fig. 4a and 4b analysis while being mindful of suitable S/N for data processing. A narrow distribution of singly charged OH-PDMS oligomers is observed in Fig. 4d. The number average mass (M_n) for this distribution was determined to be 1200 Da. Comparatively, Fig. 4e contains narrow distributions of doubly charged and singly charged OH-PDMS oligomers. The M_n calculated from Fig. 4e was determined to be 2050 Da. Thus it seems that the current experimental

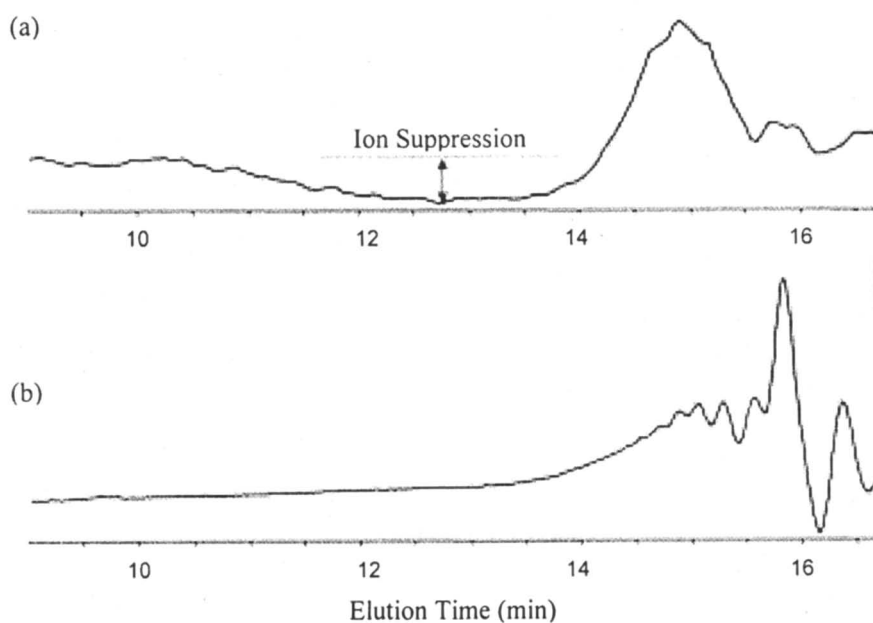


Figure 3. Total ion chromatogram (a) and dRI chromatogram (b) of the OH-PDMS sample in on-line GPC-ESI-TOF MS experiments

design described in Fig. 2b is an improvement compared to our previous design (Fig. 2a) based on the observation of higher mass oligomers. The fundamental question is “what event in this set-up enhances transformation of high mass oligomers into the gas phase?” Since the charging agent solution is not split in the new experimental design (Fig. 2b), an excess of charge is introduced into the ESI solution. This concomitant with the lower flow rate may provide an ideal ratio of *excess* charge to total number of analyte molecules in the ESI droplets as

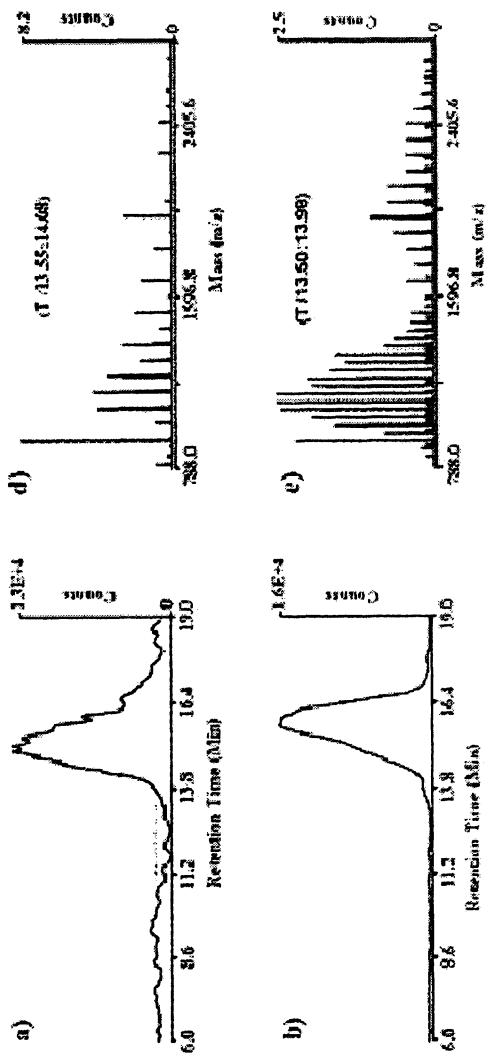




Figure 4. (a-c) Total ion chromatograms (TIC) from GPC-ESI MS analysis of OH-PDMS: (a) using NaI as the charging agent and the experimental configuration denoted in Fig. 2a. (b) using NaI as the charging agent and the experimental configuration denoted in Fig. 2b. (c) using $\text{NH}_4\text{Acetate}$ as the charging agent and the experimental configuration denoted in Fig. 1b. (d-f) A summation of mass spectra from thirty seconds elution time of the highest mass fraction observed from (d) Fig. 4a, (e) Fig. 4b, and (f) Fig. 4c analysis.

proposed by Wang et al.(33) Here, we are evaluating a mass and concentration distribution of oligomers as a function of time. This further suggests that an optimal excess charge to analyte ratio is mass dependent. Specifically with regard to the precipitation of high mass oligomers, the excess charge may in the revised GPC set-up may act as an anti-coagulant (or suppressant of aggregation) for the high mass OH-PDMS oligomers. The like charges on different oligomers could repel each other during desolvation, thus providing a more even oligomer distribution within the droplet such that coagulation of the increasingly concentrated oligomers is minimized during the desolvation process. A more even distribution of OH-PDMS oligomers in the droplet would increase the probability that some of these oligomers reach the surface of the droplet for gas phase transfer. Considering this point, it would be expected that different cation reagents having different affinities for adduct formation with OH-PDMS oligomers would provide different results. Fig. 4c illustrates the TIC from analysis of the same OH-PDMS polymer under constant experimental conditions as that obtained in Fig. 4b, however ammonium (NH_4^+) trifluoroacetate was used as the charging agent. The higher TIC intensity of Fig. 4c compared to Fig. 4b indicates that the NH_4^+ cation has a higher affinity for ion adduct formation with the OH-PDMS oligomers. The highest mass distribution observed from analysis with NH_4^+ is illustrated in Fig. 3f. This mass spectrum contains a singly and doubly charged state distribution of ammoniated OH-PDMS oligomers. The M_n calculated from Fig. 4f was determined to be 3300 Da, which is 1250 Da higher than the analysis in Fig. 4e performed with NaI charging agent.

On-line GPC-MALDI MS: On-line hyphenation of MALDI-MS with GPC is not as straightforward because of the incompatibilities associated with the complex sample preparation schemes required for MALDI and the intrinsically pulsed nature of the laser source with a continuous beam of eluent from GPC. Fei and Murray first demonstrated on-line GPC-MALDI-TOF MS by mixing the eluent from the GPC with a matrix solution, and by irradiating the resulting spray with a laser to promote MALDI.(34)

Off-line GPC-MALDI MS: In contrast to on-line hyphenation, off-line hyphenation of MALDI-TOF MS with GPC is more commonplace. In one off-line approach, GPC fractions are collected and then prepared individually for MALDI-TOF MS analysis. Fig. 5 illustrates MALDI-TOF MS spectra of GPC fractions obtained for the same HB-PDMS sample as illustrated in Fig. 1. In Fig. 5 each fractionated polymer spectrum obtained contains a well-defined monodisperse MMD with the expected decrease in average mass with increasing GPC elution time. The combination of GPC with MALDI-TOF MS serves to simplify the complexity of the polydisperse MMD such that higher mass oligomers can be observed. Comparatively oligomers up to 12,000 Da were observed with approximately the same S/N as that observed for the 4,000 Da

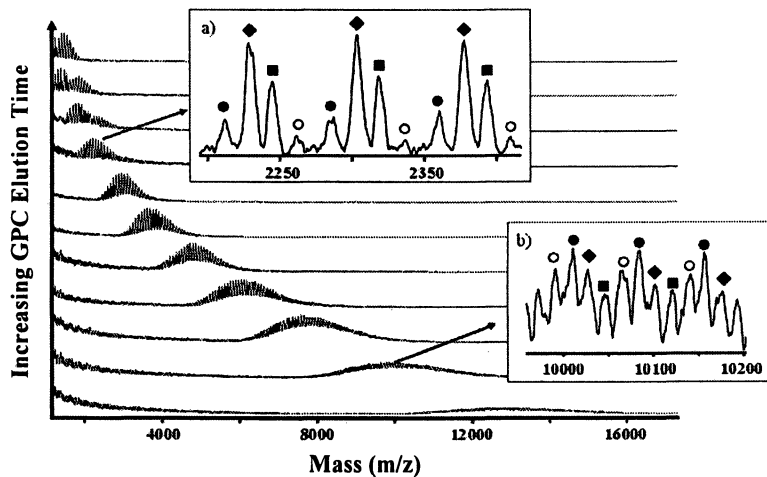


Figure 5. MALDI-TOF MS spectra of GPC fractions collected off-line and obtained for HB-PDMS. (a) Inset of MALDI-TOF MS from fraction 8. (b) Inset of MALDI-TOF MS from fraction 2. The symbols refer to types of oligomers listed in Table 1.

oligomers from Fig. 1. Fig. 5a provides an inset from fraction 8 and illustrates the four poly(dimethylsiloxane) distributions noted in Table 1. Figure 5b provides an inset from fraction 2. Here it is noted that at 10,000 Da there is inter-distribution resolution that allows one to evaluate the relative change in distribution varieties as a function of increasing mass, that is from fraction 10 to fraction 2. It should be noted here that fraction 1 was excluded from this statement because inter-distribution resolution was lost at the high mass end (>13,000 Da) of this fraction. Furthermore fraction 11 was excluded from this statement because we believe the peaks occurring in this spectrum are unlike the linear PDMS distributions discussed so far for this sample (Table 1). To understand this detailed information more completely one must look closely at fractions 9 and 10 where the typical symmetrically shaped fractionated distribution is skewed in fractions 9 (containing drawn-out front peaks) and 10 (bimodal). This would be expected if two different distributions having different average masses co-eluted because they have similar hydrodynamic volumes. This would be typical for linear and cyclic (or branched) fractions that have the same repeat unit sequence. It should be noted that this detailed information was not available from the direct MALDI-TOF MS analysis in Fig. 1. This is a method which has been used for characterizing silicone extracts (35) and silicone pre-polymers used to construct oxygen-permeable films (25), but it is tedious and not amenable to high throughput.

To increase throughput for off-line GPC coupled to MALDI MS, we have been developing an automated approach. In its initial form, automated off-line GPC was achieved by directing the eluent from the GPC through a liquid chromatography transform (LCT) platform onto a MALDI sample target (36). The LCT is a thermal deposition device which uses a long capillary nozzle for solvent elimination. A flowing stream of heated sheath gas surrounds the capillary through which the GPC eluent passes, transferring heat to the eluent. As the eluent proceeds down the capillary, its temperature increases while the pressure decreases, partially vaporizing the solvent. The resulting aerosol is then sprayed onto a moving stainless steel foil that is pre-coated with a thin layer of matrix (2,5-dihydroxybenzoic acid, DHB) which is now ready for subsequent off-line MALDI MS analysis. In the initial report, the combined hyphenation of GPC off-line with MALDI-TOF MS enabled detection of a minor product for linear poly(tetramethyleneglycol) (PTMEG) not observed in conventional dried-drop MALDI-TOF, with masses 18 Da lower than the expected oligomers, likely due to elimination of water during polymer cyclization (36). Moreover, as shown in Fig. 6, poly(methyl methacrylate) (PMMA) with a broad PD (2.43) could be size separated by GPC and directed onto the DHB target by the LCT to obtain MALDI-TOF mass spectra which were not obtainable without fractionation; this enabled collection of a series of MALDI mass spectra to characterize the broad PD PMMA. Refinements to this approach are illustrated in the diagram in Fig. 7, and include addition of a post-column mixing tee for GPC eluent and matrix solution for MALDI prior to entering the thermal deposition unit (37) and an x-y rasterable MALDI sample plate translated in a serpentine pattern (38). Conceptually, this latter innovation is equivalent to translating a temporal separation (on-column) to a spatial separation for subsequent MALDI analysis. This enabled highly automated analysis of polymer blends of PMMA and PDMS while avoiding the need for a pre-treated matrix foil.

Comparison of Methods Using GPC for Molar Mass Determination. GPC has long been utilized to measure relative molar mass and MMD for polymeric materials. In addition to MS detection, GPC can also be coupled to a variety of detection systems including light scattering, differential viscometry, photodiode array detection, NMR, and FT-IR. A major focus of our research has been to evaluate different GPC-MS combinations in comparison with the traditional GPC detection methods for determination of molar mass and MMD for polymeric materials used in biological implant devices. The following discussion summarizes our findings.

Toluene extracts of a silicone rubber revealed three major molar mass fractions at 210 kDa, 1,490 Da, and 300 Da, as shown in the GPC trace (using differential refractive index detection) in Fig. 8a. (35) This represents a broad MMD which is beyond the capability of MS to determine accurately. Most of

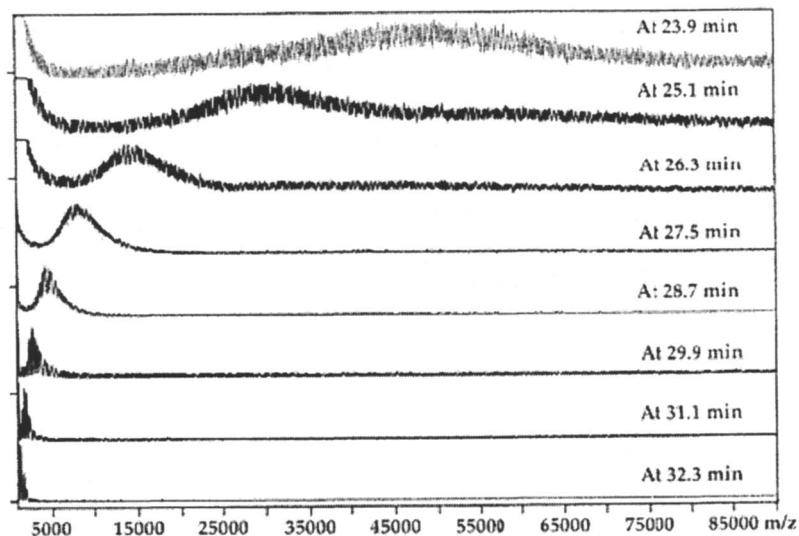


Figure 6. MALDI mass spectra of GPC eluent fractions from the broad PMMA sample applied to a DHB substrate target by the LCT.

the extractable material was in the 1,490 Da fraction. MALDI-TOF MS of the lower molar mass fractions (Fig. 8b) revealed a 74 Da repeat unit mass consistent with PDMS, although the mass resolution in Fig. 8b is insufficient to determine end group composition. Using methyl-terminated PDMS as an internal standard for mass calibration in the reflectron mode, MALDI-TOF and ESI-TOF MS analysis revealed that the predominant oligomer series was macrocyclic PDMS.

Soon after developing the combined hyphenation of GPC off-line using thermal deposition followed by MALDI-TOF MS, it became quickly apparent that pre-fractionation by GPC significantly extended the observed mass range for PDMS (37). This finding was confirmed in a comparison of molar masses and MMD for between unfractionated and GPC fractionated OH-PDMS followed by MALDI-TOF MS (32). The comparison of molar masses and MMD for OH-PDMS was also extended to GPC (refractive index detector), ESI-TOF MS, and on-line GPC-ESI-TOF MS. Average molar mass values and polydispersities for a sample of OH-PDMS by these techniques are summarized in Table 1. Lower M_n and M_w values were obtained for MALDI-TOF MS and ESI-TOF MS vs. GPC with refractive index detection, with PD values 20.0% and 24.3% lower, respectively. The GPC vs. ESI MS result was consistent with previous ESI-FTMS of narrow MMD PDMS, indicating discrimination against the high mass oligomers; that study also showed MALDI-TOF MS performed comparably to

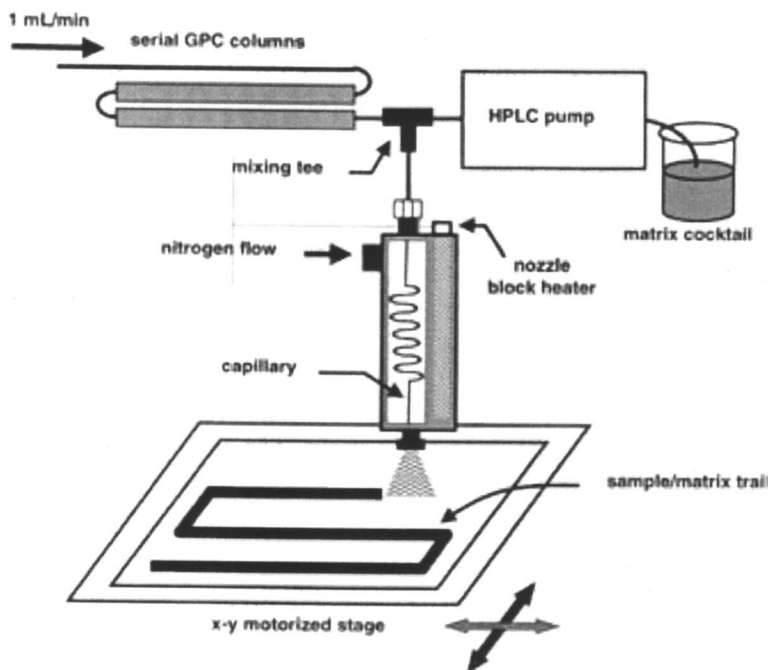


Figure 7. Simplified schematic of the thermal sample deposition apparatus for off-line coupling of GPC with MALDI-TOFMS.

GPC for narrow MMD PDMS (39). Moreover, off-line coupling of GPC with MALDI-TOF MS or on-line coupling of GPC with ESI-TOF MS provides PD values closer to that of GPC (32).

Further comparisons of molar mass and MMD determination of polymeric materials were made between conventional GPC (differential refractometer detector), GPC MS methods, and GPC with triple detection (right angle light scattering detector, differential refractometer, and differential viscometer) (40). Table 2 summarizes the average mass data for methyl-terminated PDMS obtained by direct ESI MS, conventional GPC, GPC with triple detection, and GPC-ESI MS experiments. In addition to the information of absolute molar masses and MMD, GPC with triple detection is the only technique that provides information of the weight-average intrinsic viscosity (IV) and weight-average radius of gyration (R_g) of oligomers in the given solvent at the given temperature of the experiment. The calculated M_n and M_w values by direct ESI MS are 61.7 and 69.7% less than the values determined by GPC with triple detection. The M_n and M_w values determined by conventional GPC are 57.4 and 39.4% higher than

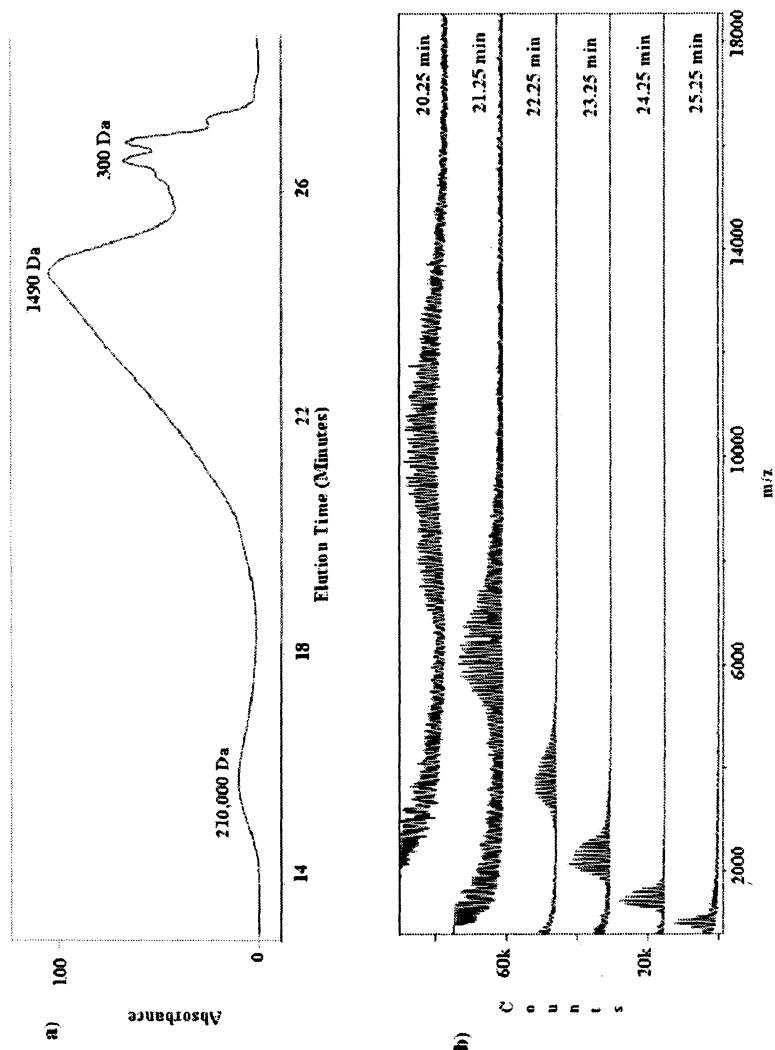


Figure 8. Silicone extracts legend.

Table 1. Average molecular mass values and molecular weight distributions of the OH PDMS obtained from different analytical techniques

MW	M_n	M_w	M_z	Polydispersity (M_w/M_n)
Analytical techniques				
Conventional GPC	796	1112	2221	1.40
MALDI-TOF MS	751	844	945	1.12
ESI-TOF MS	635	672	722	1.06
GPC-MALDI-TOF MS by spectra-summing	1830	2909	3910	1.59
GPC-MALDI-TOF MS by recalibration	1063	1400	3311	1.32
GPC-ESI-TOF MS by spectra-summing	623	731	933	1.17
GPC-ESI-TOF MS by recalibration	641	867	1782	1.35

Table 2. Average mass values and other properties of methyl-terminated PDMS measured by different analytical techniques

Techniques	M_n (Da)	M_w (Da)	M_z (Da)	PD	IV (dl/g)	Weight- average R_g (nm)
Conventional GPC with PS calibration standards	5178	7504	11834	1.45	na ^a	na
ESI MS (direct infusion)	1260	1633	1877	1.30	na	na
GPC-ESI MS	3317	5547	15872	1.67	na	na
GPC with triple detection	3290	5384	15217	1.64	0.19 ^b	2.45 ^b

^anot applicable, ^b Value determined in toluene at 45°C

that by GPC with triple detection. This may be explained by the fact that polystyrene has a different hydrodynamic volume compared to PDMS at the same mass in toluene (although they have similar linear conformations). It is notable that the M_n value calculated by the on-line GPC-ESI MS is less than 1.0% deviated from that determined by GPC with triple detection, which is less than one dimethyl siloxane repeat unit! The M_w values obtained from GPC-ESI MS are less than 5.0% from those determined by GPC with triple detection, demonstrating remarkable agreement. This study clearly indicated that on-line GPC-ESI MS is an excellent technique for determination of absolute molar masses and MMD of polymeric materials.

Approaches for the Analysis of Intractable Polymers

One of the primary analysis challenges facing polymer chemists is the ability to characterize intractable polymers, i.e. polymers with high glass transition temperatures (T_g) in concert with low thermal degradation temperatures or polymers with high molar mass. This includes polymers such as polyethylene (PE), poly(tetrafluoroethylene) (PTFE) and many of the conducting polymers, such as polyaniline (PANI) and polypyrrole (PPy). Because of their insolubility, direct analysis of intractable polymer materials are limited to techniques which can probe their properties in the solid state, and include FTIR, solid state NMR, x-ray photoelectron spectroscopy (XPS), laser light scattering, as well as MS. A common approach to process such polymers has been to employ volatile solvents (41) or low molar mass crystalline materials (42) to lower the processing viscosity or processing temperature. However, volatile solvents have to be

removed to regain polymer properties, and when combined with crystalline materials the polymeric properties are also affected. An attractive alternative has been to solvate the intractable polymeric materials in supercritical CO₂ (43). Recently, attenuated total reflectance (ATR)-FTIR has been demonstrated for miscible systems of polyvinylpyrrolidone (PVP) and poly(ethylene glycol) (PEG) (44).

A few MS techniques have been available for the analysis of intractable polymers for a number of years. The most significant of these are laser desorption/ionization (LDI) (45) and secondary ion mass spectrometry (46). The major drawback with these techniques is the low production of intact molecular ions for the oligomers, especially with increasing molar mass. Another approach has been to use chemical modifications in order to make the polymer soluble in a particular solvent so that MS analysis can be conducted. However, these modifications are both time consuming and alter the original molecular structure of the polymer of interest.

In its conventional mode, MALDI MS would not be possible with intractable polymers because formation of a crystalline matrix/polymer mixture is necessary. However, an exciting new development called "solvent-less" MALDI has been developed in an effort to perform MS of intractable polymers. (47-52). In the method, the polymeric material, the matrix, and the charging agent are all mixed and ground together using a mortar and pestle or ball mill. After grinding, the mixture can be further diluted with the matrix to tune the polymer/matrix ratio. Subsequently, the resulting mixture can be applied onto a probe tip coated with double-sided sticky tape, as a pressed pellet, or via the use of heat (to melt the mixture). Preliminary results for solvent-less MALDI MS were compared with those of traditional solvent-based MALDI for polymers such as poly(methyl methacrylate) and revealed that no fundamental differences in the quality of the obtained mass spectra. The solvent-free sample preparation indicated some advantages over the traditional method, most notably quick and easy applicability. Solvent-less MALDI MS showed improvements with respect to reproducibility and mass discrimination effects in comparison to the traditional solvent-based MALDI MS sample preparation (48).

This encouraged us to examine solvent-less MALDI MS for PANI materials. Preliminary work in our laboratory indicated that low molecular mass oligomers of PANI could be produced which were slightly soluble and therefore amenable to analysis by ESI (53), but in general this approach could not be employed for most PANI materials. Subsequently, we compared LDI-TOF and solvent-less MALDI-TOF MS for the analysis of insoluble PANI (54). Direct LDI-TOF MS of solid PANI results in extensive phenyl ring fragmentation, leading to virtually uninterpretable mass spectra. With the addition of a matrix material, solvent-less MALDI-TOF produces mass spectra that result in the detection of higher molar mass oligomers of PANI than with LDI, an example of which is given in Fig. 9 using 7,7,8,8-tetracyano-quinodimethane (TCNQ) as the

matrix. The main distribution of oligomers in Fig. 9 corresponds to an equal number of amine and phenyl groups in the backbone of the oligomer, indicated by the symbol *. The second series (identified with the @ symbol) represents oligomers which have an additional amine group present at the terminus of the chain, and thus are terminated at both ends by an amine group. These results suggest that solvent-less MALDI MS may be suitable for other intractable, conductive polymers like PPy and poly(vinyl ferrocene).

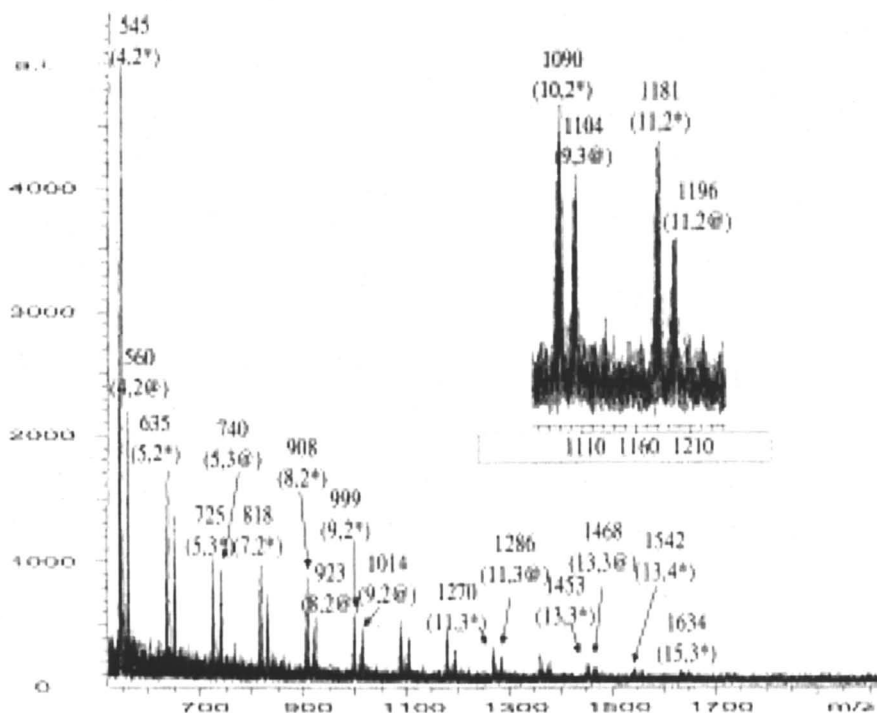


Figure 9. Solventless MALDI-TOF mass spectrum of PANI in a 1:50 molar ratio with TCNQ. This spectrum contains only two different series of PANI with differing end groups, as indicated in the inset, an expanded region of the mass spectrum around the 12-mer and 13-mer.

Concluding Remarks

Despite the fact that polymeric materials are complex mixtures of high molar mass substances, MS methods have become increasingly important in

characterizing these materials. The advent of ionization techniques such as MALDI and ESI to generate gas-phase ions coupled with innovations in mass analyzers such as reflectron-TOF and FT-ICR have greatly extended the capabilities of MS to provide ever-increasing detail on the nature of polymeric materials. The coupling of GPC, either off-line or on-line, to MALDI and ESI has helped to circumvent mass discrimination effects so that MS is amenable to much broader MMD than it was previously. Increased mass resolution and accuracy permits greater detail about even minor components in polymeric materials to be assessed, especially with regard to composition of repeat and end groups. New developments in solvent-less MALDI techniques also promise to open up characterization of some of the most challenging low-solubility polymeric materials. Indeed, we echo the comments of our colleague Scott Hanton, who wrote several years ago “The future of mass spectrometry of polymers continues to be bright” (3). The ever evolving improvements in MS techniques and instrumentation, especially when coupled to hyphenated techniques like GPC, will likely be extended to increasingly more complex and challenging polymeric materials.

References

1. Montaudo, G.; Lattimer, R. *Mass spectrometry of polymers*; CRC Press: Boca Raton, Fla., 2002.
2. Brady, R. F. *Comprehensive desk reference of polymer characterization and analysis*; American Chemical Society ; Oxford University Press: New York, 2003.
3. Hanton, S. D. *Chem. Rev.* 2001, 101, 527-569.
4. Karas, M.; Bachmann, D.; Bahr, U.; Hillenkamp, F. *Int. J. Mass Spec. Ion Proc.* 1987, 78, 53-68.
5. Tanaka, K.; Waki, H.; Ido, Y.; Akita, S.; Yoshida, Y.; Yoshida, T. *Rapid Commun. Mass Spectrom.* 1988, 2, 151-153.
6. Yamashita, M.; Fenn, J. M. *J. Phys. Chem.* 1984, 88, 4451-4459.
7. Weidner, S.; Kuhn, G.; Friedrich, J. *Rapid Communications in Mass Spectrometry* 1998, 12, 1373-1381.
8. Knochenmuss, R.; Lehmann, E.; Zenobi, R. *European Mass Spectrometry* 1998, 4, 421-426.
9. Busch, K. L. *Spectroscopy* 1999, 14, 14-16.
10. Schriemer, D. C.; Li, L. *Anal. Chem.* 1996, 68, 2721-2725.
11. Hanton, S. D.; Cornelio-Clark, P. A.; Owens, K. G. *J. Am. Soc. Mass Spectrom.* 1999, 10, 104-111.
12. Kassis, C. E.; DeSimone, J. M.; Linton, R. W.; Remsen, E. E.; Lange, G. W.; Friedman, R. M. *Rapid Commun. Mass Spectrom.* 1997, 11, 1134-1138.

13. Hensel, R. R.; King, R. C.; Owens, K. G. *Rapid Commun. Mass Spectrom.* **1997**, *11*, 1785-1793
14. Axelsson, J.; Hoberg, A. M.; Waterson, C.; Myatt, P.; Shield, G. L.; Varney, J.; Haddleton, D. M.; Derrick, P. J. *Rapid Communications in Mass Spectrometry* **1997**, *11*, 209-213.
15. Yun, H.; Olesik, S. V.; Marti, E. H. *J. Microcol. Sep.* **1999**, *11*, 53-61.
16. Prokai, L.; Simonsick, W. J., Jr. *Rapid Commun. Mass Spectrom.* **1993**, *7*, 853-856..
17. Danis, P. O.; Karr, D. E. *Macromolecules* **1995**, *28*, 8548-8551
18. Mamyryn, B. A.; Karataev, V. I.; Smikk, D. V.; Zagulin, V. A. *Soviet Phys. JETP* **1973**, *37*, 45-48.
19. Morris, H. R.; Paxton, T.; Dell, A.; Langhorne, J.; Berg, M.; Bordoli, R. S.; Hoyes, J.; Bateman, R. H. *Rapid Commun. Mass Spectrom.* **1996**, *10*, 889-896..
20. Comisarow, M. B.; Marshall, A. G. *Chem. Phys. Lett.* **1974**, *25*, 282-283.
21. Montaudo, G.; Garozzo, D.; Montaudo, M. S.; Puglisi, C.; Samperi, F. *Macromolecules* **1995**, *28*, 7983.
22. Yalcin, T.; Dai, Y. Q.; Li, L. *J. Am. Soc. Mass Spec.* **1998**, *9*, 1303-1310.
23. Guttman, C. M.; Blair, W. R.; Danis, P. O. *J. Polym. Sci. Part B--Polym. Phys.* **1997**, *35*, 2409.
24. Guttman, C. M.; Wetzler, S. J.; Blair, W. R.; Fanconi, B. M.; Girard, R. J. G.; Wallace, W. E.; VanderHart, D. L. *Anal. Chem.* **2001**, *73*, 1252-1262.
25. Maziarz, E. P.; Liu, X. M.; Quinn, E. T.; Lai, Y. C.; Ammon, D. M.; Grobe, G. L. *Journal of the American Society for Mass Spectrometry* **2002**, *13*, 170-176.
26. Axelsson, J.; Scrivener, E.; Haddleton, D. M.; Derrick, P. J. *Macromolecules* **1996**, *29*, 8875-8882.
27. Hunt, S. M.; Sheil, M. M.; Derrick, P. J. *Eur. Mass Spectrom.* **1998**, *4*, 475-486.
28. Schreimer, D. C.; Li, L. A. *Anal. Chem.* **1997**, *69*, 4169-4175.
29. Schreimer, D. C.; Li, L. A. *Anal. Chem.* **1997**, *69*, 4176-4183.
30. Zhu, H.; Yalcin, T.; Li, L. *J. Am. Soc. Mass Spectrom.* **1998**, *9*, 275-281.
31. Vitalini, D.; Mineo, P.; Scamporrino, E. *Rapid Commun. Mass Spectrom.* **1999**, *13*, 2511-2517.
32. Liu, X. M.; Maziarz, E. P.; Heiler, D. J.; Grobe, G. L. *Journal of the American Society for Mass Spectrometry* **2003**, *14*, 195-202.
33. Wang, G.; Cole, R. B. *Anal Chem* **1995**, *67*, 2892-2900.
34. Fei, X.; Murray, K. K. *Anal. Chem.* **1996**, *68*, 3555-3560.
35. Liu, X. M.; Maziarz, E. P.; Price, F.; Heiler, D. J.; Grobe, G. L. *European Journal of Mass Spectrometry* **2001**, *7*, 473-480.
36. Hanton, S. D.; Liu, X. M. *Anal. Chem.* **2000**, *72*, 4550-4554.
37. Maziarz, E. P.; Liu, M. *European Journal of Mass Spectrometry* **2002**, *8*, 397-401.

38. Maziarz, E. P.; Liu, X. M.; Baker, G. A. *Rapid Communications in Mass Spectrometry* **2003**, *17*, 2450-2454.
39. Yan, W.; Ammon, D. M., Jr.; Gardella, J. A., Jr.; Maziarz, E. P., III; Hawkrigde, A. M.; Grobe, G. L., III; Wood, T. D. *Eur. Mass Spectrom.* **1998**, *4*, 467-474.
40. Liu, X. M.; Maziarz, E. P.; Heiler, D. J. *Journal of Chromatography A* **2004**, *1034*, 125-131.
41. Smith, P.; Lemstra, P. J. *Journal of Materials Science* **1980**, *15*, 505-514.
42. Chung, C. I. *Journal of Applied Polymer Science* **1986**, *31*, 2739-2751.
43. Garcia-Leiner, M.; Lesser, A. J. *Journal of Applied Polymer Science* **2004**, *93*, 1501-1511.
44. Fleming, O. S.; Chan, K. L. A.; Kazarian, S. G. *Polymer* **2006**, *47*, 4649-4658.
45. Brenna, J. T.; Creasy, W. R.; Zimmerman, J. *Am. Chem. Soc. Symp. Ser.* **1993**, *236*, 129-154.
46. Van Vaeck, L.; Adriaens, A.; Gijbels, R. *Mass Spectrometry Reviews* **1999**, *18*, 1-47.
47. Przybilla, L.; Brand, J. D.; Yoshimura, K.; Rader, H. J.; Mullen, K. *Analytical Chemistry* **2000**, *72*, 4591-4597.
48. Timpin, S.; Rouhanipour, A.; Az, R.; Rader, H. J.; Mullen, K. *Rapid Communications in Mass Spectrometry* **2001**, *15*, 1364-1373.
49. Marie, A.; Fournier, F.; Tabet, J. C. *Analytical Chemistry* **2000**, *72*, 5106-5114.
50. Trimpin, S.; Grimsdale, A. C.; Rader, H. J.; Mullen, K. *Analytical Chemistry* **2002**, *74*, 3777-3782.
51. Hanton, S. D.; Parees, D. M. *Journal of the American Society for Mass Spectrometry* **2005**, *16*, 90-93.
52. Trimpin, S.; Deinzer, M. L. *Journal of the American Society for Mass Spectrometry* **2005**, *16*, 542-547.
53. Dolan, A. R.; Wood, T. D. *Synthetic Metals* **2004**, *143*, 243-250.
54. Dolan, A. R.; Wood, T. D. *Journal of the American Society for Mass Spectrometry* **2004**, *15*, 893-899.

Chapter 11

Synthesis and Properties of Functional Poly(vinylpyrrolidinone) Hydrogels for Drug Delivery

Louise E. Smith¹, Stephen Collins², Zuifang Liu², Sheila Mac Neil¹, Rachel Williams³, and Stephen Rimmer^{2,*}

Departments of ¹Engineering Materials, Kroto Research Institute, and ³Chemistry, University of Sheffield, Sheffield S3 7HQ, United Kingdom

²Department of Clinical Engineering, University of Liverpool, Liverpool L69 3GA, United Kingdom

Poly (N-vinylpyrrolidinone) has many uses in biotechnology and medicine. Here we review our recent work on materials based on this polymer that have applications in drug release or as potential mitogens. The synthesis of crosslinked PNVP hydrogels and highly branched polymers is covered.

Introduction

Poly(N-vinylpyrrolidinone) (PNVP) has been used in medical applications for many years. Its history can be traced back to the Second World War where in its un-crosslinked form it was used as a blood plasma expander (1). This un-crosslinked PNVP when added to iodine forms a complex, in solution this complex is better known as Povidone-iodine or by its trade name Betadine®, a surgical antiseptic. PNVP is also used as a binder in many pharmaceutical tablets as low molecular weight PNVP can be removed from the body by the kidneys. These polymers have also been investigated for use as wound dressings, drug

delivery devices and vitreous substitutes; PNVP is also a major constituent in soft, gas permeable contact lenses. Research into PNVP as a potential vitreous substitute by the group of T.V. Chirila (2-5) showed that in static cultures PNVP hydrogels with water contents comparable to that of natural vitreous $\approx 99\%$ could increase the viability of 3T3 Swiss mouse fibroblasts after the injection of the hydrogel into the culture system (3). However this was dependent on the crosslinker used. In serum free conditions cell viability increased when a PNVP hydrogel containing 1wt% 2-Hydroxyethyl methacrylate (HEMA) and 0.25wt% DEGDMA (Diethyleneglycol dimethacrylate) having an equilibrium water content (EWC) of 95% was injected into the culture system to levels approaching that of cells cultured with serum. This hydrogel also increased cell viability in cultures containing serum. Conversely a PNVP hydrogel containing 10% HEMA when added to the culture system decreased cell viability in both serum free and with serum culture systems. When this data is combined with the *in vivo* data obtained by Vijayasekaran et al (5) and Hong et al (4) polymers based on PNVP appeared ideal to incorporate into our research on the development of wound dressings.

Hydrogels also have uses in slow release systems, which allow for controlled administration of therapeutics. Thus prior to using these polymers for drug release we first investigated the biocompatibility / potential mitogenic effect of the PNVP polymer in contact with cells and then looked at release of drugs from this polymer.

Biocompatibility

In our recently published biocompatibility study (6) we showed that PNVP hydrogel networks crosslinked with 1wt% ethyleneglycol dimethacrylate [1] with an EWC of 92.2% were less effective at increasing the viability of human dermal fibroblasts than PNVP crosslinked with 1wt% diethylene glycol bisallylcarbonate [2] with an EWC of 96.2%. This study also showed that physical separation between the cells and the hydrogel was required to reliably obtain this increase in cell viability. The results from cultures carried out in the presence of P(NVP-co-1) or P(NVP-co-2) are summarised in figure 1. After 30 repeated experiments we observed a clear difference between these two series of polymers with P(NVP-co-2) being more effective at enhancing cell viability.

The effect of the detailed structure of PNVP on cell viability appears to be associated with polymer microstructure. NVP copolymerises with 2 in an almost random, statistical manner whereas copolymerization of NVP with 1 is only effective at low concentrations of 1. The effect of this mismatch of the reactivity ratios (r_{NVP} and r_2) is to produce networks in which units of 1 are clustered together in blocky structures. Although, the mechanistic details behind these

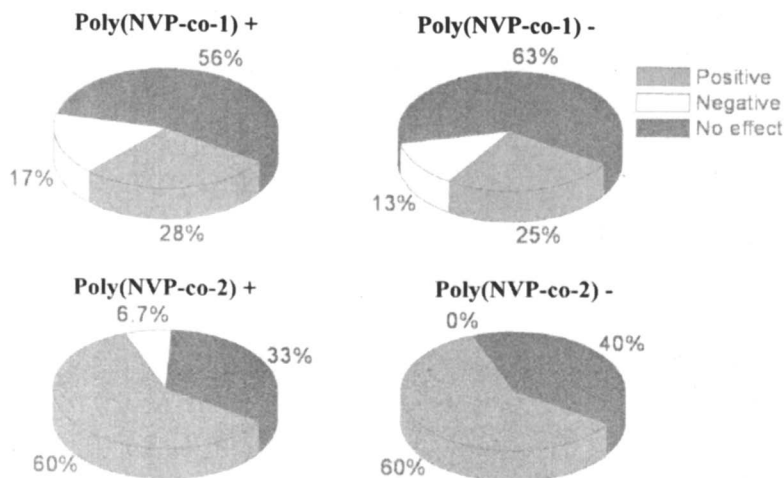
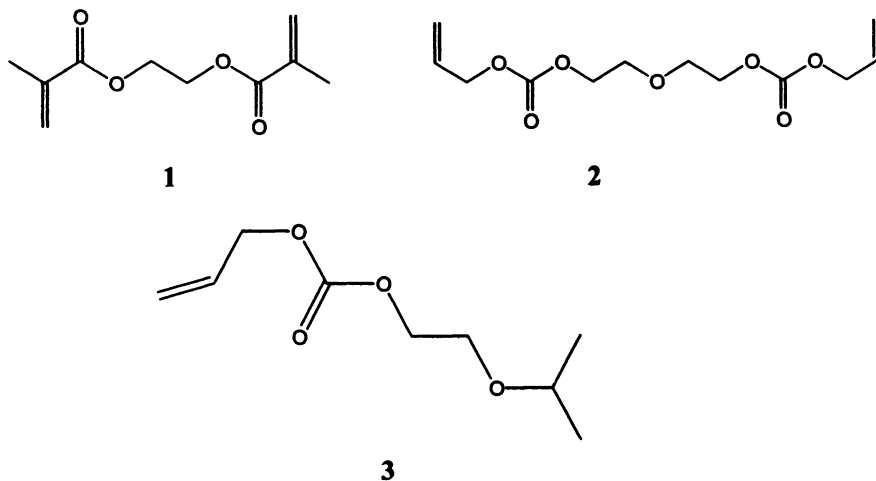


Figure 1. MTT (cell viability) data—the pie-charts show the results of 30 repeated experiments. Positive results indicate an enhancement of viability and negative results indicate a decrease in viability. No effect indicates that viability was not significantly different from the control cell cultures. The + or – indicates that the experiment was conducted in the presence (+) or absence (-) of foetal calf serum in the culture medium.

phenomena are yet to be elucidated, these block structures appear to be less effective at increasing cell viability than the random copolymer structures produced by copolymerization of NVP and 2.

These observations have prompted us to prepare soluble analogues of P(NVP-co-2). In order to prepare these polymers we used a modification of our route to highly branched poly(vinyl acetate) (7), which involves copolymerization of NVP with allyl 2-isopropoxyethyl carbonate, 3.

Polymerizations of NVP in the presence of 3 carried out at 60 °C, in butyl acetate, produced crosslinked networks. However, increasing the reaction temperature to 150 °C produced completely soluble branched polymers. The gelation process at 60 °C is a result of bimolecular termination by combination of propagating branches. At 150 °C this process is slower than termination by transfer to 3 so that gelation does not occur. Figure 2 shows an H-NMR spectrum of a typical polymer prepared in this manner. Resonances derived from methylene groups in residues of 3 (protons 1 and 3 in figure 2) were observed at $\delta \approx 4.2$ and 3.6.

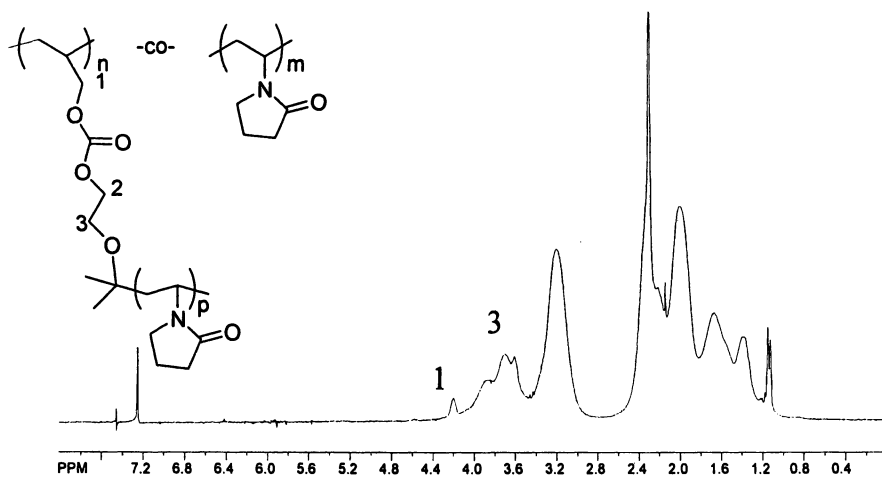
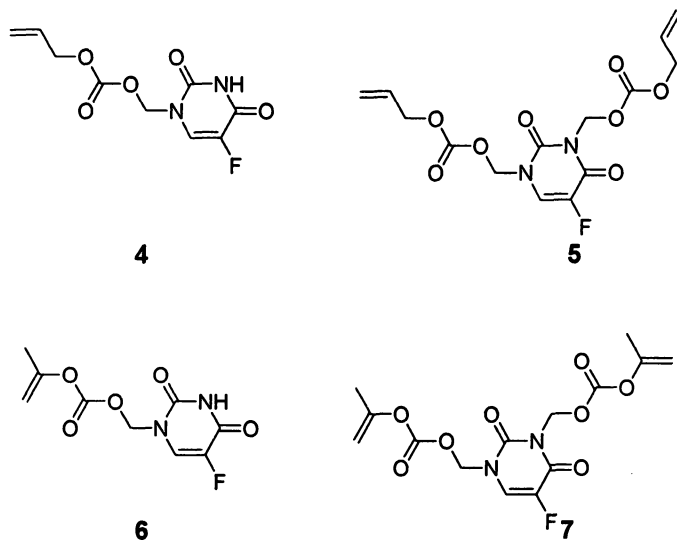


Figure 2. ^1H NMR spectrum of poly (NVP-co-3), synthesised at 150°C

Branching fractions of 0.036 and 0.064 branches per repeat unit were obtained by using 0.104 and 0.091 mole fractions of branching agent respectively. Cytotoxicity testing of these polymers is currently underway and will be reported in due course.

Drug release from Hydrogels

Two drugs were explored; *5-Fluouracil (5-FU)* and *4-methyl umbelliferone (4-MU)*. Functionalized hydrogels incorporating the cytotoxic drug 5-Fluouracil (5-FU) were synthesised by copolymerizing derivatives of oxycarbonyloxymethyl-5-fluorouracil monomers with NVP (8). Methylation of 5-FU gave mixtures of N-1-hydroxymethyl-5-fluorouracil, N-3-hydroxymethyl-5-fluorouracil, 3-bis(hydroxymethyl-5-fluorouracil). The N-1-hydroxymethyl-5-fluorouracil and N,N'-1,3-bis(hydroxymethyl-5-fluorouracil) monomers were modified with allyl chloroformate or isopropenyl chloroformate to yield carbonate monomers 4, 5, 6 and 7. 4, 5, 6 and 7 could be readily copolymerised with NVP to give either linear polymers (copolymerization with 4 or 6) or hydrogel networks (copolymerization 5 or 7).



Polymerization with the monofunctional monomers (4 and 6) was used to estimate the reactivity ratios for copolymerization with NVP ($r_5 = 0.32$, $r_{\text{NVP}} = 0.97$ and $r_7 = 0.61$, $r_{\text{NVP}} = 1.31$). This study showed that both these allyl carbonate and isopropenyl carbonate monomers copolymerize in an almost statistical manner and that copolymerization with 5 and 7 could be predicted to produce random copolymer networks without significant block formation. We produced materials containing 5, 10, 15 and 20 wt% of 5-FU by copolymerization with 5 and 7. However, degradation of the allyl carbonate crosslinks in copolymers with 5 appears to be very slow and these materials were

not examined further. Drug release from copolymers of NVP with 7 occurred over 50 days (9). The degradation of the carbonate groups followed the increase in swelling as the crosslink density decreased, as shown in figure 3.

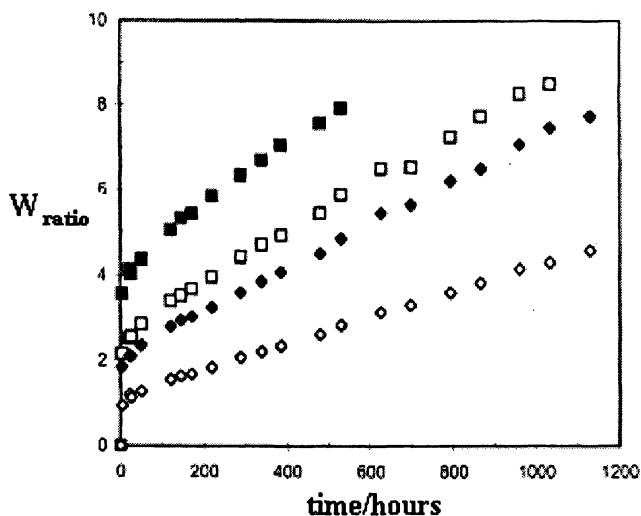


Figure 3. Increase in swelling ratio (W_{ratio}) over time due to degradation of carbonate crosslinking groups at 37°C. Wt% 7 in feed: ■ = 5; □ = 10; ◆ = 15; ◇ = 20

The release of 5-FU from these system was monitored using the power law relationship developed by Peppas (10) as shown in figure 5, and exponents of 0.13 – 0.23. These values indicate that as expected the diffusion is not Fickian but is dominated by degradation of the carbonate crosslinking groups. The total amount of 5-FU realised from these hydrogels is also a function of initial composition of the monomer feed, i.e. the amount released is a function of the loading.

5-FU is a cytotoxic drug that has applications in cancer and other disease states and post-operative conditions involving over proliferation. In order to examine the effect of the release of 5-FU, cytotoxicity studies were performed on hydrogels prepared by copolymerization with 5, 10, 15 and 20wt% of 7 in the monomer feed. Cytotoxicity studies were performed using retinal pigment epithelial cells in a static model. Cell contact assays were performed by seeding cells 12 hours prior to the addition of the polymers in either a Labtek® chamber slide system (Nunc) for live/dead staining with calcein AM and Ethd-1 or in a 24

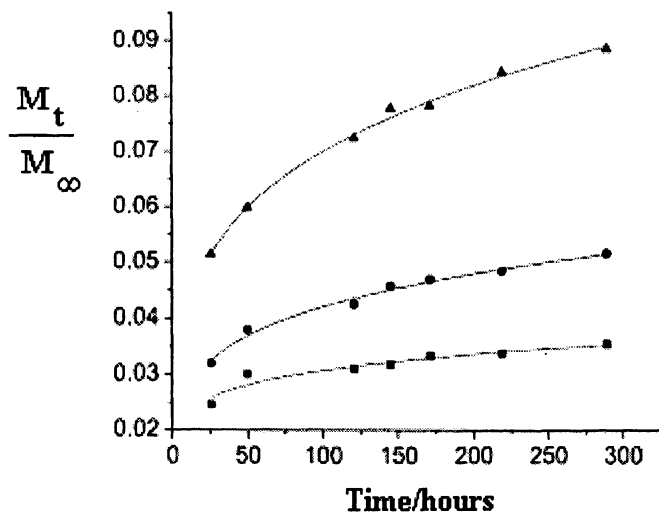


Figure 4. Plot of fractional release of 8 against time $Wt\%$ 7 in feed: ■ = 10; ● = 15; ▲ = 20

well plate for the trypan blue assay. After 12 hours the polymers were placed on top of the cells and cell viability was assessed at 12, 24 and 48 hours. The trypan blue assay suggested that the wells containing polymer with the 5FU functionality were not viable and this was confirmed by the calcein AM/Ethd-1 staining. It was also apparent that cell proliferation but not viability was reduced in the presence of the polymers lacking the 5-FU group, i.e. hydrogels that were similar in structure to those studied in reference 6.

Preliminary data from current studies of the P(NVP-co-2) hydrogels show that these hydrogels can also be used for drug delivery. Delivery of another model compound, 4-methyl umbelliferone (4-MU), an inhibitor of hyaluronan synthesis which may be useful in the treatment of scarring, loaded into P(NVP-co-2) hydrogels from solutions containing 1mMol or 4mMol 4-MU, see figure 5, shows non-Fickian release with exponents of 0.655 and 0.614 respectively.

In summary we find PNVP hydrogels to have a slight mitogenic effect when adjacent to cells and to give promising hydrogels for sustained release of drugs over several days.

Acknowledgements

The authors would like to thank the EPSRC for doctoral training awards for L. Smith and S Collins and a post doctoral fellowship for Z Liu.

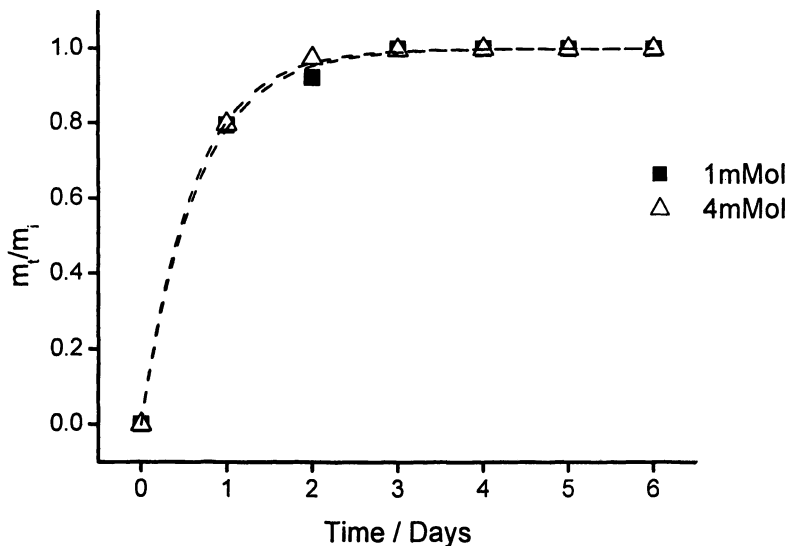


Figure 5. Fractional release of the model compound 4-methyl umbelliferone from P(NVP-co-2) hydrogels over a period of 6 days assessed using fluorescence, excitation 360nm emission 440/460nm, $n=6$.

References

1. Robinson, B.V.; Sullivan, F.M.; Borzelleca, J.F.; Schwartz, S.L.; *PVP: a critical review of the kinetics and toxicology of polyvinylpyrrolidone (povidone)*. 1 ed. Lewis Publishers, Michigan, USA, 1990.
2. Chirila, T.V.; Hong, Y.; Dalton, P.D.; Constable, I.J.; Refojo, M.F. *Prog. Polym. Sci.* **1998**, *23*, 475-508.
3. Hong, Y.; Chirila, T.V.; Fitton, H.; Ziegelaar, B.W.; Constable, I.J. *Bio-Med Mater Eng.* **1997**, *7*, 35-47.
4. Hong, Y.; Chirila, T.V.; Vijayasekaran, S.; Shen, W.; Lou, X.; Dalton, P.D. *J. Biomed. Mater. Res.* **1998**, *39(4)*, 650-659.
5. Vijayasekaran, S.; Chirila, T.V.; Hong, Y.; Tahija, S.; Dalton, P.D.; Constable, I.J.; McAllister, I.L. *J. Biomater. Sci.-Polym. Ed.* **1996**, *7(8)*, 685-696.
6. Smith, L.E.; Rimmer, S.; MacNeil, S. *Biomaterials*, **2006**, *27(14)*, 2806-2812.
7. Rimmer, S.; Collins, S.; Sarker, P. *Chem Comm.* **2005**, *48*, 6029-6031.
8. Liu, Z.; Fullwood, N.; Rimmer, S. *J. Mater. Chem.* **2000**, *10*, 1771-1775.
9. Liu, Z.; Rimmer, S. *J. Control. Release.* **2002**, *81*, 91-99
10. Peppas, N.A.; Bures, P.; Leobandung, W.; Ichikawa, H. *Eur. J. Pharm. Biopharm* **2000**, *50*, 27-46.

Chapter 12

Enzymatically Synthesized Pegylated Polymers as Nanomicellar Drug Delivery Systems

Rajesh Kumar^{1,3,*}, Mukesh K. Pandey¹, Rahul Tyagi¹,
Virinder S. Parmar^{1,2}, Arthur C. Watterson¹, and Jayant Kumar¹

¹Institute for Nano-Science Engineering and Technology and Center for Advanced Materials, Departments of Chemistry and Physics, University of Massachusetts, Lowell, MA 01854

²Bioorganic Laboratory, Department of Chemistry, University of Delhi, Delhi 110 007, India

³Current address: Pfizer Global Research and Development, Pfizer Inc., Groton, CT 06340

*Corresponding author: rkumar26@gmail.com

The enormous potential of enzymes has been recently applied to polymer material synthesis and modifications. This recent application has made biocatalysis a popular topic for polymeric research in academia and industry. Enzyme catalysis has provided a new synthetic strategy for useful polymers most of which are otherwise very difficult to produce by conventional chemical catalysis. This paper overviews our recent work on the use of a variety of enzymes in the synthesis of novel pegylated multifunctional polymers for applications in drug and gene delivery.

Improving the therapeutic index (*I*) of drugs is a major impetus for innovation in many therapeutic areas such as cancer, inflammatory, and infectious diseases. The search for new drug-delivery concepts and new modes of action are the major driving force in polymer therapeutics (2-5). A number of macromolecular delivery systems are under investigation to improve the potential of the respective drug. Generally, these can be classified as nanoparticulate drug-delivery systems or as drug-polymer conjugates. Particulate delivery systems in which the drugs are physically incorporated into nanoparticles include emulsions, liposomes, and noncovalent polymeric carrier systems. In drug-polymer conjugates, however, a drug is covalently linked to polymers such as proteins, polysaccharides, or synthetic polymers.

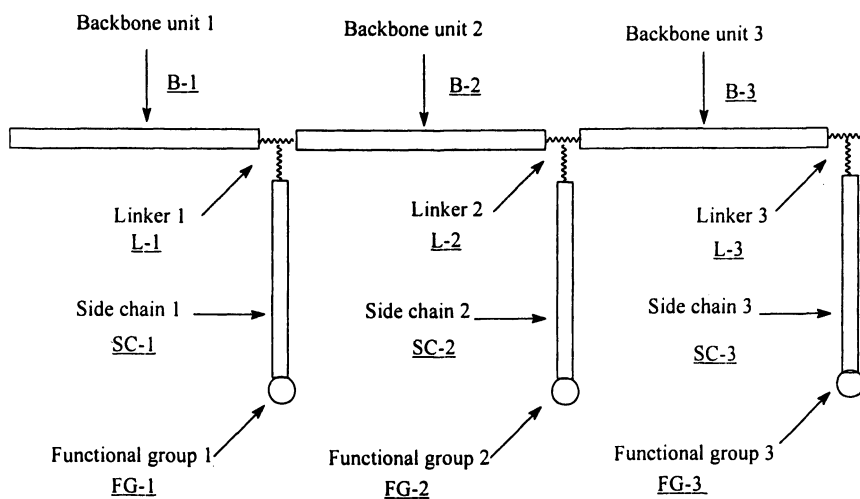


Figure 1. Schematic representation of polymer design.

The enormous potential of enzymes has been recently applied to polymeric materials synthesis and modifications. This recent application has made biocatalysis a popular topic for polymeric research in academia and industry (6-10). Enzymatic catalysis has provided a new synthetic strategy for useful polymers most of which are otherwise very difficult to produce by conventional chemical catalysis. This is an area having exponential increase in interest since a variety of well-defined molecular architects can be constructed using enzymatic catalysis. Recently, we have developed an extremely flexible chemo-enzymatic synthetic methodology to prepare well-defined structures as may be illustrated in Figure 1. This synthetic platform is designed to vary any of the parameters indicated in Figure 1. The simplest of these variations would have all backbone units (Figure 1, B-1 = B-2 = B-3, etc.), and linkers (Figure 1, L-1 = L-2 = L-3, etc.) the same structures. In some cases the same polymeric structure may be prepared by

chemical methods (11), although many of the advantages of enzymatic reactions, such as energy reduction with lower temperature of reaction, reduction of toxic solvent use, reuse of catalyst, are lost with these methods. This article overviews our recent work on the use of a variety of enzymes in the synthesis of first, second and third generation of novel pegylated multifunctional amphiphilic polymers based on the platform shown in Figure 1, for applications in drug and gene delivery, and other industrial applications.

Pegylated Polymers

The unique properties of poly (ethylene glycols) (PEGs), including solubility in wide range of solvents, lack of toxicity, absence of antigenicity and immunogenicity, non-interference with enzymatic activities and conformations of polypeptides, and ease of excretion from living organisms, make them ideal drug carriers (12-13). The two hydroxyl end groups of PEGs have been suitably functionalized prior to coupling (14) with ligands of biological relevance, although the hydroxyl groups themselves have been used as well (15-18). Because the number of terminal groups of linear PEGs (only two) to attach with drugs limits their drug loading capacity, extensive work has been done to functionalize them by copolymerizing PEGs with various functional monomers. Amphiphilic block copolymers with hydrophilic and hydrophobic segments have been extensively exploited for various applications in drug delivery (19-22). Kwon et al.(23-24) synthesized AB block copolymers of poly (ethylene oxide) (PEO) and poly (β -benzyl-L-aspartate) (PBLA). The distribution of hydrophobic moieties into the PEO-PBLA micelles was investigated by UV spectroscopy using pyrene as a model. Recent efforts in the design of drug delivery systems have led to the development of vehicles that circulate for prolonged periods in the vascular system. A common feature of the new drug vehicles is PEO at their surfaces. PEO is a nontoxic, highly hydrating polymer (through hydrogen bonding) that sterically stabilizes surfaces in aqueous systems, and this is effective for preventing the adsorption of proteins and adhesion of cells (25). The polymeric system and design described in this paper are very unique and highly flexible as compared to already reported PEG based systems. Most of the PEG modified systems are diblock polymeric systems. The flexibility in adjusting the ratio of hydrophilic segments (PEGs) and hydrophobic segments (modified diester compounds) provides easy access to tailor the polymer solution properties. PEGs of different molecular weights were used for the polymerization as well as three different sets of hydrophobic monomers were used. The critical micelle concentration (CMC) values of polymers have been investigated and determined by surface tension measurements. Intrinsic viscosities were studied based on polymer backbone length (PEGs effect) and nature of the pendant groups (diesters effect) and these were found to be dependent on molecular weights of the PEGs.

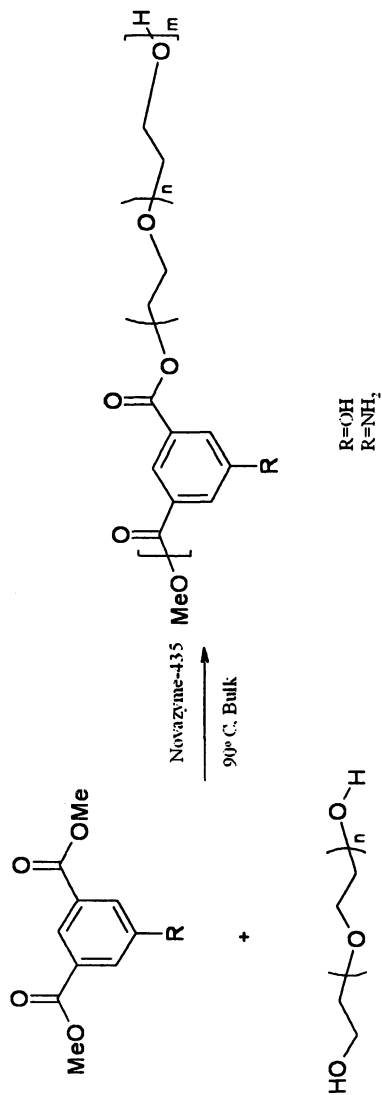
First Generation of pegylated polymers

Amphiphilic block copolymers with hydrophilic and hydrophobic segments have been investigated extensively not only because of their unique self-organization characteristics but also for their wide range of potential applications, such as in drug delivery and separation technology systems (26). The micellar characteristics of amphiphilic diblock copolymers depend on the nature of each block and the surface properties of self-organized micelles are highly dependent on the structures of the hydrophilic blocks (27-29). Based on the platform shown in Figure 1, the first generation of amphiphilic polymers consists of identical backbone and a trifunctional linker molecule with long alkyl chains. The main motivation behind this work was to develop functional, safe and biodegradable amphiphilic polymers having the characteristics:

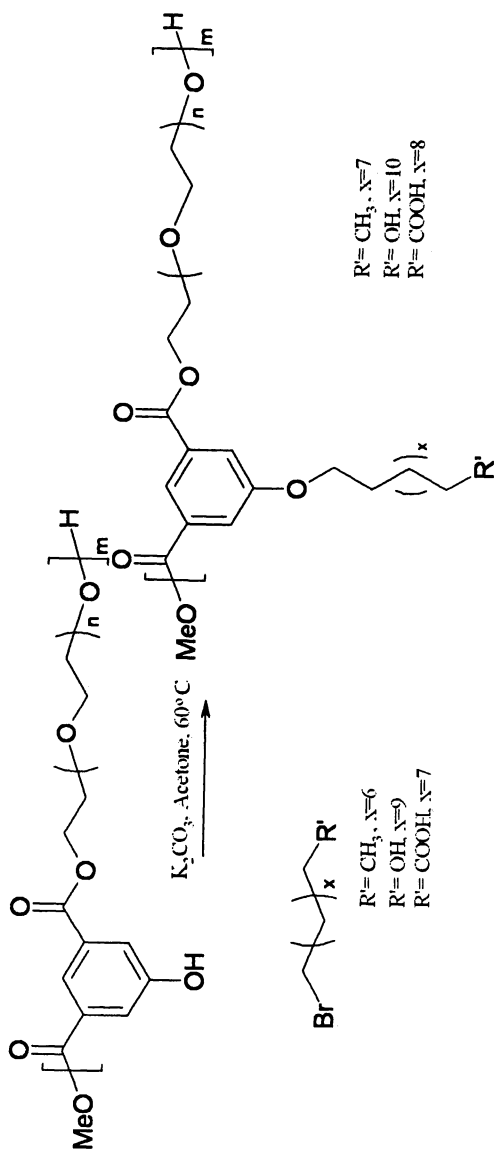
- (1) Flexibility to change the size of hydrophilic and hydrophobic segments in the polymer, as the right balancing of hydrophobic to hydrophilic segments in the repeating units may lead to lower CMCs,
- (2) The functional monomer should have sites so that it can be tailored under mild conditions,
- (3) The copolymers should be of sufficiently high molecular weight to allow them to have desirable physical properties.

In view of above stated facts we have developed and used enzymes for the synthesis of various functionalized polymers for a wide range of applications. More so, because many families of enzymes can be utilized for transformation of not only their natural substrates but a wide range of unnatural substrates to yield a variety of useful compounds. The use of enzymes in organic synthesis has several advantages also, such as superior catalytic power and high selectivity under mild conditions with regard to temperature, pressure, and pH, promising substrate conversion efficiency, high diastereo-, regio-, and chemo- selectivities as well as regulating stereochemistry to provide development of new reactions. The naturally occurring polymers are produced in vivo by enzyme catalysis. These features allow the generation of functional compounds for pharmaceutical and agrochemical sectors employing non-toxic natural catalyst with "green appeal," additional advantages including catalyst recyclability and use in bulk reaction media avoiding organic solvents. So we performed the condensation polymerization of polyethylene glycols (back bone) with dimethyl 5-hydroxyisophthalate (linker) catalyzed by lipase from *Candida antarctica* as shown in Scheme 1.

The main advantage of this reaction is that the hydroxyl/amino substituents at the C-5 position of the isophthalate moiety didn't participate in the reaction and may be further exploited for attaching different groups. For controlled aggregation, the balance between hydrophilic and hydrophobic groups is very critical. Therefore a series of amphiphilic polymers were synthesized by



Scheme 1. Synthesis of first generation polymers by enzyme catalysis



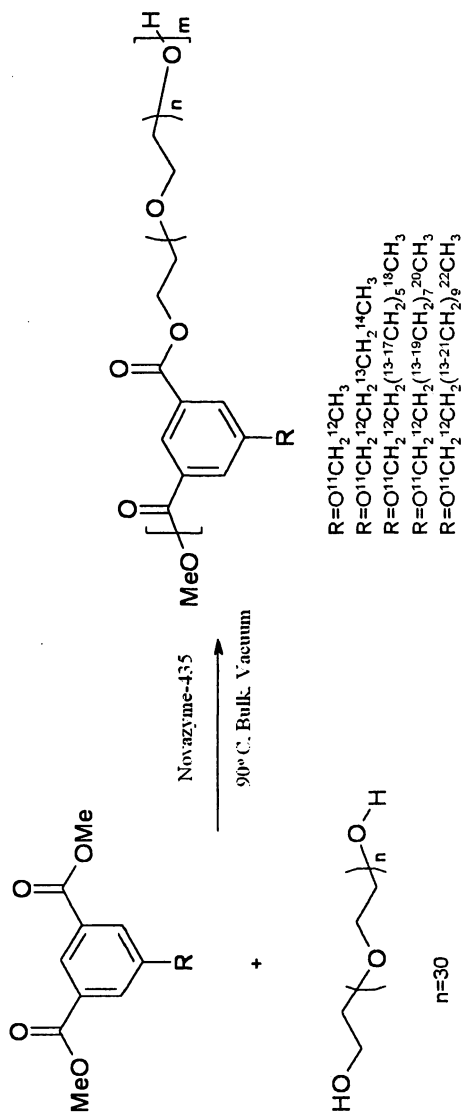
Scheme 2. Functionalization of polymers with alkyl side chains.

attaching the alkyl chains of different length (C-3 to C-12) (Scheme 2) to the hydroxy/amino substituents at C-5 position of the isophthalate linker in the polymers. Light-scattering data suggest that the alkyl chains of C-9 to C-12 confer enough hydrophobicity to the polymeric system to self-assemble in aqueous medium forming nanospheric particles with a hydrophobic core surrounded by hydrophilic PEG units. The inherent core-shell structure of our polymeric assemblies is ideally suited for targeted drug delivery. The hydrophobic core can serve as a nonaqueous reservoir for the drug, which is also protected, to some degree, against in vivo degradation (e.g., metabolism). The hydrophilic shell is composed of nontoxic, biodegradable PEG units that have a dual role in stabilizing the micellar assembly while also dictating the pharmacokinetics and bio-distribution of the carrier.

We have also investigated the synthesis of amphiphilic copolymers in a single step starting from corresponding 5-alkoxyisophthalates and polyethylene glycols using an environmentally benign catalyst, and under solventless conditions to make the process "Green" (Scheme 3). The monomers, 5-alkoxyisophthalates, were prepared by the alkylation of dimethyl 5-hydroxyisophthalate with corresponding alkyl bromides (11). Novozyme-435 catalyzed condensation polymerization reactions of 5-alkoxyisophthalates with polyethylene glycol (M_n 1500) were performed at 90°C in bulk (solvent-free conditions) under vacuum.

We observed that with an increase in the size of the chain length attached to the phenolic hydroxyl group, both the % conversions and degrees of polymerization to products decrease. This may be due to the increase in the hydrophobicity of the monomer with the increase in the size of the chain length thus making it difficult for the hydroxyl of serine residue to form an activated complex with the monomers which results in a slow or no reaction depending upon the size of the alkyl chain.

We have carried out the reaction of dimethyl 5-hydroxyisophthalate with PEG of varying molecular weights (300, 600, 900 and 1500). It was observed that with an increase in the molecular weight of the macromer (PEG), the isolated yield and number average molecular weights of the copolymer increased. In the case of PEG 300, there was very small conversion to copolymer and the reaction produced only dimers and trimers. The low copolymer yield and number average molecular weight obtained in the case of low molecular weight polyethylene glycol units are perhaps due to the difficult solubilization of the diester monomer by PEGs of low molecular weights as these reactions are being done in solvent-free conditions. When we use one equivalent of high molecular weight PEGs, the amount of PEG used will be more than the case when one equivalent of low molecular weight PEG is used, e.g. if one uses one mmol of PEG 300 and 1 mmol of PEG 1500, then the corresponding amounts of PEG in terms of weights will be 300 mg and 1.5 g for the same amount of the monomer. This implies that in the case of PEG 1500, the amount of the PEG used is :

Scheme 3. *Candida Antarctica lipase B-catalysed polymerization*

times more as compared to PEG 300. Therefore the solubilization of isophthalate-based monomer will be much better in PEG 1500 as compared to that in PEG 300, simply because it is present in larger amounts. We have repeated these experiments a few times without problem, and get consistent and reproducible results. These self-organized nanomicelles (Figure 2) are highly efficient drug delivery vehicles for hydrophobic drugs both transdermally and orally as they have the ability to encapsulate guest molecules during self-organization. In addition, the functionality of the polymeric nanomicelles can be modified simply by changing the chemical structure of the amphiphilic copolymers, which in turn helps in encapsulating not only hydrophobic drugs but partially hydrophilic drugs as well and thus increases the therapeutic potential of the drugs.

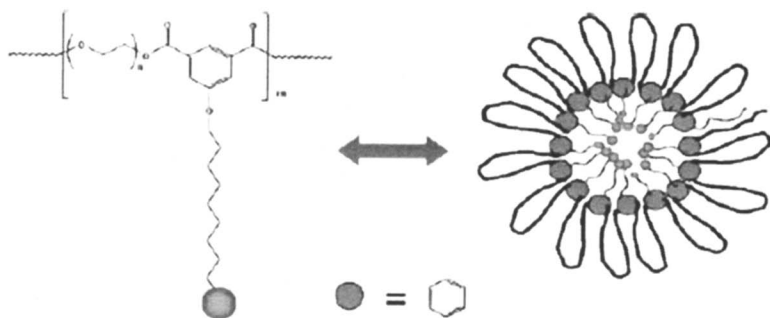


Figure 2. Self-assembly of the amphiphilic polymers in aqueous media to form polymeric nanomicelles.

The process of micellization of the amphiphilic copolymers was observed using ^1H NMR longitudinal relaxation time (T_1) studies, because the formation of micelles, viz. aggregation of the hydrophobic segments in water, may influence the proton spin relaxation. On the basis of these studies, we have observed that in water, the hydrophobic segments have strong tendency to aggregate and become the core of the micelle, while the hydrophilic segments extend themselves in the bulk solvent water. Further, we have studied the supramolecular organization of the amphiphilic polymers in water by light scattering techniques (static and dynamic) as they readily dissolved in water. The critical micelle concentration (CMCs) values of these pegylated amphiphilic polymers in aqueous media were determined by static light scattering technique; these were found to be about 0.035-0.056 mmol/mL. These pegylated amphiphilic polymers have been successfully used as drug carriers with some model hydrophobic anti-inflammatory agents such as aspirin and naproxen. The formation of the

nanospheres in the presence of drugs was monitored by static light scattering technique. The *in vivo* testing results with freshly prepared nanospheres were compared with the same dose of aqueous preparation of commercially available naproxen sodium and aspirin (acetyl salicylic acid). Application of these loaded nanospheres to the right auricle of the mice for 2 h after treatment with the pro-inflammatory compound, croton oil, resulted in a significant reduction of inflammation. The % reduction in inflammation using nanospheres containing aspirin and naproxen was 62 and 64%, respectively; however, the empty nanospheres also exhibited some anti-inflammatory activity (18%). The study also showed that our nanosphere-mediated delivery of same dose (800 μg) of aspirin and naproxen has significantly better results as compared to same dose (800 μg) aqueous preparation of commercially available naproxen sodium (34%) and aspirin (32%) (Figure 3a,b). The nanosphere mediated delivery increased the efficacy by 1.8-2.0 times.

With fewer side effects as a result of nanosphere-mediated topical delivery, aspirin will not only continue to provide therapeutic benefits for the inhibition of thrombosis but also for reduction in inflammation (32) during asthma attacks (33) and act as potential mediators of cardiovascular risk due to smoking (34). Similarly, topical delivery of naproxen via nanoparticles will allow for more efficient delivery and better management of inflammation with this drug as reported during intraocular lens implantation (35), osteoarthritis (36) and rheumatoid arthritis (37). Our ability to topically deliver anti-inflammatory agents using the novel polymeric nanospheres formed by amphiphilic copolymers generated through chemoenzymatic routes offers additional advantage of "Green appeal" and further enhances its widespread application potential as an important strategy.

Second Generation of pegylated polymers

We have extended our study to further improve the ability of these nanomicelles in terms of better drug uploading and releasing capacity and have also developed polymeric systems for gene delivery (38,39). In this direction, we have designed and synthesized novel nano-carriers containing Vitamin E, the synthesized nano-carriers are unique due to the flexibility of both bound as well as encapsulated vitamin E. This allows a better control over the release and bioavailability of Vitamin E and can be used in combination of other bioactive agents. The amphiphilic nature of these nanocarriers make them soluble in both hydrophilic and lyphophilic medium. The synthetic approach for these nano-carriers is shown in Scheme 4 and Scheme 5.

The synthesized nano-carriers have the flexibility of further encapsulating Vitamin E or other bioactive agents, and allows a handle for controlling the concentration of Vitamin E in various preparations for cosmetic and pharmaceutical applications.

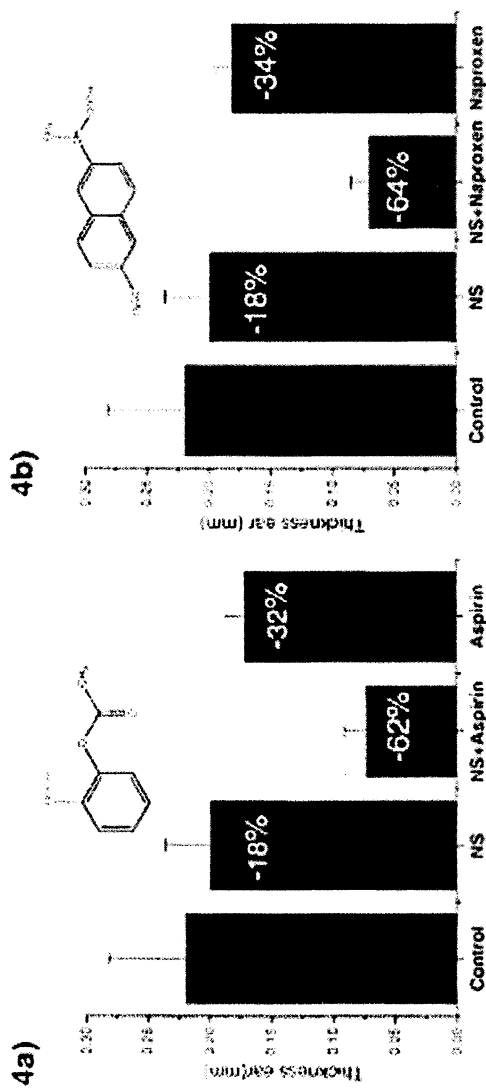


Figure 3. Anti-inflammatory properties of PEG nanospheres containing (a) aspirin and (b) naproxen.

In terms of gene delivery we have synthesized cationic polymers as they have the capacity to interact with negatively charged DNA/RNA as well as with the phosphate groups at the cell surface. Our polymeric system is composed of amino/guanidine functional groups and PEG units (Scheme 6). The guanidine group is an important structural component in many biologically active compounds. Because of its strongly basic character ($pK_a:12.5$), it remains protonated over a wide pH range. The positive charge thus imposed on the molecule forms the basis for specific interactions between ligand and receptor or enzyme and substrate. The PEG units may form a characteristic micelle structure with a hydrophilic shell layer surrounding the core of the polyion complex (PIC) formed between DNA and the cation segments (PIC micelles).

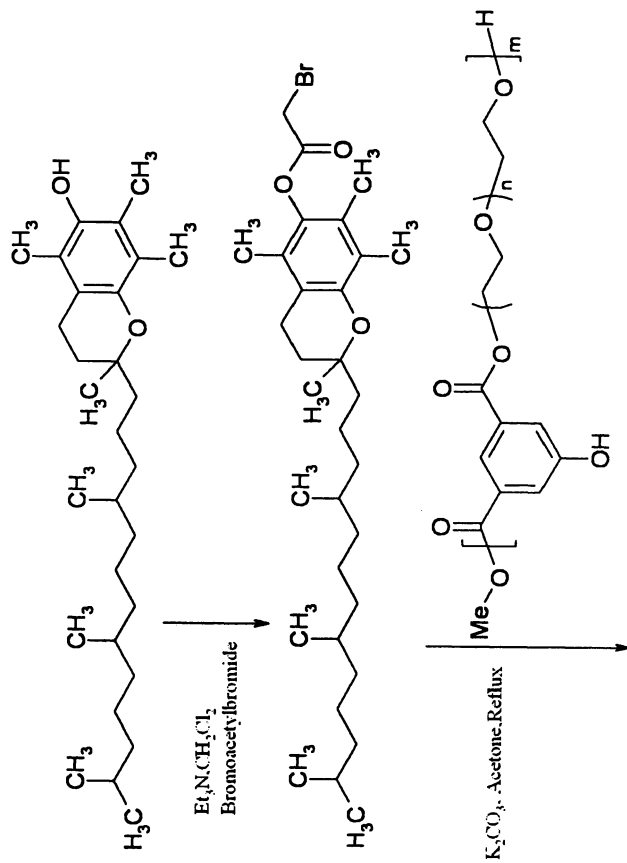
Third generation of pegylated polymers

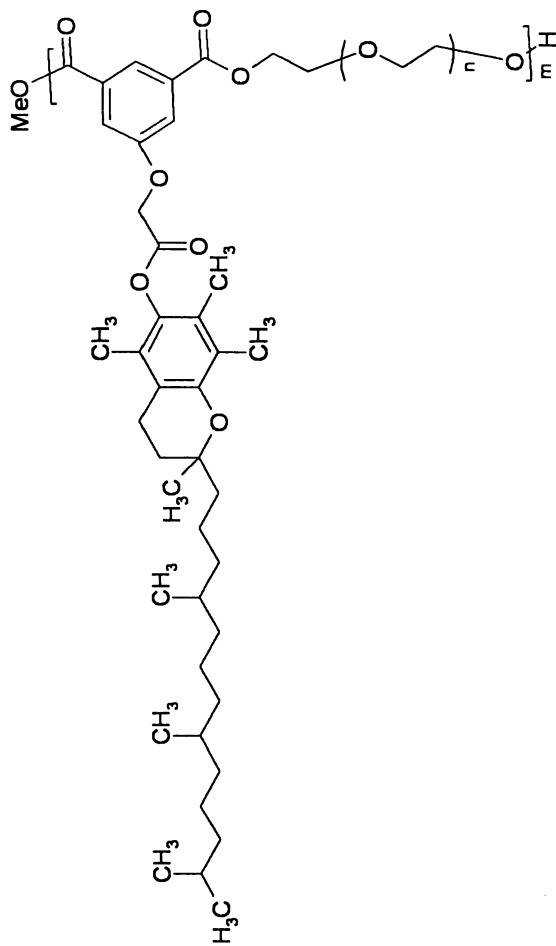
Current medical imaging techniques, CT and MRI, provide detailed anatomical snapshots of the body but fail to provide accurate, basic information necessary to manage the patient's disease optimally. The limitations are manifested in several ways:

- (1) Small primary tumors go undetected. Even under the best conditions, tumors smaller than 2 mm (roughly 500,000 cells) cannot be seen.
- (2) Metastatic disease is grossly underdiagnosed, and patients with negative scans for metastases at initial presentation routinely go on to develop, and die, from metastatic cancer.
- (3) Treatment response to therapy is poorly measured. "Measurable disease" is absent after surgical excision of many tumors.

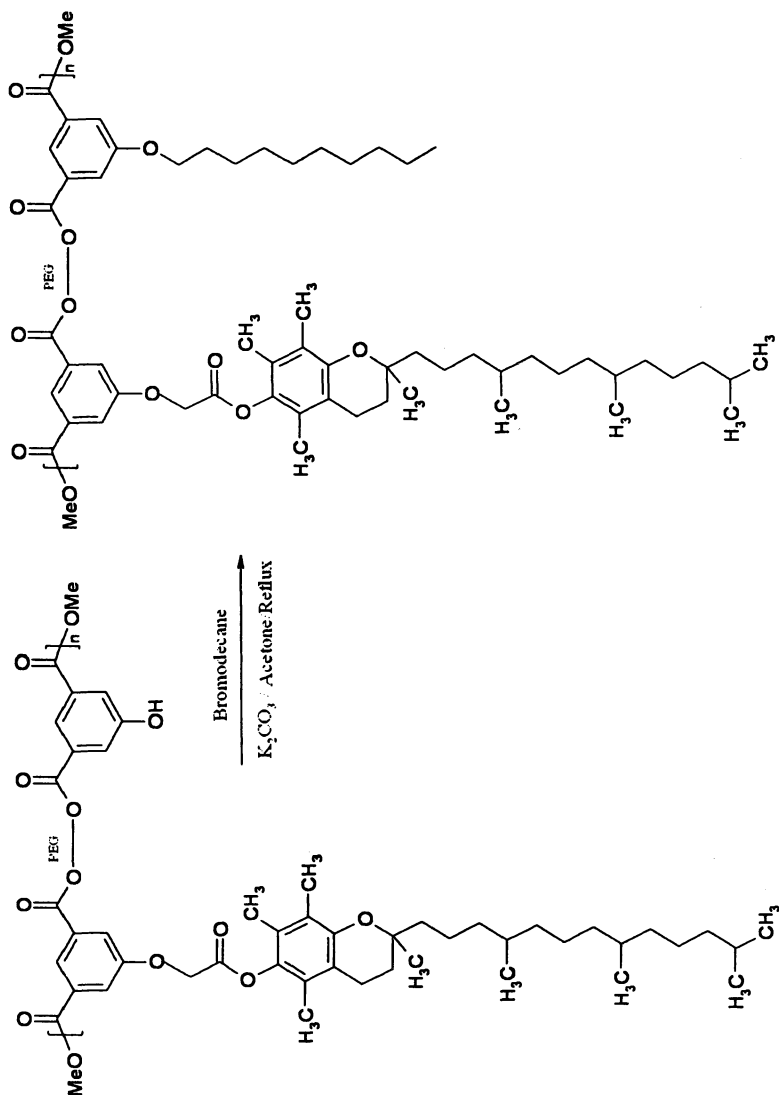
The standard of care is to blindly treat with chemotherapy selected by convention using prior retrospective studies and to consider this treatment a success or failure only in retrospect (e.g., failure is when a relapse occurs in less than 5 years). Residual metastatic disease can expand undetected. When metastatic disease leads to a tumor that is large enough to be detected (stage 4), it is often too late for anything but a modest extension in patient lifetime with available treatments. Research over the past three decades has led to unimagined progress in understanding of the cancer process at the genetic, molecular, and cellular levels. Search for the most effective ways to apply these insights to the prevention, early detection, and management of cancer as a disease process, has led to integration of science and technology. Nanotechnology has emerged as a key strategy for imaging telltale molecular features of cancer that are notoriously difficult to detect.

Supra-molecular assemblies that can be made to form nanospherical structures for carrying a contrast agent or drug, such as liposomes (40,41) and

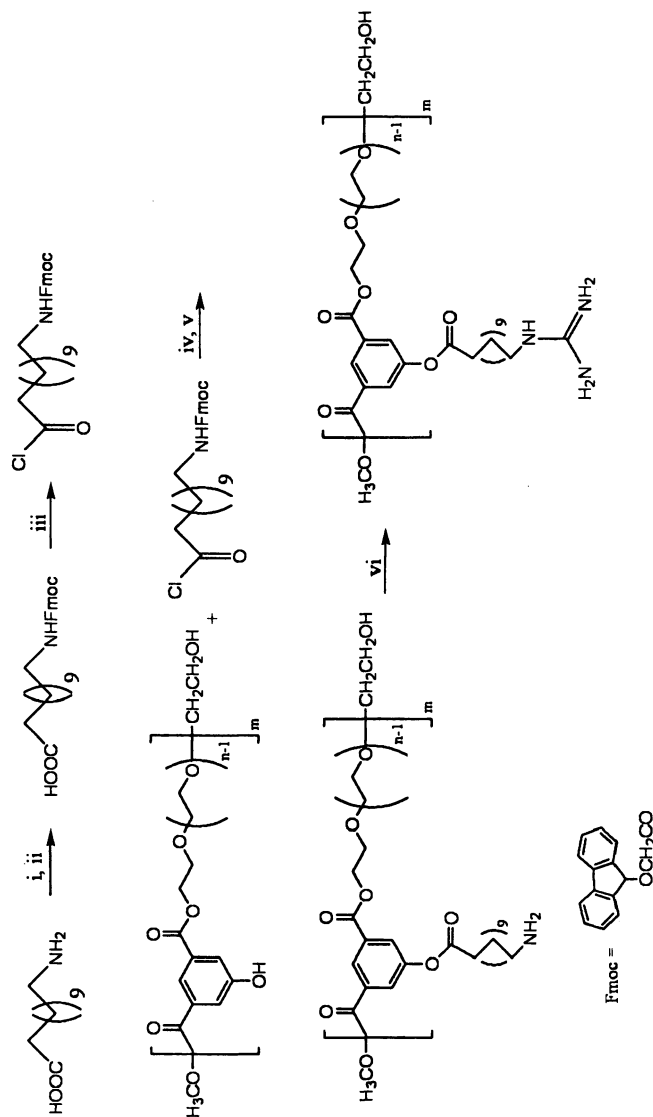




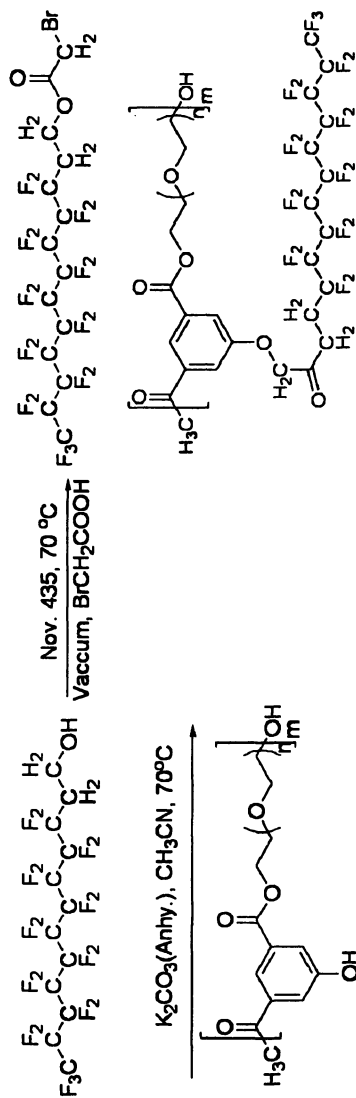
Scheme 4. Synthesis of Vitamin E conjugated copolymer of dimethylisophthalate and PEG600



Scheme 5. Synthesis of amphiphilic polymer containing vitamin E



Scheme 6. Synthesis of cationic amphiphilic polymers for gene delivery.



Scheme 7. Synthesis of perfluorinated amphiphilic polymers.

polymer micelles (42,43), offer potential for improving various imaging modalities and therapeutic drug delivery. With a few exceptions, results with liposomes have been disappointing (44). Our research focuses over the last couple of years have been in the area of nano drug delivery systems (45-47). We have successfully developed and used nano drug delivery systems for the encapsulation and transport of various bioactive compounds. We understand that the key problem in the treatment of cancer is the limitation with current imaging techniques for detecting cancer in very early stages and treating it. This has lead us to design and develop a nano platform, capable of not only imaging cancer cells but also deliver the therapeutics for destroying these cancerous cell.

A novel nanotechnology platform for *in vivo* imaging and delivery of multifunctional thererapeutics of cancer has been designed based on perfluorinated amphiphilic copolymers. We chose perfluorinated polymers because of the several advantages:

- (1) It makes use of ^{19}F -MRI, which allows for much better signal-to-noise ratio and greater sensitivity compared to protons because of the absence of ^{19}F background signals in the tissues.
- (2) The fluorine is prepared at high concentration in the form of a perfluorocarbon contained within unique self-assembling nano polymeric micelles that is small enough to be taken up by cells.

The perfluorinated amphiphilic polymer was synthesized using a chemoenzymatic methodology as shown in Scheme 7 (48). This designed nano probe is highly unique because of its ability to image and treat the cancer tumor by delivering the drugs to the cancer tumors. The methodology developed for the synthesis of perfluorinated copolymers is highly flexible and efficient. The *in vitro* and *in vivo* studies on these nano probes are in progress.

Conclusions

In summary, we have developed green route to pegylated amphiphilic polymers with the use of immobilized enzyme *Candida antartica* lipase. The ability of these polymers to form the nano-micelles has given them enormous potential for application not only in drug delivery but also in the diagnosis of cancer by imaging which is an important tool used to determine the stage (tell how advanced the cancer is) and the precise site of cancer, to aid in directing surgery and other cancer treatments, and to check to see if cancer is recurring.

References

1. The therapeutic index of a drug is defined as the ratio of the toxic dose to the therapeutic dose.

2. The term “polymer therapeutics” was coined by Helmut Ringsdorf and Ruth Duncan. Other research groups use the more general term “nanomedicine”.
3. Gros L.; Ringsdorf H.; Schupp H.; *Angew. Chem.* **1981**, *93*, 311.
4. Duncan R.; *Nat. Rev. Drug Discovery* **2003**, *2*, 347.
5. R. Duncan in *Encyclopedia of Molecular Cell Biology and Molecular Medicine*, Vol. 14 (Ed.: Meyers R. A.) Wiley-VCH, Weinheim, **2005**, pp. 163.
6. Gross, R.A.; Kumar, A.; Kalra, B. *Chem. Rev.* **2001**, *101*, 2097.
7. Kobayashi, S.; Uyama, H.; Kimura, S. *Chem. Rev.* **2001**, *101*, 3793.
8. Drauz, K.; Waldmann, H. *Enzyme Catalysis in Organic Synthesis*, **2002**, Vol. I Wiley-VCH, Weinheim.
9. Khmel'nitsky, Y.L.; Rich, J.O. *Curr. Opin. Chem. Biol.* **1999**, *3*, 47.
10. Carrea, G.; Riva, S. *Angew. Chemie Int.* **2000**, *39*, 2226.
11. Danprasert, K.; Kumar, R.; Cheng, M.H.; Gupta, P.; Shakil, N.A. Prasad, A.K.; Parmar, V.S.; Kumar, J.; Samuelson, L.A.; Watterson, A.C. *Euro. Poly. Journal*, **2003**, *39*, 1983.
12. Topchiyeva, IN.; *Polym Sci USSR* **1990**, *32*, 833.
13. Zalipsky, S.; Lee, C.; Harris, J.M; Poly (ethylene glycol) chemistry: biotechnical and biomedical applications. New York: Plenum Press; **1992**. p. 347.
14. Zalipsky, S; Gilon, C; Zilkha, A.; *Eur Polym J.* **1983**, *19*, 1177.
15. Harris, J.M.; *J Macromol Sci, Rev Macromol Chem Phys* **1985**, *C25*, 325.
16. Cecchi, R.; Rusconi, L.; Tanzi, M.C; Danusso, F.; *J Med Chem* **1981**, *24*, 622.
17. Zunino, F.; Pratesi, G.; Micheloni, A.; *J Controlled Release* **1989**, *10*, 65.
18. Abuchowski, A.; Davis, F.F.; Holsenburg, J.; Roberts, J.; editors. *Enzymes as drugs*. New York: Wiley; **1981**. p. 367.
19. (a) Cameron, N.S.; Corbierre, M.K.; Eisenberg, A.; *Can J Chem* **1999**, *77*, 1311. (b) Gref, R.; Minamitake, Y.; Peracchia, M.T.; Trubestskoy, V.; Torcchilin, V.; Langer, R.; *Science* **1994**, *263*, 1600. (c) Xu, R.; Winnik, A.; Hallett, F.R.; Riess, G.; Croucher, M.D.; *Macromolecules* **1991**, *24*, 87. (d) Kataoka, K.; Kwon, G.S.; Yokoyama, M.; Okano, T.; Sakurai, Y.; *J Controlled Release* **1993**, *24*, 119.
20. Kwon, G.S; Suwa, S; Yokoyama, M.; Okana, T.; Sakurai, Y.; Kataoka, K.; *J Controlled Release* **1994**, *29*, 17.
21. Gao, Z.; Varshney, S.K.; Wong, S.; Eisenberg, A.; *Macromolecules* **1994**, *27*, 7923.
22. Yu, K.; Eisenberg, A.; *Macromolecules* **1996**, *29*, 6359.
23. Kwon, G.S.; Naito, M.; Okano, T.; Colloid, Surf.; *B: Biointerfaces* **1994**, *2*, 429.
24. Kwon, G.S.; Kazunori, K.; *Adv Drug Deliver Rev* **1995**, *16*, 295.
25. Piskin, E.; Kaitian, X.; Kucukyavuz, Z.; *J Biomater Sci Polym Edn* **1995**, *7*, 395.

26. Cameron, N.S.; Corbierre, M.K.; Eisenberg, A. *Can J Chem* **1999**, *77*, 1311; b) Gref, R.; Minamitake, Y.; Peracchia, M.T.; Trubetsky, V.; Torchilin, V.; Langer, R. *Science*, **1994**, *263*, 1600; c) Xu, R.; Winnik, A.; Hallett, F.R.; Kwon, G.S.; Yokoyama, M.; Okano, T.; Sakurai, Y. *J Controlled Release* **1993**, *24*, 119.
27. Kwon, G.S.; Suwa, S.; Yokoyama, M.; Okano, T.; Sakurai, Y.; Kataoka, K. *J Controlled Release* **1994**, *29*, 17.
28. Gao, Z.; Varshney, S.K.; Wong, S.; Eisenberg, A. *Macromolecules* **1994**, *27*, 7923.
29. Yu, K.; Eisenberg, A. *Macromolecules* **1996**, *29*, 6359.
30. (a) Burchard, W.; *Adv. Polym. Sci.* **1983**, *48*, 1. (b) Checot, F.; Lecommandoux, S.; Gnanou, Y.; Klok, H. A. *Angew. Chem., Int. Ed.* **2002**, *41*, 1339.
31. Reader, D. J. *New Engl. J. Med.* **2000**, *343*, 1179.
32. Alaimo, N. L.; Alves, V. L.; Phillips, D. R. *Circulation* **2003**, *107*, 1123.
33. Berges-Gimeno, M. P.; Simon, R. A.; Stevenson, D. D. *Ann. Allergy, Asthma, Immunol.* **2003**, *90*, 338.
34. Mainous, A. G.; Pearson, W. S. *Fam. Med.* **2003**, *35*, 112.
35. Papa, V.; Milazzo, G.; Santocono, M.; Servolle, V.; Sourdille, P.; Santiago, P. Y.; Darondeau, J.; Cassoux, N.; LeHoang, P. J. *Cataract Refract. Surg.* **2002**, *28*, 321.
36. Makarowski, W.; Zhao, W. W.; Bevirt, T.; Recker, D. P. *Osteoarthritis Cartilage* **2002**, *10*, 290.
37. Collantes, E.; Curtis, S. P.; Lee, K. W.; Casas, N.; McCarthy, T.; Melian, A.; Zhao, P.; Rodgers, D.; McCormick, C.; Lee, M.; Lines, C.; Gertz, B. *BMC Fam. Pract.* **2002**, *3*, 1
38. Sharma, S.K.; Sharma, A.K.; Kumar, R.; Parmar, V.S.; Samuelson, L.A.; Kumar, J.; Watterson, A.C. *Polymer Preprints* **2003**, *44*, 791.
39. Sharma, S.K.; Sharma, A.K.; Samuelson, L.A.; Kumar, J.; Watterson, A.C.; Parmar, V.S. *J. Macromol. Sci.-Pure Appl. Chem.* **2004**, *A41*, 1459.
40. Caride, V. J. *Critical Reviews in Therapeutic Drug Carrier Systems* **1985**, *1*, 121.
41. Phillips, W. T. *Advanced Drug Delivery Reviews* **1999**, *37*, 13.
42. Trubetsky, V. S. *Advanced Drug Delivery Reviews* **1999**, *37*, 81.
43. Torchilin, V. P. *Advanced Drug Delivery Reviews* **2002**, *54*, 235.
44. Lasic, D. D. *Handbook of Biological Physics* **1995**, *1*, 491.
45. Kumar, R.; Shakil, N.A.; Chen, M. H.; Parmar, V.S.; Samuelson, L.A.; Kumar, J.; Watterson, A.C. *J. Macromol. Sci.-Pure Appl. Chem.* **2002**, *39*, 1137.
46. Kumar, R.; Chen, M. H.; Parmar, V. S.; Samuelson, L. A.; Kumar, J.; Nicolosi, R.; Yoganathan, S.; Watterson, A. C. *J. Am. Chem. Soc.* **2004**, *126*, 10640.

47. Kumar, R.; Bruno, F.; Parmar, V. S.; Kumar, J.; Watterson, A. C.; Chittibabu, K. G.; Samuelson, L. A. *Chem. Commun.* 2004, 862.
48. Kumar, R.; Tyagi, R.; Parmar, V.S.; Watterson, A.C.; Kumar, J.; Zhou, J.; Hardiman, M.; Colton, C.K. *Polymer Preprints* (American Chemical Society, Division of Polymer Chemistry) **2005**, 46(2), 623.

Chapter 13

Novel Two-Photon Activated Photodynamic Therapy Agents: Design, Synthesis, and Preclinical Studies on Subcutaneous Cancerous Tumors

Aijun Gong¹, Fanqing Meng¹, Jean R. Starkey²,
Britney L. Moss², Aleksandre Rebane², Mikhail Drobizhev²,
and Charles W. Spangler^{3,*}

¹MPA Technologies, Inc., 2100 Fairway Drive, Suite 104,
Bozeman, MT 59715 (gongaj@yahoo.com)

²Montana State University, Bozeman, MT 59715

³Rasiris, Inc., Seattle, WA 98154 (spangler.charles@gmail.com)

A new highly innovative two photon activated photodynamic therapy (PDT) triad agent has been synthesized successfully, which incorporates three different functional moieties: (1) photosensitizer: a porphyrin that has been substituted on the meso positions by chromophores with large two-photon absorption and activated in the NIR in the tissue transparency window and efficiently producing singlet oxygen as the cytotoxic agent; (2) a small molecule targeting agent that can target over-expressed receptor sites on the tumor, and (3) a NIR imaging agent that can accurately image the tumor for treatment. We have also been able to successfully transfect luciferase genes into model human tumor cell lines (both breast and lung cancers) that allows visualization of the efficacy of the two-photon PDT process.

Introduction

Photodynamic therapy (PDT) as a method of cancer treatment has been improved dramatically over the past decade (1-2). Compared to other methods of treating cancerous tumors, such as the standard surgery, chemotherapy, radiation protocol, PDT is a more benign treatment that provides the patients a noninvasive alternative to surgery. The aware of its definition is necessary to make a clear understanding of the issue addressed in this paper. Raymond Bonnett (3) described that photodynamic therapy (PDT) is a part of photochemotherapy, where, in addition to light and an administered drug (photosensitizer), oxygen is also required. Photosensitizer is the core element in PDT treatment. In this case, the photosensitizer is excited by the light and induces the formation of singlet oxygen which causes cellular damage and death.

The phenomenon of photodynamic effect was first observed in 1990 by a medical student, Raab in the group of Von Tappeiner in Munich, who found that acridine (Figure 1) killed paramecia (a freshwater ciliate protozoan), but only in the presence of daylight (4). A few years later Jodlbauer and Von Tappeiner demonstrated that oxygen was crucial for this effect (5). They were also the first two who investigated treatment of cancer in this way, by using fluorescein derivatives, including eosin, in patients with basal cell carcinoma. The sensitizer was applied at or near the skin by brushing or local injection, while an arc lamp or sunlight was used as the light source. Since then second and third generation photosensitizers with improved properties for photodynamic therapy have continued to be developed. At the same time, light sources have also improved to include laser and NIR diode irradiation.

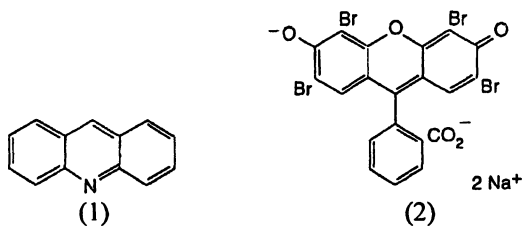


Figure 1. The molecular structure of acridine (1) and Eosin Y (2).

The first generation of tumor photosensitizers (1961-1983) were based on haematoporphyrin (Figure2), The current era of PDT began with studies by R. L. Lipson and S. Schwartz at the Mayo Clinic in 1960 who observed that injection of crude preparations of hematoporphyrin led to fluorescence of neoplastic lesions visualized during surgery. To gain an optimal tumor localizing preparation. Schwartz treated hematoporphyrin with acetic acid and sulfuric acid and obtained

a porphyrin mixture that he termed "heamatoporphyrin derivative" (HpD), which were used by Lipson et al. for tumor detection. A commercial sample used without purification consists of at least 15 different porphyrins, and its commercial name is Photofrin® in USA. It is the first drug to receive regulatory approval for PDT applications as easy made effective PDT photosensitizer. The complex mixture Photofrin®'s activity was modest and selectivity was poor, which reduced its cure efficacy. When Photofrin was injected into human tissue, it usually need 40-50 hours to accumulate on cancerous cell and over 30 days to excrete completely from human body. What's more, the weakest absorption band in the red (ca. 630 nm) not only compensated for by using high doses of drug and light, but also confined the light's penetration depth (only in millimeter) in tissue.

The second generation (1980 onwards) of PDT photosensitizers belonged to the synthesised tetrapyrrole class, such as porphyrins, chlorins, bacteriochlorins, phthalocyanines and other systems. Chlorines, bacteriochlorins have strong absorption band in the red region, and are one photon excitation photosensitizers for PDT. Phthalocyanines and porphyrins are efficient photochemical generators of singlet oxygen, and non-toxic in the absence of light, But most are activated at wavelength below 700nm.

Figure 3 shows the schematic of the energy levels for porphyrin photosensitizer and molecular oxygen of PDT treatment, where the photosensitizer is injected into a patient's blood stream, then is activated first by a visible light, usually by laser irradiation at the tumor's location (6) raising the photosensitizer to a short-lived excited state S_1 from its ground state S_0 . After a few nanosecond, the porphyrin undergoes an intersystem crossing to a triplet state T_1 with a lower energy than the S_1 state and with a much longer life time (milliseconds). From the triplet state, the energy is transferred to omnipresent oxygen molecules in the tumor blood supply by switching them from a triplet ground state $^3\Sigma_g^-$ into an excited state $^1\Delta_g$ with excitation energy of $94 \text{ kJ}\cdot\text{mol}^{-1}$. Once in the excited singlet state, the extremely reactive oxygen initiates apoptosis or necrosis in its surrounding tissue cells. A presence of excited singlet oxygen molecules ($^1\Delta_g$) in solution is usually detected by their $^1\Delta_g \rightarrow ^3\Sigma_g^-$ luminescence at about 1270 nm.

As photosensitizer candidates, how may porphyrins be improved? Based on all factors mentioned, an ideal photosensitizer, first of all, is the sensitizer that should have low or zero toxicity in the dark. Second, favourable pharmacokinetic behaviour is needed to foster selectively for tumor over normal tissue, and fast clearance after treatment to reduce generalized photosensitivity. This behavior appeared to be related to amphiphilic properties. It is clearly advantageous if the synthesis is straightforward. it is desirable that the sensitizer has a high triplet quantum yield, a triplet energy $> 94 \text{ KJ/mol}$ (the excitation energy required to generate singlet oxygen), and efficient energy transfer to produce singlet oxygen. Finally, strong absorption should occur in the near infrared (NIR), i.e. tissue transparent window (800-1000nm), since this is the part of spectrum where tissue transmits most effectively.

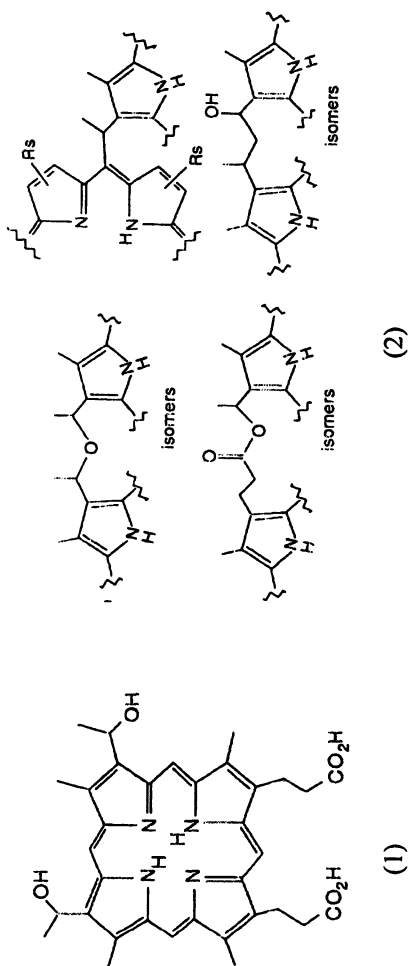


Figure 2. The structure of Haematoporphyrin (1) and its derivative HpD (photofrin)® (2).

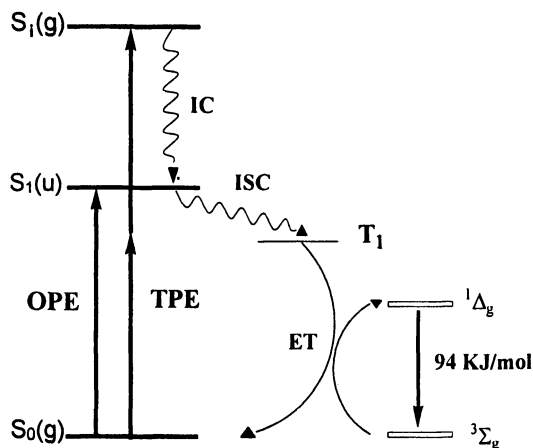


Figure 3. Schematic of the energy levels for porphyrin photosensitizer (solid bars) and molecular oxygen (open bars).

Though traditional porphyrins meet most of the required conditions, for example, they can be synthesized in high purity with constant composition, produce enough singlet oxygen to exhibit a cytotoxic effect and have low toxicity in the dark, porphyrins are the ideal candidates for PDT. However, there are still problems that need to be overcome if porphyrins can be considered to act as an ideal photosensitizer. One problem is its selectivity, accumulation rate before treatment and clearance time after treatment. At current time, it usually requires 24–96 hours for photosensitizers to accumulate at tumor sites. The other problem is activation wavelength used in PDT. Efforts have been done to shift the absorption band of porphyrin to red region. Currently FDA-approved PDT agents are limited to visible light activation at wavelengths below 700 nm, limiting the penetration depth to ca. 2–4 millimeters level, which is insufficient to treat typical deep subcutaneous cancerous tumors. In order to improve the efficacy of PDT treatment, it would be desirable to shift the irradiation wavelength to longer wavelengths in the tissue transparency window (700 – 1000 nm) (7). The revolution in design of new photosensitizers come from enhancing the intrinsic two-photon cross-sections, thus allowing porphyrin activation in the 780–900 nm region of the NIR spectrum. Two-photon absorption is a nonlinear optical process in which two photons are absorbed simultaneously, promoting the molecule to the excited state, however in order for this event to occur, the light must be tightly focused in 3D space. The high degree of focus on a target point can thus prevent damage to healthy adjacent tissue, and defines the margins of the PDT treatment protocol (see Figure 4).

Experimental and Discussion

Two photon Excited photodynamic therapeutic agent on Cancer

Since two photon excited PDT in the NIR region has obvious advantages over one-photon excitation, such as deeper penetration through the tissue, and high spatial resolution in sensitive tissue due to small focal volume, it would be an effective alternative way for PDT treatment. As the TPA cross-sections of most known porphyrin photosensitizers are too small (usually less than about $1\sim 10$ GM, $\text{GM}=10^{-50} \text{ cm}^4 \text{ s photon}^{-1} \text{ molecule}^{-1}$) to be of practical use, this requires that high intensity of laser light be used to active them which may induce hyperthermia or unreasonable prolonged laser irradiation times. Though some non-porphyrin organic systems have been developed recently that possess very high TPA cross-sections (8), their quantum efficiency of singlet oxygen generation are not satisfactory and their long-term interaction with biological tissue is unknown (9).

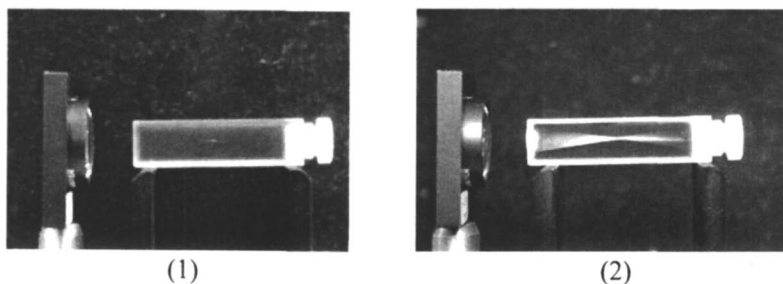


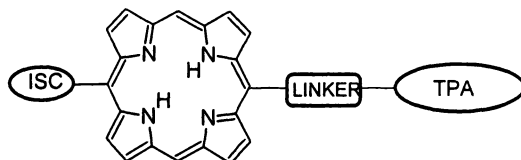
Figure 4. Chromophore excited by laser: two photon absorption (1) and one photon absorption (2).

Over the past four years we have been developing a new approach to the design of effective two-photon PDT agents using a triad concept that incorporates three components for the noninvasive treatment of subcutaneous tumors into a single therapeutic agent: tumor targeting, tumor imaging and direct two-photon PDT treatment of the imaged tumor (10-11). We reported here the design and synthesis of a novel substituted porphyrins with greatly enhanced two-photon cross sections, and corresponding nano-ensemble triads composed of a small molecule targeting agent and a NIR imaging agent combined with the porphyrin in a single therapeutic agent. This triad approach overcomes several of the disadvantages of one photon PDT agents including targeting of the tumor, discrimination between healthy cells and tumor cells allowing cleaner treatment margins, the capability of

imaging the tumor in real time, and the ability to treat tumors in the tissue transparency window. The efficacy of this ensemble in the two-photon PDT treatment of a human breast cancer tumor model (MDA-MB-231) implanted in SCID mouse mammary fat pads will be discussed below.

Porphyrins with enhanced large two-photon absorption

Since 2003 we have designed and synthesized a series of triphenylamine substituted oligomer chromophores with large two photon absorption cross sections, and by combining these oligomers into porphyrin structures, novel porphyrins with large two-photo excitation cross section were produced. We designed carefully the synthetic approach of this kind of novel asymmetrical porphyrin by coupling a substituted bilane with different aldehydes incorporating chromophores with large two photon absorption cross section, either by direct connection, or by using ethenyl or ethynyl linker groups. These donor substituents are incorporated on porphyrin *meso*- positions, and a 2, 6-dichlorophenyl group arranged on the opposite *meso*- position to facilitate the intersystem crossing (ISC) to the triplet state *via* an internal heavy atom effect that increases the singlet state quantum yield. Our research work has shown that by careful chemical modification of the porphyrin design we can increase dramatically the porphyrin's intrinsic TPA response by 2 orders of magnitude i.e., their intrinsic two-photon cross-sections for femtosecond pulses in the NIR are between 500-1000 GM units (US Patent 6,953,570) with high singlet state oxygen quantum yields around 0.8. TPA cross-section has been measured by comparing the sensitizer fluorescence intensity under two- and one-photon excitation conditions. Quantum yields of singlet oxygen production were measured by a relative method compared to tetra-phenylporphyrin (H₂TPP) as a standard reference (Φ_{Δ} of 0.68) in toluene. The steady-state spectra of $^1\Delta_g \rightarrow ^3\Sigma_g^-$ molecular oxygen luminescence at 1276 nm in air-saturated toluene were detected with a liquid nitrogen-cooled Ge detector coupled with a monochromator and a lock-in amplifier. The laser system comprised a Ti:sapphire regenerative (CPA-1000, Clark MXR), which was operated at 1 KHz repetition rate and produced 150-fs pulses at 780 nm. The instrument ensemble and experimental setup have been previously described (12). A model molecular structure is shown in (Scheme 1):



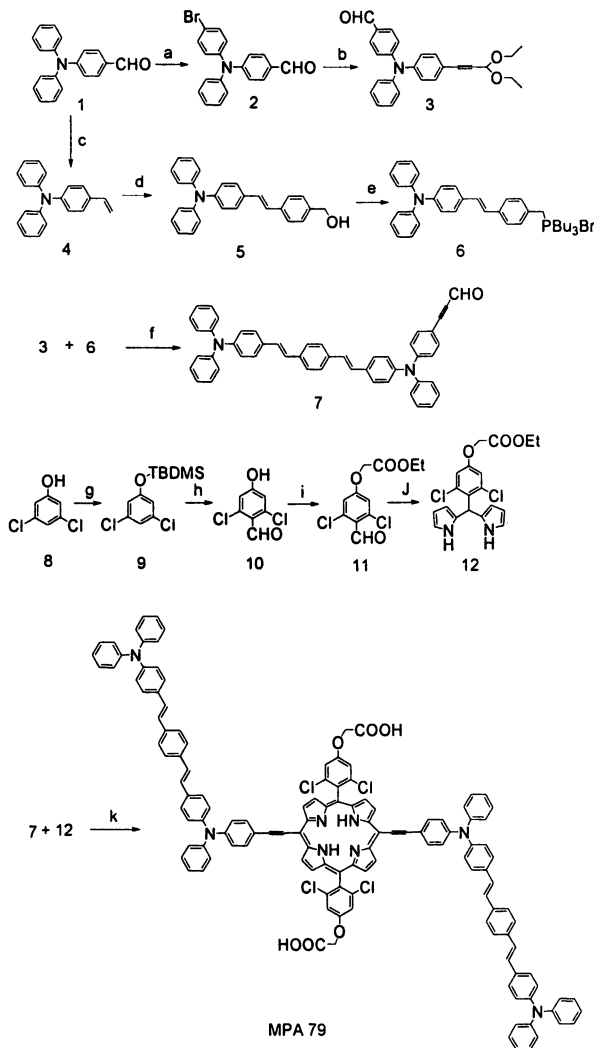
Scheme 1. Model structure of two photon excited Porphyrin.

We employed one optimized porphyrin as our target photosensitizer (MPA79) (its molecular structure and synthetic approach are shown in Scheme 2). Its TPA moiety is based on functionalized diphenylaminophenylenevinylene repeat units and it was obtained by condensing *meso*-[4-(ethyl acetate)oxy-2, 6-dichlorophenyl] dipyrromethane with aldehyde incorporating an ethynyl linker group under acidic conditions, followed by oxidation with 2, 3-dichloro-5, 6-cyano-1, 4-benzoquinone (DDQ). It was purified by column chromatography on silica gel using 40~50% methylene chloride and hexanes as eluent. MPA 79 was obtained in a moderate yield of 26.8 % at low temperature catalyzed by $\text{BF}_3 \cdot \text{Et}_2\text{O}$ following hydrolysis with ethanolic KOH solution in DMF. Its structure was confirmed by UV-VIS-NIR, ^1H and ^{13}C high field NMR as well as MALDI-TOF Mass Spectrometry.

Novel triad PDT agent – two photon excited photosensitizer with targeting and imaging agents

Classical PDT suffers from the lengthy time necessary for accumulation at the tumor site, a relative lack of discrimination between healthy and diseased tissue, particularly at the tumor margins, and difficulty in clearing from the system in a reasonable amount of time. To address these problems and considering the clinical requirements for MPA79, we designed an efficient way for making the multifunctional triad named as RA-301 (Scheme 3), which chemically conjugated a targeting agent, a NIR imaging agent to our proprietary therapeutic porphyrin photosensitizer. The targeting component would direct this ensemble to over-expressed receptor sites on the tumor surface. Once accumulated at the tumor site, the tumor could be imaged using NIR wavelengths in the tissue transparency window, and the tumor image can be potentially used to guide the two-photon PDT treatment. We chose a small cycle peptide (octreate) as our targeting moiety as it is known to target SST2 and SST5 somatostatin receptors, and is well characterized in the literature. Similarly, we utilized indodicarbocyanine and indotricarbocyanine imaging agent as their fluorescence output could easily be detected with our Kodak 2000MM Image Station.

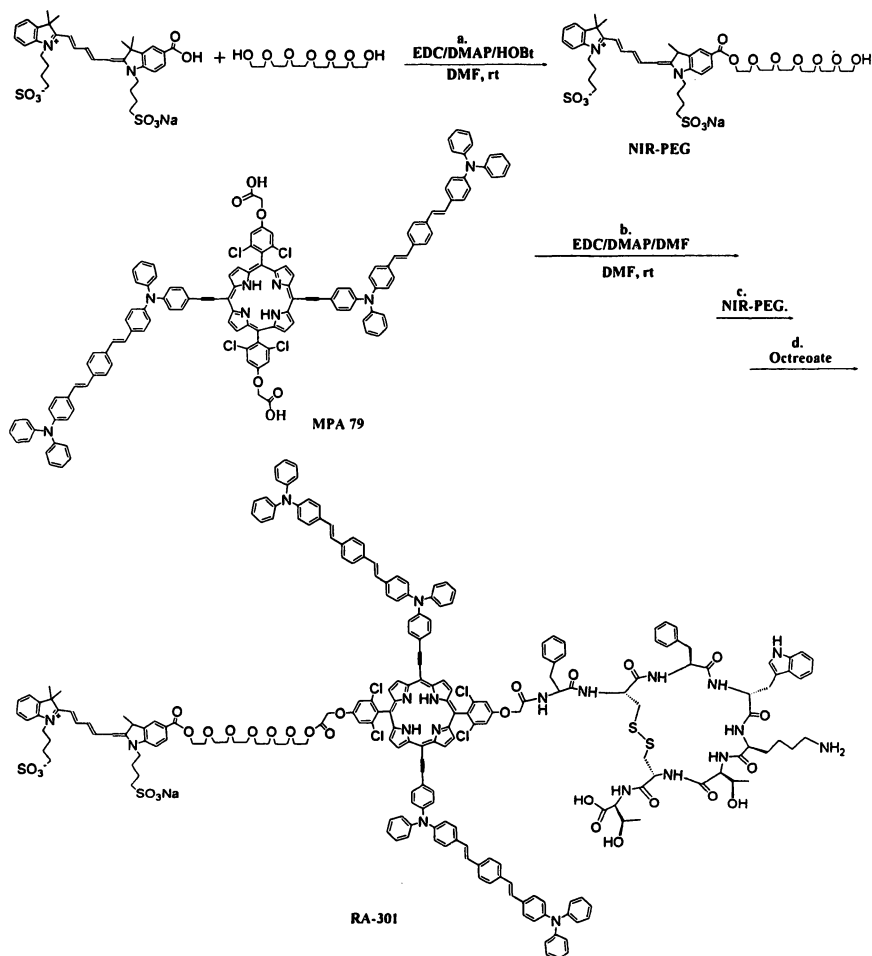
For constructing the triad photosensitizing drug, we designed several bioconjugation processes to complete these couplings, and found an efficient way to construct the triad. We first modified the carboxylic acid group of imaging agent (indodicarboxycyanine) with a hexa (ethylene glycol) as a spacer under the coupling reagent EDC and DMAP in dried DMF, and indocarboxycyanine-PEG was obtained in good yield after purification by silica gel chromatography with the elution of water/methanol (5/1). Then both of carboxylic acid groups on MPA 79 were activated in the same time in EDC and DMAP in anhydrous DMF dilute solution, which was first added and reacted with indocarboxycyanine-PEG stoichiometrically, then the octreate peptide was added following the completion of the first coupling. After precipitation in methanol three times, the dark green



Reaction conditions: (a): NBS, AcOH/CHCl₃, rt., 98.3 %; (b): Pd(PPh₃)₂Cl₂, CuI, Et₃N, Propargylaldehyde diethyl acetal, reflux, 50.0 %; (c): MePPh₃Br, KO^tBu, THF, rt., 75.9 %; (d): 4-Bromobenzylalcohol, Pd(OAc)₂, P(tri-*o*-tolyl), Et₃N, CH₃CN, reflux, 73.8 %; (e): i, PBr₃, THF, 0 °C, 100 %; ii, PBU₃, toluene, reflux, 87.2 %; (f): i, KO^tBu, THF; ii, 10 % H₂SO₄, THF, reflux, 41.3 % over two steps; (g): *tert*-Butyldimethylsilyl chloride, imadazole, DMF, 0 °C, 97.6 %; (h): i, *sec*-BuLi, DMF, THF, -78 °C; ii, 3 M HCl, 95.0 % over two steps; (i): Ethyl Bromoacetate, K₂CO₃, KI, DMF, 0 °C, 85.4 %; (j): Pyrrole, TFA, rt, 51.0 %; (k): i, BF₃·Et₂O, CH₂Cl₂, DDQ, TEA, -30 °C, 26.8 %; ii, 1 M KOH in Ethanol, DMF, 80 °C, 100 %.

Scheme 2. Synthetic approach of novel photosensitizer: MPA 79

triad drug was obtained in high yield. Its structure was established and confirmed by UV-VIS-NIR, and MALDI-TOF-MS. Its intrinsic TPA cross section is 800 GM (an acceptable value for PDT) at 850 nm with 150 fs ultrafast laser pulses. This triad is not soluble in water and methanol but moderately soluble in solutol (an FDA-approved excipient), and can be administered to the tumor-bearing mice via tail vein injection, or into the tumor directly. The reaction scheme of this novel photosensitizer RA-301 is also shown in Scheme 3.



Experiment conditions: (a) EDC, DMAP, HOBt, DMF (anhydrous), rt, 24 hours, 89%; (b) EDC, DMAP, DMF (anhydrous), rt, 30 min, (c) NIR-PEG, DMF, rt, 72 hours; (d) Octreotate, DMF, rt, 72 hours, 80 % in overall of crude product.

Scheme 3. RA-301 triad with substituted porphyrin incorporating octreotate peptide and indocarbocyanine

Pre-clinical results on breast-cancer cell line

In Figure 5, results from comparing cell kill in the phantoms (The phantoms were constructed of rat-tail collagen (2 mg/mL) to which 40% Liposin was added as a scattering agent, and 25 mM hemoglobin as an absorbing component.) are illustrated. As can readily be seen from this graphical illustration, efficient killing of the MDA-MB-231 cells (human breast cancer cell) infused with RA-301 is observed at 1, 2, 3 and 4 cm using laser light at 780 nm, 150 fs pulses for 15 minutes. Although we have not yet constructed phantoms of greater depth, the slope of the curve implies that we can expect efficient cell kills at greater depth. It should be noted that in the irradiation of the cell phantoms that had incorporated RA-301, that the efficiency of cell killing was independent of whether the irradiation was carried out using an air interface between the laser and the phantom surface, or whether the irradiation was carried out through freshly excised mouse skin. Cell kills at 2 cm in both cases was >80%. However it is clear that in comparison experiments using Photofrin®, cell kill falls off dramatically as a function of depth in the phantom, and when Photofrin® is excited through mouse skin, cell kill is severely reduced. As will be seen in our discussions of the treatment of tumor bearing SCID mice (Figure 5), this observation implies that two-photon irradiation of subcutaneous tumors directly through the skin can be an efficient process. Irradiation of cell phantoms that had incorporated Photofrin® on the other hand, show a marked decrease in PDT efficacy when the irradiation is carried out through mouse skin, with very little cell kill observed for depths beyond 1 cm.

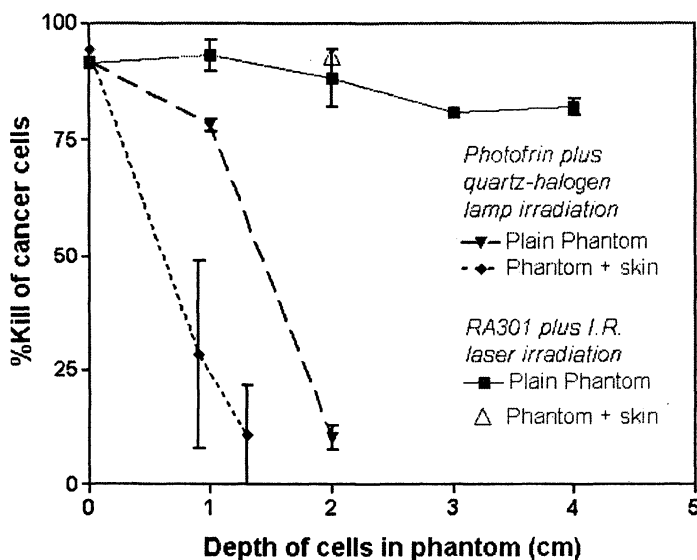


Figure 5. Comparison of PDT cell killing efficiency in collagen phantoms.

We have previously reported transfection of luciferase genes into MDA-MB-231 cell lines, and we have grown tumors incorporating this bioluminescent feature in the mammary fat pads of SCID mice. In Figure 6 we illustrate a series of irradiation experiments in which we measure the bioluminescence emanating from tumors incorporating RA-301, with and without radiation, and compared to control mice that received neither RA-301 nor irradiation. Note that only the tumors that had incorporated RA-301, and also received laser irradiation, showed a loss of luciferase signal one day after PDT treatment. Thus the conservation or disappearance of the luciferase signal can be a useful marker of the efficacy of two-photon PDT in animal models without the need to sacrifice large numbers of mice. Mice receiving PDT treatment with RA-301 recovered rapidly, and healing was rapid and uncomplicated. It is not clear at the present time whether disappearance of the luciferase signal is related to antiangiogenic effects or to direct killing of tumor cells. Studies have been initiated to elucidate mechanistic aspects of the mechanism of two-photon PDT, and will be reported in future articles.

Conclusion

A two-photon-activated therapeutic nano-ensemble triad has been synthesized incorporating imaging and targeting moieties and has been used to treat SCID

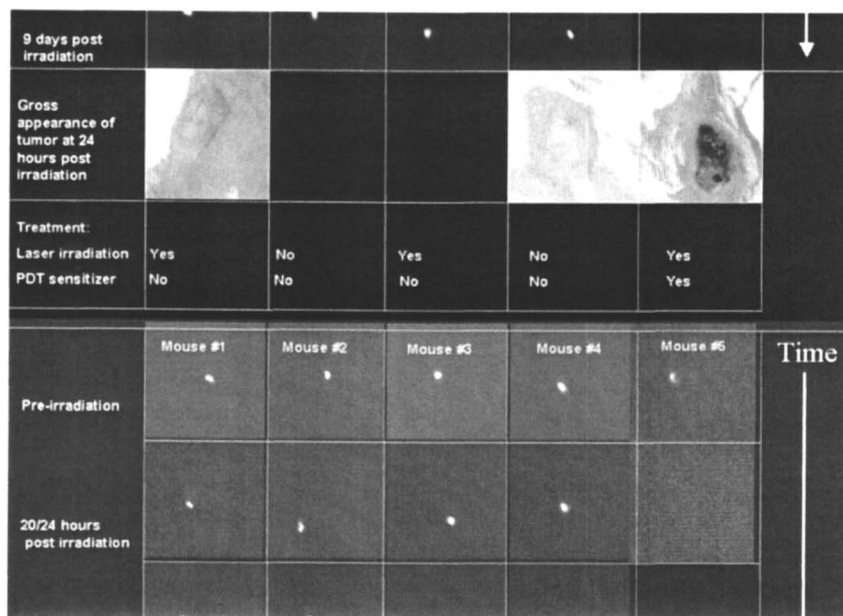


Figure 6. Luciferase activity from luc⁺ MDA-MB-231 tumor bearing mice following two-photon irradiation versus controls.

mice with human breast cancer tumors implanted in the mammary fat pads. In these mouse models we have demonstrated the imaging and direct two-photon PDT treatment of subcutaneous tumors grown from human cell lines without surgical intervention. We have also demonstrated that this new triad is efficient in killing human breast cancer cells in scattering/absorbing collagen phantoms to at least 4 cm, which is much more effective than traditional one-photon agents such as Photofrin® under similar experimental conditions, especially when irradiation is carried out directly through skin samples. In order to test the depth efficacy of this treatment protocol, large animal studies (canine) on spontaneous tumors will be carried out in the near future.

Acknowledgements

The authors would like to acknowledge financial support from Pacific Horizon Ventures, and The Montana Board of Research and Commercialization Technology.

References

1. Dennis, E.J.G.J. D.; Dai, F.; Rakesh, K. J. *Nature*, May 2003, 3, 380.
2. Korbelik, M.; Sun, J.H.; *Cancer Immunol. Immunother.* 2006, 55 (8), 900.
3. Bonnett, R. *Rev. Contemp. Pharmacother.* 1999, 10 (1), 1.
4. Baab, O. Z. *Biol.* 1900, 39, 524.
5. Jodlbaucer, A.; Von Tappeiner, H. *Münch. Med. Wochenschr.* 1904, 52, 1139.
6. Karotki, A.; Kruk, M.; Drobizhev, M.; Rebane, A.; Nickel, E.; Spangler, C.W. *IEEE J. Sel. Top. Quant. Electronics*, 2001, 7(6), 971.
7. Wan, S.; Parrish, J. A.; Anderson, R. R.; Madden, M. *Photochem. Photobio.*, 1981, 34, 679.
8. Rumi, M.; Ehrlich, J.E.; Heikal, A.A.; Perry, J.W.; Barlow, S.; Hu, Z.Y.; McCord-Maughon, D.; Parker, T.C.; Rockel, H.; Thayumanavan, S.; Marder, S.R.; Beljonne, D.; Bredas, J.L. *J. Am. Chem. Soc.* 2000, 122, 9500.
9. Frederiksen, P. K.; Jørgensen, M.; Ogiby, P.R. *J. Am. Chem. Soc.* 2001, 123, 1215.
10. Meng, F.Q.; Nickel, E.; Drobizhev, M.; Kruk, M.; Karotki, A.; Dzenis, Y.; Rebane, A.; Spangler, C.W. *Poly. Mater.: Sci. & Eng.* 2003, 89, 462.
11. Spangler, C.W.; Meng, F.Q.; Gong, A.J.; Drobizhev, M.; Aleksander, R.; Karotki, A.; Spangler, B.D.; Suo, Z.Y.; Tarter, E.S. *Functional Nanomaterials*; American Scientific Publications : California, USA, 2005.
12. Mikhail Drobizhev, Aliaksandr Karotki and Aleksander Rebane, *Chem. Phy. Lett.*, 2001, 334(1-3), 76.

Chapter 14

Synthesis and Characterization of Carborane Functionalized Dendronized Polymers as Potential Boron Neutron Capture Therapy Agents

S. Rahima Benhabbour and Alex Adronov*

Department of Chemistry, McMaster University, Hamilton,
Ontario L8S 4M1, Canada

Dendronized carborane containing polymers were successfully synthesized by the “graft-from” approach using a divergent dendron growth up to the fourth generation. Nitroxide mediated polymerization (NMP) proved effective in polymerizing the carborane-functionalized styrenic monomer to produce a well defined polymer with high boron content (~26% B by weight) and narrow polydispersity index (PDI < 1.1). Dendronization of the carborane functionalized polymer was achieved via deprotonation of the acidic carborane proton in the *para* position followed by reaction of the polyanion with a benzylidene protected bisMPA anhydride. Complete removal of the benzylidene protecting group was achieved by a combination of Pd-catalyzed hydrogenolysis and acid-catalyzed deprotection. This chemistry proved effective in the preparation of monodisperse, high-generation hydroxyl-terminated dendrons appended to the carborane-functionalized polymer backbone. The fourth generation polymer, [G-4]-(OH)₁₆, having a molecular weight of 114 kDa, was found to be water soluble at a concentration of 1 mg/mL and afforded a B content of approximately 12% by weight. All of the products were characterized by NMR and SEC.

Introduction

Carborane-containing macromolecules have attracted attention due to the unique properties of the icosahedral boron-rich carborane clusters. Due to the thermodynamic stability of carboranes, these compounds have been postulated as potential flame retardant materials. In addition, the extremely high neutron capture cross section of ^{10}B atoms, the highest of all light elements, not only makes them ideal neutron shields, but also enables their use in chemotherapy (1). Boron Neutron Capture Therapy (BNCT) is one of the most extensively studied experimental methods for tumor treatment. This method relies on the cytotoxic effect produced as a result of the nuclear fission reaction that occurs when a ^{10}B nucleus absorbs a thermal neutron (2). The radiation emitted from this reaction is mainly composed of lithium ions and alpha particles (^7Li and α), which are high linear energy transfer (LET) particles with a significant ability to destroy biological molecules (3). These particles have a penetration path length of about 10 μm in biological tissues, which is approximately equivalent to one cell diameter (4). Therefore, it is theoretically possible to destroy tumor cells without affecting adjacent healthy cells if a sufficiently high ^{10}B concentration is selectively delivered to the tumor cells. This poses a major challenge to BNCT, as it has been difficult to achieve selective delivery of adequate concentrations of ^{10}B , a minimum of 10^9 ^{10}B atoms per cell or approximately 30 μg ^{10}B per gram of tumor tissue (5,6). One of the most effective ways to address this issue is to incorporate a high number of B atoms within drug delivery vehicles (7).

Carboranes have attracted much attention in the synthesis of boron-rich compounds. The high B content within each carborane unit, their high stability in aqueous media, ease of chemical modification, and charge neutrality all make them a very promising tool for BNCT applications (8,9). However, the lipophilic nature of carboranes prohibits their direct intravenous delivery to target tissues. To overcome this difficulty, studies have been focused on the development of drug conjugates capable of combining high B content, water solubility and enhanced specific uptake by tumor tissues. Among these studies, conjugation of carborane units with sugars, peptides, DNA (10), antibodies, liposomes (11), and numerous other compounds has received much attention (6,12,13).

Recently, dendritic macromolecules have been investigated as potential drug carriers due to their well-controlled architecture, monodispersity, multivalency, and unique tendency to adopt a globular shape (14). Several studies have reported the use of dendrimers as systems for drug delivery (15), complexation agents for DNA (16), as catalytic nanoreactors (17), and numerous other applications (18,19). Several examples of carborane-containing dendrimers have also been reported. Of these, the most relevant for BNCT applications is an example using the aliphatic polyester dendrimer backbone, which is water soluble, biocompatible, and biodegradable (13). Although these structures were prepared up to the fifth generation, the molecular weight of these high-

generation structures did not exceed 30 kDa, which is well below the renal filtration cutoff. We therefore have turned our attention to a similar class of branched macromolecules that can more easily reach molecular weights of greater than 100 kDa.

“Dendronized” polymers (19) represent an interesting new class of macromolecules having a unique cylindrical shape and a large number of functionalizable groups at the dendron’s periphery (20). These molecules are a hybrid between dendrimers and linear polymers, exhibiting the potential for producing high molecular weight linear structures while retaining, to some extent, the molecular precision and three-dimensionality of dendrimers. Recently, the preparation of dendronized polymers functionalized with aliphatic polyester dendrons, having a high degree of water solubility, has been reported (20). Herein, we have applied a similar strategy to the synthesis of carborane-containing dendronized polymers as an interesting addition to the family of macromolecules with potential for application to BNCT. As far as the authors know, this is the first report on carborane-containing dendronized polymers, combining high molecular weight, water solubility, high B content, and narrow polydispersity.

Results and Discussion

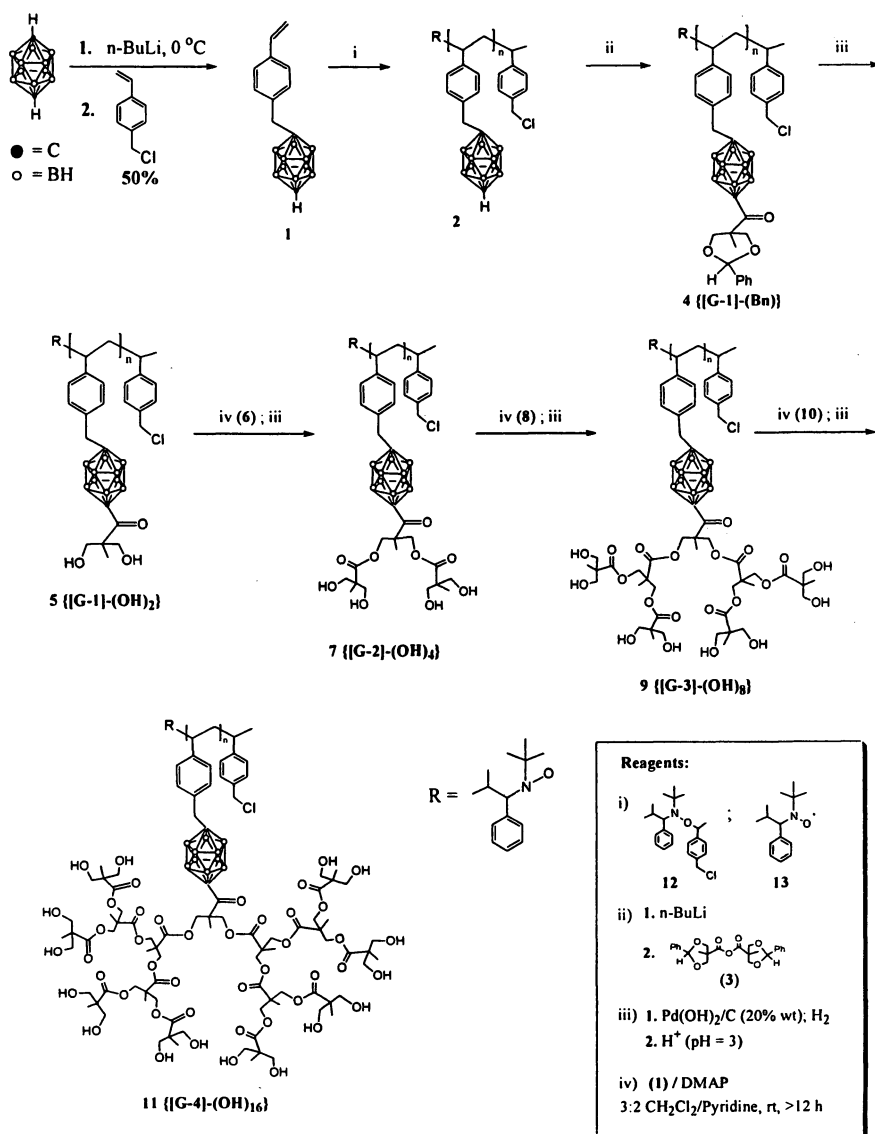
Synthesis of Carborane-containing Monomer (1)

The preparation of dendronized polymers can be carried out in a number of ways, including (a) polymerization of dendron-functionalized macro-monomers, (b) grafting of dendrons to a linear polymer backbone or (c) the divergent dendronization of appropriately functionalized linear polymers. In our present study, we chose to use a combination of methods (b) and (c). This approach involves the initial synthesis of a linear carborane-functionalized polymer, followed by deprotonation of the remaining carbon vertex allowing reaction with an appropriate synthon to install the first dendron generation. Subsequent dendrimer growth steps would allow divergent dendrimer growth, similar to what has been previously reported (20,21). To accomplish this, we began with the preparation of a carborane-functionalized styrene monomer **1**. The preparation of this carborane containing monomer was accomplished by reacting the relatively acidic protons of the *p*-carborane unit ($pK_a = 26.8$) (22) with *n*-butyllithium (*n*-BuLi) in THF to give a statistical mixture of three products, including a monoanion, a dianion, and the starting material (Scheme 1) (13). The anions generated from this reaction were treated with 1 equiv. of 4-vinylbenzyl chloride to give the *p*-functionalized carborane monomer **1** in 50% yield after purification by column chromatography in dichloromethane (Scheme 1).

Polymerization of Macromonomer 1 using NMP. The carborane functionalized polystyrene was synthesized using nitroxide-mediated polymerization (NMP) (23). In the present work, all NMPs were carried out using the alkoxyamine initiator **12**, developed by Hawker and coworkers (24), to afford polymers with narrow PDIs. The alkoxyamine initiator was found effective for the polymerization of monomer **1** under optimized conditions of monomer concentration and polymerization time at 125°C. This procedure resulted in polymers with high molecular weights and narrow PDI, with a typical yield greater than 90% (Table 1). The polymerization involved 80 equiv. of monomer **1** in the presence of 1 equiv. of the alkoxyamine initiator **12** and catalytic amounts of the free nitroxide radical **13** (0.05 mol equiv.) and acetic anhydride (1.8 mol equiv.). After degassing under N₂ for 1 h, the polymerization was carried out for different time periods at 125°C. We have found that higher $M_w > 16$ kDa and narrow PDI < 1.1 were afforded with a monomer concentration of 5.0 M and a polymerization time of 7 h. These optimized conditions were chosen to carry out all further polymerizations. The carborane loaded linear polymer was dendronized with the first generation dendron using a “graft onto” approach followed by an iterative deprotection and coupling approach to yield higher generation dendrons, up to the fourth generation.

Table 1. Optimization of polymerization conditions for the carborane containing monomer 1

Monomer Conc. (M)	Reaction Time (hr)	Polymer M_w (g/mol)	PDI	Nature of Polymer
3.8	12	25,000	1.4	Monomodal
3.8	10	17,800	1.2	Monomodal
3.8	8	16,500	1.09	Monomodal
3.8	7	12,500	1.08	Monomodal
5.0	7	15,200	1.1	Monomodal



Scheme 1. Synthesis of [G-1]-(OH)₂ to [G-4]-(OH)₁₆-Dendronized Polymer

Dendronization of the Preformed Linear Carborane-Functionalized Polymer. NMP proved effective in polymerizing the carborane-functionalized monomer **1** to produce a well defined polymer **2** with high boron content ($M_w = 21$ kDa, PDI = 1.1). Taking advantage of the acidic carborane proton in the para position, this polymer could be dendronized via reaction with anhydride **3**. The polymer was first reacted with a 1:1 stoichiometric ratio of n-BuLi to the remaining carbon vertex proton in THF. The resulting polyanion was subsequently reacted with excess benzylidene anhydride to afford the [G-1]-(Bn) dendronized polymer. The key to the success of this dendronization step was the optimization of the polymer **2** concentration. We have found that when the reaction was carried out at polymer concentrations greater than 0.6 mM, the high anion concentration generated upon deprotonation in the presence of n-BuLi results in gelation and the formation of products having broad, bimodal molecular weight distributions (Table 2). This is likely the result of inter- and/or intramolecular nucleophilic attack of the generated anions onto the chloromethyl end group of the polymer.

The degree of functionalization was determined by ^1H NMR of the preformed polymer **3** prior to and after dendronization. The ratio of the aromatic

Table 2. Optimization of dendronization of preformed carborane containing polymer, SEC analysis.

Polymer M_w (g/mol)	PDI	Polymer Conc. (mmol/L)	Reaction Time (hr)	Nature of Polymer
17,000	1.1	0.88	24	Multimodal
17,800	1.2	1.1	24	Bimodal
12,500	1.08	0.8	24	Bimodal
12,500	1.08	0.4	24	Monomodal
				Very minimal dendronization
15,200	1.1	0.7	24	Bimodal with major peak
15,200	1.1	0.6	24	Monomodal with ~ 70% dendronization

protons from the polymer backbone to the benzylic proton in the protecting group gives the number of functionalized carborane units within the polymer (Figure 1). This analysis indicated that approximately 70% functionalization was achieved. Dendron growth was carried out up to the fourth generation using the iterative esterification and deprotection approach to make aliphatic polyester dendrimers (Scheme 1) (25).

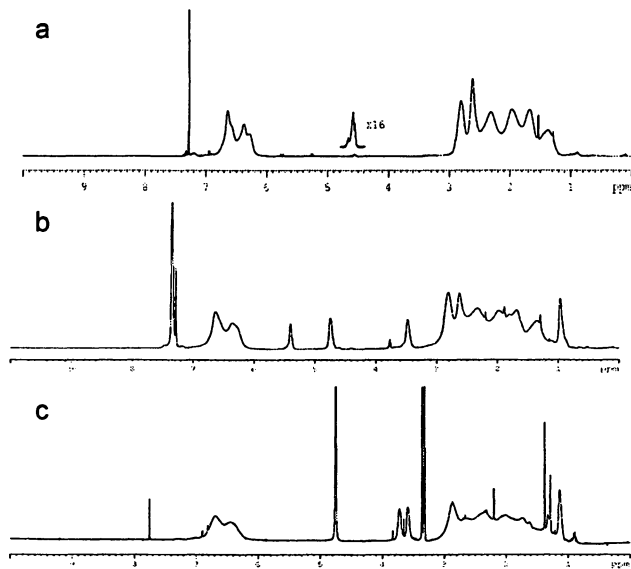


Figure 1. ^1H NMR of: a) [G-0]-polymer, b) [G-1]-(Bn)-dendronized polymer, c) [G-1]-(OH) $_2$ -dendronized polymer.

In our study, although it was necessary to use the acid-catalyzed deprotection to achieve complete conversion, we found it more efficient to carry out a nearly quantitative Pd-catalyzed deprotection first, followed by the acid-catalyzed deprotection. The deprotection reaction was followed by NMR (^1H , ^{13}C , 600 MHz) and SEC analysis to verify the completion of the deprotection, reflected by the absence of the protons from the benzylidene protecting group in the ^1H NMR, as well as the absence of any higher M_w shoulders in the SEC analysis. Therefore, the homogenous acid-catalyzed deprotection was carried out following every hydrogenolysis reaction. The acid-catalyzed step was crucial to drive the deprotection to completion and eliminate the small percentage of trans-acetalization byproduct obtained during the Pd-catalyzed hydrogenolysis (20). It was found that, when this acid-catalyzed step was omitted, it was not possible to achieve complete deprotection, and high-generation dendronized polymers exhibited multimodal molecular weight traces (Figure 2).

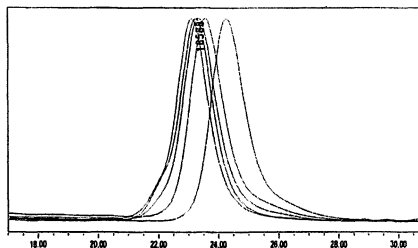


Figure 2. SEC Analysis of [G-1]-(Bn) – [G-4]-(Bn)₈; Generation growth after Pd-catalyzed deprotection followed by acid-catalyzed deprotection.

Molecular Weight Determination by SEC. In this study, SEC was utilized to evaluate the molecular weight of the carborane containing dendronized polymers. The observed M_w values and polydispersity indices (PDI) obtained by SEC are summarized in Table 3. The M_w of the preformed [G-0]-carborane-functionalized polystyrene was evaluated by SEC and ¹H NMR. The ¹H NMR data gave a more accurate M_w by relative integration of the two chloromethyl protons ($\delta = 4.5$ ppm) to the styrene aromatic protons of the polymer backbone. The estimated M_w by NMR analysis (~19 kDa) was higher than the one calculated from the SEC analysis (~12 kDa). The M_w underestimation by SEC is caused by the significant difference in the hydrodynamic radii of the dendronized polymers as compared to the polystyrene standards. This effect becomes more pronounced for the higher generation dendronized polymers, where the observed M_w values were significantly smaller than the theoretical values (Table 3). For example, the M_w of 11 obtained from SEC analysis was ~23 kDa, which is about 6 times smaller than the theoretical value of ~140 kDa. Furthermore, the [G-4]-(OH)₁₆ could not be characterized by SEC due to its poor solubility in THF. Similar results have been reported previously by Yoshida *et al.* on dendronized polymers (20).

The highest generation, [G-4] hydroxylated carborane containing dendronized polymer 11 has an estimated theoretical M_w over 100 kDa. This dendronized polymer is water soluble at a concentration of 1 mg/mL with a theoretical B content of about 12%. To our knowledge, this is the first report of the synthesis of carborane containing polymers using NMP and dendronized carborane containing polymers using the divergent approach. The high M_w and B content with an overall water solubility at higher generations makes this family of dendronized polymers potential agents for BNCT applications.

Conclusion. We have successfully prepared a well-defined carborane loaded polymer with high M_w ($M_w > 15$ kDa) using NMP. This pre-made polymer was successfully dendronized up to the fourth generation via a combination of the graft onto approach of a first generation dendron, and the divergent dendron

Table 3. Characterization of Dendronized Polymers Determined by Size Exclusion Chromatography (SEC)

Compound	Theor. MW ^b	SEC (THF) ^a		NMR Calc. MW
		M _w	PDI	
<i>p</i> -CPS (2)	21 000	12 000	1.14	21 000
[G-1]-(Bn)-CPS (4)	37 000	16 000	1.16	32 000
[G-1]-(OH) ₂ -CPS (5)	27 000	16 000	1.19	29 000
[G-2]-(Bn) ₂ -CPS (6)	49 000	21 000	1.18	54 000
[G-2]-(OH) ₄ -CPS (7)	40 000	18 000	1.16	45 000
[G-3]-(Bn) ₄ -CPS (8)	84 000	22 000	1.16	92 000
[G-3]-(OH) ₈ -CPS (9)	65 000	19 000	1.16	74 000
[G-4]-(Bn) ₈ -CPS (10)	153 000	23 000	1.16	164 000
[G-4]-(OH) ₁₆ -CPS (11)	115 000	N/A	N/A	114 000

^a PS standard was used. ^b Based on the SEC data of 2

growth to higher generations. The molecular weights of the synthesized dendronized polymers were calculated using both ¹H NMR and SEC. We have found that SEC underestimates the M_w in comparison to the expected theoretical MW. This effect can be attributed to the major difference in the hydrodynamic radii between the rod-like dendronized polymers and the random coil linear PS standards. ¹H NMR was utilized to obtain a more accurate estimation of the MWs, which were in good agreement with the theoretical MWs. Our target solubility in water (1mg/mL) was achieved with the fourth generation dendronized polymer, with an estimated MW exceeding 100 kDa, which is much greater than the renal cut off MW (50 kDa). The combination of water solubility, high boron content, high MW and narrow PDI makes these dendronized polymers potential candidates for BNCT, which will be the focus of our future studies.

Experimental Section

Materials. 4-vinylbenzyl chloride, 4-(dimethylamino)pyridine (DMAP), 2,2-bis(hydroxymethyl) propionic acid (bisMPA), benzaldehyde dimethyl acetal, *p*-toluene sulfonic acid-monohydrate (*p*-TSAOH), and *n*-butyl lithium (2.5M) were purchased from Sigma-Aldrich. Benzylidene-2,2-bis(oxymethyl)propionic acid and its anhydride were prepared following a literature procedure (25). Dichloromethane (DCM) was distilled under nitrogen from calcium hydride immediately prior to use. Tetrahydrofuran (THF) was distilled under nitrogen from sodium/benzophenone immediately prior to use. All other reagents were commercially obtained and used without further purification.

Characterization. NMR spectra were collected on Bruker DRX 500 MHz and Avance 600 MHz spectrometers. ^1H spectra were recorded at 600 MHz, ^{11}B spectra were recorded at 190 MHz, and ^{13}C NMR spectra were recorded at 150 MHz in CDCl_3 or methanol- d_4 . The non-deuterated solvent signal was used as internal standard for both ^1H and ^{13}C spectra. Where aliphatic ^1H NMR signals from the dendrimer overlap with signals from the B-H in the carborane cage or with the broad polymer signals, an accurate integration could not be assigned. In these cases, theoretical values are provided in parentheses { }. High Resolution Mass spectroscopy Electrospray Ionization (HRMS (EI+)) experiments were conducted for the synthesized macromonomers on Micromass Quattro Ultima Triple Quadrupole mass spectrometer using electrospray ionization with positive ion mode. Size exclusion chromatography (SEC) using THF as a mobile phase was performed at 40 °C using a Waters 2695 Separation Module, equipped with a photodiode array detector, a refractive index detector, and a multi-wavelength fluorescence detector. Narrow molecular weight distribution polystyrene standards were used for calibration. The flow rate was 1.0 mL/min.

General Procedure for Polymer Synthesis Using Nitroxide-Mediated Living Free Radical Polymerization (NM-LFRP). To a flame-dried round-bottom flask charged with *p*-carborane styrene macromonomer **6** in chlorobenzene was added the alkoxyamine initiator along with a 9 mM solution of the free nitroxide radical and a catalytic amount of acetic anhydride. The solution was degassed under N_2 for 1 h and heated to 125 °C for 7 h. The polymer was precipitated from methanol as a white solid and recovered by filtration through a glass fritted funnel. The collected solid was dried in a vacuum oven overnight to give the polymer as a white powder with typical yield of greater than 90%.

General Procedure for Dendronization of Pre-formed Polymer. To a flame-dried round-bottom flask, under argon atmosphere, *p*-carborane polystyrene **9** was dissolved in dry THF. The reaction mixture was cooled to 0 °C and *n*-BuLi was introduced dropwise, and the mixture was allowed to react for 30 minutes at 0 °C. Benzylidene anhydride **1** was added and the reaction mixture was stirred for an extra 8 h at room temperature. The crude reaction mixture was precipitated into methanol to give the polymer as a white powder. The polymer was recovered by filtration through a glass fritted funnel and dried in a vacuum oven overnight to give the [G-1]-(Bn)-dendronized polymer **10** as a white powder with typical yield of 85% and a degree of functionalization of 75%.

General Procedure for the Pd-Catalyzed Deprotection of the Benzylidene Protecting Group. To a round-bottom flask charged with the first generation protected carborane polymer, [G-1]-(Bn), was added a 1:1 mixture of CH_2Cl_2 :methanol (total of 20 mL). Subsequently, $\text{Pd}(\text{OH})_2/\text{C}$ (20%) was added and the flask was evacuated and back-filled with H_2 three times (H_2 pressure: 1

atm). The reaction mixture was stirred vigorously overnight at room temperature under H_2 (1 atm). The catalyst was removed by filtration through a plug of celite and washed with methanol. The filtrate was evaporated to dryness on a rotary-evaporator in vacuo, yielding the desired product as a white foam in quantitative yield.

General Procedure for Acid-Catalyzed Deprotection of the Benzylidene Protecting Group. Due to the equilibrium between the benzaldehyde, (or benzaldehyde dimethyl acetal) generated as a deprotection byproduct, and the benzylidene protected dendrons, a small percentage (< 10%) of benzylidene groups usually remained after Pd-catalyzed hydrogenolysis. Therefore, the product was subjected to an acid-catalyzed deprotection to achieve complete deprotection of the benzylidene group. To a round bottom flask charged with partially protected polymer (0.5 g, 2.8×10^{-5} mol) dissolved in THF/methanol (4:3 v/v), concentrated sulfuric acid (2% v/v, pH 3) was added to the flask, and the solution was allowed to stir overnight at room temperature. The sulfuric acid was neutralized with a 7N solution of ammonia in methanol, to precipitate ammonium sulfate as a white solid. The precipitate was removed by filtration, and the filtrate was concentrated in vacuo. The viscous liquid was washed several times with THF to remove all the remaining ammonium sulfate. The polymer was recovered as a white foam (0.45g, 95%).

General Procedure for the Divergent Dendron Growth from Using the "Graft Onto" Approach. To a flame-dried round-bottom flask equipped with a magnetic stir bar (under argon atmosphere), the benzylidene protected anhydride, the hydroxyl-terminated dendronized polymer (generation 1 through 3), and 4-dimethylaminopyridine (DMAP) were dissolved in a 3:2 ratio of CH_2Cl_2 and pyridine. The reaction mixture was stirred for 12 h at room temperature, after which 2 mL of water was added and the reaction was stirred for an extra 18 h to quench the excess anhydride. The product was isolated by diluting the mixture with CH_2Cl_2 (100 mL) and washed with 1 M $NaHSO_4$ (3×100 mL), 10% Na_2CO_3 (3×100 mL), and brine (100 mL). The organic layer was dried over anhydrous $MgSO_4$ and filtered through a glass fritted funnel. The filtrate was evaporated to dryness on a rotary-evaporator in vacuo. The polymer was isolated by precipitation from methanol as a white powder. Yields decreased with increasing dendron generation.

References

1. Soloway, A. H.; Tjarks, W.; Barnum, B. A.; Rong, F. G.; Barth, R. F.; Codogni, I. M.; Wilson, J. G. *Chem. Rev.* **1998**, *98*, 1515-1562.
2. Diaz, A. Z.; Coderre, J. A.; Chanana, A. D.; Ma, R. *Ann. Med.* **2000**, *32*, 82-85.

3. Hawthorne, M. F.; Lee, M. W. *J. Neuro-Oncol.* **2003**, *62*, 33-45.
4. Yanagie, H.; Maruyama, K.; Takizawa, T.; Ishida, O.; Ogura, K.; Matsumoto, T.; Sakurai, Y.; Kobayashi, T.; Shinohara, A.; Rant, J.; Skvarc, J.; Ilic, R.; Kuhne, G.; Chiba, M.; Furuya, Y.; Sugiyama, H.; Hisa, T.; Ono, K.; Kobayashi, H.; Eriguchi, M. *Biomed Pharmacother* **2006**, *60*, 43-50.
5. Alam, F.; Soloway, A. H.; Mcguire, J. E.; Barth, R. F.; Carey, W. E.; Adams, D. *J. Med. Chem.* **1985**, *28*, 522-525.
6. Ma, L.; Hamdi, J.; Wong, F.; Hawthorne, M. F. *Inorg. Chem.* **2006**, *45*, 278-285.
7. Hawthorne, M. F. *Angew. Chem., Int. Ed. Engl.* **1993**, *32*, 950-984.
8. Valliant, J. F.; Guenther, K. J.; King, A. S.; Morel, P.; Schaffer, P.; Sogbein, O. O.; Stephenson, K. A. *Coord. Chem. Rev.* **2002**, *232*, 173-230.
9. Tietze, L. F.; Bothe, U.; Nakaichi, M.; Hasegawa, T.; Nakamura, H.; Yamamoto, Y. *ChemBioChem* **2001**, *2*, 236-334.
10. Tietze, L. F.; Griesbach, U.; Bothe, U.; Nakamura, H.; Yamamoto, Y. *ChemBioChem* **2002**, *3*, 219-225.
11. Tomita, T.; Watanabe, M.; Takahashi, T.; Kumai, K.; Tadakuma, T.; Yasuda, T. *Biochim Biophys Acta* **1989**, *978*, 185-190.
12. Raddatz, S.; Marcello, M.; Kliem, H. C.; Troster, H.; Trendelenburg, M. F.; Oeser, T.; Granzow, C.; Wiessler, M. *ChemBioChem* **2004**, *5*, 474-482.
13. Parrott, M. C.; Marchington, E. B.; Valliant, J. F.; Adronov, A. *J. Am. Chem. Soc.* **2005**, *127*, 12081-12089.
14. De Winne, K.; Vanderkerken, S.; Hoste, K.; Dubruel, P.; Schacht, E. *J. Bioact. Compat. Pol.* **2004**, *19*, 367-382.
15. Gillies, E. R.; Frechet, J. M. J. *Drug Discov. Today* **2005**, *10*, 35-43.
16. Gossel, I.; Shu, L.; Schluter, A. D.; Rabe, P. J. *J. Am. Chem. Soc.* **2002**, *124*, 6860-6865.
17. Piotti, M. E.; Rivera, F.; Bond, R.; Hawker, C. J.; Frechet, J. M. J. *J. Am. Chem. Soc.* **1999**, *121*, 9471-9472.
18. Haag, R.; Kratz, F. *Angew. Chem. Int. Ed.* **2006**, *45*, 1198-1215.
19. Schluter, A. D.; Rabe, J. P. *Angew. Chem. Int. Ed.* **2000**, *39*, 864-883.
20. Yoshida, M.; Fresco, Z. M.; Ohnishi, S.; Frechet, J. M. J. *Macromolecules* **2005**, *38*, 334-344.
21. Malkoch, M.; Carlmark, A.; Woldegiorgis, A.; Hult, A.; Malmstrom, E. E. *Macromolecules* **2004**, *37*, 322-329.
22. Leites, L. A. *Chem. Rev.* **1992**, *92*, 279-323.
23. Hawker, C. J.; Bosman, A. W.; Harth, E. *Chem. Rev.* **2001**, *101*, 3661-3688.
24. Benoit, D. C., V.; Braslau, R.; Hawker, C. J. *J. Am. Chem. Soc.* **1999**, *121*, 3904-3920.
25. Ihre, H. R.; Omayra, L.; De Jesus, P.; Frechet, J. M. J. *J. Am. Chem. Soc.* **2001**, *123*, 5908-5917.

Chapter 15

Biodegradable Ionomers for the Loading and Release of Proteins: Formation, Characterization, Mechanism, and Consequence of Water Uptake

Fredrik Nederberg¹, Björn Atthoff¹, Tim Bowden¹, Ken Welch²,
Maria Strömme², and Jöns Hilborn¹

¹Department of Materials Chemistry, Polymer Chemistry, The Ångström Laboratory, Uppsala University, Uppsala, Sweden

²Department of Engineering Sciences, The Ångström Laboratory, Uppsala University, Uppsala, Sweden

The increased understanding of proteins and the human genome point towards a future in which selective proteins may replace synthetic drugs in the general cure of disease. In this scenario the ability of controlled and gentle release of proteins provide the key for successful treatment. To address the ability of full protein delivery we have developed a series of telechelic biodegradable ionomers based on poly (trimethylene carbonate) carrying zwitterionic, anionic or cationic functional groups. The introduction of polar end-groups provides a material with unique properties that directs the introduced functionality within the material bulk but also to the material surface if water is introduced. Bulk aggregation provide a low elastic modulus material and the ability to surface enrich provide the on-set of water swelling. The latter finally results in a co-continuous water-ionomer structure that engulfs and stores proteins simply by soaking the material in an aqueous protein solution. Following protein loading the material can be dried and re-immersed in water so that release occurs. Our results, including both the careful synthesis and the ability to load and release proteins, provides new possibilities for full protein delivery.

In this chapter the increased understanding of the water swelling properties and the subsequent formation of bulk water domains in biodegradable poly(trimethylene carbonate) (PTMC) ionomers is presented. The recent discovery that bifunctional PTMC may be functionalized with polar ω -phosphoryl choline (PC) end groups and that the resulting telechelic zwitter ionomer forms an interesting low elastic modulus material has encouraged and directed the use of biodegradable ionomers in new areas of biomaterial research (1). Present findings now suggest that the scope of the synthesis may be broadened to provide telechelic ionomers with additional functionalities (2) and also that the water absorbing properties of such ionomers indicate their potential to serve as novel carriers for the loading and release of proteins (3).

Introduction

In an effort to extend the scope from synthetic biodegradable polymers to materials that are able to dissolve or disperse both hydrophilic and hydrophobic substances, we have developed biomimetic zwitterionic, cationic and anionic ionomers. In order for those materials to perform as temporary hosts, to load and release active substances, pathways of their transport must be provided for. Possibly the most intriguing transport pathway is a linear swelling front of water which can provide an open porous material with a resulting co-continuous structure of both water and the swollen material. Such swelling mechanism is unique in that it may provide for zero order release kinetics or a constant rate of release from a biodegradable reservoir. This chapter describes the synthesis of such materials, their interaction with hydrophobic and hydrophilic substances, and the successful linear propagation of a distinct swelling front to produce an open porous structure. Finally we apply these materials by demonstrating how loading and release of proteins is achieved without the use of solvents or elevated temperatures.

In our initial work on biodegradable ionomers it was postulated that the unique material properties of these ionomers originated from bulk aggregates of polar PC groups embedded in a hydrophobic PTMC matrix such that physical cross links were formed (1). A schematic representation is shown in *Figure 1*. This was further supported by the fact that the resulting material, as compared to non-functional PTMC, swelled significantly in water. Still the question has been: How does this swelling actually occur and what are the consequences for the material? (3a)

To address this question we will currently introduce new results regarding the mechanism by which the material absorbs water and providing additional information on how the interior co-continuous (water and ionomer) structure is formed and what it looks like. Furthermore, supporting observations from dielectric spectroscopy measurements are provided as a direct means for

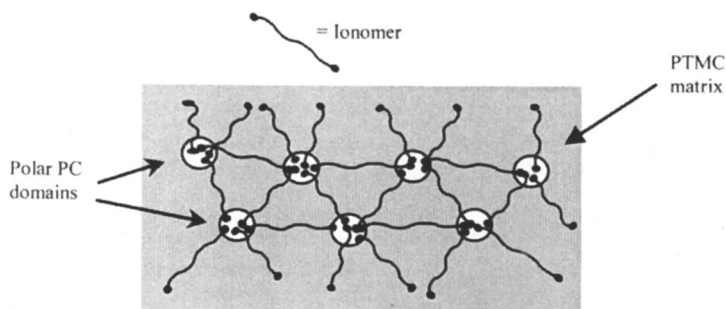


Figure 1. Schematic representation of polar PC bulk aggregates in the hydrophobic PTMC matrix.

studying of bulk PC aggregates and the dynamics of such aggregates with the introduction of water (4).

Synthesis

Our ionomers are designed based on a hydrophobic PTMC backbone. The preparation consists of stannous octanoate catalyzed ring opening polymerization (ROP) of the cyclic trimethylene carbonate monomers initiated from butanediol. PTMC diols of predictable molecular weights were formed in accordance to *Figure 2a*. The resulting alcohols were further quantitatively converted to result in three different biomimetic telechelic oligomers, shown in *Figure 2b*.

The first anionomer has a sulphate end functionality similar to that of heparin. Heparin has been shown to be responsible for the binding of a magnitude of proteins *in-vivo* (5). To prepare the anionic moiety having sulphonic acid at both chain ends, the PTMC diol was employed as a nucleophile to the electrophilic sulfur trioxide trimethylamine complex, giving the PTMC disulphonate as a product.

The second material is an end functionalized cation with trimethylammonium carrying the positive charge. This functionality is similar to that of *in-vivo* carnitine, which functions as a complexing carrier for the transport of long chain activated fatty acids into the mitochondrial matrix (6). The second material is prepared in two steps: initially 4-chlorobutyl chloride is reacted onto the ω -hydroxyl end-group of PTMC, finally trimethylamine displaces the chloride to introduce the cationic ammonium group.

The third material is equipped with zwitterionic chain ends by the initial phosphorylation with ethylene chlorophosphate in the presence of a base

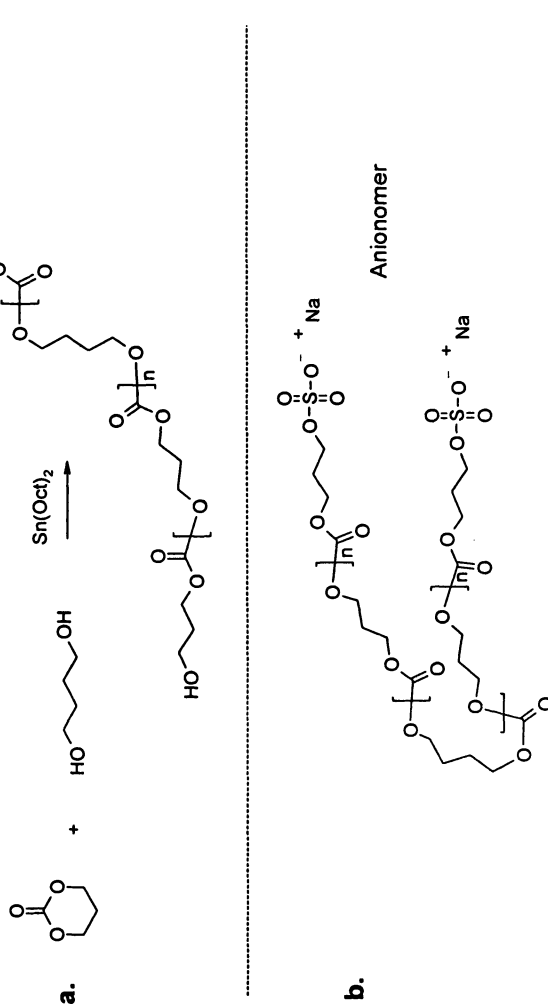
followed by the ring opening of the intermediate cyclic phosphate with trimethylamine at 60°C under pressure (7). This results in the formation of chain end functionalized phosphoryl choline which is analogous to the polar head group in the most common phospholipids in cellular membranes. It is noteworthy that all post transformations on the PTMC diol resulted in complete conversion as judged by ^1H NMR and formation of only the pure desired products (2,8).

Properties and Characterization

The newly synthesized materials showed completely new properties as compared to PTMC. While the starting material was tacky and with poor film forming capabilities, the functionalized material was firm, showed more elastic properties, and could be cast into solid films. We believe that the anticipated ionomeric behavior explained by microscopic phase separation into zwitterionic aggregates result in the drastic change of the material characteristics. In order to obtain more data regarding the mechanical performance of the material and thus support the presence of ionomers, rheology measurements were performed. Specifically, an oscillating torque experiment, in which the PC ionomer was compared with PTMC at a frequency of 1Hz was used. *Figure 3* shows the storage shear modulus (G') as function of temperature of the two materials.

At ambient conditions PTMC behaves as an amorphous melt with no mechanical integrity whereas the ionomer, as anticipated, behaves like a rubber with a G' value of ~ 2 MPa. In addition, *Figure 3* reveals a rubbery plateau of the ionomer, stretching from 5°C to about 40°C and the viscous region is not reached until 70°C. These results demonstrates that one could benefit from the rubbery behavior at physiological conditions ($\sim 37^\circ\text{C}$). Moreover, one can observe an interesting shift in the glass transition temperature (T_g) of the two materials. For PTMC the T_g is located at -16°C since the contribution of flexible end-groups is significant. For the PC ionomer however, a large difference was observed, as the T_g shifted to -5°C . Most likely the end-groups of the ionomer are captured in zwitterionic aggregates forming physical cross-links that restrains molecular mobility that raise T_g instead of lowering it. The higher temperature needed for the onset of translational mobility agrees well with the behavior of ionomers reviewed by Eisenberg as early as 1971 (9). The behavior of the anionic and cationic ionomers was similar to the PC ionomer (1,2).

The observed shift of the glass transition was further analyzed by thermal analysis. Differential scanning calorimetry (DSC) was used and the results are shown in *Figure 4*. A similar shift to that found in the rheometer was observed, Without the frequency dependence however, the T_g was -27°C for the starting PTMC as compared to -16°C for the PC ionomer.



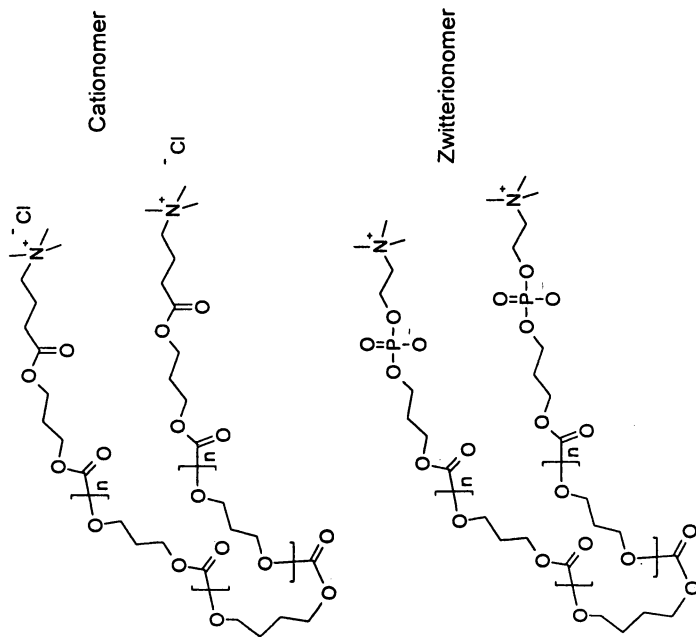


Figure 2. (a) Ring opening polymerization of trimethylene carbonate initiated from butane diol and catalyzed from stannous octanoate. (b) Three different telechelic ionomers, anionomer, cationomer and zwitterionomer.

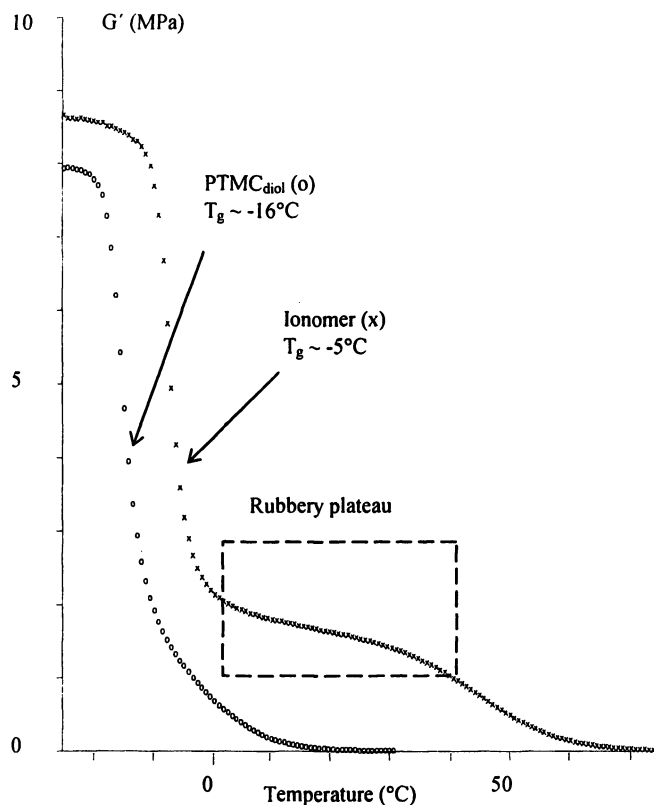


Figure 3. Results of oscillating rheology measurement of PTMC and PC ionomer. (Insets: T_g and rubbery plateau of PC ionomer)

To further analyze the bulk domains and the dynamics involved, dielectric spectroscopy measurements were performed. More specifically the real part of the dielectric loss was measured as function of frequency and temperature. The non functional PTMC was used as reference and any additional relaxation present in the spectra of the PC ionomer could be attributed to the dipolar vector of the PC group that interacts with the applied alternating electrical field. A common characteristic of essentially all amorphous polymers is that they exhibit both a principal relaxation related to the dynamic glass transition, termed the α -relaxation, and a secondary relaxation called the β -relaxation. It is generally accepted that the α -relaxation is due to segmental motion (i.e. conformational changes) along the polymer chain. On the other hand, the dielectric β -relaxation stems from localized rotational fluctuations of the dipole vector. In addition to the presence of α - and β -relaxations (found in both PTMC and the PC

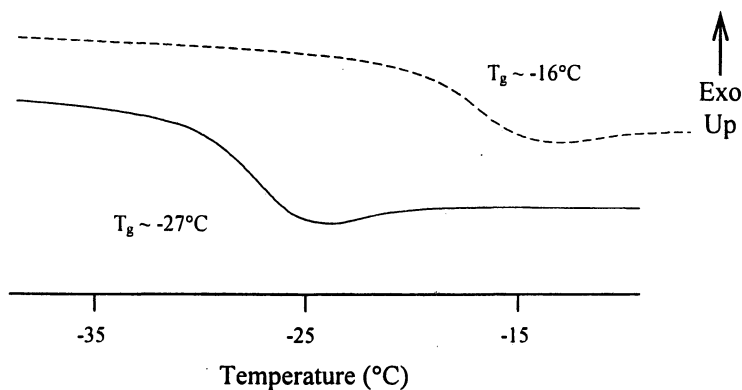


Figure 4. DSC curves of PTMC (solid line) and PC ionomer (dotted line). T_g measured on 2nd heating.

ionomer) two additional relaxations were found in the PC ionomer that were related to the presence of PC domains (4). These additional relaxations were called α -ionomer and λ . The dielectric spectra of the PC ionomer and PTMC are shown below in Figure 5.

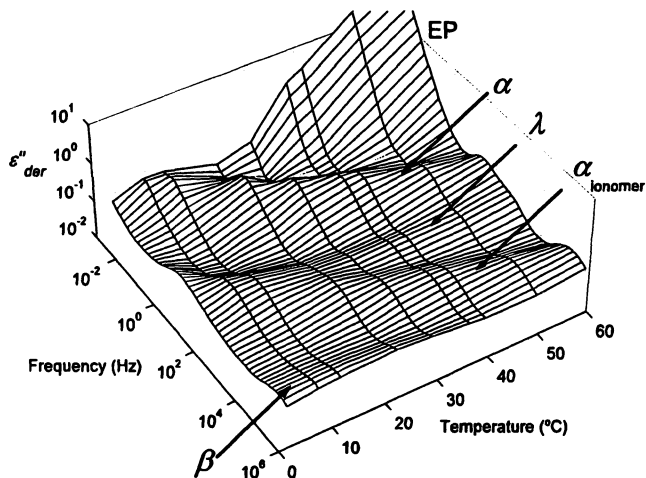
The α -ionomer relaxation was found to be directly related to the conformational changes of individual PC dipoles, whereas the λ relaxation most likely is related to movement of adjacent PC groups in the zwitterionic aggregates. This observation will be further discussed below.

Formation and Mechanism for Water Swelling

As further evidence of the existence of polar bulk domains, a separate study has shown that the PC ionomer swells in water and that this behavior could be utilized to load and release proteins (3a). Initially it was believed that water was absorbed through gas phase diffusion such that the polar PC domains would swell and finally coalesce to form interior water channels in the material. Osmosis would trigger the swelling and the PC groups would minimize their energy by enriching the water interphase. The latter is similar to the surface enrichment of polar PC groups when introducing water to the material surface (8,10).

In a study of a cationic ionomer however, a very interesting finding was observed that demonstrates how surface properties can affect water absorption (3b). When the cationic surface was pretreated with the negatively charged heparin (Mw 5000-30000 g/mol), the material did not swell at all even upon prolonged (5 months) storage in water. The lack of swelling is most likely due to

a



b

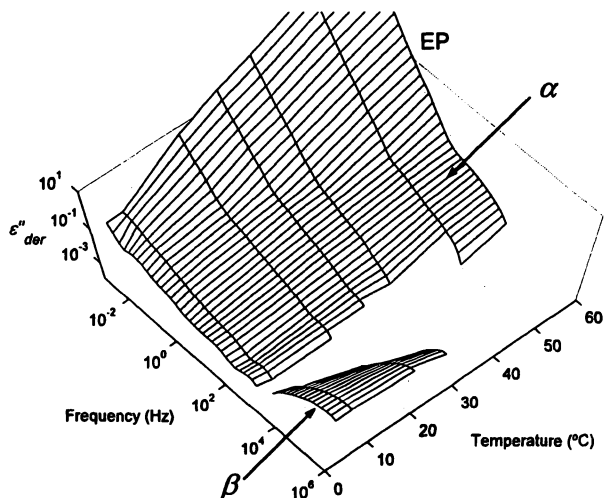


Figure 5. Dielectric loss ϵ''_{der} spectra as a function of frequency and temperature for a) PC ionomer and b) PTMC.

polyelectrolyte adsorption which creates a charged blocking layer on the surface. Thus, an immobilized layer of a few nm thickness inhibits the mechanism responsible for the entrance of water into the structure. If one takes into account the rapid surface rearrangement upon water immersion due to the migration of ionic chain ends to the material-water interface, it seems plausible that this mobility is associated with the swelling phenomena. Following, or accompanying, the surface rearrangement is the formation and opening of channels guiding water into the structure. Hence, water soluble species may be charged into these materials by simply placing a solution of this in direct contact. The water "channels" will open allowing passage into the material. Evaporation by drying removes only water and leaves the cargo inside the material. In fact, as the material is well above its T_g , the channels will close to encapsulate the content. Re-immersion into water will again open the diffusion pathways to allow for a release that might be possible to be controlled by the swelling front only. A schematic picture of how the material engulfs and store proteins is shown in *Figure 6*. These materials may offer attractive opportunities for delivery of macromolecules, where the delivery system protects the protein against denaturation by body fluids and provides for constant and sustained release.

A microscopic investigation of the swelling revealed a sharp swelling front having a linear propagation rate of between $0.5\mu\text{m}/\text{min}$ (PC ionomer) to $20\mu\text{m}/\text{min}$ (cationic ionomer). The formed interior structure left by the propagating water front shows a porous structure with pore sizes between 1 and $10\mu\text{m}$, as determined by cryo SEM (*Figure 7*).

By dissolving the red emitting hydrophobic fluorophore Rhodamine DHPE (LissamineTM rhodamine B 1,2-dihexadecanoyl-*snglycero*-3-phospho ethanolamine trimethylammonium salt) into the polymer and the green emitting BODIPY 492/515 disulfonate (4,4-difluoro-1,3,5,7,8-pentamethyl-4-bora-3a,4a-diaza-*s-indacene*-2,6-disulfonic acid disodium salt) in the swelling water, shown in *Figure 8*, it becomes evident that the porosity is open allowing free passage of green water into the structure.

The dynamics involved when water is absorbed was further supported by comparing the dielectric spectra of a dry sample with a sample which was left in the measurement cell for a period of one month and allowed to equilibrate with the surroundings at 37% relative humidity. As can be seen in *Figure 9* the α -ionomer relaxation has shifted to a higher frequency, indicating that the moiety responsible for this relaxation now has a higher mobility. Moreover, the λ relaxation has almost completely disappeared. If this relaxation is associated with adjacent PC groups in the aggregate as was suggested earlier, the swelling of the aggregates could result in a decreased interaction between PC end-groups and a subsequent decrease in the relaxation strength.

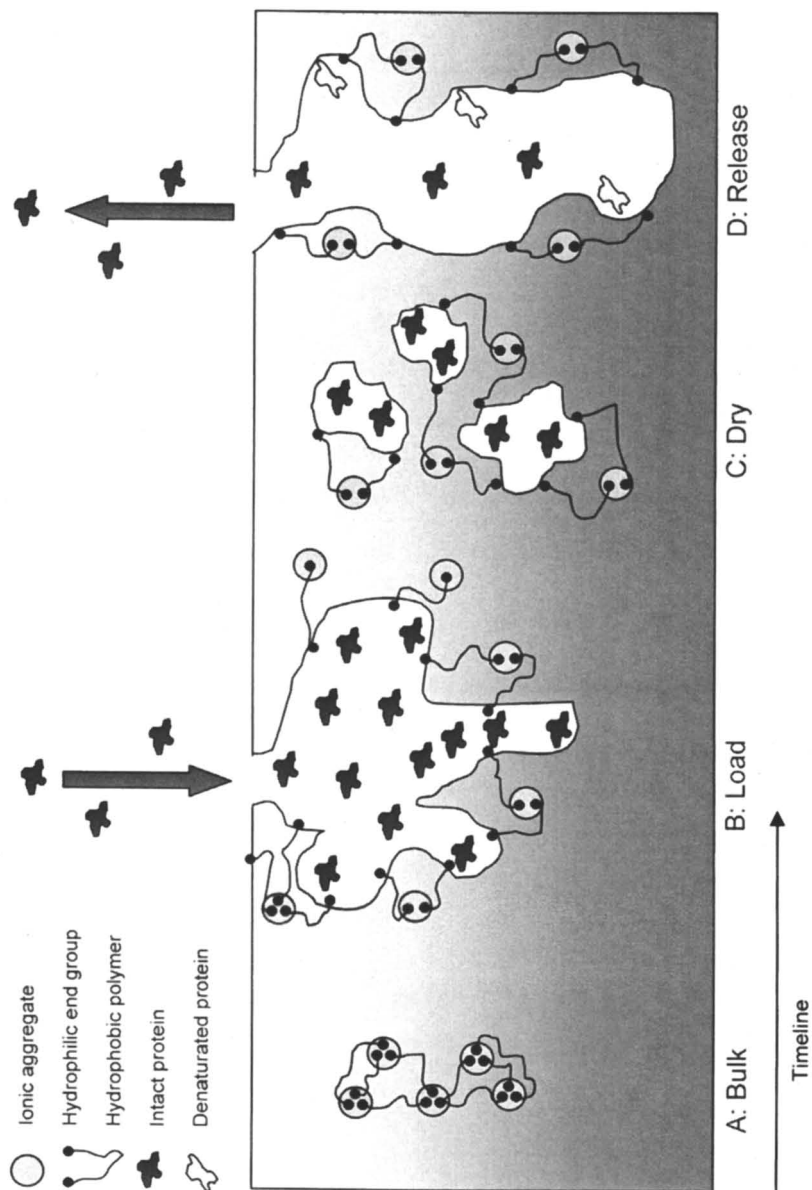


Figure 6. Schematic representation of the mechanism of protein loading and release.

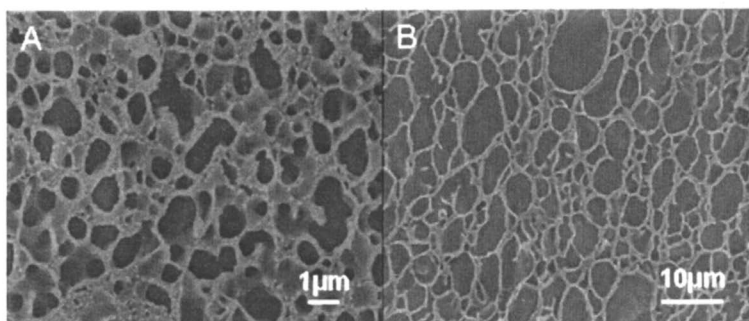


Figure 7. Cryo SEM revealing the inner structure of swelled ionomers.

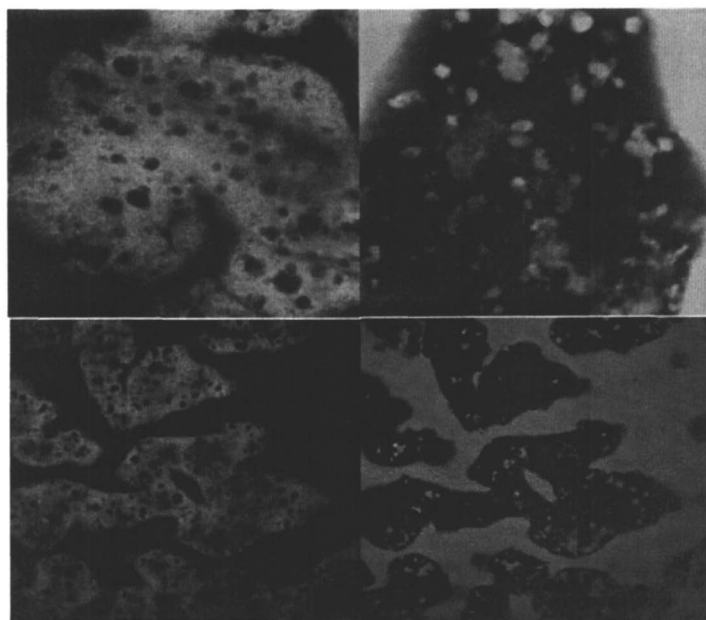


Figure 8. Confocal micrograph Hydrophobic PTMC stained with red Rhodamine DHPE and the water phase stained with green BODIPY.

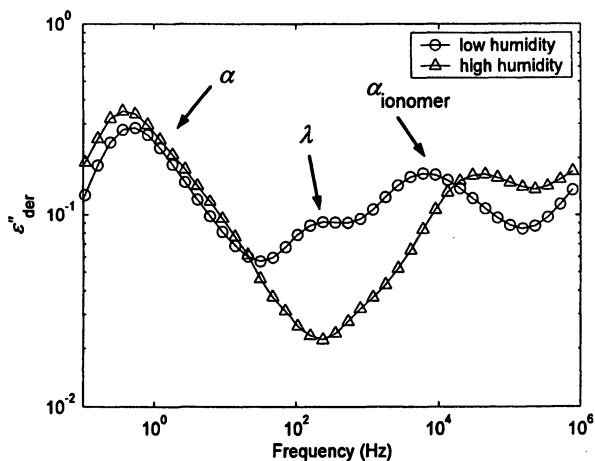


Figure 9. Two ϵ''_{der} spectra for the same PC ionomer sample collected at 30 °C, but with different moisture content. In the spectra corresponding to higher moisture content, the α -ionomer relaxation has shifted to higher frequencies while the λ relaxation appears to have disappeared.

Protein Loading and Release

Following the careful investigation of how our telechelic ionomers absorb water and how the swollen structure forms, and appears we wanted to investigate if this absorption ability could be utilized for protein loading and release. To test this question, discs of known dimensions were compression molded and allowed to equilibrate for a known time in different aqueous protein solutions. Following loading and sometimes drying (freeze drying or air drying) the discs were re-immersed in water and the release was measured. In these studies various proteins were used including insulin, albumin, carboxyhemoglobin (COHb), and cytochrome C. The latter two both carry the red iron containing heme group and upon denaturation change their colour from red to green, blue, or brown (11). COHb and cytochrome C therefore provide advantageous visual markers when studying if protein activity is retained following release from the substrate.

Shown in Figure 10 is a selective release profile after freeze drying of discs incubated in an aqueous albumin solution. In this example, the release is about 60% after one week. Under milder drying conditions (air drying) or without any drying step, the protein release was near quantitative as was shown using COHb and cytochrome C (Figure 11).

In addition, the released proteins maintained their activity since their respective UV spectra maintained constant before and following release (Figure 12) (3b).

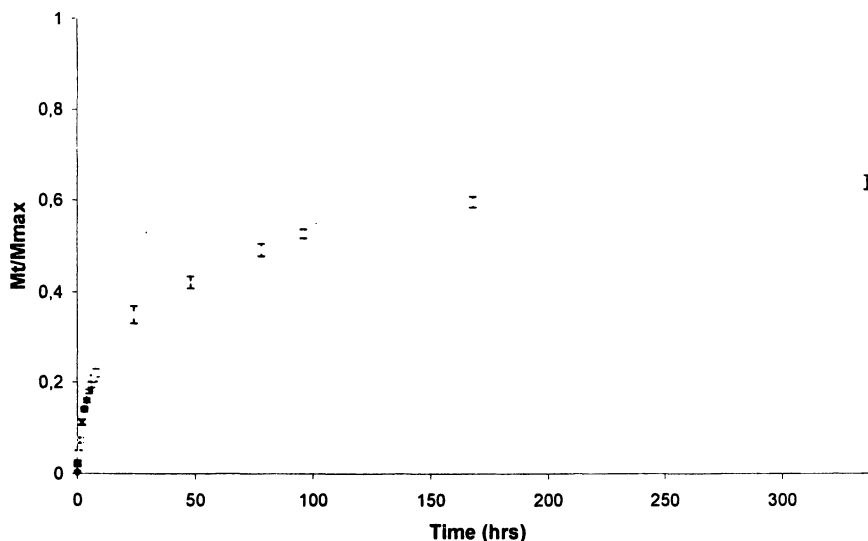
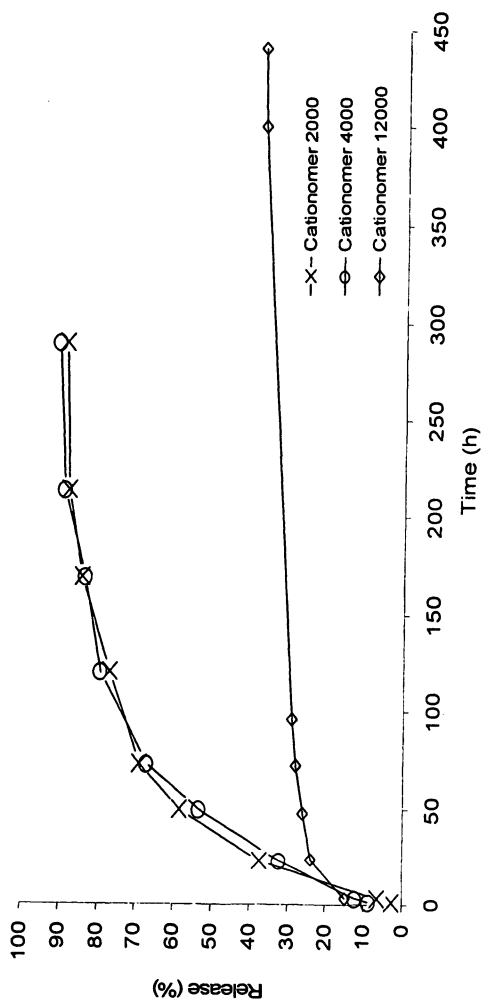


Figure 10. Release profile of albumin viewed as the release at time t (M_t) normalized with the maximum release (M_{max}) as function of time.

Conclusion

Throughout the course of this work we have demonstrated a new route to biomimetic and telechelic ionomers carrying either phosphoryl choline, sulphonate, or quaternary ammonium functional end-groups. The careful synthesis allows for complete conversion of the hydroxyl functionalised PTMC to the PTMC containing desired functionality, which results in a low elastic modulus material due to the bulk agglomeration of polar groups. The presence of physical cross-links has been confirmed using both spectroscopy and mechanical analysis. Water swelling is an additional feature of the resulting materials and a thorough evaluation has shown that water is absorbed from the surface, leaving an open co-continuous (water-ionomer) structure. The ability to absorb water and the open swollen structure was utilized for protein loading simply by letting the material swell in an aqueous protein solution. Near quantitative release was achieved either directly after loading or following an additional drying step. Protein activity is maintained following release, suggesting that the material may favourably interact with guest proteins such that denaturation is suppressed. The gentle and overall behaviour in which proteins are loaded and released has shown that full protein delivery is possible.



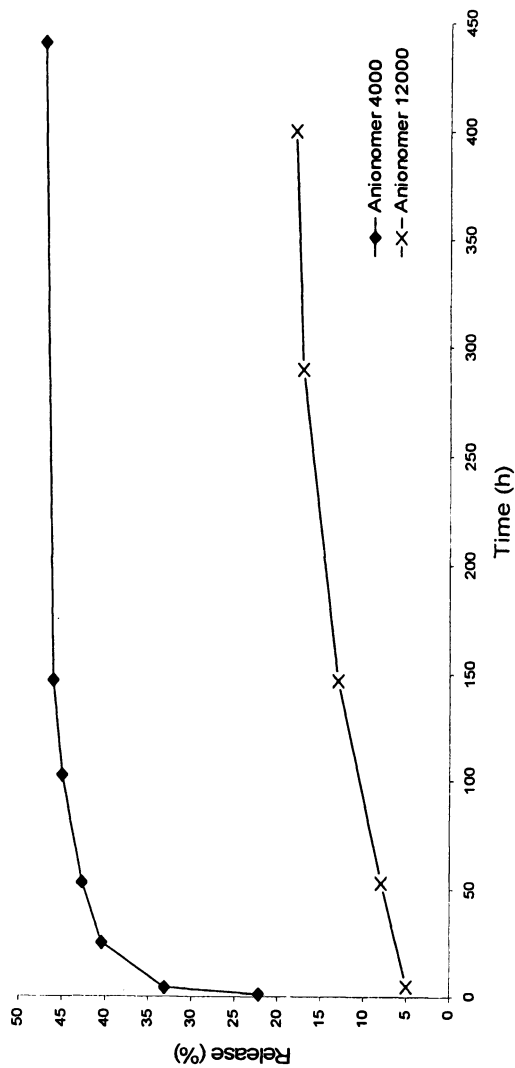


Figure 11. Curves showing the release of COHb and Cytochrome C from dried discs. Top, cationomers of three different molecular weight 2000, 4000 and 12000 g/mol, below the release from 4000 and 12000g/mol anionomer.

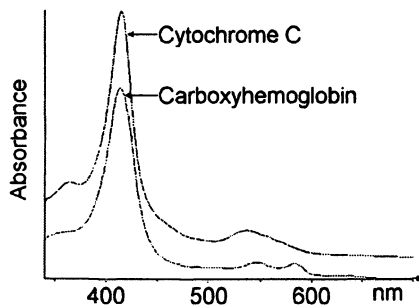


Figure 12. UV-Vis spectra of Cytochrome C and carboxyhemoglobin.

References

1. Nederberg, F.; Bowden, T.; Nilsson, B.; Hong, J.; Hilborn, J. *J. Am. Chem. Soc.* **2004**, *126*, 15350.
2. Atthoff, B.; Nederberg, F.; Hilborn, J.; Bowden, T. *Macromolecules*, **2006**, *39*, 3907-3913.
3. a) Nederberg, F.; Hilborn, J.; Bowden, T.; Watanabe, J.; Ishihara, K. *Biomacromolecules*, **2005**, *6*(6), 3088. b) Atthoff, B.; Nederberg, F.; Soederberg, L.; Hilborn, J.; Bowden, T. *Biomacromolecules*, **2006**, *7*(8), 2401-2406.
4. Welch, K.; Nederberg, F.; Bowden, T.; Hilborn, J.; Strømme, M. **2006**, submitted manuscript.
5. Petitou, M.; van Boeckel, C.A.A. *Angew. Chem. Int. Ed.*, **2004**, *43*, 3118-3133.
6. J. M. Berg, J. L. Tymoczko, L. Stryer, *Biochemistry*, 5th int. ed: W. H. Freeman and Company, New York, **2002**, 304.
7. See also: Ishihara, K.; Ueda, T.; Nakabayashi, N. *Polym. J.*, **1990**, *22*(5), 355-360.
8. Nederberg, F.; Bowden, T.; Hilborn, J. *Macromolecules*, **2004**, *37*(3), 954-965.
9. Eisenberg, A. *Macromolecules*, **1971**, *4*, 125-128.
10. Nederberg, F.; Bowden, T.; Hilborn, J. *Polym. Adv. Technol.*, **2005**, *16*, 108.
11. Szebeni, J.; Di Iorio, E.E.; Hauser, H.; Winterhalter, K.H. *Biochemistry*, **1985**, *24*, 2827-2832.

Chapter 16

An Overview of the Biocompatibility of Polymeric Surfaces

Katherine C. Glasgow¹ and Dibakar Dhara²

¹GE Plastics, 1 Lexan Lane, Mt. Vernon, IN 47620

²GE Plastics, John F. Welch Technology Centre, Bangalore, India

This review of the biocompatibility of polymeric surfaces concentrates on the observed differences of hydrophilic, hydrophobic, and heterogenic materials as measured by their interactions with proteins and platelets. Emphasis is placed on materials for use in injection molding applications.

Introduction

The desire to understand the ability of the human body and its components to tolerate exposure to synthetic materials can be first dated to 1588, when the use of gold to repair a cleft palate was recorded (1). Every advance in the fields of both medicine and material science has expanded the possible uses of synthetic materials in medical applications. Table 1 provides a list of some common medical applications of synthetic materials; the ideal material choice for each particular application depends on the biocompatibility and mechanical property requirements in each case (2).

The application type defines the desired form of the synthetic material. A coating may be spin cast or solvent cast upon a substrate. The preparation of membranes is not trivial, as many techniques have been developed to give the desired properties; methods include solution casting, melt pressing, and solvent precipitation. Detailed accounts of membrane preparation can be found elsewhere (3). Other material forms required by medical applications include powders (for bone cement) and films. This review will focus on applications that require injection molding of engineering thermoplastics.

Table 1. Common synthetic materials and their biomedical applications

<i>Material Examples</i>	<i>Application</i>
PDMS, PEU, PEO, PEG	Coatings on devices
PEU, PET, PC, COC	Medical devices
PE, PMMA	Implants
PE, PDMS, PEU, PC	Catheters and Tubing
PTFE, PET	Vascular Grafts
PSU, PTFE, PDMS, PES	Membranes
PP, EVA, PDMS, PVA	Drug delivery

See reference (2) for abbreviation expansion

In injection molding, plastic pellets are melted and injected into a hollow mold. The cooled plastic is then removed, giving the desired shape. Automated injection molding systems provide an economical production cost while maintaining tight dimensional tolerances. Injection molding is used to produce medical device components such as surgical tools, insulin pens, blood glucose meters, nebulizers, blade shields, IV components, dialyzer housings, and lab diagnostic equipment, to name a few applications. The medical device market, including those devices, which use injection molded components, was estimated to have sales of \$93.8 billion in 2004; the market is estimated to grow between 6 and 8% annually (4).

Injection-molded devices used in medical applications such as blood separation, cardiovascular surgery, and renal care may all involve direct contact with blood or blood fluids. Depending on the nature of the application, minimizing platelet adsorption, protein adsorption, or clotting may be desired so that the device is most effective. For applications that require minimal blood response to the synthetic material of the medical device, there are a limited number of options that can be used to increase the hemocompatibility, or inertness, of the synthetic material. The interaction of blood with synthetic materials involves a complex cascade of protein responses (5). Due in part to the complex nature of biological responses to synthetic materials, there is currently no ability to predict a biological response to different surfaces based solely upon the physical and chemical measurements of the surfaces. Coatings and grafts have been shown to be effective in reducing the immunological response to the synthetic material (6). While coatings are effective, they are expensive and require a secondary operation to render the medical device suitable for use. Furthermore, coatings may adversely impact some of the additional requirements of injection-molded devices, namely clarity and suitability for sterilization.

A lack of uniform test protocol further compounds the complicated nature of evaluating materials for blood contact applications. While ISO and FDA guidelines do exist, the standards do not take the various application conditions

into account (7). Testing recommendations are made based upon type of use, but neglect to adjust for significant variations such as temperature, length of exposure time, or presence of anticoagulant. Thus, test protocols are developed for each particular application, leading to the lack of an industry standard. As a result, *in vitro* tests may not predict actual *in vivo* and/or *ex vivo* applications. Different methods for evaluating the interaction of blood with synthetic materials are shown below in Table 2 (8). In general, techniques that are found in the literature either measure the platelets (or related cells) themselves, the formation of the clot, or the level of complement proteins in the blood. Complement proteins have been shown to correspond to platelet activation (8), and ELISA kits are now commercially available for the measurement of some complement proteins.

Table 2. Selected methods for evaluating blood response of exposure to synthetic materials.

Cell Count	Platelet Retention Platelet Adhesion Platelet-Leukocyte Aggregates Platelet Microparticles Hemolysis
Coagulation Time	Prothrombin Time Partial Thromboplastin Time Unactivated Partial Thromboplastin Time
Clotting Factors	C3a Generation SC5b-9 Generation C5a Generation

Understanding protein adhesion to polymer surfaces is advantageous for several reasons. While it is accepted that protein binding plays a role in platelet activation, the mechanisms are not entirely understood. Additionally, there are commercial applications of polymers in biopharmaceutical applications wherein low protein adsorption on the sides of vials or devices is desirable. In general, a hydrophilic surface (low contact angle, high surface energy) results in low protein adsorption, although exceptions can occur. The ability to predict the interaction of surfaces with proteins is relatively developed, since a hydrophilic surface has been shown to generally adsorb less protein (9). By contrast, hydrophobic surfaces have been shown to be useful for the protein adhesion required for artificial scaffolding (10). Protein adhesion or uptake can be relatively easily monitored, and may be paired with more sophisticated techniques to measure the degree of protein denaturation (11).

Despite the ubiquitous presence of polymeric materials in clinics and hospitals, a detailed understanding of how synthetic surfaces interact with biological fluids is still lacking. Detailed herein are some examples of hydrophilic, hydrophobic, and heterogenic surfaces which have been evaluated for biocompatibility.

Surface Modification by Coating

Modifying a polymeric surface through the use of additives is limited by several practical considerations. First, the modifier has to have sufficient thermal stability to survive high temperatures during extrusion and injection molding. While the additive should be surface active in order to impart the desired properties, it cannot adversely affect the bulk properties of the polymer, nor can it be fully immiscible leading to phase separation. All of these potential limitations can be overcome by modifying the polymer surface after molding the article by secondary operations like coatings, surface grafting, and plasma modification. These methods have been used successfully to impart biocompatibility in polymers, albeit with increased cost. While the coating of polymers will not be described in detail, two examples of biocompatible coatings are presented below to illustrate the use of coatings in medical devices.

The use of phospholipids to mimic cell walls has been one commercially successful coating strategy. To create a polymer surface with phospholipid-type properties, two routes are possible. The polymer surface can be modified by the attachment of the biological molecule of interest, as described in the modification of polymer surfaces with phosphorylcholine (12-14), amphiphilic molecules (15) or liposomes. Alternatively, phosphorylcholine moieties have been incorporated into artificial surfaces by using polymerizable precursors; the most representative monomer is 2-methacryloxyethylphosphorylcholine (MPC) (16, 17). Block copolymers of phosphorylcholine with other hydrophobic comonomers like lauryl methacrylate (18) also have been found to be effective.

Another commercially available coating uses the anticoagulant heparin. Heparin coatings have two different mechanisms of imparting hemocompatibility. Heparin-releasing surfaces slowly release bound heparin, in an effective but impermanent route to hemocompatibility (19). Another way of utilizing heparin is to immobilize the molecule by covalent linkage with the polymer surface (19, 20).

Coatings have been shown to be effective in reducing the immunological response to the synthetic material. While coatings are effective, they are expensive and require a secondary operation to render the medical device suitable for use. Some coatings have a limited time of use, or are quite fragile and not compatible with all sterilization methods.

Hydrophilic Materials

A hydrophilic, or “water loving” polymer, is most easily visualized as a material with such a high compatibility with water that a surface droplet will spread out into an aqueous film. Thus, the contact angle of water to an extremely hydrophilic surface would be 0° . The contact angle measurement, as shown in Figure 1, is a widely accepted measurement of the hydrophilicity (low contact angle) or hydrophobicity (high contact angle) of a surface relative to the fluid (water) that is used in the measurement. Methods such as Sessile drop, Wilhelmy plate, and captive bubble are all accepted methods of measuring the contact angle; surface energy, measured in dyne/cm, is another relative measure of the free energy difference between liquids and polymers (21).

It is generally accepted that hydrophilic materials are biocompatible via a hydrogen bonding mechanism in which strongly solvated water molecules generate a biologically inert surface. The solvated water layer minimizes interactions of biological molecules with the synthetic surface, resulting in low protein adhesion and reduced platelet interaction (9, 22). While it is accepted that protein binding plays a role in platelet activation, the mechanisms are not entirely understood (23). Furthermore, while hydrophilic surfaces in general are resistant to protein and platelet adhesion, the degree of hydrophilicity has not been observed to play a role. Furthermore, while hydrophilic surfaces in general are resistant to protein and platelet adhesion, the degree of hydrophilicity has not been observed to play a role. In other words, a more hydrophilic surface is not necessarily more biocompatible than a less hydrophilic surface (22, 24).

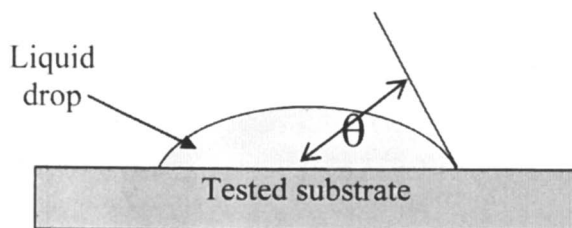


Figure 1. Schematic of contact angle measurement by the Sessile Drop method.

Furthermore, while hydrophilic surfaces in general are resistant to protein and platelet adhesion, the degree of hydrophilicity has not been observed to play a role. In other words, a more hydrophilic surface is not necessarily more biocompatible than a less hydrophilic surface (22, 24). On the other hand, the

Kohn group has established that surface hydrophilicity, along with several other descriptors, can be used to predict the cellular response to a set of polyarylate films (25). It is a provoking thought that the surface's hydrophilicity may be a key component, but not the definitive predictor, of biocompatibility.

The most well known inherently hydrophilic materials are hydrogels, which are cross-linked hydrophilic polymer networks. These hydrogels have enough cohesive strength to be used in contact lenses or medical implants, and also have porosity defined by the degree of crosslinking, a useful property for drug delivery applications (26). Some hydrogel polymers and their typical applications are shown below in Table 3 (27). While hydrogels have found widespread use in medical applications, they have limited mechanical strength and are not engineering thermoplastics.

Polyurethanes are another class of materials that can have hydrophilic properties (28). The ability to tailor the "soft" polyether block and the "hard" isocyanate block allows for optimization of surface properties and mechanical properties, depending on the application requirements. The ability to generate hydrophilic surfaces has made polyurethanes useful in catheter applications, where protein resistance is an important requirement (29). Another characteristic of some polyurethane catheters is that they soften upon use, providing a degree of patient comfort (30).

Polyurethane materials are also easily modified via grafting, which can be achieved via several methods, including reactions with hexamethylene diisocyanate (31), gamma irradiation (22*d*), or radical initiators (32), to name a few. The chemical moieties that can be grafted onto polyurethanes are also numerous, and include polyethylene glycol (PEG), polyethylene oxide (PEO), heparin, and phosphorylcholine type appendages (22*d*, 28, 31-32). In general, the grafting of hydrophilic materials improves the protein resistance and hemocompatibility of the polyurethane material. Polyurethanes are especially suited to surface functionalization, but materials as different as polyethylene terephthalate (PET)(33) and Teflon (34) can also be functionalized through grafting. Relatively hydrophobic polyurethanes grafted with hydrophilic pendant groups may be more correctly characterized as having a heterogeneous hydrophilic/hydrophobic surface, which will be described later. Treatments that make polyurethanes even more hydrophobic have been shown to react more strongly with blood proteins, in a reduction of hemocompatibility (6*a*).

The hemocompatibility of hydrophilic materials is relevant for standard blood-contacting medical devices, but there are additional applications for which the protein-resistant properties are useful. Hydrophilic materials play a large role in the membrane industry, where improved wet-out improves solution flow through the membrane; additionally, hydrophilic membranes show less protein fouling (35). In the realm of engineering thermoplastics, low protein binding materials are useful in lab equipment and in biopharmaceutical applications

Table 3. Medical applications of hydrogel polymers

<i>Hydrogel</i>	<i>Medical application</i>
Poly(hydroxyethyl methacrylate) [pHEMA] copolymerized with: N-vinyl-2-pyrrolidone Methacrylic acid Butyl methacrylate Methyl methacrylate	Contact Lenses
pHEMA/poly(ethylene terephthalate) Cellulose acetate Poly(N-vinyl-2-pyrrolidone) Poly(vinyl alcohol) Methyl methacrylate	Artificial organs/cartilage
Poly(acrylamide) Poly(acrylic acid) Poly(dimethylaminoethyl methacrylate) Poly(N-isopropyl acrylamide) Poly(lactic acid) Poly(glycolic acid) Chitosan Dextran Polycyanoacrylates	Controlled Drug Delivery

where protein handling is involved. There are some engineering thermoplastics that are inherently hydrophilic, notably polyethersulfone (PES). The hydrophilicity of PES can be further enhanced via a secondary sulfonation step (36). Non-polyurethane hydrophilic block copolymers have been characterized (37), but the adverse effects of PEG or PEO blocks on hydrolytic stability, mechanical properties, and heat deformation temperatures have limited their utility. Furthermore, while a hydrophobic domain has an energetic driving force to migrate to the surface, no such driving force exists for a hydrophilic domain. It is no surprise, then, that the most effective method to impart hydrophilicity to a surface involves the direct functionalization of that surface.

Hydrophobic Materials

Hydrophobic polymers, by common perception, are those, which have a definite contact angle of water (typically > 75 degrees). Most of the commonly used plastics in everyday life are hydrophobic by this definition. These polymers

have a wide range of properties and applications starting from stiff, brittle material like poly(methyl methacrylate) (PMMA) or polystyrene (PS) or high-heat and high-impact materials like polycarbonate, to rubbery materials like polybutadiene or polysiloxanes. Good mechanical properties and ease of processability make these hydrophobic polymers suitable for biomedical applications, especially for molding of medical devices with complex shapes. Moreover, due to absence of significant water uptake by these polymers (typically less than 0.4% at room temperature), their mechanical properties do not suffer while in contact with biological fluids like blood. Also, these hydrophobic polymers can be effectively sterilized by different well-known techniques; for example, irradiation by gamma rays, ethylene oxide (EtO) sterilization, and autoclaving. These attributes make hydrophobic polymers very effective materials for biological applications. The low surface energies of hydrophobic materials can be measured by Zisman's Critical Surface Tension (CST) concept (38). This method gives the maximum possible surface tension of a liquid that completely wets the solid surface (zero contact angle), calculated by extrapolating the surface tension values of several liquids on a particular surface to zero contact angle. In injection molding applications, a part with low surface energy may also resist staining, have lower surface friction, and easily eject from molds.

The potential advantage of hydrophobic materials in blood compatibility was demonstrated early in the literature. Lister (39) demonstrated in 1863 that blood coagulation in a rubber container was a slower process than in glass. Thereafter, Bordet and Gengou (40) showed that a surface coated with paraffin was effective in preventing plasma coagulation to a greater extent than glass.

A complete correlation between hydrophobicity and biocompatibility, as defined by protein adsorption or blood compatibility, has not yet been fully established. As polar liquids like water do not wet the surface of hydrophobic materials, similarly an aqueous biological fluid could also be expected to be repelled from a hydrophobic surface, minimizing any interactions. Quite to the contrary, hydrophobic surfaces do react quite strongly with aqueous fluids. Lambert (41) was one of the pioneers in laying down some of the principles that would help in identifying a blood-compatible surface. According to his work, the clotting time of blood is inversely proportional to the "wettability" of the surface. However, wettability can only be a rough estimate of the surface energy, since other factors such as hydrogen bonding may also influence the surface characteristics. Rose et al (42, 43) challenged this idea and also found several examples that did not follow Lambert's proposed theory. Lyman and coworkers (44) later demonstrated that for hydrophobic surfaces with no possibility of hydrogen bonding or ionic bonding, the clotting time for dog's blood decreased linearly with the logarithm of CST. There were some exceptions; Teflon, for example, exhibited a short clotting time in spite of its very low surface energy.

One more widely accepted hypothesis is that blood compatibility is optimum within a short range of surface energies that induce some favorable interactions with plasma proteins. It has been found that blood compatibility is optimum when the CST lies between 20 to 30 dynes/cm (45). However, some hydrophobic polymers that find applications in blood-contacting devices do not possess CST values within this range. Andrade hypothesized that smaller interfacial energies between blood and polymer surface actually implies a better blood compatibility (46).

Whenever a foreign material is introduced into a living environment, the first event that takes place is protein adsorption at the interface. The adsorbed protein may either retain its original structure or may undergo changes in orientation or conformation (47). The properties of this adsorbed protein layer further dictate the interactions at the cellular level, which determine the performance of the foreign body as a biomaterial. The conformational change occurring in the adsorbed protein layer can have different consequences; it can make the material bio-reactive, or it can result in recognition of the protein as a foreign body. Either action results in the organism initiating biological cascades such as coagulation and complement activation. (48). The nature of the surface plays a major role in determining the composition and biological state of the adsorbed proteins. When the adsorbed protein does not interact with the cellular elements, which is the case with adsorbed albumin, then the surface is biocompatible. However, when the adsorption of proteins such as fibrinogen results in accelerated platelet adsorption on the surface, then it can initiate coagulation cascade. In case of hydrophobic surfaces, fibrinogen is the main protein adsorbed (49), although competitive adsorption of proteins is a very complex phenomenon.

Some authors have correlated the surface free energy and surface chemistry of materials with their biocompatibility, as characterized by *in vitro* activation of coagulation, fibrinolysis and platelet adsorption (50,51). The most hydrophobic surfaces appeared to cause least activation of platelets. However, studies also exist wherein no such relationship was detected. Nurdin et al (52) did not find such a correlation between water contact angle and hemocompatibility when evaluating polymers such as low density polyethylene (LDPE), PDMS, and PMMA. Similar observations were made by Oeveren et al (53), in his studies of the interactions of hydrophobic materials like polyethylene (PE), poly(vinyl chloride) (PVC), polyurethanes (PEU), PDMS and PTFE with blood. There are also experiments that have found that hydrophobic materials strongly interacted with blood components. Sefton et al (6a) have found that reducing surface energy by modifying PE with CF_4 did not improve biological responses towards the surface; in fact PE- CF_4 was found most reactive by several assays than PE. Similar observations correlating fluorine content to reduced hemocompatibility have been made in several studies (54).

In a review of the literature the evidence suggests that among the unmodified hydrophobic surfaces, PE and PDMS show some degree of biocompatibility. Fluorinated compounds have markedly poorer performance; the lower surface energy of fluorinated polymers induces more fibrinogen adsorption, which in turn initiates platelet activation and clotting. There are contradictory reports of fluorinated polymers being more biocompatible; it is possible in these cases that the adsorption of albumin or fibrinogen was not followed by conformational changes of the proteins, thus the cascading biological response was not initiated (55). It should also be noted that the performance of materials in contact with biological fluids depends heavily upon the evaluation method that is employed, which can lead to contradictory conclusions from different laboratories for similar polymers.

Heterogenic Materials

Previous sections have described the observed trend that hydrophilic polymers in general are more biocompatible than hydrophobic polymers, ostensibly because of the ability of hydrophilic surfaces to reject proteins. However, there is no thermodynamic driving force for higher surface energy hydrophilic components to bloom to an injection-molded surface.

Polymer surfaces containing micro-domains of both hydrophilic (polar) and hydrophobic (nonpolar) regions have been of recent interest for their favorable interactions with proteins that leads to improved blood-compatibility. One way to achieve this is by adding surface modifying additives (SMAs) in the polymer formulation while processing. These SMAs typically are block copolymers having blocks of both hydrophobic and hydrophilic character. Having lower surface energy, the hydrophobic portion of the copolymer migrates to the surface on molding; by this process they carry the hydrophilic portion along as well. This kind of surface migrating ability of the additives enables their use in relatively small amounts, retaining most of the bulk properties. Examples of such hemocompatibility-improving block copolymers include polylactone-polysiloxane (56), polyurethane-PEG-PDMS (57), and polycaprolactone-PDMS-polycaprolactone triblock copolymers (58). The use of SMA additives as coatings has been proven in medical device studies. Clinical studies of SMA-coated cardiopulmonary bypass circuits demonstrated reduced thrombogenicity and inhibited platelet interactions with SMA-enhanced surfaces (59, 60). A similar approach was used to coat a polymer surface with poly(2-methoxyethylacrylate) (PMEA), which has a hydrophobic backbone and a mildly hydrophilic residue (19, 60, 61).

There are few potential disadvantages with SMAs, especially those with lower molecular weight. They could leach out from the surface and cause

reduced efficacy. Also, no surface replenishment will occur if the surface is eroded or abraded during use, due to the low mobility of these SMAs in solid state. One way to overcome this potential problem is the use of surface migrating end groups in place of additives as demonstrated by Ward (62), who developed the strategy of surface active oligomeric end groups. However, the number of surface end groups that can be placed in a polymer of given molecular weight limits this approach. To have a high concentration of end groups, the molecular weight of the polymer chains must be low; thus, mechanical properties will be adversely affected.

Other block copolymers having hydrophobic and hydrophilic blocks have also been found to improve protein and blood-compatibility. Okano *et al* have synthesized ABA type block copolymers composed of hydrophilic 2-hydroxyethylmethacrylate (HEMA) and hydrophobic styrene monomer. These copolymers were shown to have different morphologies depending upon the relative ratio of HEMA and styrene in the block copolymers. The microphase-separated structures were antithrombogenic, resisting platelet adhesion more effectively than the comparable homopolymers and random copolymers that lacked microphase-separated morphologies (63). Similar antithrombogenic behavior was found by the same group in cases of diblock copolymers of poly(HEMA) and either styrene or PDMS; these block copolymers also exhibited a hydrophilic-hydrophobic microphase separated structure (64). Examples of other hydrophobic-hydrophilic block copolymers include polydimethylsiloxane-poly(γ -benzyl L-glutamate) block copolymers (65), and poly(propylene oxide)-polyamide copolymers (66). Although the mechanism of action by which SMAs and microphase-separated structures decreases blood protein and cellular activation is not precisely known, the mosaic structure of microdomains with different polarity may lead to more uniform fibrinogen adhesion such that platelet receptor sites are unexposed or unavailable for interaction (62,63).

In conclusion, synthetic surfaces can be described as hydrophilic, hydrophobic, or heterogenic. For each of these types of surfaces, studies exist which show general trends in the improvement of biocompatibility. However, there is not a single theory or predictive tool that can predict the biocompatibility of a wide range of materials.

References

1. Lyman, D. J. *Intern. J. Polymeric Mater.* **1973**, *2*, 319-333.
2. Prasad Shastri, V. *Curr. Pharm. Biotech.* **2003**, *4*, 331-337. Polymer definitions are as follows: PDMS – polydimethylsiloxane; PEU – poly(ether urethane); PEO – poly(ethylene oxide); PEG – poly(ethylene glycol); PET –

poly(ethylene terephthalate); PC – polycarbonate; COC – cyclic olefin copolymer; PE – polyethylene; PMMA – poly(methyl methacrylate); PTFE – poly(tetrafluoroethylene); PSU – polysulfone; EVA – ethylene vinyl acetate copolymer; PVA – poly(vinyl alcohol).

3. (a) Baker, R. W. *Membrane Separation Systems – Recent Developments and Future Directions*; William Andrew Publishing: Noyes, 1991; (b) Abetz, V. et al. *Adv. Eng. Mater.*, **2006**, *8*, 328.
4. (a) Sources: *U.S. Industrial Outlook* and *U.S. Industry and Trade Outlook*, as reported by *Medical Device & Diagnostic Industry*, 2005; (b) Stewart, R. *Plastics Engineering*, 2005, *61*, 20-27.
5. Stryer, L. *Biochemistry*; 3rd edn, W. H. Freeman and Company: NY, **1988**.
6. (a) Sefton, M. V.; Sawyer, A.; Gorbet, M.; Black, J. P.; Cheng, E. Gemmell, C.; Pottinger-Cooper, E. *J. Biomed. Mater. Res.* **2001**, *55*, 447-459. (b) Ishihara, K. *Trends in Polymer Science* **1997**, *5*, 401-407. (c) Li, J. et al. *J. Biomater. Sci. Polymer Edn.* **1999**, *10*, 235-246. (d) Elam, J.-H.; Elam, M. *Biomaterials* **1993**, *14*, 861. (e) Keuren, J. F. W.; Wielders, S. J. H.; Willems, G. M.; Morra, M.; Cahalan, L.; Cahalan, P.; Lindhout, T. *Biomaterials* **2003**, *24*, 1917-1924. (f) Yuan, Y. L.; Zhang, J.; et al. *J. Biomater. Sci. Polymer Edn.* **2002**, *3*, 1081-1092.
7. "Biological Evaluation of Medical Devices, Part 1: Guidance on Selection of Tests," ISO 10993-1, EN 30993-1, Geneva, International Organization for Standardization (ISO), 1992; "Required Biocompatibility Training and Toxicology Profiles for Evaluation of Medical Devices," *Blue Book Memorandum G95-1*, Rockville, MD, FDA, Center for Devices and Radiological Health (CDRH), Office of Device Evaluation, 1995.
8. (a) Berger, M.; Broxup, B.; Sefton, M. V. *J. Mater. Sci. Materials in Medicine* **1994**, *5*, 622-627. (b) Rinder, C. S.; Rinder, H. M.; Smith, B. R.; Fitch, J. C.; Smith, M. J.; Tracey, J. B.; Matis, L. A.; Squinto, S. P.; Rollins, S. A. *J. Clin. Invest.* **1995**, *96*, 1564-1572. (c) Gemmell, C. H.; Ramirez, S. M.; Yeo, E. L.; Sefton, M. V. *J. Lab. Clin. Med.* **1995**, *125*, 276-287. (d) Resmi, K. R. Varghese, N.; Krishnan, L. K. *Thrombosis Research* **2004**, *114*, 121-128.
9. (a) Hester, J. F.; Banerjee, P.; Mayes, A. M. *Macromolecules* **1999**, *32*, 1643-1650. (b) Childs, M. A.; Dorgan, J. R.; Ohno, T. *Biomacromolecules* **2001**, *2*, 526-537. (c) Ostuni, E.; Chapman, R. G.; Holmlin, R. E.; Takayama, S.; Whitesides, G. M. *Langmuir* **2001**, *17*, 5605-5620
10. (a) Yun, J. K. DeFife, K.; Colton, E.; Stack, S.; Azeez, A.; Cahalan, L.; Verhoeven, M.; Cahalan, P.; Anderson, J. M. *J. Biomed. Mater. Res.* **1995**, *29*, 257-268. (b) Fujimoto, K. *Recent Research Developments in Biomaterials* **2002**, 123-135.
11. (a) Kumar, V.; Krishnan, S.; Steiner, C.; Maldarelli, C.; Couzis, A. *J. Phys. Chem. B* **1998**, *102*, 3152-3159. (b) Tzoneva, R.; Heuchel, M.; Groth, T.;

- Altankov, G.; Albrecht, W.; Paul, D. *J. Biomater. Sci., Polymer Edn.* **2002**, *13*, 1033-1050. (c) Tanaka, M.; Motomura, T.; Kawada, M.; Anzai, T.; Kasori, Y.; Shiroya, T.; Shimura, K.; Onishi, M.; Mochizuki, A. *Biomaterials* **2000**, *21*, 1471-1481.
12. (a) Orban, J. M.; Faucher, K. M.; Dluhy, R. A.; Chaikof, E. L. *Macromolecules* **2000**, *33*, 4205-4212. (b) Hayward, J. A.; Chapman, D. *Biomaterials* **1984**, *5*, 135-142
13. (a) Lu, J. R.; Murphy, E. F.; Su, T. J.; Lewis, A. L.; Stratford, P. W.; Satija, S. K. *Langmuir* **2001**, *17*, 3382-3389. (b) Hall, B.; Bird, R. R.; Kojima, M.; Chapman, D. *Biomaterials* **1989**, *10*, 219-224.
14. Yamasaki, A.; Imamura, Y.; Kurita, K.; Iwasaki, K.; Nakabayashi, N.; Ishihara, K. *Colloids Surf. B: Biointer.* **2003**, *28*, 53-62.
15. Liu, H.; Faucher, K. M.; Sun, X-L. June, F.; Johnson, T. L.; Orban, J. M.; Apkarian, R. P.; Dluhy, R. A.; Chaikof, E. L. *Langmuir* **2002**, *18*, 1332-1339.
16. Ishihara, K.; Fujita, H.; Yoneyama, T.; Iwasaki, Y. *J. Biomater. Sci. Polym. Ed.* **2000**, *11*, 1183-1195.
17. Iwasaki, Y.; Tojo, Y.; Kurosaki, T.; Nakabayashi, N. *J. Biomed. Mater. Res.* **2003**, *A65A*, 164-169.
18. Lewis, A. L.; Hughes, P. D.; Kirkwood, L. C.; Leppard, S. W.; Redman, R. P.; Tolhurst, L. A.; Stratford, P. W. *Biomaterials* **2000**, *21*, 1847-1859.
19. Rubens, F. D. *J. Biomater. Sci. Polym. Ed.* **2002**, *13*, 485-499.
20. Wendel, H. P.; Ziemer, G. *Eur. J. Cardiothorac. Surg.* **1999**, *16*, 342-350.
21. (a) Wu, S. *Polymer Interface and Adhesion*; Marcel Dekker, Inc.: NY, 1982. (b) Isrealachvili, J. *Intermolecular Forces and Fields*, 2nd Edition; Academic Press: NY, 1992. (c) van Oss, C. *Interfacial Forces in Aqueous Media*; Marcel Dekker, Inc.: NY, 1994. (d) Kwok, D.; Neumann, A. *Adv. Coll. Interf. Sci.* **1999**, *81*, 167.
22. Hari, P. R.; Sharma, C. P. *J. Biomed. Appl.* **1991**, *6*, 170.
23. (a) Lindon, J. N.; McManama, G.; Kushner, L.; Merrill, E. W.; Salzman, E. W. *Blood* **1986**, *68*, 355-362. (b) Anderson, A. B.; Tran, T. H.; Hamilton, M. J.; Chudzik, S. J.; BP Hastings, Melchior, M. J.; Hergenrother, R. W. *American Journal of Neuroradiology* **1996**, *17*, 859-863. (c) Kim, S. W.; Lee, E. O. *J. Polym. Sci., Polym. Symp.* **1979**, *66*, 429-441.
24. Ostuni, E.; Chapman, R.G.; Liang, M. N.; Meluleni, G.; Pier, G.; Ingber, D. E.; Whitesides, G. M. *Langmuir* **2001**, *17*, 6336-6343.
25. Kholodovych, V.; Smith, J.; Knight, D.; Abramson, S.; Kohn, J.; Welsh, W. *Polymer* **2004**, *45*, 7367-7379.
26. (a) Hoffman, A. S. *Adv. Drug Deliv. Rev.* **2002**, *43*, 3-12; (b) Park, K.; Shalaby, W. S. W., Park, H. *Biodegradable Hydrogels for Drug Delivery*; Technomic Publishing: Lancaster and Basel, 1993.
27. Hin, T. S. *Engineering Materials for Biomedical Applications*; World Scientific, 2004.

28. Zdrahala, R. J.; Zdrahala, I. J. *J. Biomater. Appl.* **1999**, *14*, 67-90.
29. (a) Scierholz, J. M.; Beuth, J. *J. Hosp. Infect.* **2001**, *49*, 87-93. (b) Schierholz, J.; Beuth, J. *Med Dev Tech* **2000**, *11*, 12-17
30. Onwunaka, T.; Lambert, J. US Patent 5,266,669, 1993.
31. (a) Han, D. K.; Jeong, S. Y.; Kim, Y. H. *J. Biomed. Mater. Res. Applied Biomaterials* **1989**, *23*, 211-228. (b) Yoo, H. J.; Kim, H. D. *J. Appl. Polym. Sci.* **2004**, *91*, 2349-2357.
32. Korematsu, A.; Takemoto, Y.; Nakaya, T.; Inoue, H. *Biomaterials* **2002**, *23*, 263-271.
33. Wang, J.; Pan, C.J.; Huang, N.; Sun, H.; Yang, P.; Leng, Y.X.; Chen, J.Y.; Wan, G.J.; Chu, P.K. *Surface & Coatings Technology* **2005**, *196*, 307-311.
34. Elam, J.-H.; Elam, M. *Biomaterials* **1993**, *14*, 861.
35. Porter, M. C. in *Handbook of Industrial membrane Technology*, William Andrew Publishing, 1990.
36. Li, Y. et al, *Polymer*, **2006**, *47*, 4210-4217..
37. Merrill, S. H.; Petrie, S. E. *J. Polym. Sci. Part A Gen. Pap.* **1965**, *3*, 2189.
38. Fox, H. W.; Zisman, W. A. *J. Collid. Sci.* **1952**, *7*, 109-121.
39. Lister, J. *Proc. Roy. Soc.* **1863**, *B12*, 580.
40. Bordet, J.; Gengou, O. *Ann. Inst. Pasteur.* **1903**, *17*, 822-833.
41. (a) Lampert, H. *Muench. Med. Wochschr.* **1930**, *77*, 586.; (b) Brash, J. L. *Ann. N.Y. Acad. Sci.* **1977**, *283*, 357-371
42. Rose, J. C.; Broida, H. P. *Proc. Soc. Exp. Biol. Med.* **1954**, *86*, 384-386.
43. Ross, J.; Greenfield, L. J.; Bowman, R. L.; Morrow, A. G. In *Prosthetic Valves for Cardiac Surgery Merendino, K. A. Eds.* **1961**, pp 212-223.
44. Lyman, D. J.; Muir, W. M.; Lee, I. J. *Trans. Amer. Soc. Artif. Int. Organs.* **1965**, *11*, 301-306.
45. Baier, R. E.; Gott, V. L.; Furuse, A. *Trans. Amer. Soc. Artif. Int. Organs* **1970**, *16*, 50-57.
46. (a) Andrade, J. D. *Med. Instum.* **1973**, *7*, 110.; (b) Andrade, J. D.; Lee, H. B.; John, M. S.; Kim, S. W.; Hibbs, J. B. *Trans. Am. Soc. Artif. Internal Organs* **1973**, *19*, 1.
47. (a) Castner, D. G.; Ratner, B. D. *Surf. Sci.* **2002**, *500*, 28. (b) Brash, J. L. Hobett, T. In *Blood compatible materials and devices; Perspective toward the 21st century*; Sharma, C.; Szycher, M. Eds. Technomic Publishing Co. Lancaster, PA 1992, pp 3-24. (c) Gaebel, K.; Feuerstein, I. *Biomaterials* **1991**, *12*, 597-602.
48. Brash, J. L.; Horbett, T. A. In *Proteins at Interfaces II: Fundamentals and Applications*; Hobett, T. A.; Brash, T. A. Eds. ACS Symposium Series, Vol. 602, 1995, pp 1-50.
49. Yu, J.; Sundaram, S.; Weng, D.; Courtney, J. M.; Moran, C. R.; Graham, N. B. *Biomaterials* **1991**, *12*, 119.
50. Kashiwagi, T.; Ito, Y.; Imanishi, Y. *J. Biomater. Sci. Polymer. Ed.* **1993**, *5*, 157-166.

51. Kiaei, D.; Hoffman, A. S.; Ratner, B. D.; Horbett, T. A. *J. Appl. Polymer Sci. Appl. Polymer Symp.* **1988**, *42*, 269-283.
52. Nuridin, N.; Francois, P.; Mugnier, Y.; Krumeich, J.; Moret, M.; aronsson, B.-O.; Discounts, P. *Eur. Cells. Mater.* **2003**, *5*, 17-28.
53. Van Oeveren, W.; Hann, J.; Lagerman, P.; Schoen, P. *Artif. Org.* **2002**, *26*, 506-511.
54. (a) Absolom, D.R.; Zingg, W.; Neumann, A.W.; *J. Biomed. Mater. Res.* **1987**, *21*, 161-171. (b) Kiaei, D.; Hoffman, A.S.; Horbett, T.A. *J. Biomater. Sci. Polym. Ed.* **1992**, *4*, 35-44. (c) Bohnert, J.L.; Fowler, B.C.; Horbett, T.A.; Hoffman, A.S. *J. Biomater. Sci. Polym. Ed.* **1990**, *1*, 279-297.
55. (a) Kanazaki, S.; Kawakami, H.; Nagaoka, S.; Kubota, S. *J. Biomater. Sci. Polymer Ed.* **2003**, *14*, 469-479. (b) Balasubramanian, V.; Grusin, N. K.; Bucher, R. W.; Turitto, V. T.; Slack, S. M. *J. Biomed. Mater. Res.* **1999**, *44*, 253-260
56. (a) Ward, R. S.; Riffle, J. S. US patent 4,663,413, 1987. (b) Voorhees, M.; Forrestal, L.; Fisher, H. US patent. 5,643,681, 1997.
57. (a) Ward, R. S. US patent 4,675,361, 1987. (b) Ward, R. S. US patent 4,861,830, 1989.
58. (a) Tang, L.; Sheu, M.; Chu, T.; Huang, Y. *Biomaterials* **1999**, *20*, 1365-1370. (b) Lovinger, A. J.; Han, B. J.; Padden, F.J.; Mirau, P.A. *J. Polym. Sci.* **1993**, *31*, 115-123. (c) Tsai, C-C.; Deppisch, R. M.; Forrestal, L. J.; Ritzau, G. H.; Oram, A. D.; Gohl, H. J.; Voorhees, M. E. *ASAIO J.* **1994**, *40*, M619-M624.
59. (a) Rubens, F. D.; Labow, R. S.; Lavalley, G. R.; Watson, M. I.; Robblee, J. A.; Voorhees, M. E.; Nathan, H. J. *Ann. Thorac. Surg.* **1999**, *67*, 689-696. (b) Martens, S.; Matheis, G.; Wimmer-Greinecker, M.; Scherer, M.; Doss, M.; Moritz, A. *Cardiovasac. Surg.* **2003**, *11*, 159. (c) Gu, Y. J.; Boonstra, P. W.; Rinjsburger, A. A.; Hann, J.; van Oeverwn, W. *Ann. Thorac. Surg.* **1998**, *65*, 1342-1347.
60. Farrar, D. J. et. al. *J. Thorac. Cardiovasac. Surg.* **1988**, *95*, 191-200.
61. Suhara, H.; Sawa, Y.; Nishimura, M. et. al. *Ann. Thorac. Surg.* **2001**, *71*, 1603-1608.
62. Ward, R. S. *Medical Plastics and Biomaterials*, PTG Scientists, CA. 1995, pp 34-41.
63. Okano, T.; Nishiyama, S.; Shinohara, I.; Akaike, T.; Sakurai, Y.; Kataoka, K.; Tsuruta, T. *J. Biomed. Mater. Res.* **1981**, *15*, 393-402.
64. Okano, T.; Aoyagi, T.; Kataoka, K.; Abe, K.; Sakurai, Y. *J. Biomed. Mater. Res.* **1986**, *20*, 919-927.
65. Kang, I.; Ito, Y.; Sisido, M.; Imanishi, Y. *Biomaterials* **1988**, *9*, 138-144.
66. Yui, N.; Sanui, K.; Ogata, N.; Kataoka, K.; Okano, T.; Sakurai, Y. *J. Biomed. Mater. Res.* **1986**, *20*, 929-943.

Chapter 17

Reactive Polymer Coatings for Biological Applications

**Himabindu Nandivada, Hsien-Yeh Chen, Yaseen Elkasabi,
and Joerg Lahann***

**Departments of Chemical Engineering and Materials Science
and Engineering, and Macromolecular Science and Engineering,
University of Michigan, Ann Arbor, MI 48109**

The design of biologically active surfaces offers a new dimension to the development of advanced materials for biomedical and microfluidic applications. Our approach to creating these surfaces is via the fabrication of vapor-based reactive polymer coatings, which provide sophisticated functional groups for the immobilization of biological ligands. Chemical vapor deposition (CVD) polymerization has been used to prepare a wide spectrum of functionalized poly(*p*-xylylenes). The applicability of a few of these reactive surfaces as stable platforms for biomimetic modifications is discussed in this review.

Introduction

In the past few decades, biomaterials have assumed a central role in the development of therapeutic and diagnostic systems for biomedical and pharmaceutical applications (1-3). These materials have been developed from mostly modified-commodity materials or naturally occurring materials to a new generation of synthetic designer materials and have found applications in drug delivery devices, prosthetics, implants, microfluidics devices, biosensors, biofouling and tissue engineering (4). However, there is a need to modulate the interactions between the biological environment and the material surfaces, since the first interaction between the ambient environment and the foreign surface occurs at the interface (5). This can be achieved by optimizing the physical, chemical and biological properties of the surfaces through biologically-inspired surface engineering. In other words, materials can be engineered to mimic (biomimetic) the biological environment with the desired bio-functionalities (6,7). The substrate must therefore possess reactive groups that support the coupling step for covalent binding between a substrate and a ligand. However, most substrates of interest lack such groups. So, they must be introduced either in a proper surface functionalization step or via the deposition of functionalized thin-film coatings.

Surface functionalization is a key step to generate a favorable reaction when any surface comes in contact with a biological environment (8). Towards this goal, a variety of physical, mechanical, chemical and biological methods such as silanization, plasma polymerization and self-assembled monolayers are being used (9). Plasma polymerization is a physico-chemical process in which gaseous monomers, stimulated through plasma, deposit on substrates as highly cross-linked layers. For instance, plasma polymer coatings have been used to achieve an excellent adhesion of parylene coating on a smooth aluminum alloy. Functionalizing the surface via plasma treatment also makes the hydrophobic polymer paintable (10). However, the monomers may be at least partly degraded in the plasma, so preserving the chemical structures of the monomers is challenging, resulting in cross-linked and disordered polymeric structures and thus reducing the specificity and reproducibility of the process. Another technique that is widely used to tailor the interfacial properties of metals, metal oxides and semiconductor surfaces is the use of self-assembled monolayers (SAMs) (11). Based on the terminal functional groups exposed on the surface of a SAM, the reactivity of the surface can be varied. SAMs have been used for the direct immobilization of DNA, polypeptides and proteins (12). However the use of SAMs is limited due to the relative chemical instability of the monolayer and the specificity of the substrates.

Over the past few years, vapor-based polymer coatings have emerged as a promising solution for surface modification due to their advanced processibility

and excellent intrinsic biocompatibility. Chemical vapor deposition (CVD) is a well established technique for the formation of inorganic layers, and it has been extended to generate thin conformal polymer coatings. This is a room temperature process that does not require any catalyst, initiator or solvent and no byproducts are generated. Other advantages of this process include control of the composition and architecture of the films, high accuracy, and good adhesion to a wide variety of substrates (including biomedical and microfluidic devices). Functionalized poly(*p*-xylylenes) can be deposited via CVD polymerization to generate thin polymer films (20-100nm) and, due to the pre-defined chemical functionalities, provide a flexible solution to surface engineering challenges as they decouple surface design from bulk properties. Hence, the technology comprises essentially a one-step coating procedure to generate functionalized surfaces without requiring any non-biological post-treatment on the deposited films (13). The simplicity in providing a wide range of functional groups, the excellent adhesion to various substrates, and its applicability to devices with three-dimensional geometries are key advantages when compared to polymers deposited by solvent-based methods.

Biomimetic Modifications of the Reactive Coatings

In principle, CVD-based polymers are well suited as a platform for tailoring the desired surface properties. For instance, a specific vapor-deposited polymer (poly(*p*-xylylene) or parylene) is already being used in FDA approved drug-eluting stents as an adhesion promoter. However, these commercially-available coatings lack functionalities for surface modification and hence do not allow the immobilization of biomolecules. A suitable immobilization platform is essential for the successful fabrication of biologically active surfaces. The biomolecules should be stable on the surface and the immobilization chemistry should preserve the conformation and accessibility of the ligands on the surface (14). The reaction chemistry should have fast reaction kinetics and the linkage should be stable. Our approach to the creation of these surfaces is the fabrication of a reactive polymer coating, which has adjustable functional groups that can be used for the covalent-binding of ligands. The strategy used is based on the fact that the reactive functional groups on the polymer can be modulated based on the specific immobilization chemistry of the ligand. These surfaces bring the physical and mechanical advantages of the non-functional commercial polymer films together with the reactivity of the functional groups.

In the recent past, chemical vapor deposition (CVD) polymerization of substituted [2,2]paracyclophanes has been instrumental in creating a wide array of functionalized poly(*p*-xylylenes) with a diverse class of functional groups, such as amines (15,16), esters (17-19) and alcohols (7,20,21), which facilitate

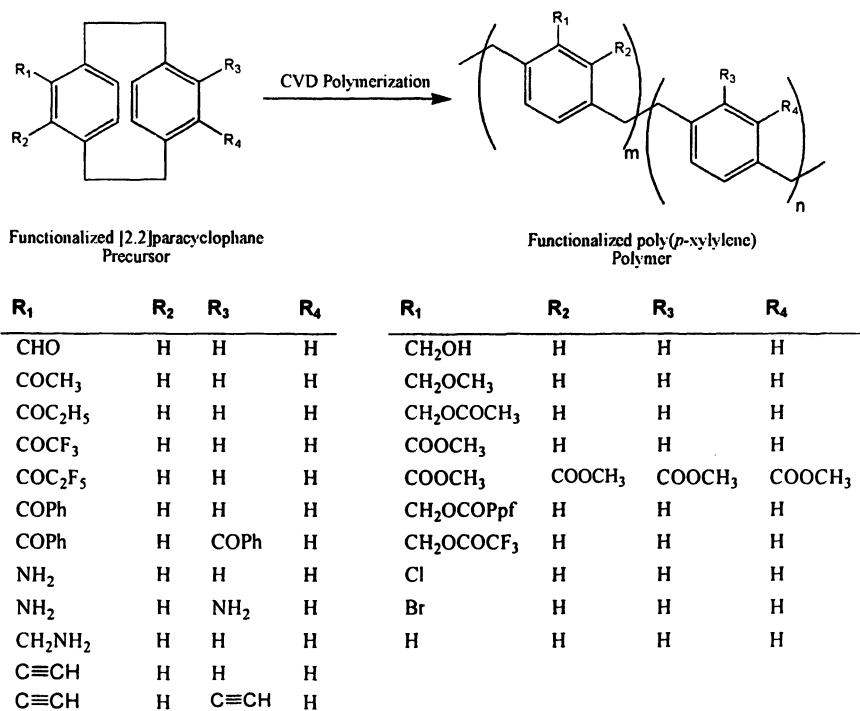


Figure 1. CVD polymerization of functionalized [2.2]paracyclophanes.

the immobilization of biomolecules (Figure 1). Coronary stents which were coated with a functionalized CVD polymer and then used to immobilize the thrombin inhibitor r-hirudin showed a remarkable decrease in the platelet activity (22). CVD polymerization has also been used to synthesize polymeric coatings to immobilize proteins and antibodies inside microfluidic devices which can be further used for cell-based bioassays (19). On the other hand, a novel photodefinable polymer was prepared by CVD polymerization and used for the fabrication of hydrogel elements (23).

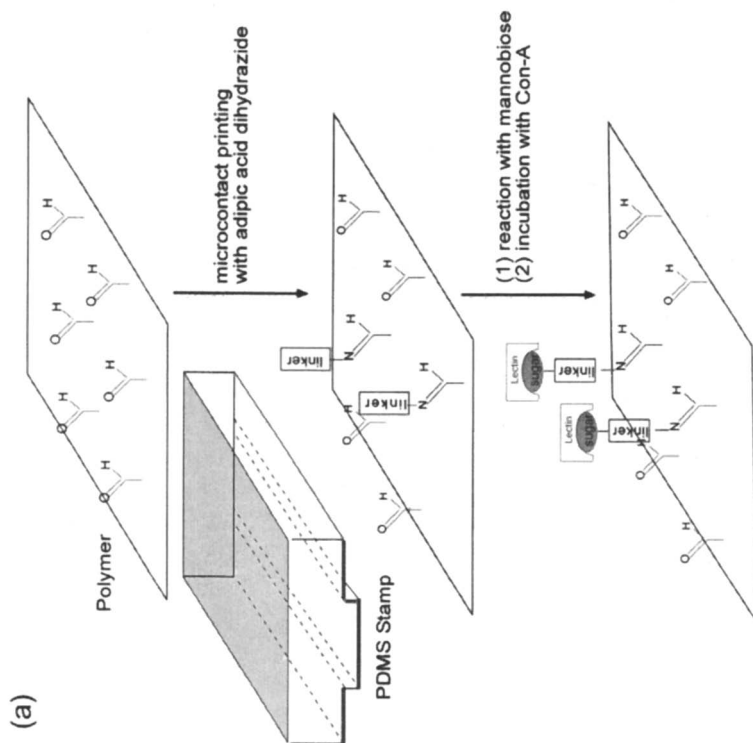
Recently, a polymer surface displaying aldehyde functionality, poly[(4-formyl-*p*-xylylene)-co-(*p*-xylylene)], was utilized to immobilize proteins and saccharides, taking advantage of the reaction between the hydrazide and the carbonyl groups (24). This method benefits from the rapid reaction kinetics and the relative inactivity of both the hydrazide and carbonyl functionalities towards other biomolecules or biological functionalities such as amines, acids and thiols. Dihydrazide linkers were used to tether model sugars onto the aldehyde-functionalized surfaces by microcontact printing and the sugar molecules were detected using a sugar-specific lectin (Figure 2).

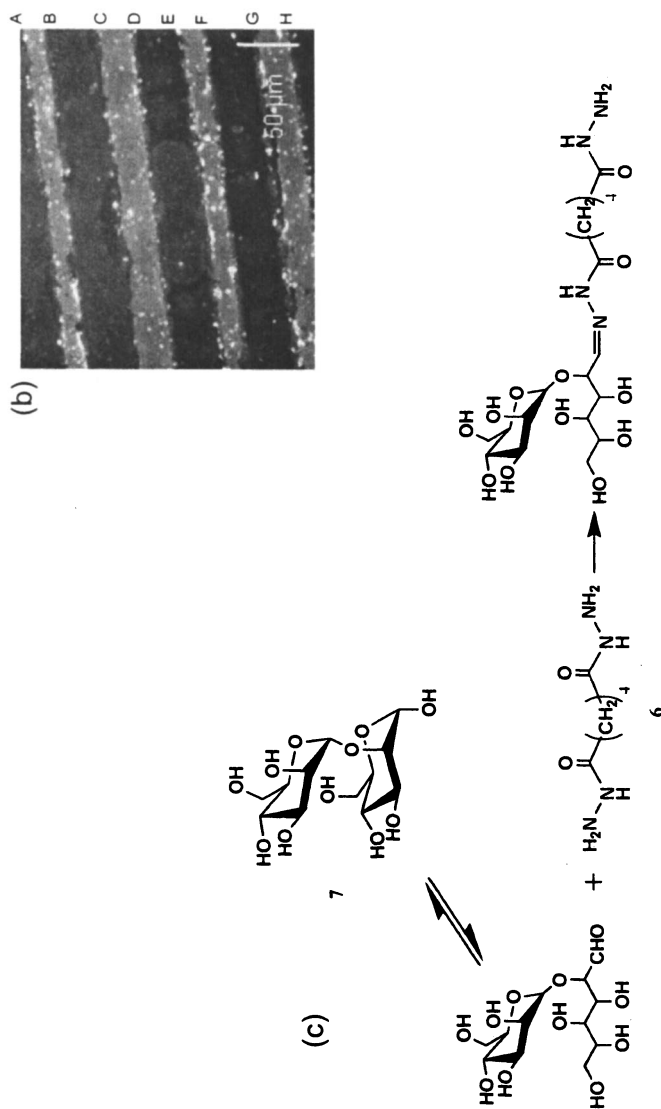
A new type of bifunctional surface based on alkyne-containing vapor-deposited polymer coatings has shown remarkable reactivity towards azide-functionalized moieties (25). These reactive coatings, poly(4-ethynyl-*p*-xylylene-co-*p*-xylylene), are applicable to a wide range of substrates and can be modified by subsequent spatially directed “click chemistry”. The most widely used click reaction is the Huisgen 1,3-dipolar cycloaddition between azides and terminal alkynes (26). The alkyne groups on the polymer surface were used as anchors for the immobilization of azide-functionalized biotin which was further used for the binding of streptavidin (Figure 3). This regioselective immobilization strategy could be further applied in the fields of biosensors, biomedical device coatings and diagnostics.

Surface Modification of Microfluidic Devices

Microfluidic systems are widely used for the separation, detection, and analysis of biochemical reagents (27,28). The continuously increasing complexity of microfluidic systems necessitates the development of methods for the precise and stable fabrication of functional surfaces and controlled spatial surface patterns (29-32). Defined and stable surface properties along with the capability to immobilize active biomolecules onto a surface are key features for the development of miniaturized biodevices, such as micro total analysis systems (μ TAS) (33), microfabricated cell sorters (34), microseparators for DNA (35) and proteins (36-38), cell-based assays, (39) and embryonic patterning networks (40). Typically, polydimethylsiloxane (PDMS) is utilized in microfluidic systems due to ease in manufacturing and favorable mechanical properties (41,42). The major disadvantages of PDMS are its hydrophobic nature, propensity for non-specific protein adsorption and lack of functional groups (43). In the past, several methods such as graft polymerization (44,45), plasma treatment (46), UV-ozone treatment (47), silanization (48), have been utilized to modify the PDMS surface but these methods have not been successful for long-term applications (49).

Development of technologies for the modification of two- as well as three-dimensional surfaces is one of the major challenges faced in the field of biotechnology. Keeping this in mind, a novel photodefinable CVD polymer, poly[4-benzoyl-*p*-xylylene-co-*p*-xylylene], was developed which can crosslink molecules in close proximity to the surface. Taking advantage of this property, non-fouling molecules, specifically polyethylene oxides (PEOs), were spatially confined in microchannels and their non-fouling characteristics were further demonstrated using a variety of proteins (Figure 4) (50). Prior to photopatterning, the polymer-coated substrate was exposed to a PEO solution. A photomask was then brought into contact with the substrate and the reactive coating was illuminated with UV radiation. In the regions exposed to the UV





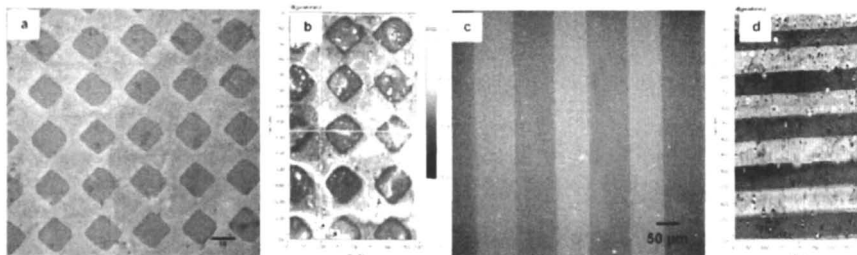
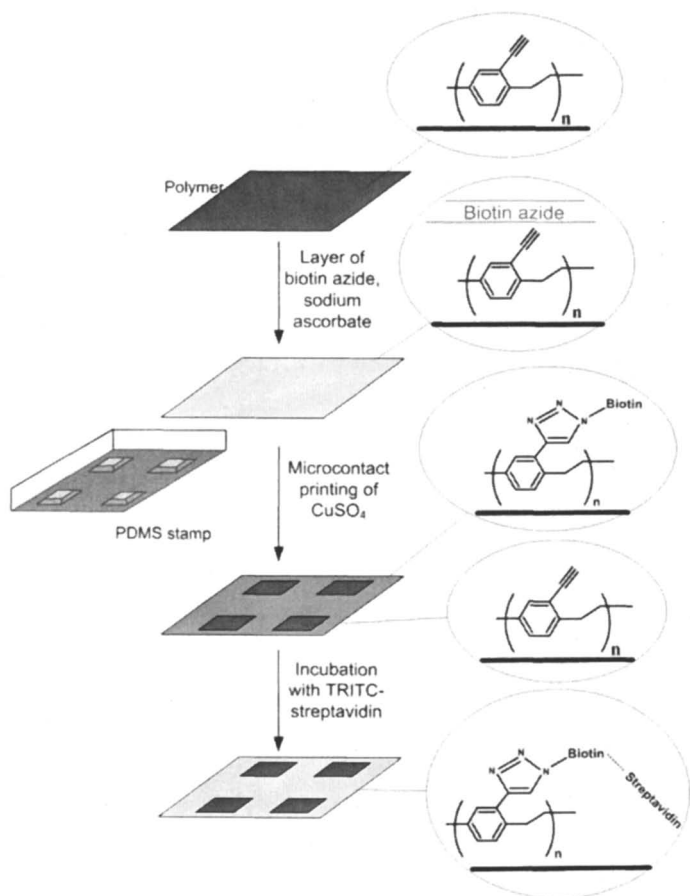


Figure 3. Immobilization of azide-functionalized biotin via microcontact printing. Subsequent binding of TRITC-streptavidin is shown in the fluorescence micrographs (a, b) and the corresponding thickness maps (b, d). (Adapted from reference 25 with permission. Copyright 2006 Wiley Interscience)

radiation, PEO molecules were crosslinked to the photoactive CVD polymer creating spatially-controlled islands of non-fouling molecules. The whole substrate was then incubated in fluorescently-labeled proteins which specifically adsorbed to regions without PEO.

This versatile technique was further extended into preparing a wide range of reactive coatings within complex confined microgeometries. The ability of this process to coat reactive polymer films within previously assembled devices was successfully demonstrated (Figure 5) (51). The polymer films deposited within the microchannels were able to maintain reactivity towards their corresponding binding partners. Compared to conventional solution-based methods, this method provides a simple route that is well-defined, permanent and is not limited to short term applications.

Multi-Potent Reactive Coatings

The surface modification strategies discussed thus far involve immobilization of only one ligand to a chemically homogenous surface. As surface design problems become more interdisciplinary, solutions will eventually require the simultaneous manipulation of several variables such as wettability, surface charge, and reactivity. Functionalized poly(*p*-xylylenes) provide a flexible strategy which can be simply extended to create multi-reactive coatings. With regards to reactivity, there has been considerable interest in the immobilization of multiple ligands simultaneously on one surface, in controlled ratios. Cell shape and adhesion studies (52), advanced bioassay development (53,54), and scaffold design (55) are some areas that would benefit from this approach.

Using the same experimental setup as the homopolymer system, CVD has also been used to deposit poly(*p*-xylylene) copolymer thin films (56). These films possess the same mechanical integrity as their homopolymer counterparts but with dual reactivity. CVD copolymerization of aminomethyl and trifluoroacetyl functionalized precursors led to the formation of poly[(4-aminomethyl-*p*-xylylene)-co-(4-trifluoroacetyl-*p*-xylylene)-co-*p*-xylylene]. The aminomethyl and trifluoroacetyl groups were chosen because of their ability to react independently without cross-competition. The two functional groups were further utilized to immobilize different ligands (Figure 6).

As a proof of concept, two fluorescent ligands were immobilized on the copolymers with varying monomer ratios. Subsequently, the fluorescence intensities of each ligand were measured, and plotted with respect to aminomethyl concentration. The results (Figure 7) show that the fluorescence intensities varied in a linear fashion. As the amine-reactive dye intensity increases, that of the trifluoroacetyl-reactive dye decreases, which indicates immobilization in controlled ratios.

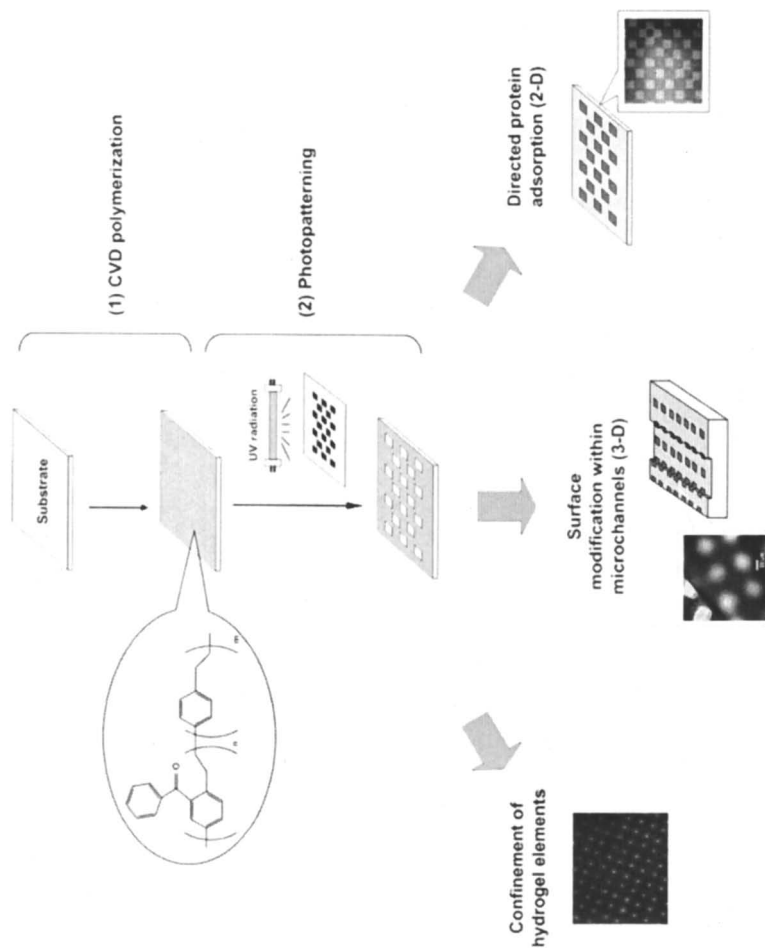


Figure 4. Photopatterning process by using photodefinable reactive polymer. (Highlighted in Analytical Chemistry, November 2005 by James P. Smith and Vicki Hinson-Smith)

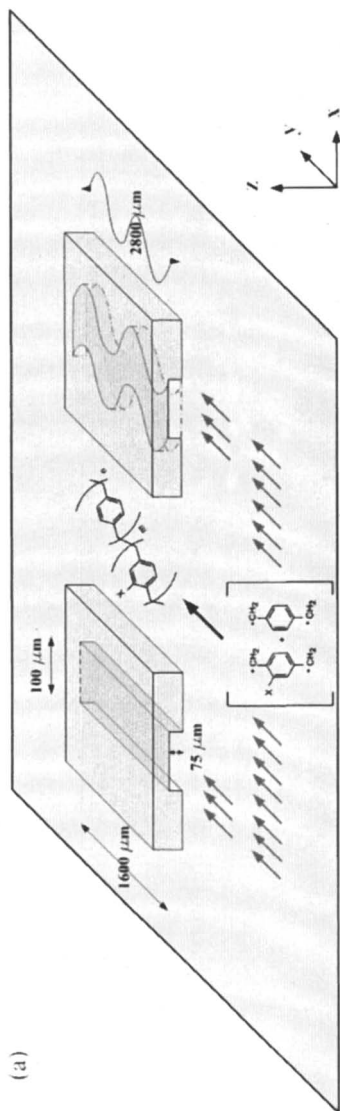


Figure 5. Chemical vapor deposition (CVD) polymerization to render various types of functional poly(p-xylylenes) within confined microgeometries. [51] (Reproduced from reference 51 with permission. Copyright 2006 American Chemical Society) Continued on next page.

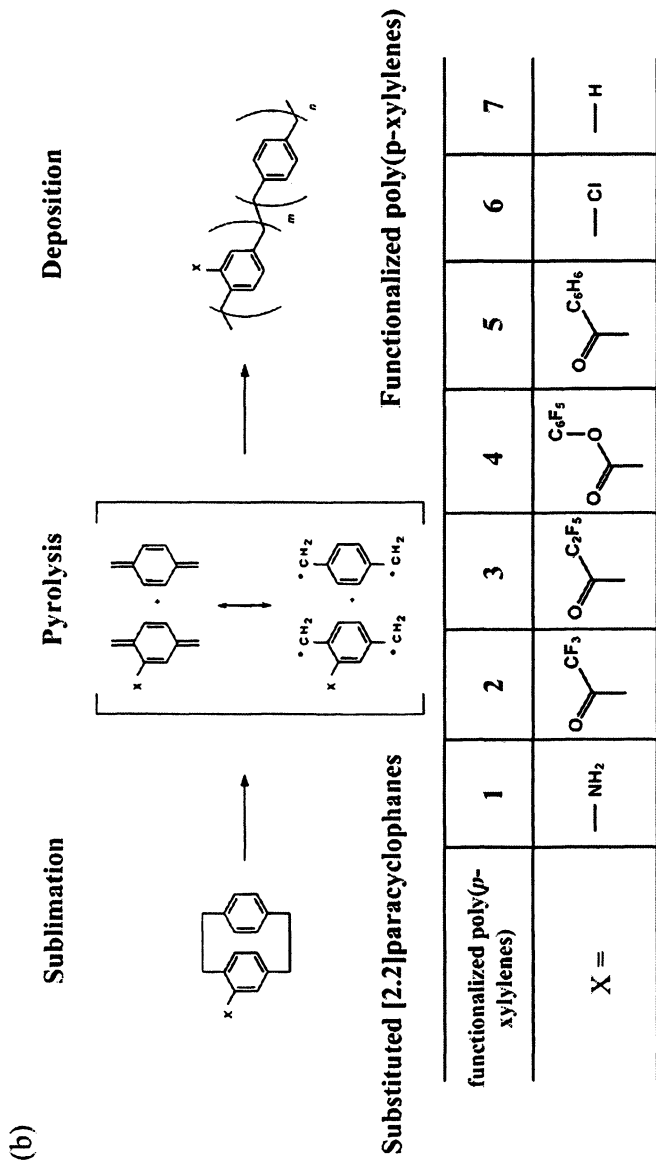


Figure 5. Continued.

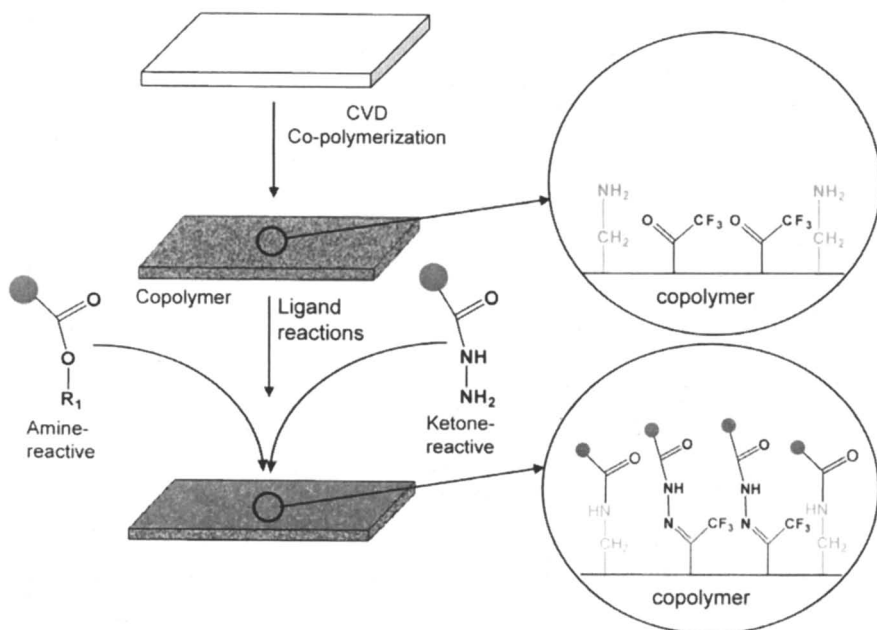


Figure 6. Schematic outlining the steps to produce a multifunctional surface with parallel reactivity. The aminomethyl group only reacts with the ester, and the trifluoroacetyl group only reacts with the hydrazide. (Reproduced from reference 56 with permission. Copyright 2006 Wiley Interscience)

Conclusions

Future developments in the fields of biomedical and microfluidic technology strongly depend on the ability to perform precise surface engineering. Functionalized vapor-based polymeric coatings have emerged as prime candidates for achieving this goal. Simplicity in providing reactive groups, applicability to a wide variety of substrates, and inherent biocompatibility make CVD an attractive option for the fabrication and modification of device architectures.

Acknowledgments

JL gratefully acknowledges support from the NSF in form of a CAREER grant (DMR-0449462) and funding from the NSF under the MRI program (DMR-0420785)

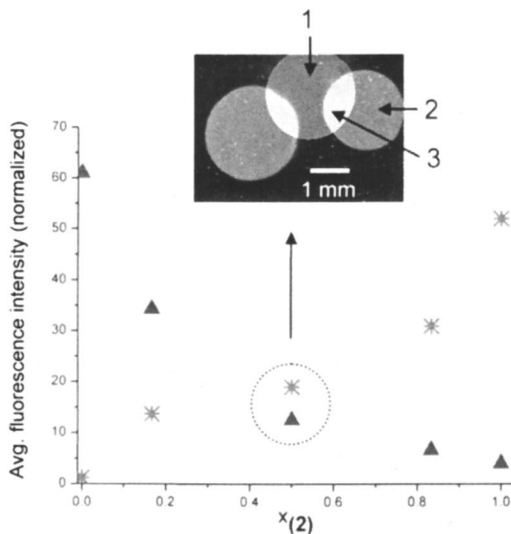


Figure 7. Fluorescence intensities of amine-reactive ligand (*) and ketone-reactive ligand (▲), with respect to mole fraction aminomethyl-functionalized paracyclophane. (Reproduced from reference 56 with permission. Copyright 2006 Wiley Interscience)

References

1. Langer, R.; Peppas, N. A. *AIChE J.* **2003**, *49*, 12, 2990-3006.
2. Langer, R.; Tirrell, D. A. *Nature* **2004**, *428*, 487-492.
3. Ratner, B. D.; Bryant, S. J. *Annu. Rev. Biomed. Eng.* **2004**, *6*, 41-75.
4. Kopecek, J. *Eur. J. Pharm. Sci.* **2003**, *20*, 1-16.
5. Kasemo, B. *Curr. Opin. Solid St. M.* **1998**, *3*, 451-459.
6. Kohn, J. *Nature Materials* **2004**, *3*, 745-747.
7. Chilkoti, A.; Hubbell, J. A. *MRS Bulletin* **2005**, *30*, 175-176.
8. Hildebrand, H. F.; Blanchemain, N.; Mayer, G.; Chai, F.; Lefebvre, M.; Boschini, F. *Surf Coat. Tech.* **2006**, *200*, 6318-6324.
9. *Biomaterials Science: An Introduction of Materials in Medicine*; Ratner, B. D.; Hoffman, A. S.; Schoen, F. J.; Lemons, J. E., Eds.; 2nd edition; Academic Press, San Diego, CA, 2004.
10. Yu, Q.; Deffeyes, J.; Yasuda, H. *Prog. Org. Coat.* **2001**, *41*, 4, 247-253.
11. Love, J. C.; Estroff, L. A.; Kriebel, J. K.; Nuzzo, R. G.; Whitesides, G. M. *Chem. Rev.* **2005**, *105*, 4, 1103-1169.
12. Falconnet, D.; Csucs, G.; Grandin, H. M.; Textor, M. *Biomaterials* **2006**, *27*, 16, 3044-3063.

13. Lahann, J.; Langer, R. *Macromolecules* **2002**, *35*, 11, 4380-4386.
14. Hermanson, G. T.; *Bioconjugate Techniques*; 1st edition; Academic, San Diego, CA 1996.
15. Lahann, J.; Choi, I. S.; Lee, J.; Jensen, K.; Langer, R. *Angew. Chem. Int. Ed.* **2001**, *40*, 3166-3169.
16. Lahann, J.; Höcker, H.; Langer, R. *Angew. Chem. Int. Ed.* **2001**, *40*, 726-728.
17. Lahann, J.; Klee, D.; Höcker, H. *Macromol. Rapid Commun.* **1998**, *19*, 441-444.
18. Lahann, J.; Balcells, M.; Rodon, T.; Lee, J.; Choi, I. S.; Jensen, K. F.; Langer, R. *Langmuir* **2002**, *18*, 9, 3632-3638.
19. Lahann, J.; Balcells, M.; Lu, H.; Rodon, T.; Jensen, K. F.; Langer, R. *Anal. Chem.* **2003**, *75*, 2117-2122.
20. Lahann, J.; Langer, R. *Macromol. Rapid Commun.* **2001**, *22*, 12, 968-971.
21. Schürmann, K.; Lahann, J.; Meyer, J.; Klosterhalfen, H.; Vorwerk, D.; Klee, D.; Günther, R. W. *Radiology* **2004**, *230*, 1, 151-162.
22. Lahann, J.; Klee, D.; Pluester, W.; Hoecker, H. *Biomaterials* **2001**, *22*, 8, 817-826.
23. Suh, K. Y.; Langer, R.; Lahann, J. *Adv. Mater.* **2004**, *16*, 1401-1405.
24. Nandivada, H.; Chen, H. Y.; Lahann, J. *Macromol. Rapid Commun.* **2005**, *26*, 1794-1799.
25. Nandivada, H.; Chen, H. Y.; Bondarenko, L.; Lahann, J.; *Angew. Chemie Int. Ed.* **2006**, *45*, 20, 3360-3363.
26. Huisgen, R.; *1,3-Dipolar Cycloaddition Chemistry*; Padwa, A.; Eds. Wiley, New York, 1984, p.1-176.
27. Quake, S. R.; Scherer, A. *Science* **2000**, *24*, 290, 1536-1540.
28. Burns, M. A.; Johnson, B. N.; Brahmasandra, S. N.; Handique, K.; Webster, J. R.; Krishnan, M.; Sammarco, T.; Man, P. M.; Jones, D.; Heldsinger, D.; Mastrangelo, C. H.; Burke, D. T. *Science* **1998**, *282*, 484-487.
29. Hu, S. W.; Ren, X. Q.; Bachman, M.; Sims, C. E.; Li, G. P.; Allbritton, N. L. *Anal. Chem.* **2004**, *76*, 1865-70.
30. Grzybowski, B. A.; Haag, R.; Bowden, N.; Whitesides, G. M. *Anal. Chem.* **1998**, *70*, 4645-4652.
31. Yang, T. L.; Jung, S. Y.; Mao, H. B.; Cremer, P. S. *Anal. Chem.* **2001**, *7*, 165-169.
32. Duffy, D. C.; McDonald, J. C.; Schueller, O. J. A.; Whitesides, G. M. *Anal. Chem.* **1998**, *70*, 4974-4984.
33. Berg, A.; Olthius W.; Bergveld P. *Micro Total Analysis Systems 2000*; Kluwer Academic Publishers; **2000**.
34. Fu, A.Y.; Spence, C.; Scherer, F.H.; Arnold, F.H.; Quake, S.R. *Nat. Biotechnol.* **1999**, *17*, 1109-1111.
35. Effenhauser, C.S.; Bruin, J.M.; Paulus, A.; Ehrat, M. *Anal. Chem.* **1997**, *69*, 3451-3457.

36. Huber, D. L.; Manginell, R. P.; Samara, M. A.; Kim, B. I., Bunker, B. C. *Science* **2003**, *301*, 352-354.
37. Mao, H.; Yang, T.; Cremer P.S. *Anal. Chem.* **2002**, *74*, 379-385.
38. Chen, S.H.; Sung, W.C.; Lee, G.B.; Lin, Z.Y.; Chen, P.W.; Liao, P.C. *Electrophoresis* **2001**, *22*, 3972-3977.
39. Li, P., Harrison, D.J. *Anal. Chem.* **1997**, *69*, 1564-1568.
40. Lucchetta, E. M.; Lee, J. H.; Fu, L. A.; Patel, N. H.; Ismagilov, R. F. *Nature* **2005**, *434*, 1134-1138.
41. McDonald, J. C.; Whitesides, G. M. *Accounts Chem. Res.* **2002**, *35*, 491-499.
42. Johnson, T.J.; Ross S.; Gaitan M.; Locascio L.E. *Anal. Chem.* **2001**, *73*, 3656-3661.
43. Ocvirk, G.; Munroe, M.; Tang, T.; Oleschuk, R.; Westra, K.; Harrison, D.J. *Electrophoresis* **2000**, *21*, 107-115.
44. Hu, S.; Ren, X.; Bachman, M.; Sims, C. E.; Li, G. P.; Allbritton, N. L. *Analytical Chemistry* **2004**, *76*, 1865-1870.
45. Hu, S.; Ren, X.; Bachman, M.; Sims, C. E.; Li, G. P.; Allbritton, N. L. *Analytical Chemistry* **2002**, *74*, 4117-4123.
46. Duffy, D. C.; Mcdonald, J. C.; Schueller, O. J. A.; Whitesides, G. M. *Anal. Chem.* **1998**, *70*, 4974-4984.
47. Berdichevsky, Y.; Khandurina, J.; Guttman, A.; Lo, Y.-H. *Sensors Actuat, B- Chem.* **2004**, *97*, 402-408.
48. Grzybowski, B. A.; Haag, R.; Bowden, N.; Whitesides, G. M. *Anal. Chem.* **1998**, *70*, 4645-4652.
49. Makamba, H.; Kim, J. H.; Lim, K.; Park, N.; Hahn, J. H. *Electrophoresis* **2003**, *24*, 3607-3619.
50. Chen, H.-Y.; Lahann, J. *Anal. Chem.* **2005**, *77*, 6909-6914.
51. Chen, H.-Y.; Elkasabi, Y.; Lahann, J. *J. Am. Chem. Soc.* **2006**, *128*, 1, 374-380.
52. Chen, C.S.; Alonso, J.L.; Ostuni, E.; Whitesides, G.M.; Ingber, D.E. *Biochem. Bioph. Res. Co.* **2003**, *307*, 355-361.
53. Tani, H.; Maehana, K.; Kamidate, T. *Anal. Chem.* **2004**, *76*, 6693-6697.
54. Kato, K.; Sato, H.; Iwata, H. *Langmuir* **2005**, *21*, 7071-7075.
55. Liu, X.; Won, Y.; Ma, P. X. *J. Biomed. Mater. Res. A* **2005**, *74A*, 84-91.
56. Elkasabi, Y; Chen, H.-Y.; Lahann, J. *Adv. Mater.* **2006**, *18*, 1521-1526.

Chapter 18

Optimization of Microdomain Structure to Control Osteoblast Attachment on Poly(ethylene glycol)–Poly(caprolactone) Polyurethanes

Gracy Wingkono and Carson Meredith

School of Chemical and Biomolecular Engineering, Georgia Institute of Technology, Atlanta, GA 30332–0100

Combinatorial libraries were employed to optimize microphase domain size and shape of polyethylene glycol (PEG) - poly(caprolactone) (PCL) polyurethanes, and their blends with PCL. Polyurethanes are used as biomaterials in a variety of applications, and the ability to tune microdomain size to enhance cell attachment is a desirable objective. These materials incorporate biocompatible PCL microdomains, to which cells can adhere, into a relatively non-adhesive PEG-PCL matrix. A region of chain extender composition and curing temperature, with controllable spherical-, wormlike-, and ribbon-shaped microdomains, was located through a series of increasingly focused libraries. Osteoblast-like cells (MC3T3-E1) cultured directly on selected libraries showed attachment density correlated with the distance to and size of nearby PCL microdomains.

Introduction

The role of material surface features in biomaterial design is significant but poorly understood. Spatial control of cellular adhesion and growth is critically important in tissue engineering and related fields (1-4). Metals and plastics that are widely used for medical implants lack the molecular sequence and patterns crucial for normal cell function, and therefore often trigger aberrant cell responses in long term implantation (5). One promising approach is to introduce chemical or physical patterns on biomaterial surfaces, to achieve cell functions more representative of in vivo behavior.

For physically-patterned surfaces, roughness, geometric spacing and size of adhesive areas, as well as surface mechanical properties can influence the attachment, function, shape, and fate of anchorage-dependent cells (1-6). Much of this research has used carefully-designed surfaces created with microlithography (5). In contrast to the regular geometric spacing created with microlithography, polymers (and metals) used in biomaterials applications often exhibit random or semi-ordered features on their surfaces. Such features arise from phase separation and ordering phenomena, such as crystallization, as well as processing steps (physical roughening for example). Furthermore, phase-separated patterns, while being somewhat randomly distributed, do offer control via composition, temperature, and processing conditions and allow patterning in 2D and 3D structures. An example is polyurethanes, which are networks of polyester or polyether 'soft' segments linked with diisocyanates to 'hard' segment diols to form linear or branched copolymers. Hard segments typically phase-separate into crystalline domains that act as physical crosslinks, giving the material its elastomeric character. Polyurethanes are robust biomaterials that can be used in mechanically-challenging environments (connective tissues, vasculature), but they are fairly complex in the number of parameters that can be adjusted to achieve microdomain control. Much remains to be learned about the influence of their physical microstructures on cell behaviors. Hence, this material class is a prime candidate for combinatorial exploration in which a wide range of compositions can be explored on the same sample, prepared under consistent conditions.

In this paper, we report on the investigation of phase-separated microdomains in a PEG-PCL polyurethane and their effect on osteoblast adhesion. The design concept explored herein is the use of two different soft segments, one that is known to promote osteoblast adhesion (PCL) and one that is known to repel adhesion (PEG). Gradient library approaches are employed to search for regions of composition and annealing temperature that allow control over the shape and size of PCL microdomains distributed in a PEG matrix. Following identification of composition / temperature regions that produce such microstructures, the effect of these surface structures on osteoblast adhesion is investigated by culturing cells directly on the libraries.

Experimental

Combinatorial Micropatterned Polyurethanes Preparation

Poly(ethylene glycol) (PEG, $M_w=2,000$, Sigma-Aldrich), poly(caprolactone) (PCL $M_w=80,000$, $M_w/M_n=1.43$, Aldrich) solutions were prepared in chloroform (CHCl_3 , Aldrich). The PEG/PCL composition-annealing temperature (Φ/T) two-dimensional libraries were prepared on $22\text{mm}\times 22\text{mm}$ silicon chips pretreated with piranha solution (30% hydrogen peroxide/70% sulfuric acid) for an hour, then etched with buffered oxide etchant (BOE) 1:6 (JT Baker). Annealing temperature (T , $80\text{--}120^\circ\text{C}$) and PCL composition (Φ_{PCL} , $0\text{--}0.3$, mass fraction) gradients were generated along orthogonal directions (7,8). Briefly, a PCL solution in CHCl_3 was pumped into a mixing vial initially containing a PEG solution while another syringe pumped in a mixture of 4,4 methylene bis-phenyl diisocyanate (MDI, Sigma-Aldrich) and Pluracol[®] ($M_w=430$, BASF) in tetrahydrofuran (THF, EMD). This resulted in a linear increase in PCL composition in the vial. A third automated syringe extracted the Φ_{PCL} -gradient solution from the vial and deposited it as a thin stripe on the substrate. A knife-edge coater spread the liquid as a film orthogonal to the composition gradient. The Φ_{PCL} -gradient films were annealed on a custom aluminum T-gradient heating stage overnight, with the T gradient orthogonal to the Φ_{PCL} -gradient, and were immediately quenched to room temperature (5).

Cell Culture and Assays

After sterilization (70% EtOH solution, 30 min), mouse osteoblast-like cells (MC3T3-E1 subclone 4 from ATCC, Rockville, MD, passage 6 or 7) were seeded onto combinatorial chips of surface lateral patterns at a density of $5,000$ cells/ cm^2 and were cultured in DMEM with 10% fetal bovine serum, L-glutamine and streptomycin at 37°C in a humidified 5% CO_2 atmosphere for 4 hours. Cell counter staining is done with Hoechst 33342 (Invitrogen). The MC3T3-E1 cell line was chosen based on previous experience culturing them on PCL, and based upon their ability to reproduce certain behaviors of normal mouse osteoblast (9).

Image Acquisition

Surface lateral patterns and cell density were studied by cross-polarized optical and fluorescent microscopy. These two different types of images were acquired sequentially over a grid of positions on each library by using a multi-

channel microscope equipped with a robotic image acquisition system. Typically, for a 22mm×22mm library, at 10× magnification rate, 324 images from distinct locations (1,200μm×1000μm) were acquired. Quantitative descriptions of surface lateral patterns and cell proliferation were attained by image processing and analysis using ImageJ (NIH) and Matlab™ software.

Results and Discussion

Optimization of the trifunctional crosslinker (Pluracol) was performed first using combinatorial libraries such as that depicted in Figure 1. Pluracol composition was varied while PCL-to-PEG weight ratio was kept constant throughout at 0.2. The desired result was minimum weight loss at less than 10% of initial weight upon immersion into aqueous solution for 3 days. This minimum weight loss area corresponds to an optimal formation of PEG crosslinks, and the ability to control PCL microdomain shape and size.

The optimal composition was found to be approximately 50% mol ratio of Pluracol to PEG at a curing temperature of ~110°C, shown in Figure 1. The bright areas shown under cross-polarized light are the crystalline PCL domains, while the amorphous PEG-rich background is shown as the dark area. PEG crystallization is suppressed due to formation of crosslinks in the polyurethane. The combinatorial library of surface lateral patterns covers a range of diverse shapes and sizes from circular islands of several microns to ~70 μm ribbon patterns. The height of the features ranges from 0 to 1 μm. The results are shown in Figure 2 and 3.

The image analysis results from the library in Figure 3 are shown in Figure 4 (top) for the PCL feature size. Osteoblast density after 1 day of culture growth on the library is shown in Figure 4 (bottom). Note that the chosen surface metrics, area coverage of PCL and cell density, are plotted versus the actual library preparation variables, annealing temperature and PCL concentration. There is an apparent “negative” correlation between crystalline PCL area coverage and cell density. For example, within the triangular boundaries in Figure 4 top and bottom, high crystalline area coverage corresponds to low cell density. In the oval boundaries in Figure 4 top and bottom, low crystalline area coverage corresponds to high cell density. However, there are regions where this negative correlation was not followed as well. The presentation of microstructural and cell-adhesive results as a function of library preparation conditions in Figure 4 is not a robust method for observing structure-function relationships. Rather, we desire direct knowledge of the correlation between cell density and the local microdomains surrounding cells. In particular, the consideration of % coverage of crystalline area probably overlooks other factors

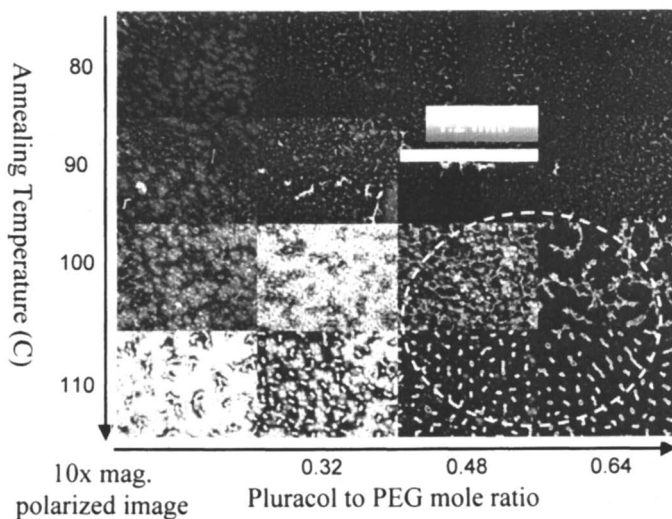


Figure 1. Combinatorial library with Pluracol (chain extender) composition and annealing temperature gradient. The oval marked an optimal region, selected for minimized water solubility and generation of microstructures.

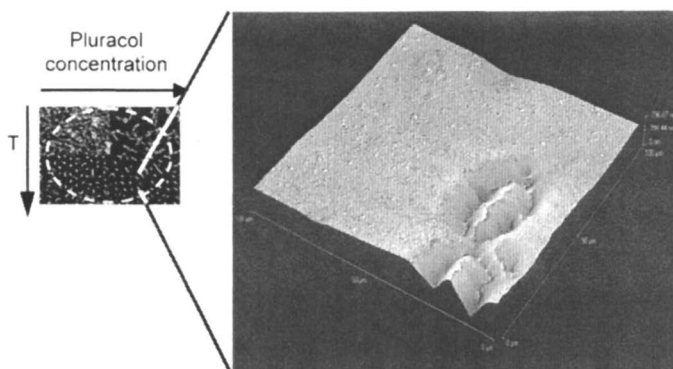


Figure 2. AFM scanning of the 'ribbon pattern' – 100x100 μm scan, max range: 797 nm high.

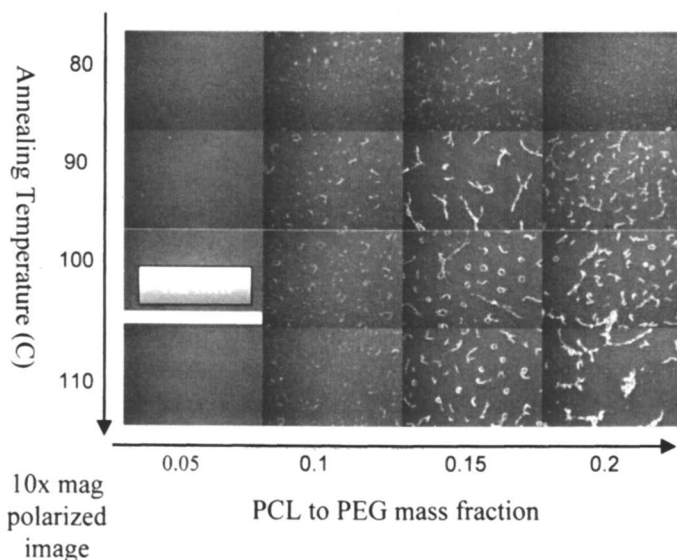


Figure 3. Focused combinatorial library in which PCL composition (blended with the optimal PEG-PCL polyurethane of Fig 1) is explored along with curing temperature. (16 points from 22x22 mm sample). Pattern shapes range from circular islands, to linear chains, looped chains, fully-closed rings, and twisted ribbons.

that influence cell function. This includes the ‘local’ distance between each cell and the neighboring PCL islands. This information cannot be captured by looking ‘globally’ at the variation of parameters over the library surface, as Fig 4 does. Further investigation into the details of the surface lateral patterns is needed so that we can better describe the cell-biomaterial interaction.

Therefore, the data from each image on the library in Figure 4 were analyzed with local cell-feature histograms (LCFH) (10), obtained by sorting various surface parameters and the cell density into bins. This approach offers several advantages: (a) the local interactions between cells and their immediate neighbors is considered, (b) the actual physical dimensions on the surface are illuminated, and (c) a wide range of surface feature descriptors (anything that can be calculated from image analysis) can be used as independent variables. Figure 5 presents a LCFH analysis of the data from Figure 4. Two candidate surface parameters are the area of a PCL-crystalline domain and its distance from each adherent cell. Figure 5 was constructed by sorting the distance between each cell and the PCL-crystalline features of a certain size, and counting the occurrences of each combination. The peaks in Figure 5 show that cells

adhere preferably to certain combinations of distance and PCL size, and that other combinations are not preferable. This presentation, in terms of the local microstructural parameters surrounding each cell, allows a more direct exploration of the cell-surface relationships than Figure 4. However, in order to interpret LCFH correctly, one must consider the experimental results relative to random sampling, e.g., a random distribution of cells around the PCL islands will also produce certain distinct peaks. The ratio of the experimental to random reference histogram can be used to determine a probability distribution for cell attachment and to identify features that can act to influence, positively or negatively, cell attachment. This work is under way at present and will be the subject of future publications (10).

Conclusion and Future Direction

Optimization of PEG-PCL polyurethanes was performed to identify microdomains suitable for osteoblast-like cell adhesion. Patterned shapes of the optimized microdomains ranged from circular islands, linear or looped chains, to fully-closed rings and twisted ribbons. Osteoblast density after 1 day of culture growth on the libraries showed that attachment density correlated to the distance to and area of nearby PCL microdomains. It was concluded that plotting the culture data as a histogram of cell density relative to local surface features was superior to plotting as a function of library preparation conditions. Ongoing work will investigate the effects of combinations of distance and size of PCL microdomains, as well as other surface properties like shape, on osteoblast function.

Acknowledgements

The authors would like to thank Dr. Andres García, Woodruff School of Mechanical Engineering, Georgia Institute of Technology, for helpful discussions and use of laboratory equipment, and also Jing Su, Charlene Rincon, and Pedro Zapata for helpful discussions. In addition, we are grateful for funding provided by NIH under the following grants: NCR# R21 RR17425-01 and NHLBI# 1R21 HK072039-01.

References

1. Brocchini, S., K. James, V. Tangpasuthadol, and J. Kohn, *J. Amer. Chem. Soc.* **1997**, *119*, 4553.

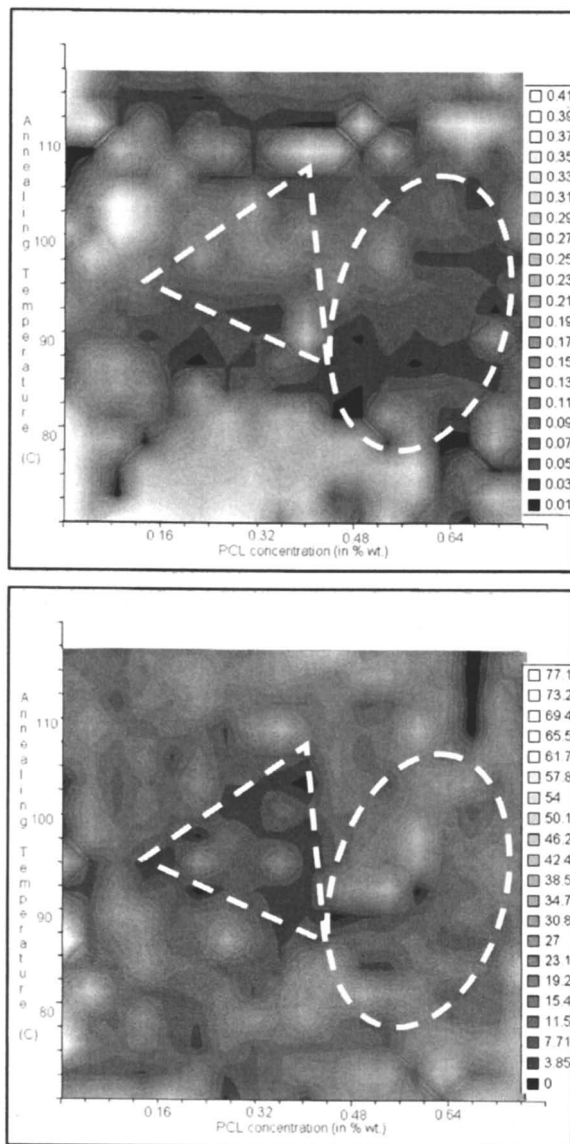


Figure 4. Results from image analysis. **Top:** area coverage (%) of crystalline features at each points of interest. **Bottom:** cell density (# of cells per 1.2 mm^2) at each points of interest. – image comprised of 324 points from $22 \times 22 \text{ mm}$ sample, each point is $1,200 \times 1,000 \mu\text{m}$ size).

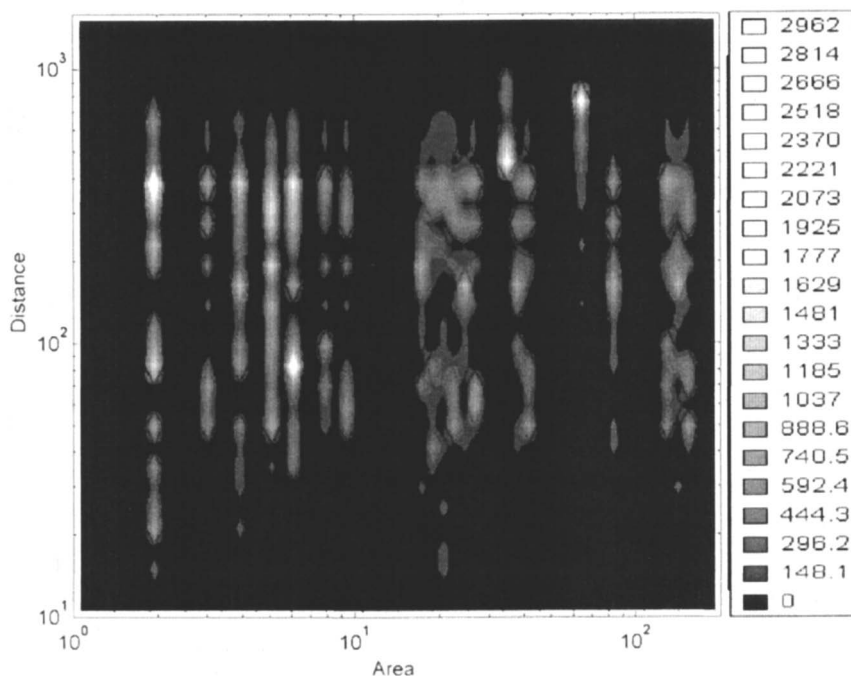


Figure 5. Number of cells observed within distance (μm) from a PCL-crystalline feature of area (μm^2).

2. C. S. Ranucci, P.V.M.. *Tissue Eng.* **1999**, *5*, 407.
3. Evangelos Tziampazis, J.K., Prabhas V. Moghe, *Biomaterials.* **2000**, *21*, 511.
4. Chen, G., Y. Imanishi, and Y. Ito, *J Biomed Mater Res.* **1998**, *42(1)*, 38.
5. Chen CS, e.a., *Biochemical and Biophysical Research Communication.* **2003**, *307*, 355.
6. Kao, W.J., *Biomaterials.* **1999**, *20*, 2213.
7. J. C. Meredith, J. L. Sormana, B. Keselowsky, A. García, A. Tona, A. Karim, and E. J. Amis, *Journal of Biomedical Materials Research*, **2003**, *66A*, 483.
8. J. C. Meredith, A. Karim, and E. J. Amis, *Macromolecules*, **2000**, *33*, 5760.
9. Byers, B.A., Pavlath, G.K., Murphy, T.J., Karsenty, G., García, A.J. *J of Bone and Mineral Res* **2002**, *17*, 1931.
10. Su, J., Meredith, C. *in preparation* **2006**.

Chapter 19

Polymers for Tissue Engineering

Wei He¹, Yu Feng¹, Zuwei Ma², and Seeram Ramakrishna³

¹Graduate Program in Bioengineering, Centre for Life Sciences #05–01,
28 Medical Drive, Singapore 117456

²Department of Orthopedics, University of Massachusetts Medical School,
55 Lake Avenue North, Worcester, MA 01605

³Department of Mechanical Engineering, National University of Singapore,
9 Engineering Drive 1, Singapore 117576

Recently it has been the main trend for the application of polymer materials in the interdisciplinary tissue engineering area. Polymer materials have shown their versatility and played main roles in constructing tissue engineering scaffolds. This book chapter briefly reviews the materials requirements for tissue engineering application, and focus on polymer materials including both natural and synthetic polymers. The frequently used and newly developed fabrication technologies for constructing tissue engineering scaffolds are described. Some surface modification/functionalization approaches to the tissue engineering scaffolds are also discussed. Recent advances for the development of polymer scaffolds in skin, cartilage, blood vessel, and nerve tissue engineering are also summarized.

Tissue engineering was defined as “an interdisciplinary field that applies the principles of engineering and the life sciences toward the development of biological substitutes that restore, maintain, or improve tissue functions.” (1). As an interdisciplinary field, tissue engineering combines the knowledge from engineering areas such as materials engineering, chemical engineering, and even computer engineering *etc* with the knowledge from biological areas such as cell biology, molecular biology, and anatomy *etc*. Tissue engineering is promising to resolve the problem of donor organ shortage which is faced by lots of patients waiting for organ transplantation. The ideal tissue engineering approach is to isolate specific cells through a small biopsy from a patient, to grow them on a 3-D scaffold under precisely controlled culture conditions, to implant the construct to the diseased site in the patient’s body, and to direct new tissue formation into the scaffold that can be degraded over time (2-3). Each step indispensably guarantees the success of engineered new tissue, amongst which biodegradable scaffolds may be the core element. There are some general requirements for the materials used as tissue engineering scaffolds such as biocompatibility, biodegradation, and suitable mechanical properties. Detailed descriptions of each property are listed in Table I.

Table I. Requirements of tissue engineering scaffolds

Requirements	Explanation
Biocompatibility	non-toxic, non-carcinogenic, non-immunogenic, resistant to infection; in application of blood contact, additional requirement including haemocompatible, lack of thrombogenicity, non-inflammatory
Biodegradability	by-products of the biodegradation won't cause any infection or inflammatory reaction; by-products of the biodegradation should not be toxic, allergenic, thrombogenic nor carcinogenic; appropriate degradation rate is required to be equal to that of regenerating tissue
Mechanical property	capable of supporting initial wound healing stress and maintaining the integrity of the predesigned tissue structure

Polymers (macromolecules) are the primary materials for various tissue engineering scaffolds such as skin, cartilage, bone *etc*. Limited number of inorganic materials is used in bone and mineralized tissue engineering applications. In this chapter, the most commonly used polymers in tissue engineering are reviewed.

Commonly used polymers as tissue engineering scaffolds

Polymers used in tissue engineering can be naturally derived, synthetic or a combination of both. There are advantages and disadvantages for both synthetic and natural polymer when used as tissue engineering scaffolds which is summarized in Table II.

Table II. Comparison between synthetic and natural polymers

Polymer	Advantages	Disadvantages
Synthetic	easily synthesized with controlled molecular weight and other physical properties like mechanical properties	lack of intrinsic biological activity
Natural	possess intrinsic biological activity; enzymatically degradable	source-related variability and contamination; limited control over parameters such as molecular weight; the potential for adverse immunological responses; variation in degradation rates due to difference in host enzyme levels; inferior mechanical properties

Biodegradable synthetic polymers including polyesters, poly(amides), poly(phosphoester), poly(phosphazenes), poly(orthoesters) and polyanhydrides have been widely used in biomedical applications such as drug delivery and tissue engineering, amongst which polyesters are most commonly used in tissue engineering area. Here we mainly focus on 3 types of polyesters: Poly(glycolic acid), Poly(lactic acid), and Poly(ϵ -caprolactone) which are most frequently used in tissue engineering (4). Structures and properties of these polyesters are summarized in Table III. Copolymers of lactide/glycolide and lactide/caprolactone such as PLGA and PCL-PLLA are also extensively used in tissue engineering area.

As the major requirement of tissue engineering scaffolds, those polyesters and their monomers should be biocompatible with human bodies. Polyesters degrade by hydrolysis of the ester bond. PGA is hydrophilic in nature and it degrades rapidly *in vitro* aqueous solution or *in vivo* fast. PLA is more hydrophobic than PGA because of the extra methyl group in the repeating units,

which leads to a slower hydrolysis. To get intermediate degradation rates between PGA and PLA, copolymers of PLGA are synthesized. It needs to be mentioned that PGA, PLA and PLGA are approved by US Food and Drug Administration (FDA) for some human clinical applications. PCL degrades at a significantly slower rate than PGA, PLA and PLGA which makes PCL a good candidate for long-term tissue engineering implants applications. Except for biocompatibility and biodegradation, these polymers should be fabricated into scaffolds with suitable mechanical properties in accordance with the implanted tissues. Mechanical properties of scaffolds fabricated by these polymers are decided mainly by the shape of scaffolds they are made into. The thermal properties of polymers are summarized in Table IV.

Table III. Commonly used biodegradable synthetic polymers, polyesters, in tissue engineering

Polymer	Structure	Properties
PGA Poly (glycolic acid)		Relatively hydrophilic; semi-crystalline polymer; degradable through hydrolysis at the ester bond in aqueous solution or <i>in vivo</i> (2-4 weeks);
PLA Poly (lactic acid)		More hydrophobic than PGA; chirality; degradable in months or even years ;
PCL Poly (ε-caprolactone)		Hydrophobic; semi-crystalline; degrade at a much slower rate than PGA and PLA

Natural derived polymers are usually extracellular macromolecules. There are two main classes of natural polymers: (1) fibrous protein such as collagen, elastin and fibronectin *etc* and (2) polysaccharide which are polymers of five-carbon (pentose) or six-carbon (hexose) sugar molecules. Polysaccharides can be classified into several groups regarding the sources of polysaccharides. Glycosaminoglycans (GAGs) are unbranched polysaccharide chains composed of repeating disaccharide units, which are commonly found in extracellular matrix of mammalian. In invertebrates and plants, other types of polysaccharides are often found such as cellulose in higher plants, chitin/chitosan in arthropod exoskeletons, and alginate from marine brown algae. We will limit our

Table IV. Thermal and mechanical properties of polyesters

Synthetic Polymer	Mw	T _g , °C	T _m , °C	Tensile Strength, MPa	Tensile Modulus, MPa	Elongation(%)	
						Yield	Break
PGA	50,000	35	210	NA	NA	NA	NA
L-PLA	50,000	54	170	28	1,200	3.7	6.0
L-PLA	100,00-	58	159	50	2,700	2.6	3.3
L-PLA	300,000	59	178	48	3,000	1.8	2.0
DL-PLA	107,000	51	---	29	1,900	4.0	5.0
PCL	44,000	-62	57	16	400	7.0	80

SOURCE: Reproduced from Reference (5). Reprinted from *Biomaterials* 1991, 12, 292-304, with permission from Elsevier.

discussion to the most commonly used natural polymers including collage, chitosan and GAGs, whose structures and properties are summarized in Table V.

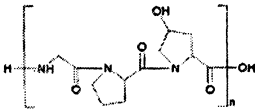
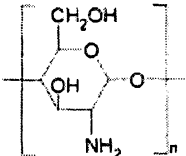
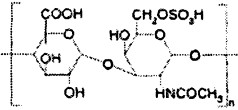
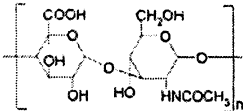
To date, 27 types of collagen have been found in which type I collagen is most common type. As tissue engineering scaffolds, collagen has been utilized in the form of sponges, gels, woven and non-woven meshes, and decellularized tissue matrices. One concern with use of collagen is mechanical properties because collagen used as tissue engineering scaffolds are generally isolated by either enzymatic digestion or acid extraction from collageneous animal tissues, thus the original crosslinked triplehelix structure was destroyed. However mechanical properties of collagen scaffolds can be strengthened by chemical crosslinking. Chitosan, similar to collagen, has been processed into porous structures for use in tissue engineering. The mechanical properties of chitosan scaffolds are mainly dependent on the pore size and pore orientation. As natural ECM can be simply described as the protein network in association with GAGs hydrogels, GAGs are always used in combination with protein, growth factors to constructed composite tissue engineering scaffolds. For example, crosslinked collagen-chondroitin sulfate complexes have demonstrated superior healing and regeneration in skin and nerve applications (6,7).

For tissue engineering applications, both synthetic and natural polymers need to be processed into scaffolds with suitable structure and chemical properties that match the reproduced tissue. The following part will introduce some commonly used methods of fabricating tissue engineered scaffolds.

Fabrication Strategies for Tissue Engineering Scaffolds

The natural extracellular matrix (ECM) plays an important role in the integrity of most tissues. It serves as a natural web of micro/nanofibers that

Table V. Commonly used natural polymers: collagen, chitosan, and GAGs

Natural Polymer	Structure	Properties
Collagen		Triple helix structure; each polypeptide chain has general sequence of Glycine-X-Y where X and Y are often proline and hydroxyproline; adhesive functions
Chitosan		Deacetylated derivatives of chitin; structure is similar to cellulose; stable and crystalline; normally insoluble in aqueous solutions above PH 7; cationic ; hydrolysable by enzyme <i>in vivo</i>
GAGs	 (chondroitin-6-sulfate)	Unbranched; highly negatively charged; there are four groups; strongly hydrophilic; usually covalently linked to proteins in the form of proteoglycans which form hydrated gels to resist compressive forces in mammalian ECM
	 hyaluronan	

anchors cells, provides sufficient mechanical strength to stabilize the tissue's structure, and also takes part in regulating the behaviors of cells contacting it. Therefore, fabrication of scaffolds that can mimic the structure and functions of natural ECM is of great importance to tissue engineering. Different materials and fabrication techniques have been explored for this purpose: electrospinning, molecular self-assembly, fabrication methods for 3-D porous composite scaffolds, and hydrogels. We will introduce these techniques in more details in the following four sub-sections.

Electrospinning

Recently, electrospinning has attracted increasing attentions as a simple method to generate nonwoven mats of nano/microscale fibers because of its simplicity, versatility, low cost, and scale-controllability. This process was first patented by Formhals in 1934 (8) and until 1990s it has regained more

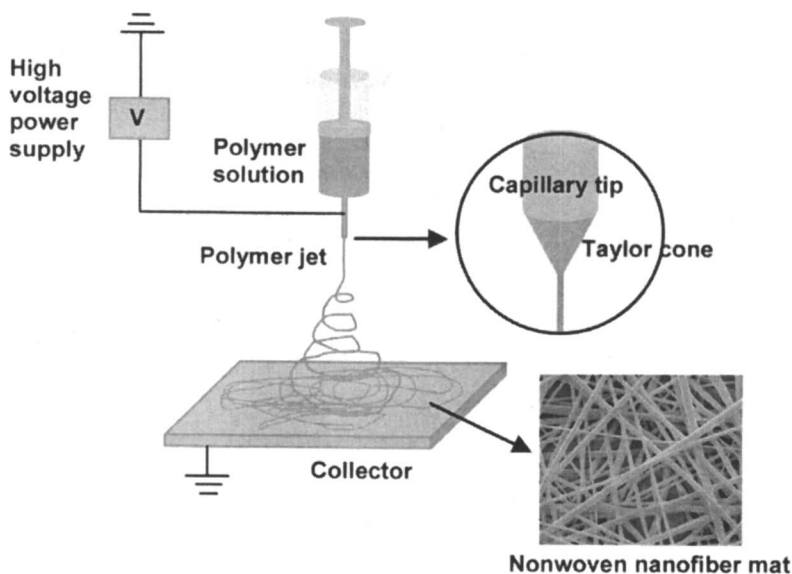


Figure 1. Schematic diagram of electrospinning setup.

attentions. Successful electrospinning requires the use of a high voltage supplier, a capillary tube with a small-diameter needle, an appropriate polymer solution or melt system, and a metal collector (Fig. 1). In electrospinning, a strong electric field is generated between the capillary tip containing a polymer solution or melt and the metallic collector. This induces charging of the polymer droplet at the capillary tip held by its surface tension. Mutual charge repulsion and the attraction between the charged droplet surface and the collector cause a force that acts against the surface tension (9). At a critical voltage, this droplet is elongated to form a conical shape known as the Taylor cone (10). When the applied voltage exceeds this critical voltage, the repulsion electrostatic force overcomes the surface tension and a stable jet could be ejected from the tip of the Taylor cone. The charged jet is accelerated towards the metallic collector and undergoes bending instability, elongation, and solvent evaporation or jet solidification in the case of polymer melt during this period, which leads to rapid thinning of the jet and deposition of dry fibers in a random manner onto the collector (11). Besides random nanofibers, uniaxially aligned nanofibers are also obtained successfully by electrospinning (12). The electrospinning process can be adjusted to control fiber diameter and favor formation of uniform nanofibers without beads by varying solution concentration, strength of the electric field, charge density of the solution, and solution feeding rate (13).

Many naturally derived and synthetic polymers have been used to produce nanofibrous scaffolds through electrospinning (14-16). Naturally derived polymers, such as collagen, can provide innate binding site for cells and promote cell adhesion and growth. However, these materials are usually isolated from animal tissues, thus they are normally not available in large amount and have batch-to-batch variations. On the contrary, synthetic polymers, such as poly(ϵ -caprolactone) (PCL), poly(lactic acid) (PLA), poly(lactic-co-glycolic acid) (PLGA), and poly(glycolic acid) (PGA), can be manufactured reproductively on a large scale, and can also be processed into nanofibrous scaffold in a more controllable manner. The scaffold's macro/micro structure, mechanical properties, and degradation rate can be easily tuned and manipulated for different applications.

Nonetheless, a major drawback of synthetic polymer scaffolds is that they are not biologically active like the nature ECM: they do not present specific motifs on their surface for specific cell targeting and binding, nor do they provide soluble factors for correct cell growth and development. To make up for this shortage, people have tried different approaches to incorporate bioactive molecules into the polymer scaffolds. RGD-containing sequences and many other cell adhesive peptides, saccharides, and proteins have been successfully embedded onto the nanofiber surfaces using adsorption or covalent grafting methods to add biological cues to the scaffold's surfaces. Enhanced cell adhesion and improved cell functions have been observed through these treatments (17-19). To make scaffolds capable of releasing soluble factors, electrospun blended nanofibers were developed. Growth factors (20), heparin (21), and DNA (22) have been incorporated into nanofibrous scaffolds through this method for different applications. Sustained release was observed in these systems, but harsh initial burst release was inevitable. Moreover, in solution preparation and the following blending electrospinning process, bioactive molecules were mixed with carrier polymers in harsh organic solvent all the time, which could possibly cause denaturing of those bioactive molecules. Another newly emerged approach that can encapsulate soluble factors inside the polymer nanofibers is coaxial electrospinning (23-25). In this process, two components can be concomitantly ejected out through two coaxial channels to generate a core-shell structured nanofiber. Those bioactive soluble factors that are not electrospinnable can still be electrospun as the core component as long as the shell fluid is electrospinnable (26). The core component can be protected inside the shell of the resultant fibers, which could also prevent the initial burst release of the core. Coaxial electrospinning has been used to produce protein- and/or drug-encapsulating core-shell fibers and their release profiles have been investigated (23-25). All these studies revealed a sustained release profile with no or alleviated initial burst release, as compared to the release profile of blended nanofibers (20-25).

Electrospun nanofibers have been actively explored for applications in the area of tissue engineering because of the specific properties they have: easy to manufacture, scale-controllability, high porosity, high spatial interconnectivity, and potential of “biological” fine-tuning toward particular applications. Electrospun nanofibrous scaffolds have been attempted in engineering a number of tissues including epithelia (27), cartilage (28), bone (29), blood vessel (12), nerve (30), and heart (31). Nanofibrous membranes also have great potentials in wound healing as a novel wound dressing material (32). Further advances in the areas of fundamental matrix biology and electrospinning may enable the fabrication of more complex 3-D nanofiber matrices with molecular and structural information closer to the natural ECM.

Molecular self-assembly

Many natural biomolecules, like peptides and proteins, interact and self-assemble to form delicate structures that are associated with specific functions (33). Ligaments and hair, for example, are assembled from collagen and keratin, respectively. DNA transcription is initiated by self-assembly of transcription factors, RNA polymerase, and DNA. Systematic studies and analysis of these natural existing self-assembly systems provide insight into the chemical and structural principles of peptide self-assembly, which inspires the development of molecular self-assembly as a new approach for fabrication of novel supramolecular architectures.

By definition, molecular self-assembly is “*the spontaneous organization of molecules under thermodynamic equilibrium conditions into structurally well-defined and rather stable arrangements through a number of noncovalent interactions*” (34). Therefore, design of finely tailored molecular building blocks that can assemble in multiple steps from bottom up through formations of numerous non-covalent bonds is the key principle for engineering molecular self-assembly. Typical non-covalent bonds include hydrogen bonds, ionic bonds, van der Waals’ bonds, electrostatic, and hydrophobic interactions (35). These bonds are individually weak but once they are working together to hold the structure as a whole, they can control the structural confirmation and form stable materials. So far, a number of molecular self-assembly systems have been designed and developed. These materials have considerable potentials in the area of tissue engineering as scaffolds, drug reservoir for delivery, or bioactive coatings.

Many research groups have worked on the peptide and protein self-assembly systems. One example is the ionic self-complementary peptides or “molecular Lego”, which can form stable β -strand and β -sheet structures in aqueous solution with two distinct hydrophilic and hydrophobic surfaces (36). These peptides are around 5 nm in size with alternating polar and nonpolar pattern. In aqueous solutions, the nonpolar residues shelter themselves from water while the charged

residues form complementary ionic interactions with regular repeats on the hydrophilic surfaces (37). The complementary ionic sides have been classified into different moduli i.e., modulus I, II, III, *etc.* and mixtures. This classification is based on the number of alternating positively charged and negatively charged amino acids on the hydrophilic surfaces of the molecules. For example, charge arrangement for modulus I is $- + - + - + - +$, for modulus II is $-- + + -- + +$, for modulus III is $--- + ++$. Different charge orientation can result in entirely different molecules. These well-defined sequences make highly ordered self-assembly become possible. Additionally, a broad range of peptides and proteins have been shown to self-assemble into stable nanofiber structures (also called amyloid fibers) with similar scale to the extracellular matrices (38). A number of mammalian cell types have been encapsulated or grown in this 3-D peptide scaffolds and promising results of cell attachment, proliferation, differentiation, migration, and ECM secretion were observed (37-39).

Amphiphilic molecules have also been intensively studied as building blocks for self-assembly (40-42). A typical example of amphiphilic molecules from nature is phospholipids, which are molecules containing distinct hydrophobic and hydrophilic segments. Amphiphilic molecules readily partition in water and undergo self-assembly to form various structures including micelles, vesicles, and tubules. This is largely due to the hydrophobic forces that drive the hydrophobic region of each molecule away from water and towards each other. Nanotubules have been successfully fabricated from lipids (40), surfactant-like peptides (41), and polyglutamines (42). Synthesis of self-assembly amphiphilic molecules that allow incorporation of specific biomolecular signals is also demonstrated (43), which underlines the potential of such molecular self-assembly system in incorporating both biomechanical and biomolecular cues.

Molecular self-assembly can be used as coating to modify chemical and physical properties of other materials' surface. Peptides that can interact with cells and adhere to other surfaces after self-assembly have been developed (44). These peptides usually have three general regions: a ligand for specific cell recognition, an anchor for covalent bonding to the surface, and a linker in between (44). Through this method, different complex cell patterns can be generated, which might provide a new way to study the cell-cell interactions (45).

Fabrication methods of 3-D porous composite scaffold

There are mainly four fabrication techniques that can produce 3-D composite scaffolds with highly interconnected pores: thermally induced phase separation, solvent casting, rapid prototyping, and microsphere sintering.

Thermally induced phase separation can generate 3-D polymer scaffolds with high porosity (~97%). Briefly, under certain conditions, a homogeneous

polymer solution become thermodynamically unstable and tends to separate into two phases to lower the system's free energy, a polymer-rich phase and a polymer-poor phase. After removing the solvent, the polymer-rich phase solidifies and forms a 3-D porous composite scaffold. The obtained scaffolds have highly interconnected pore structures and anisotropic tubular architectures. The pore morphology, mechanical properties, bioactivity and degradation rate of the scaffold can be controlled by varying the preparation conditions (46). The primary disadvantages of thermally induced phase separation are time consuming, possibility of shrinkage, and small scale production (47). Recently, 3-D polymer composite scaffolds containing TiO₂ and Bioglass[®] have been synthesized by thermally induced phase separation and enhanced cell adhesion and function is demonstrated (48). This method has been widely used to prepare scaffolds for various tissues, including nerve, muscle, tendon, ligament, intestine, bone, and teeth (46,47).

In solvent casting, polymer is dissolved in an organic solvent, which is then cast into a pre-designed 3-D mold. Subsequently the solvent is removed (49). Pre-synthesized microspheres, salt or sugar particles can be added to the polymer solution as porogens before casting and will be leached away after polymer solidification to generate 3-D scaffolds with more controlled porosity (50). Main advantage of this method is easy to fabrication, while disadvantages include shape limitations, possibility of toxic organic solvent remaining in the scaffolds which could cause denaturing of bioactive molecules incorporated in the scaffolds, *etc.* Little work has been done to produce bioactive scaffolds using this method, probably due to its major drawback of low pore interconnectivity, since many of the porogen might be still trapped in the polymer scaffold after leaching (51).

Rapid prototyping is the method that allows precise control of 3-D pore architecture of the scaffolds with the help of computer. Scaffolds of complex shapes are accurately designed using digital data generated by an imaging source such as computer tomography (52). Examples of rapid prototyping techniques include solid freeform fabrication (53), fused deposition modeling (54), and stereo lithography (55), all of which have been explored for scaffold fabrication. However, rapid prototyping technique has its inherent disadvantages such as limited material selection, increased scaffold fabrication time, inadequate resolution, and structural heterogeneity of the resultant scaffolds.

In microsphere sintering, pre-synthesized polymer microspheres or polymer/ceramic/bioactive addition composites are sintered to produce a 3-D porous scaffold (56). Bioactive scaffolds can be fabricated through this technique, and they are demonstrated to be supportive to human osteoblast-like cells' adhesion, growth, and mineralization (57). Scaffolds fabricated through this technique can have graded porosity structures. Mechanical properties close to cancellous bone also become possible when the microspheres are sintered into

cylindrical shapes (57). However, production of interconnected pores in the scaffolds remains to be a challenge for microsphere sintering technique.

Hydrogels

Hydrogels are crosslinked hydrophilic polymers whose molecular architecture has similar diffusive transportation, viscoelastic, and interstitial flow characteristics with natural ECM (58). Hydrogels contain large amount of water without dissolution. The excellent physiochemical similarity of the hydrogels to the natural ECM makes them attractive candidates for certain tissue engineering applications and promising results have been presented (59). Poly(ethylene glycol) (PEG) is the most frequently studied synthetic hydrogel and has been explored for potentials as scaffolds. However, lack of degradability is the major drawback of PEG hydrogel. To overcome this problem, enzymatic degradation sequences are introduced to the PEG backbone and copolymers are formulated degradable polymers and PEG (60,61). Other hydrogels attempted for applications in tissue engineering include semi-interpenetrating polymer networks (62), diblock copolypeptide amphiphiles containing polar and nonpolar segments (63), crosslinked alginates and polysaccharides (64), collagen (65), fibrin [66], and artificial proteins developed with recombinant DNA technology (67).

Tissue Engineering Applications of polymers

Tissue engineering has been successfully used for repair of chronic wounds and burns and at the experimental study level, in repair of cartilage defects. The advancement in tissue engineering is also permeating all previously synthetic areas. In the following part, four main tissue engineering application areas: skin, cartilage, blood vessel and nerve will be discussed mainly in terms of polymer materials used. The main principle of designing tissue engineering scaffolds and choosing polymer materials is to mimic the natural ECM around cells. Thus the structure and ECM properties of each organ will be introduced as the basis for understanding why specific polymer materials are constructed in specific scaffold shape.

Skin

Skin is the largest organ in human body and an adult has about 2m² areas of skin totally. It has lots of functions such as thermoregulation, protection,

sensation *etc.* Basically skin is a three-layer structure composed of epidermis, dermis and hypodermis. The epidermis is composed of stratified squamous epithelium consisting of epithelial cells, and the matrix producing keratinocytes together with the melanin producing melanocytes. The dermis is made up of dense connective and fibroblasts. The hypodermis is comprised of a looser connective tissue (68) .

Damage to skin can be caused by heat (burning), chemicals, electricity, ultraviolet or biting etc which results in 3-degree of skin trauma into epidermis, dermis and hypodermis respectively. As skin grafts, tissue engineering approach has evolved from simple cultured autologous epidermal sheets to more complex bilayered cutaneous substitutes (69).

Principle goals in skin graft are to achieve rapid wound closure and a functional and aesthetic scar. The skin graft should be porous to allow diffusion of nutrients, wasters and excess water, and prevent dehydration. The graft should encourage cell migration and have similar mechanical properties as that of native skin. Also the graft should degrade at properly rate which match tissue regeneration. Finally the graft should prevent bacteria infection (70).

Natural and synthetic polymers and hybrid of both have been used widely in constructing the scaffold part of skin grafts. Choice between these materials is one of the major concerns regarding fate of constructed skin grafts. There are some commercialized skin grafts mainly constructed from collagen and biodegradable PLGA which are summarized in Table VI.

The future requirement for the polymers would be biomimetic properties contain chemical signals, soluble growth factors, physical properties, mechanical properties which are similar to natural ECM and more conductive for epidermis and dermis regeneration.

Cartilage

There are three types of cartilage: hyaline cartilage, fibrocartilage and elastic cartilage. Hyaline cartilage is the predominant form of cartilage in the body and coats the surfaces of all articulating joints. Elastin cartilage forms the ear and nose and fibrocartilage is found at the end of tendons and ligaments. Articular cartilage is mainly composed of hyaline cartilage which consists of chondrocyte (1 % volume of cartilage) and several ECM molecules (mainly collagen type II and proteoglycans-aggreacan). Fibrocartilage is composed of mainly of type I collagen and proteoglycans such as versican. The ECM composition and organization of fibrocartilage provides much lower mechanical compressive strength as compared to hyaline cartilage (77). Elastic cartilage is composed of elastin as the name suggests. Current research has focused on hyaline cartilage.

Table VI. Polymers used as skin grafts

Polymer	Scaffold constructed	Cell used	Skin graft type
Polyurethane	sheet	keratinocyte	Epidermis Epicel™ (71)
PLGA	3-D matrix	Allogenic fibroblast	Dermis Dermagraft™ (72)
Collagen (bovine type I)	gel	Allogenic fibroblast and keratinocyte later	Bilayer Apigraft™ (73)
Collagen and GAG and silicone	3-D matrix	no	Acellular bilayer Integra™ (74)
Collagen	Gel and scaffold	Keratinocyte in gel and fibroblast in scaffold	Bilayer OrCell™ (75)
PLGA	Microsphere (70-130 μm in diameter)	Fibroblast and keratinocyte	Bilayer Bench study (76)

Osteoarthritis is the most prevalent disorder of the skeletal system and as many as 36 million Americans suffer from some forms of arthritis. Cartilage damage from sport injure is also common. Articular cartilage has a limited capacity for repair after injure because it contains no vascular supply and articular chondrocytes entrapped in dense ECM have limited mobility and low capability of contributing wound healing process (78-79).

The advantage for cartilage regeneration is articular cartilage contains no vasculature, nerves, or lymphatic vessels which is relatively easy to be reproduced compared with other complicated organs. However the challenge is regenerated cartilage needs to be supportive of loading since normal articular cartilage of the hip, for example, can withstand compressive stresses up to 20 MPa. Thus the important criterias for cartilage graft include sufficient mechanical properties to support join loading, capability of supporting cell infiltration, maintaining phenotype of chondrocyte, desirable degradable rate to match tissue regeneration. Ideally the regenerated cartilage should be

indistinguishable from the native articular cartilage in terms of zonal organization, biochemical composition, and mechanical properties (69).

Both synthetic and natural polymers have been used to construct cartilage graft. Nonbiodegradable polymers have also been used because they can provide good mechanical support. But biodegradable polymers are the trend in tissue engineering approach. There are some good reviews regarding the polymer materials used in cartilage regeneration which we won't repeat here (80-81).

Recently electrospinning has been widely used in cartilage tissue engineering because nanopopography of electrospun nanofibers was believed to provide a favorable condition for the growth of chondrocytes. PLGA (82) (75:25), PCL (83), type II collagen (84) were electrospun into nanofibers and behavior of chondrocytes grown on them were studied. It was found that PLGA nanofiber structure could better maintain phenotype of chondrocyte compared with the PLGA film (83). Also redifferentiation was observed in chondrocytes cultured on PCL electrospun scaffold in serum free media while other 3-D scaffolds such as alginate beads require additional growth factors for cell redifferentiation (84).

Blood vessel

Normal blood vessel (except capillary) has a trilamellar structure, with each layer having specific functional properties. The intima layer contains the endothelium, which is a single endothelial cell sheet functioning to prevent spontaneous blood clotting in the vessel. As the interface between dynamic blood flow and static vessel wall, ECs are directly exposed to flow and the associated shear stress and pressure, which made ECs elongate in response to flow and orient their major axis with the direction of flow (85). Also ECs attached to a connective tissue bed of basement membrane. This is adjacent to the internal elastic lamina which is a band of elastic tissue, found most prominently in the larger arteries. The media layer is composed of smooth muscle cells (SMCs) and variable amount of connective tissue such as collage, elastin, and proteoglycans. Specially, the SMCs and collagen fibers have a marked circumferential orientation to withstand the higher pressures in the circulation, as well as its ability to contract or relax in response to external stimuli. The adventitia, composed primarily of fibroblasts and loose connective tissue fibers, have the blood supply of the artery and innervations (86).

Ideally, a vascular graft should have characteristics similar to those of health recipient's vessels. Table VII summarizes the requirements which vascular graft should fulfill. When we design novel tissue engineered vascular scaffolds, we should consider all those factors.

There are generally three methods of constructing tissue engineered vascular grafts by applying collagen gel, cell-sheet and biodegradable polymer scaffolds,

Table VII. Requirements for tissue engineered vascular grafts

Requirements	Explanation
Biocompatibility	Haemocompatible, lack of thrombogenicity, non-inflammatory, nontoxic, non-carcinogenic, nonimmunogenic, resistant to infection
Biodegradability	By-products of polymer degradation is not toxic; degradation rate should match that of tissue regeneration
Porosity	Allow cell infiltration from the adventitial; maintaining hemostasis; sufficient mass transfer of gases and nutrients
mechanical property	Burst strength to withstand the physiological blood pressure and cyclic loading; compliant; elastic; good suturability, kink resistance
surface chemistry	Bioactivity for cell adhesion, proliferation, differentiation
Others	Off the shelf availability in various diameters and lengths; Uncomplicated storage or preparation requirements ;Ease of handling; Ease of adequate sterilization; Ease and low cost fabrication

amongst which, the last one is the main trend of current research. Table VIII shows the summary of the three methods. A review of detailed information on those methods is presented by Robert M. Nerem and will not be repeated here (87).

It can be seen from Table VIII that biodegradable polymer scaffolds approach went faster into clinical practice than the other two. Synthetic scaffolds enable us better control over physical properties such as mechanical properties. Also varieties of surface modification methods like protein and peptide immobilization, plasma treatment can provide better biocompatibility to the original polymer materials.

Nerve

Nervous system consists of the central nervous system (CNS) and the peripheral nervous system (PNS). CNS mainly includes the brain and the spinal cord, which receives sensory information and coordinates body activities. PNS mediates connections between the CNS and the peripheral of the body. In order to conduct information throughout the body, the nervous system possesses a large number of communication units by using electrical signals through nerve cells (neurons). While nerves are bundles of fibers made up of neurons through which sensory stimuli and motor impulses pass between the brain and other parts of CNS and other parts of the body. If nerves are severely damages, they can't

Table VIII. Summary of 3 methods of constructing tissue engineered vascular grafts

TEVG	Materials	Advantages	Disadvantages	Current Status
Collagen Gel (88-90)	Collagen Type I and III	Good tissue remodeling	Poor mechanical property; immunological mismatch	Bench study
Cell Sheet (91-92)	None	Elimination of immunological mismatch	Minimum 3 months until implantation	Reported clinical application on human in 2006 (92)
Biodegradable Scaffolds (93-98)	Polyester	Good mechanical property; Good patency if combined with cell		Reported clinical application on human in 1999 (99). PCL-PLLA tube reinforced with woven PGA.

send signals through the body in a normal way, and the signal communication inside the body is interrupted (100).

Damages to the nervous system may be raised by trauma from vehicle accidents, disease such as Alzheimer disease, Parkinson's disease, and after surgery. Among these injuries, spinal cord injury is most serious. To date, greater success has been achieved in repair of the PNS. Repair of CNS represents a greater challenge. The appearance of polymer nerve conduit may answer this challenge. Nerve conduits can direct axons sprouting from the regenerating nerve end, provide a conduit for diffusion of neurotropic and neurotrophic factors secreted by the damaged nerve stumps, and minimize infiltration of fibrous tissue (101). Ideal tissue engineered polymer nerve conduit should act as the substitutes of extracellular matrix (ECM) around nerves and the carriers of neurotrophic factors, growth-promoting molecules, neuronal support cells or genetically engineered cells or neural stem cells. Some related contents about nerve conduits have been well reviewed by several researchers in detail (102-104).

Here we restrict our discussion to the use of polymer materials as nerve conduit. To select proper polymer materials, there are some general requirements which all nerve conduits should follow: easily formed into a conduit with desired dimensions; sterilizable; tear resistant; easy to handle and suture; biodegradable *etc* (101).

ECM-based proteins such as collagen, fibronectin, and laminin and GAGs such as Hyaluronic acid, together with polysaccharides such as alginate and agarose have been used to construct or modify the nerve conduits. A number of synthetic polymers have also been explored for use in constructing nerve conduits. Polyesters such as PLA, PCL, PLGA were the first types of synthetic polymers being studied because of their availability, ease of processing, biodegradation, and approval by FDA.

Our group fabricated electrospun PLA (105) and PLGA (106) nanofibers to construct nerve conduit. Neural stem cells (NSC) seeded on the PLA nanofibrous scaffold were found to interact favorable with the environment with good cell attachment and differentiation as shown by the neurite outgrowth (105). In an animal study, PLGA (10:90) conduit was implanted into the right sciatic nerve of a rat. The porous nanofibrous scaffold allows the entry of nutrients into the lumen to promote nerve regeneration but at the same time act as a barrier to unwanted tissues infiltration. Positive reflex responses were observed in 45% of the rats one month after implantation and eight out of eleven rats had regenerated cable inside the conduits with no inflammation response (105).

Conclusion

Both synthetic and natural polymers such as polyesters and extracellular macromolecules have been widely used to construct tissue engineered scaffolds.

Besides traditional 3-D scaffolds fabrication methods, electrospinning and molecular self-assembly are newly developed techniques to construct biomimetic polymer scaffolds. Scaffolds fabricated by those techniques are mainly used in four tissue engineering areas: skin, cartilage, blood vessel, and nerve.

References

1. Langer, R.; Vacanti, J. P. Tissue engineering. *Science* **1993**, *260*, 920-926.
2. Shin, H.; Jo, S.; Mikos, A. G. Biomimetic materials for tissue engineering. *Biomaterials* **2003**, *24*, 4353-4364.
3. Hubbell J. A. Biomaterials in tissue engineering. *Bio-Technology* **2000**, *13*, 565-576.
4. Ma, P. X. Scaffolds for tissue fabrication. *Materials today* **2004**, *May*, 30-40.
5. Engelberg, I.; Kohn, J. Physico-mechanical properties of degradable polymers used in medical applications: a comparative study. *Biomaterials* **1991**, *12*, 292-304.
6. Ellis, D. L.; Yanna, I. V. Recent advances in tissue synthesis in vivo by use of collagen-glycosaminoglycan copolymers. *Biomaterials* **1996**, *17*, 291-299.
7. Yannas, I. V. Applications of ECM analogs in surgery. *J. Cell. Biochem.* **1994**, *56*, 188-191.
8. Formhals, A. Process and apparatus for preparing artificial threads. US Patent No. 1,975,504, 1934.
9. Fang, X.; Reneker, D. H. DNA fibers by electrospinning. *J. Macromolecular Sci-Phys* **1997**, *B36*, 169-173.
10. Taylor, G. I. Electrically driven jets. *Proc. R. Soc. London, Ser. A* **1969**, *313*, 453-475.
11. Reneker, D. H.; Yarin, A. L.; Fong, H.; Koombhongse, S. Bending instability of electrically charged liquid jets of polymer solutions in electrospinning. *J. Appl. Phys.* **2000**, *87*, 4531-4547.
12. Xu, C. Y.; Inai, R.; Kotaki, M.; Ramakrishna, S. Aligned biodegradable nanofibrous structure: a potential scaffold for blood vessel engineering. *Biomaterials* **2004**, *25*, 877-886.
13. Deitzel, J. M.; Kleinmeyer, J.; Harris, D.; Tan, N. C. B. The effect of processing variables on the morphology of electrospun nanofibers and textiles. *Polymer* **2001**, *42*, 261-272.
14. Matthews, J. A.; Wnek, G. E.; Simpson, D. G.; Bowlin, G. L. Electrospinning of collagen nanofibers. *Biomacromolecules* **2002**, *3*, 232-238.
15. Min, B. M.; Lee, G.; Kim, S. H.; Nam, Y. S.; Lee, T. S.; Park, W. H. Electrospinning of silk fibroin nanofibers and its effect on the adhesion and

- spreading of normal human keratinocytes and fibroblasts in vitro. *Biomaterials* **2004**, *25*, 1289-1297.
16. Kim, K.; Yu, M.; Zong, X.; Chiu, J.; Fang, D.; Seo, Y. S.; Hsiao, B. S.; Chu, B.; Hadjiargyrou, M. Control of degradation rate and hydrophilicity in electrospun non-woven poly(D,L-lactide) nanofiber scaffolds for biomedical applications. *Biomaterials* **2003**, *24*, 4977-4985.
 17. Kim, T. G.; Park, T. G. Biomimicking extracellular matrix: cell adhesive RGD peptide modified electrospun Poly(D,L-lactic-co-glycolic acid) nanofiber mesh. *Tissue Eng.* **2006**, *12*, 221-33.
 18. Chua, K. N.; Lim, W. S.; Zhang, P.; Lu, H.; Wen, J.; Ramakrishna, S.; Leong, K. W.; Mao, H. Q. Stable immobilization of rat hepatocyte spheroids on galactosylated nanofiber scaffold. *Biomaterials* **2005**, *26*, 2537-2547.
 19. He, W.; Ma, Z.; Yong, T.; Teo, W. E.; Ramakrishna, S. Fabrication of collagen-coated biodegradable polymer nanofiber mesh and its potential for endothelial cells growth. *Biomaterials*. **2005**, *26*, 7606-15.
 20. Chew, S. Y.; Wen, J.; Yim, K. F.; Leong, K. W. Sustained release of proteins from electrospun biodegradable fibers. *Biomacromolecules* **2005**, *6*, 2017-2024.
 21. Van, E. L.; Grondahl, L.; Chua, K. N.; Leong, K. W.; Nurombe, V.; Cool, S. M. Controlled release of heparin from poly(ϵ -caprolactone) electrospun fibers. *Biomaterials* **2006**, *27*, 2042-2050.
 22. Luu, Y. K.; Kim, K.; Hsiao, B. S.; Chu, B.; Hadjiargyrou, M. Development of a nanostructured DNA delivery scaffold via electrospinning of PLGA and PLA-PEG block copolymers. *J. Control. Release* **2003**, *89*, 341-353.
 23. Jiang, H. L.; Hu, Y. Q.; Li, Y.; Zhao, P.; Zhu, K. J.; Chen, W. L. A facile technique to prepare biodegradable coaxial electrospun nanofibers for controlled release of bioactive agents. *J. Control. Release* **2005**, *108*, 237-243.
 24. Huang, Z. M.; He, C. L.; Yang, A. Z.; Zhang, Y. Z.; Han, X. J.; Yin, J. L.; Wu, Q. S. Encapsulating drugs in biodegradable ultrafine fibers through coaxial electrospinning. *J. Biomed. Mater. Res.* **2006**, *77A*, 169-179.
 25. Zhang, Y. Z.; Wang, X.; Feng, Y.; Li, J.; Lim, C. T.; Ramakrishna, S. Coaxial electrospinning of (fluorescein isothiocyanate-conjugated bovine serum albumin)-encapsulated Poly(ϵ -caprolactone) nanofibers for sustained release. *Biomacromolecules*, **2006**, *7*, 1049-1057.
 26. Yu, J. H.; Fridrikh, S. V.; Rutledge, G. C. Production of submicrometer diameter fibers by two-fluid electrospinning. *Adv. Mater.* **2004**, *16*, 1562-1566.
 27. Rho, K. S.; Jeong, L.; Lee, G.; Seo, B. M.; Park, Y. J.; Hong, S. D.; Roh, S.; Cho, J. J.; Park, W. H.; Min, B. M. Electrospinning of collagen nanofibers: effects on the behavior of normal human keratinocytes and early-stage wound healing. *Biomaterials* **2006**, *27*, 1452-61.

28. Fertala, A.; Han, W. B.; Ko, F. K. Mapping critical sites in collagen II for rational design of gene-engineered proteins for cell-supporting materials. *J. Biomed. Mater. Res.* **2001**, *57*, 48-58.
29. Yoshimoto, H.; Shin, Y. M.; Terai, H.; Vacanti, J. P. A biodegradable nanofiber scaffold by electrospinning and its potential for bone tissue engineering. *Biomaterials* **2003**, *24*, 2077-82.
30. Chew, S. Y.; Wen, J.; Yim, E. K.; Leong, K. W. Sustained release of proteins from electrospun biodegradable fibers. *Biomacromolecules* **2005**, *6*, 2017-2024.
31. Zong, X.; Bien, H.; Chung, C. Y.; Yin, L.; Fang, D.; Hsiao, B. S.; Chu, B.; Entcheva, E. Electrospun fine-textured scaffolds for heart tissue constructs. *Biomaterials* **2005**, *26*, 5330-8.
32. Zhang, Y. Z.; Lim, C. T.; Ramakrishna, S.; Huang, Z. M. Review: Recent development of polymer nanofibers for biomedical and biotechnological applications. *J. Mater. Sci. Mater. Med.* **2005**, *16*, 933-946.
33. Benyus, J. M. *Biomimicry: Innovation Inspired by Nature*; Quill-William Morrow: New York, 1997.
34. Zhang, S. G. Emerging biological materials through molecular self-assembly. *Biotechnol. Advan.* **2002**, *20*, 321-339.
35. Pauling, L. *Nature of the Chemical Bond and the Molecular Crystals: An Introduction to Model Chemistry* 3rd ed; Cornell University: Ithaca, NY, 1960.
36. Zhang, S.; Marini, D.; Hwang, W.; Santoso, S. Designing nanobiological materials through self-assembly of peptides and proteins. *Curr. Opin. Chem. Biol.* **2002**, *6*, 865-871.
37. Zhang, S.; Holmes, T.; DiPersio, C. M.; Hynes, R. O.; Su, X.; Rich, A. Self-complementary oligopeptide matrices support mammalian cell attachment. *Biomaterials* **1995**, *16*, 1385-1393.
38. Fandrich, M.; Fletcher, M. A.; Dobson, C. M. Amyloid fibrils from muscle myoglobin. *Nature* **2001**, *410*, 165-166.
39. Holmes, T.; Delacalle, S.; Su, X.; Rich, A.; Zhang, S. Extensive neurite outgrowth and active neuronal synapses on peptide scaffolds. *Proc. Natl. Acad. Sci. USA* **2000**, *97*, 6728-6733.
40. Singh, A.; Price, R.; Schoen, P. E.; Yager, P.; Schnur, J. M. Tubule formation by hetero biofunctional polymerizable lipids: synthesis and characterization. *Polymer Preprints* **1986**, *27*, 393-394.
41. Santoso, S.; Hwang, W.; Hartman, H.; Zhang, S. Self-assembly of surfactant-like peptides with variable glycine tails to form nanotubules and nanovesicles. *Nano Lett.* **2002**, *2*, 687-691.
42. Perutz, M. F. Glutamine repeats and neurodegenerative diseases. *Brain Res. Bull.* **1999**, *50*, 467.
43. Niece, K. L.; Hartgerink, J. D.; Donners, J. J.; Stupp, S. I. Self-assembly

- combining two bioactive peptide-amphiphile molecules into nanofibers by electrostatic attraction. *J. Am. Chem. Soc.* **2003**, *125*, 7146-7147.
44. Zhang, S.; Yan, L.; Altman, M.; Lassle, M.; Nugent, H.; Frankel, F.; Lauffenburger, D. A.; Whitesides, G. M.; Rich, A. Biological surface engineering: a simple system for cell pattern formation. *Biomaterials* **1999**, *20*, 1213-1220.
 45. Zhang, S. G. Review: fabrication of novel biomaterials through molecular self-assembly. *Nature* **2003**, *21*, 1171-1178.
 46. Boccaccini, A. R.; Maquet, V. Bioresorbable and bioactive polymer/bioglass (R) composites with tailored pore structure for tissue engineering applications. *Compos. Sci. Technol.* **2003**, *63*, 2417-2429.
 47. Ma, P. X.; Zhang, R. Microtubular architecture of biodegradable polymer scaffolds. *J. Biomed. Mater. Res.* **2001**, *56*, 469-477.
 48. Boccaccini, A. R.; Blaker, J. J.; Maquet, V.; Chung, W.; Jerome, R.; Nazhat, S. N. PDLA foams with TiO₂ nanoparticles and PDLA/TiO₂-Bioglass foam composites for tissue engineering scaffolds. *J. Mater. Sci.*, in press.
 49. Laurencin, C. T.; Lu, H. H.; Y. K. *Methods of tissue engineering*; Academic Press: California, 2002; p 705.
 50. Ma, P. X.; Choi, J. W. Biodegradable polymer scaffolds with well-defined interconnected spherical pore network. *Tissue Eng.* **2001**, *7*, 23-33.
 51. Rezwan, K.; Chen, Q. Z.; Blaker, J. J.; Boccaccini, A. R. Review: biodegradable and bioactive porous polymer/inorganic composite scaffolds for bone tissue engineering. *Biomaterials* **2006**, *27*, 3413-3431.
 52. Hutmacher, D. W. Scaffolds in tissue engineering bone and cartilage. *Biomaterials* **2001**, *21*, 2529-2543.
 53. Xiong, Z.; Yan, Y. N.; Wang, S. G.; Zhang, R. J.; C. Z. Fabrication of porous scaffolds for bone tissue engineering via low-temperature deposition. *Scr. Mater.* **2002**, *46*, 771-776.
 54. Hutmacher, D. W.; Schantz, T.; Zein, I.; Ng, K. W.; Teoh, S. H.; Tan, K. C. Mechanical properties and cell cultural response of polycaprolactone scaffolds designed and fabricated via fused deposition modeling. *J. Biomed. Mater. Res.* **2001**, *55*, 203-216.
 55. Sodian, R.; Loebe, M.; Hein, A.; Martin, D. P.; Hoerstrup, S. P.; Potapov, E. V.; Hausmann, H.; Lueth, T.; Hetzer, R. Application of stereolithography for scaffold fabrication for tissue engineered heart valves. *ASAIO J.* **2002**, *48*, 12-16.
 56. Khan, Y. M.; Dhirendra, D. S.; Katti, S.; Laurencin, C. T. Novel polymer-synthesized ceramic composite-based system for bone repair: an in vitro evaluation. *J. Biomed. Mater. Res. A* **2004**, *69A*, 728-737.
 57. Lu, H. H.; EL-Amin, S. F.; Scott, K. D.; Laurencin, C. T. Three-dimensional, bioactive, biodegradable, polymer-bioactive glass composite

- scaffolds with improved mechanical properties support collagen synthesis and mineralization of human osteoblast-like cells in vitro. *J. Biomed. Mater. Res. A* **2003**, *64A*, 465-474.
58. Lutolf, M. P.; Hubbell, J. A. Review: synthetic biomaterials as instructive extracellular microenvironments for morphogenesis in tissue engineering. *Nature* **2005**, *23*, 47-55.
 59. Peppas, N. A.; Huang, Y.; Torres-Lugo, M.; Ward, J. H.; Zhang, J. Physicochemical foundations and structural design of hydrogels in medicine and biology. *Annu. Rev. Biomed. Eng.* **2000**, *2*, 9-29.
 60. Lutolf, M. P.; Lauer-Fields, J. L.; Schmoekel, H. G.; Metters, A. T.; Weber, F. E.; Fields, G. B.; Hubbell, J. A. Synthetic matrix metalloproteinase-sensitive hydrogels for the conduction of tissue regeneration: engineering cell-invasion characteristics. *Proc Natl Acad Sci U S A.* **2003**, *100*, 5413-5418.
 61. Behraves, E.; Jo, S.; Zygourakis, K.; Mikos, A. G. Synthesis of in situ cross-linkable macroporous biodegradable poly(propylene fumarate-co-ethylene glycol) hydrogels. *Biomacromolecules* **2002**, *3*, 374-381.
 62. Stile, R. A.; Healy, K. E. Poly(N-isopropylacrylamide)-based semi-interpenetrating polymer networks for tissue engineering applications. 1. Effects of linear poly(acrylic acid) chains on phase behavior. *Biomacromolecules* **2002**, *3*, 591-600.
 63. Nowak, A. P.; Breedveld, V.; Pakstis, L.; Ozbas, B.; Pine, D. J.; Pochan, D.; Deming, T. J. Rapidly recovering hydrogel scaffolds from self-assembling diblock copolypeptide amphiphiles. *Nature* **2002**, *417*, 424-428.
 64. Atala, A.; Kim, W.; Paige, K. T.; Vacanti, C. A.; Retik, A. B. Endoscopic treatment of vesicoureteral reflux with a chondrocyte-alginate suspension. *J Urol.* **1994**, *152*, 641-643.
 65. Hildebrand, K. A.; Jia, F.; Woo, S. L. Response of donor and recipient cells after transplantation of cells to the ligament and tendon. *Microsc Res Tech.* **2002**, *58*, 34-38.
 66. Grassl, E. D.; Oegema, T. R.; Tranquillo, R. T. Fibrin as an alternative biopolymer to type-I collagen for the fabrication of a media equivalent. *J Biomed Mater Res.* **2002**, *60*, 607-612.
 67. Tamura, T.; Yamaoka, T.; Kunugi, S.; Panitch, A.; Tirrell, D. A. Effects of temperature and pressure on the aggregation properties of an engineered elastin model polypeptide in aqueous solution. *Biomacromolecules* **2000**, *1*, 552-555.
 68. Parenteau, N. L.; Yong, J. H.; Ross R. N. *Principle of Tissue Engineering*; Academic Press, San Diego, 2000; p 879-890.
 69. Seal, B. L.; Otero, T. C.; Panitch, A. Polymeric biomaterials for tissue and organ regeneration. *Mat. Sci. Eng. R.* **2001**, *34*, 147-230.
 70. Clark, R. A. F.; Singer, A. J. *Principle of Tissue Engineering*; Academic Press, San Diego, 2000; p 857-878.

71. Wright, K. A.; Nadire, K. B.; Busto, P.; Tubo, R.; McPherson, J. M.; Wentworth, B. M. Alternative delivery of keratinocytes using a polyurethane membrane and the implications for its use in the treatment of full-thickness burn injury. *Burns* **1998**, *24*, 7-17.
72. Marston, W.A. Dermagraft, a bioengineered human dermal equivalent for the treatment of chronic nonhealing diabetic foot ulcer. *Expert. Rev. Med. Devices*. **2004**, *1*, 21-31.
73. Falanga, V.; Margolis, D.; Alvarez, O.; Auletta, M.; Maggiacomo, F.; Altman, M.; Jensen, J.; Sabolinski, M.; Hardin-Yong, J. Rapid Healing of Venous Ulcers and Lack of Clinical Rejection With an Allogeneic Cultured Human Skin Equivalent. *Arch. Dermatol.* **1998**, *134*, 293-300.
74. Ojeh, N. O.; Frame, J. D.; Navsaria, H. A. *In vitro* characterization of an artificial dermal scaffold. *Tissue. Eng.* **2001**, *7*, 457-472.
75. Auger, F. A.; Berthod, F.; Moulin, W.; Pouliot, R.; Germain, L. Tissue-engineered skin substitutes: from *in vitro* constructs to *in vivo* applications. *Biotechnol. Appl. Bioc.* **2004**, *39*, 263-275.
76. LaFrance, M. I.; Armstrong, D. W. *Tissue. Eng.* **1999**, *5*, 153.
77. McPherson, J. M.; Tubo, R. *Principle of Tissue Engineering*; Academic Press, San Diego, 2000; p 697-709.
78. Temenoff, J. S.; Mikos, A. G. Review: tissue engineering for regeneration of articular cartilage. *Biomaterials* **2000**, *21*, 431-440.
79. Risbud, M. V.; Sittering, M. Tissue engineering: advances in *in vitro* cartilage regeneration. *Trends. Biotechnol.* **2002**, *20*, 351-356.
80. Lu, L.; Zhu, X.; Valenzuela, R. G.; Currier, B. L.; Yaszemski, M. J. Biodegradable polymer scaffolds for cartilage tissue engineering. *Clin. Orthop. Relat. Res.* **2001**, *391*, S251-70.
81. Frenkel, S. R., Dicesare, P. E. Scaffolds for articular cartilage repair. *Ann. Biomed. Eng.* **2004**, *32*, 26-34.
82. Shin, H. J., Lee, C. H., Cho, I. H., Kim, Y. J., et al., Electrospun PLGA nanofiber scaffolds for articular cartilage reconstruction: mechanical stability, degradation and cellular responses under mechanical stimulation *in vitro*. *J. Biomater. Sci. Polym. Edn.* **2006**, *17*, 103-119.
83. Li, W.J., Danielson, K. G., Alexander, P. G., Tuan, R. S., Biological response of chondrocytes cultured in three-dimensional nanofibrous poly(ϵ -caprolactone) scaffolds. *J. Biomed. Mater. Res.* **2003**, *67A*, 1105-1114.
84. Shields, K. J., Beckman, M. J., Bowlin, G. L., Wayne, J. S., Mechanical Properties and Cellular Proliferation of Electrospun Collagen Type II. *Tissue. Eng.* **2004**, *10*, 1510-1517.
85. Dewey, C. F. Jr.; Bussolari, S. R.; Gimbrone, M. A. Jr.; Davies, P. F. The dynamic response of vascular endothelial cells to fluid shear stress. *J. Biomech. Eng.* **1981**, *103*, 177-185.
86. Niklason, L. E.; Seruya, M. *Methods of Tissue Engineering*; Academic Press, San Diego, 2002; p 905-913.

87. Nerem, R. M.; Seliktar, D. Vascular tissue engineering. *Annu. Rev. Biomed. Eng.* **2001**, *3*, 225-243.
88. Weinberg, C. B.; Bell, E. A blood vessel model constructed from collagen and cultured vascular cells. *Science* **1986**, *231*, 397-400.
89. L'Heureux, N.; Germain, L.; Labbe, R.; Auger, F. A. *In vitro* construction of a human blood vessel from cultured vascular cells: amorphologic study. *J. Vasc. Surg.* **1993**, *17*, 499-509.
90. Tranquillo, R. T.; Girton, T. S.; Bromberek, B.A.; Triebes, T. G.; Mooradian, D. L. Magnetically orientated tissue-equivalent tubes: application to a circumferentially orientated media-equivalent. *Biomaterials* **1996**, *17*, 349-357.
91. L'Heureux, N.; Paquet, S.; Labbe, R.; Germain, L.; Auger, F. A. A completely biological tissue engineered human blood vessel. *Faseb. J.* **1998**, *12*, 47-56.
92. L'Heureux, N.; Dusserre, N.; Konig, G.; Victor, B.; Keire, P.; Wight, T. N.; Chronos, N. A. F.; Kyles, A. E.; Gregory, C. R.; Hoyt, G.; Robbins, R. C.; McAllister, T. N. Human tissue-engineered blood vessels for adult arterial revascularization. *Nat. Med.* **2006**, *12*, 361-365.
93. Niklason, L. E.; Gao, J.; Abbott, W. M.; Hirschi, K. K.; Houser, S.; Marini, R.; Langer, R. Functional arteries grown *in vitro*. *Science* **1999**, *284*, 489-493.
94. Shum-Tim, D.; Stock, U.; Hrkach, J.; Shinoka, T.; Lien, J.; Moses, M. A.; Stamp, A.; Taylor, G.; Moran, A. M.; Landis, W.; Langer, R.; Vacanti, J. P.; Mayer, J. E. Jr. Tissue engineering of autologous aorta using a new biodegradable polymer. *Ann. Thorac. Surg.* **1999**, *68*, 2298-2305.
95. Niklason, L. E.; Gao, J.; Abbott, W. M.; Hirschi, K. K.; Houser, S.; Marini, R.; Langer R. Functional arteries grown *in vitro*. *Science* **1999**, *284*, 489-493.
96. Watanabe, M.; Shin'oka, T.; Tohyama, S.; Hibino, N.; Konuma, T.; Matsumura, G.; Kosaka, Y.; Ishida, T.; Imai, Y.; Yamakawa, M.; Ikada, Y.; Morita, S. Tissue-engineered vascular autograft: inferior vena cava replacement in a dog model. *Tissue. Eng.* **2001**, *7*, 429-439.
97. Hoerstrup, S. P.; Zund, G.; Sodian, R.; Schnell, A. M.; Grunenfelder, J.; Turina, M. I. Tissue engineering of small caliber vascular grafts. *Eur. J. Cardiothorac. Surg.* **2001**, *20*, 164-169.
98. Hoerstrup, S. P.; Kadner, A.; Breymann, C.; Maurus, C. F.; Guenter, C. I.; Sodian, R.; Visjager, J. F.; Zund, G.; Turina, M. I. Living, autologous pulmonary artery conduits tissue engineered from human umbilical cord cells. *Ann. Thorac. Surg.* **2002**, *74*, 46-52.
99. Shin'oka, T.; Imai, Y.; Ikada, Y. Transplantation of a tissue-engineered pulmonary artery. *N. Engl. J. Med.* **2001**, *344*, 532-533.
100. Fine, E. G.; Valentini, R. F.; Aebischer, P. *Principle of Tissue Engineering*; Academic Press, San Diego, 2000; p 785-798.

101. Schmidt, C. E.; Leach, J. B. Neural tissue engineering: strategies for repair and regeneration. *Annu. Rev. Biomed. Eng.* **2003**, *5*, 293-347.
102. Belkas, J. S.; Shoichett, M.S.; Midha, R. Peripheral nerve regeneration through guidance tubes. *Neurol. Res.* **2004**, *26*, 151-160.
103. Meek, M. F.; Coert, J. H. Clinical use of nerve conduits in peripheral-nerve repair: Review of the literature. *J. Reconstr. Microsurg.* **2002**, *18*, 97-109.
104. Strauch, B. Use of nerve conduits in peripheral nerve repair. *Hand. Clin.* **2000**, *16*, 123-130.
105. Yang, F., Xu, C. Y., Kotaki, M., Wang, S., Ramakrishna, S., Characterization of neural stem cells on electrospun poly(L-lactic acid) nanofibrous scaffold. *J. Biomater. Sci. Polymer Edn.* **2004**, *15*, 1483-1497.
106. Bini, T. B., Gao, S., Tan, T. C., Wang, S., Electrospun poly(L-lactide-co-glycolide) biodegradable polymer nanofibre tubes for peripheral nerve regeneration. *Nanotechnology* **2004**, *15*, 1459-1464.

Chapter 20

Cell-Container Prepared with Cytocompatible Phospholipid Polymers for Cell and Tissue Engineering

Tomohiro Konno and Kazuhiko Ishihara

Department of Materials Engineering, School of Engineering, and Center for NanoBio Integration, The University of Tokyo, Hongo, Bunkyo-ku, Tokyo 113-8656, Japan

We propose a novel polymeric hydrogel system as a cell container that can encapsulate cells in the polymer networks reversibly. A phospholipid polymer bearing 2-methacryloyloxyethyl phosphorylcholine units and *p*-vinylphenylboronic acid (PMBV) was synthesized to form a covalently cross-linking hydrogel with a polymer having multivalent hydroxyl groups such as poly (vinyl alcohol) (PVA). The hydrogel was formed not only in water but also even in the biological medium. However it was dissociated by addition of low molecular weight divalent hydroxyl compounds such as glucose. After fibroblast cells were added to PMBV solution and mixed with PVA, the cells were immobilized into the hydrogel. After dissociation of the hydrogel, the cells were adhered and proliferated as usual on a conventional cell culture plate. That is, the hydrogel system is useful to maintain the cells as a cell container.

It is extremely important to handle cells to progress the tissue growth and engineering. In this study, we propose a new hydrogel system "cell-container" which can encapsulate and maintain the functional cells and proteins with high viability and activity. It was considered that the reversible polymeric hydrogel satisfied the requirements. Preparation of a recoverable hydrogel with water-soluble polymers will provide a new fixation method for target biomolecules, cells and tissues. Cross-linking of the polymer chains under mild condition in physiological conditions would be necessary for this purpose to avoid reduction of activity of the immobilized cells and the entrapped biomolecules. Also, cytocompatibility of the hydrogel would be important for its application as a cell container. To obtain the cytocompatibility of hydrogel, we focused on the cell membrane structure. We have reported that 2-methacryloyloxyethyl phosphorylcholine (MPC) polymers containing phospholipid polar group in the side chain have an excellent biocompatibility due to their ability to inhibit protein adsorption following biological responses (1).

In our previous studies, we have succeeded in spontaneous gelation of water-soluble phospholipid polymers from their aqueous solutions by hydrogen bonding without any physical treatments (2-7). Also, the hydrogel formed could be dissociated by change in pH, however, the pH inside of the hydrogel was low ($\text{pH} < 4$), which would be required in order for its application as a cell container.

It is well known that the boronic acid in a tetrahedral anionic structure makes stable complexes with diol compounds including PVA, glucose, sorbitol and so on (8-11). Moreover, the hydrogel formed by cross-linking between boronic acid and polyol compound can dissociate by addition of low molecular weight substances such as glucose. The hydrogels containing boronic acid moiety have attracted attention in the affinity chromatography of biological agents (10). Also, this reaction mechanism is well known as glucose concentration responsive hydrogels with application in glucose sensors (11). We propose the new hydrogel system based on this cross-linking mechanism will be useful to preserve the cells as cell container (Figure 1).

In this study, we synthesized a new water-soluble phospholipid polymer containing a *p*-vinylphenylboronic acid unit, that is, poly[MPC-*co*-*n*-BMA-*co*-*p*-vinylphenylboronic acid (VPBA)](PMBV). Also, we reported the synthesis and characterization of the polymer, formation and properties of polymeric hydrogel with PVA, and behavior of fibroblast cells in the hydrogel.

Materials and Method

Materials

MPC was synthesized by a previously reported method and used after recrystallization from acetonitrile (12). *n*-Butyl methacrylate (BMA) was

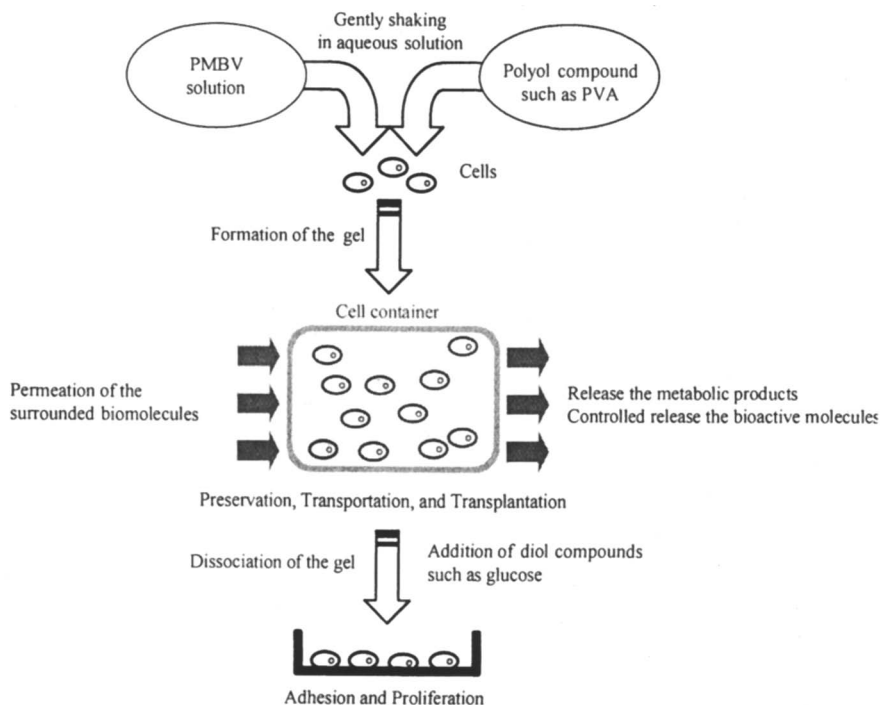


Figure 1. Basic concept of cell-container using with reversible polymer hydrogel system

purchased from Nakalai Tesque Co. Ltd. (Tokyo, Japan) and purified by distillation under reduced pressure. *p*-Vinylphenylboronic acid (VPBA) was kindly provided from Osaka Organic Chemical Industry Ltd. (Osaka, Japan). Poly(vinyl alcohol)(PVA, polymerization degree 1500, saponification value 86-90 mol%) was purchased from Wako Pure Chemical Industries Ltd. (Osaka, Japan). Other organic reagents and solvents were commercially available reagents of extra-pure grade and were used without further purification.

Cell culture medium (Dulbecco's modified eagle medium, DMEM), phosphate buffered saline (PBS), and other substances for cell culture were purchased from Invitrogen Corporation, Grand Island, NY, USA.

Synthesis of Phospholipid Polymers

Poly(MPC-*co-n*-BMA-*co*-VPBA)(PMBV) were synthesized by a conventional radical polymerization technique using α,α' -azobis-isobutyronitrile (AIBN) as an initiator. The synthesis procedure was as follows; MPC (M.W.=295.27), BMA (M.W.=142.2) and VPBA (M.W.=147.8) were placed in

a glass ampoule, and the mixture was diluted with ethanol to 1 mol/L of monomer concentration. AIBN was dissolved in a mixture solution (1 mmol/L). Argon gas was bubbled into the solution to eliminate oxygen for 5 min, and then the glass ampoule was sealed. The polymerization was performed at 60 °C for given time. After cooling the glass ampoule, the contents were poured into a large amount of mixture of diethyl ether and chloroform (8/2 by volume) to eliminate remaining monomer and precipitate the polymer. The polymer as a precipitate was filtered off using glass-filter and dried in vacuum. Chemical structure of the polymer was confirmed by ¹H-NMR and FT-IR measurements. The mole fraction of each component in the copolymer was determined by the ¹H-NMR measurement. Molecular weight of polymers was measured by a gel permeation chromatography system (JASCO Co. Ltd., Tokyo Japan). The chemical structure and synthetic results of polymers are summarized in Figure 2 and Table 1.

Fibroblast Cell Culture in the Hydrogel

To preserve the cells in the hydrogel, mouse fibroblast cell line, L929, was used as model cells. L929 cells were routinely cultured in Dulbecco's modified eagle minimum essential medium (GIBCO[®], Invitrogen Corp., Grand Island, NY), supplemented with 10% fetal bovine serum (GIBCO[®], Invitrogen Corp., Grand Island, NY) at 37 °C in a 5 % CO₂ atmosphere. After trypsinization, the cell density was adjusted to 5 x 10³ cells/mL by the cell culture medium containing 5 wt% of PMBV631. The L929/PMBV631 solution was mixed with 5 wt% of PVA solution, and gently shaken to form the PMBV hydrogel containing L929 cells. The shape and morphology of the L929 cells was observed by using a phase-contrast microscope (BX60, OLYMPUS, Tokyo, Japan). After 5 days, the hydrogel was dissociated, and the inner L929 cells were plated on the tissue culture polystyrene (TCPS).

Results and Discussion

Both water-soluble and water-insoluble phospholipid polymers containing VPBA were synthesized by the conventional radical polymerization. The water-solubility of polymers depended on the MPC mole fraction in polymer. The chemical structure and synthetic results of polymers are summarized in Figure 2 and Table 1.

The water-soluble phospholipid polymer bearing both MPC units and VPBA units, PMBV631, formed a hydrogel after mixing with PVA aqueous solution. Figure 3 shows the schematic representation of the covalent cross-linking between PMBV631 and PVA. The gelation mechanism was covalent

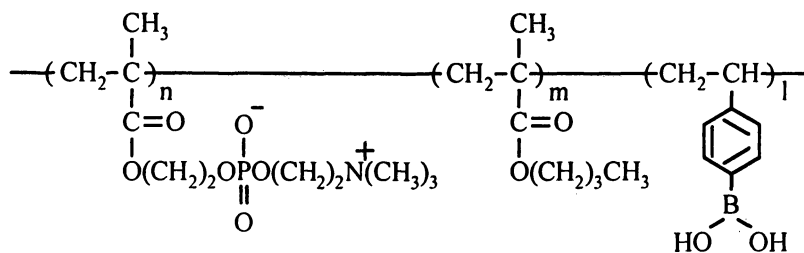


Figure 2. Chemical structure of poly(MPC-co-n-BMA-co-VPBA)(PMBV)

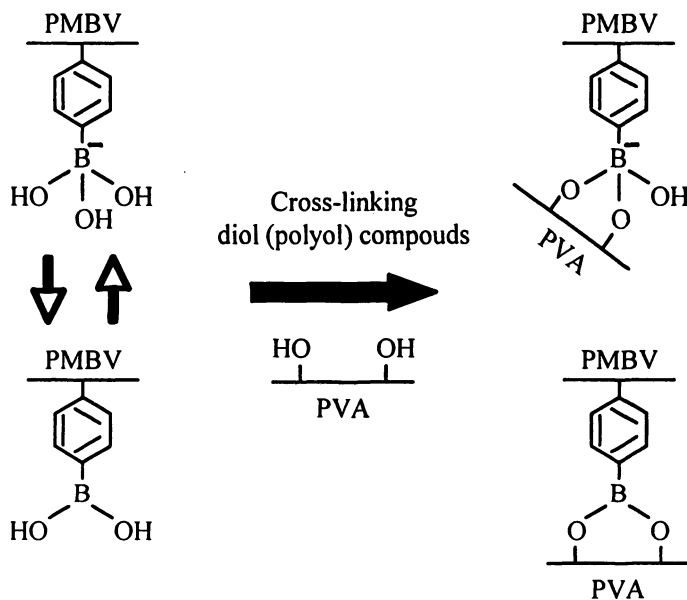


Figure 3. Cross-linking mechanism between the PMBV631 and the diol-compound (PVA)

Table 1. Synthetic results of PMBV

Abbreviation	In feed (mole fraction) MPC/BMA/VPBA	In polymer (mole fraction) MPC/BMA/VPBA	Polymerization time (h)	Yield (%)	Solubility in water	M.W. (10^{-3})	Mw/Mn
PMBV631	0.6 / 0.3 / 0.1	0.6 / 0.3 / 0.1	6	71	+	54	2.6
PMBV361	0.3 / 0.6 / 0.1	0.4 / 0.5 / 0.1	3	62	-	88	1.6

cross-linking between the phenylboronic acid of VPBA and hydroxyl groups of PVA. Before mixing, both polymer aqueous solutions were low viscosity liquids. After mixing, the viscosity gradually increased, and finally, the mixture formed the hydrogel. The combination of PMBV631 and PVA that formed the hydrogels are summarized in Table 2. Also, the typical image of the hydrogel is shown in Figure 4. Figure 5 shows SEM images of the cross section of the PMBV hydrogel after lyophilization. Every gel had a porous structure. The pore size of the network was almost 1 μm under the dry condition. The gelation between PMBV631 and PVA was confirmed even though phosphate buffered saline and cell culture medium were used. It is hypothesized that this hydrogelation mechanism does not affect the ionic strength of saline and medium.

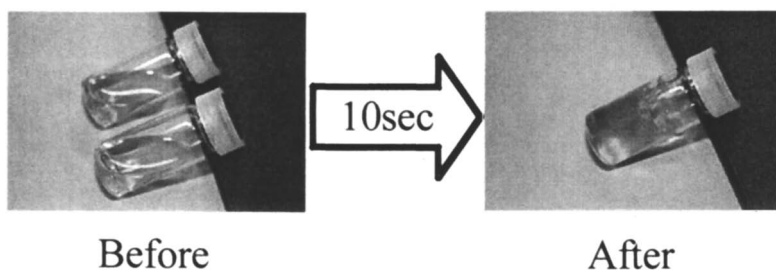


Figure 4. Typical image of PMBV hydrogel before and after shaking

Table 2. Composition dependency of hydrogel formation

(wt%)		PMBV631					Abb.	PMBV631 (wt%)	PVA (wt%)
		5.0	2.5	1.2	0.6	0.3			
PVA	5.0	○	○	×	×	×	#001	5.0	5.0
	2.5	○	○	×	×	×	#002	5.0	2.5
	1.2	○	×	×	×	×	#003	2.5	5.0
	0.6	○	×	×	×	×	#004	2.5	2.5
	0.3	×	×	×	×	×			

To demonstrate the application of the hydrogel as a cell-container, mouse fibroblast (L929) cells were cultured (preserved) in the hydrogel. In this culture method, the PMBV631 was dissolved using cell culture medium containing PBS. Previous reports have observed that the phospholipid polymer containing

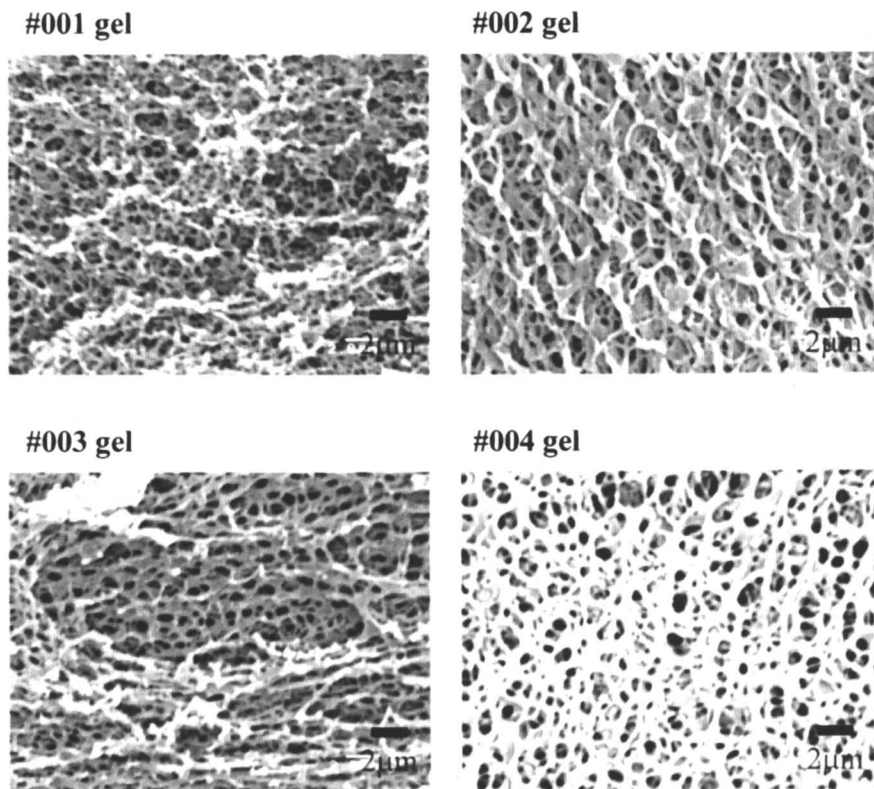


Figure 5. SEM images of the cross section of the various PMBV hydrogels

MPC units reduced the nonspecific interaction between proteins and cells (13). The cells were suspended in 2.5 wt% of PMBV631 medium solution. The PMBV medium solution containing the cells was mixed with 5.0 wt% of PVA aqueous solution. The gelation was confirmed after gently shaking. Figure 6 shows the phase contrast microscope images of the cells in the gel. The cell morphology was circular and the cells did not spread in the network. Furthermore, the cells did not aggregate each other. When the cells were cultured on the phospholipid polymer surface, they locally aggregated each other. Thus, it was considered that this hydrogel could hold the individual cells. After 5 days culture without changing the medium, the hydrogel was dissociated and the inner cells were seeded on the conventional tissue culture polystyrene plate. The cells immediately adhered and proliferated normally on the TCPS. Namely, the cells had enough viability even in the PMBV hydrogel during 5 days. It was considered that the PMBV hydrogel functioned only as a cell

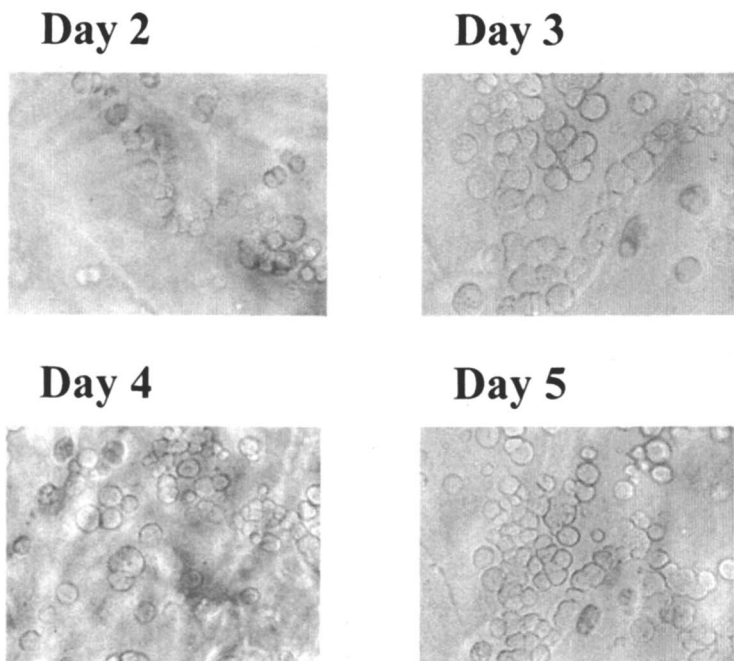


Figure 6. Phase contrast microscope images of L929 fibroblast cell cultured in the PMBV hydrogel 2.5 wt% PMBV and 5.0 wt% PVA)

holding matrix. Also, this result indicated that the PMBV hydrogel has a good cytocompatibility to apply as a platform matrix for its use as cell-container.

Conclusion

We prepared water-soluble and water-insoluble phospholipid polymers bearing both MPC units and VPBA units. The gelation between the phospholipid polymer and PVA spontaneously occurred after mixing the two kinds of polymer aqueous solutions. The gelation mechanism was based on covalently cross-linking between phenylboronic acid moiety of phospholipid polymer and hydroxyl groups of PVA. The hydrogel formed not only in water but also in saline including cell culture medium. The viability of the cells was not affected from the hydrogel. It was concluded that the novel hydrogel system based on the phospholipid polymer might be applied as cell container to preserve and transport the cells.

References

1. Ishihara, K.; Nomura, H.; Mihara, T.; Kurita, K.; Iwasaki, Y.; Nakabayashi, N. *J. Biomed. Mater. Res.* **1998**, *39*, 323.
2. Nam, K.; Watanabe, J.; Ishihara, K. *Polymer* **2005**, *46*(13), 4707.
3. Kimura, M.; Fukumoto, K.; Watanabe, J.; Takai, M.; Ishihara, K. *Biomaterials* **2005**, *26*(34), 6853.
4. Kimura, M.; Fukumoto, K.; Watanabe, J.; Ishihara, K. *J. Biomater. Sci. Polym. Edn.* **2004**, *15*(5), 631
5. Nam, K.; Watanabe, J.; Ishihara, K. *Eur. J. Pharm.* **2004**, *23*(3), 261.
6. Nam, K.; Watanabe, J.; Ishihara, K. *Biomacromolecules* **2002**, *3*(1), 100.
7. Nam, K.; Watanabe, J.; Ishihara, K. *J. Biomater. Sci. Polym. Edn.* **2002**, *13*(11), 1259.
8. Kitano, S.; Koyama, Y.; Kataoka, K.; Okano, T.; Sakurai, J. *Control. Rel.* **1992**, *19*, 161.
9. Weith, H.; Wiebers, J.; Gilham, P. *Biochemistry* **1970**, *9*(22), 4396.
10. Kikuchi, A.; Suzuki, K.; Okabayashi, O.; Hoshino, H.; Kataoka, K.; Sakurai, Y.; Okano, T. *Anal. Chem.* **1996**, *68*, 823.
11. Matsumoto, A.; Yoshida, R.; Kataoka, K. *Biomacromolecules* **2004**, *5*(3), 1038
12. Ishihara, K.; Ueda, T.; Nakabayashi, N. *Polym. J.* **1990**, *22*, 355.
13. Sawada, S.; Sakaki, S.; Iwasaki, Y.; Nakabayashi, N.; Ishihara, K. *J. Biomed. Mater. Res.* **2003**, *64A*(3), 411.

Chapter 21

Evaluation of a Bioabsorbable Polyester Blend for Use in Medical Devices: CRANIOSORB™, a Novel Cranial Fixation System

Kevin Cooper¹, Yufu Li¹, Bruce Lowenhaupt¹, David Overaker²,
Tom Poandl³, Susan Trenka-Benthin⁴, J. Yuan³,
and M. Zimmerman⁵

¹Center for Biomaterials and Advanced Technologies, Medical Devices Group, A Division of Ethicon, A Johnson & Johnson Company, Route 22 West, Somerville, NJ 08876

²Cordis, A Johnson & Johnson Company, 7 Powder Horn Drive, Warren, NJ 07059

³Ethicon, A Johnson & Johnson Company, Route 22 West, Somerville, NJ 08876

⁴Consulting Veterinary Pathologist, 24 Poor Farm Road, Pennington, NJ 08534

⁵Betalogics, A Johnson & Johnson Company, 199 Grandview Road, Skillman, NJ 08558

*Corresponding author: kcooper@ethus.jnj.com

A novel cranial fixation system, Craniosorb™, was developed using bioabsorbable, aliphatic polyester blends comprising a 50:50 mole:mole poly(50,50 D,L-lactide) (D,L-PLA) and a 95:5 mole:mole poly(ϵ -caprolactone-co-p-dioxanone) (PCL:PDO). It was determined that compositions containing less than 10 weight percent of the PCL:PDO copolymer form an opaque, semi-crystalline blend that upon heating above the melting point of the copolymer soften and appear clear until cooled below the copolymer's melting point to yield a visual cue to allow the surgeon to non-destructively contour the now flexible plate to the irregularly shaped cranial and facial bones. Additionally, a novel, easy to deliver fastener system composed of an interference fitting poly(L-lactide) rivet/pin was developed. Physico-mechanical testing of the plate and

rivet/pin system demonstrated sufficient strength retention for cranio-facial fracture fixation. It was also found that the absorbable plate and rivet/pin device was biocompatible and elicited minimal inflammatory response. Good bone healing was observed across the defect site. Additional biocompatibility studies demonstrated that the polymer is non-cytotoxic, non-mutagenic, and non-sensitizing.

Introduction

Internal fixation with metal plates and screws is widely used in cranio-maxillofacial surgery. Advantages compared to wiring include: the ability to more closely approximate normal skeletal morphology; prevention of bone graft collapse; fewer drill holes; decreased bone graft mobility; and elimination of sharp wire syndrome. Although fixation using metal plate and screw systems is a reliable method to achieve osteosynthesis, it has several potential post-operative complications. Depending on the location and types of replacement it may be necessary to remove bone plates and screws after bone healing because of the restriction of cranial growth and transcranial migration. Long-term corrosion may cause inflammatory reactions. Palpability, especially at regions with minimal soft tissue coverage, hardware loosening, temperature sensitization when placed under a thin skin cover, and sinus infections from protruding screws are other complications that have been reported (1-3).

Metal implants also interfere with radiological studies and postoperative radiation therapy. The use of metal miniplate and microplate fixation has also been shown to result in restricted skeletal growth when placed across suture lines (1,2,4).

Bioabsorbable rigid fixation devices can eliminate a majority of the problems because bioabsorbable materials can provide sufficient fixation during the bone healing process and then are gradually resorbed by the body. Thus, bioabsorbable polymers are excellent candidates for replacing metal plating systems in cranio-maxillofacial trauma procedures. LactoSorb™ plates and screws made from poly(lactide-co-glycolide)s were developed for craniofacial fixation and were found to be a satisfactory system in many preclinical and clinical cases (5-7). The polymer plates provided osteotomy line healing comparable to that of the metal plating system. Eppley and Sadove (3) also investigated the use of resorbable bone fixation devices in immature rabbits and human infants. In both studies, a resorbable plate and metal microscrews were used. Plating across a coronal suture in the immature rabbit model resulted in complete device resorption and increased screw distance after 8 months post-operatively. In the clinical study, twenty infants with calvarial deformities were implanted with thin, straight resorbable plates and metal microscrews. A total of

231 fixation devices were implanted without complications after 12 months post-operatively.

Resorbable fixation plating systems are especially attractive for pediatric patients, because they permit cranial plate growth while the plate is degrading. Polymer type and device size must be carefully tailored to the dynamics of the skeletal sites (4,5,8). In all of these cases, it was demonstrated that the use of absorbable plating devices in cranial-facial trauma procedures is effective in maintaining good stability across the bony defect site until healing occurs, while eliminating many of the concerns of metal plating.

Ahn et al. (6) demonstrated the effectiveness of a biodegradable plate and an adhesive osteosynthesis technique in a Yorkshire pig model with a frontal sinus fracture. The stability and bone healing characteristics of this rigid fixation method were studied and compared with a standard method using metal plates and screws. The animals were sacrificed at 8 weeks. There were no significant differences between the two methods.

Although absorbable plates have been relatively successful for these applications, there are limitations. Deforming the polymer plates prematurely can cause damage and weaken plates, and absorbable screws often require tapping of the bone resulting in over-tapping of drilled holes for screw insertion (9). Another concern is the application of excessive torsional forces that result in the failure between the head of the screw and the shaft.

To design a successful bioabsorbable craniofacial fixation-plating device to replace metallic systems, several factors such as mechanical functionality, biocompatibility, and biodegradation should be reviewed and appropriate material and design considerations changed or modified to the absorbable system to enhance its applicability in such procedures.

This article describes the material characteristics and design modifications that have led to an innovative bioabsorbable craniofacial bone fixation plate/rivet-pin system (10-12). The system imparts better ease-of-use through a unique visual cue plating device and a novel fastener system that yields more than sufficient strength retention required for cranial-facial fixation. Polymer composition, plate/rivet-pin system design, and mechanical evaluation of the plating and rivet/pin device are detailed. Additionally, the novel, easy to deliver fastener system yields more than sufficient *in-vitro* strength retention. This article also describes both *in-vitro* and *in-vivo* studies designed to evaluate the safety and effectiveness of our biodegradable plating system.

Experimental

Polymer Composition

The plating and rivet/pin devices are composed of several polymers. The rivet/pin is formed from a poly(L-lactide) (referred to as PLA) obtained from

Purac Biochem. The plating systems are formed from a polymer blend comprising a 50:50 mole:mole poly(D,L-lactide) (referred to as D,L-PLA) and a 95:5 mole:mole poly(ϵ -caprolactone-co-p-dioxanone) (referred to as 95:5 PCL:PDO). The D,L-PLA was also obtained from Purac Biochem.

The PCL:PDO copolymer was prepared in-house by a method consisting of reacting the ϵ -caprolactone and p-dioxanone lactone monomers via a ring opening polymerization at temperatures of 100°C to 230°C for 2 to 24 hours under an inert nitrogen atmosphere until the desired molecular weight and viscosity were achieved.

The polymer blends were prepared by individually charging the D,L-PLA and PCL:PDO polyesters into a conventional mixing vessel such as a Brabender or extruder. The homopolymers and copolymers are mixed at a temperature of 100°C to 230°C for 5 to 90 minutes until a uniformly dispersed polymer blend is obtained.

Analytical Testing

The blends, polymers and monomers were characterized for chemical composition and purity (NMR), thermal analysis (DSC), molecular weight (inherent viscosity), and baseline and *in-vitro* mechanical properties (Instron stress/strain).

Proton Nuclear Magnetic Resonance (NMR) was performed on a 400 MHz Varian Unity Plus NMR using deuterated chloroform (CDCl_3) as a solvent and tetramethylene silane (TMS) as a reference. Samples were prepared by dissolving 250 mg of polymer in 20 ml of CDCl_3 . Aliquots of 0.7 ml of the solution were used in each measurement.

An accelerated hydrolysis study was also performed using NMR to identify the hydrolysis products of the plate and rivet/pin. Approximately 5 mg of a plate or rivet/pin sample was placed into a NMR tube containing 0.7 ml of deuterated buffer (pH 7.3). The samples were placed in an oven at 90°C until complete hydrolysis occurred.

Inherent viscosities (I.V., dL/g) of the blends and polymers were measured using a 50 bore Cannon-Ubbelohde dilution viscometer immersed in a thermostatically controlled water bath at 25°C utilizing chloroform as the solvent at a concentration of 0.1 g/dL. Typical inherent viscosities ranged from 1.4 to 2.2 dL/g.

Thermal analysis of polymers and blends was performed on a TA Instruments 2910 Modulated Differential Scanning Calorimeter (DSC). Modulated DSC analysis was used to characterize the morphological properties of the D,L-PLA and PCL:PDO blends. During the DSC scan, the sample was heated to 70°C at 1°C/min linear ramp while the modulation was at an amplitude of +/- 1°C every 30 seconds.

The sample was then cooled to 37°C and held at isotherm for 60 minutes. The materials were then reheated to see how much crystallinity was restored. The glass transition temperature, melt temperature, crystallinity levels, and crystallization of the D,L-PLA/PCL:PDO blends were measured.

Scanning electron microscopy (SEM) was also used to study the crystalline domains in the blends. The materials were fractured by immersion in liquid nitrogen for a few seconds until well below T_g , and then broken by hand. The fracture surfaces were mounted perpendicular to the beam.

A thermal shaping and recovery study of the D,L-PLA/PCL:PDO blends was conducted by immersing the coupons in 60°C saline for 1 minute and then shaping the coupons to a predetermined curvature. The thermo-shaped coupons were then placed in 37°C saline and the curvature recovery was recorded for up to 30 hours.

Baseline and *in-vitro* mechanical properties of the devices were performed on an Instron model 4201. *In-vitro* studies were determined in a buffered deionized water solution (pH=7.4) at a temperature of 37°C for periods of 1, 3, 6, 9 and 12 weeks. Ten samples were placed in 500 ml of buffered solution. The buffered solution was replaced on a weekly basis. Flexural properties of compression molded test coupons of the blends were also measured by ASTM standard D790M. Ethylene oxide sterilization of devices used in these studies was conducted at Ethox, Inc.

Finite Element Analysis

A finite element model of the rivet and pin system was developed to analyze rivet deployment and optimize the design of the system. The model includes the rivet body and pin and a cylindrical portion of bone. A finite sliding contact analysis with friction (Abaqus Version 5.8) was conducted in two steps: placement of the rivet body into a hole in bone; and insertion of the pin into the rivet body. The material properties were as follows: Bone $E=2$ GPa, Poisson's ratio=0.3; and polymer $E=2.5$ GPa, Poisson's ratio=0.45. The friction coefficient on all surfaces was 0.1.

In-vitro Push-out test

A custom designed push-out test was performed to simulate the fixation of a burr hole defect using a burr hole cover plate and 6 rivet/pins. A polyurethane sawbone product (#40) obtained from Pacific Research Labs, Inc. Vashon, WA was used to simulate calvarial bone.

The sawbone was cut into 35 x 35 x 6 mm pieces. An 8 mm center hole was machined into the sawbone plate to simulate a trephine burr hole defect, and 0.078" pilot holes were drilled at specific intervals to match the holes in the circular burr hole cover plate that was used for the tests. A burr hole cover plate

was then fixed to the sawbone plate by six rivet/pins. The sawbone/plate assembly was then mounted to a testing fixture with the plate face down and the entire assembly of sawbone/plate and testing fixture jig was attached to an Instron tester with a 444.8N compression load cell. The testing jig was aligned in the Instron with a 30 mm metallic probe and placed directly above the center point of the trephine defect site. The probe was then moved downward toward the center point at a rate of 1 mm/min and the plate and rivet/pin were tested to failure. The force versus displacement curve and failure mode was recorded. The test was terminated after the displacement reached 5 mm.

In-vitro push-out tests were also performed in the same fashion. The sawbone/plate and rivet/pin assemblies (5 samples in one 500 ml bottle) were immersed in 37°C phosphate buffered saline solution and then tested at 1, 3, 6, 9, and 12 weeks. The phosphate buffered saline solution was replenished every week. Ethylene oxide sterilization of devices used in these studies was conducted at Ethox, Inc.

Biocompatibility Studies

The cytotoxic, mutagenic, and sensitizing potential of the cranial plate was evaluated in a series of *in-vitro* and *in-vivo* studies. The poly(L-lactide) rivet/pins were not evaluated for biocompatibility because PLA containing devices have been shown to be biocompatible when implanted in animals and because of the long clinical history of safe use of various of PLA devices including bone screws and suture anchors.

In-Vitro Cytotoxicity

The cytotoxic potential of the cranial plate was evaluated in cultures of L929 mouse fibroblast cells following standardized procedures for the agar overlay assay (15). A subconfluent monolayer of L929 cells was prepared in Dulbecco's modified Eagle's Medium (DMEM) with 10% fetal bovine serum. One percent BBL agar in complete medium supplemented with 5% fetal bovine serum was overlaid on the monolayer and samples (cut to approximately 1 cm) of the cranial plate and positive (latex gloves) and negative (dosing rings) control articles were placed on the agar (in triplicate). After 18-24 hours, the cranial plates and control samples were removed, the monolayers were stained with 0.01% neutral red solution in saline, and the samples were evaluated microscopically for cytotoxicity following USP Guidelines (15). The cytotoxicity of saline extracts of the cranial plate was also evaluated in cultures of L929 cells. Saline extracts of the cranial plate, latex gloves, and dosing rings were prepared by extracting the materials at a test material/saline ratio of 6 cm²/mL for 24 hours at 37°C. Five hundred microliters of the appropriate extracts and controls were added to subconfluent cultures of L929 cells in 1.5 ml

of fresh DMEM (in triplicate). After a 48-hour incubation period, the test and control extracts were removed and the monolayers were stained with 0.01 % neutral red solution in saline and evaluated microscopically for cytotoxicity following USP Guidelines.

In-Vitro Mutagenicity Assay

The mutagenic potential of saline and ethanol extracts of the cranial plates was evaluated by measuring the ability of the extracts to induce reverse mutations at select loci of 4 strains of *Salmonella typhimurium* and at the tryptophan locus of *Escherichia coli* WP2 *uvrA* in the presence and absence of S-9 activation. Saline and ethanol extracts of the cranial plates were prepared by extracting the plates at a surface area to volume ratio of 3 cm³/mL of extraction medium for 72 hours at 37°C (without agitation). After extraction, the extracts were allowed to cool to ambient room temperature, decanted and aseptically transferred to serum vials, and used within 24 hours. A minimum of five dose levels of each extract (1 to 100 µL per plate, in triplicate) along with the appropriate vehicle and positive controls were plated with tester strains TA98, TA100, TA1535, TAI 537, and WP2 *uvrA* in the presence and absence of rat liver S-9 activation following standard procedures for the plate incorporation assay (16-18). After 48-72 hours incubation, the bacterial background lawn was evaluated for evidence of toxicity and the number of revertant colonies counted with an automated colony counter or manually if necessary due to test article precipitate.

Guinea Pig Sensitization

The potential of saline and cottonseed oil extracts of the cranial plates to cause delayed contact hypersensitivity was evaluated in guinea pigs following minor modifications of standard procedures (19,20). The experimental design complied with the International Organization for Standardization (ISO) Guideline 10993-12, 1996. Saline and cottonseed oil extracts of the cranial plates were prepared by extracting the plates at a surface area to volume ratio of 3 cm³/mL of extraction medium for 72 hours at 37°C (without agitation). After extraction, the supernatants (extracts) were allowed to cool to ambient room temperature, aseptically decanted and transferred to serum vials, and used within 24 hours. The cranial plate extracts and extract blanks were prepared fresh for each induction and challenge phase. Forty Hartley-derived, male albino guinea pigs were assigned randomly to one of 5 groups (5/group in Groups 1 and 3, 10/group in Groups 2, 4, and 5). Group 1 received the saline vehicle, Group 2 received the saline extract of the cranial plate, Group 3 received the cottonseed oil vehicle, Group 4 received the cottonseed oil extract of the cranial plate, and Group 5 received the DNCB positive control solution. The Phase I induction

doses were administered as intradermal injections to the shaved inter-scapular region on Day 1 of the study (along with injections of Freund's Complete Adjuvant (FCA) and appropriate cranial plate extract or extract blank mixed with FCA). The Phase II induction doses were administered on Day 8 and consisted of topical applications of the neat saline and cottonseed oil extracts, blanks, or the positive control (dinitrochlorobenzene [DNCB]) to the skin of the shaved back of each animal. On study Day 22, the appropriate challenge dose was applied topically to the shaved flank of each animal for a period of 24 hours. The challenge sites were scored for sensitization expressed as erythema and/or edema approximately 24, 48, 72, and 96 hours after removal of the challenge dose.

Preclinical Studies: Rabbit Trephine Defect Model

An 8-mm circular trephine defect, centered on the sagittal suture line, was made in the calvarium of 42 skeletally mature male New Zealand white rabbits. A cranial fixation burr hole cover plate was attached over the defect site. The absorbable plating and rivet/pin devices were composed of the polymers described above. The metal burr hole cover plate and screws are made of titanium (Bioplate™).

The rabbits were partitioned into two groups, one having standard metallic plates and screws and the other having the absorbable polymeric plate and rivet/pin fasteners. Half of the animals in each group had the bone cap replaced (CR), which was initially removed when the defect was created, reattached by securing it to the plate before the device was fixed in place. In the remaining group of animals, the defect was created and covered with the absorbable or metallic plate (no bone cap, NC). An equal number of animals in each group were sacrificed at one, three, and six months. A limited number of animals with the absorbable system alone were also sacrificed at 18, 22, and 27 months. The details of the surgical procedure are described below.

A surgical plane of anesthesia was obtained in each rabbit by intramuscular injections of ketamine hydrochloride (55-mg/kg), acepromazine maleate (1.0 mg/kg), and xylazine (5 mg/kg), and maintained with supplemental doses of either xylazine or ketamine, both at one quarter the initial level. A local anesthetic, 0.5% bupivacaine hydrochloride, was administered directly to the surgical site at a dose of 0.25 ml/site. Analgesia was achieved with buprenorphine hydrochloride (0.02 mg/kg), with an initial dose being administered two to three hours prior to the initiation of the procedure and a second dose delivered post-operatively, after the rabbits regained sterna recumbency. Antibiosis was assured by a preoperative intramuscular injection of penicillin G (60,000 IU/kg). Ophthalmic ointment was placed gently onto the conjunctiva of each eye and the surgical site was prepared for aseptic surgery.

A 3 cm long mid-sagittal incision was made through the skin and galea. The periosteum was elevated and an 8-mm diameter trephine craniotomy was made immediately proximal to the coronal suture in the parietal bone, without dural involvement. The circular cranial plates were secured to the skull and the soft tissues were closed with 4-0 Vicryl™ suture using simple interrupted stitches. The skin wound was closed in a standard manner with staples.

Animal experimentation was conducted at an AAALAC approved and USDA regulated facility, in accordance with care and use guidelines promulgated by the Animal Welfare Act (PL 99-198: 1985) and the PHS Public Health Policy on Humane Care and Use of Laboratory Animals.

At sacrifice, the surgical site was examined grossly and the portion of the calvarium containing the implant site was excised *en bloc*. Bone tissue samples were fixed in 10% neutral buffered formalin. All specimens were radiographed in a standard manner and assessed for qualitative gray level densities indicative of healing. They were then dehydrated in increasing concentrations of ethanol to 100%, followed by infiltration and embedding in poly(methylmethacrylate) (PMMA). Once the PMMA polymerized, thin sections were prepared from both the sagittal and transverse planes, allowing for the viewing of bone formation in two perpendicular planes. For illustrative micrographs, sections containing the absorbable implant were stained with Goldner's Trichrome and with Stevenel's blue for metal implants.

For all animals sacrificed at 18 months and later, following fixation, the tissues were decalcified. The decalcified tissues were trimmed in a variety of transverse planes in order to maximize sectioning of the plate and rivets. Trimmed tissues were processed for standard paraffin embedding, sectioned at 5 μ and stained with hematoxylin and eosin. Following identification of a birefringent, apparently crystalline material within macrophages at the site of the absorbing plate material, additional tissue sections were trimmed, deparaffinized and stained with H&E or left unstained. These additional sections were sent to Surface Science Laboratories, Mountain View, CA for microRaman spectroscopy on the birefringent material. The purpose of the spectroscopy was to attempt to identify the chemical nature of this material. Polymer samples of D,L-poly(lactide), poly(ϵ -caprolactone-co-p-dioxanone) and a polymer blend of these two polymers (91/9 wt/wt blend) were also submitted as controls.

Results

Plate Composition Effects on Visual Cue, Mechanical Function and Absorption

It is desirable that polymer compositions when molded into medical devices have improved functionality. The ideal bioabsorbable polymer for bone fixation should have sufficient initial stiffness and strength to fix the fracture and then

degrade gradually while the bone heals. Additionally, such plates should be heat deformable to allow the surgeon to manipulate the device during surgery to match the contours of bony structures on the cranium or face. However, one drawback of previously described devices is their lack of a visual cue to aid the surgeon in knowing the precise time that they can begin deforming the device. This is critical to a plating system, because premature bending or otherwise manipulating it before it has relaxed (i.e., heated above its T_g or T_m) can cause stresses to form in the part and thereby weaken the device.

To prevent premature bending, blends that comprised a dispersed phase of a low melting PCL:PDO copolymer in an amorphous D,L-PLA were prepared (11,12). By having a dispersed phase composed of a low melting, semi-crystalline copolymer such as PCL:PDO, it was believed that the blend would contain scattering centers that upon heating would become transparent. This would provide the surgeon a visual cue of when to bend and shape the medical device. This is critical to making the device easier and simpler to use in applications that require shaping the plate over a variety of bony contours such as in cranial-facial procedures. Table 1 shows a series of polymer blends of D,L-PLA and PCL:PDO and their corresponding weight ratios and other characteristics. Figure 1 depicts photomicrographs of the blend in a burr hole cover plate configuration at a weight ratio of 91/9 D,L-PLA/PCL:PDO that displays the visual cue concept.

The addition of the second phase polymer, PCL:PDO, also affects the mechanical properties of the D,L-PLA by two competing mechanisms. PCL:PDO has a much lower T_g (-60°C). This can result in lower stiffness and strength when compared to D,L-PLA. Therefore, by preparing blends of D,L-PLA and PCL:PDO, a lower modulus and strength could be rendered. However, PCL:PDO can also crystallize. The 5wt% PCL:PDO blend, for example, has a heat of fusion (H_f) of 6.501 J/g and the 9wt% PCL:PDO blend, H_f was 11.52 J/g. This results in a material that forms stiffer semi-crystalline domains that can yield higher stiffness and strength (Table 2). Therefore, although the addition of a higher proportion of lower modulus PCL:PDO in the blend should result in a lower strength and stiffness, the 9wt% blend has higher strength and stiffness due to its higher crystallinity. This indicates that the 9wt% blend is close to an optimum composition with respect to these critical characteristics. Evidence of the existence of a second dispersed phase of PCL:PDO is shown in an SEM micrograph that depicts the PCL:PDO phase as distinct small domains (Fig. 2).

Moreover, the addition of PCL:PDO and its subsequent low levels of crystallinity affect the plate's thermal shaping and creep recovery character. One would like to have plates that when shaped resist creeping back to their original shape. Thus, flex coupons were shaped by immersing in 60°C water for one minute over a 2 inch diameter mandrel. One end of each of the flex coupons was then attached to the mandrel with a metallic screw and creep recovery changes were recorded. Results are shown in Table 1.

Table 1. D,L-PLA/PCL-PDO Blends Creep Recovery

Recovery Time (h) and Shape Changes

D,L-PLA/PCL-PDO	4 h	8h	24h	30h
100/0	Minimal	Small	Significant	Original Shape
98/2	Minimal	Small	Significant	Original Shape
95/5	Minimal	Small	Significant	Original Shape
91/9	Minimal	Small	Small	Half curvature
80/20	Minimal	Small	Significant	Slightly curved

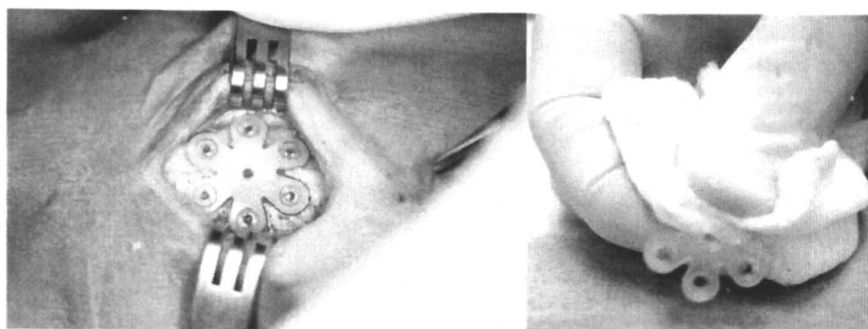


Figure 1. Photomicrographs showing the visual cue of the 91/9 wt/wt D,L-PLA/PCL-PDO blend burr hole cover plate after (right) heating above the melting transition of the PCL-PDO copolymer and after the plate has cooled to body temperature and been implanted in a rabbit cranium (left)

Table 2. Flexural Modulus and Yield Strength of D,L-PLA/PCL-PDO blends

D,L-PLA/PCL-PDO	Flexural Modulus (GPa)	Yield Strength (MPa)
100/0	3.5	81
98/2	3.1	70
95/5	2.7	61
91/9	3.0	72
80/20	2.3	60

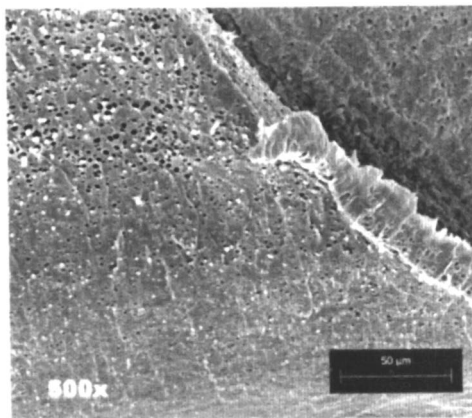


Figure 2. SEM depicting the PCL-PDO copolymer as distinct small domains dispersed in the D,L-PLA polymer

As expected, the blends with little or no PCL:PDO showed little resistance to creep recovery, while the higher 9wt% blend showed good resistance. Unexpectedly, however, despite its semi-crystallinity the 20wt% blend did not show good resistance to creep. It is believed that although this 20wt% blend was semi-crystalline, the higher proportion of lower modulus PCL:PDO has a greater effect, and thus, the blend had less resistance to creep. Therefore, based on these experiments and the other information, the blend composition of 91wt% of D,L-PLA and 9wt% PCL:PDO was chosen as the candidate material for the cranial plating system.

Safety of the product was also a concern. To demonstrate that this blend hydrolyzed to the same by-products present in other absorbable medical implants, an accelerated hydrolysis study was performed to identify the by-products of the plate and rivet/pin. Approximately 5 mg of a plate or rivet/pin sample was placed into a NMR tube containing 0.7 ml of deuterated buffer (pH 7.4). The samples were placed in an oven at 90°C until complete hydrolysis occurred. The NMR spectrum for each sample was examined and the hydrolysis products were identified. The results for the breakdown products for each of the materials studied are shown in Table 3.

The resulting hydrolysis products observed by proton NMR were as expected, showing that the plate and rivet/pin hydrolyze to the same nontoxic by-products as FDA approved and marketed Panacryl™ and Monocryl™ sutures, and the Orthosorb Pin™. Note that the presence of 6-hydroxycaproic acid in the NMR spectrum in the Panacryl suture hydrolysis was a result of breakdown products of the suture's coating (a poly(ϵ -caprolactone-co-glycolide)).

Plate and Rivet/Pin Design Optimization through Mechanical Evaluation

Due to the inherent material differences, polymer plates generally have lower stiffness and strength compared to the same size metal plate. Polymer screws are not hard enough for self-tapping. Hence, tapping the threads must be performed before screws can fix the plate. Tapping is also a tedious process that few surgeons wish to undertake. Taking these factors into consideration, a bioabsorbable rivet and pin fastener system was developed to eliminate the tapping procedure.

Figure 3 displays the rivet/pin and plate devices. The rivet is composed of a head at a one end and three legs extending distally from the head. In practice, the pin is inserted into the rivet where upon it contacts the internal surface of the legs of the rivet, forcing the legs of the rivet outwardly and creating an interference fit in a predrilled hole in the bone. If several rivet/pins are applied through holes in a device such as a plate and through predrilled holes in the bone, it will fix the plate to the site and hold the fracture in place (Fig. 4).

To demonstrate the rivet fixation feasibility, a series of mechanical tests were performed to demonstrate that the plate and rivet/pin device would provide

Table 3. Hydrolysis By-Products of a series of Absorbable Polyester Medical Devices

Device	Hydrolysis By-Products
Panacryl™ Suture	glycolic acid, lactic acid, 6-hydroxycaproic acid
Monocryl™ Suture	glycolic acid, 6-hydroxycaproic acid
Orthosorb™ Pin	2-hydroxyethoxy acetic acid
Craniosorb™ Plate	lactic acid, 6-hydroxycaproic acid, 2-hydroxyethoxy acetic acid
Craniosorb™ Rivet/Pin	lactic acid

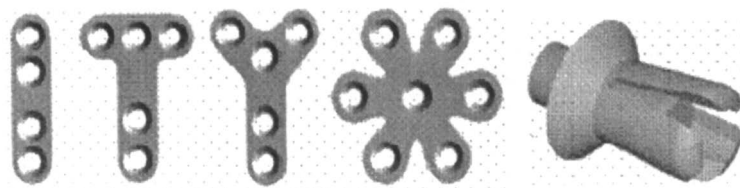


Figure 3. Various Plate Devices (Straight, "T", "Y", Burr Hole Cover) and the Rivet/Pin

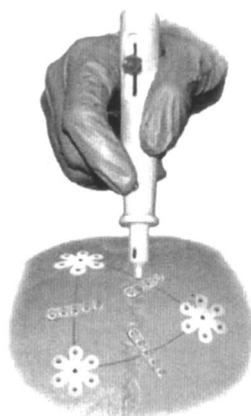


Figure 4. A Rivet/Pin being applied through a plate and predrilled holes in the cranium to fix the plate to the site and hold the incision in place

sufficient strength both initially and over time *in-vitro*. The first of these tests was a pullout experiment to verify that the rivet/pin device could adequately fix a plate to bone. The pull-out test is performed using a U-shaped test fixture mounted in an Instron mechanical testing device. Bone was simulated using a polyurethane sawbone product (#40) obtained from Pacific Research Labs, Inc. with the appropriate stiffness and elasticity (human bone was also simulated using rabbit, canine, or porcine cranial bone). The sawbone was cut into 60 mm long, 12 mm wide and 12 mm thick slabs. Holes of various diameters were then drilled into the sawbone. The U-shaped fixture (which simulates the absorbable plate thickness of 1 mm) was then placed over the hole and the rivet/pin was driven into the hole. The assembly was then placed in the Instron with a 200 lb. load cell, aligned and a tensile test was performed at a rate of 1 mm/min until the rivet/pin failed. Failure mode and pull-out force were recorded. Results are an average of 3 specimens. The pull-out strength was calculated as the pull-out force divided by the contact area between pilot hole and fastener. The results of the pullout tests are shown in Table 4.

Pull-out strengths were determined for three systems using sawbone and calvarial bone. For each type of fastener, the pull-out strengths were very similar when tested with sawbone or cranial bone. Among the three fasteners systems, the Bioplate metal systems had the highest pull-out strength, followed by the single-piece PLA rivet/pin system and the Biomet Lactosorb™ screw. Although the Biomet Lactosorb™ screws and the PLA rivet/pin fasteners have much lower pull-out strengths than that of the metal screws, they can still achieve stability of the fracture fixation for low load-bearing cranial-maxillofacial applications (13).

Failure modes for each fastener system were also different. The major failure mode for Bioplate metal screws tested with both sawbone and canine cranial bones was screw pull-out. Occasionally, the sawbone was broken before the screw pulled out. The Biomet Lactosorb™ PLA/PGA screws, however, failed just below the screw head when tested with sawbone, but pulled out of cranial bone with little or no damage to the threads or screw head. The failure mode for the rivet/pins was pull-out from both the sawbone and cranial bone.

Besides the pull-out test to measure the function of the rivet/pin fastener, a push-out test was designed to test the plate and rivet/pin system fixation to cranial bone. As before, sawbone #40 from Pacific Research was used as the cranial bone simulation material. Sawbone was cut into 35 x 35 x 6 mm thick pieces. An 8 mm center hole was machined into the sawbone plate to simulate a trephine burr hole defect, and various sized pilot holes (for rivet/pin insertion) were drilled at specific intervals to match up with holes in a circular burr hole cover plate that was used for the tests. A burr hole cover plate was then fixed to the sawbone plate by six rivet/pins (Fig. 5). The sawbone/plate assembly was then mounted to a testing fixture with the plate face down and the entire assembly of sawbone/plate and testing fixture jig attached to an Instron tester with a 200 lb. load cell. The testing jig was aligned in the Instron with a 30 mm

Table 4. Pull-out strength of fasteners tested with sawbone, or canine and rabbit cranial (calvarial) bone

Device	Pull-out Strength (lb/in ²)
Bioplate™ metal screw in sawbone	80
Bioplate™ metal screw in canine calvarial bone	72
Biomet screw in sawbone	28
Biomet screw in rabbit cranial bone	20
Two-piece PLA Rivet/Pin in sawbone	28
Two-piece PLA Rivet/Pin in rabbit cranial bone	23
Single-piece PLA Rivet/Pin in sawbone	35

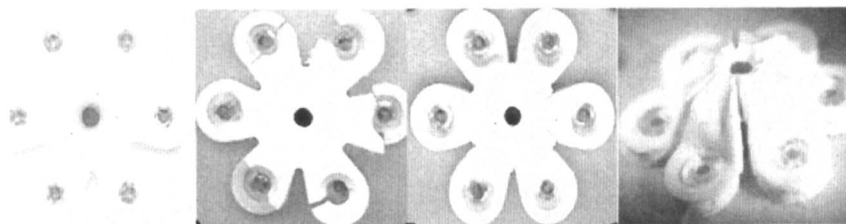


Figure 5. A burr hole cover plate fixed to sawbone plate by 6 rivet/pins (far left); burr hole cover plate tested after 3 weeks in vitro (left; note plate breakage and rivet pull out failures); burr hole cover plate tested after 12 weeks in vitro (right and far right; note plate deformation but no breakage)

metallic probe and then placed directly above the center point of the trephine defect site. The probe was then moved downward towards the center point at a rate of 1 mm/min and the plate and rivet/pin were tested to failure. The failure mode was recorded. The test was terminated after the displacement reached 5 mm. Results are an average of 10 specimens.

In-vitro push-out tests were also performed in the same fashion on both sterile and non-sterile devices (Table 5). The sawbone/plate and rivet/pin assemblies were immersed in 37°C phosphate buffered deionized water solution and then tested at 1, 3, 6, 9, and 12 weeks. The PBS solution was replenished every two weeks.

During the push-out test, a central downward force loads the plate and rivet/pin system. The plate experiences complex loading conditions including both tensile and bending. The rivet/pin experiences a pull-out force and a transverse shear force. The failure modes were varied with *in-vitro* exposure. For the zero-day, non-sterilized plating system, it was observed that the plate had permanent bending deformation in the central region, the fingers of the burr hole cover plate cracked or broke close to the rivet hole, and some rivet/pins pulled out of the sawbone (Fig. 5). Similar failure modes occurred at 1 and 3 weeks. At 6, 9 and 12 weeks, the failure modes changed. There was permanent bending deformation in the central part of the plate and breakage of the fingers of the plate, but no rivet/pins were pushed out (Fig. 5). The deformation of the plate was also more dramatic in comparison to the coupons with less *in-vitro* exposure.

Sterilized devices had similar failure modes as the non-sterilized plate and rivet/pins. Differences, however, did exist. For the zero day and 1 week tests, in addition to bending of the plate, breakage of the fingers, and push out of the rivet/pins, breakage of the rivet head and legs also occurred. At 3 weeks and longer, the major failure modes were surface cracks, and cracks and breakage of the fingers of the burr hole cover plate. The permanent bending deformation of the plate was less compared to the non-sterilized plating systems.

Push-out tests also showed decreasing maximum loads for both non-sterilized and sterilized plating systems with the increased *in-vitro* exposure. It was also observed that the maximum load for the sterilized plating system was lower than the non-sterilized plating system at each *in-vitro* exposure. However, the differences diminished at 6 week and longer *in-vitro* exposures. It is theorized that the reasons for the changing failure modes, especially the permanent bending deformation of the plate and the lower maximum loads for the sterilized plating system, are likely due to the changes of the materials properties caused by sterilization.

Finite Element Analysis

The peak insertion load obtained from the analysis was found to be 117 N (26 lb), which compared well with experimental tests. This indicates that the

Table 5. Push-out strength of Plate and Rivet/Pin

Time (weeks)	Peak Load (N)	
	Non-sterile devices	Sterile devices
0	260	220
1	160	98
3	125	65
6	51	49
9	51	45
12	--	40

estimated friction properties are appropriate since they produce analytical results that agree with the experimental data.

The stress results are shown in Figure 6. The plot on the left in Figure 6 shows contours of minimum principal stress, which reflect compressive stresses associated with the interference fit in the radial direction. The peak compressive stresses are found in the lower portion of the device (rivet legs and pin) where the interference fit with the hole is greatest. The stress values in the lower portion of the device are at or slightly above the compressive yield point of the material (approximately 110 MPa). The plot on the right in Figure 6 shows contours of maximum principal stress in the rivet body, which reflect tensile stresses along the axis of the device due to friction between the pin and rivet body. Notice that the rivet leg is in tension along its length because of friction with the pin that is being driven downward. The peak tensile stresses occur at the rivet leg/head junction, where the cross-sectional area is lowest. The stress values are at the tensile yield point of the material (approximately 70 MPa) for only a small portion of the minimum cross-section so that minimal yielding will occur for the given conditions.

Biocompatibility Studies

No evidence of cytotoxicity was observed in the L929 cells exposed to the cut sections of the cranial plates or the saline extracts of the cranial plates. Similarly, there was no evidence of cytotoxicity in the L929 cultures exposed to the negative (saline) or media controls or the saline extracts of the negative controls. In contrast, the positive controls (cut sections of latex gloves and saline extracts of the latex gloves) showed moderate to severe cytotoxicity. No evidence of cytotoxicity or significant increase in mutation frequency (mean revertants/plate) was observed in *Salmonella rypimurium* tester strains TA 98, TA 100, TA 1535, and TA 1537 or *Escherichia coli* strain WP2 *uvrA* exposed to the saline or ethanol extracts of the cranial plates in the presence or absence of S-9 activation. In contrast, the positive controls for each bacterial tester strain produced an increase in revertant mutants within the expected historical range in

the presence and absence of S-9 activation, demonstrating the validity of the assay. In the guinea pig sensitization assay, no erythema or edema (all scores of 0) was observed at any of the challenge dose sites exposed to the saline or cottonseed oil extracts of the cranial plates at any of the scoring periods (24-96 hours post-dose) in any of the Group 2 or 4 animals. Similarly, no erythema or edema was observed in any of the Group 1 or 3 animals exposed to the appropriate saline or cottonseed oil extract blanks. In contrast, the majority of the positive control animals (Group 5) exhibited slight to well-defined erythema at the time of removal of the DNCB challenge dose and 24 - 96 hours post-dose removal. The severity of the erythema remained the same in most DNCB-challenged animals through 72 hours post-dose removal and lessened between the 72 hour and 96 hour observation. The results of these studies demonstrate that the cranial plate, and extracts thereof, are non-cytotoxic, non-mutagenic, and non-sensitizing.

Preclinical Studies: Rabbit Trephine Defect Model

The polymeric plate and fasteners had acceptable tissue reactions at all periods. At 1 and 3 months, these reactions consisted of minimal numbers of macrophages and minimal to slight fibrous encapsulation which was equivalent to that seen at the metallic control sites. At 6 months, the plate portion of the polymeric device had undergone significant absorption and there was a slight to moderate macrophagic infiltration within the absorbing polymer mass. The percentage of apparently degraded but extracellular plate polymer was estimated to be approximately 25-40%. There was no evidence of absorption of the polymeric rivets out to 6 months. These features are highlighted in representative photomicrographs from the 1, 3, and 6 month periods (Fig. 7-9). All of the figures show bone in direct contact with the rivet and plate. At 6 months, remnants of the plate still exist but there is almost complete bridging of the defect, demonstrating that plate resorption was not inhibiting new bone formation in this calvarial defect model.

Histologically, healing of the calvarium, as evidenced by new bone formation at the trephine defect edges, could be seen in all test and control sections. In the CR specimens, the new bone could be seen in horizontal sections to almost totally bridge the gap between the trephined cut edge and the cap in all metal sites. At 1 and 3 months, there was slightly more variability in the degree of bridging in the polymer sites, although significant bridging was seen in most sites. By 6 months, the degree and nature of the bridging was similar in both test and control CR sites in that there was almost complete mature bone in the gap between the calvarial cap and the defect edge. In the NC cohort, the amount of new bone in the calvarial defect was significantly greater in both extent and "robustness" in the polymer group at 1 month, than in the 1 and 3-month metal and the 3-month polymer specimens. By 6 months, the linear

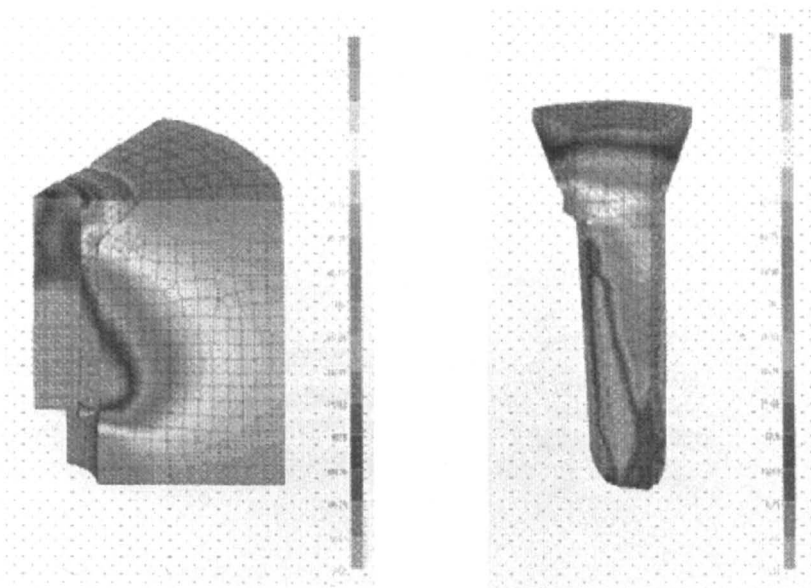


Figure 6. Stresses in the rivet/pin after pin insertion (minimum principal stresses on left and maximum principal stresses on the right)

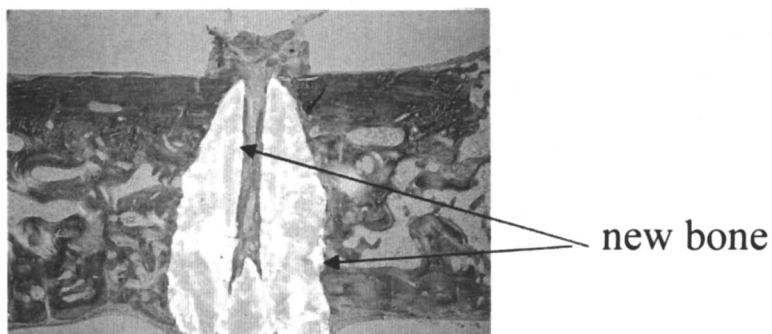


Figure 7. Photomicrograph at one month showing new bone growth apposed to rivet (note new bone between rivet legs)

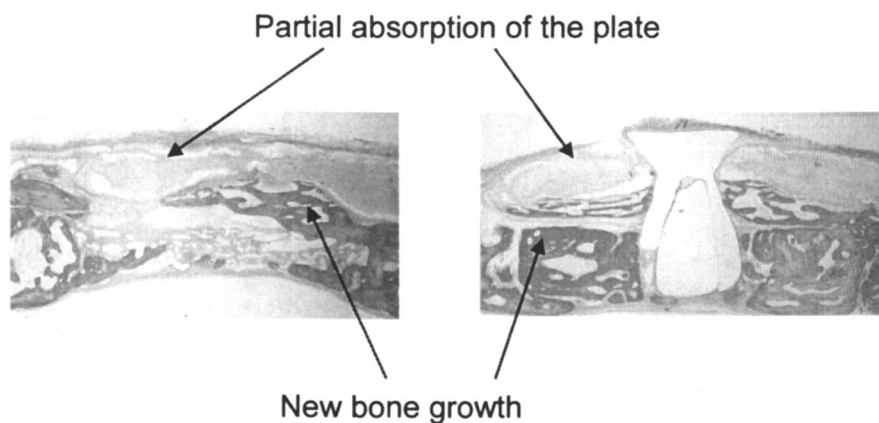


Figure 8. Photomicrographs at three months showing new bone growth apposed to rivet (right), partial absorption of the plate and bone growth across the defect site (left)

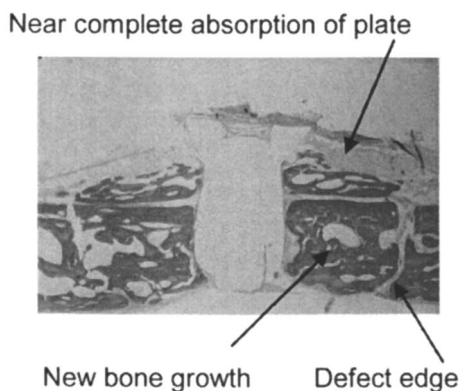


Figure 9. Photomicrograph at six months showing new bone growth apposed to rivet and nearly complete absorption of the plate

extent of the defect filling in both test and control sites was equivalent to or greater than that seen in the 1 month polymer sites. Although bridging new bone formation was significant at some sites, it was not complete at any of the test or control sites. With the exception of the 1 month polymer sites in which bone formation was in the dorsal-ventral extent of the defect, most of the new bone in the defect had formed at the ventral surface of the plates, slightly dorsal to (but often connected to) the periosteal new bone originating from the dorsum of the calvarium.

A low level of calvarial bone remodeling was more apparent at the metal screw versus the polymer rivet sites at 1 and 3 months. At 6 months, inadequacy of the fastener site specimens (both number and quality) made an evaluation of remodeling at some metallic sites impossible and rather limited at all other sites. At all periods, the bone surrounding the rivets appeared to be either totally unchanged, or had a minor degree of remodeling, including occasional minor foci of bone resorption. There were relatively long zones of apparent direct or close to direct contact of the polymer rivets with the bone. This is evident in figure 7. None of the bone remodeling changes at the sites of either test or control fasteners were considered to be abnormal.

In the limited set of longer-term animals, the plate component had undergone complete absorption by 27 months. At 18 and 22 months, there was still minor evidence of degraded polymer in the form of birefringent, apparently crystalline particles, ranging from $< 1 \mu$ (not resolvable with the microscope) to approximately $1 \times 5 \mu$, located intracellularly (macrophages) and extracellularly in the area of the absorbing plate. By Raman spectroscopy, these crystalline particles showed an association to the poly(ϵ -caprolactone-co-p-dioxanone) copolymer component of the plate polymer blend. Raman bands at 1033, 1065, 1109, 1286, 1305, 1442, 1468, 1729, 2874, and 2929 cm^{-1} are identical in both the crystallites and the polymer spectra indicating that the birefringent particles are in fact remnants of the polymer.

By 27 months, the rivets were showing slight absorptive changes, especially in the head region. Adjacent to the rivets there were minor calvarial bone changes, similar to those seen at earlier periods. Healing of the calvarium was complete in all except for the area of the central hole in the plate.

Discussion

The goal of the present work was to characterize a truly novel absorbable plate and rivet system. The plate was fabricated from a unique polymer formulation that allows the plate to be deformed at an elevated temperature that is tolerable to the surgeon and local tissues. If not quite correct, the plate can be reheated and deformed multiple times until the proper curvature is attained. If

not quite perfect, the final shaping can be accomplished by applying saline soaked surgical sponges over the plate and warming the plate in place. No deleterious effects were observed regarding local tissue damage at the temperatures and times used in this study.

The other advantage of this plate is that the heating of the plate can be accomplished by simply warming saline to 60°C and placing the plate in the saline. Because of the unique aspect of the polymer blend, as the plate is heated to the transition temperature of the polymer, the plate changes from an opaque white color to clear indicating that the plate can be deformed without damaging the plates physical structure. Upon cooling the plate becomes opaque again. The working malleable time for the plate is approximately 2 minutes. This "visual cue" is a significant advantage of this polymeric system.

The rivet and pin system is also a novel design as it provides a rapid fixation technique with no need for tapping of the drill holes. The fixation strength of the rivets was 35 pounds. This is comparable to absorbable screw fixation of similar dimensions. A user-friendly rivet applicator has also been developed (14). A secondary advantage of the rivet design is the lack of a sharp tip that is often found on metal screws. Thus, the placement of the rivet beyond the inner cranial surface poses less risk of a dural tear.

The *in-vitro* degradation studies demonstrated different failure modes as the plates hydrolyzed. There was permanent bending deformation in the central part of the plate and breakage of the fingers of the plate, but no rivet/pins were pushed out at time zero. The pushout tests showed decreasing maximum loads for the cranial plating system with the increased *in-vitro* exposure. As Eppley (7) has described, calvarial bone healing is essentially an unloaded fracture fixation application. Since calvarial bone heals in 6 to 8 weeks for pediatric patients and the plating system had measurable strength out to 12 weeks, it is safe to conclude that more than adequate strength was retained for fracture healing.

The hydrolysis study demonstrated that the products of the plate and rivet/pin include lactic acid, 6-hydroxycaproic acid, and 2-hydroxyethoxy acetic acid. These are non-toxic by-products that are results of polymer hydrolysis. They are the same hydrolysis products generated by other absorbable devices currently used clinically, such as FDA approved and marketed Panacryl™ and Monocryl™ sutures, and the Orthosorb Pin™.

The toxicity studies demonstrated no evidence of cytotoxicity, mutagenicity, or sensitization. The preclinical biocompatibility studies confirmed the biocompatibility of the polymers and designs in the calvarial model. There was no adverse response to either the plate or the rivet. An unexpected and interesting finding was the observation of crystalline particles in the area of the absorbing plate at 18 and 22 months. Micro-Raman spectroscopy was performed on this material and it was found to have an association to the poly(ϵ -caprolactone-co-p-dioxanone) copolymer component of the plate polymer blend.

The presence of this minor amount of residual material was probably responsible for the slight residual cellular infiltrations seen at these periods. The polymers in this study were carefully characterized regarding molecular weight, monomer content, and residual ethylene oxide levels both pre- and post-processing. Specifications were strictly enforced for this study and may account for the excellent tissue response observed.

Physal growth and expansion is a key aspect of an absorbable fixation device for children. Eppley and Sardine (4,8) found that the changes in shape of absorbable fixation plates after the initiation of degradation were more important than the complete degradation of the material. Further material biocompatibility within the physes is a key success parameter for absorbable materials.

Clinical trials of absorbable fixation methods showed that absorbable fixation methods can provide satisfactory fixation for craniofacial procedures (3,5,6,7). Eppley et al.(3) found that polymer fixation hardware was no longer palpable and there was radiographic evidence of facial fracture healing in 28% (7 out of 25) of the patients that received LactosorbTM implants 9-12 months after surgery. Because only 25-40% of the polymer plates blend was left in this study, a very similar clinical result would be expected at 9-12 months.

In summary, the data from this study including push-out strength retention and hydrolysis of the polymer systems demonstrates that the current absorbable plate and rivet/pin fixation system is biocompatible, has sufficient *in-vitro* strength retention, and is as effective as metal plates and screws for providing stable support for osteotomized bone fractures in cranio-facial fixation.

Conclusions

In the present study, we evaluated the mechanical, morphological and absorption characteristics of a series of plate and rivet/pin fixation devices for use in cranio-facial, and other low-load bearing bone fixation applications. The cranio-facial devices are composed of a bioabsorbable, aliphatic polyester blend comprising a 50:50 mole:mole poly(D,L-lactide) and a 95:5 mole:mole poly(ϵ -caprolactone-co-p-dioxanone). It was determined that compositions containing less than 10 weight percent of the PCL:PDO copolymer form an opaque, semi-crystalline blend that upon heating above the melting transition of the copolymer would soften and appear clear until cooled below the copolymer's melting point. This behavior has been utilized to form unique plating devices that upon heating to contour it to an anatomical site, yields a visual cue to the surgeon to impart ease-of-use. Additionally, a novel, easy to deliver fastener system composed of an interference fitting poly(L-lactide) rivet/pin is depicted. Together, physico-mechanical testing of the plate and rivet/pin system has been demonstrated to provide sufficient *in-vitro* strength retention. It was found that the absorbable

plate and rivet/pin device was biocompatible and elicited minimal inflammatory response. Good fracture healing and defect filling was observed across the defect sites.

References

1. Thaller, S.; Moore, C.; Tesluk, H.; Holmes, R., *Journal of Craniofacial Surgery*, 7(1), 54, 1996.
2. Polley, J.; Figueroa, A.; Hung, K.; Cohen, M.; Lakars, T., *Journal of Craniofacial Surgery*, 6(2), 132, 1995.
3. Eppley, B.; Prevel, C.; Sadove, A.; Sarver, D., *Journal of Cranio-Maxillofacial Trauma*, 2(1), 56, 1996.
4. Eppley, B.; Sadove, A., *Journal of Craniofacial Surgery*, 3(4), 190, 1992.
5. Eppley, B.; Sadove, A., *Journal of Craniofacial Surgery*, 6(6), 477, 1995.
6. Ahn, D.; Sims, C.; Randolph, M.; O'Connor, D.; Butler, P.; Amarante, M.; Yaremchuk, M., *Plastic and Reconstructive Surgery*, 99(6), 1508, 1997.
7. Eppley, B.; Sadove, A., *Plastic and Reconstructive Surgery*, 96(2), 316, 1995.
8. Eppley, B.; Sadove, A., *J. Craniofacial Surg.*, 5(2), 110, 1994.
9. Montag, M.; Morales, L.; Daane, S., *The Journal of Craniofacial Surgery*, 8(2), 100, 1997.
10. Cooper, K.; Yuan, J.; Overaker, D.; Hoppe, C.; Li, Y.; Lowenhaupt, B.; Monisera, A., *Transactions of The Society for Biomaterials*, 23(2), 903, 2000.
11. Cooper, K.; Arnold, S.; Scopelianos, A., *U.S. Pat.* 5641501, 1997.
12. Cooper, K.; Arnold, S.; Scopelianos, A., *U.S. Pat.* 5705181, 1998.
13. Sarver, D.; Eppley, B.; D'Alessio, K.; Pietrzak, W.; Sander, T., *U.S. Pat.* 5569250, 1996.
14. Yuan, J.; Zimmerman, M.; Poandl, T.; Trenka-Benthin, S.; Cooper, K., *Transactions of The Society for Biomaterials*, 23(1), 119, 2000.
15. Biological Reactive Test In Vitro, *U.S. Pharmacopeia* 23, *U.S. Pharmacopeial Convention*, 1697, 1995.
16. Ames, B.; McCann, J.; Yamasaki, E., *Mutation Research*, 31, 347, 1975.
17. Green, M.; Muriel, W., *Mutation Research*, 38, 3, 1976.
18. Maron, D.; Ames, B., *Mutation Research*, 113, 173, 1983.
19. Magnusson, B.; Kligman, A., *Journal of Investigative Dermatology*, 52, 268, 1969.
20. Kligman, A.; Basketter, D., *Contact Dermatitis*, 32, 129, 1995.

Chapter 22

Biopolymers for Biosensors: Polypeptide Nanotubes for Optical Biosensing

Hatice Duran¹, King Hang Aaron Lau¹, Anke Lübbert¹,
Ulrich Jonas¹, Martin Steinhart², and Wolfgang Knoll¹

¹Max Planck Institute for Polymer Research, Ackermannweg 10,
55128 Mainz, Germany

²Max Planck Institute of Microstructure Physics, Weinberg 2,
06120 Halle, Germany

In this work, N-carboxy anhydride (NCA) monomer molecules were condensed on the pore walls of an initiator-coated nanoporous alumina template, leading to polypeptide (poly(γ -benzyl-*L*-glutamate), PBLG) film formation. Three different ways were followed for peptide nanotube formation: NCA polymerization in solution, in melt and polymerization from surface-initiated vapor deposition. While the NCA monomer was polymerized within the pores, the wall thickness of the resulting polypeptide was tuned by changing the polymerization time. This polypeptide-coated alumina membrane will be used as planar optical waveguide to monitor both the changes in the refractive index and fluorescent signals of the composite membrane through specific binding of a bio-analyte. We monitored for the first time the in-situ formation of an initiator layer (3-Aminopropyltriethoxysilane, APTE) inside the pores of an alumina membrane via optical waveguide spectroscopy. Attachment of initiator molecule effectively changed the dielectric constants of the interfaces, resulting in detectable shifts of the waveguide modes. We have previously demonstrated that unmodified nanoporous alumina waveguide sensor having a 10 times higher sensitivity than surface plasmon spectroscopy (SPR). The sensitivity may be further increased if the pores are coated with PBLG polypeptides, which has many functional sites on each polypeptide chain.

Nowadays, carbon nanotubes (CNTs) are very attractive substances as potential building blocks for high technology applications. Many of these applications require both uniform dispersion of CNTs in solution and further functionalization of their inner or outer wall in order to have a useful signal which is also a prerequisite for the use in biosensor devices. A major concern about carbon nanotubes for biological applications is their potential toxicity unless they are functionalized or coated with a biocompatible agent (1). For example, research over the past several years has shown that, when inhaled, carbon nanotubes can accumulate in the lungs and cause inflammation. Polymeric nanotubes, on the other hand, can be potential candidates to overcome such severe obstacles. They are also regarded as promising building blocks for a multitude of applications. Polypeptides are polymers of exceptional interest because of the close relationship they bear to proteins. Synthetic polypeptides offer a unique opportunity for exploring the interrelation of these fundamental properties, which determine protein structure and function (2); their flexibility in functionality and their molecular-recognition properties distinguish them from other materials. The ability of peptide-based nanotubes to target specific cells makes them attractive for biomedical applications (e.g. smart drug-delivery). This type of nanotubes can be inserted into cell membranes and can mimic the ion channels in membranes (3). Furthermore, inner surfaces can be designed that have properties distinct from the outer surfaces. For example, one can fabricate them with hydrophobic outer surfaces and hydrophilic inner surfaces. Since polypeptide nanotubes are non-toxic to cells and they are biocompatible, this makes them even more valuable for future in vivo experiments in biosensor and biomolecular filters applications. Peptide nanotubes could be formed via self-assembly by stacking cyclic peptide monomers (4). Self-assembled peptide nanostructures can be organized into nanowires, nanotubes, or nanoparticles via their molecular recognition function (4). Peptide rings are stacked through backbone-backbone hydrogen bonds between neighboring amide groups to form peptide nanotubes. Most recently, dendritic peptide monomers have been used to form polypeptide nanotubes (5) via hydrogen bonding. One of the disadvantages of nanotube formation using cyclic peptide monomers is that in order to produce larger-diameter peptide nanotubes, the ring diameters of the cyclic peptide monomers need to be larger. However, many cyclic monomers can only be synthesized between 10 to 20 Å in diameter to maintain a stable cyclic structure, and nanotubes need to be bundled to obtain larger nanotube diameters (6). In order to achieve a wide range of peptide-nanotube sizes, it may be more advantageous to fabricate them via template-directed synthesis. Martin et al. (7, 8) have pioneered template-assisted fabrication of hybrid nanostructures by combining the tools of synthetic chemistry and material science. They grew organic materials within the pores of anodic alumina templates, which are characterized by regularly arranged parallel pores with uniform pore depth

(9, 10). Using this approach, one can now produce polymeric nanotubes in confined geometries for applications in biosensor technology.

In the present work, poly(γ -benzyl-L-glutamate) (PBLG) polypeptide nanotubes have been fabricated for optical biosensor applications. This technique is based on the synthesis of nanostructures within the pores of a nanoporous membrane (7, 11). PBLG (12) is a polymer with non-linear optical properties. This polymer is attractive not only because of its large intrinsic dipole moments and birefringence but also because its ester side chains may be easily modified. So far, the tethering of polypeptides onto flat substrates (13) has been studied extensively. However, this concept still presents a challenge due to the low surface area coverage, resulting in a smaller amount of functional or reactive sites. Our technique overcomes these drawbacks. Its advantages include reproducibility, flexibility regarding the aspect ratios of the nanotubes, large-scale production, and sharp distributions of length and diameter. Furthermore, the nanoporous structure of the alumina membrane results in a very high internal surface area. Consequently, we increased the effective surface density of functional peptide groups. This is particularly important since the sensitivity and the precise quantification of analyte molecules depend on the number of active biofunctional groups. However, a problem still to be solved is the recycling of the alumina templates. Functionalities can be enriched in nanotubes through well-established chemical or non-covalent attachment of functional molecules (14) to the peptide nanotubes. This feature enables decoration of the inside and outside walls of peptide nanotubes with different functionalities, which provides the flexibility to further control the nanotube structure and behavior at the molecular level. The hollow structure of nanotubes offers functionalisation and/or templating various molecules inside the nanotubes. These nanotubular polypeptides can be further designed to have distinct functional groups (-COOH or -NH₂) depending on the analyte of interest. Furthermore, debenzylated polypeptide nanotubes act as polyelectrolytes and might be useful for monitoring changes in pH for in vivo cell studies. The polypeptide nanotubes embedded in the robust alumina template form a mechanically stable biosensor membrane so that aggregation and mechanical deformation of the nanotubes are prevented. In this way, polypeptide probes have a sufficiently long lifetime and during this period it is easy to functionalize and calibrate them.

Experimental

Materials and Templates

The N-carboxy anhydride (NCA) monomer of PBLG was synthesized by phosgenation of L-glutamic acid (Merck Biosciences) with stoichiometric

quantities of triphosgene (Sigma-Aldrich) in dry ethyl acetate (Fluka) (15). Then, the monomer was purified two times by recrystallization. $^1\text{H-NMR}$ spectra were recorded on a Bruker Dpx250 spectrometer, using the residual proton resonance signal of the deuterated dichloro methane (CD_2Cl_2) as the internal standard.

$^1\text{H NMR}$ (CD_2Cl_2 250 MHz): δ (ppm): 2.17 (m, $\beta\text{-CH}_2$), 2.52 (m, $\gamma\text{-CH}_2$), 4.32 (t, C-H), 5.14 (s, $\text{-CH}_2\text{-benzylic}$), 6.31 (s, N-H), 7.41 (s, Ar-H)

3-Aminopropyltriethoxysilane (APTE) (Sigma-Aldrich) was used as initiator. The initiator was dried and distilled prior to usage for better polymerization. For substrate directed growth of PBLG, it is immobilized in the alumina pores by liquid phase silanization as described below.

For the polymerization of NCA monomer in a solvent for PBLG powder:

In a dry box, NCA was dissolved in DMF (150-200mg NCA per ml solvent) and placed inside a syringe attached with a Rotilator-Syringe filter (pore diameter $5\mu\text{m}$) on it. Then, transferred in a 25mL Schlenk tube from the top which was sealed with a Teflon stopcock. An aliquot of APTE was rapidly added via syringe to the flask, while continuously stirring the monomer solution. A stirrbar was added and the flask was sealed, removed from the dry box, and stirred in a thermostated bath at 25°C for 5 days. Polymer was isolated by addition of the reaction mixture as small drops to a distilled water flask (the amount of water is X10 that of the solution) causing precipitation of the polymer. The polymer was then dissolved in THF and reprecipitated by addition to water. The white precipitated PBLG was filtered and dried in vacuo overnight to give a white solid.

$^1\text{H NMR}$ (DMSO, 500 MHz at 323K): δ (ppm): 2.06 (m, $\beta\text{-CH}_2$), 2.28 and 2.48 (m, $\gamma\text{-CH}_2$), 3.95 (t, C-H), 5.03 (s, $\text{-CH}_2\text{-benzylic}$), 7.26 (s, Ar-H), 8.25 (s, N-H).

$^{13}\text{C NMR}$ (DMSO, 500 MHz at 323K): δ (ppm): $^{\gamma}$ $^{\beta}$ ($\beta\text{-CH}_2$), 29.50 ($\gamma\text{-CH}_2$), 57.38 ($\text{-CH}_2\text{-benzylic}$), 64.86 (C-H), 127.17, 128.18, 135.48 (Ar-H), 170.88, 174.32 (C=O).

The number average molecular weight (83,200 g/mol with a degree of polymerization of 380 and an average chain length of 57nm) and polydispersity index (1.73) were measured with GPC in DMF against standard PS.

Silicon substrates (Si-Mat, double side polished) were cleaned by immersing them in a mixture of NH_3 (8 mL, 25%), H_2O_2 (8 mL, 35%) and Millipore water (100 mL) at $80\text{-}85^\circ\text{C}$, for 20-25 min. Afterwards, the substrates were rinsed with copious amount of Millipore water and dried under N_2 .

Self-ordered porous alumina templates (pore diameter ranges from 25nm to 380nm; pore depth is from $5\mu\text{m}$ to $100\mu\text{m}$) were prepared according to protocols reported elsewhere (16, 17).

Deposition of Thin Alumina Films on LaSFN9 Substrates for Optical Waveguide Studies

Glass substrates (LaSFN9, Hellma Optik, Halle) were cut into 25 mm x 25 mm pieces and sonicated in 2% Hellmanex solution (Hellma Optik). Before aluminum deposition, 3 nm Cr followed by 45 nm Au were deposited as an optical coupling layer by thermal evaporation, both at a rate of 0.1 nm/s and at $\sim 1 \times 10^{-6}$ mbar (BOC Edwards Auto300). Al (500~1000 nm) was deposited by DC magnetron sputtering (BOC Edwards Auto500) in an Ar plasma, at a rate of 1 nm/s/A using the following conditions: 0.7 A (300 W) or 1.4 A (600 W), process pressure at 3×10^{-3} mbar, base pressure at $< 1 \times 10^{-6}$ mbar.

Al was anodized at a constant potential of 40V at 1-2°C. The sample was placed in a beaker containing 0.3 M oxalic acid and a Pt counter electrode. The edges of the sample were protected from the acid solution by nail polish. Anodization was normally complete after 35 minutes, and a distinct color change was observed. After anodization, the pores were widened by immersing the samples in 5 wt.% H_3PO_4 for 20 min.

Liquid-Phase Silanization with APTE

Prior to silanization, alumina templates were cleaned with oxygen plasma (2min). Silanization was performed in either an aqueous or a methanol solution. A 1% silane solution in Milli-Q water and Acetate buffer (pH=5.3) was stirred for 20 min and filtered through a 0.2- μm polytetrafluoroethylene (PTFE) syringe filter before use. Then, the alumina substrates were immersed in the silane solution for 30 min, washed with Milli-Q water, and baked at 95 °C for 1h. For in-situ optical waveguide spectroscopy, 1 mM methanol solution was used. The templates were immersed in it overnight, rinsed and then annealed. After washing with a solvent sequence (acetone, Milli-Q water, acetone, and tetrahydrofuran) the templates were sonicated in acetone in order to remove physisorbed silane molecules. Fourier transform infrared resonance spectroscopy, FT-IR and ellipsometry results (data not shown) revealed that the initiator layers produced in this way have a high amine surface density and multiple molecular layers.

Grafting of Poly(γ -Benzyl-L-Glutamate) to the Inner Walls of Alumina by N-Carboxyanhydride Polymerization

We applied three different techniques for the growth of polypeptide films inside the pores. Depending on the envisioned applications, each technique has its own advantages.

1. Solution Polymerization

The initiator (APTE) coated nanoporous alumina substrates were immersed in a solution of 3.7mM NCA in anhydrous tetrahydrofuran. The formation of the polypeptide films by ring opening polymerization was initiated by APTE. The reaction was performed to proceed under vacuum (100mbar) at room temperature for 72h. After polymerization, the substrates were cleaned with tetrahydrofuran and deionized water. Figure 1 depicts the details of the polypeptide film formation within the inner walls of the alumina template.

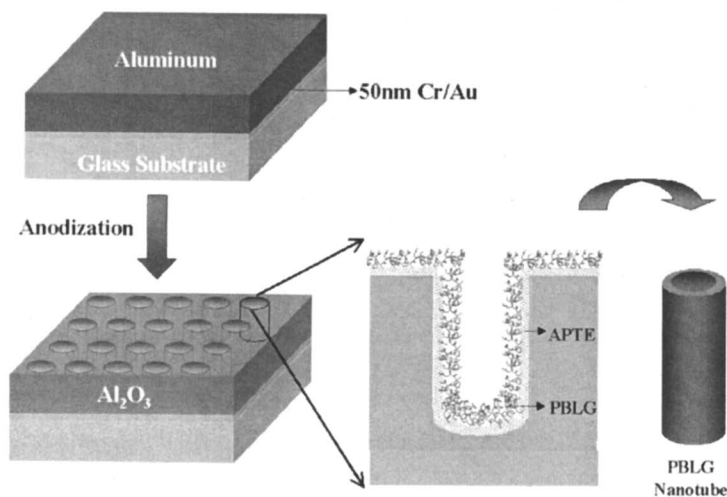


Figure 1. Schematic diagram of initiator deposition and polymerization; polypeptide films formed on the pore walls of a thin anodic alumina membrane. (See page 1 of color inserts.)

2. Template-Wetting Method

In this technique, an APTE-modified alumina template with uniform porosity was used as the mold. First, NCA monomer was spread on top of pores. Then, the substrate was located in vacuum furnace under Ar atmosphere. The temperature was adjusted to a value 10-15 K above the melt temperature (95-97°C) of the monomer. The monomer melt covers the pore wall coated with APTE molecules and NCA monomer molecules are in direct contact with the initiator molecules polymerize and ultimately forms a PBLG polymer layer inside the pores. Since the nanotubes are replicas of the template pores, their

dimensions could be exactly controlled by using templates with proper pore diameters and depths.

3. Surface-Initiated Vapor Deposition Polymerization (SI-VDP)

The SI-VDP of NCA in which gas phase monomer molecules are condensed onto an initiator-immobilized surface lead to polypeptide growth was conducted following previously published work by C. W. Frank et al. (18,19). The initiator coated template was placed in a sealed glass reactor and a small amount of NCA monomer was placed on the bottom of the reactor. Vapor-deposition polymerization involves a reaction between the vaporized NCA molecules and surface-immobilized amine groups, after increasing the temperature above the melting point of the monomer. The NCA monomers polymerize through a ring opening polymerization mechanism. Figure 2 depicts PBLG nanotube formation within the inner walls of the alumina template via the SI-VDP technique.

Etching Alumina Templates

Free-standing PBLG nanotubes were obtained by selective dissolution of the template using an aqueous HF (25-45%) solution at 0°C for 1.5 h. Then, PBLG nanotubes were filtered off by Sterlitech stainless steel syringe equipped with PTFE laminated membrane disc filters (pore diameter of 0.2 μ m), removing the supernatant liquid, and adding deionized water. This procedure was repeated several times until the solution became neutral. Finally, PBLG nanotubes were collected by back-filtering.

Characterization Techniques

Scanning Electron Microscopy (SEM)

After etching the alumina layer, free standing polypeptide nanotubes were deposited on metal holders covered with conductive tape. SEM measurements were performed with a LEO Gemini 1530 SEM with 3.5nm resolution. The electron acceleration voltage was used around 6kV.

Differential Scanning Calorimetry (DSC)

Mettler Toledo DSC 822 equipped with a cooling chamber was operated with liquid nitrogen as a purging and cooling medium. Polypeptide nanotubes in

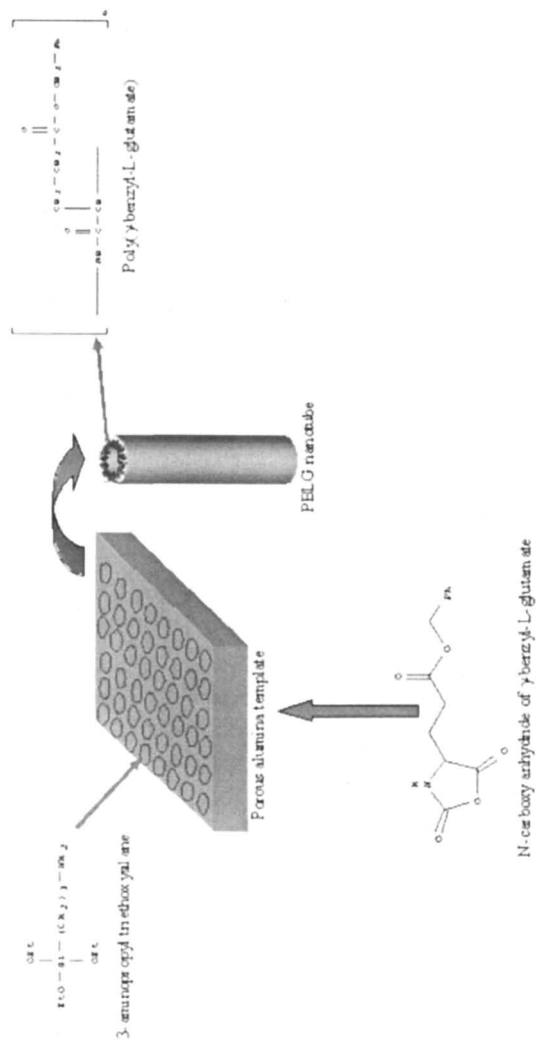


Figure 2. PBLG nanotube formation within the inner walls of alumina template via surface-initiated vapor deposition technique. (See page 1 of color inserts.)

the recommended amount of 5-10 mg were hermetically sealed in aluminum pans. DSC experiments were performed in the temperature range of -10°C to 200°C with a 10 K/min ramp in order to determine the glass transition temperature (T_g) and the nematic-isotropic transition temperature of the polypeptide nanotubes. The thermal decomposition temperatures were measured with a Thermal Gravimetric Analyzer (Mettler Toledo TGA 851) and found to be $\sim 320^{\circ}\text{C}$.

X-ray Diffraction (XRD)

For flat alumina substrate covered with PBLG film, wide-angle X-ray diffraction measurements were made using a Bruker-AXS D8 diffractometer in the reflection geometry. The $\text{CuK}\alpha$ radiation ($\lambda=0.154$ nm) was used operating at 40kV and 40mA. Measurements were made in the 2Θ range from 1° to 80° in steps of 0.05° . $\Theta/2\Theta$ in reflection mode were performed on polypeptide nanostructures which were aligned within the anodic alumina template pores, using a Philips X'pert MRD diffractometer with cradle and secondary monochromator for $\text{CuK}\alpha$ radiation ($\lambda=0.154$ nm). Prior to the measurements the residual material on the surface of the templates was carefully removed with a sharp blade.

Optical Waveguide Spectroscopy (OWS)

OWS was performed on a home-built system set up in the Kretschmann configuration (20). The alumina membrane thin film created on the glass substrate was used as a slab waveguide. A Teflon flow cell was clamped on top of the anodic alumina membrane. Thus, the solvent in the cell acts as the cladding over layer and the Cr/Au film deposited between the alumina membrane and glass substrate acts as the coupling layer. Excitation of waveguide modes were measured as sharp minima in intensity as a laser (632.8 nm) is reflected at different angles off the Au-glass interface under total internal reflection. The thickness and the refractive indices of the film, cladding and coupling layers were then measured by fitting these angle minima to Fresnel calculations, which is simple, highly developed and precise (21). The highest angle (lowest order) waveguide mode was chosen for measurement. Angle resolution better than 0.005° was obtained. The refractive indices used for the alumina component of the film and for adsorbed APTE are 1.58 and 1.45, respectively.

Results And Discussions

The ideal reaction conditions were first optimized by means of flat silicon substrates, onto which the polypeptides were grafted. Varying the polymerization temperature and time allows adjusting the thickness of the films. Ordered porous alumina templates with pore diameters ranging from 25 nm and pore depths ranging from 5 μm to 100 μm were used for the template assisted polymerization. The fabrication of polypeptide nanotubes was verified by scanning electron microscopy (SEM). Figure 3 shows a bird's eye view of alumina templates before and after the polypeptide nanotube/nanorod formation.

The pores were either partially or completely filled with polypeptide (Figure 3(b) and (c), respectively) depending on the polymerization time. At 115 $^{\circ}\text{C}$ and for 1h deposition time, hollow structures were obtained with a wall thickness around 80nm. A further increase in polymerization time up to 2h converted these nanotubes into solid nanorods (Figure 3(c)). Besides the polymer formation inside the pores, a thick polypeptide film covered the surfaces of the porous alumina templates. The excess film on top of the alumina templates was removed with a Microtome Ultra Cutter. These nanorods were released from the template

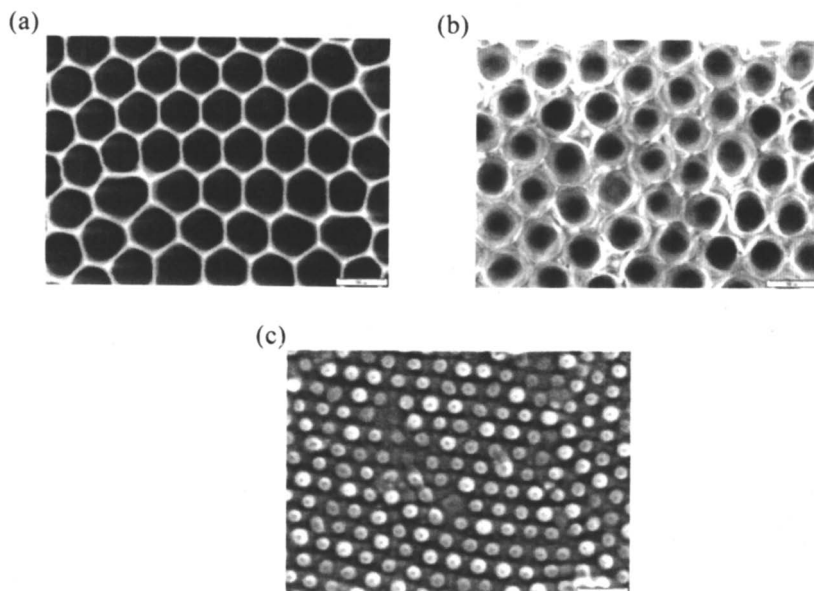


Figure 3. Top view SEM images of (a) an empty alumina templates before modification, after the SI-VDP of NCA at (b) 115 $^{\circ}\text{C}$ for 1h at 4×10^{-3} mbar and (c) 115 $^{\circ}\text{C}$ for 2h at 2×10^{-3} mbar; pore diameter is 380nm and pore depth is 100 μm

by etching with HF solution to form well-aligned bundles (Figure 4(a) and (b)). The nanorods from the vapor phase polymerization show a particular surface structure with many small protrusions <10nm at the wall surface, leading to a much larger surface area compared to smooth walls. This might be of advantage in applications that rely on the surface of the nanorods (e.g. enhanced sensitivity for biosensing).

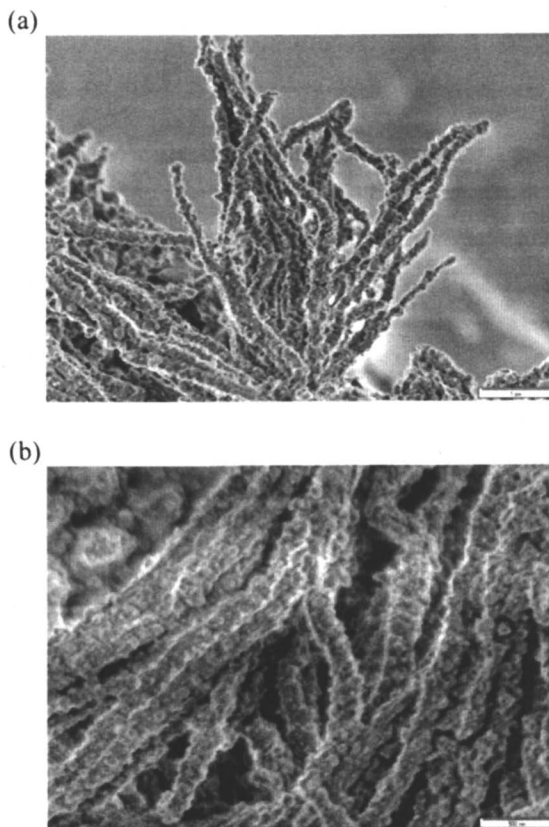


Figure 4. SEM images of PBLG nanorods after HF etching (25%) at 0°C for 1.5 h. NCA polymerized by SI-VDP at 115°C for 2h at 2×10^{-3} mbar.

On the basis of the template-wetting method, we also prepared PBLG nanotubes (Figure 5). The main reason to use this alternative technique is because of the difficulties for controlling the nanotube wall thickness. SI-VDP technique showed a non-linear growth profile and the polymer film wall thickness varied substantially between each experiment. In contrast to the SI-

VDP method, polypeptide nanotubes obtained with template wetting technique had a very smooth surface. They were stacked together after removal of alumina with HF etchant. Surprisingly, these nanotubes and rods appeared to be very flexible judging from the bends seen in the SEM images of Figure 5(b). As expected, these tubes have an outside diameter that are equivalent to the pore diameter of the template.

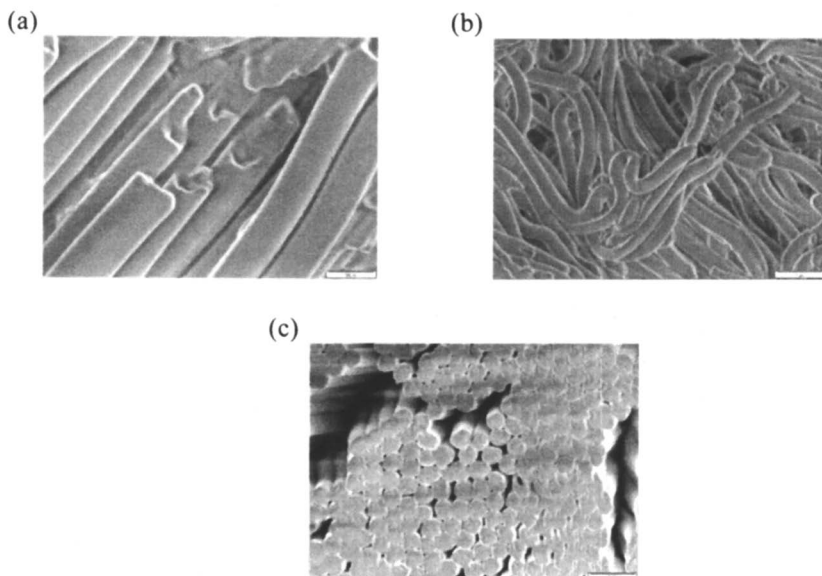


Figure 5. SEM images of free standing PBLG (a) nanotubes and nanorods (b), with (c) the top view of b after HF etching (45%) at 0°C for 1.5 h. NCA polymerized by template-wetting technique in vacuum oven at 105°C for (a) 20h, (b) and (c) 72h.

In order to investigate any orientation and ordering effects of the nanostructures at the molecular level of the polypeptide chains, XRD measurements were performed. For this purpose, $\theta/2\theta$ scans were measured on PBLG films on flat substrate and nanotubes located within the template pores prepared by template-wetting technique. NCA polymerized on both (flat and porous alumina) substrates modified with APTe initiator layer by the template-wetting technique in a vacuum furnace at 105°C for 20h. The wall thickness was 50nm. The $\theta/2\theta$ scan (beam direction normal to the film surface) of the PBLG film on a flat alumina substrate (Figure 6(a)) shows the characteristic, strong peak of the lyotropic liquid crystalline phase at $2\theta = 6.7^\circ$. This reflection

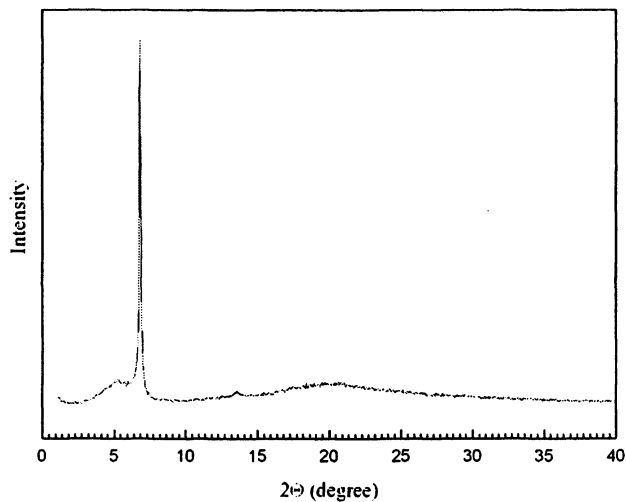
corresponds to an intermolecular spacing of α -helical chains (12, 22) with a spacing of 13.2 Å. The second peak (5°) is relatively weak and had higher spacing (17.7 Å). There is another very weak peak at 13.4° with a spacing of 6.6 Å, which might be due to secondary polypeptide structure formation. The broad peak at $2\theta \approx 20^\circ$ corresponds to amorphous polymer portion. Figure 6(b) shows XRD patterns of PBLG inside the anodic alumina pores. Only one peak at $2\theta = 6.5^\circ$ ($d = 13.2$ Å) appears. Compared with PBLG films on flat substrate, this peak is weaker and broader. The second peak at 5° , on the other hand, completely disappeared. These two peaks might fall together into a broader and weaker peak. The reflection at a Bragg angle of $2\theta = 6^\circ$ - 9° corresponds to the ($\bar{1}0\bar{1}0$) plane of a hexagonal lattice for the α -helix crystal form of PBLG (23-25). It seems that the pore geometry does not induce any noticeable chain ordering in the polymer tubes formed inside the alumina template with 380 nm pore size. In order to elucidate any detailed ordering effect of the pores, a more detailed investigation with systematic variation of the template pore size and polymer wall thickness would be required.

Differential scanning calorimetry was employed to obtain the glass transition temperature of both PBLG powder and polypeptide nanotubes and to determine the melting point of the NCA monomer (Figure 7). PBLG powder synthesized by the solution polymerization technique exhibited a glass transition temperature (T_g) at 8°C and a broad endothermic peak which can be an indication of a first-order phase transition, at around 60°C during the heating run. The PBLG nanotubes, on the other hand, exhibited a T_g at around $20 \pm 2^\circ\text{C}$. The shift in T_g might not be correlated the molecular weight of the polypeptide since we used similar chain lengths; 57 nm for PBLG powder and 50 nm for PBLG nanotube. Unlike a PBLG powder, any noticeable endothermic peak for PBLG nanotubes was not observed, although these two experiments were measured under the same conditions.

Optical Waveguide Studies

Figure 8(a) shows a scanning electron micrograph of a thin porous alumina film covered with PBLG molecules. The pores were either partially or completely filled with polypeptide by solution polymerization of NCA. In this way, it was possible to obtain polypeptide nanostructures with smaller diameters. The inset of the figure shows an empty porous alumina membrane with a distribution in pore diameters, ranging from 25nm to 75nm. The openings to the larger pores are relatively elliptical in shape while the smaller ones are more circular. Notwithstanding, Figure 8(b) shows the cross section of the PBLG coated membrane, demonstrates that the pores run parallel to each other and rods have similar diameters. The height of the porous alumina layer is approximately 600nm, which is sufficiently thick to allow for optical waveguide modes within the alumina template for the characterization of internal adsorption processes.

(a)



(b)

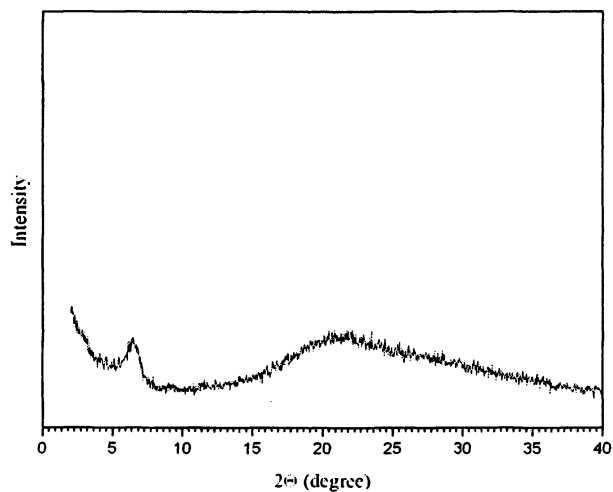


Figure 6. Wide-angle x-ray diffraction profiles of (a) PBLG film grown on a flat alumina surface and (b) inside the alumina pores.

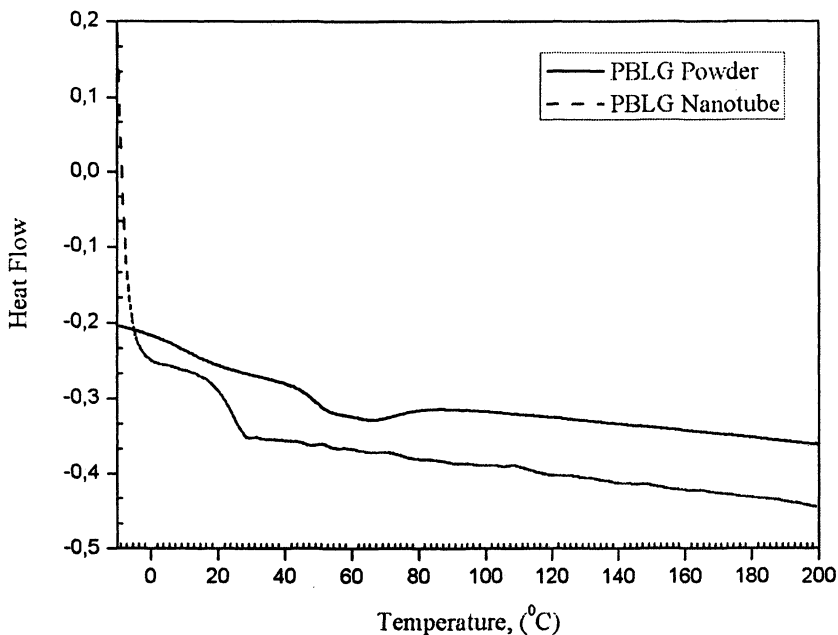


Figure 7. Differential Scanning Calorimetry scans for PBLG powder (from solution polymerization) and PBLG nanotubes of $D=380\text{nm}$, $L=100\mu\text{m}$ kept in a vacuum oven at $105\text{ }^\circ\text{C}$ for 20h.

As proof of concept, we monitored in-situ APTE immobilization inside the pores in methanol. Observation of guided optical modes is a highly sensitive approach for monitoring adsorption processes within the pores of anodic alumina films (21). Using the Kretschmann prism setup, guided optical modes are observed as sharp minima in reflectivity vs. incidence angle scans (R vs. θ). If the pore walls of the alumina membrane are covered with APTE molecules, the effective refractive index (n_{eff}) of the film changes, causing a shift in the mode coupling angles to higher values (Figure 9(a)). Tracking the temporal change of the angle (0.4°) of a waveguide mode in time gives the adsorption kinetics (20), as shown in Figure 9(b). The curve thus obtained is in agreement with a 2-step first order diffusion limited model (26), which is a reasonable description given the high aspect ratio of the pores. Around 80% of the final adsorbed thickness is achieved within 2 hours during the initial fast adsorption. In the subsequent slow adsorption regime, we also observe a slight, continuous increase in film thickness, which could be correlated with physisorbed APTE multilayers. Calculations using simple first and second order kinetics cannot describe the data. The increase in n_{eff} is calculated from the angle shifts and related to the thickness increase of the APTE layer using effective medium theory (9, 27).

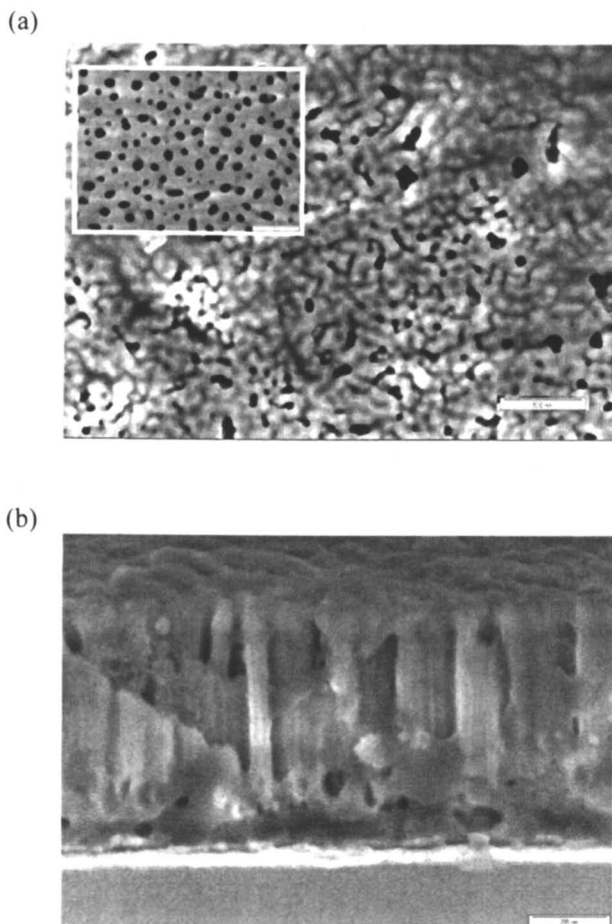


Figure 8. Scanning electron micrographs of a thin porous anodic alumina film covered with PBLG molecules (a) top view, (inset: empty membrane) and (b) side view.

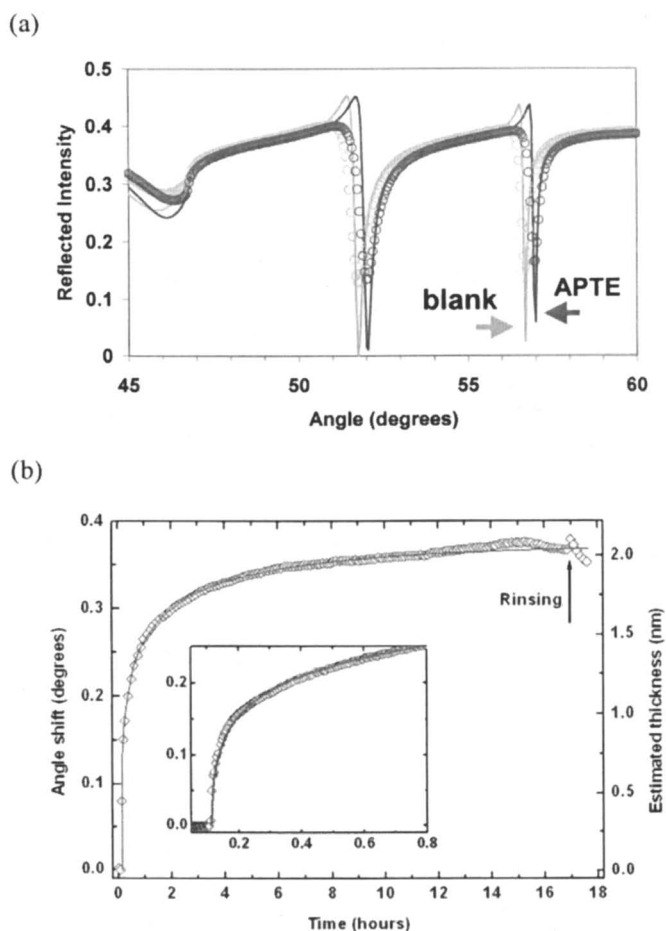


Figure 9. (a) Waveguide mode patterns of a thin alumina film before and after functionalization with APTE in 1mM methanol solution. (b) In-situ kinetics of APTE adsorption was followed using the right-most guided mode in (a). Open diamonds are data, and the solid line is fitted with a 2-step diffusion limited model. (See page 2 of color inserts.)

Around 2 nm of material was adsorbed (Right axis, Figure 9(b)), which corresponds to the value obtained for flat silicon oxide substrates measured with optical ellipsometry (not shown.) The results reported here suggest that optical waveguide characterization can also be used to study the formation of the polypeptide-nanoporous alumina hybrid systems in particular since much more material is deposited during NCA polymerization, which should lead to even much stronger shifts of the waveguide modes. As seen in Figure 9(a), film thickness changes corresponding to the sub-angstrom level is detected, and the difference between an empty and a surface functionalized membrane is discerned at very high resolution.

Conclusion

We have shown that polypeptide nanotubes can be fabricated in a porous alumina template by using three different techniques. The polypeptide synthesis was successfully performed within thin film layers of nanoporous anodic alumina templates. First, the inner wall of the alumina templates was functionalized with APTe, which is used as initiating sites for ring opening polymerization of NCA monomers for polypeptide synthesis. At present, we have been able to follow in-situ initiator layer formation via an optical waveguide spectroscopy. Future work aims at the monitoring of in-situ polypeptide formation inside the pores, side chain activation reactions as well as real-time detection of specific target DNA or protein sequences. Besides the final detection of the biological targets in a biosensor set-up, the real-time kinetics of each step in the course of the preparation of complex hybrid structures inside the pores can be monitored. This includes the functionalisation of the pore walls with initiator molecules followed by polypeptide film formation up to specific peptide modification inside the pores.

Acknowledgment

Financial support from the Deutsche Forschungsgemeinschaft (DFG) through the priority program (Schwerpunktprogramm) SPP 1165 (KN 224/15-1) and the Volkswagen Foundation (Az. I/80 780) is gratefully acknowledged. The authors would like to thank Robert Brandscheid for technical support. H. D. thanks Prof. Curtis W. Frank for valuable discussions and the European Union for the Marie Curie Intra-European Fellowship (MEIF-CT-2005-024731).

References

1. Bertozzi, C. R.; Zettl, A.; Chen, X *J. Am. Chem. Soc.* **2006**, *128*, 6292.
2. Doty, P.; Bradbury, J. H. and Holzer, A. M. *J. Am. Chem. Soc.* **1956**, *78*, 947.
3. Gao, X. and Matsui, H. *Adv. Mater.* **2005**, *17*, 2037.
4. De Santis, P.; Morosetti, S. and Rizzo, R. *Macromolecules* **1974**, *7*, 52.
5. Percec, V.; Dulcey, A. E.; Balagurusamy, V. S. K.; Miura, Y.; Smidrkal, J.; Peterca, M.; Nummelin, S.; Edlung, U.; Hudson, S. D.; Heiney, P. A.; Hu, D. A.; Magonov, S. N.; Vinogradov, S. A. *Nature* **2004**, *430*, 764.
6. Bong, D. T.; Clark, T. D.; Granja, J. R.; Ghadiri, M. R. *Angew. Chem. Int. Ed.* **2001**, *40*, 988.
7. Martin, C. R. *Science*, **1994**, *266*, 1961.
8. Martin, C. R. *Adv. Mater.* **1991**, *3*, 457.
9. Nielsch, K.; Choi, J.; Schirn, K.; Wehrspohn, R. B.; Gosele, U. *Nano Lett.* **2002**, *2*, 677.
10. Steinhart M.; Wehrspohn, R. B.; Gösele, U. and Wendorff, J. H. *Angew. Chem. Int. Ed.* **2004**, *43*, 1334.
11. Hulteen, J. C. and Martin, C. R. *J. Mater. Chem.* **1997**, *7*, 1075.
12. H. Block, *Poly(γ -Benzyl-L-Glutamate) and Other Glutamic Acid Containing Polymers*, 1st Ed.; Gordon and Breach Science Publishers Inc.: New York, **1983**
13. Chang, Y.-C., Frank, C. W. *Langmuir*, **1996**, *12*, 5824.
14. Djalali, R.; Chen, Y. -F.; Matsui, H. *J. Am. Chem. Soc.* **2003**, *125*, 5873.
15. Daly, W. H. and Poché, D. *Tetrahedron Letters*, **1988**, *29*, 5859.
16. a) Masuda, H. and Fukuda, K. *Science* **1995**, *268*, 1466. (b) Masuda, H.; Hasegawa, F. and Ono, S. J. *Electrochem. Soc.* **1997**, *144*, L127. (c) Masuda, H.; Yada, K. and Osaka, A. *Jpn. J. Appl. Phys. Part 2* **1998**, *37*, L1340.
17. Nielsch, K.; Choi, J.; Schwirn, K.; Wehrspohn, R. B.; and Gösele, U. *Nano Lett.* **2002**, *2*, 677.
18. Chang, Y. -C. and Frank, C. W. *Langmuir* **1996**, *12*, 5824.
19. Chang, Y. -C. and Frank, C. W. *Langmuir* **1998**, *14*, 326.
20. Knoll, W. *Ann. Rev. Phys. Chem.* **1998**, *49*, 569.
21. Lau, K. H. A; Tan, L- -S.; Tamada, K.; Sander, M. S. and Knoll, W. *J. Phys. Chem. B.* **2004**, *108*, 10812.
22. Bamford, C. H.; Elliott, A. and Hanby, W. E. *Synthetic Polypeptides*, Academic Press New York, **1956**, p.239.

-
23. Rao, M. V. R.; Pantar, A. V. and Atreyi, M. *Int. J. Biol. Macromol.* **1987**, *9*, 337.
 24. Hayashi, T; Anderson, J. M. and Hiltner, P. A. *Macromolecules*, **1977**, *10*, 352.
 25. McKinnon, A. J. and Tobolsky, A. V. *J. Phys. Chem.* **1968**, *72*, 1157.
 26. Peterlinz, K. A.; Georgiadis, R. *Langmuir*, **1996**, *12*, 4731.
 27. Galca A. C.; Kooij E. S.; Wormeester H.; Salm C.; Leca V.; Rector J. H.; Poelsema B. *J. Appl. Phys.* **2003**, *94*, 4296.

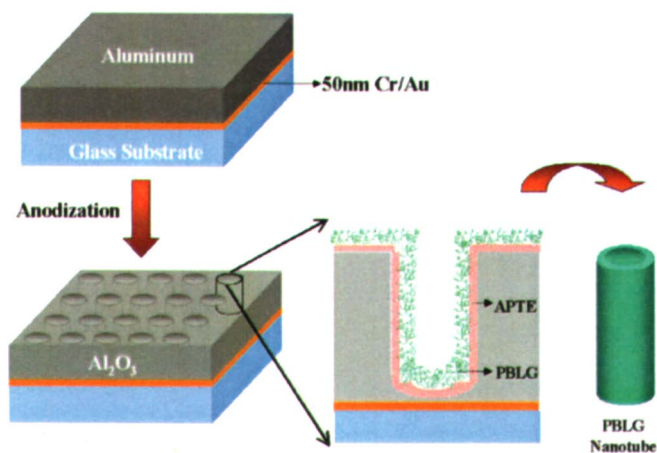


Figure 22.1. Schematic diagram of initiator deposition and polymerization; polypeptide films formed on the pore walls of a thin anodic alumina membrane.

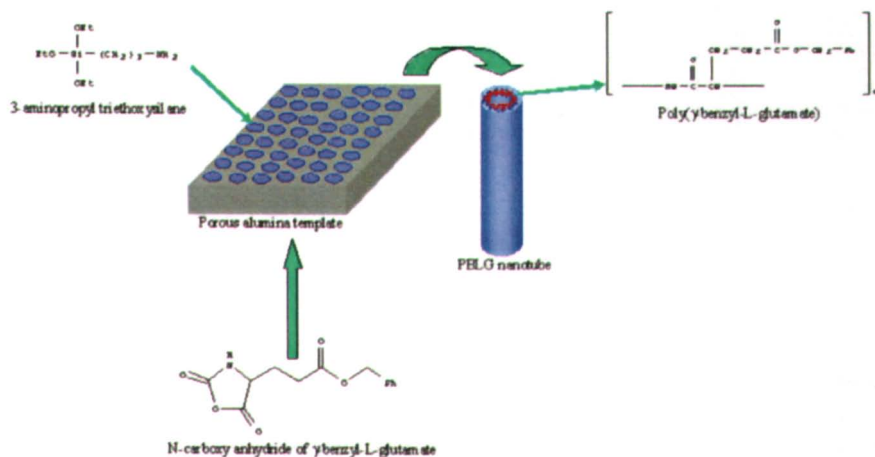


Figure 22.2. PBLG nanotube formation within the inner walls of alumina template via surface-initiated vapor deposition technique.

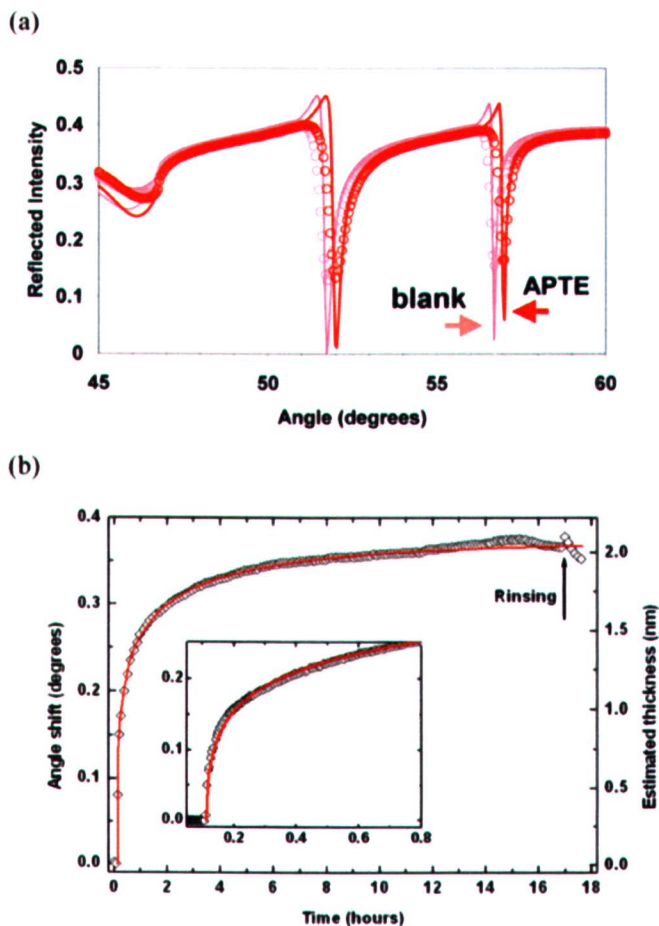


Figure 22.9. (a) Waveguide mode patterns of a thin alumina film before and after functionalization with APTE in 1mM methanol solution. (b) In-situ kinetics of APTE adsorption was followed using the right-most guided mode in (a). Open diamonds are data, and the solid line is fitted with a 2-step diffusion limited model.

Author Index

- Adronov, Alex, 238
Atthoff, Björn, 250
Benhabbour, S. Rahima, 238
Bowden, Tim, 250
Chen, Hsien-Yeh, 283
Chiang, Martin Y. M., 118
Chirachanchai, Suwabun, 27
Collins, Stephen, 196
Cooper, Kevin, 51, 346
Da, Jane, 10
DeFife, Kristin M., 10
Dhara, Dibakar, 268
Drobizhev, Mikhail, 225
Duran, Hatice, 371
Elkasabi, Yaseen, 283
Eugene, Dawanne M., 37
Fangkwangwanwong, Juthathip, 27
Feng, Yu, 310
Fiore, Gina L., 95
Fraser, Cassandra L., 95
Glasgow, Katherine C., 268
Gomurashvili, Zaza, 10
Gong, Aijun, 225
Grako, Kathryn A., 10
Grayson, Scott M., 37
Haddleton, David M., 78
Hassan, Mohammad K., 153
He, Wei, 310
Henderson, Lori A., 118
Hilborn, Jöns, 250
Hughes, Jonathan, 10
Ishihara, Kazuhiko, 336
Jenkins, Turner D., 10
Jonas, Ulrich, 371
Katsarava, Ramaz, 10
Kipper, Matt J., 118
Knoll, Wolfgang, 371
Konno, Tomohiro, 336
Kulshrestha, Ankur S., 1
Kumar, Jayant, 204
Kumar, Rajesh, 204
Lahann, Joerg, 283
Lambert, Leanne, 10
Lau, King Hang Aaron, 371
Laurent, Boyd A., 37
Li, Yufu, 346
Liu, X. Michael, 170
Liu, Zuifang, 196
Lowenhaupt, Bruce, 346
Lübbert, Anke, 371
Ma, Zuwei, 310
MacPherson, Cassandra, 10
Mahapatro, Anil, 1
Mantovani, Giuseppe, 78
Mauritz, Kenneth A., 153
Maziarz, E. Peter, III, 170
Meng, Fanqing, 225
Meredith, Carson, 299
San Miguel, Veronica, 78
Moss, Britney L., 225
Nandivada, Himabindu, 283
Nederberg, Fredrik, 250
Mac Neil, Sheila, 196
Nicolas, Julien, 78
Overaker, David, 346
Pandey, Mukesh K., 204
Parmar, Virinder S., 204
Poandl, Tom, 346
Ramakrishna, Seeram, 310
Rebane, Aleksandre, 225
Rimmer, Stephen, 196

- Scopelianos, Angelo, 51
Smith, Louise E., 196
Spangler, Charles W., 225
Starkey, Jean R., 225
Steinhart, Martin, 371
Storey, Robson F., 153
Strömme, Maria, 250
Trenka-Benthin, Susan, 346
Turnell, William G., 10
Tyagi, Rahul, 204
Vassilev, Vassil, 10
Watterson, Arthur C., 204
Welch, Ken, 250
Wiggins, Jeffrey S., 153
Williams, Rachel, 196
Wingkono, Gracy, 299
Wood, Troy D., 170
Wu, Mark, 10
Yuan, J., 346
Zhang, Huashi, 10
Zimmerman, M., 346

Subject Index

A

- 4-Acetoxy styrene, polymerization for cyclic polymers, 47
- Acridine, molecular structure, 226*f*
- Active polycondensation (APC) method
- copolymers of poly(ester amides) (PEAs), 14, 16–17, 18
 - poly(ester amides) (PEAs), 11–12
 - polymeric biomaterials, 2–3
 - See also* Poly(ester amides) (PEAs)
- Adhesive bond, cell and surface for tissue engineering, 128
- Albumin, protein loading and release from biodegradable ionomers, 262, 263*f*
- Alumina templates, poly(γ -benzyl-L-glutamate) (PBLG) nanotubes by etching, 377, 380–381
- American Society for Testing and Materials (ASTM), tissue engineering industry, 120
- Amphiphilic copolymers, process of micellization, 212–213
- Amphiphilic molecules, molecular self-assembly, 319
- Architectures. *See* Cyclic polymers
- Aromatic diacids, poly(ester amide) (PEA) copolymers based on, 20–22
- Aromatic poly(anhydride)s
- bis(p-carboxyphenoxy)alkane poly(anhydride)s synthesis, 54, 56
 - cobalt (γ) radiation on test coupons, 58, 61
 - controlled drug delivery, 52
 - copolymerization of 1,4-bis(acetoxycarboxyphenoxy)butane and 1,6-bis(acetoxycarboxyphenoxy)hexane, 75, 77
 - cylindrical dumbbell molded properties, 58, 59*t*, 60*t*, 61
 - elemental analysis of bis-1,n-(p-carboxyphenoxy)alkane aromatic acids, 55*t*
 - experimental, 64, 66–77
 - fibers and films, 52
 - fiber tensile properties of, as function of draw ratio, 58, 59*t*
 - ^1H NMR of poly[1,6-bis(p-carboxyphenoxy)hexane anhydride], 73*f*
 - ^1H NMR of poly[1,6-bis(p-carboxyphenoxy)hexane anhydride] after cobalt irradiation, 76*f*
 - inherent viscosities of poly[1,6-bis(carboxyphenoxy)hexane anhydride] as function of time, 55*t*, 62*t*
 - in vivo physical properties of annealed BTC-1, 64, 65*t*
 - in vivo physical properties of annealed PGA, 64, 66*t*
 - in vivo physical properties of unannealed poly[1,4-bis(carboxyphenoxy)butane anhydride], 63*t*
 - isothermal melt viscosity of poly[1,6-bis(p-carboxyphenoxy)hexane anhydride], 76*f*
 - mechanical property requirements, 52
 - monofilament fibers, 57–58
 - physical properties of annealed poly[1,4-bis(carboxyphenoxy)-butane anhydride], 58, 60*t*

- physical properties of annealed poly[1,6-bis(carboxyphenoxy)hexane anhydride], 58, 59*t*
- physical properties of unannealed irradiated poly[1,4-bis(carboxyphenoxy)butane anhydride], 62*t*
- physical properties of unannealed poly[1,2-bis(carboxyphenoxy)ethane anhydride], 65*t*
- physical properties of unannealed poly[1,4-bis(carboxyphenoxy)butane anhydride], 58, 60*t*, 63*t*
- physical properties of unannealed poly[1,6-bis(carboxyphenoxy)hexane anhydride], 64*t*
- polymer and monomer characterization methods, 66–67
- polymerization of 1,4-bis(acetoxycarboxyphenoxy)butane, 70, 72*f*
- polymerization of 1,6-bis(acetoxycarboxyphenoxy)hexane from recrystallized anhydride monomer, 73–74
- polymerization of 1,6-bis(acetoxycarboxyphenoxy)hexane via Domb and Langer method, 75
- polymerization of 1,6-bis(acetoxycarboxyphenoxy)hexane via modified Domb and Langer method, 74
- potential of high molecular weight, for melt processing methods, 57
- preparation for high molecular weights, 53
- purity of dicarboxylic acid in first step, 54, 55*t*
- radiation sterilizable, 3
- sterilization practice, 52–53
- synthesis of 1,4-bis(acetoxycarboxyphenoxy)butane, 70, 72*f*
- synthesis of 1,4-bis(*p*-carboxyphenoxy)butane with *N*-methylpyrrolidinone (NMP) recrystallization, 67–69
- synthesis of 1,6-bis(acetoxycarboxyphenoxy)hexane and recrystallization with acetic anhydride, 71, 73
- synthesis of 1,6-bis(*p*-carboxyphenoxy)hexane with dimethylacetamide recrystallization, 71
- synthesis of 1,*n*-bis(*p*-carboxyphenoxy)alkane, 68*f*
- three-step process for preparation, 53–54
- Artificial organs, hydrogel polymers, 274*t*
- Aspirin
- anti-inflammatory properties of nanospheres, 213, 214*f*
 - pegylated amphiphilic polymers carrying, 212–213
- Atomic force microscopy (AFM), ribbon pattern in poly(ethylene)-poly(caprolactone) polyurethane, 302, 303*f*
- Atom transfer radical polymerization (ATRP)
- macrocyclic poly(styrene) synthesis, 43*f*
 - preparation of functionalized linear precursors, 40
- See also* Cyclic polymers
- B**
- Bioabsorbable polyester blend factors in designing, 348
- See also* Cranial fixation system

- Biocompatibility of polymeric surfaces**
 application type, 268
 block copolymers, 277–278
 blood compatibility, 275–276
 contact angle measurement, 272
 copolymers and additives, 277–278
 hemocompatibility of hydrophilic materials, 273–274
 heparin coatings, 271
 heterogenic materials, 277–278
 human body tolerating exposure, 268
 hydrogels, 273, 274*t*
 hydrophilic materials, 272–274
 hydrophobic materials, 274–277
 injection-molded devices in medical applications, 269
 lack of uniform test protocol, 269–270
 medical applications of hydrogel polymers, 274*t*
 methods for evaluating blood response of exposure to synthetic materials, 270*t*
 phospholipids mimicking cell walls, 271
 polyurethane materials, 273
 surface modification by coating, 271–272
 synthetic materials and biomedical applications, 269*t*
 wettability of surface, 275–276
- Biocompatibility studies**
 cranial plate, 351, 363–364
See also Cranial fixation system
- Bioconjugates.** *See* Protein-polymer bioconjugates
- Biodegradable ionomers**
 anionomer, 254*f*
 biodegradable poly(trimethylene carbonate) (PTMC), 251
 cationomer, 255*f*
 confocal micrograph hydrophobic- and water-phase stained PTMC, 259, 261*f*
 cryo-scanning electron microscopy (cryo-SEM) of inner structure of swelled ionomers, 261*f*
 cyclic trimethylene carbonate ring opening polymerization (ROP), 252, 254*f*
 dielectric spectroscopy, 256–257, 258*f*
 differential scanning calorimetry (DSC) of PTMC and ω -phosphoryl choline (PC) ionomer on second heating, 253, 257*f*
 formation and mechanism for water swelling, 257, 259
 oscillating rheology measurement of PTMC and PC ionomer, 256*f*
 properties and characterization, 253, 256–257
 protein loading and release, 260*f*, 262
 release curves of
 carboxyhemoglobin (COHb) and cytochrome C, 262, 264*f*, 265*f*
 release profile of albumin, 262, 263*f*
 schematic of polar PC bulk aggregates, 252*f*
 swelling mechanism, 251
 synthesis, 252–253
 telechelic ionomers, 254*f*, 255*f*
 UV-vis spectra of cytochrome C and COHb, 266*f*
 zwitterionomer, 255*f*
- Biodegradable polyester scaffolds, constructing vascular grafts, 324, 326*t***
- Biodegradation**
 in vitro enzyme catalyzed, of copoly(ester amides) (co-PEAs), 17, 20

- poly(ester amides) (PEAs), 12
 polyesters and co-polyesters, 154
 studies of PEAs, 15
See also Broadband dielectric spectroscopy
- Biological characterization, tissue engineering, 129*t*
- Biomaterials
 applications, 5–6, 284
 biosensors, 5–6
 characterization, 4
 drug delivery, 3
 health care industry, 1
 polymeric surfaces, 4–5
 polymers, 2
 surface features, 300
 synthetic approaches and polymer based, 2–4
 tissue engineering, 5
 widespread uses, 2
- Biomaterials engineering. *See* Tissue engineering
- Biomedical applications
 biomaterials, 284
 synthetic materials, 268, 269*t*
- Biomedical devices, sterilization, 52–53
- Biomimetic modifications, reactive coatings, 285–287
- Biomolecules, molecular self-assembly, 318
- Biosensors
 biomaterials, 5–6
 carbon nanotubes (CNTs), 372
 characterization techniques, 377, 379
 deposition of thin alumina films on LaSFN9 substrates for optical waveguide studies, 375
 differential scanning calorimetry (DSC) method, 377, 379
 DSC of poly(γ -benzyl-L-glutamate) (PBLG) powder and polypeptide nanotubes, 383, 385*f*
 etching alumina templates, 377
 experimental, 373–379
 filling pores with polypeptide depending on polymerization time, 380–381
 grafting of PBLG to inner walls of alumina by *N*-carboxylanhydride polymerization, 375–377
 kinetics of 3-aminopropyltriethoxysilane (APTE) adsorption, 387*f*, 388
 liquid-phase silanization with APTE, 375
 materials and templates, 373–374
 nanotubular polypeptides, 373
 optical, of PBLG polypeptide nanotubes, 373
 optical waveguide spectroscopy (OWS), 379
 optical waveguide studies, 383, 385, 388
 release of nanorods from template by etching with HF, 380–381
 scanning electron microscopy (SEM) method, 377
 schematic of initiator deposition and polymerization for polypeptide film formation, 376*f*
 SEM of thin porous alumina film with PBLG molecules, 383, 386*f*
 SEM verifying fabrication of peptide nanotubes, 380
 solution polymerization, 376
 surface-initiated vapor deposition polymerization (SI-VDP), 377, 378*f*
 template-wetting method, 376–377
 template-wetting method for preparing PBLG nanotubes, 381–382
 waveguide mode patterns of thin alumina film before and after functionalization with APTE, 385, 387*f*

- X-ray diffraction (XRD) method, 379
- XRD profiles of PBLG films on alumina surface and inside alumina pores, 382–383, 384*f*
- Biotin, immobilization of azide-functionalized, via microcontact printing, 290*f*
- Bipyridine ligands. *See* Polymeric metal complexes
- Block copolymers, additives and biocompatibility of polymer surfaces, 277–278
- Blood response
 hydrophobic materials, 275–276
 methods for evaluating, of synthetic materials, 270*t*
See also Biocompatibility of polymeric surfaces
- Blood vessel, tissue engineering with polymers, 324–325
- Boronic acid
 hydrogels containing, 337
See also Phospholipid polymers
- Boron neutron capture therapy (BNCT)
 carboranes, 239
 polymeric biomaterials, 3
 tumor treatment, 239
See also Carborane functionalized dendronized polymers
- Bovine serum albumin (BSA)
 characterization and synthesis of BSA-macroinitiator, 85–87
 fluorescent bioconjugates, 85–89
 spectral properties of BSA
 fluorescent bioconjugates, 87, 88*f*, 89
See also Protein-polymer bioconjugates
- Broadband dielectric spectroscopy
 broadening in polymer blends, 166–167
 concentration fluctuation model, 167
 conductivity contribution
 subtracted for fixed temperature, 163*f*
 curve fitting using WinFit program, 161, 164*t*
 data analysis using Havriliak-Negami (HN) and Vogel-Fulcher-Tammann-Hesse (VFTH) equations, 161–164
 dielectric spectra of hydrolyzed polymers, 157–159
 dielectric spectra of undegraded poly(D,L-lactide), 156–157
 distribution of relaxation times for untreated and 95 days degraded samples, 166*f*
 effect of degradation on, spectra, 159–161
 effect of degradation on relaxation times distribution, 165–167
 experimental, 155–156
 HN equation, 161
 hydroxyl-terminated poly(D,L-lactide) preparation, 155–156
 measurement method, 156
 modern, 154
 segmental relaxation, 163–164
 untreated control sample vs. temperature, 162*f*
 VFGH plots for untreated and 95 days degraded samples, 164, 165*f*
- Bipyridine, polyesters macroligands, 98, 99*f*
- ## C
- Calvarial bone. *See* Cranial fixation system
- Cancer treatment
 imaging and delivery of therapeutics, 221
 luciferase activity from tumor bearing mice following two-

- photon irradiation vs. controls, 235, 236*f*
- pre-clinical results on breast-cancer cell line, 235–236
- two photon excited photodynamic agent, 230–231
- See also* Photodynamic therapy (PDT)
- Candida antarctica* lipase. *See* Pegylated polymers
- Carborane functionalized dendronized polymers
- characterization methods, 247
 - degree of functionalization by ^1H NMR, 243–244
 - dendronization of preformed linear, 243–244
 - experimental, 246–248
 - general polymer synthesis using nitroxide-mediated living free radical polymerization (NM-LFRP), 247
 - general procedure for acid-catalyzed deprotection of benzylidene protecting group, 248
 - general procedure for dendronization of pre-formed polymers, 247
 - general procedure for divergent dendron growth using "graft onto" approach, 248
 - general procedure for Pd-catalyzed deprotection of benzylidene protecting group, 247–248
 - ^1H NMR of polymer and dendronized polymers, 244*f*
 - materials, 246
 - molecular weight determination by size exclusion chromatography (SEC), 245, 246*t*
 - optimization of dendronization of preformed carborane containing polymer, 243*t*
 - optimization of polymerization for carborane containing monomer, 241*t*
 - polymerization of macromonomer using NMP, 241
 - synthesis of carborane-containing monomer, 240, 242
- Carboxyhemoglobin (COHb)
- release profiles from biodegradable ionomers, 262, 264*f*, 265*f*
 - UV-vis spectra of cytochrome C and, 266*f*
 - See also* Biodegradable ionomers
- Cartilage
- hydrogel polymers, 274*t*
 - tissue engineering with polymers, 322–324
- Cell count, evaluating cell response to synthetic materials, 270*t*
- Cell density
- number of cells within distance from poly(caprolactone) (PCL)-crystalline feature of area, 307*f*
 - PCL concentration in polyurethanes, 302, 306*f*
- Cell engineering
- hydrogel system "cell-container", 337
 - See also* Phospholipid polymers
- Cell migration on bioactive gradient materials
- assaying cell migration, 137–138, 141
 - cell population migration parameters, 143, 144*f*
 - cell tracks at three fields of view along peptide gradient surface, 138, 140*f*
 - durotaxis, 136
 - haptotaxis, 135–136
 - high-throughput technique with combinatorial sample preparation, 137, 139*f*

- modeling, with persistent random walk models, 141–143
- peptide gradient surfaces, 136–137
- topotaxis, 136
- See also* Tissue engineering
- Cell morphology and migration on rigid surfaces
- competing destabilizing and stabilizing forces, 146, 148
- effects of substrate rigidity, 147*f*
- thermodynamic model examining morphology, 143, 145
- total free energy in cell-substrate systems, 145–146, 148
- See also* Tissue engineering
- Cell motility
- function of material surface design, 130
- See also* Tissue engineering
- Cell sheet, constructing vascular grafts, 324, 326*t*
- Cell-surface interactions
- cell attachment, 128
- cell response to mechanical stimuli, 131, 135
- cell response to peptide gradients, 129–131
- mechanical deformation of cells, 135
- phenomena leading to cell migration, 131, 134*f*
- theoretical descriptions of cell migration, 132*t*, 133*t*
- See also* Tissue engineering
- Cellulose, naturally derived superabsorbent polymer, 28
- Cell viability, poly(*N*-vinylpyrrolidinone) (PNVP) hydrogels, 197, 198*f*
- Central nervous system (CNS), tissue engineering with polymers, 325, 327
- Chemical-physical characterization, tissue engineering, 129*t*
- Chemical vapor deposition (CVD) copolymerization for multifunctional reactivity, 291, 295*f*
- immobilization of saccharides on CVD polymer, 288*f*
- photodefinable reactive polymer, 292*f*
- polymeric surfaces, 5
- polymerization for functionalized poly(*p*-xylylenes), 293*f*, 294*f*
- polymerization of functionalized [2.2]paracyclophanes, 286*f*
- technique for inorganic layers, 285
- See also* Reactive polymer coatings
- Chitosan, tissue engineering scaffolds, 314, 315*t*
- Chitosan water-soluble system
- chitin-chitosan for superabsorbent polymer, 28–29
- Fourier transform infrared (FTIR) spectra of chitosan, chitosan-hydroxybenzotriazole (HOBt), and chitosan-poly(ethylene glycol) (PEG3350), 31, 32*f*
- ¹H NMR spectra of HOBt and mixture with chitosan, 31, 32*f*
- hydrogels, 27–28
- impregnation of hydroxyapatite (HAp), 30–31
- materials and methods, 30–31
- naturally derived superabsorbent polymer, 28
- space filling scaffold for tissue engineering, 33–34
- superabsorbent gel for tissue engineering, 29–30
- swelling ratio of gels with PEG 1450 and PEG 3350, 33, 34*f*
- synthesis of chitosan-PEG superabsorbent gel, 30, 31, 33–34
- synthesis of dicarboxylated poly(ethylene glycol), 30

- thermogravimetric analysis (TGA)
of chitosan-PEG3350 by
soaking cycle, 33–34, 35*f*
- α -Chymotrypsin, biodegradation
profiles of co-poly(ester amides),
20, 21*f*
- "Click"-type cyclization reaction
Huisgen cycloaddition, 40
macrocyclic poly(styrene)
synthesis, 43*f*
See also Cyclic polymers
- Clotting factors, evaluating cell
response to synthetic materials,
270*t*
- Coagulation time, evaluating cell
response to synthetic materials,
270*t*
- Coatings, surface modification by,
271–272
- Coaxial electrospinning, polymer
nanofibers for encapsulation, 317
- Cobalt irradiation, aromatic
poly(anhydride)s, 58, 61
- Coherent anti-Stokes Raman
spectroscopy (CARS), tissue
engineering, 125, 126*f*
- Collagen
cartilage tissue engineering, 322–
324
constructing vascular grafts, 324,
326*t*
scaffolds through electrospinning,
317
skin grafts, 323*t*
tissue engineering for nerves, 327
tissue engineering scaffolds, 313–
314, 315*t*
- Commercial support, tissue
engineering, 120
- Concentration fluctuation model,
polymer blends, 166–167
- Contact angle, biocompatibility and,
surface, 272
- Contact lenses, hydrogel polymers,
274*t*
- Controlled delivery polymer,
Gliadel®, 20
- Controlled drug delivery
hydrogel polymers, 274*t*
See also Drug delivery
- Copolymers
additives and biocompatibility of
polymer surfaces, 277–278
aromatic poly(anhydride)s, 64, 75,
77
biodegradable, 154
unique properties of poly(ethylene
glycol) (PEG), 206
See also Broadband dielectric
spectroscopy; Cranial fixation
system; Pegylated polymers;
Poly(ester amides) (PEAs)
- Cranial fixation system
absorption effects, 355, 358
advantages, 347
advantages in heating plate, 368
analytical testing, 349–350
bioabsorbable rigid devices, 347–
348
biocompatibility in calvarial model,
368–369
biocompatibility studies, 351, 363–
364
blends of poly(D,L-lactide) (D,L-
PLA) and poly(ϵ -caprolactone-
co-*p*-dioxanone) (PCL:PDO),
348–349
burr hole cover plate fixed to
sawbone plate, 361*f*
calvarial bone remodeling, 367
craniofacial procedure use, 369
D,L-PLA/PCL-PDO blends creep
recovery, 355, 356*t*
experimental, 348–354
factors for designing successful,
348
failure modes as plates hydrolyze,
368
finite element analysis, 350, 362–
363

- flexural modulus and yield strength of D,L-PLA/PCL-PDO blends, 355, 357*t*
- growth and expansion for children, 369
- guinea pig sensitization, 352–353
- healing of calvarium, 364, 367
- hydrolysis by-products of series of absorbable medical devices, 358, 359*t*
- in vitro cytotoxicity, 351–352
- in vitro mutagenicity assay, 352
- in vitro push-out test, 350–351
- mechanical function, 355, 358
- palpability, 347
- photomicrographs showing new bone growth, 365*f*, 366*f*
- photomicrographs showing visual cue of D,L-PLA/PCL-PDO blend, 356*f*
- plate and rivet/pin design optimization, 358, 360, 362
- plate composition effects, 354–355, 358
- plate devices and rivet/pin, 359*f*
- preclinical studies, 353–354, 364, 367
- pull-out strengths in sawbone and calvarial bone, 360, 361*t*
- push-out strength of plate and rivet/pin, 362, 363*t*
- rabbit trephine defect model, 353–354, 364, 367
- reheating and deformation for proper curvature, 367–368
- rivet and pin system design, 368
- rivet/pin through plate and predrilled holes, 359*f*
- scanning electron microscopy (SEM) showing PCL-PDO copolymer as domains dispersed in D,L-PLA, 355, 357*f*
- stresses in rivet/pin, 363, 365*f*
- visual cue to surgeon, 355, 356*f*
- Craniosorb™. *See* Cranial fixation system
- Critical surface tension (CST), hydrophobic materials, 275–276
- Crystalline features, poly(ϵ -caprolactone) concentration in polyurethanes, 302, 306*f*
- Cyclic polymers
- application of unimolecular micelles, 41–42
 - behavior of invertible unimolecular micelles in polar and nonpolar solvents, 42*f*
 - challenge of preparing, 37–38
 - challenges of synthetic design, 38
 - "click"-type cyclization reaction, 40
 - cyclic polystyrene (PS) by coupling ends of α -alkynyl- ω -azido poly(styrene), 42–43
 - extending methodology to 4-acetoxystyrene, 47
 - gel permeation chromatography (GPC) of linear PS and unoptimized mixture of cyclic and oligomeric products, 46*f*
 - GPC of linear and cyclic PS, 46*f*
 - ¹H NMR spectra of terminal benzyl bromide and terminal benzyl azide protons, 44*f*
 - ideal systems for preparing functionalized linear precursors, 40
 - infrared (IR) spectra of terminal bromide and terminal azide, 45*f*
 - invertible unimolecular micelles, 41
 - macrocycles by "cyclic" ruthenium ring opening metathesis polymerization (ROMP) catalyst, 38–39
 - macrocyclic PS via atom transfer radical polymerization (ATRP) and "click" coupling, 43*f*

- matrix assisted laser desorption ionization-time of flight mass spectrometry (MALDI-TOF MS), 44, 47*f*
- optimizing cyclization reactions, 43–44
- polymer concentration of linear precursors, 43
- preparing cyclic poly(4-acetoxystyrene) and hydrolysis to cyclic poly(hydroxystyrene), 47, 48*f*
- scheme of coupling of α,ω -heterodifunctional polymers, 38, 39*f*
- slow addition technique via syringe pump, 40–41
- synthesis of cyclic poly(hydroxystyrene), 47–48
- synthesis of unimolecular reverse micelles from linear polymer precursors, 41*f*
- synthetic design, 39–42
- Cylindrical dumbbells
preparation, 67
preparation and properties of aromatic poly(anhydride)s, 58, 59*t*, 60*t*
- Cytochrome C
release profiles from biodegradable ionomers, 262, 264*f*, 265*f*
UV-vis spectra of, and carboxyhemoglobin (COHb), 266*f*
See also Biodegradable ionomers
- Cytotoxicity
cranial plate, 351–352, 363
See also Cranial fixation system
- D**
- Degradation, hydrolytic
effect of degradation time on dielectric relaxation spectra, 159–161
- See also* Broadband dielectric spectroscopy
- Dendritic macromolecules, potential drug carriers, 239–240
- Dendronized polymers
new class of macromolecules, 240
See also Carborane functionalized dendronized polymers
- Deoxyribonucleic acid/ribonucleic acid (DNA/RNA), cationic polymers for gene delivery, 215, 219
- Depolymerization, aromatic poly(anhydride)s, 54
- Design challenges, cyclic polymers, 37–38
- Design principles
definition, 121
information network, 123, 124*f*
iterative optimization approach, 121, 122*f*
tissue engineering, 121, 123
- Dibenzoylmethane, polyesters in polymeric metal complexes, 98, 100
- Dibenzoylmethane ligands. *See* Polymeric metal complexes
- Dielectric spectroscopy
biodegradable ionomers, 256–257, 258*f*
description, 154–155
See also Broadband dielectric spectroscopy
- Drug delivery
controlled-delivery polymer wafer, 20–22
hydrogel polymers, 274*t*
hydrogels of poly(*N*-vinylpyrrolidone) (PNVP), 196–197
metal based drugs, 96
peptide-based nanotubes, 372
polymeric biomaterials, 3
potential for dendritic macromolecules, 239–240

search for new concepts, 205
See also Pegylated polymers;
 Poly(*N*-vinylpyrrolidinone)
 (PNVP)

Drug encapsulation, coaxial
 electrospinning, 317

Drug release
 aromatic poly(anhydride)s, 52
 poly(ester amides) (PEAs), 12

E

Electrospinning

cartilage tissue engineering, 324
 coaxial, 317
 fabricating tissue engineering
 scaffolds, 315–318
 nanofibers, 318
 natural and synthetic polymers,
 317
 schematic, 316*f*
See also Tissue engineering
 scaffolds

Electrospray ionization (ESI)
 technique, 172, 173

See also Mass spectrometry (MS)

Elemental analysis, aromatic
 poly(anhydride)s, 54, 55*t*

Endothelial cell viability, copolymers
 of poly(ester amides), 15, 25

Engineering. *See* Polymers for tissue
 engineering; Tissue engineering

Enzyme catalysis

Candida antarctica lipase B-
 catalyzed polymerization, 210,
 211

first generation pegylated polymers
 by, 207, 208

lipase from *C. antarctica*, 207, 208

potential in synthetic strategy, 205–

206

See also Pegylated polymers

Eosin Y, molecular structure, 226*f*

Etching alumina templates, poly(γ -
 benzyl-L-glutamate) nanotubes,
 377, 380–381

Extracellular matrix (ECM), role in
 integrity of tissues, 314–315

F

Fiber formation

aromatic poly(anhydride)s, 52
 monofilament fiber production by
 aromatic poly(anhydride)s, 57–
 58

Film formation, aromatic
 poly(anhydride)s, 52

Fixation system. *See* Cranial fixation
 system

Fluorescent bioconjugates

bovine serum albumin (BSA), 85–
 89

lysozyme, 89, 91

preparation, 82–84

See also Protein-polymer
 bioconjugates

5-Fluouracil (5-FU)

drug release from hydrogels, 200–
 202

See also Poly(*N*-
 vinylpyrrolidinone) (PNVP)

Food and Drug Administration (FDA),
 tissue engineering industry, 120

Fumaric acid, poly(ester amide)
 copolymers based on, 22, 23

G

Gamma irradiation, aromatic
 poly(anhydride)s, 58, 61

Gel permeation chromatography
 (GPC)

broad poly(methyl methacrylate)
 (PMMA), 184, 185*f*

- comparing methods using, for molar mass determination, 184–185, 189
- coupling off-line to matrix-assisted laser desorption ionization mass spectrometry (MALDI MS), 182–184
- coupling on-line to MALDI MS, 182
- GPC electrospray ionization time-of-flight (GPC–ESI–TOF) mass spectra of OH-terminated poly(dimethylsiloxane) (OH-PDMS), 177–179
- See also* Mass spectrometry (MS)
- Gene delivery
- polymeric systems for, 213, 215
 - See also* Pegylated polymers
- Glass transition temperatures, copolymers of poly(ester amides), 17, 19*f*
- Glycosaminoglycans (GAGs)
- skin grafts, 323*t*
 - tissue engineering for nerves, 327
 - tissue engineering scaffolds, 313–314, 315*t*
- "Grafting from" strategy, synthesizing bioconjugates, 79
- "Grafting to" strategy, synthesizing bioconjugates, 79
- Guinea pig, sensitization with cranial plates, 352–353
- H**
- Haematoporphyrin
- structure, 228*f*
 - tumor photosensitizer, 226–227
- Havriliak Negami (HN) equation
- degradation vs. untreated polymer samples, 164*t*
 - dielectric data analysis, 161
 - distribution of relaxation times, 165–166
- See also* Broadband dielectric spectroscopy
- Health care industry, biomaterials, 1
- Hemocompatibility
- hydrophilic materials, 273–274
 - hydrophobic materials, 276–277
- Heparin coating, surface modification by, 271
- Heterogenic materials, biocompatibility, 277–278
- Huisgen cycloaddition, "click"-type cyclization reaction, 40
- Human body. *See* Biocompatibility of polymeric surfaces
- Hydrogels
- "cell-container" concept, 337, 338*f*
 - fibroblast cell culture, 339, 342–344
 - hydrophilic materials, 273
 - medical applications, 274*t*
 - reversible system, 337, 338*f*
 - superabsorbent polymer (SAP), 28
 - three dimensional network, 27
 - tissue engineering scaffolds, 321
 - See also* Chitosan water-soluble system; Phospholipid polymers; Poly(*N*-vinylpyrrolidinone) (PNVP)
- Hydrolytic degradation. *See* Broadband dielectric spectroscopy
- Hydrophilic materials
- biocompatibility, 272–274
 - hemocompatibility, 273–274
 - medical applications of hydrogels, 274*t*
- Hydrophobic materials, biocompatibility, 274–277
- Hydroxybenzotriazole (HOBt)
- complexation of chitosan with, 29, 31
 - crosslinking of chitosan-HOBt in water, 31, 33
 - ¹H NMR spectra of, and mixture of chitosan and HOBt, 32*f*

- See also* Chitosan water-soluble system
- Hydroxyl-terminated poly(D,L-lactide). *See* Broadband dielectric spectroscopy
- Hydroxystyrene, polymerization for cyclic polymers, 47–48

I

- Immersive visualization, tissue engineering, 125, 127*f*
- Information network, tissue engineering design principle, 123, 124*f*
- Inherent viscosity, aromatic poly(anhydride)s, 55*t*, 56, 62*t*, 76*f*
- Injection-molded devices, medical applications, 269
- International Organization of Standards, tissue engineering industry, 120
- Intractable polymers, analysis challenges, 189–191
- Intramolecular cyclization
coupling α,ω -heterodifunctional polymers, 38, 39*f*
See also Cyclic polymers
- Ionization sources
techniques for large molecules, 171–173
See also Mass spectrometry (MS)
- Ionomers. *See* Biodegradable ionomers
- Iron bipyridine
poly(acrylic acid) metal complexes, 108–109
poly(ethylene glycol), 101–102
See also Polymeric metal complexes
- Iterative optimization, tissue engineering design principle, 121, 122*f*

L

- Laser desorption/ionization (LDI), analysis of intractable polymers, 190
- Lipase, weight loss profiles of copoly(ester amides) films, 17, 20*f*
- Living radical polymerization (LRP) fluorescent bioconjugates, 3, 79
See also Protein-polymer bioconjugates
- Local cell-feature histograms (LCFH), poly(caprolactone)-crystalline domain, 304–305
- Luciferase activity, tumor bearing mice following two-photon irradiation vs. controls, 235, 236*f*
- Lysozyme
fluorescent bioconjugates, 89, 91
spectral properties of BSA fluorescent bioconjugates, 89, 91, 92*f*, 93*f*
synthesis of lysozyme-macroinitiator, 89
See also Protein-polymer bioconjugates

M

- Macroinitiators. *See* Protein-polymer bioconjugates
- Macroscopic polarization, dielectric spectroscopy, 154–155
- Mass resolution, mass analyzers, 173–174
- Mass spectrometry (MS)
analysis of hydroxyl-terminated poly(dimethylsiloxane) (OH-PDMS) using gel permeation chromatography–electrospray ionization MS (GPC–ESI–MS), 177–179
approaches for analysis of intractable polymers, 189–191

- average mass values and properties of methyl-terminated-PDMS, 189*f*
- average molecular mass values and molecular weight distributions (MWD) of OH-PMDS, 188*f*
- characterization of polymeric materials, 171
- comparing methods using GPC for molar mass determination, 184–185, 189
- conventional GPC–ESI–MS, 177, 178*f*
- electrospray ionization (ESI), 172, 173
- formulae for molecular weights (MW) and MW distributions (MWD), 175
- importance of, in polymer analysis, 174–175
- ionization techniques, 171–173
- MALDI (matrix-assisted laser desorption ionization), 172
- MALDI–MS coupling with time-of-flight (TOF), 173–174
- MALDI–MS of GPC fractions from broad poly(methyl methacrylate) (PMMA) sample, 184, 185*f*
- MALDI–TOF–MS analysis of α,ω -bis(4-hydroxybutyl poly(dimethylsiloxane) (HB-PDMS), 175, 176*f*
- MALDI–TOF–MS spectra of GPC fractions collected off-line and for HB-PDMS, 183*f*
- mass analyzers, 173–174
- mass resolution, 173–174
- minimizing mass discrimination effects, 176–177
- off-line GPC–MALDI–MS, 182–184
- OH-PDMS oligomers, 180*f*, 181*f*, 182
- on-line GPC–ESI–MS, 177–182
- on-line GPC–MALDI–MS, 182
- schematic of improved GPC–ESI–MS experimental setup, 178*f*
- silicone extracts legend, 184–185, 187*f*
- solvent-less MALDI–MS for poly(aniline) (PANI), 190, 191*f*
- tandem mass spectrometry (MS/MS), 174
- thermal sample deposition apparatus for off-line coupling of GPC with MALDI–TOF–MS, 184, 186*f*
- Matrix assisted laser desorption ionization (MALDI) technique, 172
- See also* Mass spectrometry (MS)
- Measurable disease, treatment response, 215
- Medical applications
- injection-molded devices, 269
- poly(*N*-vinylpyrrolidinone) (PNVP), 196–197
- See also* Biocompatibility of polymeric surfaces
- Metals
- reactive centers of materials, 96
- See also* Polymeric metal complexes
- 4-Methyl umbelliferone (4-MU)
- drug release from hydrogels, 200–202
- See also* Poly(*N*-vinylpyrrolidinone) (PNVP)
- Micelles
- behavior of invertible unimolecular, in polar and nonpolar solvents, 41–42
- nanomicelles as drug delivery vehicles, 210, 212
- synthesis of unimolecular reverse, from linear polymer precursors, 41*f*
- therapeutic drug delivery, 215, 221

See also Cyclic polymers;
 Pegylated polymers

Micellization process, amphiphilic copolymers, 212–213

Microcontact printing
 immobilization of azide-functionalized biotin, 287, 290*f*
 immobilization of saccharides, 286, 288*f*

Microfluidic devices, surface modification, 287, 291

Microlithography, surface features, 300

Micropatterned polyurethanes
 preparation of combinatorial, 301
See also Poly(ethylene glycol)-poly(caprolactone) (PEG-PCL) polyurethanes

Microsphere sintering, porous 3-D polymer scaffolds, 320–321

Modeling. *See* Tissue engineering

Molar mass determination
 comparing methods using gel permeation chromatography (GPC), 184–185, 189
 formulas, 175
 resolution, 173–174
See also Mass spectrometry (MS)

Molecular dipoles, dielectric spectroscopy, 154–155

Molecular dynamics, broadband dielectric spectroscopy, 154

Molecular mass distribution (MMD), physical property, 171

Molecular motions, entangled polymer chains, 155

Molecular self-assembly
 definition, 318
 tissue engineering scaffolds, 318–319

Molecular weight (MW), average molar mass, 171

N

Nanofibers, electrospinning, 318

Nanotubes. *See* Biosensors

Naproxen
 anti-inflammatory properties of nanospheres, 213, 214*f*
 pegylated amphiphilic polymers carrying, 212–213

National Institute of Standards and Technology (NIST), tissue engineering industry, 120

Natural polymers
 scaffolds through electrospinning, 317
 tissue engineering scaffolds, 312*t*

Nerve, tissue engineering with polymers, 325, 327

Nitroxide mediated polymerization (NMP)
 carborane functionalized polystyrene, 241
See also Carborane functionalized dendronized polymers

O

Optical imaging with collinear optical coherence and confocal fluorescence microscopy (OCM–CFM), tissue engineering, 125, 126*f*

Optical waveguide spectroscopy (OWS). *See* Biosensors

Osteoarthritis, tissue engineering of cartilage, 323

P

[2.2]Paracyclophanes
 chemical vapor deposition (CVD) polymerization of

- functionalized, 286*f*
- fluorescence intensities of amine- and ketone-reactive ligands, 291, 296*f*
- Pediatric patients, resorbable fixation plating systems, 348
- Pegylated polymers
 - anti-inflammatory properties of poly(ethylene glycol) (PEG) nanospheres with aspirin and naproxen, 213, 214*f*
 - cancer treatment, 215, 221
 - Candida antarctica* lipase B-catalyzed polymerization, 210, 211
 - copolymers, 206
 - drug carriers of aspirin and naproxen, 212–213
 - enzymatic catalysis, 205–206
 - first generation, 207, 210, 212–213
 - functionalization with alkyl side chains, 209
 - functionalizing, 206
 - gene delivery, 213, 215
 - lipase from *C. antarctica*, 207, 208
 - nanotechnology platform for in vivo imaging and delivery of multifunctional therapeutics of cancer, 221
 - process of micellization of amphiphilic copolymers, 212
 - schematic of polymer design, 205*f*
 - search for new drug-delivery concepts, 205
 - second generation, 213, 215
 - self-organized nanomicelles, 212*f*
 - synthesis of amphiphilic copolymers in single step, 210, 211
 - synthesis of amphiphilic polymer containing vitamin E, 213, 218
 - synthesis of cationic amphiphilic polymers for gene delivery, 215, 219
 - synthesis of first generation, by enzyme catalysis, 208
 - synthesis of perfluorinated amphiphilic polymers, 220
 - synthesis of vitamin E conjugated copolymer of dimethylisophthalate and PEG600, 213, 216, 217
 - third generation, 215, 221
- Peptides, molecular self-assembly, 318–319
- Peripheral nervous system (PNS), tissue engineering with polymers, 325, 327
- Persistent random walk models, cell migration, 141–143
- Phase separation
 - polyurethanes, 300
 - thermally induced, for porous 3-D polymer scaffolds, 319–320
 - See also* Poly(ethylene glycol)-poly(caprolactone) (PEG-PCL) polyurethanes
- Phospholipid polymers
 - composition dependency of hydrogel formation, 342*t*
 - concept of cell containing using reversible polymer hydrogel system, 338*f*
 - containing p-vinylphenylboronic acid (VPBA), 337
 - covalent crosslinking, 339, 340*f*
 - fibroblast cell culture in hydrogel, 339
 - hydrogel as cell-container, 342–344
 - materials and methods, 337–339
 - 2-methacryloyloxyethyl phosphorylcholine (MPC) polymers with phospholipid in side chain, 337
 - phase contrast microscope images of fibroblast cell in PMBV hydrogel, 344*f*
 - PMBV [poly(MPC-*co-n*-butyl methacrylate-*co*-VPBA)]

- hydrogel before and after shaking, 342*f*
- scanning electron microscopy (SEM) images of PMBV hydrogels, 343*f*
- spontaneous gelation of water-soluble, 337
- structure of PMBV, 340*f*
- synthesis method, 338–339
- synthetic results of PMBV, 341*t*
- water-soluble, with MPC and VPBA units, 339, 342
- Phospholipids, surface modification by, 271
- Photocrosslinking
 - change of Young's modulus after, UPEA, 24*f*
 - unsaturated poly(ester amides) (UPEAs), 22, 23
- Photodynamic therapy (PDT)
 - biomaterials, 3
 - cancer treatment, 226
 - chromophore excited by laser, 229*f*
 - comparing cell killing efficiency in collagen phantoms, 235*f*
 - energy levels for porphyrin photosensitizer and molecular oxygen of PDT treatment, 227, 229*f*
 - first generation of tumor photosensitizers, 226–227
 - haematoporphyrin and derivative (HpD), 226–227, 228*f*
 - improving candidates, 227–228
 - luciferase activity after PDT treatment, 233, 235, 236*f*
 - model structure of two photon excited porphyrin, 231
 - molecular structure of acridine and Eosin Y, 226*f*
 - MPA 79 optimized porphyrin as target photosensitizer, 230–231
 - novel triad RA–301: two photon excited photosensitizer with
 - targeting and imaging agents, 232, 234
 - phenomenon of photodynamic effect, 226
 - porphyrins with enhanced large two-photon absorption, 231–232
 - pre-clinical results on breast-cancer cell line, 235–236
 - reaction conditions for MPA 79 synthesis, 233
 - second generation of PDT photosensitizers, 227
 - synthesis of triad RA–301, 234
 - synthetic approach to MPA 79, 233
 - two photon excited photodynamic therapeutic agent on cancer, 230–231
- Photofrin®
 - structure, 228*f*
 - tumor photosensitizer, 226–227
- Photopatterning
 - photodefinable reactive polymer, 292*f*
 - polyethylene oxides, 287, 291, 292*f*
- Photosensitizers
 - energy levels of porphyrin, and oxygen, 227, 228*f*
 - improving candidates, 227–228
 - two photon excited, with targeting and imaging agents, 232, 234
 - See also* Photodynamic therapy (PDT)
- Plasma polymerization, reactive coatings, 284
- Poly(acrylic acid) (PAA)
 - iron bipyridine in PAA-polyacrylate based complexes, 108–109
 - ruthenium bipyridine initiators, 107
 - See also* Polymeric metal complexes
- Poly(anhydride)s
 - radiation sterilizable aromatic, 3
 - See also* Aromatic poly(anhydride)s

- Poly(aniline) (PANI)**, solventless matrix-assisted laser desorption ionization time-of-flight mass spectrometry, 190, 191*f*
- Poly(caprolactone) (PCL)**
 correlation between crystalline PCL area and cell density, 302, 306*f*
 image analysis for PCL feature size, 302, 306*f*
 scaffolds through electrospinning, 317
 tissue engineering for nerves, 327
See also Poly(ethylene glycol)-poly(caprolactone) (PEG-PCL) polyurethanes
- Poly(ϵ -caprolactone-*co-p*-dioxanone) (PCL:PDO)**. *See* Cranial fixation system
- Poly(dimethylsiloxane) (PDMS)**
 average mass values and properties of methyl-terminated PDMS, 189*t*
 average molecular mass values and molecular weight distributions of OH-terminated PDMS, 188*t*
 GPC electrospray ionization time-of-flight (GPC-ESI-TOF) mass spectra of OH-PDMS, 177–179
 mass spectra of α,ω -bis(4-hydroxybutyl PDMS) (HB-PDMS), 175, 176*f*
 microfluidic systems, 287
 molar mass determination, 184–185, 189
See also Mass spectrometry (MS)
- Poly(ester amides) (PEAs)**
 active polycondensation (APC) method, 12
 amino acid-based bis-nucleophilic monomers, 15–16
 α -amino acid-based PEAs, 11
 biodegradation and drug release, 12
 change of Young's modulus after photocrosslinking of unsaturated PEA (UPEA), 24*f*
 controlled delivery polymer wafer, 20
 co-PEA film degradation weight loss profiles in α -chymotrypsin, 20, 21*f*
 co-PEA synthesis by solution APC, 14
 deprotection of polymeric benzyl esters, 14
 endothelial cell viability, 15, 25
 experimental, 12–15
 functionalizing polymer backbone and end-groups, 11–12
 general structure of bis-electrophilic monomers, 16
 glass transition temperatures of co-PEAs, 17, 19*f*
 in vitro enzyme catalyzed biodegradation, 17, 20
 in vitro enzyme catalyzed biodegradation studies, 15
 lipase-mediated weight loss profiles of co-PEA films, 20*f*
 materials, 12
 mechanical properties of co-PEAs, 17, 19
 monomer synthesis, 15–16
 monomer synthesis procedures, 12–13
 PEA copolymers based on aromatic diacids, 20–22
 PEA copolymers based on fumaric acid, 22, 23
 solution or interfacial polycondensation, 11
 structures of selected PEA copolymer, 18
 synthesis of PEA copolymers, 16–17
 tensile properties of co-PEA, 17, 19*t*

- therapeutic PEAs, 22, 24–25
 UV-crosslinking of UPEA, 22, 23
- Polyester blends. *See* Cranial fixation system
- Polyesters
- biodegradable, 154
 - dibenzoylmethane for,
 - macroligands and polymeric metal complexes, 98, 100
 - hydroxyl functionalized bipyridines as initiators, 98, 99*f*
 - poly(ϵ -caprolactone) (PCL), 312, 313*t*
 - poly(glycolic acid), 312, 313*t*
 - poly(lactic acid) (PLA), 312, 313*t*
 - thermal and mechanical properties, 314*t*
 - tissue engineering for nerves, 327
 - tissue engineering scaffolds, 312–313
- See also* Broadband dielectric spectroscopy; Polymeric metal complexes
- Poly(ethylene) (PE)
- analysis challenge, 189
 - hemocompatibility, 276
- Poly(ethylene glycol) (PEG)
- attenuated total reflectance Fourier transform infrared (ATR–FTIR), 190
 - iron bipyridine centered PEG ligands, 101–102
 - model systems, 104*f*
 - potential as tissue engineering scaffold, 321
 - ruthenium bipyridine for PEG systems, 102–103
- See also* Chitosan water-soluble system; Pegylated polymers; Polymeric metal complexes
- Poly(ethylene glycol)-poly(caprolactone) PEG-PCL polyurethanes
- atomic force microscopy (AFM)
 - scanning of ribbon pattern, 302, 303*f*
 - cell culture and assays, 301
 - cells preferably adhering to
 - combinations of distance and PCL size, 304–305, 307*f*
 - combinatorial library with Pluracol (chain extender) composition and annealing temperature gradient, 303*f*
 - combinatorial micropatterned polyurethanes preparation, 301
 - crystalline PCL area coverage
 - correlation with cell density, 302, 306*f*
 - experimental, 301–302
 - future directions, 305
 - image acquisition, 301–302
 - local cell-feature histograms (LCFH), 304–305
 - optimal composition, 302, 304*f*
 - optimization of trifunctional crosslinker, 302, 303*f*
 - structure-function relationships, 302, 304
- Poly(ethylene oxides) (PEOs), photopatterning, 287, 291, 292*f*
- Poly(ethylenimine) (PEI)
- ruthenium tris(bipyridine) PEI complexes, 105, 106*f*
 - system for gene delivery, 103, 105
- See also* Polymeric metal complexes
- Poly(γ -benzyl-L-glutamate) (PBLG)
- grafting to inner walls of alumina, 375–377
 - monomer synthesis, 373–374
 - polypeptide nanotubes, 373
 - scanning electron microscopy (SEM) verifying polypeptide nanotubes, 380

- solution polymerization, 376
 surface-initiated vapor deposition
 polymerization (SI-VDP), 377,
 378*f*
 template-wetting method, 376–377
See also Biosensors
- Poly(glycolic acid) (PGA), scaffolds
 through electrospinning, 317
- Poly(lactic acid) (PLA)
 scaffolds through electrospinning,
 317
 tissue engineering for nerves, 327
- Poly(lactic-co-glycolic acid) (PLGA)
 cartilage tissue engineering, 324
 scaffolds through electrospinning,
 317
 skin grafts, 323*t*
 tissue engineering for nerves,
 327
- Poly(D,L-lactide) (D,L-PLA). *See*
 Broadband dielectric spectroscopy;
 Cranial fixation system
- Polymer blends, concentration
 fluctuation model, 166–167
- Polymer chemistry tools. *See* Mass
 spectrometry (MS)
- Polymeric metal complexes
 biocompatible and biodegradable
 polymers modifying ligands and
 metal complexes, 97
 biomaterial poly(ethylene glycol)
 (PEG), 100–103
 biomaterials based on poly(acrylic
 acid) (PAA), 107–109
 biomedical applications, 96
 design criteria and strategies, 96–
 97
 dibenzoylmethane for polyester
 macroligands, 98, 100
 hydroxyl functionalized bipyridine
 as initiators for polyesters, 99,
 99*f*
 iron bipyridine for PAA, 108–109
 iron bipyridine for PEG
 macroligands, 101–102
 macroligand chelation and
 metalloinitiation approaches to,
 with bipyridine polyester
 macroligands, 99*f*
 materials based on
 poly(ethyleneimine) (PEI), 103,
 105, 106*f*
 polyesters, 97–100
 routes to poly(lactic acid) (PLA)
 macroligands and polymeric Fe
 complexes based on
 dibenzoylmethane, 99*f*
 ruthenium bipyridine for PAA-
 based materials, 107
 ruthenium bipyridine for PEG
 macroligands, 102–103, 104*f*
 schematic, 96*f*
 synthesis of iron tris(bipyridine)
 centered PEG stars, 101*f*
 two stage degradation mechanism,
 96*f*
- Polymeric surfaces
 chemical vapor deposition (CVD)
 polymerization, 5
 modification by coating, 271–272
 protein adhesion, 270
See also Biocompatibility of
 polymeric surfaces
- Polymers. *See* Biomaterials
- Polymers for tissue engineering
 applications, 321–327
 blood vessel, 324–325
 cartilage, 322–324
 chitosan, 313–314, 315*t*
 collagen, 314, 315*t*
 common, scaffolds, 312–314
 commonly used biodegradable
 synthetic polymers, 313*t*
 comparison between synthetic and
 natural polymers, 312*t*
 electrospinning, 315–318
 fabrication methods of 3-D porous
 composite scaffold, 319–321
 glycosaminoglycans (GAGs), 313–
 314

- hydrogels, 321
 methods for constructing tissue engineered vascular grafts, 324, 326*t*
 molecular self-assembly, 318–319
 natural polymers, 315*t*
 nerve, 325, 327
 poly(ϵ -caprolactone) (PCL), 313*t*
 poly(glycolic acid) (PGA), 313*t*
 poly(lactic acid) (PLA), 313*t*
 polysaccharides, 313–314
 requirements for tissue engineered vascular grafts, 325*t*
 skin, 321–322
 skin grafts, 323*t*
 thermal and mechanical properties of polyesters, 314*t*
See also Tissue engineering scaffolds
- Poly(methyl methacrylate) (PMMA)
 biocompatibility, 275, 276
 matrix assisted laser desorption ionization mass spectra of gel permeation chromatography of broad, 184, 185*f*
- Poly(*N*-vinylpyrrolidinone) (PNVP)
 biocompatibility, 197–199
 cell viability, 197, 198*f*
 copolymerizing derivatives of drugs with NVP, 200–202
 drug release from hydrogels, 200–202
 drugs 5-fluoracil (5-FU) and 4-methyl umbelliferone (4-MU), 200
 fractional release of 4-MU from hydrogel, 203*f*
 hydrogel networks, 197, 198
 increase in swelling ratio over time due to degradation of carbonate crosslinking groups, 201*f*
 medical applications, 196–197
 plot of fractional release against time, 202*f*
 typical ^1H NMR spectra of crosslinked network, 199*f*
- Polypeptides, potential of polymeric nanotubes, 372
- Poly(*p*-xylylene)
 chemical vapor deposition (CVD) polymerization of functionalized [2.2]paracyclophane, 286*f*
 CVD polymerization for functionalized, 293*f*, 294*f*
 multi-potent reactive coatings, 291, 295*f*
- Poly(pyrrole) (PPy), analysis challenge, 189
- Polysaccharides
 tissue engineering for nerves, 327
 tissue engineering scaffolds, 313–314
- Poly(styrene) (PS)
 biocompatibility, 275
 nitroxide mediated polymerization of carborane functionalized, 241, 247
See also Cyclic polymers
- Poly(tetrafluoroethylene) (PTFE), analysis challenge, 189
- Poly(urethanes)
 hemocompatibility of low density, 276
 hydrophilic, and medical applications, 273
 phase-separated patterns, 300
 skin grafts, 323*t*
See also Poly(ethylene glycol)-poly(caprolactone) (PEG-PCL) polyurethanes
- Poly(vinyl alcohol) (PVA). *See* Phospholipid polymers
- Poly(vinylchloride) (PVC), hemocompatibility, 276
- Poly(vinylpyrrolidone) (PVP)
 attenuated total reflectance Fourier transform infrared (ATR–FTIR), 190

- See also* Poly(*N*-vinylpyrrolidinone) (PNVP)
- Porous composite scaffold, fabrication of three-dimensional, 319–321
- Porphyrins, enhanced large two-photon absorption, 231–232
- Protein. *See* Biodegradable ionomers
- Protein adhesion, polymer surfaces, 270
- Protein-polymer bioconjugates
absorption and emission spectra of rhodamine B methacrylate monomer, 85*f*
analytical techniques, 80–81
bioconjugate synthesis monitoring by sodium dodecyl sulfate polyacrylamide gel electrophoresis (SDS–PAGE), 86, 87*f*
bioconjugation, 79
bovine serum albumin (BSA) fluorescent bioconjugates, 85–89
BSA-macroinitiator preparation, 81–82
emerging research area, 79
experimental, 80–84
"grafting to" and "grafting from" routes, 79
living radical polymerization (LRP), 79, 91
lysozyme fluorescent bioconjugates, 89, 91
lysozyme-macroinitiator, 82
materials, 80
preparation of fluorescent bioconjugates, 82–84
preparation of protein-macroinitiators, 81–82
reverse phase-high performance liquid chromatography (RP–HPLC) of BSA, control, and BSA-macroinitiator, 88*f*
SDS–PAGE of native lysozyme and lysozyme-macroinitiator, 89, 92*f*
SEC (size exclusion chromatography)–HPLC with fluorescence detection for fluorescent monomer, 89, 90*f*
SEC–HPLC with fluorescence detection of lysozyme bioconjugate and rhodamine B methacrylate monomer, 89, 91, 93*f*
spectral properties of BSA fluorescent bioconjugates, 87, 88*f*, 89
synthesis and characterization of BSA-macroinitiator, 85–87
synthesis and characterization of lysozyme fluorescent bioconjugate, 89, 91, 92*f*
synthesis of lysozyme fluorescent bioconjugates by LRP, 91
synthesis of rhodamine B methacrylate monomer, 81, 84–85
- Proteins
molecular self-assembly, 318–319
See also Biodegradable ionomers
- R**
- Rabbit trephine defect model
cranial fixation plate, 364, 367
preclinical studies, 353–354
See also Cranial fixation system
- Random walk models, cell migration, 141–143
- Rapid prototyping, porous 3-D polymer scaffolds, 320
- Reactive polymer coatings
biomimetic modifications of, 285–287
chemical vapor deposition (CVD) polymerization for

- functionalized poly(p-xylylenes), 293*f*, 294*f*
- CVD polymerization of functionalized [2.2]paracyclophanes, 286*f*
- fluorescence intensities of amine- and ketone-reactive ligands, 296*f*
- immobilization of azide-functionalized biotin via microcontact printing, 290*f*
- immobilization of saccharides, 288*f*, 289*f*
- modulating interactions between biological environment and surfaces, 284
- multi-potènt, 291, 295*f*
- photopatterning process using photodefinable, 292*f*
- plasma polymerization, 284
- schematic producing multifunctional surface with parallel reactivity, 295*f*
- surface functionalization, 284
- surface modification of microfluidic devices, 287, 291
- vapor-based polymer coatings, 284–285
- Recrystallization, synthesis of aromatic poly(anhydride)s, 54, 56, 69, 71, 73
- Regeneration, tissue engineering of cartilage, 323–324
- Regulatory acceptance, tissue engineering industry, 120
- Resorbable fixation plating systems pediatric patients, 348
See also Cranial fixation system
- Reverse micelles. *See* Cyclic polymers
- Reversible hydrogels, concept of cell-container, 337, 338*f*
- Rhodamine B methacrylate monomer synthesis, 81
- synthesis as fluorescent probe, 84–85
- See also* Protein-polymer bioconjugates
- Ring opening metathesis polymerization (ROMP), ruthenium catalyst for cyclic polymers, 38–39
- Rubbery gel, aromatic poly(anhydride)s, 54
- Ruthenium bipyridine poly(acrylic acid) (PAA) metal complexes, 107
- poly(ethylene glycol), 102–103, 104*f*
- poly(ethylenimine) (PEI), 103, 105, 106*f*
- See also* Polymeric metal complexes
- S**
- Scaffolds. *See* Tissue engineering scaffolds
- Self-assembled monolayers, reactive surfaces, 284
- Sessile drop method, contact angle measurement, 272
- Skeletal surgery. *See* Cranial fixation system
- Skin polymers as skin grafts, 323*t*
- tissue engineering with polymers, 321–322
- Solution polymerization, grafting poly(γ -benzyl-L-glutamate) (PBLG) to alumina, 376
- Solvent casting, porous 3-D polymer scaffolds, 320
- Spectrometry. *See* Mass spectrometry (MS)
- Spectroscopic imaging with broadband coherent anti-Stokes Raman spectroscopy (CARS), tissue engineering, 125, 126*f*

- Sterilization, biomedical devices, 52–53
- Structural characterization, tissue engineering, 129*t*
- Styrenic polymers. *See* Cyclic polymers
- Superabsorbent polymer
chitin-chitosan for, 26–29
naturally derived, 28
See also Chitosan water-soluble system
- Surface features
biomaterial design, 300
See also Poly(ethylene glycol)-poly(caprolactone) (PEG-PCL) polyurethanes
- Surface-initiated vapor deposition polymerization (SI-VDP), grafting poly(γ -benzyl-L-glutamate) to alumina, 377, 378*f*
- Surface modifications, microfluidic devices, 287, 291
- Surface modifying additives, biocompatibility of polymer surfaces, 277–278
- Swelling, formation and mechanism for water, of biodegradable ionomers, 257, 259
- Synthetic polymers
scaffolds through electrospinning, 317
tissue engineering scaffolds, 312*t*
- T**
- Template-wetting method
grafting poly(γ -benzyl-L-glutamate) (PBLG) to alumina, 376–377
PBLG nanotube preparation, 381–382
- Tensile properties, copolymers of poly(ester amides) (co-PEAs), 17, 19*f*
- Testing protocol, lacking for biocompatibility, 269–270
- Thermally induced phase separation, porous 3-D polymer scaffolds, 319–320
- Tissue engineering
assaying cell migration, 137–138, 141
biological characterization properties, 129*t*
biologically active peptides on surfaces, 129–130
biomaterials, 5
cell migration model study on bioactive gradient materials, 135–143
cell motility as function of surface design and properties, 130
cell population migration parameters, 143, 144*f*
cell response to mechanical stimuli, 131, 135
cell response to peptide gradients, 129–131
cell tracks for three fields of view, 138, 140*f*
chemical-physical characterization properties, 129*t*
commercial support in United States, 120
competing destabilizing and stabilizing forces, 146, 148
contributions from cell-surface interactions, 128–135
definition, 119*n*, 311
design of bioactive materials for, 128
design principles, 121, 123
drotaxis, 136
effects of substrate rigidity on cell morphology and migration, 147*f*
global assessment, 119
global regulatory issues, 120
haptotaxis, 135–136

- high-throughput technique with combinatorial sample preparation, 137, 139*f*
- immersive visualization using Rave Engine, 125, 127*f*
- important properties in characterizing, materials, 129*t*
- information network, 123, 124*f*
- interdisciplinary approach, 125, 128
- iterative optimization approach, 121, 122*f*
- mechanical deformation of cells, 135
- modeling cell migration with persistent random walk models, 141–143
- model study of cell morphology and migration on rigid surfaces, 143, 145–148
- multivariate analysis of peptide gradient libraries, 138, 141
- National Institute of Standards and Technology (NIST), 120
- optical imaging with collinear optical coherence and confocal fluorescence microscopy (OCM–CFM), 125, 126*f*
- peptide gradient surfaces, 136–137
- phenomena leading to cell migration, 131, 134*f*
- requirements of, scaffolds, 311*t*
- role of extracellular matrix (ECM), 314–315
- spectroscopic imaging with broadband coherent anti-Stokes Raman spectroscopy (CARS), 125, 126*f*
- strategic approaches to design principles, 121, 123
- structural characterization properties, 129*t*
- superabsorbent gel for, 29–30
- theoretical descriptions of cell migration, 132*t*, 133*t*
- therapeutic and diagnostic applications, 125, 128
- thermodynamic model examining cell morphology, 143, 145
- tools and methodologies to model bioactive materials, 123, 125, 128
- topotaxis, 136
- total free energy in cell-substrate systems, 145–146, 148
- "try it and see" approach, 130–131
- See also* Phospholipid polymers; Polymers for tissue engineering
- Tissue engineering scaffolds
- 3-D porous composite scaffold, 319–321
- amphiphilic molecules, 319
- chitosan, 314, 315*t*
- collagen, 314, 315*t*
- common polymers as, 312–314
- comparing synthetic and natural polymers, 312*t*
- electrospinning, 315–318
- electrospun nanofibers, 318
- fabrication strategies, 314–321
- glycosaminoglycans (GAGs), 313–314, 315*t*
- hydrogels, 321
- microsphere sintering, 320–321
- molecular self-assembly, 318–319
- natural polymers, 313–314
- peptide and protein self-assembly, 318–319
- poly(ϵ -caprolactone) (PCL), 312, 313*t*
- poly(glycolic acid) (PGA), 312, 313*t*
- poly(lactic acid) (PLA), 312, 313*t*
- polyester types, 312, 313*t*
- polysaccharides, 313–314
- rapid prototyping, 320
- requirements, 311*t*
- role of extracellular matrix (ECM) in integrity of tissues, 314–315
- solvent casting, 320

- thermal and mechanical properties of polyesters, 314*t*
See also Polymers for tissue engineering
- Tumors. *See* Photodynamic therapy (PDT)
- Two-photon absorption
 chromophore excited by laser, 229*f*
 porphyrins with enhanced large, 231–232
See also Photodynamic therapy (PDT)
- U**
- Unimolecular reverse micelles
 behavior of invertible, in polar and nonpolar solvents, 41–42
 synthesis from linear polymer precursors, 41
See also Cyclic polymers
- United States, commercial support for tissue engineering, 120
- V**
- Vascular grafts
 methods for constructing, 324, 326*t*
 requirements for tissue engineered, 325*t*
- Versailles Advanced Materials and Standards (VAMAS), tissue engineering industry, 120
- Virtual reality environment, tissue engineering, 125, 127*f*
- Visual cue, cranial fixation plate, 354–355, 356*f*
- Vitamin E
 nano-carriers for, 213
 synthesis of, conjugated copolymer, 216, 217
 synthesis of amphiphilic polymer containing, 218
- Vogel–Fulcher–Tammann–Hesse (VFTH) equation
 parameters for degraded vs. untreated polymer samples, 164*t*
 plot for untreated and degraded polymer samples, 164, 165*f*
 segmental relaxation, 163–164
See also Broadband dielectric spectroscopy
- W**
- Water swelling, formation and mechanism for, in biodegradable ionomers, 257, 259
- X**
- X-ray diffraction. *See* Biosensors
- Z**
- Zisman's critical surface tension (CST), hydrophobic materials, 275–276